Advanced Structured Materials

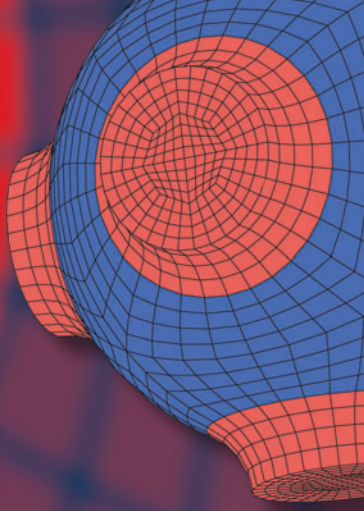

Zishan Husain Khan *Editor*

Recent Trends in Nanomaterials

Synthesis and Properties

Springer

Advanced Structured Materials

Volume 83

More information about this series at http://www.springer.com/series/8611

Zishan Husain Khan
Editor

Recent Trends in Nanomaterials

Synthesis and Properties

Springer

Editor
Zishan Husain Khan
Department of Applied Sciences
and Humanities
Jamia Millia Islamia
New Delhi, Delhi
India

ISSN 1869-8433 ISSN 1869-8441 (electronic)
Advanced Structured Materials
ISBN 978-981-10-3841-9 ISBN 978-981-10-3842-6 (eBook)
DOI 10.1007/978-981-10-3842-6

Library of Congress Control Number: 2017935822

Printed on acid-free paper

This Springer imprint is published by Springer Nature
The registered company is Springer Nature Singapore Pte Ltd.
The registered company address is: 152 Beach Road, #21-01/04 Gateway East, Singapore 189721, Singapore

Foreword

Since the announcement of the establishment of the US National Nanotechnology Initiative (NNI) in the year 2000 by President William Jefferson Clinton, NNI-supported research and development is producing many scientific and technological innovations. The initiative has spawned many countries around the world to invest in their own nanotechnology initiatives that have led to the invention and commercialization of products that are used every day in consumer products that will make our lives more productive and sustainable. Nanotechnology is pervasive in many different areas such as energy, health, materials, electronic devices, advanced manufacturing, computing, and related technologies. Nanotechnology-based electronics are making devices smaller and faster and are developing alternative fuel sources that will eventually replace the use of fossil fuels. Nanoscale understanding provides researchers the unique ability to diagnose diseases and to target bespoke treatments, thereby increasing the chances of a longer life. Manufacturing issues such as scalability, reliability, and cost are critical for nanotechnology products to live up to our expectations. Nanotechnology research has also led to the development of materials that are lighter, stronger, and more resistant to damage when compared to traditional materials. These achievements have been driven by scientific curiosity, demand, and financial support by Government agencies and multinational corporations.

The future holds great promise for new and disruptive innovations that are not possible without the properties that exist at the nanoscale. The ability to control and manipulate information, multifunctional and self-healing structures, energy-scavenging technologies, personalized medicine, and many other inventions have yet to be discovered. This book is intended to inform the reader of the current state of the art in nanomaterials and their applications. I salute Prof. Zishan Husain Khan for compiling such a collection of very well-written and informed chapters associated with current thinking and understanding of using and developing nanomaterials. Chapter 1 presents a review of the research work reported on the synthesis and characterization of graphene oxide and the challenges still facing scientists in perfecting this material. Chapter 2 focuses on the wear of nanocomposites, its mechanisms, types, and analysis of wear debris. Wear behavior of metals, ceramics,

and polymers is also described along with a special focus on iron-alumina metal matrix nanocomposites and a mechanism to reduce the overall wear rate in any system. Chapter 3 is mainly focused on the targeted drug delivery using nanoparticles. The mechanism of action of targeted delivery is discussed in detail with the applications of different types of nanoparticles in targeted delivery. This chapter also explains the synthetic procedures of producing nanoparticles for use in targeted drug delivery. Chapter 4 describes the application of graphene quantum dots used in the fields of biomedicine, biosensing, optoelectronics, and energy conversion and storage. Chapter 5 presents an overview of progress made in the fabrication of hybrid nanostructured transparent conductive film (TCF) based on the assembly of one-dimensional metal nanowires and two-dimensional graphene films. The concept of nanostructured hybrid films is expected to open up possibilities for developing next-generation TCF with multiple functionalities. Chapter 6 illustrates the antibacterial properties of nanoscale materials and describes the effect of pure and doped ZnO nanoparticles on the antibacterial activity against two Gram-negative *Escherichia coli* and *Pseudomonas aeroginosa* and two Gram-positive *Bacillus subtilis* and *Staphylococcus aureus* bacteria. Chapter 7 focuses on the synthesis of large area graphene in an affordable, non-toxic way. This chapter describes microwave-assisted synthesis of graphene and electrochemical exfoliation methods with applications in the fields of electro-magnetic shielding and field-effect transistors. Chapter 8 is aimed at understanding the recent progress in the development and characterization of a new group of nanomaterials, in freestanding forms, such as fiber/yarns, paper/sheet, and bulk forms of supply, which were derived from graphene nanosheets using various fabrication technologies. Chapter 9 illustrates how laser-assisted molecular beam epitaxy growth affects the properties of GaN nanowall networks for the improvement of products and devices. Chapter 10 provides a lucid description of the density functional theory of two- and three-dimensional networks, while the final chapter of the book provides an understanding of how nanostructured zirconium oxides (ZrO_2) have emerged as versatile and promising materials in the biomedical field due to their biocompatibility and excellent physicochemical properties. Readers of this volume are encouraged to throughly read and understand these informative chapters in the hope of stimulating further research in the exciting field of nanotechnology.

I wish to thank all the contributing authors of this volume who have provided a wide scope of knowledge in the area of nanomaterials. I also wish to thank and acknowledge the efforts of Prof. Zishan Husain Khan for his knowledge and ability to compile such a first-class book on the advanced in nanomaterials, and hope that experienced researchers and graduate students alike will use the book as a source of reference on nanomaterials in the years to come.

Prof. Mark J. Jackson, Ph.D., D.Sc.
McCune and Middlekauff Endowed Professor and Academic Program Leader
College of Technology and Aviation Kansas State University
Salina, KS, USA

Acknowledgements

First and foremost, I am thankful to God. In the process of putting this book together, I realized how true this gift of writing is for me. You have given me the power to believe in my passion and pursue my dreams. I could never have done this without the faith I have in you, the Almighty.

I would like to express my gratitude to all the authors for their significant contributions to this book. It would not have been possible to undertake this challenging work and enabling me to accomplish it without your support and timely response. All the authors have justified their contribution in this book by presenting the work on latest areas of nanomaterials and their applications. I owe them a lot.

I would like to thank Prof. Talat Ahmad, Vice-Chancellor, Jamia Millia Islamia, New Delhi (India), for his ongoing support and encouragement for creating an academic environment in the pursuit of higher education. His pearls of wisdom coupled with motivation have contributed largely to the completion of this book.

I would like to express my gratitude to Prof. Mushahid Husain, Vice-Chancellor, MJP Rohilkhand University, Bareilly (Uttar Pradesh), India, and Prof. Haroon Sajjad, Department of Geography, Jamia Millia Islamia, New Delhi (India), for their valuable suggestions and motivation during the compilation of this book. I admire their distinguished helping nature.

I am grateful to all who saw me through this book and to all those who provided support, talked things over, read, wrote, offered comments, and assisted in the editing, proofreading, and design. My thanks are due to all of Ph.D. students especially Mohd. Bilal Khan, Mohd. Parvaz, and Sutan Ahmad, who helped me a lot in completing this work.

I would also like to acknowledge the support and guidance provided by the editorial team of Springer without whom this endeavor would not have been a reality.

Last but not least, my deepest gratitude goes to my family for their unflagging love and support throughout the process of compilation of this book. They have been a constant source of inspiration and I dedicate this book to them. I am also indebted to my mother for her encouragement and allowing me to follow my

ambitions throughout my childhood. I am grateful to my wife Rubina Mirza for her constant support and for standing beside me throughout my career. She has been my inspiration and motivation for continuing to improve my knowledge and move my career forward. I also thank my wonderful children Ayanab, Alina, and Ali for always making me smile and for understanding on those weekend mornings when I was working on this book instead of playing games with them. I hope that one day they can read this book and understand why I spent so much time in front of my computer.

As an editor, I would love to receive suggestions and feedback for the book at zishan_hk@yahoo.co.in.

Contents

About the Editor

Dr. Zishan Husain Khan Professor at Department of Applied Sciences & Humanities, Faculty of Engineering & Technology, is working in the field of nanotechnology since December 2001. He has almost 20 years of research experience in semiconductor physics and nanotechnology. He has published more than 102 research papers in various international reputed journals and guided a number of Ph.D. students. He has presented many research papers in various national and international conferences. He has completed several research projects on various topics in nanotechnology. He has worked at several positions in the universities abroad.

In 2001, Dr. Khan was selected for pursuing postdoctoral research in nanotechnology at the Center of Nanoscience and Nanotechnology, National Tsing Hua University, Taiwan. He joined this research program in December 2001 and completed it in February 2005. During the postdoctoral fellowship, he worked on different aspects of nanomaterials with special emphasis on carbon nanotubes. His work on I-V characteristics on individual carbon nanotubes (CNTs) for CNT-based FET (field-effect transistor) was highly appreciated by the scientific community. To carry out this research work, he employed the technique of photolithography to design a mask and subsequently used e-beam lithography to connect an individual carbon nanotube (CNT) to fabricate a nanodevice.

With this significant experience in nanotechnology, he was selected to establish Center of Nanotechnology

at King Abdul Aziz University, Jeddah, Saudi Arabia, in 2007. Dr. Khan worked as an associate professor at this center until July 2012. During his stay there, he established the world-class facilities in nanotechnology with clean room of level 100. He also was actively involved in designing various courses in nanotechnology. He also acted as a reviewer for many international journals of high repute. In addition, he has edited several special issues for reputed international journals. Dr. Khan has edited two books entitled "*Recent Trends in Nanotechnology & Renewable Energy*" published by Bharti Publications, Delhi (India), and "*Advances in Nanomaterials*" published by **Springer**.

Chapter 1
Graphene Oxide: Synthesis and Characterization

Mohd. Bilal Khan, Mohd. Parvaz and Zishan Husain Khan

1.1 Introduction

Carbon is one of the most vital elements found on earth. The word carbon is taken from the Latin word carbo, which means charcoal. Carbon is capable of forming many allotropes due to its valency. Well-known crystalline forms of carbon are diamond and graphite. On the other hand, amorphous forms of carbon include coal, soot and carbide-derived carbons. However, these materials are not amorphous in true crystallographic sense; rather, they are polycrystalline, consisting of combination of graphitic and diamond crystals. With the development of science and technology at small scale, known as nanotechnology, many more allotropes and forms of carbon have been discovered, which includes buckminsterfullerene, carbon nanotubes and graphene (Fig. 1.1).

Buckminsterfullerenes are cage-shaped molecules of carbon with molecular formula C_{60}, which were discovered in 1985 by a group of scientists from Rice University and University of Sussex, and three of them got 1985 Chemistry Nobel Prize. Its shape resembles a football made up of 20 hexagons and 12 pentagons with a carbon atom at each vertex of each polygon and a bond along each polygon edge [1]. The name of buckminsterfullerene is in reference to Buckminster Fuller, a US architect, because the structure of C-60 resembled the geodesic dome invented by him. Buckminsterfullerene can withstand very high amounts of heat and pressure. After that, fullerenes having higher number of atoms, open-cage fullerenes, quasifullerenes were prepared, isolated and investigated [2]. Buckminsterfullerene, higher-order fullerenes and other derivatives of fullerene family found their applications in the field of medical and biological sciences [3] and photovoltaics [4] etc.

Mohd.B. Khan · Mohd. Parvaz · Z.H. Khan (✉)
Department of Applied Sciences and Humanities, Jamia Millia Islamia,
New Delhi 110025, India
e-mail: zishanhk@jmi.ac.in

Z.H. Khan (ed.), *Recent Trends in Nanomaterials*,
Advanced Structured Materials 83, DOI 10.1007/978-981-10-3842-6_1

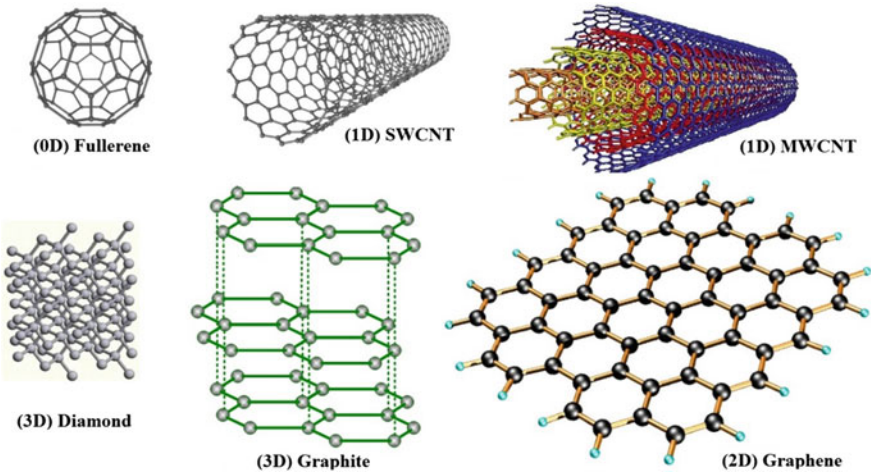

Fig. 1.1 Allotropes of carbon

The discovery of fullerenes triggered the scientists towards the preparation and isolation of other allotropes of carbon.

In 1991, a Japanese electron microscopist, Sumio Iijima, discovered a new form of carbon resembling a tube, called carbon nanotube. These are long hollow structures with their walls made up of single atomic layer of sp^2-hybridized carbon [5]. According to the number of rolled atomic layers of carbon, carbon nanotubes can be categorized into multiwalled and single-walled carbon nanotubes. Single-walled carbon nanotube has only one rolled atomic layer of carbon, while multiwalled carbon nanotubes have two or more atomic layers of carbon rolled along single axis forming the concentric cylinders. According to the manner in which the carbon atomic layer/layers is/are rolled, carbon nanotubes can be categorized into armchair, zigzag and chiral. Normally, armchair nanotubes are metallic, while chiral and zigzag nanotubes are semiconducting in nature. Carbon nanotubes possess extraordinary physical properties [6, 7]. These are the stiffest and strongest material, very good conductor of heat and electricity with various other interesting properties. Since their discovery, carbon nanotubes have been employed into various applications such as electronic, optoelectronic, mechanical and medical applications due to their extraordinary properties [8].

Graphene is a single atomic layer of carbon which exists in the form of Van der walls stacked sheets in graphite [9] and in the rolled form in carbon nanotubes [10]. Theoretically, it was predicted long back that the stacked atomic layers of graphite can be isolated. It has likely been unknowingly produced in small quantities for centuries, through the use of pencils and other similar applications of graphite. It was actually observed in electron microscopes in 1962, but only studied while supported on metal surfaces [11]. The material was later rediscovered, isolated and characterized in 2004 by Andre Geim and Konstantin Novoselov at the University of Manchester [12, 13]. Since its discovery, graphene has proved to be one of the

most promising materials due to its extraordinary properties. It is finest, strongest and stiffest material as well as a wonderful conductor of electricity and heat. With these excellent properties, graphene is being used as the building block for different applications in electronics and material science [13–16], electrochemistry [17], sensor technology [18, 19], biological engineering [20, 21], filtration [21, 22] and energy storage [23–25], etc.

Although graphene has a lot of interesting properties and applications, there are some drawbacks associated with it. The physical methods to synthesize graphene are so complex that its mass scale production is very difficult. On the other hand, graphene is a semimetal and is not suitable for semiconducting applications. Due to these limitations, researchers shifted their attention towards graphene oxide, which is an oxygenated derivative of graphene. These oxygenated graphene sheets have the same structure as graphene except oxygen-containing functional groups on their basal planes and edges (Fig. 1.2). Graphene oxide (GO) can be easily dispersed in water and is easy to process. It can be produced in large quantities easily. Most interestingly, it can be reduced (partly) to form reduced graphene oxide (rGO). The properties and behaviour of reduced graphene oxide depend on the oxygen content in it. The increasing degree of reduction decreases the oxygen content, which induces the properties and behaviour of rGO to shift towards graphene.

As-prepared and reduced graphene oxide can be extensively used in a variety of applications, especially for the mass scale production of graphene. Graphene oxide (GO) films can be deposited on any substrate and can be converted into a conductor (via reduction). This makes it suitable for the use in the production of transparent conductive films, flexible electronics, solar cells and chemical sensors [26–29]. Graphene oxide has a high surface area and can be suitable for the use as electrode material for batteries and capacitors [29–31]. GO can easily be mixed with different polymers and other materials to enhance their properties like tensile strength, elasticity and conductivity of composite materials [32]. In solid form, graphene oxide flakes are attached to one another to form thin and stable flat structures that can be folded, wrinkled and stretched. Such graphene oxide structures can be used for applications in hydrogen storage, ion conductors and nanofiltration membranes [14, 33]. Graphene oxide is a fluorescent material, which makes it appropriate for

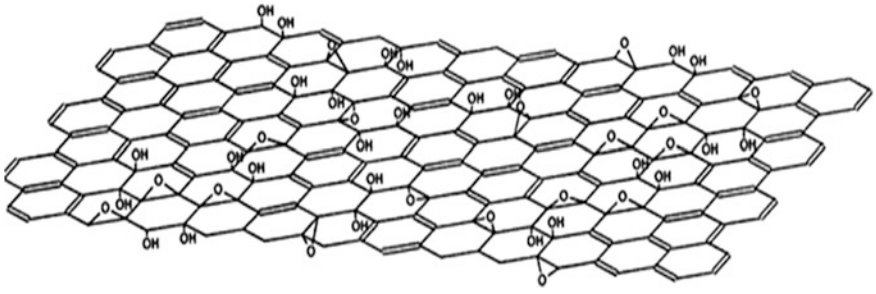

Fig. 1.2 Structure of graphene oxide (Lerf-Klinowski model) (reprinted with permission from [11])

various medical applications. Biosensing and disease detection, drug carriers and antibacterial materials are just some of the possibilities GO holds for the biomedical applications [34, 35].

1.2 Synthesis of Graphene Oxide/Reduced Graphene Oxide

As mentioned earlier, graphite consists of several graphene layers stacked by weak van der Waals forces. Graphite oxide has more or less same structure of graphite with a little difference. Graphite can be oxidized using strong oxidizing agents to change hybridization of carbon atoms and attach oxygen. This transition not only increases the interlayer spacing of graphite, but it also enhances the hydrophilic nature of the system. Due to this property, GO can be dispersed more easily in aqueous or other polar solvents to get isolated graphene oxide layers. Various reduction strategies can be used to get reduced graphene oxide (rGO) sheets having oxygen content specifically required for desired applications (Fig. 1.3).

1.2.1 Oxidation of Graphite

Oxidation of graphite to get graphite oxide is the first step towards the synthesis of graphene oxide. The oxidation methods utilize strong oxidation agents such as potassium chloride and potassium permanganate in the strong acidic medium. The main methods for the synthesis of graphite oxide include Broodie's method, Hummer's method and Tour's method. Among these three methods, Hummer's method is the most popular one, which is being widely used by the researchers worldwide with or without modifications.

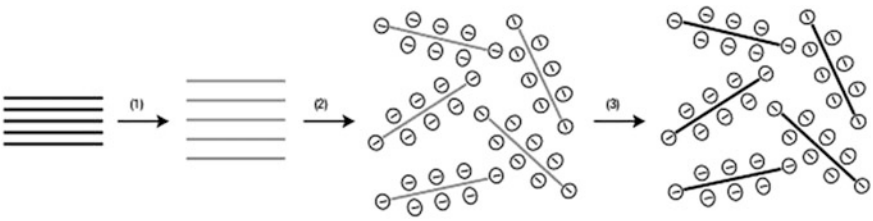

Fig. 1.3 Schematic showing the chemical route for the synthesis of aqueous graphene dispersions. *1* Oxidation of graphite (*black blocks*) to graphite oxide (*lighter coloured blocks*) with greater interlayer distance. *2* Exfoliation of graphite oxide. *3* Reduction of graphene oxide [16]

1.2.1.1 Broodie's Method

The very first report on the ability of graphite to get oxidized using oxidizing agents and strong acids was published by a British chemist B.C. Brodie in 1859 [36]. In this report, a mixture of $KClO_3$ as the oxidizing agent in the presence of fuming nitric acid was used to prepare graphene oxide (GO). The investigation of chemical composition of resulting product suggested the presence of carbon, oxygen and hydrogen. The resulting product was washed to make it salt-free and dried at 100 °C. Further, the oxidized batch was kept in oxidizing environment using three sequential steps to obtain a blackish yellow material which did not change with additional oxidation. After elemental analysis, the chemical composition of the resulting material came out to be $C_{11}H_4O_5$. Although an effort was made to analyse the chemical composition, structural properties and thermal decomposition process of oxidized graphite, these analyses were limited by the available characterization techniques at that time, leaving room for further improvement in the process. In 1898, Staudenmaier [37, 38] proposed an improvement over the method introduced by Broodie's et al. [36] by adding H_2SO_4 to increase the acidic nature of the reaction medium. He further added multiple aliquots of potassium chlorate solution into the mixture several times during the reaction. These improvements enhanced the oxidation process of graphite in the single step and ruled out the need for repeated oxidation steps. In 1937, Hofmann et al. [39] reported further improvement in the process by using non-fuming nitric acid. This method provided an enhancement in the oxidation process of graphene oxide. However, these methods have several shortcomings such as the danger of explosion due to the evolution to chlorine dioxide [40].

1.2.1.2 Hummer's Method

The method proposed by Hummer et al. [41] has been popularly used by the researchers worldwide with and without modifications. In their report, they used a mixture of sulphuric acid (H_2SO_4), sodium nitrate ($NaNO_3$) and potassium permanganate ($KMnO_4$) to oxidize graphite at a temperature of 20 °C [41]. KMO_4 is a commonly used strong oxidizing agent. In Hummer's method, dimanganese heptoxide (Mn_2O_7), formed by the reaction of $KMnO_4$ with H_2SO_4, acts as the active species [42]. It is more reactive than KMO_4 and acts as a strong oxidizing agent [43, 44]. The original Hummer's process lasted for 2 h, and the resulting graphite oxide had a higher degree of oxidation than that of Staudenmaier's method [45]. It was found that the Hummer's method provided oxidation of the outer shell of graphite, leaving the graphite core unoxidized. Hummer's method can be improved by the pre-treatment of graphite with a mixture of H_2SO_4, P_2O_8 and $K_2S_2O_8$ [46] prior to the employment of Hummer's method or by taking small-sized graphite flakes. Other commonly used modified Hummer's methods include the use of increased amount of $KMnO_4$ [46]. Hummer's methods involve several purification and filtration steps, which make them quite lengthy and complicated. Despite this fact, the

Hummer's method and its modified forms remain to be the most popular method used for the oxidation of graphite.

1.2.1.3 Tour's Method

The development of carbon nanotechnology inspired the researchers to discover new and improved methods to synthesize new carbon nanomaterials. Several methods for the synthesis of graphite oxide have also been proposed. Graphene oxide is considered as an intermediate material formed during the facile synthesis of graphene. Most of these methods may be regarded as the modified forms of Hummer's methods. Some modifications in Broodie's and Staudenmaier's methods also came into the light. Among different methods reported in the first decade of twenty-first century, the method proposed by Tour et al. [47] made several modification and improvements over the earlier methods and it was established as the new method. In their method reported in 2010, Tour et al. [47] avoided the use of $NaNO_3$ and introduced H_3PO_4 in the method originally proposed by Hummer's et al. Their method provided graphite oxide having an improved degree of oxidation. Other features of their protocol are the absence of toxic gases such as NO_2 and N_2O_4, more intact sp^2 hybridized graphitic plane [47] and improved yield.

1.2.2 Exfoliation of Graphene Oxide

1.2.2.1 Chemical Exfoliation of Graphene Oxide

The oxidation of graphite increases the interlayer spacing between the atomic layers. The increase in the interplanner spacing decreases the degree of staking between the oxidized graphene sheets. Graphene oxide dispersions can be achieved by dissolving graphite oxide in aqueous and organic solvents using simple sonication [48–52]. Due to the hydrophilic nature of graphene oxide, stable dispersions with concentration up to 3 mg/ml can be achieved. The colour of these dispersions has been reported between yellowish brown to dark brown. Modification of graphene oxide sheets with organic molecules is also reported to be helpful to achieve stable graphene oxide suspension in polar and non-polar organic solvents [50]. In the repost published by Stankovich et al. [50], a dispersion of 1 mg/ml was achieved by treating GO with isocyanate followed by dissolution in organic aprotic solvent. The treatment of GO with organic isocyanates can lead to the derivatization of both the edge carboxyl and surface hydroxyl functional groups via formation of amides or carbamate esters, respectively (Fig. 1.4). These amide and carbamate functionalities can be used for covalent linking of variety of materials with GO [50]. Different dispersing agents used for preparing stable graphene oxide dispersions are presented in Table 1.1.

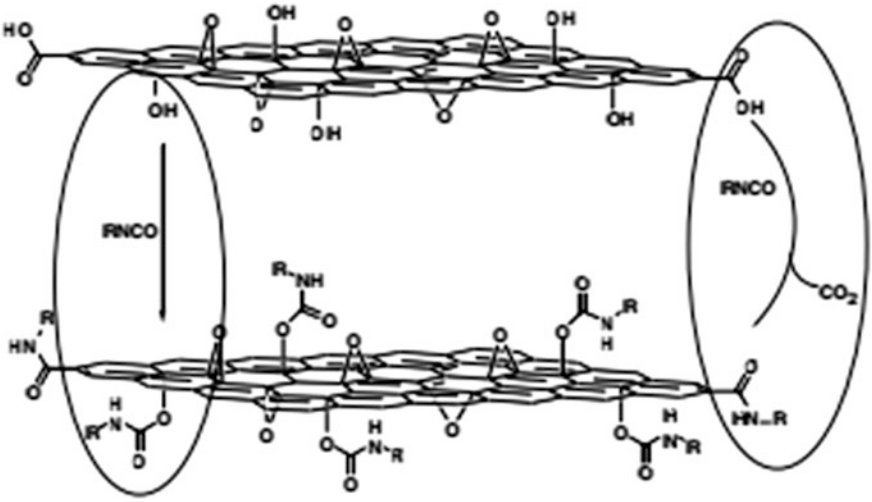

Fig. 1.4 Formation of amide and carbamate functionalities on treating graphite oxide with isocyanates (reprinted with the permission from [50])

Although, ultrasonication in organic polar or aqueous medium has been proven to be the faster and more efficient way to exfoliate graphite oxide to graphene oxide sheets, it is also reported that ultrasonic method also induces structural damages and breaks the graphene oxide sheets [48]. As an alternative approach, graphite oxide can be exfoliated thermally via rapid heating of the graphite oxide powder.

1.2.2.2 Thermal Exfoliation of Graphene Oxide

When graphite oxide is put at high temperature, its exfoliation occurred due to the generation of high pressure between the layers of graphite oxide. This high pressure is the consequence of the conversion of carboxylic and other oxygen-containing groups into CO_2 and CO [66, 67]. Akhawan et al. [67] put the alumina boat filled with graphite oxide in the pre-heated tube furnace at 1050 °C. They kept the boat till 30 s and then rapidly moved the boat out of the furnace to get graphene oxide sheets.

1.2.3 Reduction of Graphene Oxide

The most attractive property of graphene oxide is its partial reduction, which can convert it into reduced graphene oxide (rGO), having properties similar to that of pristine graphene. The shift in the properties of reduced graphene oxide towards

Table 1.1 Different starting materials, methods for preparation and dispersing solvents used by different groups

S. No.	Starting materials	Dispersible solvents	Concentration (mg ml^{-1})	Lateral size	Thickness (nm)	Ref.
1	GO/MH	Water	1	–	–	[44]
2	GO/MH	Water	0.5	Several hundred nm	~1	[53]
3	GO/MH	Water	0.1	–	~1.7	[54]
4	GO/MH	Water	7	Several hundred nm	~1	[55]
5	GO/H	Water/methanol, acetone, acetonitrile mixed solvents	3–4	Several hundred nm	~1.2	[56]
6	GO/MH	DMF, NMP, DMSO, HMPA	1	~560 nm	~1	[50]
7	GO/H	Water, acetone, ethanol, 1-propanol, ethylene glycol, DMSO, DMF, NMP, pyridine, THF	0.5	100–1000 nm	1.0–1.4	[51]
8	GO/O	DMF, THF, CCl_4, DCE	0.5	–	0.5–2.5	[57]
9	GO/S	DMF, DMAc, NMP	1	Several hundred nm	1.8–2.2	[58]
10	GO/MH	Hydrazine	1.5	Up to 20 μm × 40 μm	~0.6	[59]
11	GO/S	THF	<0.48	–	1–2	[60]
12	GO/S	NMP, DMF, DCB, THF, nitromethane	0.1	100–2500 nm	1.1–3.5 (ave.1.75)	[61, 62]
13	GO/H	Ethanol	1	Several hundred nm	~2	[63]
14	GO/H	Ethanol	3.33	–	–	[64]
15	GO/MO	Water	–	–	–	[65]

GO Graphene oxide, *H* Hummers method, *S* Staudenmaier, *MH* modified Hummer's method, *O* own method, *DMF* dimethylformamide; *DMAc N,N′*-dimethylformamide; *DMSO* dimethylsulphoxide; *NMP N*-methyl pyrrolidone; *THF* tetrahydrofuran; *MC* dichloromethane; *DCE* 1,2-dichloroethane; *DCB* 1,2 dichlorobenzene; *HMPA* hexamethylphosphoramide; *GBL* γ-butyrolactone; *DMEU* 1,3 dimethyl-2-imidazolidinone

Reproduced in modified form with permission from [48]

graphene depends upon the degree of reduction. The reduction of graphene oxide is achieved by the removal of oxygen-containing groups. Various efforts have been made to reduce graphene oxide completely into graphene, but this ultimate goal is still a dream.

1.2.3.1 Thermal Annealing

Graphene oxide can be reduced by annealing at the temperatures greater than 1200 °C. In fact, thermal annealing was initially used to exfoliate graphite oxide [66, 67]. The exfoliation of graphene oxide occurs due to the generation of CO and CO_2 by the thermal decomposition of oxygen-containing groups. In this way, thermal annealing not only exfoliates the graphite oxide into graphene oxide, but also removes the oxygen-containing groups from the graphite oxide and reduces it into reduced graphene oxide [66–68]. However, thermal annealing procedure creates lattice defects and breakage in the graphene sheets. This is due to the fact that the decomposition of carboxylic groups in the reduction process utilizes the carbon atoms of the graphene lattice. These lattice defects and breakages badly affect the conductivity of the resulting reduced graphene oxide sheets. The reported conductivity of the resulting reduced graphene oxide (rGO) is 10–23 S/cm, which is several orders lower than the pristine graphene [68, 69] (Fig. 1.5).

The most popular way to exfoliate graphite oxide into graphene oxide is sonication in variety of aqueous or organic solvents. In this way, large-area graphene oxide sheets can be deposited and subsequently reduced using thermal heating [70]. The reduction of pre-exfoliated graphene oxide depends upon the annealing temperature and the annealing atmosphere. At high temperatures, the degree of reduction increases, but increased chances of reaction of oxygen present in the atmosphere compensate the loss of oxygen achieved via thermal annealing. Therefore, vacuum or inert atmosphere is required for high degree of reduction. Sometimes a reducing gas such as hydrogen or ammonia is used to create reducing atmosphere to enhance the reducibility [68]. Youn et al. analysed the effect of hydrazine vapours to create the reducing atmosphere for efficient thermal reduction of graphene oxide [71].

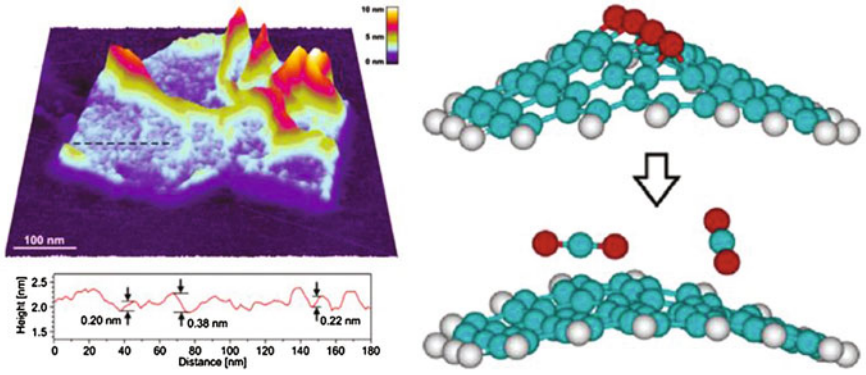

Fig. 1.5 Pseudo-3D representation of a 600 nm × 600 nm AFM scan of an individual graphene sheet showing the wrinkled and rough structure of the surface, and an atomistic model of the graphite oxide to graphene transition (reprinted with permission from [68])

1.2.3.2 Reduction Using High-Energy Radiations

High-energy radiations such as microwave [72, 73], gamma radiation [74], camera flash radiation [75, 76] and UV radiation [77, 78] may be used to reduce graphene oxide. Microwave radiation heats GO more rapidly than conventional heating. The time taken for the reduction of GO under microwave radiation is reported to be less than 1 min [72] (Fig. 1.6).

Cote et al. [75] reduced graphene oxide using camera flash. Camera flash induces rapid heating which reduces graphene oxide instantaneously. Matsumoto et al. [77] reported the reduction of graphene oxide using UV radiation in the mild atmosphere of H_2 and N_2. The UV radiation destroys the epoxy groups attached to the basic graphene lattice to convert graphene oxide into reduced graphene oxide. Laser radiation also reduces graphene oxide very efficiently. While the photo- and UV radiations need prolonged interaction with graphene oxide to convert it into

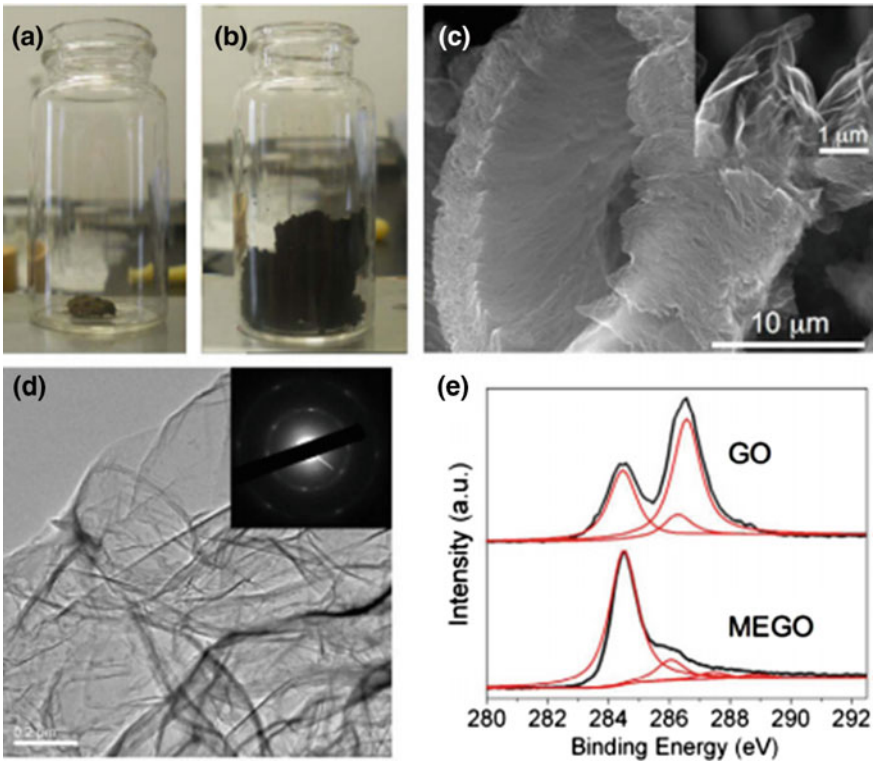

Fig. 1.6 Optical photographs of GO before (**a**) and after (**b**) treatment in a microwave oven for 1 min. **c** Typical SEM image of as-prepared rGO by microwave irradiation with a high-magnification SEM image in the inset showing the crumpled rGO sheets. **d** Typical TEM image of the rGO and the corresponding electron diffraction pattern. **e** XPS C 1s spectra of GO and rGO (reprinted with permission from [72])

reduced graphene oxide, laser radiation reduces graphene oxide ultimately fast [78]. Gamma radiation may also be used to reduce graphene oxide in alcohol/water [79]. Gamma radiation converts water or alcohol molecules into the highly reactive reductive species, which deoxidize the graphene oxide and convert it into reduced graphene oxide [79].

1.2.3.3 Chemical Reduction of Graphene Oxide

Chemical reduction is the most popular and one of the earliest reported methods to reduce graphene oxide. Hydrazine is one of the very first chemical reagents to be used to reduce graphene oxide in aqueous solution. Unlike other common strong reducing agents, hydrazine does not react with water; this property makes it most popular reducing agents for graphene oxide dispersed in aqueous solution [80]. Although the reaction mechanism of reduction of graphene oxide via hydrazine is not well supported, the proposed mechanism is presented in Scheme 1.1 [80].

rGO obtained after reduction is often aggregated due to increased hydrophobicity as a result of oxygen-containing groups [81]. Tung et al. [59] used pure hydrazine to reduce graphene oxide to get highly dispersed monolayers of graphene oxide.

Other nitrogen-containing compounds such as hydroxylamine [82], pyrrole [83], benzylamine [84], 5 *p*-phenylenediamine [85], ethylenediamine [86], urea [87], dimethyl ketoxime [88], hexamethylenetetramine [89], polyelectrolyte [90] and poly(amidoamine) [91] were used as the reducing agent to reduce graphene oxide.

Hydrohalic acids such as HI, HBr and HCl are used in electrophilic addition and nucleophilic substitution in synthetic chemistry. In addition to this, their capability of opening epoxides makes them good candidates for the reduction of graphene oxide [81]. Moon et al. [92] used the mixture of hydroiodic acid and acetic acid for the liquid-phase as well as solid-phase reduction of graphene oxide. They further tested the mixture of hydroiodic acid and trifluoroacetic acid and found that the latter reduces the graphene oxide more effectively due to strong acidic nature of trifluoroacetic acid. The more interesting point with the latter mixture is that it can reduce GO at sub-zero temperature [92, 93]. Pure hydroiodic acid [94] and hydrobromic [95] acid were also used to reduce graphene oxide. The conductivity of reduced graphene oxide obtained by the use of hydrobromic acid was low, which was attributed to the presence of residual bromides [95].

Metal hydrides such as sodium hydride, sodium borohydride and lithium aluminium hydride are considered as the strong reducing agents. Sodium borohydride ($NaBH_4$) was used, which was proved as better reducing agent than hydrazine [96]. $NaBH_4$ effectively reduces C=O species, but it shows less reducibility for epoxy and alcoholic groups [97]. An additional treatment with sulphuric acid, after the $NaBH_4$ treatment, improves the reduction of graphene oxide [98].

Oxygen-containing compounds, such as common alcohols, L-ascorbic acid and hydroquinone, have also been used to reduce graphene oxide [96]. Su et al. demonstrated that the graphene oxide reduced by high-temperature alcohol vapours

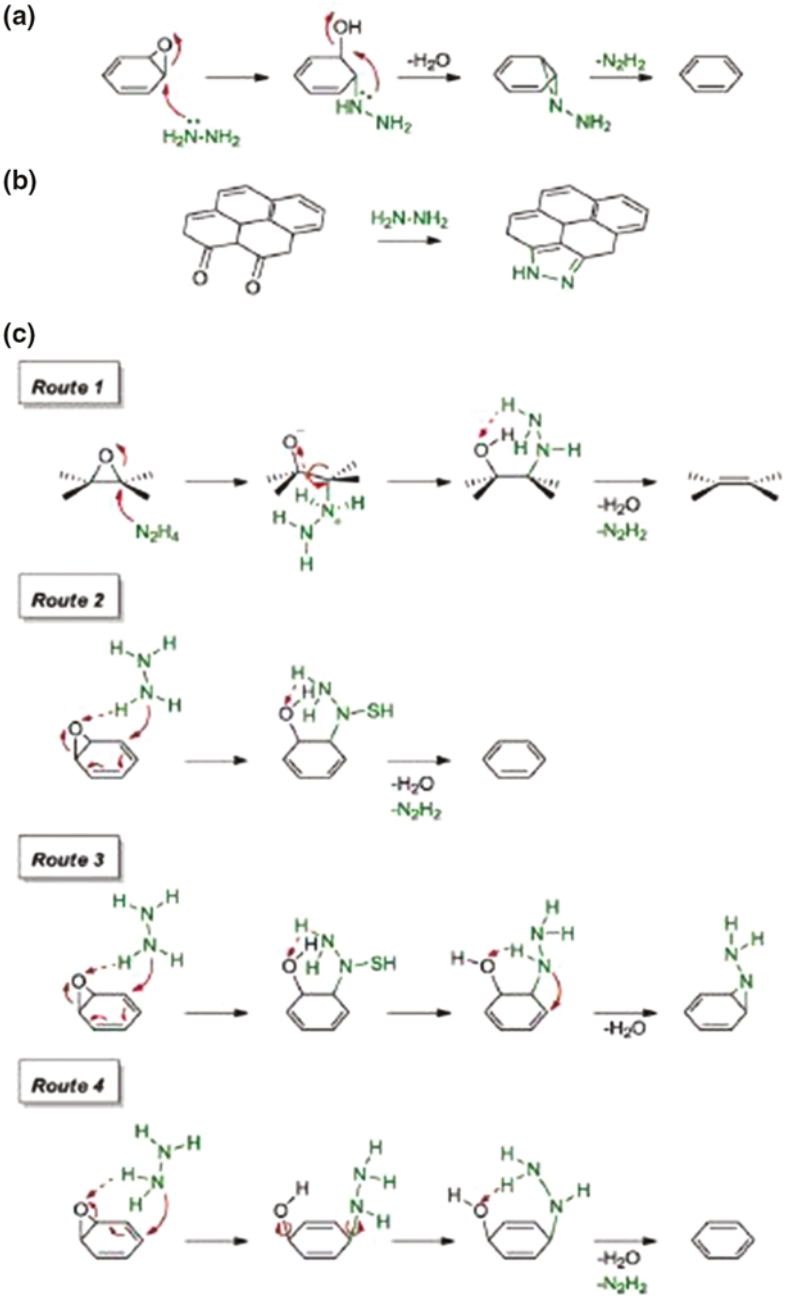

Scheme 1.1 **a** Proposed mechanism for the reduction of the epoxide group with hydrazine. **b** Formation of the pyrazole ring upon usage of hydrazine as a reducing agent. **c** Proposed mechanisms for the reduction of epoxide groups with hydrazine via four different routes [80] (reprinted with permission from [81])

has excellent graphitic structure [99]. Keeping in view of good antioxidant property of L-ascorbic acid, commonly known as vitamin C, some groups used L-ascorbic acid as the reducing agent for graphene oxide and produced good quality rGO [100, 101].

Sulphur-containing compounds such as thiourea dioxide, ethanethiol–aluminium chloride, Lawessons's reagent and thiourea [81] have also been used to reduce graphene oxide. Thiourea dioxide is a common reducing agent used in the paper and textile industry. It is used to reduce ketones, aromatic nitro-azo, azoxy and organosulphur compounds. It was used with NaOH [102] and with NH_3 [103] by different groups for the reduction of GO.

Different metals in acid as well as alkaline environment have the potential to be used for the reduction of graphene oxide. Aluminium [104, 105], iron [106], zinc [107], tin [108] and magnesium [109] metals were used in HCl medium, while zinc was used with H_2SO_4 [110] to reduce graphene oxide. Some alkaline metal combinations such as Zn + NH_3 [111], Zn + NaOH [105, 112], Al + NaOH [105] and Na + NH_3 [113] were tried and successfully proven to act as the reducing agents for graphene oxide.

Most of the chemical reagents discussed so far for the reduction of GO are harmful and toxic in nature. Keeping in view of this, some researchers used natural and biocompatible materials for the reduction of GO. The use of these materials not only avoids the use of harmful and toxic materials at the processing stage, but also opens a way to the production of biocompatible rGO, which is free from metal and other toxic residuals. Amino acids are biologically important organic compounds. They contain amine and carboxyl functional groups along with a side chain. Chen et al. [114] used L-cysteine for the reduction of graphene oxide. rGO obtained in their study showed less conductivity. Further, they used glycin, L-lysine and L-glutathione to reduce graphene oxide [115–117]. The ongoing search of environment-friendly and green chemical reagents showed a new way to the researchers to utilize plant extract as the reducing agents. Suresh et al. used clove extract for the reduction of GO at 100 °C for 30 min [118]. Hatamie et al. [119] used curcumin extract to reduce chemically exfoliated graphene oxide sheets. Other plant extracts such as grape extract [120] and pomegranate juice were also used as the reducing agents for graphene oxide. Some micro-organisms, proteins and hormones have also been employed as the reducing agents for GO. Shewanella, a group of heterotrophic and facultative anaerobes, usually found in the environment, have the ability to utilize inorganic or organic compounds in their respiratory pathway as terminal electron acceptors. These organisms are also able to utilize solids as terminal electron acceptors. Salas et al. [121] highlighted the usage of Shewanella in a strictly anaerobic environment towards the reduction of graphene oxide. In other works, *E. coli* [122] and baker's yeast [123] were also used to reduce graphene oxide. Bacteriorhodopsin is a protein, which captures the light energy and utilizes it for the movement of protons across the membrane. Akhawan [124] used this property and utilized it as the reducing agent for graphene oxide. Melatonin (*N*-acetyl-5-methoxytryptamine) is a hormone found in animals and other living organisms. It has an electron-donating property, which makes it an excellent

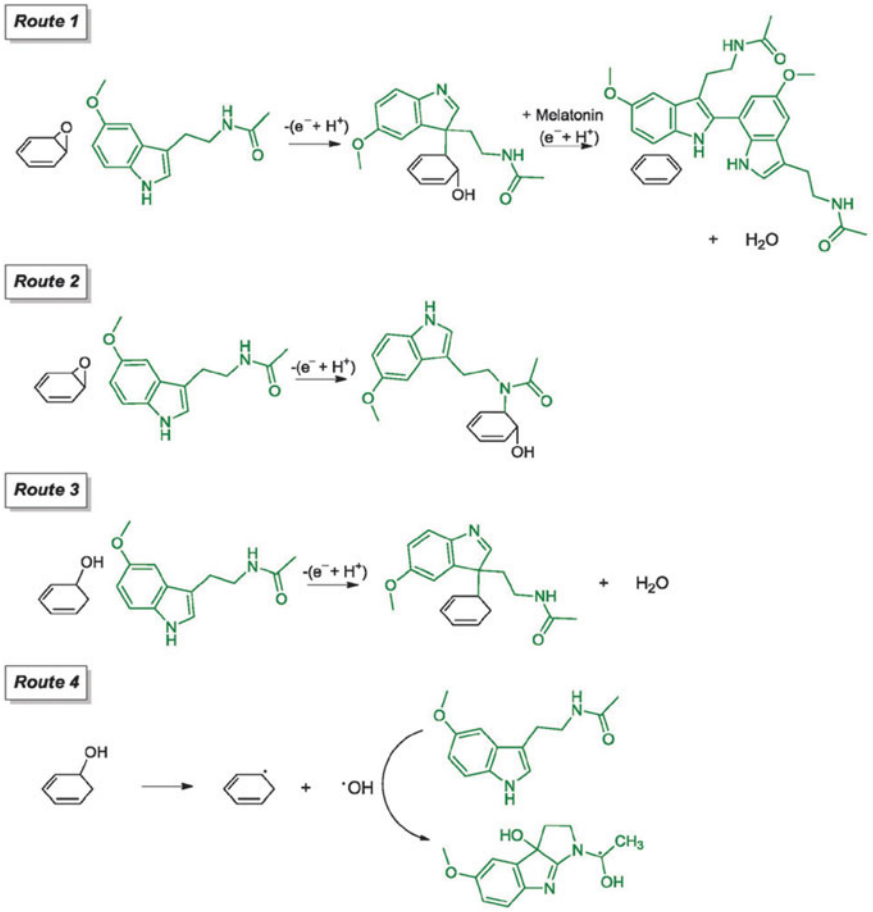

Scheme 1.2 Proposed mechanisms for the reduction of epoxide and hydroxyl by melatonin (reproduced with permission from [81])

antioxidant. Akhawan et al. [125] employed melatonin to reduce GO in the presence of NH_3. They proposed a series of reaction mechanisms to understand the reduction to epoxide and hydroxyl present in GO by melatonin, as given in Scheme 1.2.

1.3 Characterizations of Graphene Oxide

Graphene oxide is single or few atomic thick layers of carbon atoms attached to different groups such as epoxy, hydroxyl, carbonyl and carboxyl. The exact structure of graphene oxide is still a matter of debate. The nature, quantity and distribution of different groups present in graphene oxide depend upon the method

Table 1.2 Different peaks observed in ^{13}C NMR spectra of GO and their respective assignments

S. No.	Peak position [ppm]	Assignments
1	57.6 [126]	Epoxide [126]
2	60 [127–130]	Hydroxyl [128], Epoxide [127–130]
3	61 [131]	Epoxide [131]
4	69.2 [126]	Hydroxyl [126]
5	70 [128–131, 145]	Epoxide [128], Hydroxyl [128, 129–131]
6	101 [52, 126, 127, 131]	Lactol [52, 126, 127], O–C–O [131]
7	130 [127–131]	sp^2 carbon [127–131]
8	167 [52, 126, 127]	Ester carbonyl [52, 126, 127]
9	169 [131]	O=C–O [131]
10	193 [131]	C=O [131]

of synthesis, whereas the reduction depends on the method and the nature of reducing agent.

Solid-state nuclear magnetic resonance (NMR) is a good technique to analyse the structure of materials. ^{13}C and ^{1}H NMR spectra of graphene oxide exhibit three major peaks at 60, 70 and 130 pm [126]. In some studies, four peaks were found at 57.6, 69.2, 92.9 and 166.3 ppm [126]. In high resolution, ^{13}C NMR spectra of graphene oxide also feature three minor peaks at 101, 167 and 191 ppm [52, 127]. Different peaks observed in ^{13}C NMR spectra of graphene oxide and their respective assignments are summarized in Table 1.2. Figure 1.7 presents the typical ^{13}C NMR spectra for GO.

X-ray photoelectron spectroscopy (XPS) reveals the information regarding the chemical environment of carbon atoms. Therefore, it is a good technique to investigate the structure of GO and understand the degree of oxidation and reduction of graphene oxide. These features can be investigated by comparing the XPS signals of pristine graphite and graphene oxide at different oxidation and reduction stages [132]. For fully oxidized graphene oxide, five different components are observed in C 1s spectra and their respective origins are given in Table 1.3.

Some groups reported only four chemically shifted peaks in the XPS spectrum of graphene oxide. They did not find the shifted peak at 287.5 eV, which is assigned to carbonyl group [133]. As the complementary to C 1s spectra, O 1s spectra gives the additional information of groups present in the graphene oxide. In O 1s spectra, three chemically shifted peaks are observed at 531.08, 532.03 and 533.42 eV and these peaks can be assigned to C=O [133, 138], C–O and phenolic groups [61, 139]. A typical XPS spectrum is provided in Fig. 1.8.

X-ray photoelectron spectroscopy can be effectively used to determine the degree of reduction of graphene oxide. This can be done by analysing the fraction of carbon sp^2-bonded carbon atoms. The fraction of sp^2 carbon is evaluated by dividing the area under sp^2 carbon peak by the area under entire C 1s spectrum graphene oxide. The increase in this fraction depicts the increased degree of reduction [61, 133].

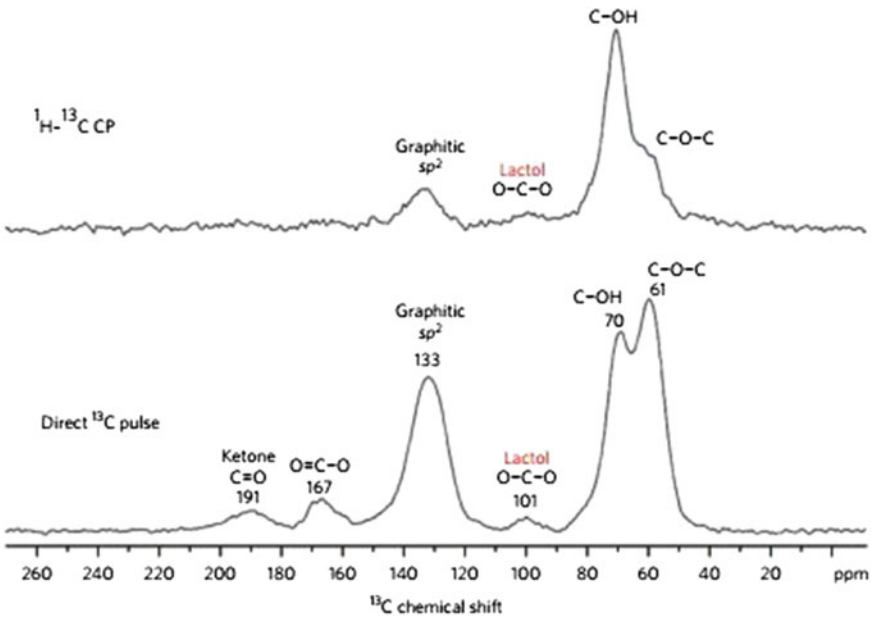

Fig. 1.7 ^{13}C NMR spectra of Go (reprinted with permission from [101])

Table 1.3 Shifted peak observed in XPS spectrum of graphene oxide and their respective origins [133–136]

S. No.	Chemically shifted signal positions (eV)	Origins
1	284.5	Sp^2 carbon atoms
2	285.86	C atom bounded to hydroxyl group
3	286.55	C atom bounded to epoxy group
4	287.5	C atom bounded to carbonyl group
5	289.2	C atom bounded to carboxyl group

Fourier transform infrared (FTIR) spectroscopy can also be used to determine the functional groups present in graphene oxide. The FTIR spectrum of graphene oxide [138] may be composed of various peaks which can be assigned to different functional groups present in graphene oxide. The assignments of these peaks to the functional groups are presented in Table 1.4 (Fig. 1.9).

At different levels of reduction, the peak positions associated with different groups diminish, some new peaks arise, and some peaks remain unaffected. This pattern depends upon the method of reduction. To understand the process of reduction, FTIR spectrum at different levels of reduction needs detailed analysis [134].

Raman spectroscopy is an excellent technique to study the carbonaceous materials. In case of graphene oxide, three different peaks are observed at 1350,

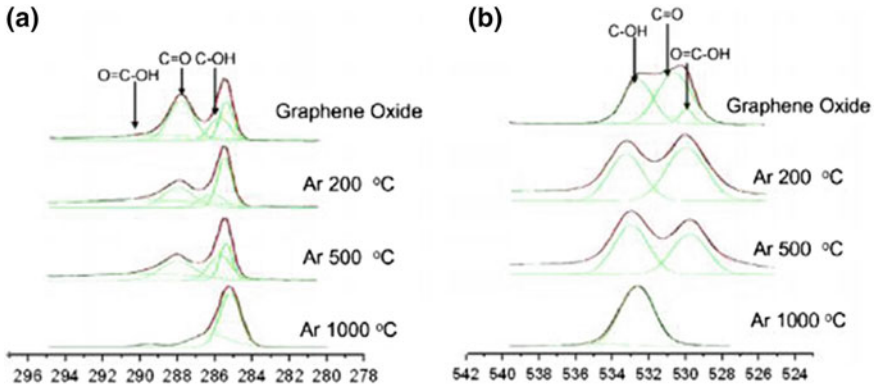

Fig. 1.8 XPS spectra for graphene oxide films after 200, 500 and 1000 °C treatment in flowing argon: **a** comparison of C 1s peaks, **b** comparison of O 1s peaks (reprinted with permission from [131])

Table 1.4 Observed IR peaks in FTIR spectrum of GO and their respective assignments [138]

S. No.	FTIR peak positions (cm^{-1})	Assignment
1	3050–3800	Hydroxyl
2	1750–1850	Carbonyl
3	1650–1750	Carboxyl
4	1500–1600	C=C
5	1000–1280	Ester and/or epoxides

1580 and 2680 cm^{-1}, which correspond to G band, D band and 2D band of carbonaceous materials. G band is the characteristic of graphitic (sp^2) carbon, D band arises due to defects and the presence of different functional groups, and 2D band, which is an overtone of D band, is the measure of the number of graphene layers [140, 141]. The ratio of intensity of D peak and that of G peak (I_D/I_G) is a good measure of degree of oxidation or reduction. Increasing degree of oxidation increases the value of I_D/I_G, while increasing degree of reduction decreases the value of I_D/I_G. Reduction in the intensity of 2D band can be attributed to the breaking of stacking order associated with oxidation reaction [142–144] (Fig. 1.10).

Transmission electron microscopy (TEM) is a good technique to study the microstructure of GO. It enables direct imaging of GO lattice and defects [145–147]. GO monolayer is highly transparent, and the samples with different oxidation levels show different transparencies [142] (Fig. 1.11). Increasing oxidation levels increase the transparency. High-resolution transmission electron microscopy (HRTEM) is capable of imaging honeycomb lattice of GO. In HRTEM image of GO, three different regions may be clearly visible. These regions may be termed as holes, graphitic and disordered regions. Holes are created by the release of CO and CO_2 during the oxidation, while graphitic region is the region with less effect of

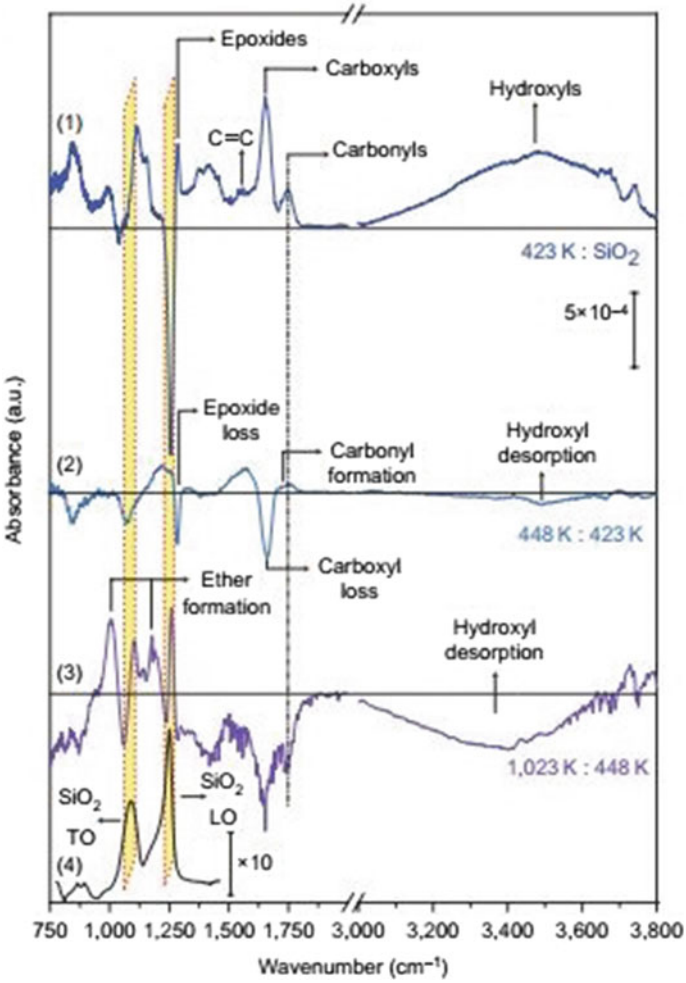

Fig. 1.9 FTIR absorbance spectra of single-layer GO. After annealing at 423 K and referenced to the bare oxidized silicon substrate, the spectrum (*1*) shows hydroxyls (broad peak at 3050–3800 cm^{-1}), carbonyls (1750–1850 cm^{-1}), carboxyls (1650–1750 cm^{-1}), C¼C (1500–1600 cm^{-1}) and ethers and/or epoxides (1000–1280 cm^{-1}). The differential spectrum after annealing to 448 K (reprinted with permission from [134])

oxidation. In the disordered region, there is a large quantity of oxygen functionalities attached to honeycomb lattice [146]. Selected-area electron diffraction (SAED) pattern shows clear diffraction spots which depict that the original graphene crystal lattice is preserved in GO [142] (Fig. 1.11).

Atomic force microscopy (AFM) is employed to investigate the thickness and lateral morphology of graphene oxide sheets. For AFM investigation, coating of graphene oxide on flat surface (usually silicon) is needed. The thickness of single or

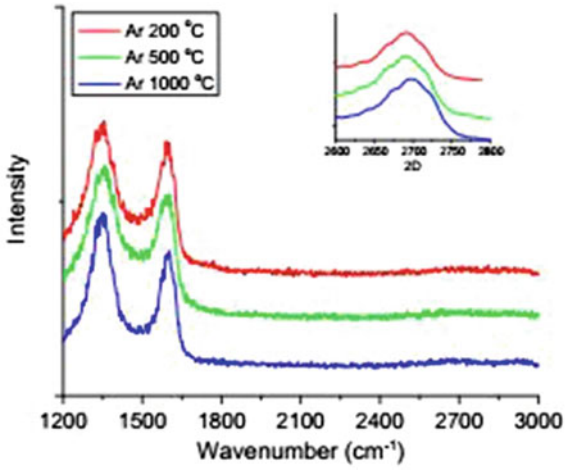

Fig. 1.10 Raman spectra of pristine and thermally reduced graphene oxide showing D, G and 2D (*inset*) bands (reprinted with permission from [134])

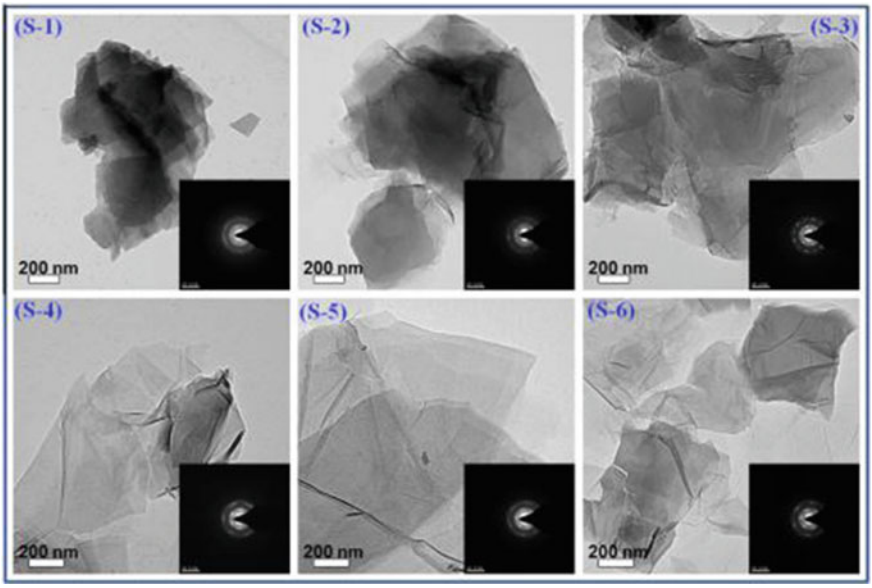

Fig. 1.11 TEM images of graphene oxide at increasing level of oxidation (S-1 to S-6) (reprinted with permission from [142])

multiple sheets can be obtained either by taking a simple line scan going across the sheets and substrate or by obtaining the histogram of the area of interest in the image [148] (Fig. 1.12). Typically, the thickness of graphene oxide sheet is about

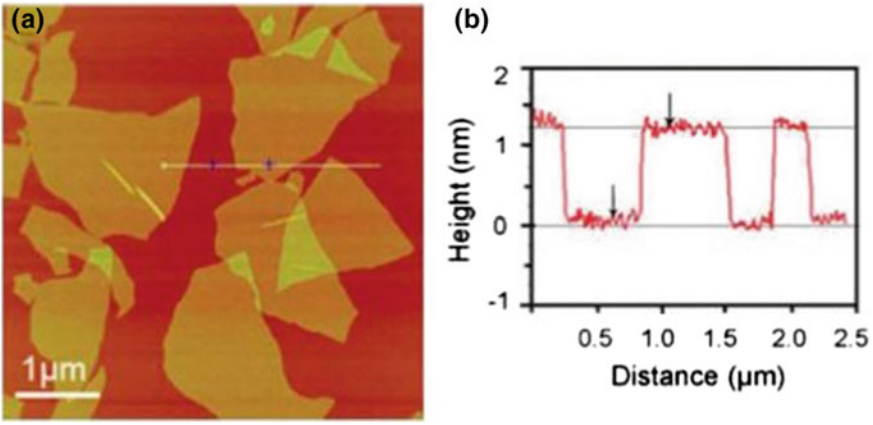

Fig. 1.12 **a** AFM image of graphene oxide. **b** Height profile of AFM image [40]

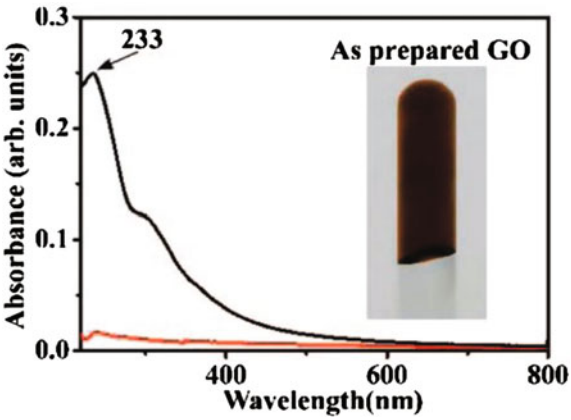

Fig. 1.13 UV–visible spectra of GO solution (reprinted with permission from [151])

1–1.3 nm which is more than that of graphene. The reason behind the increased thickness of graphene oxide is the presence of different groups attached to the graphene lattice [148, 149].

UV–visible spectroscopy is an analytical technique which is used in analytical chemistry for quantitative determination of different analytes [150]. In the case of graphene oxide, the UV–visible spectrum consists of a couple of peaks around 233 nm due to π–π^* transition of C=C bond. A broad band between 290 and 300 nm is also evident in UV–visible spectrum of graphene oxide. This band can be attributed to π–π^* transition of C=O band [151] (Fig. 1.13). Paredes et al. [51] recorded UV–visible spectra of graphene oxide dissolved in different organic solvents. They also observed a peak and a shoulder at 231 and 300 nm, respectively.

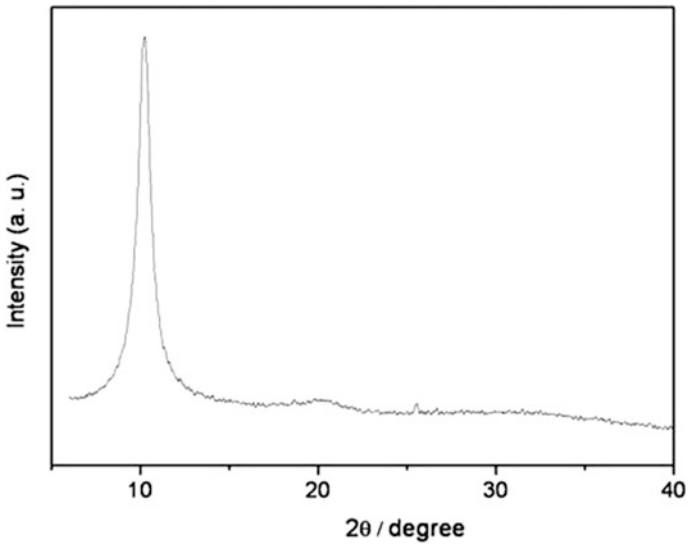

Fig. 1.14 XRD spectrum of GO (reprinted with permission from [155])

On reduction, the characteristics peak of graphene oxide around 230 nm gets red-shifted. Li and Kaner [19] reduced graphene oxide using hydrazine and observed that UV–visible peak initially located around 230 nm was red-shifted on reduction. The shift in peak position increases with increase in reaction time. The intensity of peak located around 230 nm can be used to estimate the number of layers in graphene oxide. In their report, Lai et al. [152] showed that the intensity of peak located at 230 nm in UV–visible spectrum of graphene oxide decreases with the increase in number of layers.

X-ray diffraction spectrum of graphene oxide shows a broad peak around $2\theta = 10°$ due to the interlayer distance of GO which is between 5.97 and 9.5 Å (Fig. 1.14). The XRD peak position and intensity are affected by oxidation, reduction, humidity and fractionalization [47, 153]. On reduction, the removal of oxygen-containing groups reduces the interlayer distance of graphene oxide, which, in turn, shifts the peak position towards higher 2θ values. Zhang et al. [154] reduced graphene oxide using L-ascorbic acid. They observed that the XRD peak position shifted from $2\theta = 11.1°$ to $2\theta = 24°$ which corresponded to interlayer spacing of 7.45 and 3.7 Å. The observed interlayer spacing of reduced graphene oxide, i.e. 3.7 Å, is very much close to the interlayer spacing of graphite (002) plane ($\sim$3.35 Å). Krishnamoorthy et al. [142] studied various graphene oxide samples having different levels of oxidation. They found that the XRD peak position shifts from higher values of 2θ to lower values of 2θ with decreasing degree of oxidation.

1.4 Conclusion

Graphene oxide (GO), is very promising material due to its easy synthesis and extraordinary properties. Although the structure of graphene oxide depends upon the methods of preparation, it is an insulator in its unreduced form. On reduction, the oxygen-containing groups of graphene oxide are removed and it starts to behave as a semiconductor. Further reduction improves the conductivity of graphene oxide and it shifts towards graphene, which is a semimetal. Facile synthesis and wide range of reduction recipes make graphene oxide a cost effective replacement of pristine graphene. Although there are various reduction recipes used by the researchers worldwide, no one has claimed to produce pure graphene from graphene oxide. Use of different chemicals and reagents induces different types of impurities, which affect the properties of graphene oxide. Therefore, the complete reduction of GO is still an issue to be addressed. The mass scale production of graphene can be realized only if the complete reduction of GO becomes possible.

References

1. A. Hirsch, M. Brettreich, *Fullerenes—Chemistry and Reactions* (Wiley, New York, 2004). H. Yang et al., Angew. Chem. Int. Ed. **49**, 886 (2010)
2. A. Hirsch, The era of carbon allotropes. Nat. Mater. **9**(11), 868–871 (2010)
3. N. Tagmatarchis, H. Shinohara, Fullerenes in medicinal chemistry and their biological applications. Mini. Rev. Med. Chem. **1**(4), 339–348 (2001)
4. E.A. Katz, Fullerene thin films as photovoltaic material, in *Nanostructured Materials for Solar Energy Conversion*, ed. by T. Sōga (Elsevier, Amsterdam, 2006), pp. 361–443
5. R.E. Smalley, *Carbon Nanotubes: Synthesis, Structure, Properties, and Applications*, vol. 80, ed. by M.S. Dresselhaus, G. Dresselhaus, P. Avouris (Springer Science & Business Media, 2003)
6. S.H. Jin, Single-walled carbon nanotubes (SWNTs); history and future prospects for electronic applications, in *Active-Matrix Flatpanel Displays And Devices* (*AMFPD*)*, 2016 The 23rd International Workshop on Active-Matrix Flatpanel Displays and Devices*, FTFMD (2016), pp. 38–41
7. M. Husain, Z.H. Khan (eds.), *Advances in Nanomaterials*, vol. 79 (Springer, Berlin, 2016)
8. P.M. Ajayan, O.Z. Zhou, Applications of carbon nanotubes, in *Carbon Nanotubes* (Springer, Berlin, 2001), 391–425
9. H.P. Boehm, R. Setton, E. Stumpp, Nomenclature and terminology of graphite intercalation compounds (IUPAC Recommendations 1994). Pure Appl. Chem. **66**(9), (1994), 1893–1901
10. E.T. Thostenson, Z. Ren, T.W. Chou, Advances in the science and technology of carbon nanotubes and their composites: a review. Compos. Sci. Technol. **61**(13), 1899–1912 (2001)
11. H.P. Boehm, A. Clauss, G.O. Fischer, U. Hofmann, Das adsorptionsverhalten sehr dünner kohlenstoff-folien. Zeitschrift für anorganische und allgemeine Chemie **316**(3–4), 119–127 (1962)
12. K.S. Novoselov, A.K. Geim, S.V. Morozov, D. Jiang, Y. Zhang, S.V. Dubonos, I.V. Grigorieva, A.A. Firsov, Electric field effect in atomically thin carbon films. Science **306** (5696), 666–669 (2004)
13. This Month in Physics History: October 22, 2004: Discovery of Graphene. APS News. Series II. **18**(9), 2 (2009)

14. D. Chen, H. Feng, J. Li, Graphene oxide: preparation, functionalization, and electrochemical applications. Chem. Rev. **112**(11), 6027–6053 (2012)
15. J.T. Robinson, F.K. Perkins, E.S. Snow, Z. Wei, P.E. Sheehan, Reduced graphene oxide molecular sensors. Nano Lett. **8**(10), 3137–3140 (2008)
16. V. Dua, S.P. Surwade, S. Ammu, S.R. Agnihotra, S. Jain, K.E. Roberts, S. Park, R.S. Ruoff, S.K. Manohar, All-organic vapor sensor using inkjet-printed reduced graphene oxide. Angew. Chem. **122**(12), 2200–2203 (2010)
17. S. Stankovich, D.A. Dikin, G.H.B. Dommett, K.M. Kohlhaas, E.J. Zimney, E.A. Stach, R.D. Piner, S.T. Nguyen, R.S. Ruoff, Graphene-based composite materials. Nature **442**(7100), 282–286 (2006)
18. H. Zhang, X. Lv, Y. Li, Y. Wang, J. Li, P25-graphene composite as a high performance photocatalyst. ACS Nano **4**(1), 380–386 (2009)
19. D. Li, R.B. Kaner, Graphene-based materials. Nat. Nanotechnol. **3**, 101 (2008)
20. S. Goenka, V. Sant, S. Sant, Graphene-based nanomaterials for drug delivery and tissue engineering. J. Controll. Release **173**, 75–88 (2014)
21. K. Shehzad, Y. Xu, C. Gao, X. Duan, Three-dimensional macro-structures of two-dimensional nanomaterials. Chem. Soc. Rev. **45**(20), 5541–5588 (2016)
22. Y. Han, Z. Xu, C. Gao, Ultrathin graphene nanofiltration membrane for water purification. Adv. Func. Mater. **23**(29), 3693–3700 (2013)
23. Martin Pumera, Graphene-based nanomaterials for energy storage. Energy Environ. Sci. **4** (3), 668–674 (2011)
24. Z.S. Wu, G. Zhou, L.C. Yin, W. Ren, F. Li, H.M. Cheng, Graphene/metal oxide composite electrode materials for energy storage. Nano Energy **1**(1), 107–131 (2012)
25. M.F. El-Kady, R.B. Kaner, Scalable fabrication of high-power graphene micro-supercapacitors for flexible and on-chip energy storage. Nat. Commun. **4**, 1475 (2013)
26. H. He, J. Klinowski, M. Forster, A. Lerf, Chem. Phys. Lett. **287**, 53–56 (1998)
27. X. Wang, L. Zhi, K. Müllen, Transparent, conductive graphene electrodes for dye-sensitized solar cells. Nano Lett. **8**(1), 323–327 (2008)
28. G. Eda, G. Fanchini, M. Chhowalla, Large-area ultrathin films of reduced graphene oxide as a transparent and flexible electronic material. Nat. Nanotechnol. **3**(5), 270–274 (2008)
29. X. Li, Y. Zhu, W. Cai, M. Borysiak, B. Han, D. Chen, R.D. Piner, L. Colombo, R.S. Ruoff, Transfer of large-area graphene films for high-performance transparent conductive electrodes. Nano Lett. **9**(12), 4359–4363 (2009)
30. G. Eda, Y.Y. Lin, S. Miller, C.W. Chen, Su WF, M. Chhowalla, Transparent and conducting electrodes for organic electronics from reduced graphene oxide. Appl. Phys. Lett. **92**(23), 233305 (2008)
31. S. Chen, J. Zhu, X. Wu, Q. Han, X. Wang, Graphene oxide—MnO_2 nanocomposites for supercapacitors. ACS Nano **4**(5), 2822–2830 (2010)
32. X. Zhu, Y. Zhu, S. Murali, M.D. Stoller, R.S. Ruoff, Nanostructured reduced graphene oxide/Fe_2O_3 composite as a high-performance anode material for lithium ion batteries. ACS Nano **5**(4), 3333–3338 (2011)
33. R.R. Nair, H.A. Wu, P.N. Jayaram, I.V. Grigorieva, A.K. Geim, Unimpeded permeation of water through helium-leak–tight graphene-based membranes. Science **335**(6067), 442–444 (2012)
34. L. Wang, K. Lee, Y.Y. Sun, M. Lucking, Z. Chen, J.J. Zhao, S.B. Zhang, Graphene oxide as an ideal substrate for hydrogen storage. ACS Nano **3**(10). 2995–3000 (2009)
35. C. Chung, Y.K. Kim, D. Shin, S.R. Ryoo, B.H. Hong, D.H. Min, Biomedical applications of graphene and graphene oxide. Acc. Chem. Res. **46**(10), 2211–2224 (2013)
36. B.C. Brodie, On the atomic weight of graphite. Phil. Trans. R. Soc. London **149**, 249–259 (1859)
37. L. Staudenmaier, Verfahren zur Darstellung der Graphitsäure. Ber. Dtsch. Chem. Ges. **31**, 1481–1487 (1898)
38. L. Staudenmaier, Verfahren zur Darstellung der Graphitsäure. Ber. Dtsch. Chem. Ges. **32**, 1394–1399 (1899)

39. U. Hofmann, R. Holst, Über die Säurenatur und die Methylierung von Graphitoxyd. Berichte der deutschen chemischen Gesellschaft (A and B Series), **72**(4), 754–771 (1939)
40. W. Gao, Synthesis, structure and characterizations, in *Graphene Oxide: Reduction Recipes, Spectroscopy, and Applications*, ed. by W. Gao (Springer International Publishing, 2015), pp. 1–28
41. W.S. Hummers Jr, R.E. Offeman, Preparation of graphitic oxide. J. Am. Chem. Soc. **80**(6), 1339–1339 (1958)
42. K.R. Koch, P.F. Krause, Oxidation by dimanganese heptoxide: an impressive demonstration. J. Chem. Ed **59**, 973 (1982)
43. A. Simon, R. Dronskowski, B. Krebs, B. Hettich, The crystal structure of Mn_2O_7. Angew. Chem. Int. Ed. Engl. **26**(2), 139–140 (1987)
44. S. Stankovich, R.D. Piner, X. Chen, N. Wu, S.T. Nguyen, R.S. Ruoff, Stable aqueous dispersions of graphitic nanoplatelets via the reduction of exfoliated graphite oxide in the presence of poly (sodium 4-styrenesulfonate). J. Mater. Chem. **16**(2), 155–158 (2006)
45. N.I. Kovtyukhova, P.J. Ollivier, B.R. Martin, T.E. Mallouk, S.A. Chizhik, E.V. Buzaneva, A.D. Gorchinskiy, Layer-by-layer assembly of ultrathin composite films from micron-sized graphite oxide sheets and polycations. Chem. Mater. **11**, 771–778 (1999)
46. J. Chen, B. Yao, C. Li, G. Shi, An improved hummers method for eco-friendly synthesis of graphene oxide. Carbon **64**, 225–229 (2013)
47. D.C. Marcano, D.V. Kosynkin, J.M. Berlin, A. Sinitskii, Z. Sun, A. Slesarev, L.B. Alemany, W. Lu, J.M. Tour, Improved synthesis of graphene oxide. ACS Nano **4**, 4806–4814 (2010)
48. S. Park, R.S. Ruoff, Chemical methods for the production of graphenes. Nat. Nanotechnol. **4** (4), 217–224 (2009)
49. S. Park et al., Graphene oxide papers modified by divalentions—Enhancing mechanical properties via chemical cross-linking. ACS Nano **2**, 572–578 (2008)
50. S. Stankovich, R. Piner, S.T. Nguyen, R.S. Ruoff, Synthesis and exfoliation of isocyanate-treated graphene oxide nanoplatelets. Carbon **44**, 3342–3347 (2006)
51. J.I. Paredes, S. Villar-Rodil, A. Martinez-Alonso, J.M.D. Tascón, Graphene oxide dispersions in organic solvents. Langmuir **24**, 10560–10564 (2008)
52. S. Stankovich et al., Synthesis of graphene-based nanosheets via chemical reduction of exfoliated graphite oxide. Carbon **45**, 1558–1565 (2007)
53. D. Li, M.B. Muller, S. Gilje, R.B. Kaner, G.G. Wallace, Processable aqueous dispersions of graphene nanosheets. Nat. Nanotechnol. **3**, 101–105 (2008)
54. Y. Xu, H. Bai, G. Lu, C. Li, G. Shi, Flexible graphene films via the filtration of water-soluble noncovalent functionalized graphene sheets. J. Am. Chem. Soc. **130**, 5856–5857 (2008)
55. S. Park et al., Aqueous suspension and characterization of chemically modified graphene sheets. Chem. Mater. **20**, 6592–6594 (2008)
56. Y. Si, E.T. Samulski, Synthesis of water soluble graphene. Nano Lett. **8**, 1679–1682 (2008)
57. S. Niyogi et al., Solution properties of graphite and graphene. J. Am. Chem. Soc. **128**, 7720–7721 (2006)
58. J.R. Lomeda, C.D. Doyle, D.V. Kosynkin, W.-F. Hwang, J.M. Tour, Diazonium functionalization of surfactant-wrapped chemically converted graphene sheets. J. Am. Chem. Soc. **130**, 16201–16206 (2008)
59. V.C. Tung, M.J. Allen, Y. Yang, R.B. Kaner, High-throughput solution processing of large-scale graphene. Nat. Nanotechnol. **4**, 25–29 (2008)
60. R. Muszynski, B. Seger, P.V. Kamat, Decorating graphene sheets with gold nanoparticles. J. Phys. Chem. C **112**, 5263–5266 (2008)
61. H.C. Schniepp et al., Functionalized single graphene sheets derived form splitting graphite oxide. J. Phys. Chem. B **110**, 8535–8539 (2006)
62. M.J. McAllister et al., Single sheet functionalized graphene by oxidation and thermal expansion of graphite. Chem. Mater. **19**, 4396–4404 (2007)
63. G. Williams, B. Serger, P.V. Kamat, TiO_2-graphene nanocomposites. UV-assisted photocatalytic reduction of graphene oxide. ACS Nano **2**, 1487–1491 (2008)

64. P.V. Kamat, V. Bridewell, Electrocatalytic activity of graphene oxide: mediating electron transfer between two redox couples, in Meeting Abstracts, no. 6, The electrochemical society, (2016), pp. 551–551
65. Y. Wang, L. Li, C. Luo, X. Wang, H. Duan, Removal of Pb 2+ from water environment using a novel magnetic chitosan/graphene oxide imprinted Pb 2+. Int. J. Biol. Macromol. **86**, 505–511 (2016)
66. Z.S. Wu, W. Ren, L. Gao, B. Liu, C. Jiang, H.M. Cheng, Synthesis of high-quality graphene with a pre-determined number of layers. Carbon **47**(2), 493–499 (2009)
67. O. Akhavan, M. Choobtashani, E. Ghaderi, Protein degradation and RNA efflux of viruses photocatalyzed by graphene–tungsten oxide composite under visible light irradiation. J. Phys. Chem. C. **116**(17), 9653–9659 (2012)
68. S. Pei, H.M. Cheng, The reduction of graphene oxide. Carbon **50**(9), 3210–3228 (2012)
69. K.N. Kudin, B. Ozbas, H.C. Schniepp, R.K. Prud'homme, I.A. Aksay, R. Car. Raman spectra of graphite oxide and functionalized graphene sheets. Nano Lett. **8**(1), 36–41 (2007)
70. H.A. Becerril, J. Mao, Z. Liu, R.M. Stoltenberg, Z. Bao, Y. Chen, Evaluation of solution-processed reduced graphene oxide films as transparent conductors. ACS Nano **2**(3), 463–470 (2008)
71. S.C. Youn, J. Geng, B.S. Son, S.B. Yang, D.W. Kim, H.M. Cho, H.T. Jung, Effect of the exposure time of hydrazine vapor on the reduction of graphene oxide films. J. Nanosci. Nanotechnol. **11**(7), 5959–5964 (2011)
72. Y. Zhu, S. Murali, M.D. Stoller, A. Velamakanni, R.D. Piner, R.S. Ruoff, Microwave assisted exfoliation and reduction of graphite oxide for ultracapacitors. Carbon **48**(7), 2118–2122 (2010)
73. H.M.A. Hassan, V. Abdelsayed, A.E.R.S. Khder, K.M. AbouZeid, J. Terner, M.S. El-Shall et al., Microwave synthesis of graphene sheets supporting metal nanocrystals in aqueous and organic media. J. Mater. Chem. **19**(23), 3832–3837 (2009)
74. S. Sharin, I.A. Rahman, A.F. Ahmad, H.M.K. Mohd, F. Mohamed, S. Radiman, M.S. Yasir, S. Sarmani, M.T. Ayob, I.S.A. Bastamam, Reduction of graphene oxide to graphene by using gamma irradiation. Malays. J. Anal. Sci. **19**(6), 1223–1228 (2015)
75. L.J. Cote, R. Cruz-Silva, J. Huang, Flash reduction and patterning of graphite oxide and its polymer composite. J. Am. Chem. Soc. **131**(31), 11027–11032 (2009)
76. Y. Zhang, L. Guo, S. Wei, Y. He, H. Xia, Q. Chen et al., Direct imprinting of microcircuits on graphene oxides film by femtosecond laser reduction. Nanotoday **5**(1), 15–20 (2010)
77. Y. Matsumoto, M. Koinuma, S.Y. Kim, Y. Watanabe, T. Taniguchi, K. Hatakeyama, H. Tateishi, S. Ida, Simple photoreduction of graphene oxide nanosheet under mild conditions. ACS Appl. Mater. Inter. **2**(12), 3461–3466 (2010)
78. P. Kumar, K.S. Subrahmanyam, C.N.R. Rao, Graphene produced by radiation-induced reduction of graphene oxide. Int. J. Nanosci. **10**(04n05), 559–566 (2011)
79. B. Zhang, L. Li, Z. Wang, S. Xie, Y. Zhang, Y. Shen, M. Yu et al., Radiation induced reduction: an effective and clean route to synthesize functionalized graphene. J. Mater. Chem. **22**(16), 7775–7781 (2012)
80. D.R. Dreyer, S. Park, C.W. Bielawski, R.S. Ruoff, The chemistry of graphene oxide. Chem. Soc. Rev. **39**(1), 228–240 (2010)
81. C.K. Chua, M. Pumera, Chemical reduction of graphene oxide: a synthetic chemistry viewpoint. Chem. Soc. Rev. **43**(1), 291–312 (2014)
82. X. Zhou, J. Zhang, H. Wu, H. Yang, J. Zhang, S. Guo, J. Phys. Chem. C **115**, 11957–11961 (2011)
83. T. Sakura, Y. Nagasaki, Preparation of gold colloid using pyrrole-2-carboxylic acid and characterization of its particle growth. Colloid Polym. Sci. **285**(12), 1407–1410 (2007)
84. S. Liu, J. Tian, L. Wang, X. Sun, A method for the production of reduced graphene oxide using benzylamine as a reducing and stabilizing agent and its subsequent decoration with Ag nanoparticles for enzymeless hydrogen peroxide detection. Carbon **49**(10), 3158–3164 (2011)

85. Y. Chen, X. Zhang, P. Yu, Y. Ma, Stable dispersions of graphene and highly conducting graphene films: a new approach to creating colloids of graphene monolayers. Chem. Commun. **30**, 4527–4529 (2009)
86. J. Che, L. Shen, Y. Xiao, A new approach to fabricate graphene nanosheets in organic medium: combination of reduction and dispersion. J. Mater. Chem. **20**(9), 1722–1727 (2010)
87. Z. Lei, L. Lu, X.S. Zhao, The electrocapacitive properties of graphene oxide reduced by urea. Energy Environ. Sci. **5**(4), 6391–6399 (2012)
88. P. Su, H.L. Guo, L. Tian, S.K. Ning, An efficient method of producing stable graphene suspensions with less toxicity using dimethyl ketoxime. Carbon **50**(15), 5351–5358 (2012)
89. X. Shen, L. Jiang, Z. Ji, J. Wu, H. Zhou, G. Zhu, Stable aqueous dispersions of graphene prepared with hexamethylenetetramine as a reductant. J. Colloid. Interf. Sci. **354**(2), 493–497 (2011)
90. S. Zhang, Y. Shao, H. Liao, M.H. Engelhard, G. Yin, Y. Lin, Polyelectrolyte-induced reduction of exfoliated graphite oxide: a facile route to synthesis of soluble graphene nanosheets. ACS Nano **5**(3), 1785–1791 (2011)
91. T. Wu, X. Wang, H. Qiu, J. Gao, W. Wang, Y. Liu, Graphene oxide reduced and modified by soft nanoparticles and its catalysis of the Knoevenagel condensation. J. Mater. Chem. **22** (11), 4772–4779 (2012)
92. I.K. Moon, J. Lee, R.S. Ruoff, H. Lee. Reduced graphene oxide by chemical graphitization. Nat. Commun. **1**(73), (2010)
93. P. Cui, J. Lee, E. Hwang, H. Lee, One-pot reduction of graphene oxide at subzero temperatures. Chem. Commun. **47**(45), 12370–12372 (2011)
94. S.F. Pei, J.P. Zhao, J.H. Du, W.C. Ren, H.M. Cheng, Carbon **48**, 4466–4474 (2010)
95. Y. Chen, X. Zhang, D. Zhang, P. Yu, Y. Ma, Carbon **49**, 573–580 (2011)
96. H.J. Shin, K.K. Kim, A. Benayad, S.M. Yoon, H.K. Park, I.S. Jung et al., Efficient reduction of graphite oxide by sodium borohydride and its effect on electrical conductance. Adv. Funct. Mater. **19**(12), 1987–1992 (2009)
97. M. Periasamy, M. Thirumalaikumar, Methods of enhancement of reactivity and selectivity of sodium borohydride for applications in organic synthesis. J. Organomet. Chem. **609**(1–2), 137–151 (2000)
98. W. Gao, L.B. Alemany, L. Ci, P.M. Ajayan, New insights into the structure and reduction of graphite oxide. Nat. Chem. **1**(5), 403–408 (2009)
99. C.Y. Su, X.U. Yanping, W. Zhang, J. Zhao, A. Liu, X. Tang, C.H. Tsai, Y. Huang, L.J. Li, Highly efficient restoration of graphitic structure in graphene oxide using alcohol vapors. ACS Nano **4**(9), 5285–5292 (2010)
100. J. Gao, F. Liu, Y. Liu, N. Ma, Z. Wang, X. Zhang, Chem. Mater. **22**, 2213–2218 (2010)
101. M.J. Fernández-Merino, L. Guardia, J.I. Paredes, S. Villar-Rodil, P. Solís-Fernández, A. Martínez-Alonso, J.M.D. Tascón, J. Phys. Chem. C. **114**, 6426–6432 (2010)
102. Y. Wang, L. Sun, B. Fugetsu, Bull. Chem. Soc. Jpn. **85**, 1339–1344 (2012)
103. Q. Ma, J. Song, C. Jin, Z. Li, J. Liu, S. Meng, J. Zhao, Y. Guo, Carbon **54**, 36–41 (2013)
104. Z. Fan, K. Wang, T. Wei, J. Yan, L. Song, B. Shao, Carbon **48**, 1686–1689 (2010)
105. V.H. Pham, H.D. Pham, T.T. Dang, S.H. Hur, E.J. Kim, B.S. Kong, S. Kim, J.S. Chung, J. Mater. Chem. **22**, 10530–10536 (2012)
106. Z.-J. Fan, W. Kai, J. Yan, T. Wei, L.-J. Zhi, J. Feng, Y.-m. Ren, L.-P. Song, F. Wei, ACS Nano **5**, 191–198 (2010)
107. X. Mei, J. Ouyang, Carbon **49**, 5389–5397 (2011); P.B. Liu, Y. Huang, L. Wang, Mater. Lett. **91**, 125–128 (2013)
108. N.A. Kumar, S. Gambarelli, F. Duclairoir, G. Bidan, L. Dubois, J. Mater. Chem. A **1**, 2789–2794 (2013)
109. B.K. Barman, P. Mahanandia, K.K. Nanda, RSC Adv. **3**, 12621–12624 (2013)
110. R.S. Dey, S. Hajra, R.K. Sahu, C.R. Raj, M.K. Panigrahi, Chem. Commun. **48**, 1787–1789 (2012)
111. Y. Liu, Y. Li, M. Zhong, Y. Yang, W. Yuefang, M. Wang, J. Mater. Chem. **21**, 15449–15455 (2011)

112. S. Yang, W. Yue, D. Huang, C. Chen, H. Lin, X. Yang, RSC Adv. **2**, 8827–8832 (2012)
113. H. Feng, R. Cheng, X. Zhao, X. Duan, J. Li, Nat. Commun. **4**, 1539 (2013)
114. D. Chen, L. Li, L. Guo, Nanotechnology **22**, 325601 (2011)
115. S. Bose, T. Kuila, A.K. Mishra, N.H. Kim, J.H. Lee, J. Mater. Chem. **22**, 9696–9703 (2012)
116. J.K. Ma, X.R. Wang, Y. Liu, T. Wu, Y. Liu, Y.Q. Guo, R.Q. Li, X.Y. Sun, F. Wu, C.B. Li, J.P. Gao, J. Mater. Chem. A **1**, 2192–2201 (2013)
117. T.A. Pham, J. Kim, J.S. Kim, Y.T. Jeong, Colloids Surf. A **384**, 543–548 (2011)
118. D. Suresh, H. Nagabhushana, S.C. Sharma, Clove extract mediated facile green reduction of graphene oxide, its dye elimination and antioxidant properties. Mater. Lett. **142**, 4–6 (2015)
119. S. Hatamie, O. Akhavan, S.K. Sadrnezhaad, M.M. Ahadian, M.M. Shirolkar, H.Q. Wang, Curcumin-reduced graphene oxide sheets and their effects on human breast cancer cells, Mater. Sci. Eng. C **55**, 482–489 (2015)
120. R.K. Upadhyay, N. Soin, G. Bhattacharya, S. Saha, A. Barman, S.S. Roy, Grape extract assisted green synthesis of reduced graphene oxide for water treatment application. Mater. Lett. **160**, 355–358 (2015)
121. E.C. Salas, Z. Sun, A. Lüttge and JM Tour. ACS Nano **4**, 4852–4856 (2010)
122. O. Akhavan, E. Ghaderi, Escherichia coli bacteria reduce graphene oxide to bactericidal graphene in a self-limiting manner. Carbon **50**(5), 1853–1860 (2012)
123. P. Khanra, T. Kuila, N.H. Kim, S.H. Bae, D.S. Yu, J.H. Lee, Simultaneous bio-functionalization and reduction of graphene oxide by baker's yeast. Chem. Eng. J. **183**, 526–533 (2012)
124. O. Akhavan, Bacteriorhodopsin as a superior substitute for hydrazine in chemical reduction of single-layer graphene oxide sheets. Carbon **81**, 158–166 (2015)
125. A. Esfandiar, O. Akhavan, A. Irajizad, Melatonin as a powerful bio-antioxidant for reduction of graphene oxide. J. Mater. Chem. **21**(29), 10907–10914 (2011)
126. T. Szabó, O. Berkesi, P. Forgó, K. Josepovits, Y. Sanakis, D. Petridis, I. Dékány, Evolution of surface functional groups in a series of progressively oxidized graphite oxides. Chem. Mater. **18**(11), 2740–2749 (2006)
127. W. Cai, R.D. Piner, F.J. Stadermann, S. Park, M.A. Shaibat, Y. Ishii, D. Yang et al., Synthesis and solid-state NMR structural characterization of 13C-labeled graphite oxide. Science **321**(5897), 1815–1817 (2008)
128. H. He, T. Riedl, A. Lerf, J. Klinowski, Solid-state NMR studies of the structure of graphite oxide. J. Phys. Chem. **100**(51), 19954–19958 (1996)
129. A. Lerf, H. He, T. Riedl, M. Forster, J. Klinowski, 13C and 1H MAS NMR studies of graphite oxide and its chemically modified derivatives. Solid State Ionics. **101**, 857–862 (1997)
130. A. Lerf, H. He, M. Forster, J. Klinowski, Structure of graphite oxide revisited. J. Phys. Chem. B **102**(23), 4477–4482 (1998)
131. Q. Zhang, K. Scrafford, M. Li, Z. Cao, Z. Xia, P.M. Ajayan, B. Wei, Anomalous capacitive behaviors of graphene oxide based solid-state supercapacitors. Nano Lett. **14**(4), 1938–1943 (2014)
132. J. Zhao, L. Liu, F. Li, Structural Characterizations in *Graphene Oxide: Physics and Applications*. (Springer, Berlin Heidelberg, 2015), pp. 15–29
133. C. Mattevi, G. Eda, S. Agnoli, S. Miller, K.A. Mkhoyan, O. Celik, D. Mastrogiovanni, G. Granozzi, E. Garfunkel, M. Chhowalla, Evolution of electrical, chemical, and structural properties of transparent and conducting chemically derived graphene thin films. Adv. Funct. Mater. **19**(16), 2577–2583 (2009)
134. D. Yang, A. Velamakanni, G. Bozoklu, S. Park, M. Stoller, R.D. Piner, S. Stankovich et al., Chemical analysis of graphene oxide films after heat and chemical treatments by X-ray photoelectron and Micro-Raman spectroscopy. Carbon **47**(1), 145–152 (2009)
135. O. Akhavan, The effect of heat treatment on formation of graphene thin films from graphene oxide nanosheets. Carbon **48**(2), 509–519 (2010)

136. G. Abhijit, S. Sharma, P. Papakonstantinou, J. Hamilton, Probing the thermal deoxygenation of graphene oxide using high-resolution in situ X-ray-based spectroscopies. J. Phys. Chem. C **115**(34), 17009–17019 (2011)
137. R.J.W.E. Lahaye, H.K. Jeong, C.Y. Park, Y.H. Lee. Density functional theory study of graphite oxide for different oxidation levels. Phys. Rev. B **79**(12), 125435 (2009)
138. A. Bagri, C. Mattevi, M. Acik, Y.J. Chabal, M. Chhowalla, V.B. Shenoy, Structural evolution during the reduction of chemically derived graphene oxide. Nat. Chem. **2**(7), 581–587 (2010)
139. C. Hontoria-Lucas, A.J. Lopez-Peinado, J.D. de López-González, M.L. Rojas-Cervantes, R. M. Martin-Aranda, Study of oxygen-containing groups in a series of graphite oxides: physical and chemical characterization. Carbon **33**(11), 1585–1592 (1995)
140. A.C. Ferrari, J.C. Meyer, V. Scardaci, C. Casiraghi, M. Lazzeri, F. Mauri, S. Piscanec et al., Raman spectrum of graphene and graphene layers. Phys. Rev. Lett. **97**(18), 187401 (2006)
141. A. Gupta, G. Chen, P. Joshi, S. Tadigadapa, P.C. Eklund, Raman scattering from high-frequency phonons in supported n-graphene layer films. Nano Lett. **6**(12), 2667–2673 (2006)
142. K. Krishnamoorthy, M. Veerapandian, K. Yun, S-J. Kim. The chemical and structural analysis of graphene oxide with different degrees of oxidation. Carbon **53**, 38–49 (2013)
143. G. Eda, M. Chhowalla, Chemically derived graphene oxide: towards large-area thin-film electronics and optoelectronics. Adv. Mater. **22**(22), 2392–2415 (2010)
144. L.M. Malard, M.A. Pimenta, G. Dresselhaus, M.S. Dresselhaus, Raman spectroscopy in graphene. Phys. Rep. **473**(5), 51–87 (2009)
145. C. Gómez-Navarro, J.C. Meyer, R.S. Sundaram, A. Chuvilin, S. Kurasch, M. Burghard, K. Kern, U. Kaiser, Atomic structure of reduced graphene oxide. Nano Lett. **10**(4), 1144–1148 (2010)
146. K. Erickson, R. Erni, Z. Lee, N. Alem, W. Gannett, A. Zettl, Determination of the local chemical structure of graphene oxide and reduced graphene oxide, Adv. Mater. **22**(40), 4467–4472 (2010)
147. J. Xie, F. Tu, Q. Su, G. Du, S. Zhang, T. Zhu, G. Cao, X. Zhao, In situ TEM characterization of single PbSe/reduced-graphene-oxide nanosheet and the correlation with its electrochemical lithium storage performance. Nano Eng. **5**, 122–131 (2014)
148. K.A. Mkhoyan, A.W. Contryman, J. Silcox, D.A. Stewart, G. Eda, C. Mattevi, S. Miller, M. Chhowalla, Atomic and electronic structure of graphene-oxide. Nano Lett. **9**(3), 1058–1063 (2009)
149. M.I. Katsnelson, K.S. Novoselov, A.K. Geim, Chiral tunnelling and the Klein paradox in graphene, Nat. Phys. **2**(9), 620–625 (2006)
150. D.A. Skoog, F.J. Holler, S.R. Crouch, *Principles of Instrumental Analysis*, 6th edn. (Thomson Brooks/Cole, Belmont, CA, 2007), pp. 169–173
151. Z. Luo, Y. Lu, L.A. Somers, A.T.C. Johnson, High yield preparation of macroscopic graphene oxide membranes. J. Am. Chem. Soc. **131**(3), 898–899 (2009)
152. Q. Lai, S. Zhu, X. Luo, M. Zou, S. Huang, Ultraviolet-visible spectroscopy of graphene oxides. AIP Adv. **2**(3), 032146 (2012)
153. T. Szabó, O. Berkesi, I. Dékány, DRIFT study of deuterium-exchanged graphite oxide. Carbon **43**(15), 3186–3189 (2005)
154. J. Zhang, H. Yang, G. Shen, P. Cheng, J. Zhang, S. Guo. Reduction of graphene oxide via L-ascorbic acid. Chem. Commun. **46**(7), 1112–1114 (2010)
155. Y. Wang, L. Tang, Z. Li, Y. Lin, J. Li, In situ simultaneous monitoring of ATP and GTP using a graphene oxide nanosheet–based sensing platform in living cells. Nat. Protoc. **9**(8), 1944–1955 (2014)

Chapter 2
Wear Behavior of Composites and Nanocomposites: A New Approach

Yasmin Choudhury and Pallav Gupta

2.1 Wear

The expulsion of material from either of two strong surfaces in relative movement is termed as wear. Wear can also be defined as surface damage, because of material relocation with no net change in weight or volume. It happens as a natural result and for the most part through surface interactions at severities. It is a system response and is not a material property. Interface wear is firmly commanded by working conditions. Wear can be either desirable or undesirable. Desirable instances of wear incorporate machining, polishing, shearing, and writing with a pencil, whereas undesirable cases incorporate all machine applications, for example, gears, bearings, cams, and seals. At times, it is mistakenly expected that high friction wear implies high wear rates, but this is not valid. Interfaces with solid lubricants and polymers generally indicate low friction, however high wear. On the other hand, ceramics show moderate friction with extremely low wear. In some segregated cases, friction and wear might be corresponded. On an overall basis, friction and wear are two distinct system responses [1].

2.2 Types of Wear

Wear occurs either by a chemical process or by a mechanical process or by an amalgamation. In most of the applications, it is accelerated by thermal processes. In our day to day applications, wear is classified on the basis of (a) mechanism and

Y. Choudhury · P. Gupta (✉)
Department of Mechanical and Automation Engineering, A.S.E.T.,
Amity University, Uttar Pradesh, Noida, India
e-mail: pgupta7@amity.edu

Z.H. Khan (ed.), *Recent Trends in Nanomaterials*,
Advanced Structured Materials 83, DOI 10.1007/978-981-10-3842-6_2

(b) severity of material removal. Nonetheless, on the basis of mechanism employed, it can be extensively arranged in four principle forms:

(a) Adhesive wear
(b) Abrasive wear
(c) Corrosive wear
(d) Fatigue wear

2.2.1 Adhesive Wear

Adhesive wear takes place as a result of micro-junctions produced by welding between two contrasting severities on rubbing surfaces of the counter frames. Load that is applied to the contacting severities is so great that they distort and stick to each other forming micro-joints. Motion of two rubbing counter bodies leads to the generation of rift in between the micro-joints. Welded particle ruptures in the non-deformed regions, thereby leading to transportation of some parts by its counter body. This effect is called as galling or scuffing. At the point when a significant area of the rubbing surfaces adheres, a seizure effect is produced.

There are numerous mechanisms that are present for the development of wear particles. Archard's theory of sliding wear states that shearing of the severity junctions can occur in one of the two bodies depending upon the relative magnitude of interfacial adhesion strength and the shearing strength of surrounding native regions. Fragments of wear occur due to such shearing, whereas, when shearing occurs along the interface, no wear occurs. In another mechanism, the detachment of wear fragments results from the plastic shearing of successive layers of an asperity contact. Due to adhesion, the separated fragment may be conveyed to the mating surface. Furthermore, sliding also leads to the development of fragments. Attachment of fragments indicates that the bond between the surface and the fragment is strong, while the development of loose particles suggests that there is a weak bond between the mating surfaces. Owing to oxidation, chemical changes in the fragment occurs, which may decrease the adhesive strength and promote development of loose particles. Residual elastic energy of adherent fragments may sometimes be accountable for the development of loose particles. Fragment is heavily stressed when it is captured between the two mating surfaces and as the other surface continues to travel, only the residual elastic stresses are left behind. In case the elastic energy overcomes the adhesive energy in magnitude, then the fragment forms a loose wear particle.

A simple model of adhesive wear states that the amount of wear is directly proportional to the applied load (W) and the sliding distance (x) and is inversely proportional to the hardness (H) of the surface being worn away. The volume of wear v is given by

$$v = \frac{kWx}{H} \tag{2.1}$$

where k is a previously introduced wear coefficient dependent on the material pair and their surface cleanliness. The above Eq. (2.1) can be derived using Archard's law [1].

The factors which decrease adhesive wear are as follows:

- Harder rubbing materials.
- Lower load.
- Contaminated rubbing surfaces.
- Presence of solid lubricants.
- Anti-wear additives in oil.
- Presence of a lubrication oil.

2.2.2 Abrasive Wear

Abrasive wear also called cutting wear, takes place when a solid object is loaded against particles of a material that have a relatively greater hardness. This results in wedging, plowing, and cutting; an example of this problem is the wear of shovels on earth-moving machinery. The extent of abrasive wear is far bigger than realized. Abrasive wear takes place in the presence of hard particles [2]. There are a number of wear mechanisms acting in a sliding body which shows different properties [3].

Abrasive wear is caused by the path of relatively hard particles/asperities over a surface. A few well-known reasons of abrasive wear mechanisms are stated below:

Micro-cutting: It occurs when a hard particle cuts the softer material. Cut material is removed in the form of wear debris.
Micro-fracture: It generally occurs in brittle materials, e.g., ceramic material. The fracture of the worn surface occurs due to the merging of a number of smaller cracks.
Micro fatigue: When a ductile material is scraped by a blunt particle or asperity then the worn surface is repeatedly loaded and unloaded. In this case, the failure occurs due to fatigue.
Removal of material grains: It occurs in materials (i.e., ceramics) having relatively weak grain boundaries.

Different type of abrasive wear mechanisms are as follows:

Two-Body Abrasion

This wear mechanism occurs when two intermingling asperities are in physical contact, and where one of them is harder than other. Due to normal load, the harder asperities penetrate into softer surface and thus produce plastic deformations.

To slide, the material is displaced/removed from the softer surface by a combination of micro-plowing and micro-cutting.

Three-Body Abrasion

This type of abrasion occurs when a material is removed from a softer surface by hard loose particles, which are allowed to move and also slide over the surface, as they are not detained inflexibly. The hard particles might be created locally by oxidation or wear from the components of tribological framework. Iron oxides wear debris produced during adhesive wear brings on additional damage due to abrasion. Due to the influence of rolling, abrasive wear constant is lower in three body abrasion as compared to two-body abrasion.

From the estimations of wear constants, it is evident that the wear rate is lesser in three-body abrasion than in two-body abrasion. The reduction in three-body abrasion occurs due to energy consumed in rolling motion of free hard particles.

It was initially believed that abrasive wear due to grits or hard severities bears a resemblance to cutting by a series of file or machine tools. However, microscopic investigation has revealed that the cutting process is just estimated by the sharpest of grits and numerous other more subsidiary mechanisms involved. The particles or grits may expel material by micro-fracture, micro-cutting pulled out of individual grains [4] or fast-tracked fatigue by repeated deformations as outlined in the figure. In some practical applications such as polishing process, the abrasive particles are desired or useful since it produces refined or polished surfaces. The ridges made during abrasion process turn out to be flattened after some sliding distance and are fractured due to repeated cyclic system [5, 6].

Figure 2.1a represents cutting, where a sharp grit or hard asperity cuts the softer surface. The cut material is removed as wear debris. Fracture of the worn surface may occur, which is shown in Fig. 2.1b, if the scraped material is brittle, e.g., ceramic. In this case, wear debris is the consequence of crack intersection. When a ductile

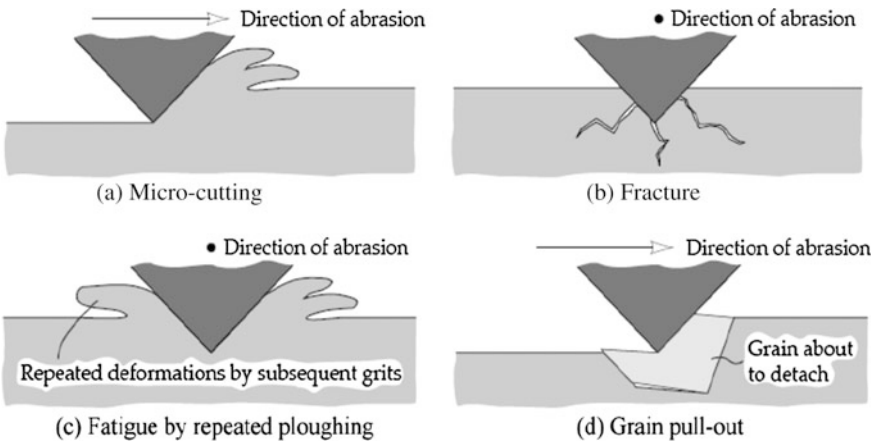

Fig. 2.1 Mechanisms of abrasive wear: micro-cutting, fracture, fatigue, and grain pullout [7]

material is scraped by a blunt grit then in this case, cutting is not likely and the surface that is worn is repeatedly deformed as shown in Fig. 2.1c. In this instance, wear debris is the outcome of metal fatigue. The final mechanism illustrated in Fig. 2.1d signifies grain pullout or grain detachment. This mechanism relates generally to ceramics, where there is a comparatively weak boundary between grains. In this mechanism, the complete grain is lost in the form of wear debris.

It has been found that the Archard wear equation derived for adhesive wear is also useful in the demonstration of abrasive wear. Consider, for an instance, the case of an abrasive surface that consists of conical severities of included angle α that plows through the surface of a softer material. Figure 2.2 illustrates abrasive wear by conical indentation. By travelling a distance x, the volume of the material removed is given by,

$$v = adx \tag{2.2}$$

But, $d = a \tan \alpha$
Therefore,

$$v = a^2 x \tan \alpha \tag{2.3}$$

Assuming that the material has yielded under normal load $= 1/2\pi\alpha^2 H$, where H is the hardness of the softer material. The volume of the displaced material in terms of load is expressed as:

$$v = \left(\frac{2W}{\pi H}\right) d \tan \alpha \tag{2.4}$$

Since it is observed that all traversals of abrasive wear do not produce loose wear debris, so Eq. (2.4) can be modified as

$$v = k\left(\frac{\tan \alpha}{\pi}\right) \frac{Wd}{H} \tag{2.5}$$

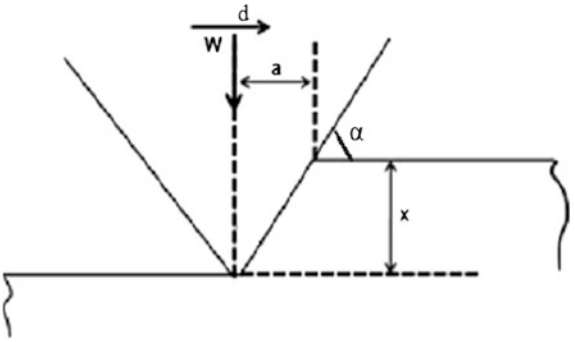

Fig. 2.2 Abrasive wear by conical indentation

where k is the proportion of events that actually result in the formation of wear particles, So

$$v = \frac{k_{\text{abr}} W d}{H} \tag{2.6}$$

where $k_{\text{abr}} = k \tan \alpha / \pi$ and is a non-dimensional wear coefficient that depends on the geometry of the abrading particle and usually ranges between 10^{-6} to 10^{-1}.

2.2.3 Corrosive Wear

When sliding prevails in a corrosive atmosphere, then it is known as corrosive wear. It is also known as chemical wear. Since the most corrosive medium in the air is oxygen, it is generally known as oxidative wear. The oxides, which are in the form of corrosive products, create a dense film on the surface, and sliding activity helps it to wear away the particles. In the non existence of sliding action, the film be likely to seize the corrosion. Thus, corrosive wear necessitates both the sliding action (rubbing) and chemical reaction (corrosion). Oxide film occasionally averts the metal-to-metal contact and hence diminishes against the stark adhesion-enhanced wear, which would otherwise occur. Corrosive wear is used in many industries such as mineral processing, mining, slurry handling, and chemical processing.

At higher temperature, oxygen can interact with the sliding surface and form oxides known as oxidative wear. For instance, oxidation of Inconel (nickel–chromium alloys containing some iron) occurs at 100 °C causing in the formation of chromium oxide (Cr_2O_3) and nickel oxide (NiO). However, when the temperature rises to 280 °C, the surface contains spinel of $NiFe_2O_4$ near the surface and Cr_2O_3 near the metal interface [8]. This results in the development of weak, mechanically incompatible corrosive or oxide layer.

In corrosive wear, tribo-chemical reaction yields a reaction layer on the surface. In the meantime, such type of layer is expelled with the help of friction. Finally, wear of reaction layers is determined by relative growth rate and removal rate of materials from the surface. In this way, representations of the reaction layer development and those of the layer removal turn out to be critical.

Archard has given a simple qualitative development of corrosive wear theory which shows the rate of wear and is given by the equation of the form

$$v = \frac{KW}{H} \tag{2.7}$$

where $K = K_3 \lambda / 2a$ is the wear coefficient, K_3 is the proportion of events which produce the wear particles, λ is the critical film thickness at which the film becomes unstable and $2a$ is the width of the asperity contact. The values of K_3 and λ are dependant on various mechanical, chemical and thermal variables.

2.2.4 Fatigue Wear

During repeated sliding and rolling, surface and sub-surface fatigue are observed, respectively. These are also termed as microscopic and macroscopic fatigue wears. Surface or subsurface cracks are formed due to repeated loading and unloading cycles. These cracks after a critical number of cycles result in the development of large fragments from the surface and leave large pits in the surface, which is known as pitting. The crack propagation depends on numerous factors. One of the important factors is the relative humidity in the air. Experimental reports suggest that the crack development occurs rapidly in high moisture environment rather than in dry air [9].

Before this final separation, minor wear occurs. In this respect, fatigue wear varies significantly from adhesive to abrasive wear, where gradual development of wear particles happens from the earliest point of running. In this way, the quantity of material expelled by fatigue wear is not vital, but rather furthermore pertinent is the useful life, in terms of number of cycles of operation before fatigue failure takes place.

2.2.4.1 Rolling Contact

Abrasive and adhesive wear mechanism is influenced by direct solid-to-solid contact and cannot function if a lubricating film separates the moving surfaces. There is no progressive noticeable wear due to abrasion or adhesion, but bearing life is restricted by fatigue, in case of a well-lubricated rolling element bearing. Although there exists no direct contact, the mating surfaces goes through large stresses that are transferred with the help of the lubricating film during the rolling motion. Due to the existence of such stresses, the maximum compressive stress occurs at the surface, while the maximum shear stress takes place at some distance underneath the surface. As rolling continues, the directions of shear stresses change sign and are accountable for energy dissipation in rolling contacts. Under high contact pressure in rolling element bearings, the amplitude of stress is above the fatigue limit of the bearing material which eventually causes fatigue failure. The materials used in rolling contact could be brittle as they are soft hardened, and this may result in crack formation at the surface and lead to surface fatigue.

The life (in millions of revolutions) for 90% of the bearings in a given population is determined by:

$$L_{10} = \left(\frac{C}{W}\right)^{p} \tag{2.8}$$

where

$p = 3$ for point contacts or ball bearings
$p = 10/3$ for line contacts or roller bearings

and C is the basic load capacity of the bearing defined as the load that 90% of the bearing can endure for 1 million revolutions under the specified running conditions, and W is the equivalent thrust or radial load.

2.2.4.2 Sliding Contact

Wear due to sliding contact occurs mainly due to abrasion and adhesion. Asperities can interact without abrading or adhering and can experience plastic deformation due to contact stresses. Cracks may nucleate at and under the surface as the deformation continues. Subsequently, due to loading and deformation, cracks outspread and propagate resulting in the formation of wear fragments at a critical number of contacts. In case of sliding contacts, the maximum shear stress occurs at the surface, which may results in surface fatigue. Rolling contacts are often accompanied by sliding and the friction stresses due to sliding which causes the maximum shear stress to be near the surface, and failure occurs due to near surface fatigue. Such type of failure often occurs in wheel rail contacts, cam roller followers, hypoid gear teeth, and in roller bearings.

2.3 Analysis of Wear Debris

The material that is detached from the worn surface has a form and shape and is the characteristic of the process that lead to its formation. In case of abrasive micro-cutting, the debris that is formed initially during run-in is in the form of finely machined chips. The debris that is formed during mild lubricated wear is in the form of a thin flake, whereas the ones formed during fatigue wear are more equiaxed. In fatigue wear, the propagation of cracks in rolling contacts is characterized by almost spherical particles and the concentration of these particles indicates the extent of propagation [10]. Thus, by monitoring the form and the amount of debris formed during the service period, we can deduce about the state of a pair of worn surfaces provided the collection of debris is before any mechanical or chemical change. By using various techniques we can find out the size, shape, structural and chemical details of particles:

1. Scanning electron microscopy (SEM)
2. Transmission and scanning transmission electron microscopy (TEM/STEM)
3. Optical microscopy
4. Auger electron spectroscopy (AES)
5. Energy dispersive and wavelength dispersive electroscopy (EDS/WDS)
6. X-ray photoelectron spectroscopy (XPS)
7. X-ray and electron diffraction, etc.

The study of the size of airborne particles is done by using particle counters, which is commonly based on the principle of scattering of light. Using Coulter principle, commercial counter particles are also available, where the debris is supported in midair with the help of electrically conductive fluid medium. This suspension is then allowed to flow through a small aperture with simultaneous flow of electric current which results in a series of pulses (proportional to the volume of the particle), which provides data that can be plotted in terms of collective particle frequency versus particle size.

Ferrography (invented by D. Scott in 1970) is a technique used in order to remove ferrous wear particle from a lubricant and analyze its arrangement according to the size with the help of a transparent substrate. A ferrography analyzer consists of the following: (a) a pump, (b) a magnet, and (c) a substrate. A pump is used in order to deliver the lubricant at a lower flow rate. The magnet provides a very high gradient magnetic field near its poles. The magnetic particles are deposited on a transparent substrate. With the help of bichromatic microscope, which uses both transmitted and reflected light, we can easily detect the magnetic particles. A direct reading ferrograph helps us to determine the operating condition of the machine by studying the size of the particles. Any increase or change in the severity wear indices denotes an abnormal wear mode.

2.4 Composites and Nanocomposites

When two or more materials are combined together to yield another material, they are known as composite materials. The two materials that combine to form the composite have very distinctive properties [11]. Composite materials generally show improved properties as compared to the base metal. Generally composites are made up of two materials. First is the matrix. It combines and ties together fragments or fibers of the other material, which is known as reinforcement. Some examples of composites are fiberglass, plywood, concrete, and fibrous composites made by combining different fibers such as Kevlar, glass, nylon and graphite.

Nanocomposites are those in which one or more phases are in the nanoscale dimensions: (a) Nanoparticles (b) Nanofibers, and (c) Nanoclays are embedded in a ceramic, metal, or polymer matrix. Nanocomposites were made in order to overcome the limitations of composite materials. Nanocomposites have small filler size and small distances between fillers which render to the high surface-to-volume ratio. They have increased ductility with no decrease in strength and scratching resistance [12]. They find a wide application in the food, medical and pharmaceutical industry. Nanocomposites have proved to be quite helpful in many uses that include producing batteries with greater power output, speeding up the healing process for broken bones, producing structural components with a high strength-to-weight ratio, making lightweight sensors with nanocomposites, flexible batteries, and making tumors easier to see and remove.

2.4.1 Classification of Composites

Composites can be classified based on various parameters; it can be classified based on the nature of reinforcement employed, for instance, fiber strengthened (l_f 0.1–250 mm, V_f up to 70%), dispersion strengthened (d_p = 0.01–0.1 mm, V_f 1–15%), and particulate strengthened (d_p > 1.0 mm, V_f 5–40%). Figure 2.3 shows the classification of composites.

Fiber-strengthened composites can be further classified into short fiber and continuous fiber (single layer composites), laminates, and hybrids (multilayer composites). Continuous fiber composites can be unidirectional or bidirectional, while discontinuous fiber composites can be categorized as random orientation and preferred orientation composites. It can also be classified on the basis of matrix material. Accordingly, there could be ceramic, polymer, metallic, intermetallic matrix composites etc. (Fig. 2.4).

2.4.1.1 Polymer Matrix Composites (PMCs)

Polymer matrix composites essentially consists of matrix of polymer and ceramic material as reinforcement. PMCs are additionally discovering its space in games merchandise such as tennis rackets, fishing rods, and bicycles and musical instruments such as guitars, violin bows, and woodwinds. Soft magnetic are also incorporating polymer matrix composites such as frequency convertors and sensor screens. Composite materials possess light weight property, which makes them a favorable choice for automotive parts. This is because fuel economy is automatically improved as the weight of the vehicle is reduced.

PMCs exhibit corrosion resistant properties, which make them suitable for marine application and other ground piping system and storage. Nowadays, PMCs are also

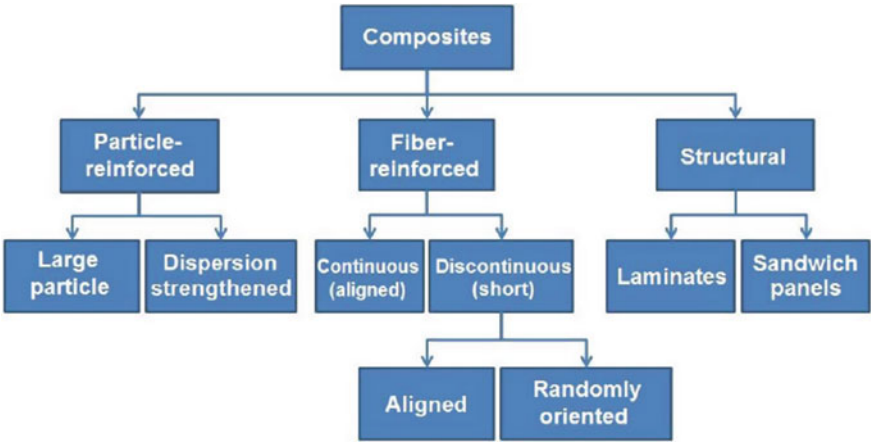

Fig. 2.3 Classification of composites

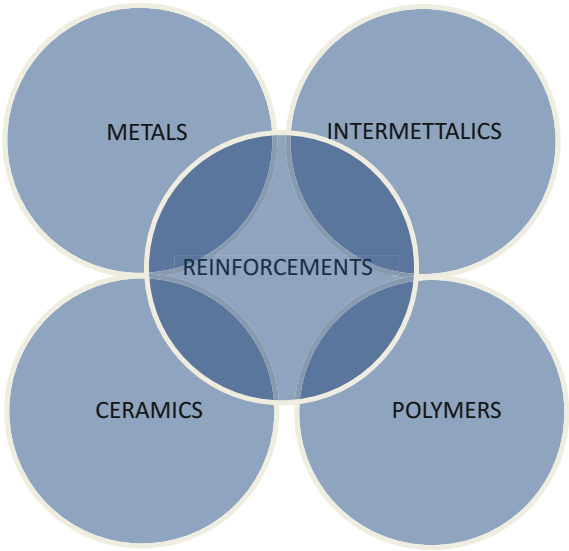

Fig. 2.4 Classification of composites according to matrix

used as a material in turbine blade production, especially for wind energy sector. Despite the fact that these composites possess a high structural properties and currently finds application in a large scale area, however, the main downside associated with these composites are that they are non-biodegradable in nature which has prompted the development of eco-friendly natural fiber polymer composites [13]. An advanced step in polymer matrix composite is the development of polymer matrix nanocomposite (PMNC). PMNCs has any of its constituent phase in nano size.

2.4.1.2 Metal Matrix Composites (MMCs)

When matrix is of metal and the reinforcement is of ceramic then it is essentially known as Metal matrix composites. Metal matrix composites are generating a wide interest in the research community. Yet they are not as widely used as their plastic counterparts. Metal matrices offer high stiffness, strength, and fracture toughness than those offered by their polymer counterparts. They have the ability to withstand high temperature in corrosive environment than polymer composites. Most metals and alloys could be used as matrices and they necessitate reinforcement materials which require stability over a wide range of temperature and should be non-reactive too. However, the determining factor for the decision depends mainly on the matrix material. In addition to the above-mentioned reasons, lighter metals form the matrix for temperature application and the reinforcements are characterized by high moduli. Most metals and alloys are said to be good matrices. However, practically, the varieties for low temperature applications are not many. Only light metals are responsive, because of their low density which proves to be an advantage. Aluminum, titanium, and magnesium are mainly useful for aircraft applications and

are the popular matrix metals which are currently in vogue. In case the metallic matrix materials have to offer high strength, they require high modulus reinforcements. The strength-to-weight ratios of resulting composites can be higher than most alloys. Service temperatures of composite are determined by the melting point, physical and mechanical properties of the composite at various temperatures. Most ceramics, metals, and compounds can be used with matrices of low melting point alloys. The decision for the reinforcements becomes more arrested, due to the increase in the melting temperature of matrix materials. Among matrix and ceramic, if any one is in nano size then it is called as Metal Matrix Nanocomposite (MMNC).

2.4.1.3 Ceramic Matrix Composites (CMCs)

In Ceramic matrix composite, the matrix as well as reinforcement both are of ceramic materials. Ceramics are defined as solid materials which display a very strong ionic bonding in general, and in few cases, covalent bonding. Stability at elevated temperatures, good corrosion resistance, high melting points, and high compressive strength are few of the properties which render ceramic-based matrix materials a favorite for applications necessitating a structural material that does not give way at temperatures above 1500 °C. Naturally, for high temperature applications ceramic matrices are the understandable choice. Most ceramics possess high modulus of elasticity and low tensile strain, which when combined causes the failure of attempts to add reinforcements to improve the strength. The reason being, at the stress levels at which ceramics rupture is that there is inadequate elongation of the matrix which keeps composite from transmitting an effective quantum of load to the reinforcement, and the composite may fail unless the percentage of fiber volume is sufficiently high. The resultant composite is improbable to have a superior level of strength, when ceramics have a higher thermal expansion coefficient than the reinforced material. If any of the phases in CMC is in nano size then it is called as Ceramic Matrix Nanocomposite (CMNC).

2.4.2 Advantages of Composites

Some of the advantages of composites are given below:

1. It leads to fuel savings due to higher performance for a given weight. Composite materials give a higher stiffness to weight and strength-to-weight ratios, which are expressed as stiffness (modulus) divided by density and strength divided by density.
2. The ply buildup and laminate patterns in a part can be custom-made to give the required mechanical properties in various directions.
3. It gives a reduced part count.
4. Since the composites can be produced by a wide variety of processes, so the production cost is reduced.

5. Composites offer excellent resistance to chemical attack, corrosion, and outdoor weathering. However, there are a few chemicals that are quite harmful to them (e.g., paint stripper). New types of strippers and paints are being cultivated to eradicate such problems. There are also a few thermoplastics that are not very resilient to some solvents.

2.4.3 Limitations of Composites

Some of the disadvantages of composites are as follows:

1. Expensive raw materials and high cost of fabrication.
2. Due to the brittle nature of composites than wrought metals, they are more likely to be damaged.
3. They have weak transverse properties.
4. Low toughness because of weak matrix.
5. Disposal and reuse might be problematic.
6. Not easier to fasten.
7. Repair presents different issues, because of the accompanying reasons:
   (i) Materials needs to be transported in refrigerated conditions and capacity should have a constrained time frame of realistic usability.
   (ii) Hot curing is vital in various instances which require special tooling.
   (iii) Hot or cold curing requires some investment.
   (iv) Analysis is troublesome.
   (v) Matrix is liable to environmental exploitation.

2.5 Wear of Metals, Ceramics and Polymers

2.5.1 Wear of Metals

High adhesion is observed in clean metals and alloys, when they are in contact with a solid surface, and thus high friction and wear is also observed. The wear rate can be very high in high vacuum. Chemical films are formed due to contamination and reduction in adhesion which results in the reduction of friction and wear. Galling and seizure result from high stresses in metal-to-metal wear tests even after a single cycle. In order to determine the galling stress, block and button galling test is carried out, where fresh samples are tested at gradually greater stress levels up until the beginning of galling. Galling generally appears as a score mark or a groove and the galling stress helps in determining the wear resistance of a given pair of material. Table 2.1 shows characteristic values of wear coefficients for various alike and unlike metals.

It is evident from the galling data that in terms of wear resistance, metal pairs do poorly as compared to dissimilar metal pairs. Wear resistance can be improved significantly when unlike metals are paired. Wear resistance can also be improved by changing the surface characteristics like by adding a coating or by surface treatment.

Table 2.1 Wear coefficient for metal pairs at normal load 20 N and sliding velocity 1.8 m/s Archard [14]

Metal pair	Wear coefficient k ($\times 10^{-4}$)	Vickers hardness (kg/mm^2)
Cd on Cd	57	20
Zn on Zn	530	38
Hg on Hg	40	43
Cu on Cu	110	95
Pt on Pt	130	138
M.S on M.S	150	158
Stainless steel on stainless steel	70	217
Cd on M.S	0.3	20
Cu on M.S	5	95
Pt on M.S	5	138
M.S on Cu	1.7	95
Pt on Ag	0.3	43

When the sliding of metallic pairs takes place under unlubricated conditions, interface temperature is formed at asperity contacts which results in thermal oxidation leading to oxide film formation. Severe wear can be prevented by the oxidation film. At low ambient temperatures, frictional heating leads to oxidation at asperity contacts. However, at high temperatures, general oxidation of the full surface takes place and influences wear. Oxidation of iron and many metals follows the parabolic law, where the oxide film thickness (h) and the average time (t) is related as, $h = ct^{1/2}$, where c is the parabolic rate constant at elevated temperature. Since the diffusion is thermally activated, during sliding, the growth rate in oxide film thickness depends on temperature that follows an Arrhenius type of relation

$$K_p = A\, e^{(-Q/RT)} \tag{2.9}$$

where K_p is the parabolic rate constant for growth of the oxide film, A is the parabolic Arrhenius constant for the reaction, Q is the parabolic activation energy associated with oxide, R is the universal gas constant, and T is the absolute temperature of the surface. The Arrhenius constant for sliding is found to be greater in magnitude than that for static conditions. This means that in under sliding conditions the oxidation is much more rapid than static conditions, and this occurs due to increased diffusion rates of ions through a growing oxide film.

A single wear map shows the effect of operating conditions, the various routines of corrosive and mechanical wear of some specific couple of rubbing materials plotted on the axes of sliding velocity (V) and the normalized pressure (p/H). The graph in Fig. 2.5 shows the wear map of soft carbon steel at room temperature. This map can be categorized into various wear regions with boundaries of contact pressure and sliding speed.

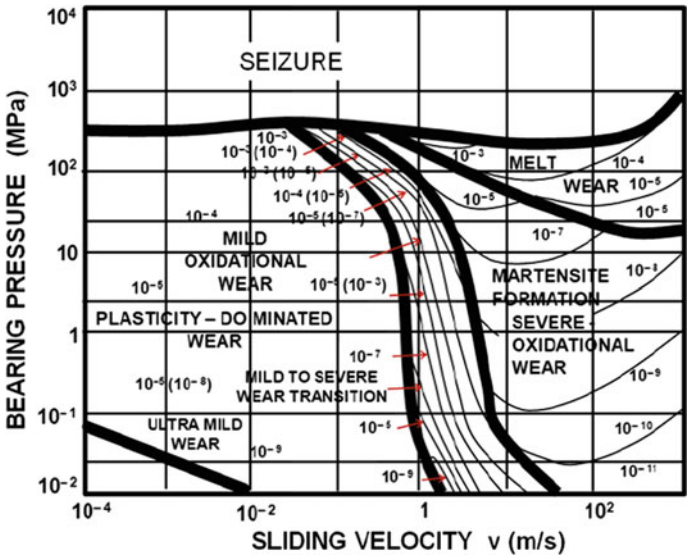

Fig. 2.5 Wear map for soft carbon steels [15]

2.5.2 *Wear of Ceramics*

Due to the nature of interatomic bonding, ceramic materials differ greatly from metals and this gives rise to a very restricted plastic flow at room temperature. Ceramics are more probable to react to stress by brittle fracture as compared to metals. In case of oxide ceramics, crack development is more likely to respond to environmental factors, which impacts the suppleness of dislocations of wear surface and thus effect plastic flow. This type of chemical and mechanical effect is called as the *Rehbinder effect*. Significant tangential forces results from unlubricated sliding of ceramics which may result in fracture rather than plastic flow. Tribo-chemical effects, plastic flow and fracture are involved in sliding wear mechanisms in case of ceramics. Transition among systems ruled by each of these usually results in severe changes in the wear rate with respect to sliding speed, load, or environmental conditions.

Mild wear in case of ceramics is linked with even surfaces, lower wear rate, steady friction traces, subtly distributed wear debris, and mechanisms of wear ruled by tribo-chemical reactions or plastic flow. Critical wear leads to high rate of wear, besides angular wear debris, rough surface, an unstable friction trace, and systems of wear ruled by brittle intergranular fracture. Ceramic materials confirm Archard's law too. For engineering ceramics experiencing critical or severe wear, the non-dimensional wear coefficient varies from 10^{-4} to 10^{-2}, which for mild wear varies from 10^{-6} to 10^{-4}.

Figure 2.6 shows the influence of sliding speed on wear rate in Si_3N_4. At low speed, Si_3N_4 forms a surface layer in moisture, and hence, this delivers the

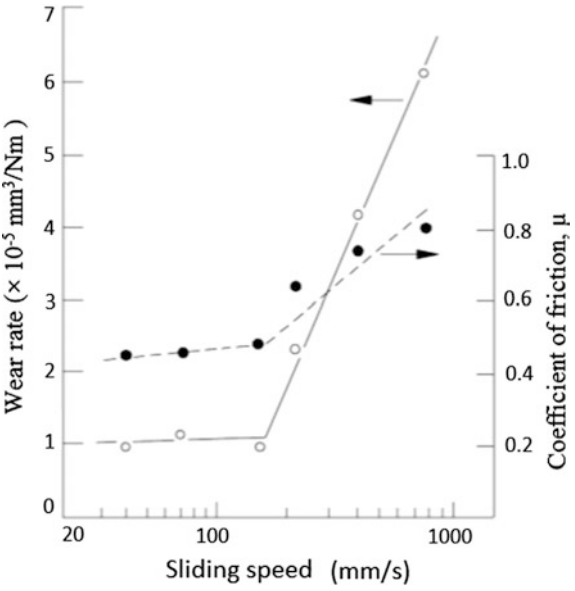

Fig. 2.6 Coefficient of friction and wear rate as a function of sliding velocity of hot-pressed silicon nitride on itself at a normal load of 10 N and ambient air tested using a pin-on-disc rig [16]

foundation for wear debris. Coefficient of friction is reduced as the shear strength of this layer is lower than the bulk ceramic. When the speed is upraised, the tribo-chemically reacted layer ceases to provide safeguard and the coefficient of friction increases. As the surface shear stress increases, it leads to cracking, and a transition occurs from mild wear-to-severe wear. The surface roughness also increases which leads to the increase in coefficient of friction.

2.5.3 Wear of Polymers

In comparison to metal and ceramic pairs, polymers (elastomers and plastics) show low friction and moderate wear. Adhesive, abrasive and fatigue wear shows dominant wear mechanisms. When the mating surfaces are smooth, adhesive wear occurs. In cases, where the sliding of polymers occurs against a rough surface, the wear mainly occurs by abrasive mechanism. Fatigue mechanism occurs in harder polymers such as thermosetting plastics, where sliding takes place against a smooth surface. The asperity malformation in polymer is generally elastic, and the wear caused by fatigue occurs as an outcome of development of cracks accompanying predominant elastic deformation. Crack transmission and consequent intersection of cracks leads to the formation of wear particles.

Polymers flow smoothly at moderate pressure and temperature. Hence, polymer and polymer composites are employed at lower speed, load, and temperature as compared to ceramics and metals. Due to low thermal conductivities, polymers lead to high interface temperatures, which are a function of the product of normal

pressure (P) and sliding velocity (V). Hence, polymers are used depending upon a PV limit, beyond which they begin to melt at the interface leading to rapid increase in wear rate. Polymers are known to be highly tolerant toward abrasive particles and are usually insensitive to corrosive environments. However, in case of some fluids, they tend to react with degradation in mechanical properties. In case of polymer composites, the wear rate is affected by the orientation of the fibers. Wear rate is affected by the surface roughness of the mating material, and its location with respect to the orientation of sliding. Exposure to environment also affects mechanical properties as well as friction and wear of polymers. Liquid lubricant interacts with polymers in different ways. For instance, in glassy thermoplastics, liquid lubricants causes improved plasticity of the surface leading to wear reduction, whereas the same polymer can experience cracking or stress grazing in different liquids, leading to greatly enhanced wear.

2.6 Factors Affecting Reduction of Wear

Wear cannot be completely eliminated when the surfaces are in relative motion. It can only be reduced to a trivial level. If the rate of expected wear is objectionable, a designer should change the system in some possible way so as to reduce wear [17, 18]. The rate of wear in a specific system is administered by the collaboration of numerous factors, which can be recognized and divided into two groups:

(a) The operating variables.
(b) The structure of the mechanical system.

The structure is defined by nature of any material present at the interface, environment and the materials making up the surfaces that are in relative motion. The operating variable involves the conditions imposed on the system during operations such as temperature, speed, and load. All these factors influence the wear rate and the designer can control most of them. Wear in a system can be controlled or reduced by changing the operating variables, by proper lubrication and by appropriate selection of materials and their surface properties. All these are performed in their so-called systems approaching to wear analysis.

2.7 Wear Behavior of Fe–Al_2O_3 Metal Matrix Nanocomposites

In the present chapter, wear behavior of Fe–Al_2O_3 metal matrix nanocomposites synthesized via powder metallurgy technique has been discussed. Specimens for the present study have been prepared by weighing the composition, ball milling, compaction, and sintering in argon atmosphere [19]. Sintering of 5% Al_2O_3 reinforced specimen was carried out in the temperature range of 900–1100 °C for

1–3 h, respectively [20]. Few specimens were also synthesized by adding cobalt oxide as dopant in iron-10% Al_2O_3 composites. Wear behavior of the nanocomposites was carried out using pin-on-disc wear and friction testing machine. Sliding velocity of 4 m/s was used in the present study. Following results were drawn from the present study:

(1) In Fe-5% Al_2O_3 metal matrix nanocomposite specimens, there was a formation of iron aluminate ($FeAl_2O_4$) phase due to the reactive sintering between iron (Fe) and alumina (Al_2O_3) particles [21].
It was revealed from the study that adhesive wear occurred at lower loads while abrasive wear took place at higher loads. It was found that the overall wear from the specimen surface was extremely low whether it be adhesive wear or abrasive wear. Figure 2.7 shows the wear rate versus load plots for the specimens 5AFe1000(1), 5AFe1000(2), and 5AFe1000(3). The amount of wear from the specimens sintered for 1, 2, and 3 h at 1000 °C is almost the same, and its values are less as compared to the specimens sintered at 900 °C.

(2) In Fe-10% Al_2O_3 nanocomposite specimens, it was revealed that the amount of iron aluminate phase has increased as compared to that of 5% Al_2O_3 reinforcement. It was found that in the present case that the wear mechanism maps are generated due to the microploughing effect.

(3) In cobalt oxide doped Fe-10% Al_2O_3 nanocomposite specimen, it was found that there is a reduction in the iron aluminate phase. Figure 2.8 shows the wear rate versus load plot for specimen (a) 10AFe0.5Co1100(1), (b) 10AFe1.0Co1100(1), and (c) Pure Fe + 0.5% CoO. Adhesive wear takes place at lower loads, whereas abrasive wear dominates at higher loads. For the 0.5% doped Cobalt oxide specimen [10AFe0.5Co1100(1)] up to a load of 1.5 kg, the adhesive wear occurred, but at 2.0 kg, load the wear behavior was abrasive in nature.

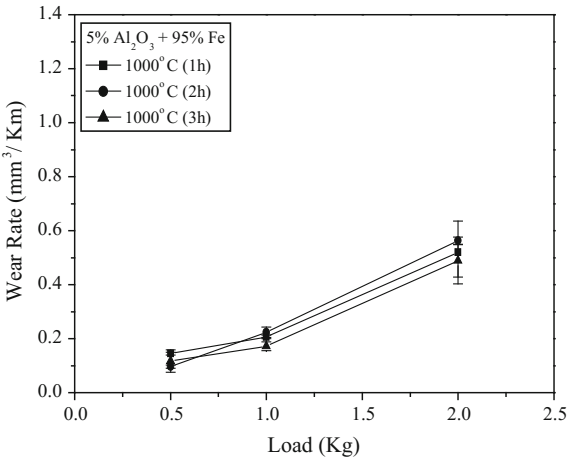

Fig. 2.7 Wear rate versus load for specimens sintered at 1000 °C [21]

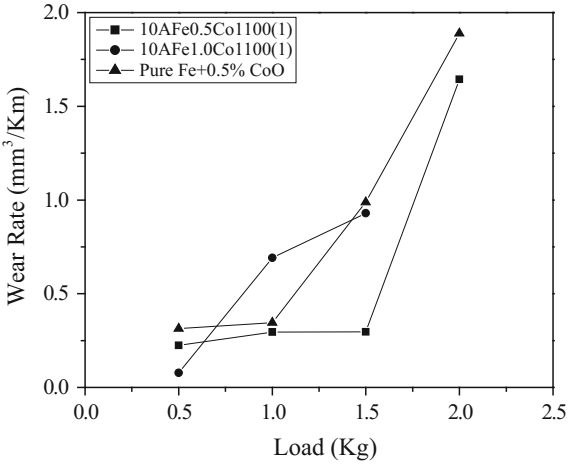

Fig. 2.8 Wear rate versus load plot for specimen **a** 10AFe0.5Co1100(1) **b** 10AFe1.0Co1100(1) and **c** pure Fe+0.5% CoO [22]

On the other hand, 1.0% cobalt oxide doped specimen [10AFe1.0Co1100(1)] showed the abrasive wear under all loads. This may also be reason for failure of the specimen during wear test at 2.0 kg load. Pure iron specimen doped with 0.5% cobalt oxide shows the highest amount of wear [22].

References

1. P. Sahoo, *Engineering Tribology* (PHI Learning Private Limited, New Delhi, 2005)
2. C.W. Bunn, E.R. Howells, Structures of molecules and crystals of fluorocarbons. Nature **174**, 549–551 (1954)
3. M.M. Khruschov, Principles of abrasive wear. Wear **28**(1), 69–88 (1974)
4. C.M. Pooley, D. Tabor, Friction and molecular structure: the behaviour of some thermoplastics. Proc. Roy. Soc. London. Ser. A **329**, 251–274 (1972)
5. K.J. Stout, T.G. King, D.J. Whitehouse, Analytical techniques in surface topography and their application to a running in experiment. Wear **43**, 99–115 (1977)
6. N.P. Suh, *Tribophysics* (Prentice-Hall Inc., Englewood Cliffs, 1986)
7. A.F. Offringa, Thermoplastic composites—rapid processing applications. Comp. Part A: App. Sci. Manuf. **27**(4), 329–336 (1996)
8. N.S. McIntyre, D.G. Zetaruk, D. Owen, XPS study of initial growth of oxide film on Inconel 600 alloy. App. Surf. Sci. **2**, 55–73 (1978)
9. K. Endo, H. Goto, Effects of environment on fretting fatigue. Wear **48**, 347–367 (1978)
10. P. Gupta, D. Kumar, M.A. Quraishi, O. Parkash, Corrosion behavior of Al_2O_3 reinforced Fe metal matrix nanocomposites produced by powder metallurgy technique. Adv. Sci. Engg. Med. **5**(4), 366–370 (2013)
11. P. Gupta, D. Kumar, O. Parkash, A.K. Jha, Structural and mechanical behavior of 5% Al_2O_3 reinforced Fe metal matrix composites (MMC) produced by powder metallurgy (P/M) route. Bull. Mater. Sci. **36**(5), 859–868 (2013)

12. P. Gupta, D. Kumar, M.A. Quraishi, O. Parkash, Effect of cobalt oxide doping on the corrosion behavior of iron-alumina metal matrix nanocomposites. Adv. Sci. Engg. Med. **5** (12), 1279–1291 (2013)
13. R. Roy, R.A. Roy, D.M. Roy, Alternative perspectives on "quasi-crystallinity": non-uniformity and nanocomposites. Mater. Lett. **4**(8–9), 323–328 (1986)
14. J.F. Archard, Contact and rubbing of flat surfaces. J. Appl. Phys. **24**, 981–988 (1953)
15. S.C. Lim, M.F. Ashby, Wear-mechanism maps. Acta Metall. **35**(1), 1–24 (1987)
16. H. Ishigaki, I. Kawaguchi, M. Isawa, Y. Toiba, in *Wear of Materials*, ed. by K.C. Ludema (Springer, New York, 1985)
17. I. Dinaharan, N. Murugan, Dry sliding wear behavior of AA6061/ZrB_2 in-situ composite. Trans. Nonferrous Met. Soc. China **22**, 810–818 (2012)
18. P. Gupta, D. Kumar, M.A. Quraishi, O. Parkash, Influence of processing parameters on corrosion behavior of metal matrix nanocomposites. J. Mater. Env. Sci. **7**(7), 2505–2512 (2016)
19. P. Garg, P. Gupta, D. Kumar, O. Parkash, Structural and mechanical properties of graphene reinforced aluminum matrix composites. J. Mater. Env. Sci. **7**(5), 1461–1473 (2016)
20. P. Jha, P. Gupta, D. Kumar, O. Parkash, Synthesis and characterization of Fe-ZrO_2 metal matrix composites. J Comp Mater **48**(17), 2107–2115 (2014)
21. P. Gupta, D. Kumar, O. Parkash, A.K. Jha, Effect of sintering on wear characteristics of Fe-Al_2O_3 metal matrix composites. Proc. Inst. Mech. Eng. Part J: J. Engg. Tribol. **228**(3), 362–368 (2014)
22. P. Gupta, D. Kumar, O. Parkash, A.K. Jha, Hardness and wear behavior of CoO doped Fe-Al_2O_3 metal matrix composite (MMC) synthesized via powder metallurgy (P/M) technique. J. Adv. Mater. Res. **585**, 584–589 (2012)

Chapter 3
Nanoparticles as Targeted Drug Delivery Agents: Synthesis, Mechanism and Applications

Rahisuddin, Pattan Sirajuddin Nayab, Akrema, Rizwan Arif and Mohammad Abid

3.1 Introduction

Efficient and targeted delivery of therapeutics to the desired location is a subject of substantial curiosity in chemotherapy. The administration of a therapeutic agent into the body might be toxic to many cell or tissue types; therefore delivering the drug specifically into the diseased cell without disturbing normal cells remains a major challenge in chemotherapeutics [1]. To address this fundamental task, significant effort has been and continues to be for the development of drug carriers which deliver chemotherapeutic drugs to the desired locations. Modern research attempts targeted drug delivery systems to overcome the limitations of conventional drug delivery system such as nonspecific bio-distribution and low therapeutic efficacy and inconvenient dosing (Fig. 3.1). Moreover, controlled release targeted drug delivery systems ensure cell/tissue specific targeting for a desired period of time leading to the minimization of drug side effects, higher therapeutic efficiency, and improved drug bioavailability. This method of approach has fascinated significant interest in the field of medicine since reducing drug consumption considerably reduces the effective cost of drug which in turn provides financial relief to the patients. As drug development is a both expensive and time-consuming process, scientists focused on drug delivery formulations which involve low cost research compared to discovering new drug candidates.

Rahisuddin (✉) · P.S. Nayab · Akrema · R. Arif
Department of Chemistry, Jamia Millia Islamia, New Delhi 110025, India
e-mail: rahisuddin@jmi.ac.in

M. Abid
Department of Biosciences, Jamia Millia Islamia, New Delhi 110025, India

M. Abid
Eppley Institute for Research in Cancer & Allied Diseases, University of Nebraska Medical Center, Omaha, NE, USA

Z.H. Khan (ed.), *Recent Trends in Nanomaterials*,
Advanced Structured Materials 83, DOI 10.1007/978-981-10-3842-6_3

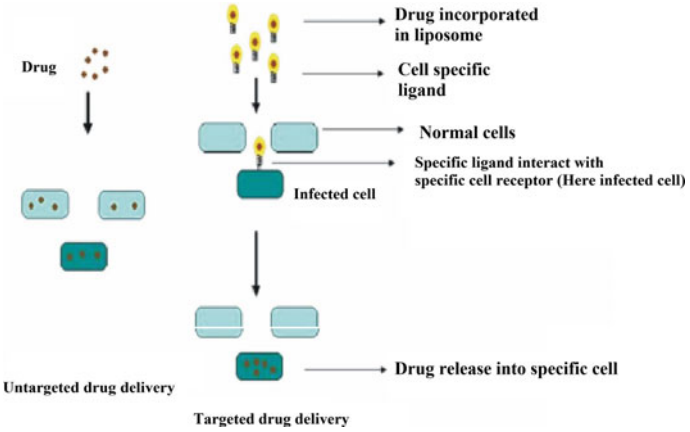

Fig. 3.1 Conventional and targeted drug delivery systems. Reprinted with permission from [1] © 2002, Elsevier

3.2 Targeted Drug Delivery

To achieve prolonged therapeutic efficacy researchers have developed different approaches to design delivery systems which continuously release the active ingredients over an extended time period after administration of single dose. Over the past three decades, sustained or controlled drug delivery systems (CDDS) have made significant progress in pharmaceutical formulations which offer several advantages over conventional therapy. CDDS maintain constant supply of therapeutic agent at—different intervals whereas sustained-release systems offer prolonged drug release at uniform intervals need not to maintain the same amount of drug release at every time.

An ideal controlled drug delivery system should offer the following features:

1. Predictable and prolonged drug release for extended durations
2. Better drug utilization, patient comfort, and compliance
3. It should maintain optimal drug plasma concentration with minimum fluctuation
4. It should enhance effective biological half-life of drugs
5. It should eradicate toxic side effects and frequent dosing.

A well designed drug delivery system deliver active pharmaceutical ingredient of desired concentration to the desired location for the accurate time and duration. The drug concentration should be within the therapeutic range, which is the concentration interval between the minimal effective concentration (MEC) and the minimal toxic concentration (MTC). Figure 3.2 displays the plasma concentration profile of different release dosage, forms after the oral administration of a drug. As

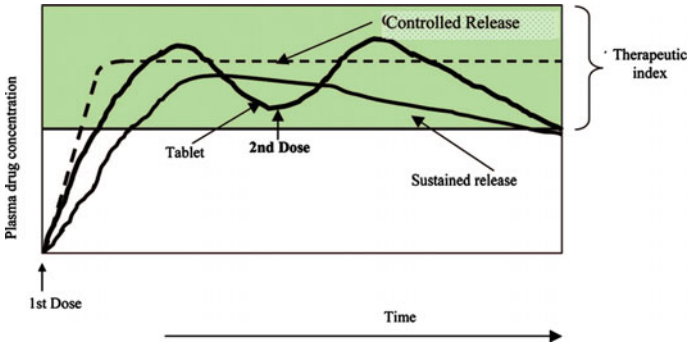

Fig. 3.2 Plasma concentration versus time profile of different-release dosage forms. Reprinted with permission from [2] © 2009, American Chemical Society

can be seen from the figure, in case of traditional tablets or injections, the plasma drug concentration rises after each first dose then reduces until the next dose while with controlled drug delivery system; the plasma drug level remains constant between minimum and maximum for extended duration [2].

3.3 Significance of Nanoparticles in Drug Delivery

Nanoparticles (NPs) are potential candidates for controlled drug delivery systems due to their distinctive properties such as nanoscale size, varied surface chemistry, and unique pharmacokinetics. NPs have great surface to volume ratio therefore can readily cross the cell membranes and penetrate deeply into tissues [3]. Recently, the emergence of nanoparticles as drug delivery vehicles has fascinated significant interest for researchers in the field of biology and medicine. They allow for drug delivery with longer circulation half-lives, passive targeting, reduced side effects, and enhanced permeability and retention (EPR) effect. The most important advantage of using NPs as drug carriers is their ability to enhance aqueous solubility of hydrophobic drugs which in turn improve drug systemic circulation and eradicates fast renal excretion of drugs [4]. Among the different carriers for drug delivery, biodegradable nanoparticles can offer many benefits such as improved encapsulation, increased bioavailability, controlled and targeted drug release with minimal toxicity.

NPs exhibit greater accumulation at disease tissues than normal ones due to the EPR effect (passive targeting) [5]. Attempts were also done for the modification of biological species such as DNA, peptides, antibodies, proteins and aptamers (active targeting) in order to bind with targetable receptors present on the target cell surface [6]. Such an active targeting strategy can enhance therapeutic efficacy of a drug by facilitating cellular uptake and intracellular retention of the drug carriers [7]. The

Table 3.1 Advantages and limitations of nanoparticulate drug delivery systems

Advantages
High stability and carrier capacity
Improved bioavailability and biodistribution
Reducing toxicity by means of biodegradable nanocarriers
Targeted delivery of therapeutic agents at cellular and nuclear level
Lowers the frequency of drug administration
Capability to control or sustain the release of drug
Improving the aqueous solubility of hydrophobic drugs
Limitations
Cytotoxicity of NPs or their degradation products
Poor in vitro-in vivo correlation
Possibility of dose dumping

emergence of environmentally responsive NPs further improved NP therapeutic efficacy. These NP formulations respond to physiochemical changes within the microenvironments of organs, tissues, and cell organelles and release the drugs at target site [8]. Investigations are also going on different targeting strategies which deliver multiple therapeutic agents with single nanocarrier (Table 3.1).

3.4 Nanoparticle-Based Drug Delivery Platforms

Literature is enriched with a number of drug carriers for controlled drug release including liposomes, magnetic nanoparticles, dendrimers, polymer carriers, silica and gold nanoparticles, polymeric micelles and hydrogel nanoparticles.

3.4.1 Liposomes

The liposomes since their discovery have been of huge interest to scientists in the field of cosmetics, biology, and medicine [9]. Liposomes are considered as most frequently studied drug carriers owing to their unique properties such as composition, morphology, biodegradability, and simple method of preparation [10]. They are microscopic vesicles consists of an aqueous comportment enclosed by a hydrophobic lipid bilayer. Liposomes are amphipathic molecules comprise of hydrophobic tail and a hydrophilic head; therefore, they can trap both lipophilic and hydrophilic drugs. The therapeutic efficacy of hydrophilic small molecule drugs is limited because of their poor intracellular absorption. Such a limitation could be potentially overcome by means of colloidal drug delivery system [11]. Although liposomes are widely used as carriers of hydrophilic small drugs, their short blood

circulation time and low stability can limit their therapeutic efficacy. Several approaches have been developed to overcome this drawback including coating liposomes with polyethylene glycol or chitin derivatives, incorporation of cholesterol into liposomes, freeze drying and polymerization.

PEG coating stabilizes liposomes against aggregation and fusion leading to enhancement in the liposomal circulation half-life and improvement in liposomal drug delivery in vivo. Many efforts have been made to design modified liposomal formulations with surface-attached ligands including antibodies, transferring, folates, and peptides to recognize and interact desired cells. A number of liposomal products are currently undergoing clinical trials as drug carriers and a few are already been approved by the Food and Drug Administration (FDA). For example, Doxil, the first FDA approved nano-drug is formulated in PEGylated nano liposome. Several PEGylated liposomal formulated drugs are also in clinical use e.g. Camptothecin and PEPO2 [12]. Apart from PEG conjugated lipids, a number of FDA approved conventional and cationic liposomal-based drugs (daunorubicin, amphotericin B, Cytarabine and Marqibo) are currently in the market, with many more in clinical trials. Despite of their wide spread applications, the clinical translation of liposome assisted drug delivery therapies not yet progressed.

3.4.2 Dendrimers

Dendrimers are well-defined, highly branched structures, comprise of a central core, repeated branches emerging from the core and surface functional groups. They display a wide variety of attributes including mono dispersity, low compressibility, high aqueous solubility, nanoscale dimensions and shape enable them highly promising candidates for drug delivery. A dendrimer drug delivery takes place by any one of the following methods. (i) Non covalent encapsulation of drugs: incorporation of drug molecules (physically entrapment) into the internal structure of dendrimer (ii) Covalent drug-dendrimer conjugates: the functional groups present on the surface of dendrimer can offer efficient conjugation to other functionalities on drug molecules. The interior core of dendrimer can accommodate hydrophobic drugs while exterior surface hold hydrophilic drugs that enhances the solubility of poorly soluble contents. Dendrimers have several advantages over liposome-based gene vectors, including high density of terminal groups, ease of surface modification and high permeability [13]. A number of dendritic derivatives including polyamidoamine (PAMAM), poly(etherhydroxylamine) (PEHAM), poly (propylene imine) (PPI), poly(esteramine) (PEA), poly-L-lysine, melamine, and polyglycerol reported as drug delivery carriers [14]. Among them, PAMAM is most extensively studied dendrimer for biomedical applications because its cationic nature helps in binding with DNA at physiological pH. PAMAM-drug conjugates also have the ability to bypass intestinal epithelial efflux pumps. Although dendrimers have wide variety of applications as drug and gene delivery vehicles, their multi step synthesis procedure limit their advancement of clinical trials.

3.4.3 Magnetic Nanoparticles

Recently, magnetic nanoparticles (MNPs) have been extensively used to develop magnetic targeted drug delivery system (MTDDS) where in magnetic field is used as an external stimulus to enhance local drug concentration at target sites. Owing to their super paramagnetic properties, ultrafine size and biocompatibility MNPs have gained significant interest in the field of biology and medicine. The release rate of active pharmaceutical ingredients from MNPs is usually regulated by external magnetic field, therefore drug delivered in a controllable way with less toxicity to healthy tissues. Another important benefit of MNPs as drug vehicles originates from their capacity to induce heat when subjected to alternating magnetic field (magnetic fluid hyperthermia). This allows to trigger the release of a loaded drug or to cause cell death by temperature-induced apoptosis [4]. Furthermore, MNPs induce a negative T2 contrast during magnetic resonance imaging enabling them to serve as efficient contrast agents. The other potential advantages of super-paramagnetic NPs over traditional cancer therapies are minimal invasiveness, accessibility of hidden tumors and reduced side effects.

MNP-drug conjugates coated with inorganic (silica, gold) or organic materials (phospholipids, polysaccharides, peptides, and polymers) exhibited greater therapeutic efficacy than the free drug [15]. For example, the conjugates of chitosan-modified magnetic nanoparticles and tissue plasminogen activator protein exhibited remarkable thrombolytic activity. Moreover, when this conjugate is used in magnetically targeted pyrolysis of in-stent thrombosis it did not induce hemorrhagic complications which are frequently observed with traditional thrombolytic therapy. MNPs embedded in polymer capsules can be used to enhance the permeability of microcapsules by applying external magnetic fields, e.g. ferromagnetic Au-coated cobalt NPs were incorporated into the polymer walls of microcapsules. Applying external magnetic fields to these conjugates disturb the capsule wall structures which in turn enhances the permeability to macromolecules. The limited clinical use of MNPs as drug carriers is mainly due to their tendency to aggregate into large clusters. This limitation can be overcome by combining MNPs with synthetic or biological polymers which could prevent aggregation.

3.4.4 Hydrogels

Hydrogels are three dimensional networks of polymer chains attracted tremendous attention in control drug delivery. The utility of hydrogels as drug carriers can be esteemed by their ability to absorb and retain large quantities of water and their swelling behavior [16]. However, they will not dissolve in aqueous environment due to their cross-linked networks. The advantageous characteristics which make them promising drug delivery candidates are flexibility, high water absorptivity, hydrophilicity, and biocompatibility. The drugs loaded in the porous structures of

hydrogel matrix could be released in a controllable way over extended period of time. Recently, smart nanogels are particularly interesting in drug delivery owing to their responsiveness to external stimuli. Entrapment of different structures into hydrogels further improves their drug release patterns. For example, hydroxyethyl cellulose-based hydrogels entrapped with liposomes have been reported for efficient release of calcein. Despite these applications, difficulty in handling low mechanical strength, high cost and macroscopic dimensions of hydrogels limit their use for in vivo applications.

3.4.5 Polymeric Micelles

Self-assembly of amphiphilic block copolymers in aqueous medium resulted in the formation of polymeric micelles (PMs). They comprise of hydrophobic core which acts as a reservoir for lipophilic drugs and a hydrophilic shell provides stabilization in aqueous solution [17]. Polymeric micelle-based DDS have proven to be promising because of their following beneficial characteristics (i) solubilization of lipophilic moieties in hydrophobic core (ii) improved blood circulation time (iii) biocompatibility (iv) structural stability (v) low toxicity. The inner core of micelles can accommodate a large amount of hydrophilic drug molecules and the exterior shell serves as a barrier by preventing them dispersity aggregation [18]. Another significant advantage of PMs make them efficient drug carriers is their larger size which suppress or eliminate renal excretion. The drawbacks of using PMs as drug delivery vehicles are slow extravasation and difficulty in polymer synthesis.

A variety of drugs have been entrapped in micellar DDS in order to enhance the therapeutic efficacy e.g. DOX encapsulated monomethoxy PEG (mPEG)-b-P(CL) micelles were studied for anti-tumor activity against B16-F10 melanoma cells. This encapsulation allows the cellular uptake of drug which in turn enhances the DOX cytotoxicity. Some PM formulated drugs are currently in clinical trials e.g. Genexol-PM conjugates developed against pancreatic, ovarian, and gastric cancer. The poor aqueous solubility of Currculin (Cur) limited its clinical applicability. This limitation was overcome by Cur-loaded biodegradable mPEG-b-P(LA) micelles exhibiting remarkable antiangiogenic and antitumor activities over free Cur. It is well known that folic acid (FA) is an important targeting moiety for DDS as folate receptor (FR) is present on the surface of most of human cancer cells. Recently, PM-drug conjugates developed by conjugating PEG-bP(LGA)-DOX and FA-PEG-b-P(LGA) diblock copolymers and studied against antitumor activity. Interestingly, FA-targeted DOX-containing micelles were efficiently accumulated at target site and showed greater activity than free DOX or nontargeted PEG-b-P (LGA)-DOX micelle. The emergence of smart PMs which responds to the environmental signals and external stimulations further extend their potential as promising DDS.

3.4.6 Gold Nanoparticles

Gold nanoparticles (AuNPs) are ideal candidates to be used in DDS since they exhibited non toxicity and non-immunogenicity [19]. The use of gold NPs as drug delivery vehicles has several advantages including inertness, greater surface area, simple procedures for synthesis, structural stability and increased half-life of the drugs. In addition to that, they can be functionalized with different targeting moieties in that they offer useful complement to platinum-based drugs. Since AuNPs exhibit strong affinity to functional groups such as thiols, carboxylates, amines and phosphates, they can be readily conjugated with wide variety of molecules like amino acids, proteins, polymers, and drugs. As it is well known, gold is highly resistant to bacteria, AuNPs can be used to prevent the bacterial growth in infections. Furthermore, AuNPs have been used extensively in the diagnosis of cancer due to their optical and photophysical properties.

Most of the human cancer cells express a protein epidermal growth factor receptor (EGFR) on their surface. Since gold is a good heat conductor, radio frequency is used to heat the AuNPs which in turn heat cancer cells that can led to destroy the malignant tumors. Researchers conjugate AuNPs to an antibody for EGFR (Anti-EGFR) enable them to accumulate to cancer cells. A number of studies have been performed on the AuNP-based drug delivery systems. PEGylated AuNPs were conjugated with TNF-α, in order to enhance the tumor damage and reduce the systemic toxicity of TNF-α. Interestingly, this nanoparticle conjugate exhibited greater therapeutic efficiency than free TNF-α. Recently, Sershen's group focused on the development of photothermally-modulated drug delivery system from the composites of hydrogel and gold nanoshells. On irradiation at 1064 nm, these conjugates release active ingredients in controlled fashion [20]. The drawbacks of AuNP-based drug delivery strategies are their acute or chronic toxicity, exhibiting difficulties in vivo kinetics, biocompatibility and display weak optical signals compared to quantum dots.

3.5 Applications of Nanoparticles in Drug Delivery

Destroying biological pathogens is easy. The point is how to destroy them while sparing the host. This is especially obvious when dealing with cancer. Despite recent progresses in the diagnosis and treatment, lung cancer still remains the leading cause of death due to tumor where worldwide gastric cancer (GC) is the fourth most common malignant disease and the second leading cause of cancer mortality worldwide [21–24]. To critically evaluate treatment wait times in CRC (colorectal cancer) patients and identify clinical and systemic barriers to treatment even the complexities of cancer, chemotherapy frequently fails for many unknown reasons. Recent technological advances, including single cell genomic technologies, anti-mitotic drugs target the reorganization of microtubules, essential for proper cell division and proliferation. The epigenetic machineries have proven roles in a wide variety of cancers [25]. For patients with metastatic or recurrent GC, the evidence supports the use of chemotherapy to prolong survival and maintain quality of life.

Advances in the treatment of ovarian cancer over the past decade, have led to emphasize the concept of managing ovarian cancer as a chronic disease [26].

A variety of polymeric nanoparticles, including polymer conjugate complexes [27, 28], nanospheres [29–31], micelles [32–34], and dendrimers [35–37] have been developed to aid in the delivery of drugs to cancerous sites and have shown great efficacy against various types of cancers. Conjugation of drug molecules to the polymer backbone allows for precise drug loading and control over release kinetics [38]. Self-assembled nanospheres, micelles, and dendrimers loaded with therapeutic agents offer sustained and controlled release through surface or bulk erosion, drug diffusion through the polymer matrix, or environmental activation or stimulation [39]. By combining an imaging agent along with the encapsulated drug within a polymeric nano-particle, researchers have been able to achieve analysis of drug distribution and release at the target site in real time. The live evaluation of drug distribution provides assistance in predicting drug response and can better facilitate treatment regimens to be specifically tailored for each individual.

A recent study of polymer nanoparticles suggested the targeted delivery of drug to cancerous liver cells. The polymer nanoparticles were synthesized using D-α-tocopherol polyethylene glycol 1000 succinate and poly(lactide) and modified with polydopamine. Galactosamine was conjugated on prepared nanoparticles to enhance the delivery of docetaxel (DTX) via ligand mediated endocytosis [40]. The study of these modified functional polymer nanoparticles in vitro showed that coumarin 6-loaded nanoparticles have the highest cellular uptake efficiency in liver cancer cell line HepG2 than other tested nanoparticles. The in vivo biodistribution experiment the modified functional polymer nanoparticles targeted specifically to the tumor cells and on injecting DTX loaded polymer nanoparticles reduced the size of tumor significantly on hepatoma bearing nude mice. The authors investigated in vitro cellular uptake and cytotoxicity assay, found that Gal-pD-TPGS-PLA/NPs approach HepG2 cells via ASGP receptor mediated recognition, and significantly inhibits cell proliferation. Furthermore, DTX-loaded Gal-pD-TPGS-PLA/NPs reduced tumor size more evidently in vivo than Taxotere, DTX-loaded TPGS-PLA/NPs or pD-TPGS-PLA/NPs, or saline. Therefore, the prepared Gal-pD-TPGS-PLA/NPs could potentially qualify as a drug delivery system targeting liver cancers or other liver diseases.

Chitosan modified single walled carbon nanotubes (SWCNTs) were constructed for controllable release of doxorubicin, an anti-cancer agent [41]. For easy transmission of drug, the delivery vehicle, chitosan modified SWCNTs were cut and purified before use. The use of chitosan in the preparation of drug delivery vehicle makes the delivery vehicle more soluble and biocompatibility of single walled carbon nanotubes and increased surface activity to bind targeted molecule. The researchers found that the biocompatibility of DOX/FA/CHI/SWCNTs was greater than bare DOX. HCC cell line (SMMC-7721) cells were exposed to FA/CHI/SWCNTs for an hour and then cultured in fresh media for additional 72 h. The viability was maintained at 86% which itself confirms the biocompatibility of the delivery vehicle. According to author's expectations, the DOX/FA/CHI/SWCNTs induced serious cytotoxicity at even much lower dose than bare DOX. The synthesized formulation also possessed low systematic toxicity as after

intravenous injection of DOX/FA/CHI/SWCNTs increased the weight of mice while after injecting bare DOX the weight decreased significantly. This observation was in consistent with the toxicity of bare DOX and proves that DOX/FA/CHI/SWCNTs have lesser toxicity compare with bare DOX. The platelet level and aminotransferase were increased due to toxicity of bare DOX [42]. However, the platelet level and aminotransferase levels were much lower than bare DOX, indicating less toxicity and low damage to liver. Hence, the DOX-SWCNTs conjugate can easily bind with the tumor sites while bare DOX is nonspecific and DOX can easily enter into the cell due to cell membrane penetration ability of SWCNTs [43, 44].

A recent study was done to develop paclitaxel loaded self-assembled nanoparticles which were prepared by using the block copolymers synthesized by ß-poly (lactide) and poly(γ-glutamic acid) [45]. The prepared composite nanoparticles were conjugated by galactosamine. The galactosamine conjugated nanoparticles (Gal-P/Nps) were compared with available paclitaxel formulation drug in the market (Phyxol®). The release profile of paclitaxel drug was almost same in the case of both P/NPs and Gal-P/NPs and it was almost a burst (Fig. 3.3a). The cell

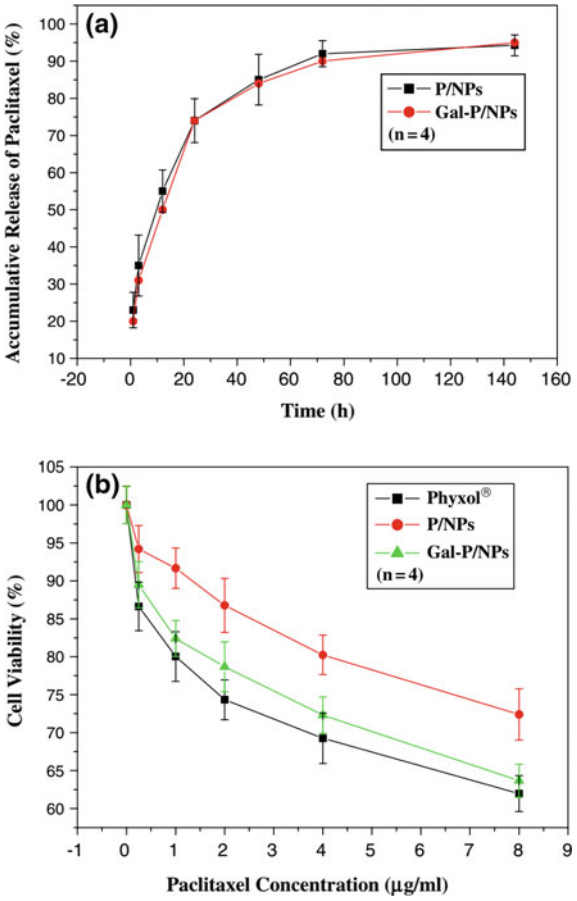

Fig. 3.3 **a** Release profiles of paclitaxel from the P/NPs or Gal-P/NPs; **b** viability of HepG2 cells treated with distinct paclitaxel formulations with varying paclitaxel concentrations. *Phyxol®* cells treated with a clinically available paclitaxel formulation; *P/NPs* cells treated with the paclitaxel-loaded NPs without galactosamine conjugation; and *Gal-P/NPs* cells treated with the paclitaxel-loaded NPs with galactosamine conjugation. Reprinted with permission from [45] © 2006, Elsevier

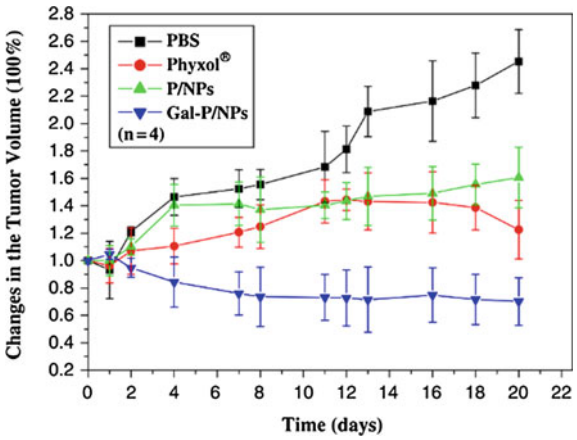

Fig. 3.4 Changes in the tumor volume of the hepatoma-tumor-bearing nude mice injected with distinct paclitaxel formulations. *PBS* mice injected with PBS; *Phyxol*® mice injected with a clinically available paclitaxel formulation; *P/NPs* mice injected with the paclitaxel-loaded NPs without galactosamine conjugation; and *Gal-P/NPs* mice injected with the paclitaxel-loaded NPs with galactosamine conjugation. Reprinted with permission from [45] © 2006, Elsevier

viability of Gal-P/NPs was comparable with the paclitaxel drug while the P/NPs showed very less cell viability (Fig. 3.3b). The author inspected the growth of tumor for 20 days in nude mice injected with PBS (control) and different paclitaxel formulations (Fig. 3.4). It was observed that the size of tumor increased significantly, which means control have no effect on tumor growth prevention. However, the other formulations inhibited the growth of tumor as compared to control. The drug loaded Gal-P/NPs group showed most significant inhibition of tumor growth among all the groups tested. The Gal-P/NPs targeted actively to the tumor sites and subsequently released the encapsulated paclitaxel which resulted in the inhibition of tumor growth. All the groups have shown the weight loss of nude mice except Gal-P/NPs group because all other formulation affected tumor cells as well as normal cells. The Gal-P/NPs formulation can be used in hepatoma tumor via the ASGP receptor-mediated recognition and may be used in liver cancer.

Lung cancer is also a major concern today and there are several bacterial species which are associated with it like *Staphylococcus aureus*, *Pseudomonas aeruginosa*, *Burkholderia cepacia*, and *Haemophilus influenza* etc. However, the available drugs in the market have many side effects to the healthy cells. In recent years, smart lipid nanoparticles have been developed as a potential system for lung delivery [46–48] due to its nontoxic, biodegradable, small size and physiochemical properties [49]. Some researchers have selected levofloxacin as the antibiotic mode for encapsulation due to its strong toxicity towards *P. aeruginosa* [50]. Although, levofloxacin is safe antibiotic among quinoline drugs, its prolong use or higher consumption may result in serious nephrotoxicity after oral dose [51]. The lipid myristyl myristate was chosen by the researchers to encapsulate levofloxacin. The properties of smart lipid nanoparticles can be improved by incorporating them into

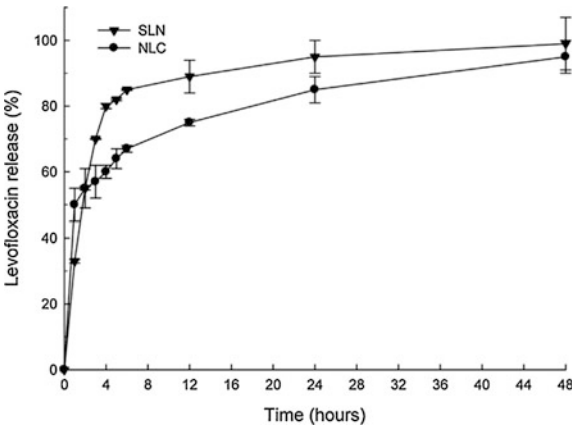

Fig. 3.5 Release profiles of Levofloxacin from smart lipid nanoparticles (SLN) and nanostructured lipid carrier (NLC) formulation (4.0 μg/ml of initial levofloxacin). Errors: SD, $n = 3$. Reprinted with permission from [50] © 2016, Elsevier

new generation of nanoparticles called nanostructured lipid carriers [52]. It has been shown that lipid nanoparticles had controlled release for about 48 h (Fig. 3.5) which help to reduce the high concentration of drug in the body and beneficial to the patient's comfort. The smart feature of these nanoparticles is the dual capability to deliver an antibiotic and a hydrolytic enzyme of DNA to reduce the biofilm formation of the bacteria and increase antimicrobial activity which improves the fight against cystic fibrosis lung infection.

3.6 Conclusions

The drug delivery to the specific target cell or tumor is an instantly growing field among the researchers. The development of new drugs is a time taking and very complicated process while improving the performance of currently available drugs is a comparable easy task. Therefore, researchers are preferring targeted controlled drug delivery system to enhance the activity of available drug. The implication of nanoparticles as a drug delivery vehicle further improved the performance of drugs by utilizing the exceptional properties of nanoparticles like biocompatibility, ability to encapsulate, aqueous stability, biodegradability, functionalization. Due to small dimensions, nanoparticulates are able to cross the blood-brain-barrier and operate on cellular level. These properties of nanoparticles are the leading attraction among scientists which are interested in the fabrication of novel multifunctional nanoparticles that can target tumor cells with more precision and specificity. Despite of having several advantages, nanoparticles formulations have some disadvantages too. The large number of functional groups on the surface of nanoparticles attach with the carrier only in a stoichiometric ratio. The oxidative stress and inflammation in different cell types have been often reported as toxic mechanisms of various types of nanoparticles. The sub-nanometer scale particles may remain in the cells and may induct chronic inflammatory response and fibrosis

of tissues. The nano drug delivery carrier should also be tested for safety in drug delivery and other biomedical applications. The drug carrier and its degraded products should ensure the safety of healthy cells. Therefore, a large amount of exploration should be done on the pharmacodynamics, metabolism in vivo, and nanocarriers are the future of medicine. Extensive research is needed to make the switching of these nano drug carriers from laboratory to market.

Acknowledgements Akrema greatly acknowledges the financial support from University Grants Commission in the form of BSR Fellowship. R. Arif also thanks to UGC for Major Research Project (F. No. 41-238/2012).

References

1. I. Brigger, C. Dubernet, P. Couvreur, Nanoparticles in cancer therapy and diagnosis. Adv. Drug Deliv. Rev. **54**, 631–651 (2002)
2. E.M. Martín del Valle, M.A. Galán, R.G. Carbonell, Drug delivery technologies: the way forward in the new decade. Ind. Eng. Chem. Res. **48**, 2475–2486 (2009)
3. A. Bansal, Y. Zhang, Photocontrolled nanoparticle delivery systems for biomedical applications. Acc. Chem. Res. **47**, 3052–3060 (2014)
4. K. Ulbrich, K. Holá, V. Šubr, A. Bakandritsos, J. Tuček, R. Zbořil, Targeted drug delivery with polymers and magnetic nanoparticles: covalent and noncovalent approaches, release control, and clinical studies. Chem. Rev. **116**, 5338–5431 (2016)
5. V. Torchilin, Tumor delivery of macromolecular drugs based on the EPR effect. Adv. Drug Deliv. Rev. **63**, 131–135 (2011)
6. H. Koo, S. Lee, J.H. Na, S.H. Kim, S.K. Hahn, K. Choi, I.C. Kwon, S.Y. Jeong, K. Kim, Bioorthogonal copper-free click chemistry in vivo for tumor-targeted delivery of nanoparticles. Angew. Chem. Int. Ed. **51**, 11836–11840 (2012)
7. E. Gullotti, Y. Yeo, Extracellularly activated nanocarriers: a new paradigm of tumor targeted drug delivery. Mol. Pharm. **6**, 1041–1051 (2009)
8. W. Gao, J. Chan, O.C. Farokhzad, pH-responsive nanoparticles for drug delivery. Mol. Pharm. **7**, 1913–1920 (2010)
9. X. Guo, F.C. Szoka, Chemical approaches to triggerable lipid vesicles for drug and gene delivery. Acc. Chem. Res. **36**, 335–341 (2003)
10. J. Lewandowska-Łańcucka, K. Mystek, A. Gilarska, K. Kamiński, M. Romek, B. Sulikowski, M. Nowakowska, Silicone-stabilized liposomes as a possible novel nanostructural drug carrier. Colloids Surf. B Biointerfaces **143**, 359–370 (2016)
11. J.O. Eloy, M. Claro de Souza, R. Petrilli, J.P.A. Barcellos, R.J. Lee, J.M. Marchetti, Liposomes as carriers of hydrophilic small molecule drugs: strategies to enhance encapsulation and delivery. Colloids Surf. B Biointerfaces. **123**, 345–363 (2014)
12. L. Sercombe, T. Veerati, F. Moheimani, S.Y. Wu, A.K. Sood, S. Hua, Advances and challenges of liposome assisted drug delivery. Front. Pharmacol. **6**, 286 (2015)
13. J. Hu, K. Hu, Y. Cheng, Tailoring the dendrimer core for efficient gene delivery. Acta Biomater. **35**, 1–11 (2016)
14. K. Madaan, S. Kumar, N. Poonia, V. Lather, D. Pandita, Dendrimers in drug delivery and targeting: drug-dendrimer interactions and toxicity issues. J. Pharm. Bioallied Sci. **6**, 139–150 (2014)
15. S.R. Mudshinge, A.B. Deore, S. Patil, C.M. Bhalgat, Nanoparticles: emerging carriers for drug delivery. Saudi Pharm. J. **19**, 129–141 (2011)

16. H.-Q. Wu, C.-C. Wang, Biodegradable smart nanogels: a new platform for targeting drug delivery and biomedical diagnostics. Langmuir **32**, 6211–6225 (2016)
17. Y. Shi, C.F. van Nostrum, W.E. Hennink, Interfacially hydrazone cross-linked thermosensitive polymeric micelles for acid-triggered release of paclitaxel. ACS Biomater. Sci. Eng. (2015) (150512181754006)
18. E.L. Cooper, TMU: brain injury. J. Exp. Clin. Med. **3**, 1–2 (2011)
19. S.D. Brown, P. Nativo, J.A. Smith, D. Stirling, P.R. Edwards, B. Venugopal, D.J. Flint, J.A. Plumb, D. Graham, N.J. Wheate, Gold nanoparticles for the improved anticancer drug delivery of the active component of oxaliplatin. J. Am. Chem. Soc. **132**, 4678–4684 (2010)
20. W. Cai, T. Gao, H. Hong, J. Sun, Applications of gold nanoparticles in cancer nanotechnology. Nanotechnol. Sci. Appl. **1**, 17–32 (2008)
21. U. Pliquett, Electrochemotherapy—a new way for enhancing cancer treatment. Chemother. **01** (2012)
22. Y. Chen, NEK1 protein kinase as a target for anticancer therapeutics. Chemother. **01**, e118 (2012)
23. C. Polenz, Adjuvant chemotherapy for colorectal cancer-timing is everything. Chemother. **02**, 110 (2013)
24. A.K. Maiti, Emerging biology of circulating tumor cells (CTCs) in cancer detection and chemotherapy. Chemother. **02** (2013); R. Alam, D. Wahi, R. Singh, D. Sinha, V. Tandon, A. Grover, Rahisuddin, Design, synthesis, cytotoxicity, HuTopoIIα inhibitory activity and molecular docking studies of pyrazole derivatives as potential anticancer agents. Bioorg. Chem. **69**, 77 (2016)
25. M.L. Thomas, K.M. Coyle, M. Sultan, A. Vaghar-Kashani, P. Marcato, Chemoresistance in cancer stem cells and strategies to overcome resistance. Chemother. **03** (2014)
26. R.S. Huang, Cancer epigenetics: mechanisms and crosstalk of a HDAC inhibitor, vorinostat. Chemother. **02** (2013)
27. A.A. Bogdanov, M. Mazzanti, G. Castillo, E. Bolotin, Protected graft copolymer (pgc) in imaging and therapy: a platform for the delivery of covalently and non-covalently bound drugs. Theranostics **2**, 553–576 (2012)
28. R. Duncan, Drug-polymer conjugates: potential for improved chemotherapy. Anticancer Drugs **3**, 175–210 (1992)
29. J.R. McCarthy, J.M. Perez, C. Brückner, R. Weissleder, Polymeric nanoparticle preparation that eradicates tumors. Nano Lett. **5**, 2552–2556 (2005)
30. C.-M.J. Hu, L. Zhang, S. Aryal, C. Cheung, R.H. Fang, L. Zhang, Erythrocyte membrane-camouflaged polymeric nanoparticles as a biomimetic delivery platform. Proc. Natl. Acad. Sci. U. S. A. **108**, 10980–10985 (2011)
31. A.K. Maiti, Emerging biology of circulating tumor cells (CTCs) in cancer detection and chemotherapy. Chemother. **02** (2013)
32. D.W. Kim, S.Y. Kim, H.K. Kim, S.W. Kim, S.W. Shin, J.S. Kim, K. Park, M.Y. Lee, D.S. Heo, Multicenter phase II trial of genexol-PM, a novel cremophor-free, polymeric micelle formulation of paclitaxel, with cisplatin in patients with advanced non-small-cell lung cancer. Ann. Oncol. **18**, 2009–2014 (2007)
33. R. Trivedi, U.B. Kompella, Nanomicellar formulations for sustained drug delivery: strategies and underlying principles. Nanomedicine (Lond). **5**, 485–505 (2010)
34. H. Xin, L. Chen, J. Gu, X. Ren, Z. Wei, J. Luo, Y. Chen, X. Jiang, X. Sha, X. Fang, Enhanced anti-glioblastoma efficacy by PTX-loaded PEGylated poly(ε-caprolactone) nanoparticles: in vitro and in vivo evaluation. Int. J. Pharm. **402**, 238–247 (2010)
35. K.T. Al-Jamal, W.T. Al-Jamal, S. Akerman, J.E. Podesta, A. Yilmazer, J.A. Turton, A. Bianco, N. Vargesson, C. Kanthou, A.T. Florence, G.M. Tozer, K. Kostarelos, Systemic antiangiogenic activity of cationic poly-L-lysine dendrimer delays tumor growth. Proc. Natl. Acad. Sci. U. S. A. **107**, 3966–3971 (2010)
36. I.J. Majoros, A. Myc, T. Thomas, C.B. Mehta, J.R. Baker, PAMAM dendrimer-based multifunctional conjugate for cancer therapy: synthesis, characterization, and functionality. Biomacromolecules **7**, 572–579 (2006)

37. R. Rupp, S.L. Rosenthal, L.R. Stanberry, VivaGel (SPL7013 Gel): a candidate dendrimer—microbicide for the prevention of HIV and HSV infection. Int. J. Nanomed. **2**, 561–566 (2007)
38. S. Aryal, C.-M.J. Hu, L. Zhang, Polymeric nanoparticles with precise ratiometric control over drug loading for combination therapy. Mol. Pharm. **8**, 1401–1407 (2011)
39. D. Peer, J.M. Karp, S. Hong, O.C. Farokhzad, R. Margalit, R. Langer, Nanocarriers as an emerging platform for cancer therapy. Nat. Nanotechnol. **2**, 751–760 (2007)
40. D. Zhu, W. Tao, H. Zhang, G. Liu, T. Wang, L. Zhang, X. Zeng, L. Mei, Docetaxel (DTX)-loaded polydopamine-modified TPGS-PLA nanoparticles as a targeted drug delivery system for the treatment of liver cancer. Acta Biomater. **30**, 144–154 (2016)
41. Z. Ji, G. Lin, Q. Lu, L. Meng, X. Shen, L. Dong, C. Fu, X. Zhang, Targeted therapy of SMMC-7721 liver cancer in vitro and in vivo with carbon nanotubes based drug delivery system. J. Colloid Interface Sci. **365**, 143–149 (2012)
42. B. Ihova, Cytostatic and immunomobilizing activities of polymer-bound drugs: experimental and first clinical data. J. Control. Release **91**, 1–16 (2003)
43. K. Kostarelos, L. Lacerda, G. Pastorin, W. Wu, S. Wieckowski, J. Luangsivilay, S. Godefroy, D. Pantarotto, J.-P. Briand, S. Muller, M. Prato, A. Bianco, Cellular uptake of functionalized carbon nanotubes is independent of functional group and cell type. Nat. Nanotechnol. **2**, 108–113 (2007)
44. L. Lacerda, S. Raffa, M. Prato, A. Bianco, K. Kostarelos, Cell-penetrating CNTs for delivery of therapeutics. Nano Today **2**, 38–43 (2007)
45. H.-F. Liang, C.-T. Chen, S.-C. Chen, A.R. Kulkarni, Y.-L. Chiu, M.-C. Chen, H.-W. Sung, Paclitaxel-loaded poly(gamma-glutamic acid)-poly(lactide) nanoparticles as a targeted drug delivery system for the treatment of liver cancer. Biomaterials **27**, 2051–2059 (2006)
46. S. Jaspart, P. Bertholet, G. Piel, J.-M. Dogné, L. Delattre, B. Evrard, Solid lipid microparticles as a sustained release system for pulmonary drug delivery. Eur. J. Pharm. Biopharm. **65**, 47–56 (2007)
47. J. Liu, T. Gong, H. Fu, C. Wang, X. Wang, Q. Chen, Q. Zhang, Q. He, Z. Zhang, Solid lipid nanoparticles for pulmonary delivery of insulin. Int. J. Pharm. **356**, 333–344 (2008)
48. J. Varshosaz, S. Ghaffari, S.F. Mirshojaei, A. Jafarian, F. Atyabi, F. Kobarfard, S. Azarmi, Biodistribution of amikacin solid lipid nanoparticles after pulmonary delivery. Biomed Res. Int. **2013** (2013)
49. N. Nafee, A. Husari, C.K. Maurer, C. Lu, C. De Rossi, A. Steinbach, R.W. Hartmann, C.M. Lehr, M. Schneider, Antibiotic-free nanotherapeutics: ultra-small, mucus-penetrating solid lipid nanoparticles enhance the pulmonary delivery and anti-virulence efficacy of novel quorum sensing inhibitors. J. Control. Release. **192**, 131–140 (2014)
50. G.A. Islan, P.C. Tornello, G.A. Abraham, N. Duran, G.R. Castro, Smart lipid nanoparticles containing levofloxacin and DNase for lung delivery. Design and characterization. Colloids Surf. B Biointerfaces. **143**, 168–176 (2016)
51. C. Carbon, Comparison of side effects of levofloxacin versus other fluoroquinolones. Chemotherapy **47**, 9–14 (2001)
52. C.-L. Fang, S.A. Al-Suwayeh, J.-Y. Fang, Nanostructured lipid carriers (NLCs) for drug delivery and targeting. Recent Pat. Nanotechnol. **7**, 41–55 (2013)

Chapter 4
Synthesis, Characterization and Applications of Graphene Quantum Dots

Jhih-Siang Yang, Dean Aidan Martinez and Wei-Hung Chiang

4.1 Introduction

Graphene quantum dots (GQDs) are zero-dimensional nanomaterials with lateral size below 100 nm [1–5]. Due to the graphene-based structure, it possesses similar physical and chemical properties to graphene including large surface area, high electronic mobility, non-toxicity and chemical stability. Besides, its nanoscale structure exhibits new phenomena due to quantum confinement and edge effects that give its distinct chemical, optical and physical properties, commonly nonzero bandgap [4] and photoluminescence [2, 6]. Based on these superior properties, GQDs attracted more attention and are applied in various fields such as bioimaging, drug/gene delivery, sensor, LED and solar cells [4, 6, 7]. The applications and its mechanism are described in Applications section in detail. Additionally, the tunable optical and physical properties by adjusting particle size and designing functional groups on GQDs make it become potential and versatile materials in different applications and theoretical research in recent years [8, 9].

4.2 Properties

4.2.1 Optical Properties

4.2.1.1 Photoluminescence

Photoluminescence is an appealing feature in GQDs materials. This characteristic is attributed to GQDs possessing semiconductor nature, which have typical bandgap

J.-S. Yang · D.A. Martinez · W.-H. Chiang (✉)
National Taiwan University of Science and Technology, Taipei, Taiwan
e-mail: whchiang0102@gmail.com

Z.H. Khan (ed.), *Recent Trends in Nanomaterials*,
Advanced Structured Materials 83, DOI 10.1007/978-981-10-3842-6_4

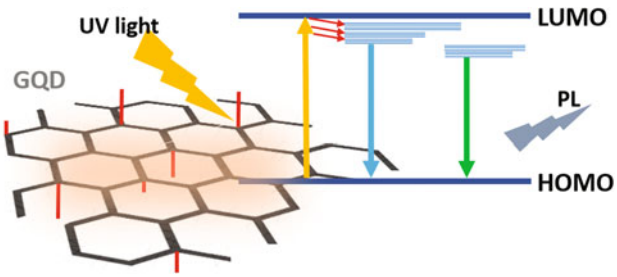

Scheme 4.1 The PL spectrum mechanism of GQDs

consisted of the highest occupied molecular orbital (HOMO) and lowest unoccupied molecular orbital (LUMO). Then, the PL spectrum can be considered as the electrons transition from the LUMO to HOMO [10]. Its mechanism is shown in Scheme 4.1. However, the bandgap is susceptible to GQDs quantum confinement and surface state such as emissive traps, functional groups, free zigzag sites and edge defects [11–13]. Those factors will change the energy density of GQDs and generate different energy levels. The typical phenomenon which is excitation-dependent PL emission could prove the various surface states and energy gaps [14–18]. Some groups attempt to interpret this phenomenon by different models [19–22]. However, there is no exact mechanism and consistent interpretation for excitation-dependent PL emission currently.

Here some researchers divided the effect factors into two main parts which are size structure and functional groups to discuss the PL phenomena. Ye et al. group presents two methods to synthesize GQDs with controllable particle size [9]. The bandgap corresponding to particle size could be observed in Fig. 4.1. In Fig. 4.1b, the particle size of GQDs decreased with increasing synthesis temperatures. Based on Fig. 4.1, the study shows that the bandgap will increase with decreasing particle size of GQDs. The small bandgap corresponded to orange luminescence shown in the inset of Fig. 4.1.

Additionally, in order to avoid other factors effect, a researcher fixes the surface state and changes the particle size of GQDs. Yeh et al. group presents a method to synthesize high-crystallinity and high-uniformity GQDs which have almost identical energy levels of oxygenated function groups, proven through theoretical calculations [23]. According to the different particle sizes, which corresponded to different sp^2 aromatic carbon structure, it will generate various bandgaps. The smaller particle size of GQDs will possess large $\pi \rightarrow \pi^*$ energy gap. It means the GQDs will emit higher energy, typically blue light. Additionally, the PL emission peak will generate redshift with increasing particle size. The diagram of bandgap and emission light is shown in Fig. 4.2. In accordance with above discussions, it could be found that a smaller size leads to a wider energy gap. It is typical size effect, also known as quantum confinement effect. This mechanism is a significant effect factor for PL emission and accepted widely by other researchers [17, 24, 25].

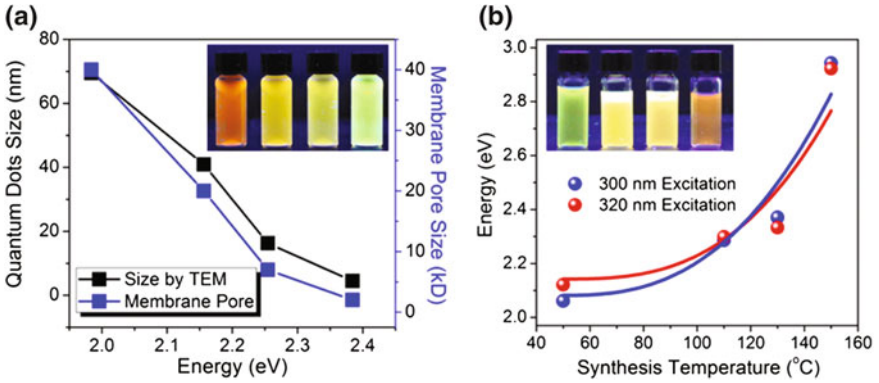

Fig. 4.1 **a** The energy gap corresponding to particle size of GQDs. **b** The peak intensities at 300 and 320 nm excitation wavelength from PLE contour map. Reprinted with permission from Ref. [9]. Copyright 2015, American Chemical Society

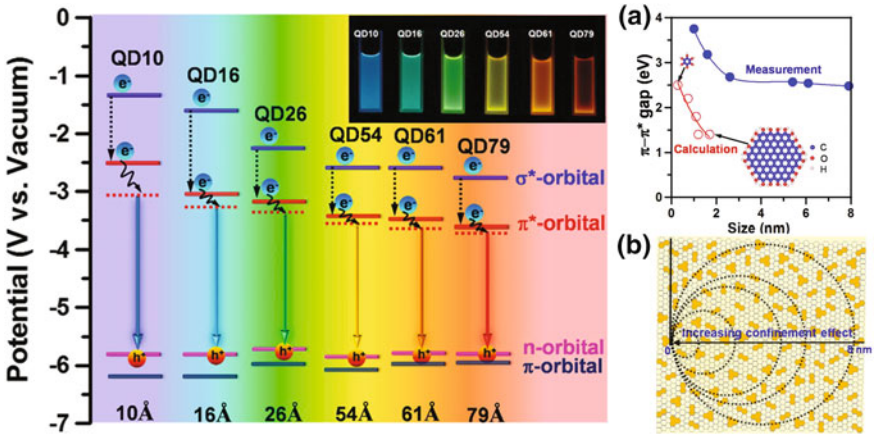

Fig. 4.2 The schematic of energy level corresponding to particle size of GOQD specimens. **a** Variation of the π–π* energy gap with the particle size for GOQDs. **b** Schematic of the mechanism underlying the decrease in the size of the continuous sp^2 phase, which surrounds the isolated sp^3 sites or islands, with a decrease in the diameter of the GOQDs. The *orange areas* represent oxygenated sp^3 sites or islands, which are homogeneously distributed in the basal plane of the GOQDs. Reprinted with permission from Ref. [23]. Copyright 2016, American Chemical Society

On the other hand, the effect of functional groups could be discussed following paper using carbon quantum dots (CQDs). Although the CQDs and GQDs have a little difference in structure such as crystalline and particle size, they almost have identical optical properties due to the structure limited by quantum confinement and edge effect. Ding et al. group mentions a method to synthesize uniform size CQDs

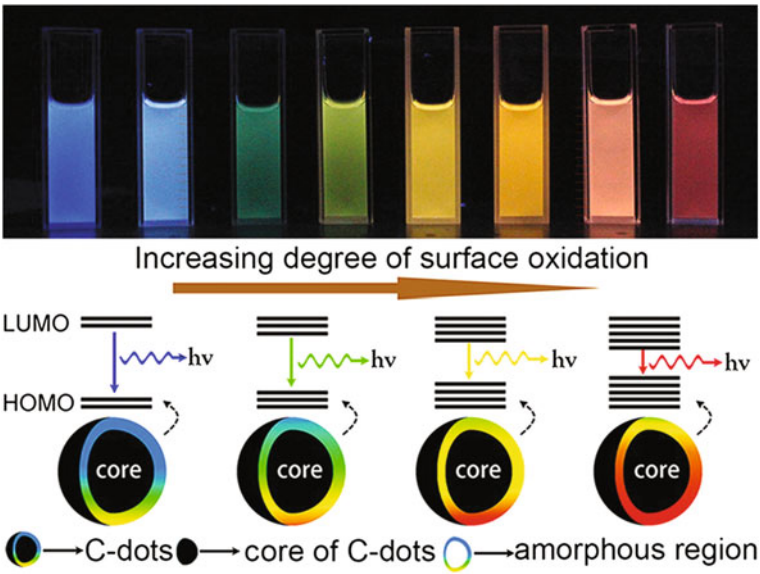

Fig. 4.3 The schematic of the GQD with different degrees of oxidation and the emission light of GQD. Reprinted with permission from Ref. [26]. Copyright 2015, American Chemical Society

with different oxygenated function groups on surface [26]. It could be found that the CQDs with high degree of oxidation will cause the PL redshift. Therefore, the emission light of CQDs will be changed from blue light to red light. It suggests that the bandgap gradually decreases with increasing oxygenated function groups. The schematic is shown in Fig. 4.3.

However, different species functional groups also bring the different electrons transitions. Tetsuka et al. group reports a molecularly designed method to synthesize the GQDs with different nitrogen-containing groups [27]. Nucleophilic substitution and the dehydration reaction of amine moieties with oxygen functional groups on the GQDs were used to produce nitrogen-functionalized graphene quantum dots (N-GQDs). Then, they utilize ab initio calculations to estimate the bandgap of different N-GQDs. The calculation results are shown in Fig. 4.4. The HOMO/LUMO energy levels could be tuned continuously by adjusting the strength of the orbital interactions using different nitrogen-containing groups and adjacent groups.

4.2.1.2 Up-conversion

Up-conversion fluorescence gradually attracts attention due to their excellent property in biology field. It could be applied in in vivo imaging widely because of deep tissue penetration of long excitation wavelength such as near-infrared (NIR).

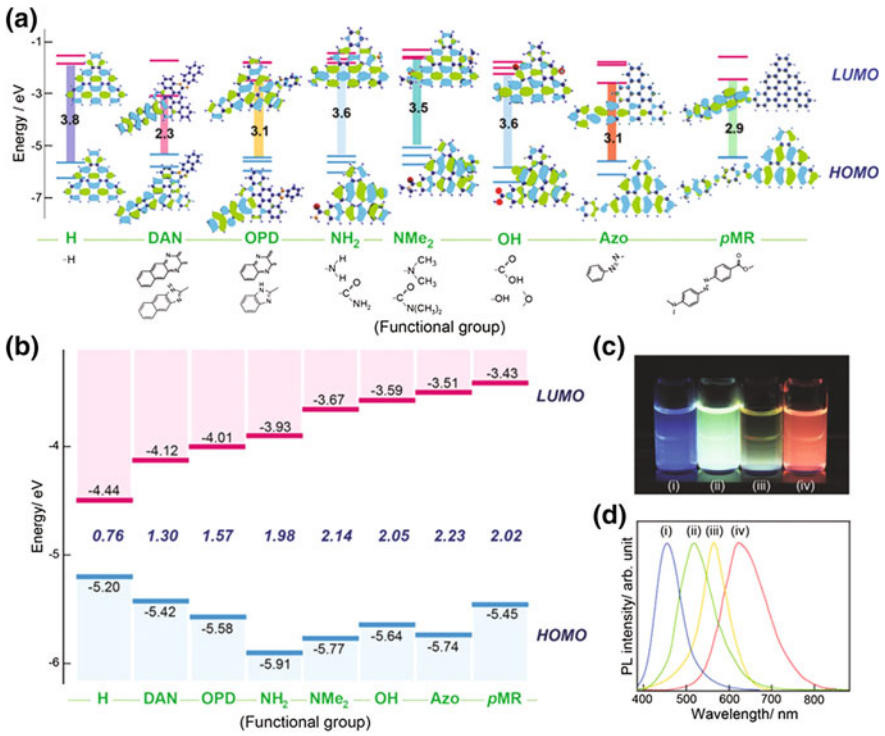

Fig. 4.4 Energy levels and photoluminescence for nitrogen-functionalized graphene quantum dots (N-GQDs). Reprinted with permission from Ref. [27]. Copyright 2016, Wiley-VCH

Up-conversion PL which means emitting shorter wavelength upon simultaneous absorption of two or sequential absorption of multiple longer-wavelength photons [6] could be attributed to two reasons, which are multi-photon active process [28–30] and anti-Stokes transition [31]. Cao et al. group mentions the up-conversion phenomena using carbon dots passivated by PPEI-EI [28]. The C-dots are found to be strongly emissive in the visible with either the argon ion laser excitation (458 nm) or the femtosecond pulsed laser for two-photon excitation in the near-infrared (800 nm). Through the overlap shown in Fig. 4.5a, b, the luminescence images could be matched well. The results demonstrate that C-dots possess multi-photon active process. The similar phenomena could be reported by Zhu et al. group [30]. The obtained GQDs possess up-conversion PL properties shown in Fig. 4.6. The GQDs will emit short wavelength by providing the long excitation wavelength. It is a typical up-conversion property which is attributed to the multi-photon active process.

However, Shen et al. group mentions that the multi-photon active process is not enough to explain the up-conversion phenomena [31]. Shen et al. group reports the

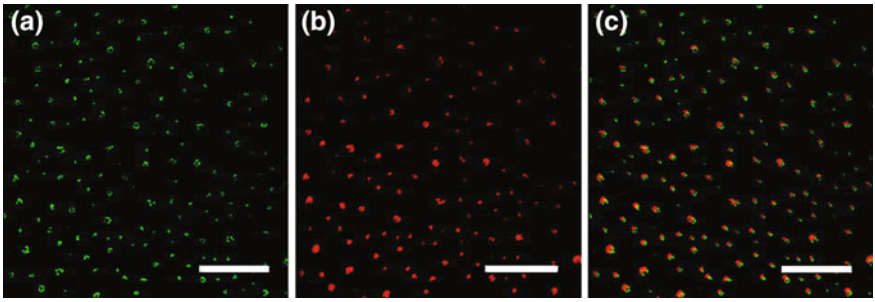

Fig. 4.5 Photoluminescence images of the C-dots by different excitation sources. **a** Argon ion laser excitation at 458 nm and **b** femtosecond pulsed laser excitation at 800 nm; **c** is an overlay of (**a**) and (**b**). Reprinted with permission from Ref. [28]. Copyright 2007, American Chemical Society

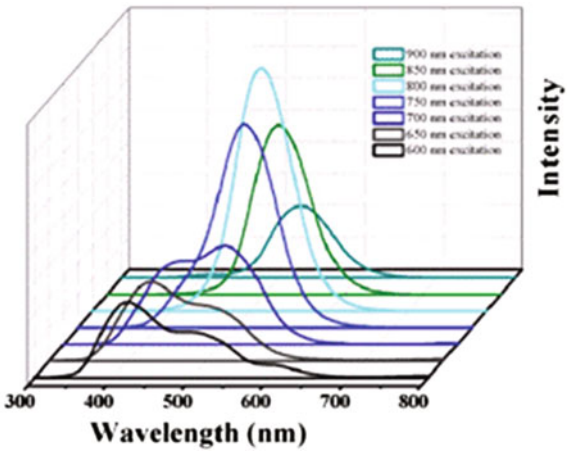

Fig. 4.6 The up-conversion photoluminescence of GQDs with different excitation wavelengths from 600 to 900 nm. Reprinted with permission from Ref. [30]. Copyright 2012, Royal Society of Chemistry

other reason to explain the up-conversion photoluminescence. The synthesized GQDs also showed the up-conversion property (Fig. 4.7a). The PL spectrum of GQDs is excited by 980 nm excitation wavelength. The relationship between PL emission and excitation could be shown in Fig. 4.7b with the inset of the energy of the excitation light as a function of the emission. The inset shows the linear relationship between E_m and E_x, and the function of the fit line is $E_m = 1.00E_x + \delta E$ ($R^2 = 0.9983$) with $\delta E = 1.1$ eV. They speculated the up-conversion PL as an anti-Stokes transition as depicted in Fig. 4.7c, where the energy levels of π and σ orbitals were provided by the carbon ground-state multiplicity. When the electrons of the π orbital are excited by certain photons, the π electrons would transition to LUMO state. Subsequently, if the electrons of LUMO turn to σ orbital, the up-conversion PL will be generated.

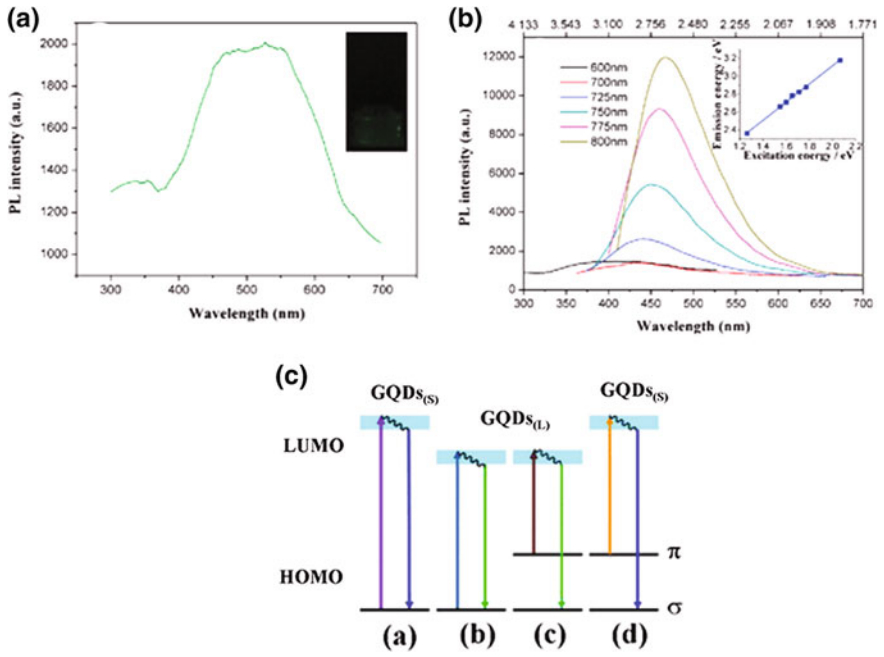

Fig. 4.7 **a** PL spectrum excited at 980-nm laser with the *inset* of photograph of the GQD aqueous solution taken under a 980-nm laser; **b** up-converted PL properties of GQDs, *inset* is the energy of the excitation light as a function of the emission; **c** a schematic illustration of various typical electronic transition processes of GQDs. Reprinted with permission from Ref. [31]. Copyright 2011, Royal Society of Chemistry

Additionally, Wen et al. group also mentions the experiment results to elaborate the up-conversion phenomena is not multiple phonon process [32]. They utilize five different synthesized CNDs and GQDs to measure the PL property. And they confirm that the up-conversion fluorescence actually originates from the normal fluorescence excited by the leaking component from the second diffraction in the monochromator of the fluorescence spectrophotometer. Therefore, the phenomenon of up-conversion PL still has no exact interpretation.

4.2.1.3 Electrochemical Luminescence

Electrochemical luminescence (ECL) is a common method for chemiluminescence detection, fundamental study and analytical applications because of their high sensitivity and wide range of working concentrations. ECL is a form of

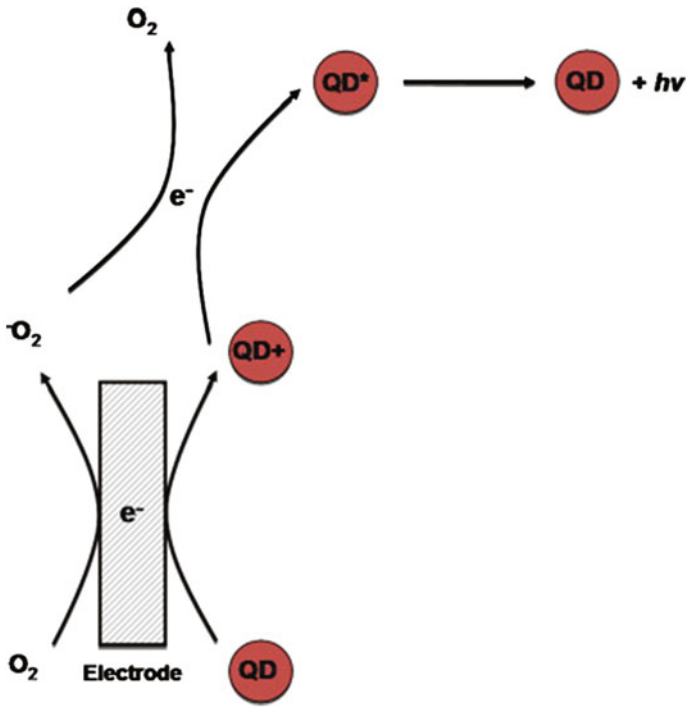

Fig. 4.8 The electrochemiluminescence mechanism of QDs. Reprinted with permission from Ref. [33]. Copyright 2015, Elsevier B.V.

chemiluminescence in which the light-emitting reaction is preceded by an electrochemical reaction. This involves the generation of reactive species, at an electrode surface, that undergo electron transfer (redox) reactions to form excited states which emit light upon an energy relaxation process [33]. The typical mechanism of ECL is shown in Fig. 4.8.

However, the most studies utilize semiconductor materials to implement ECL. But those semiconductors almost are heavy metal components, and it will limit the application for biotechnology and be limited by cost considerations. So in order to resolve this problem, low cost and compatible materials are developed. GQDs are novel materials with excellent physical and optical properties. Li et al. group reports the ECL behavior by using GQDs [34]. According to Fig. 4.9a, it could be found that the gGQDs showed an intense ECL emission at −1.45 V, with a non-set potential at about −0.9 V, which was about 9 times higher than background signal.

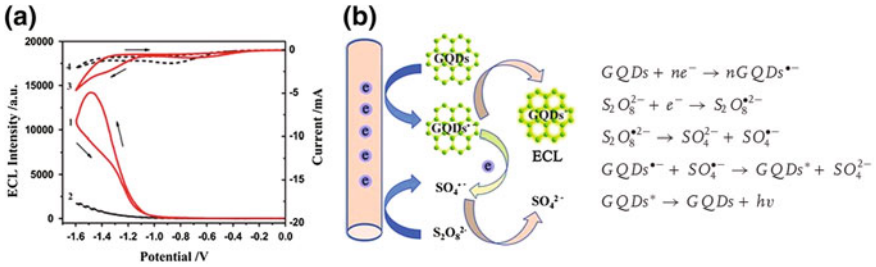

Fig. 4.9 **a** ECL potential curves and cyclic voltammograms (CVs) of the gGQDs (1,3) and background (2,4) with concentration of 20 ppm in 0.05 M Tris–HCl (pH = 7.4) buffer solution containing 0.1 M $K_2S_2O_8$. **b** Schematic illustration of the ECL mechanism of GQDs and the reaction equation. Reprinted with permission from Ref. [34]. Copyright 2012, Wiley-VCH

However, when $K_2S_2O_8$ was not added in the process, it will not generate obvious ECL. The reaction is shown in Fig. 4.9b. Based on the reaction mechanism, the chemiluminescence could be observed.

The particle applications are reported by Chen et al. and Du et al. groups in recent years [35, 36]. The similar mechanisms could be seen in their study. The ECL emission could be originated from the $GQDs^{\bullet -}$ reacted with $SO_4^{\bullet -}$ radicals. And then, when the analyte is added, the quenching mechanism will be generated. The ECL signal will be decreased with increasing the analyte.

4.2.1.4 Cytotoxicity

Cytotoxicity is an important factor in biological fields such as in vitro and in vivo imaging studies. However, most semiconductors are heavy metals, so it will limit the applications in these studies. GQDs are emerging as excellent optical materials because of semiconductor-like properties. Besides, their free metal structure makes it widely applied in transition toward clinical applications. In order to investigate the cytotoxicity of GQDs, GQDs have been evaluated by the cell viability assay [37–40]. Zhu et al. group utilizes the MG-63 (human osteosarcoma) cells to observe the cell activity by methylthiazolyldiphenyl-tetrazolium bromide (MTT) assay [37]. The results demonstrate that the cell activity does not get weak significantly (Fig. 4.10). It means that the GQDs possess low toxicity effects in biology.

The similar methods could be seen by Dong et al. and Peng et al. groups. These studies also use MTT assay to implement cell viability via MCF-7, MDA-MB-231 and T47D as cells, respectively. The results show that GQDs have low cytotoxicity and excellent biocompatibility.

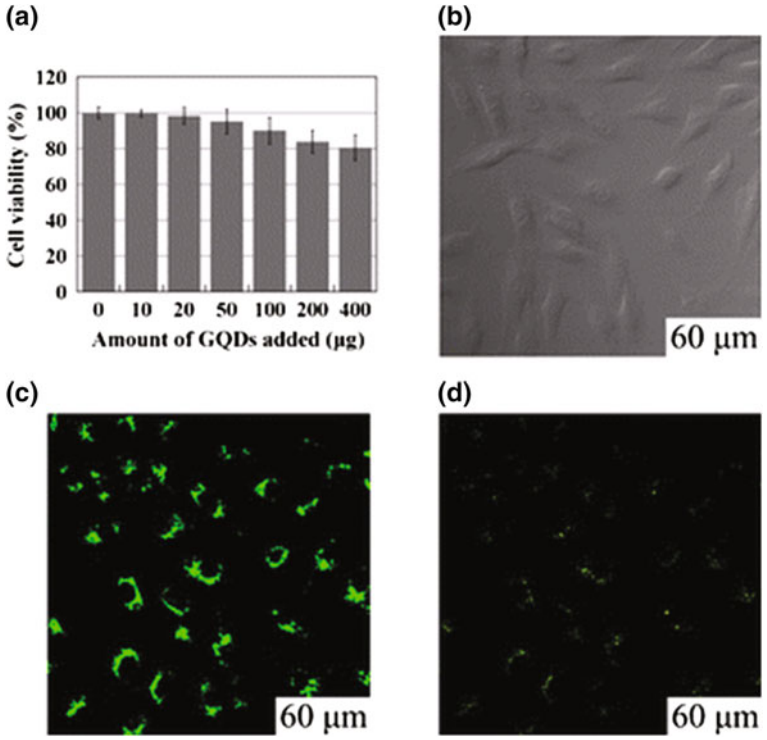

Fig. 4.10 **a** Effect of GQDs on MG-63 cells viability. **b–d** are washed cells imaged under bright field, 405- and 488-nm excitations, respectively. Reprinted with permission from Ref. [37]. Copyright 2011, Royal Society of Chemistry

4.3 Characterization

Based on above properties discussion, the GQDs possess unique optical, physical and chemical features. These properties could be measured and correlated using different characterization techniques. The characterizations including UV–Vis spectroscopy, Raman spectroscopy, photoluminescence, transmission electron microscopy (TEM), atomic force microscopy (AFM), Fourier transform infrared spectrometer (FT-IR) and X-ray photoelectron spectroscopy (XPS) are used to analyze their electron state, fluorescence property, functional group composition, surface morphology and vibrational patterns. The characterizations will be discussed below.

4.3.1 Optical Characterization

4.3.1.1 UV–Visible Spectroscopy

UV–visible spectroscopy is a useful tool for investigating the electron transition of materials. The molecule can absorb certain energy wavelength to make the electrons transition into higher-energy orbital. Recording the degree of absorption by sample at different wavelengths, we could get the absorbance of the sample. Therefore, most researchers utilize it to investigate the excitation wavelength of GQDs. According to UV–Vis spectrum analysis of GQDs, most researchers mention that the peak below 300 nm is attributed to the $\pi \rightarrow \pi^*$ which is ascribed to aromatic C=C structure [34, 41–44]. The peak between 300 and 390 nm is attributed to the electrons transition from $n \rightarrow \pi^*$ which is caused by oxygen-containing groups on GQDs surface [44–46]. However, different functional groups on GQDs surface or different surface structure will cause the wavelength shift. Based on UV–visible spectrum analysis, we could get the excitation range of GQDs and determine the possible applications.

4.3.1.2 Raman Spectroscopy

Raman spectroscopy is a scattering technique. It is based on Raman effect, i.e., frequency of a small fraction of scattered radiation is different from frequency of monochromatic incident radiation. It is based on the inelastic scattering of incident radiation through its interaction with vibrating molecules. It probes the molecular vibrations [47]. According to above principle, it could be used widely to analyze the materials. It can reveal information on the crystal structure, electronic structure and lattice vibration of material. Typical signals of G, D and 2D bands could be observed effectively in carbon-based materials by Raman spectrum. Therefore, there have been some studies on Raman spectrum of GQDs [18, 40, 41, 45, 48–51]. The G band is near 1590 cm^{-1}, representing the E_{2g} vibrational mode of aromatic domains in the 2D hexagonal lattice structure [42, 49]. The D band is located near 1350 cm^{-1}, which means disorder-activated Raman mode and the presence of sp^3 defects [48]. D band is usually observed by Raman spectrum due to the defect generated by surface functional groups or destroyed by synthesis process. Generally, most researchers use the I_D/I_G ratio to estimate the defect extent of GQDs.

4.3.1.3 Photoluminescence Spectroscopy

PL spectrum is an important measurement for GQDs due to its strong fluorescence properties. When it is provided a certain excitation wavelength, the GQDs will emit corresponding emission peaks. Through this measurement, GQDs show typical

emission light such as blue [18, 23, 31, 49], green [9, 23, 37], yellow [9, 23, 45] and red luminescence [23]. Generally, PL spectrum could be divided into excitation-dependent PL and excitation-independent PL. However, most researchers report that PL spectrum of as-produced GQDs possesses excitation-dependent PL emission behavior [13, 18, 31, 37, 49, 52], because it may result from optical selection of different size and surface state of GQDs [37].

Moreover, the other one interesting investigation is to analyze their electrons transition via measuring PL excitation (PLE). Yeh et al. group reports a PLE measurement to investigate the electrons transition situation of their GQDs [23]. The measurement result is shown in Fig. 4.11. Each PLE spectrum can be deconvoluted into three peaks that correspond to electron transitions of $n \rightarrow \sigma^*$ (blue), $\pi \rightarrow \pi^*$ (green) and $n \rightarrow \pi^*$ (red), respectively. However, according to their previous PL measurement, they find that the PLE spectra depict an energy difference between the absorptive $n \rightarrow \pi^*$ and radiative $\pi^* \rightarrow n$ transitions. They consider that the energy loss is possible through phonon scattering for achieving momentum alignment instead of the presence of trap states generally.

4.3.2 Microscopy Characterization

4.3.2.1 Transmission Electron Microscopy (TEM)

In TEM, a high-energy beam of electrons is transmitted through a very thin specimen. The electrons interact with the atoms in specimen and pass through it. The image is magnified and then formed onto a phosphor screen via collecting these electrons leaving specimen. According to above principle, the morphology information of sample could be observed. Based on paper survey, there are many studies using TEM to estimate the particle size and morphology of GQDs [40, 41, 50, 53–55]. Most sizes of GQDs are below 10 nm with circle shape. They are small enough to generate quantum effect. In addition, some researchers further focus on one dot by using HR-TEM to see the morphology in detail and crystalline structure [40, 41, 56]. Part of GQDs possesses high-degree crystallinity with the lattice parameter of 0.24 nm, representing the presence of graphene structure [40, 56]. Besides, some groups further utilize the HR-TEM to observe the defects such as vacancy [54] as shown in Fig. 4.12.

4.3.2.2 Atomic Force Microscopy (AFM)

AFM is a versatile and powerful microscopy technology. AFM uses a cantilever with a very sharp tip to scan over a sample surface. Briefly, as the cantilever is brought even closer to the surface, increasingly repulsive force takes over and causes the cantilever to deflect away from the surface. Therefore, the topography of solid surface could be measured by AFM through the tip scanning the surface.

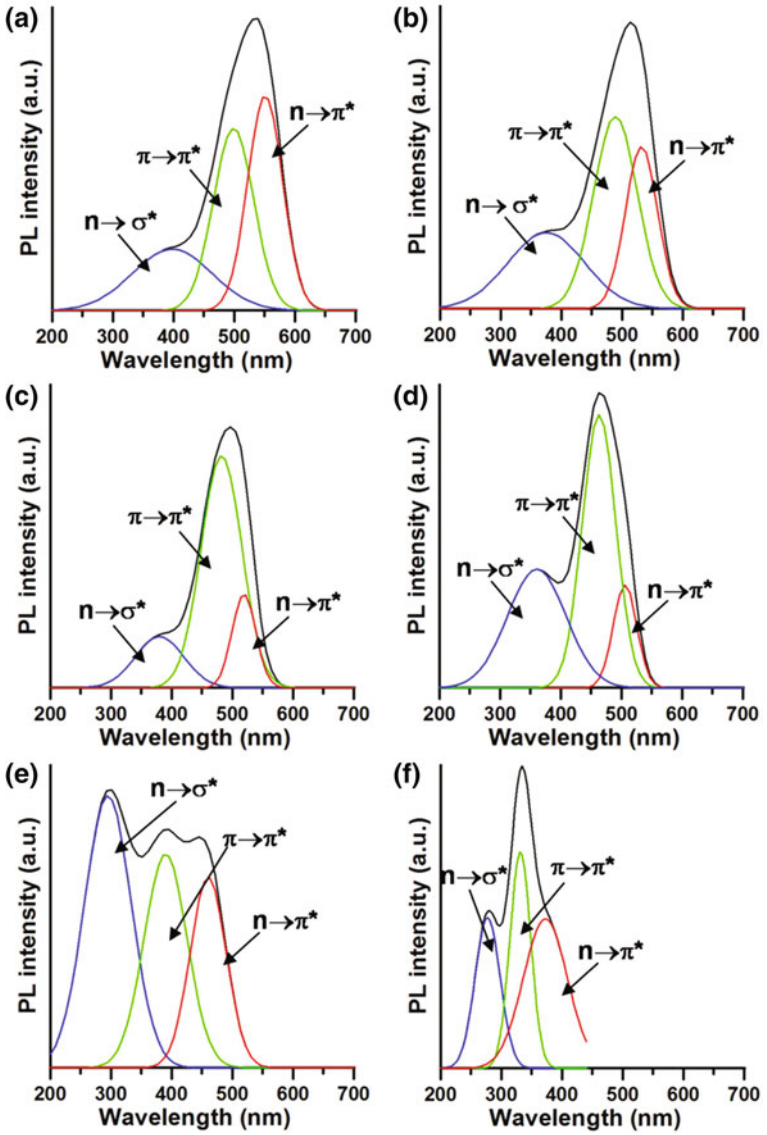

Fig. 4.11 PLE spectra of the aqueous GOQD dispersions with different particle sizes. Reprinted with permission from Ref. [23]. Copyright 2016, American Chemical Society

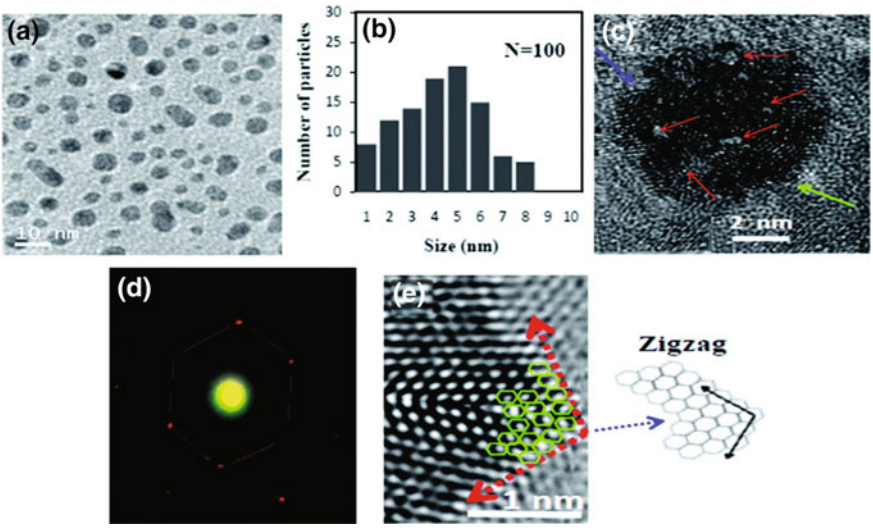

Fig. 4.12 **a** TEM image of aGQDs; **b** size distribution of synthesized aGQDs; **c** high-resolution TEM image of a typical aGQD; **d** 2D FFT of aGQD; **e** HR-TEM image of the edge of aGQD (highlighted by a *green arrow* in (**c**)) with a schematic representation of the zigzag edge termination of HR-TEM image. Reprinted with permission from Ref. [54]. Copyright 2011, Royal Society of Chemistry

It is usually used to investigate the thickness of GQDs and further estimate the graphene layers [34, 40, 41, 49, 50, 53]. The height of GQDs corresponding to graphene layer could be referred to a paper which reports an equation to calculate the graphene layers [57].

4.3.3 Surface State Characterization

4.3.3.1 Fourier Transform Infrared Spectrometer (FT-IR)

FT-IR is an important technology to identify the surface component and functional groups on materials. Briefly, in infrared spectroscopy, IR radiation is passed through a sample. Some of the infrared radiation is absorbed by the molecules vibration of sample and some of it is transmitting to the sample. Through detecting molecule vibration mode, it could create a molecular fingerprint of the sample. The researchers utilize it to investigate the functional groups on the GQDs surface [18, 40, 41, 45, 50, 55] because the functional group is an important factor for optical properties. The typical FT-IR signals of GQDs are near 3400, 1600 and 1350 cm^{-1}, representing the stretching vibrations of O–H, aromatic C=C stretching and C=O of carboxy, respectively. However, the presence of functional groups depends on different synthesis methods and precursors.

4.3.3.2 X-ray Photoelectron Spectroscopy (XPS)

XPS is an excellently quantitative spectroscopic technique which measures the elemental composition and surface chemistry. It is always used with FT-IR to study the material surface components. XPS spectra are obtained by irradiating a material with a beam of X-rays while simultaneously measuring the kinetic energy. According to measured kinetic energy, the binding energy could be derived. The corresponding characteristic peaks could be obtained. There are many studies for investigating the GQDs component by XPS spectroscopy [18, 34, 40, 41, 45, 49, 50]. GQDs have typical carbon signal which could be deconvoluted into various peaks such as C–C, C–O and C=C bonding. According to these peaks, the quantity of element could be estimated accurately.

4.4 Synthesis

Generally, the approaches of synthesis GQDs could be classified into top-down and bottom-up. Different synthesis methods will result in the different surface state and structure nature of GQDs. The common top-down approaches which are breaking bulk carbon-based materials into small fragments are chemical ablation methods, electrochemical methods and physical methods. The advantages of the most top-down approaches are large-scale production and simple precursors. But the obtained GQDs will involve high surface defects due to the aromatic framework destroyed during the process, and it will cause different physical characteristics. Additionally, it is also difficult to control the structure size and surface component [14, 58]. The results will influence the optical characteristics seriously. Conversely, the bottom-up approaches synthesize the GQDs through pyrolysis or carbonization of organic molecules to form bulk materials by cage opening of fullerene and GQDs derived from organic molecules. So it is possible to control the structure size, shape and surface state during synthesis procedure [58]. However, the disadvantages are the special organic precursors, poor solubility and strong tendency of aggregation of as-synthesized GQDs [59]. Here we introduce few common methods for synthesizing GQDs and discuss the relevant mechanism.

4.4.1 Top-Down Approach

4.4.1.1 Chemical Ablation Methods

Chemical ablation synthesis is a typical oxidation and reduction method for cutting the bulk materials into fragments. The normal starting material is always graphene oxide (GO). The synthesis procedure involves using acidic solution through hydrothermal or solvothermal route to synthesize GQDs. In the 2010, Pan et al.

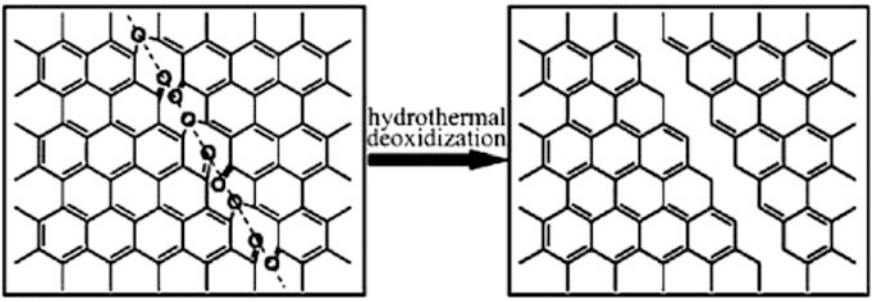

Fig. 4.13 Mechanism for the hydrothermal cutting oxidized GSs into GQD. Reprinted with permission from Ref. [18]. Copyright 2010, Wiley-VCH

group firstly presents a hydrothermal route to synthesize blue-luminescent GQDs [18]. The bulk graphite powder is starting material. After a modified Hummers method treatment, the GO could be obtained. Then, through thermal deoxidization, GO could be changed into small graphene sheets (GSs). Small GSs are oxidized in a mixture of sulfuric acid and nitric acid under mild ultrasonication. The intermediate are reduced under hydrothermal condition to generate blue-luminescent GQDs. The mechanism for hydrothermal cutting the oxidized GSs into GQDs could be described briefly (showing in Fig. 4.13). The oxidized GSs exhibit abundant oxygen-containing groups which result in surface defects. However, these defect positions are easily attacked and broken [18]. Therefore, the GQDs could be synthesized through reducing these defects under hydrothermal condition. The obtained GQDs have typical blue luminescence under UV light. The PL quantum yield measured through quinine sulfate as a reference is 6.9%. The average diameter of particle size of GQDs is 9.6 nm, and the topographic heights are almost between 1 and 2 nm, indicating 1–3 graphene layers.

Zhu et al. group reports one-step solvothermal method to synthesize green-luminescent GQDs with quantum yield of 11.4% using 9,10-bis(phenylethynyl)anthracene as a reference. Firstly, the GO is dissolved in DMF (270 mg/10 ml) and the mixture is under ultrasonication for 30 min. Then, the solution is transferred to Teflon-lined autoclave to implement solvothermal process. During the reaction, the DMF could be used as a reduction agent. Therefore, the GQDs are obtained through the reduction of GO. The average diameter of as-produced GQDs is 5.3 nm, and the heights are 1.2 nm. It suggested that the structure of GQDs possesses 1–2 graphene layers [37].

Besides, other chemical redox cutting methods are like hydrazine hydrate reduction. The GQDs synthesized via hydrazine hydrate reduction of GO with their surface passivated by polyethylene glycol (PEG) are reported by Shen et al. group [31]. Briefly, the GO which is the starting material is oxidized by nitric acid and cut into small GO sheets. Then, the small GO sheets are treated with an oligomeric PEG diamine (PEG_{1500N}) as a surface passivation agent. Finally, the GQD-PEG could be obtained through the mixture reduced by hydrazine hydration.

The reaction is shown in Fig. 4.14. The obtained GQD-PEG possesses strong blue-luminescent under 365-nm UV light and green-luminescent under 980-nm laser. It means the GQD-PEG has up-conversion PL property which is attributed to anti-Stokes photoluminescence (ASPL). The average diameter of GQD-PEG is 13.3 nm. The PL quantum yield of 7.4% is measured using rhodamine B as a reference.

However, later in 2012, Shen et al. group adds hydrothermal route into their procedure to improve the PL property of GQD-PEG [60]. Briefly, the cutting GO which is generated by similar process previously is mixed with PEG and transferred into Teflon-lined stainless steel autoclave to carry out hydrothermal process. The obtained GQD-PEG has stronger PL emission. The PL quantum yield is up to 28%. The average diameter of GQD-PEG is maintained around 13 nm.

Recently, Shin et al. group presents an acid-free and oxone oxidant-assisted solvothermal method to synthesize GQDs using different carbon sources such as graphite, multi-walled carbon nanotubes, carbon fibers and charcoal [49]. Briefly, the carbon-based materials are put in the solution consisted of potassium monopersulfate (also called oxone). The sulfate radicals ($SO^{\bullet -}$) or hydroxyl radicals ($OH^{\bullet}$) from oxone oxidize the carbon-based materials. And then, the blue-luminescent GQDs could be synthesized through the solvothermal reduction (Fig. 4.15).

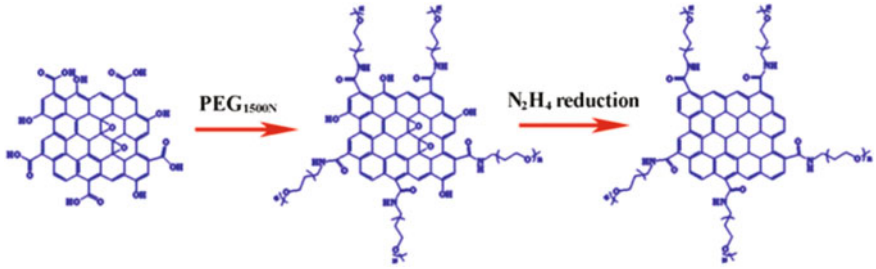

Fig. 4.14 Reaction of the GQDs containing an oligomeric PEG. Reprinted with permission from Ref. [31]. Copyright 2011, Royal Society of Chemistry

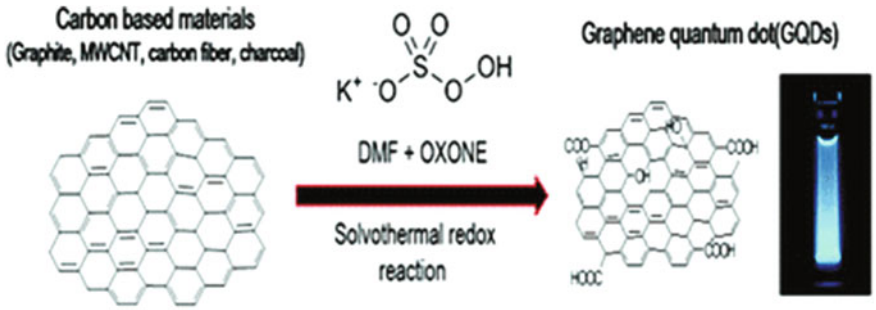

Fig. 4.15 Mechanism of GQDs synthesis by solvothermal method. Reprinted with permission from Ref. [49]. Copyright 2015, Royal Society of Chemistry

The obtained GQDs have fairly uniform size distributions of 2–8 nm. However, the topographic heights of GQDs will depend on different carbon-based materials.

4.4.1.2 Electrochemical Method

Generally, the carbon-based materials such as graphite rod [61, 62], graphite foil and MWCNTs [63] are usually used as working electrode for synthesizing carbon dots (CDs). Zhou et al. group firstly reports an electrochemical method to synthesize blue-luminescent CDs from MWCNTs [63]. The synthesis method is utilizing the three-electrode system consisted of MWCNTs as working electrode, a Pt wire as counter electrode and an $Ag/AgClO_4$ as reference electrode to implement cyclic voltammograms (CVs). The electrolyte is tetrabutylammonium perchlorate (TBAP). The blue-luminescent carbon nanocrystals could be synthesized through the MWCNT generating reaction during cycling scan. The obtained CDs have narrow size distribution being 2.8 nm in diameter. Subsequently, the Lu et al. group mentions a new strategy through electrochemical method to synthesize the CD [61]. The mechanism for synthesizing CD is shown in Fig. 4.16. Briefly, the high redox potential induces water molecule to generate hydroxyl and oxygen radicals. These oxygen radicals will make graphite oxidize and generate cleavage. The oxidation of the edge planes opens up the edge sheets, facilitating intercalation by the anionic BF_4^-, which leads to the depolarization and expansion of the graphite anode. Based on the interaction between anodic oxidation and anion intercalation, the CD should be obtained through the exfoliation from graphite rod.

This electrochemical method has further been extended to the production of GQDs. Li et al. group mentions an electrochemical approach to synthesize GQDs with green-luminescence [64]. The graphene film is used as working electrode. Pt wire and Ag/AgCl are used as counter and reference electrodes, respectively.

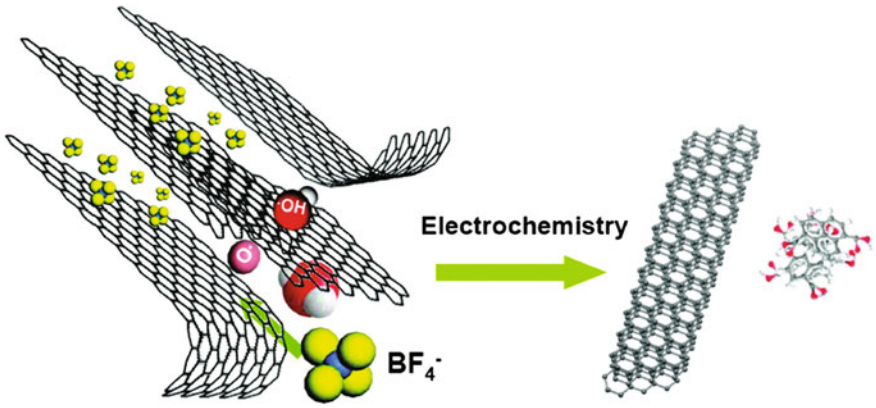

Fig. 4.16 Illustration of the exfoliation process by electrochemical method. Reprinted with permission from Ref. [61]. Copyright 2010, American Chemical Society

Through the electrochemical cycling scan, the oxidation reaction will be generated on the graphene surface under 0.1 M phosphate-buffered solution (PBS). During the repeated cycling, the GQDs could be synthesized. The as-product GQDs have a uniform diameter of ca. 3–5 nm. Through AFM analysis, the topographic heights are between 1 and 2 nm, indicating 1–3 graphene layers.

Zhang et al. group prepared highly fluorescent GQDs by electrochemical oxidation [45]. Firstly, the graphite rod and Pt foil are used as working electrode and counter electrode, respectively. Then, put them into the electrolyte consisted of 0.1 M NaOH solution. After electrochemical treatment, the oxidative radicals could be generated in the solution. Subsequently, these radicals attack the working electrode to result in graphite rod covered with epoxide and OH groups. The interaction is similar to the mechanism reported by Lu et al. group. In next step, put the hydrazine hydrate into solution to implement the reduction and modification. The yellow-luminescent GQDs could be generated. (The mechanism is shown in Fig. 4.17.)

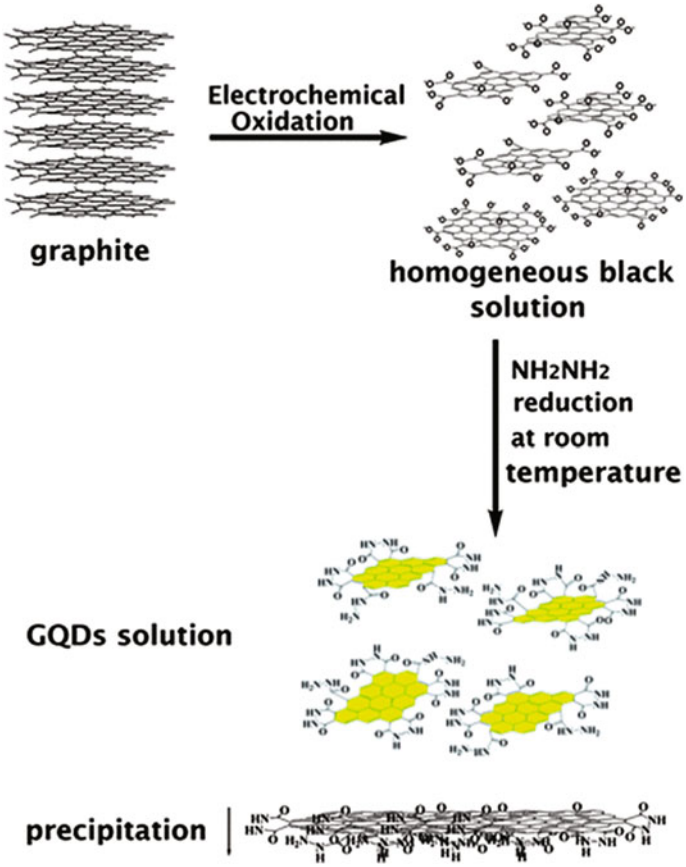

Fig. 4.17 Illustration of the GQDs synthesis process by electrochemical method. Reprinted with permission from Ref. [45]. Copyright 2011, Royal Society of Chemistry

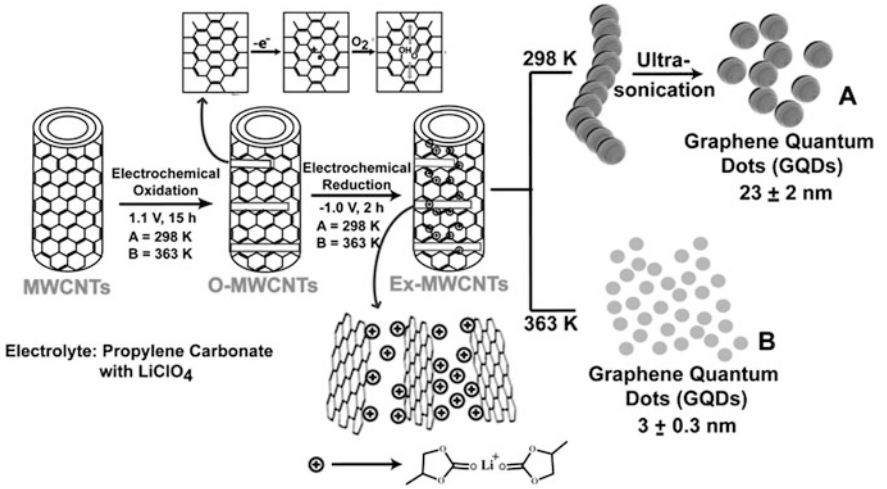

Fig. 4.18 Schematic representation of various processing stages involved in the preparation of GQDs from MWCNTs by this electrochemical approach. Reprinted with permission from Ref. [66]. Copyright 2011, Wiley-VCH

Sinde et al. group reported electrochemical unzipping of CNTs by a two-step process to synthesize GQDs [65]. In first step, the MWCNT-coated working electrode in propylene carbonate with $LiClO_4$ is applied a typical anodic potential of 1 V versus Pt QRE (quasi-reference electrode) to initiate the breaking of sp^2 carbon atoms through the electronic field. In the second step, change the potential of 1 V into −1 V to induce the intercalation of Li^+/propylene carbonate complexes resulting in exfoliation of oxidized MWCNTs. (The mechanism could be shown in Fig. 4.18.) Additionally, according to their approach, the GQDs could be synthesized with different sizes depending on the electrochemical oxidation time. The longer oxidation time they were used will result in smaller GQDs being generated. The particle size could be 3 ± 0.3, 5 ± 0.3 and 8.2 ± 0.3 nm.

In recent years, the similar intercalation mechanism is mentioned by Ananthanarayanan et al. group [66]. They use the three-electrode system consisted of working electrode covered by 3D graphene, Pt wire as counter electrode and Ag/AgCl electrode as the reference. The ionic liquid of $BMIMPF_6$ is used as electrolyte. During the reaction procedure, the GQDs could be generated through the high electrical stress by the applied voltage, PF_6^- intercalated into graphene layers and intimate interaction (pi–pi or cation–pi interaction) between $BMIM^+$ group and GQDs. The mechanism of reaction procedure is shown in Fig. 4.19. The average diameter of as-produced GQDs is 3 nm. The average heights of GQDs are near 1.25 nm, indicating mostly single-layer graphene. The obtained GQDs have typical blue luminescence with the PL quantum yield of 10% (use quinine sulfate as a reference).

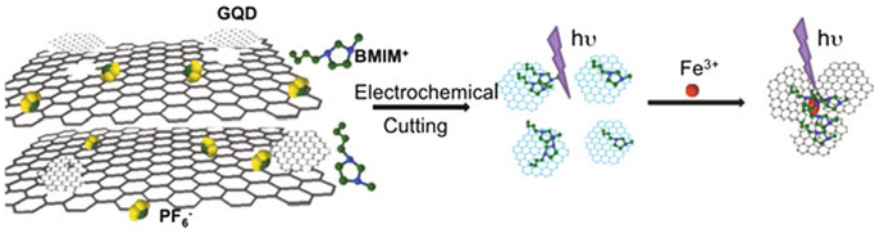

Fig. 4.19 The reaction procedure of synthesis of GQDs. Reprinted with permission from Ref. [67]. Copyright 2014, Wiley-VCH

4.4.1.3 Physical Method

The common physical method is ultrasonication which utilizes the shear forces to cut the bulk carbon structure into small fragments such as GQDs [67] or CQDs [68]. Zhuo et al. group presents ultrasonic method to prepare GQDs [67]. Briefly, the graphene which is typical bulk starting material is put in the mixture solution of sulfuric acid and nitric acid to get oxidation. After standing for 12 h, the mixture solution is implemented ultrasonication (300 W, 80 kHz) to get the GQDs. However, the mechanism is attributed to the ultrasound which generates alternating low-pressure and high-pressure waves in liquid, leading to the formation and violent collapse of small vacuum bubbles which, in turn, produce high-speed liquid jets and strong hydrodynamic shear forces to break the layered carbon structures into GQDs. The as-produced GQDs have typical blue luminescence under 365-nm UV light with the PL quantum yield of 3.4% which is measured using a fluorimeter and an integrating sphere. The diameter of as-produced GQDs is between 3 and 5 nm.

In recent years, some researchers try to use high-energy ball milling method to synthesize the QDs [27, 69] because ball milling method for materials synthesis possesses large-scale production and easily obtained starting materials [69]. Wang et al. group firstly reports the ball milling method to synthesize the CQDs with dual-wavelength photoluminescence [69]. Subsequently, Tetsuka et al. group extends the similar ball milling method which combines two mechanical methods to produce GQDs [27]. Briefly, this study uses the graphite nanoparticles (GNPs, <50 nm) as starting materials. Then, GNPs are ball-milled in ethanol/H_2O (1:1) at 8000 rpm for 1 h. After ball milling process, the suspension is ultrasonicated at high power for 3 h. Through above mechanical exfoliation, the GQDs could be synthesized.

4.4.2 Bottom-Up Approach

4.4.2.1 Cage Opening of Fullerene

Lu et al. group mentions an attractive method to synthesize GQDs by decomposition of fullerene adlayers on reactive transition metals [70]. In this process, the

study deposits the fullerene compound on the Ru substrate. The strong C_{60}–Ru interaction induces the formation of surface vacancies in the Ru single crystal and a subsequent embedding of C_{60} molecules in the surface. The fragmentation of the embedded molecules at elevated temperatures then produces carbon clusters that undergo diffusion and aggregation to form graphene quantum dots. The schematic of synthesis of GQDs is shown in Fig. 4.20. However, according to paper surveying result [10, 11], we find that one group mentions this method in top-down methods [1]. But the GQDs are synthesized finally through aggregation of fragmentations at elevated temperatures. The mechanism preferred is the bottom-up

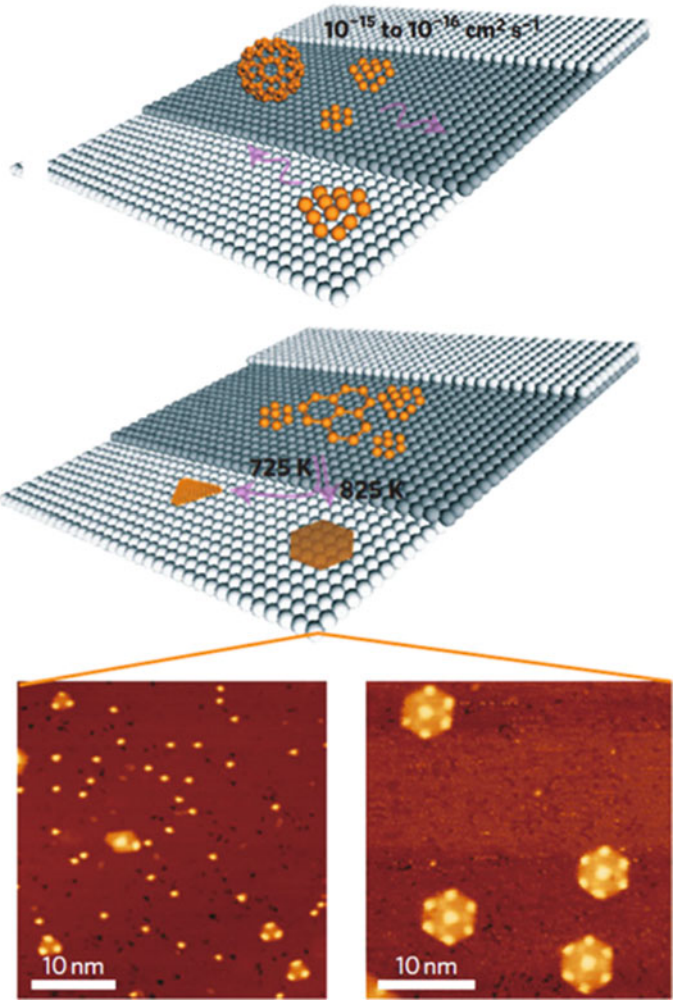

Fig. 4.20 The growth mechanism of graphene nanoislands and quantum dots using C_{60} and the corresponding STM images. Reprinted with permission from Ref. [71]. Copyright 2011, Nature

which formed bulk materials from fragment molecules. Additionally, in recent years, one group also uses the fullerene as a carbon source to synthesize the GQDs via cage opening [71]. But the synthesis method belongs to top-down. It utilizes Hummers method which induces the oxidation of fullerene by strong acid to synthesize GQDs.

4.4.2.2 GQDs Derived from Organic Molecules

Some groups use the organic molecules as carbon sources to synthesize GQDs [48, 58, 72–74] or CQDs [75] by hydrothermal or solvothermal. Most of these methods involve pyrolysis and carbonization of organic precursors [58, 72–74, 76]. Dong et al. group presents a thermal treatment method to synthesize GQDs [58]. GQDs and GO could be synthesized by tuning the carbonization degree of citric acid. The synthesis mechanism is shown in Fig. 4.21. Through heat treatment, the citric acid

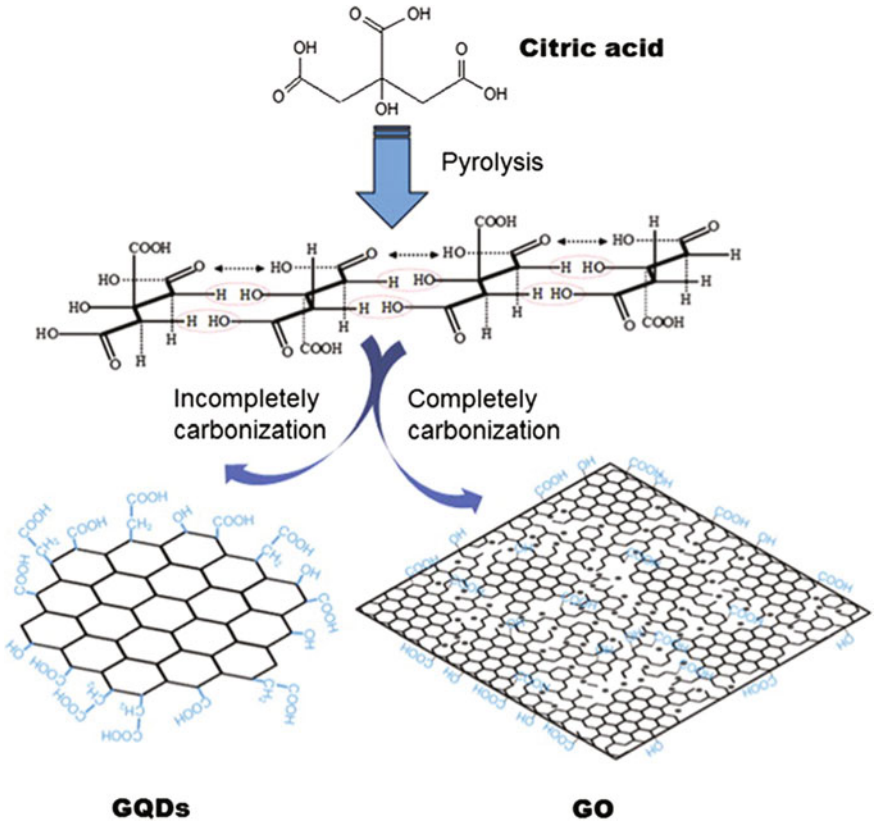

Fig. 4.21 The mechanism of GQDs synthesis. Reprinted with permission from Ref. [59]. Copyright 2012, Elsevier B.V.

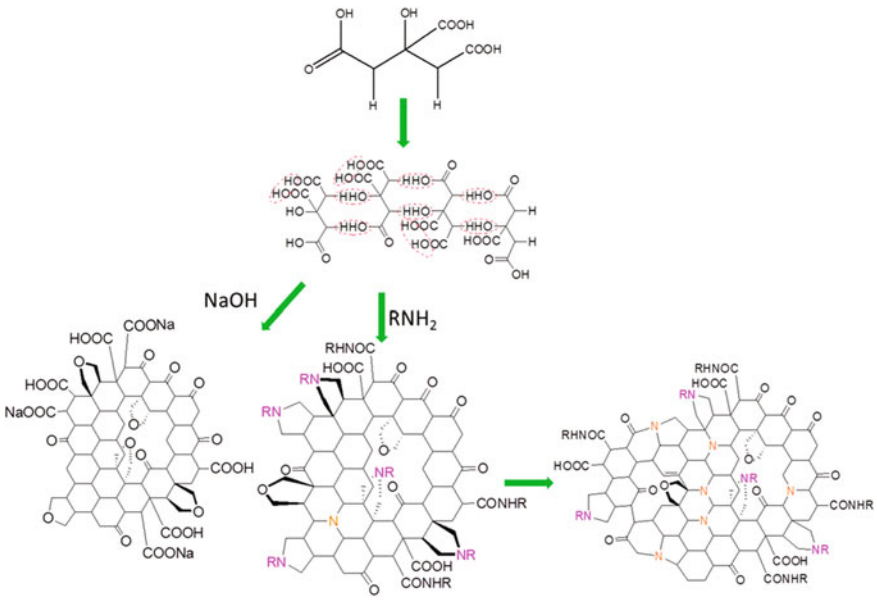

Fig. 4.22 The mechanism of GQDs synthesis. Reprinted with permission from Ref. [48]. Copyright 2012, Nature

could be pyrolyzed to generate GQDs or GO depending on different operating times. The blue-luminescent GQDs are obtained after 10-min reaction. The average size and height of GQDs are 15 and 1.4 nm, respectively. The quantum yield of GQDs is 9.0%.

Qu et al. group reports a hydrothermal process to synthesize GQDs from organic molecule and a serious of GQDs with nitrogen dopant [48]. Citric acid (CA) was used as a carbon precursor and self-assembled into sheet structure in a basic condition and formed N-free GQDs graphite framework through intermolecular dehydrolysis reaction. N-doped GQDs were prepared using a series of N-containing bases such as urea. The mechanism of synthesizing GQDs or N-GQDs via hydrothermal method is shown in Fig. 4.22. Firstly, the GQDs could be synthesized through putting CA with NaOH. Under basic condition, CA molecules will generate the self-assembled reaction to form GQDs through intermolecular dehydroxylation. Subsequently, they replace NaOH with amines to implement next reaction. The GQDs with some unreacted carboxyl and hydroxyl groups react with different amines. The study discovers that N atom enters GQDs by forming pyrrolic structure through intramolecular dehydroxylation between neighbor carboxyl groups. The obtained N-GQDs have stronger optical property than GQDs without nitrogen dopant. The average diameter and quantum yield depend on GQDs with different amines doping.

The similar methods of hydrothermal and precursors are used in recent years to discuss the structure and properties of GQDs. Gu and Permatasari et al. groups use

the citric acid as carbon source and utilize it to react with amine groups [73, 76]. These studies utilize similar mechanisms that intermediate could form cyclic aromatic hydrocarbon structure via dehydration and graphitization to synthesize GQDs. The obtained GQDs possess different structures and functional groups on surface depending on different precursors. And the PL properties also are influenced by different surface states and sizes.

4.5 Applications

Despite the plentiful and ever-growing applications of GQDs, further studies are still required to understand its innate properties. Though generally its surface area, active edge sites and modifiable structure are key players to its versatility, concern remains for these materials to be viable alternatives in future. Fortunately, continual efforts in the field have progressively opened doors for the future of its industrial applicability.

This section aims to provide a detailed account of recent progress in the development of GQD-based applications. Its performances are tabulated to show its capabilities together with the innovation of its functions in various materials and technology. With some fundamental knowledge and key points discussed, hopefully, this will guide the reader in exploring avenues for the continual improvement and molding of potential revolutionary advances to address the technical challenges of its related applications.

4.5.1 Bioimaging or Biolabelling

Various bioimaging techniques include optical imaging [77], radionuclide-based imaging [78], magnetic resonance imaging (MRI) [79], photoacoustic imaging [80], positron emission tomography (PET) imaging [79] and Raman imaging [81]. Graphene oxide has been reported applicable to all these techniques [82, 83], whereas GQDs are commonly employed as bioimaging agents for in vitro optical imaging applications primarily due to its inherent fluorescent properties. In vivo bioimaging studies for GQDs are also growing, as surface modification schemes (i.e., doping, functionalization, passivation) greatly improve its biocompatibility.

The first carbon-based nanoprobes used for cell nucleus labelling were GQDs [84]. Synthesized from the chemical oxidation of XC-72 carbon black, the single-layer GQDs together with MCF-7 cells were incubated to allow simultaneous labelling of the cell membrane, cytoplasm and the nucleus [38]. With its cytomembrane-penetrating capacity, GQDs were also found highly useful for stem cell labelling starting from a time where stem cell labelling posed a considerable challenge, refer to Fig. 4.23. Zhang et al. study proved that GQDs easily penetrated

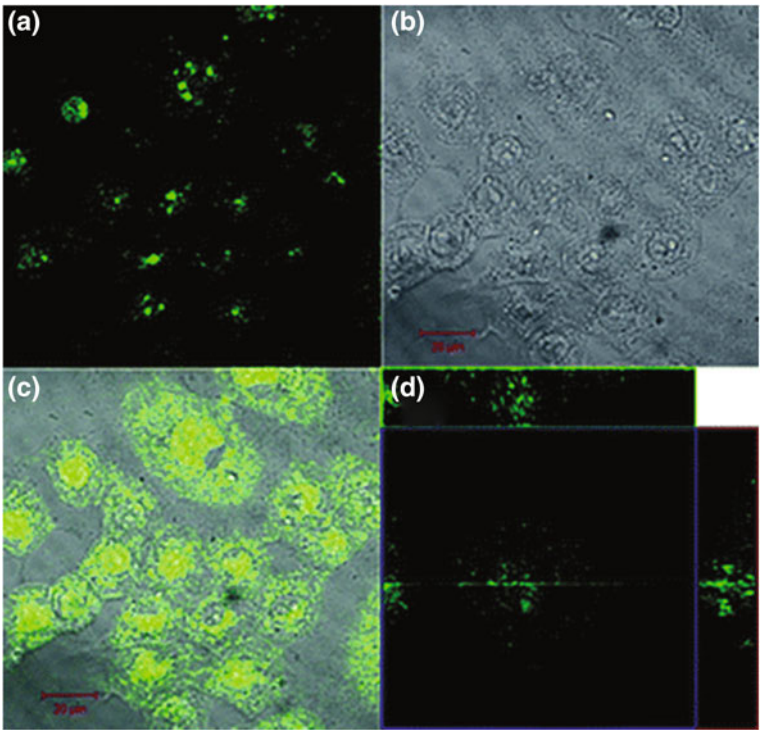

Fig. 4.23 Successful imaging of human breast cancer cells MCF-7 labelled with GQDs taken by a confocal laser scanning microscope (CLSM): **a** fluorescent image; **b** bright-field image; **c** merged fluorescent and bright-field image; **d** section analysis [38]

into the cells, but did not enter the nuclei as opposed to using CdS nanoparticles where stem cells died owing to the cytotoxicity of Cd^{2+} [45].

Until now, stem cell particularities are a continuing area for research and the search for durable and biologically compatible nanomaterials as cell scaffolds for stem cell differentiation is an ongoing endeavor. On the other hand, recent studies in GQD bioimaging involve in vivo studies. For example, a study by Jiang et al. supports results from in vitro cell imaging studies, as GQDs are mostly found in the cytoplasm and not in the nucleus of myocardial cells. This was used to study the cardiovascular biodistribution of GQDs in zebra fishes [85]. Another would be the study by Al-Nahain et al. involving the hyaluronic acid-functionalized GQDs (HA-GQDs) as tumor-targeting agents in female mice. In vivo, the HA-GQDs showed bright fluorescence from the tumor tissue, while in vitro cellular imaging exhibits strong fluorescence from CD44-overexpressed A549 cells [86]. Comprehensive review articles can be referred for the recent developments on GQD bioimaging [87–89].

4.5.2 Biosensing

GQDs in biosensing, that is, combining the use of a biological component in various substance detections, have been explored for various functions other than being a transducer material. With the high affinity of biological reagents to the desired inorganic/organic component, matched with the photoluminescent and physicochemically active nature of GQD surface, its biosensing applications have continued to grow enormously toward detecting macro- and micro-biomolecules, even down to viruses. Sensing applications itself is a huge and broad scope for GQDs, as such a separate section was made to keep a distinction on the different strategies used in biosensing.

4.5.3 Immunosensing

This sensing mechanism involves the use of signal changes caused by the formation of antigen–antibody complexes. A transducer, which happens to be a common function of GQDs, will detect property changes and convert to measurable parameters. Signal transducing in immunosensors involves either electrons, photons and masses, as such the transducers involved can be classified as electrochemical, optical and electrochemiluminescent [90]. As shown in Table 4.1, GQD studies in immunosensing have varied functions in relation to the assay type and signal transduction method involved. It can be observed that a highly sensitive or low detection limit is attained in most studies due to the highly selective and highly affinitive nature of the antigen–antibody complexes utilized.

4.5.4 Drug Delivery

The focus on improving drug delivery technology stems from improving the uptake and efficiency of drugs in nano-form. Challenge lies on the low therapeutic efficacy of using nano-formulations due to its tendency to self-aggregate at low drug concentrations [99]. Quantum dots foreseen as ideal nano-carrier materials should then be inert to the drug and have high drug-loading capacity and encapsulation efficiency, excellent biocompatibility and cytocompatibility, enough mechanical strength and stability to hold the drug, and longer residence time in vivo [100]. GQDs are expected to possess excellent drug-/gene-loading capacity due to their large specific surface area and stable interaction with various molecules through π–π stacking, hydrophobic interaction, electrostatic interaction or physisorption [6].

Drugs for fighting cancer, specifically cisplatin and doxorubicin (DOX) are typically used for drug delivery studies [101]. However, the pioneering work by Liu et al. started with the insoluble aromatic drug SN38 on (polyethylene glycol) PEGylated nanographene oxide for killing cancer cells [102]. From then on, variations of GQD conjugates have been applied on DOX delivery especially targeted

Table 4.1 Compilation of studies using GQDs as component for immunosensors

GQD	Assay type/sensor type	Function of GQD/composite	Signal transduction method	Analyte	LOD (detection range)	Ref.
Fe_3O_4@GQD	Sandwich	Immobilization support Signal amplification	Electrochemical (amperometric)	Avian leucosis virus subgroup J (ALVs-J)	115 $TCID_{50}$/mL ($10^{2.08}$–$10^{4.5}$ $TCID_{50}$/mL)	[91]
GQD	LRET	Transducer (LRET) Immobilization support	Optical (fluorescence)	Human immunoglobulin G (IgG)	10 ng/mL	[92]
GQD-coated PtPd nanochains	Sandwich	Immunological labels Signal amplification	ECL (voltammetry)	Carbohydrate antigen 199	0.96 mU/mL (0.002–70 U/mL)	[72]
GQDs/Si nanowires	Label-free (bioaffinitive)	Immobilization support Conductive electrode	PEC (voltammetry) (EIC)	Microcystin-LR	0.055 μg/L (0.1–10 μg/L)	[93]
GOx/$McAb_2$/GQD/Au@Pt	Sandwich (catalytic)	Immunological labels Signal amplification	ECL	Carcinoembryonic antigen (CEA)	0.6 pg/mL (1 pg/mL–10 ng/mL)	[94]
Ab_2/GOQDs in Ag core–shell nanocrystals	Turn-on, sandwich	Detection probe Signal amplification	Optical (fluorescence)	Prostate-specific antigen (PSA)	0.3 pg/mL (1 pg/mL–20 ng/mL)	[95]

(continued)

Table 4.1 (continued)

GQD	Assay type/sensor type	Function of GQD/composite	Signal transduction method	Analyte	LOD (detection range)	Ref.
Hydrazide-modified GQDs/AuNPs on GCE	Label-free	Conductive electrode Immobilization support	ECL	CEA	0.01 ng/mL (0.02–80 ng/mL)	[96]
afQGDs with antibody anti-cardiac troponin 1	FRET	Detection probe Immobilization support	Optical (fluorescence)	Cardiac marker antigen troponin 1	0.192 pg/mL (0.001–1000 ng/mL)	[97]
afGQDs–cGQDs	Label-free	Conductive electrode Immobilization support	ECL	PSA	0.29 pg/mL (1 pg/mL–10 ng/mL)	[98]

ECL Electrochemiluminescence, *PEC* photoelectrochemical, *BSA* bovine serum albumin, *GOx* glucose oxidase, *Ab* antibodies, *GCE* glassy carbon electrode, *afGQDs* amine-functionalized GQDs, *F/LRET* fluorescence/luminescence resonance energy transfer, *cGQDs* carboxyl GQDs

on certain sites in/on the cell. For example, PEG-GQD loaded with DOX is anchored with hyaluronic acid (HA) for targeted delivery to CD44-overexpressed tumors [103], and the mechanism was confirmed by Wang et al. by in vivo and in vitro imaging of the GQD-DOX conjugate in balb/c female mice and A549 cells [104]. Other variations include additional functions simultaneous with drug delivery, for example GQDs conjugated with folic acid (GQD-FA) targeted HeLa cancer cells for cellular imaging and DOX delivery [105], GQDs conjugated with hyaluronic acid-functionalized human serum albumin (HSA) for simultaneous bioimaging and targeted delivery of gemcitabine to pancreatic cancer cells [106].

A notable improvement in using GQDs as drug delivery platforms involves the nucleus as target location. Cell membrane receptors are the usual target locations. However, numerous therapeutic agents efficiently operate at the nucleus, making it also a beneficial area of focus [101]. As shown in Fig. 4.24, Chen et al. synthesized DOX-GQDs-PEG/TAT that allows real-time monitoring of drug release process through FRET (Förster Resonant Energy Transfer) signals. Together with the emerging trend of using 3D network structures, morphology controllable GQD–chitosan hybrid xerogels have been recently studied for in vivo imaging and pH-sensitive sodium salicylate (SS) carrier. Superior release of SS molecules occurred under alkaline conditions, contrary to that of DOX from chitosan-based nanocomposites [107].

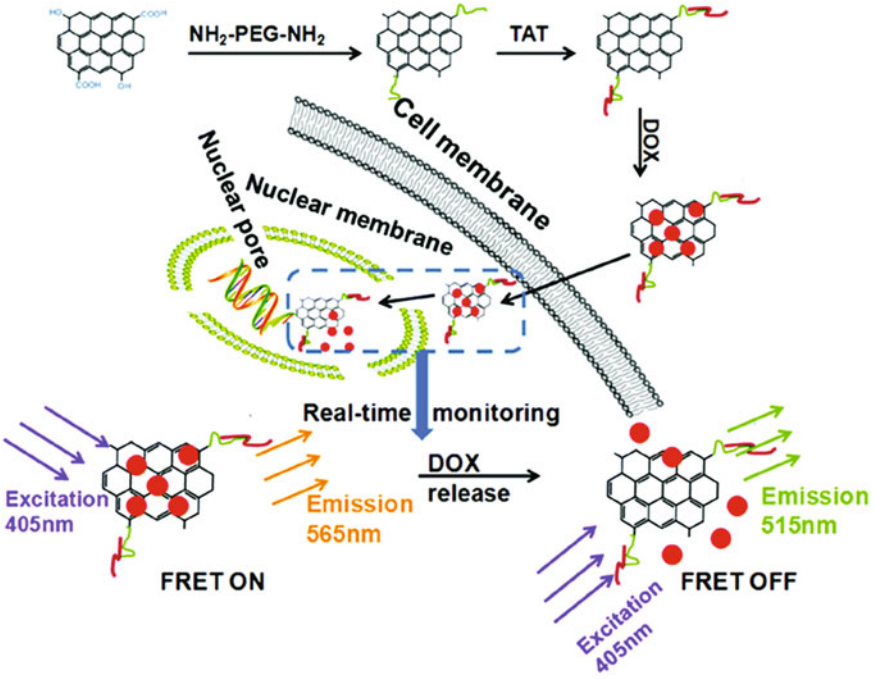

Fig. 4.24 Schematic illustration of the GQD-based FRET system for nuclear-targeted delivery allowing for real-time monitoring of drug release process [101]

4.5.5 Light-Emitting Diode

Other than biomedical applications, GQDs have demonstrated potential for optoelectronics, in particular, for their use as organic light-emitting diodes as the luminescent component for having a broad PLE band that matches well with LED chips [108–110]. Generally, both quantum dots (QDs) and carbon dots (CDs) are gaining popularity as materials for LEDs and have approached industrial applications [110]. For QDs, despite its promising convenience, a serious drawback remains for the toxicity of heavy metals used, specifically dominated by cadmium and lead chalcogenides [111, 112]. As such, carbon-based structures emerge as a non-toxic alternative [113]. In the field of organic optoelectronic devices, enormous efforts have been focused on efficiency, stability and color stability, as such white OLEDs have drawn popularity for being highly efficient, relatively cheaper, flexible, high resolution and low-energy consumption in the full-color display [114–117]. White emission requires the material to cover the whole visible region, from 380 to 780 nm, which poses a challenge in optimizing materials combination of multiple emitters incorporated into one device. GQDs then provide a feasible alternative as phosphors in white light-emitting diodes (WLEDs) or active layers in electroluminescent devices.

Only a handful of reports are available regarding white light generation using GQDs. Initial efforts conducted by Gupta et al. involve converting orange light from poly(2-methoxy-5-2(ethylhexyloxy)-1,4-phenylenevinylene) (MEH-PPV) to yellow light by blending with methylene blue GQDs (MB-GQDs) [118]. Tang et al., converted blue light from commercially available light emitting diodes to white light via coating with concentrated GQD solution, then dried at 100 °C [119]. There results shown in Fig. 4.25b, the original blue emission of LED with CIE

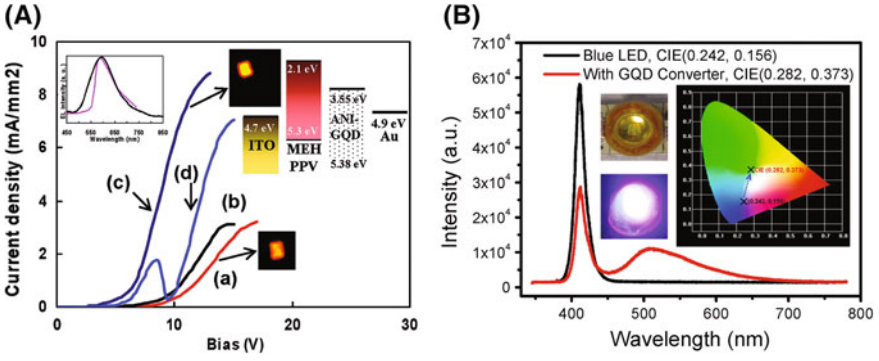

Fig. 4.25 **A** Band diagram showing enhancement of maximum light intensity after blending MEH-PPV with MB-GQDs. MEH-PPV/MB-GQDs (1%) exhibit strong yellow emission (*c*), compared to the bright orange emission of MEH-PPV (*d*) [118]. **B** Comparison of luminescence spectra of blue LED with and without GQD coating, also showing transition of CIE coordinates from blue to white and images of GQD-coated LED with and without applied voltage [119]

coordinates of (0.242, 0.156) shifted to a more whitish color of (0.282, 0.373). Notice the weakening of emission intensity of blue light and the appearance of a broad peak in the luminescence spectrum at 510 nm.

From all reported studies of GQD-WLED applications, mechanism of white light emission can be categorized into (1) coating of blue LED for conversion to white light [119–122], (2) mixing GQDs with other fluorophores [123, 124] and (3) single-phase white light-emitting phosphors [50, 125–127]. Most recent study on GQD-LED is by Luo et al., involving GQDs doped using 4,4-bis(carbazol-9-yl (biphenyl) acting as single-phase WLE phosphors in WLED device consisting of a patterned ITO anode, a 40-nm poly(ethylenedioxythiophene):polystyrene sulfonate (PEDOT:PSS) hole injection layer, a 40-nm 1,3,5-tris(*N*-phenylbenzimidazol-2-yl) benzene (TBPI) electron transport layer, a 0.8-nm LiF and 100-nm aluminum double layer as cathode, as shown in Fig. 4.26. Another recent study involves mixing GQDs with pure green fluorescence to Rhodamine B with orange red

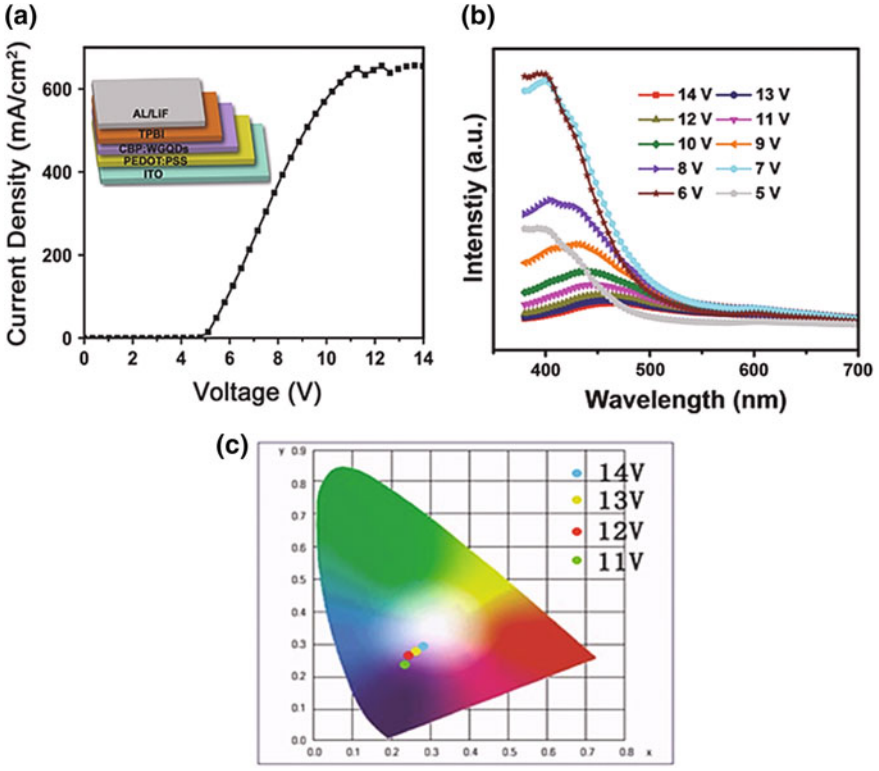

Fig. 4.26 **a** Schematic structure of WLED device by Luo et al. and its corresponding density–voltage (J–V) diagram. **b** Electroluminescent spectra of WLED with applied voltages from 5 to 14 V, blue light emitted at 5–8 V, while white light at 11–14 V. **c** CIE coordinates showing effect of different applied voltages, 14 V being nearest to white [50]

fluorescence, to emit white light under UV irradiation. Mahesh et al. synthesized GQDs via emulsion-templated carbonization of honey, citing the use of precursor to be a sustainable and easily available resource [123].

The luminous flux per input electrical power, also luminous efficiency (lumens/W), is used to evaluate energy efficiency of light sources. The color rendering index (CRI) and Commission International de L'Eclairage (CIE) coordinates (x, y) are photometric characteristics of WLEDs. CRI of 100 represents the best color rendering ability, while CIE coordinates of (0.33, 0.33) is the ideal value for white light [128]. External quantum efficiency (EQE) is the ratio of number of photons emitted from the LED to the number of electrons passing through the device, and currently the highest for using GQDs is 0.19% [50]. As shown in Table 4.2, not all studies using GQD for WLEDs show a varied set of characterization and performance parameters. It is good to mention though that in most reported cases, white light is commonly achieved by chemical modification of GQDs.

4.5.6 Sensors

Sensing mechanisms vary from multiple studies by using either solely or a combination of chemical, colorimetric, electrical and optical strategies. Light can be emitted via a number of luminescent processes, which include photoluminescence, chemiluminescence and electrochemiluminescence (ECL), as illustrated in Fig. 4.27 [130].

Luminescence, which is the generation of light without heat [130], is widely used for its simplicity and sensitivity. Various mechanisms are cited as basis for its use, specifically RET (resonance energy transfer) and fluorescence-based transduction. Electrical methods of generating luminescence are also common and can be combined with chemical and luminescent methods, which can surpass the performances of sole methods. Along with ongoing research on improving detection selectivity and efficiency comes the detection of various analytes ranging from biomolecules to environmental hazards such as those found in bodies of water and air [132] and even from other living organisms such as plants and bacteria.

4.5.7 Photoluminescence (PL) Sensor

The intrinsic fluorescent properties of GQDs due to quantum confinement and edge effects are highly useful in photoluminescent (PL) sensing. These materials show outstanding luminescent performance having stable light emission, high quantum yield, good photostability and easy modulation [3, 133]. Factors affecting GQD PL vary as some are dependent on pH [134] and others on temperature [135].

Table 4.2 Compilation of studies using GQDs as component for WLED

GQD	Function	(Precursor) synthesis	CIE	Performance	Ref.
GQD doped with CBP	W	(Graphite oxide) two-step microwave irradiation	0.27, 0.29 @ 14 V	>200 cd/m^2 EQE—0.19%	[50]
GQDs–RhB	M	(Honey) emulsion-templated carbonization	0.287, 0.31		[123]
Unmodified GOQD	W	(Graphene oxide) oxidative cutting	0.29, 0.34		[125]
GOQD-PLED	W	(Graphene oxide) modified hydrothermal deoxidation		1 cd/m^2 @ 11 V	[126]
Amino GQDs–CNF-clay	C	(Oxidized graphene nanosheets) heat treatment with ammonia	0.33, 0.37 dev A	10 mW/cm^2 for 100 h 31.6 lm/W	[120]
Edge-functionalized GQD (GQD 3c)	C	(Graphite) oxidative cutting	0.324, 0.383		[121]
GQD-QS-CPY	M	(Neem leaves) hydrothermal	0.31, 0.34	450 W/cm^2 for 1000 h	[124]
GQD dispersed in PVK	W	(Potassium sodium tartrate, graphite) controlled oxidation using graphite intercalation compounds		1000 cd/m^2 @ 16 V	[129]
GQD doped with CBP	W	(Graphite) amidative cutting		EQE—0.1%	[127]
GQD-agar	C	(Glucose) microwave-assisted pyrolysis	0.33, 0.38	42.2 lm/W @ 20 mA 61.1% for 100 h	[122]
GQD	C	(Glucose) microwave irradiation	0.282, 0.373		[119]

C light converter, *W* white light phosphor, *C* combined with other fluorophores, *PLED* poly(*N*-vinyl carbazole), *CNF* carbon nanofiber, *QS* quinine sulfate, *CPY* chlorophyll, *PVK* (poly(*N*-vinyl carbazole)), *CBP* 4,4-bis(carbazol-9-yl(biphenyl)

Typically, PL emission is excitation dependent [136]; however, excitation-independent PL emission has been reported as well [137]. Furthermore, PL tuning has been attained by doping GQDs with heteroatoms such as boron [138], fluorine [139], nitrogen [140] and sulfur [141].

PL sensors based on GQDs have so far been used mainly to detect ionic species, small organic molecules and biomacromolecules. The early uses of GQD as PL sensing platforms started with the detection of ferric ions (Fe^{3+}) [89]. Certain analytes such as Fe^{3+} have the ability to quench PL of GQDs; then via Stern–Volmer equation, LOD can be determined. Selectivity, detection range and limit of detection (LOD) are measures to assess sensing effectivity. For example, as shown

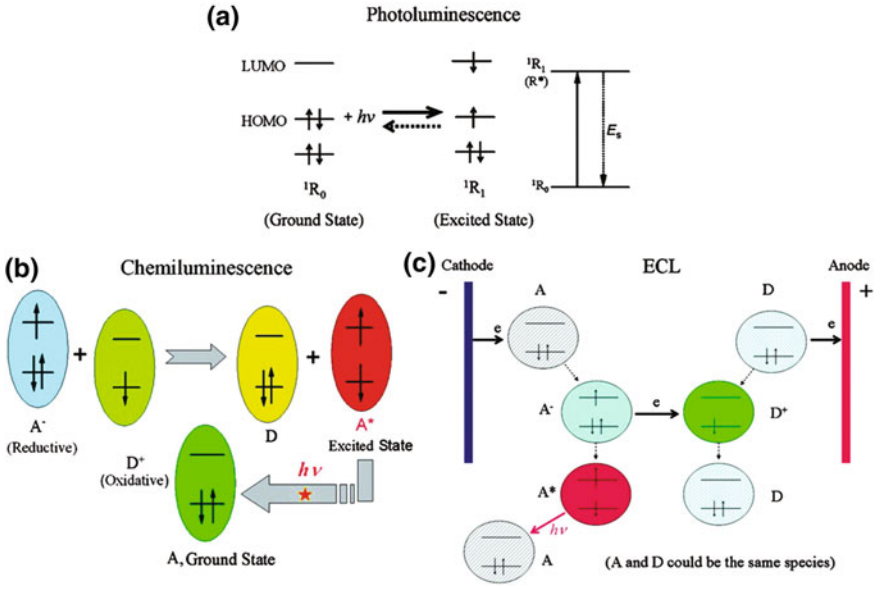

Fig. 4.27 Schematic diagrams showing the general principles of **a** photoluminescence, **b** chemiluminescence, **c** ECL [131]

in Fig. 4.28, Ju et al. used nitrogen-doped GQDs (N-GQDs) in detecting Fe^{3+}, and the quenching of N-GQD fluorescence with increasing analyte concentration provided a linear relation, useful to obtain the detection range of 1–1945 μM and LOD of 90 nM. Then selectivity was tested by applying the same conditions only using Li^+, K^+, Mn^{2+}, Co^{2+}, Ni^{2+}, Cu^{2+}, Zn^{2+}, Cd^{2+}, Pb^{2+}, Na^+, Ag^+, Al^{3+}, Cr^{3+} and Hg^{2+}. Although it was found that Hg^{2+} and Cu^{2+} may interfere with Fe^{3+} detection, the problem can be resolved by using EDTA and cystine as chelating agents for Cu^{2+} and Hg^{2+} [142].

Various GQDs have been used to detect Fe^{3+}, namely S-GQDs [143], dopamine-GQDs [144], amino acid-GQDs [145] and ($BMIM^+$)-GQDs [66], whereas various ionic species have been targets for GQD PL sensing, for example Ag^+ [146], Cu^{2+} [147], Pb^{2+} [148], Al^{3+} [138], Hg^{2+} [149], Cr^{6+} [150], ClO^- [151], PO_4^{3-} [152]. No publications about GQD-based gels in sensing are found [84].

4.5.8 *Electrochemical (EC) Sensor*

EC deals with the interconversion of chemical and electrical energy, and the relation of electricity to chemical changes in a substance. Electrons are detected by EC. Usually, not just one EC capable species is present in solution, but, especially in biological applications, ions from buffers and the analyte itself. Thus, multiple

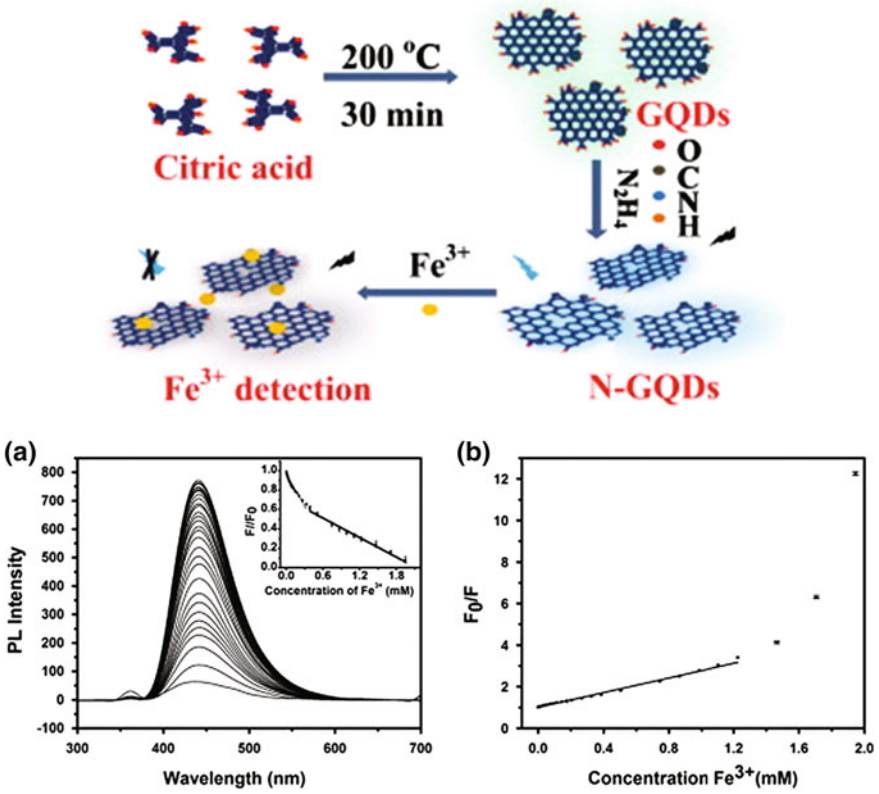

Fig. 4.28 **a** Schematic representation for the synthesis of N-GQDs and the detection of Fe^{3+}. **b** Fluorescent emission spectra of N-GQDs upon addition of different concentrations of Fe^{3+}. Stern–Volmer plot shows linear relation of increasing Fe^{3+} to degree of quenching, that is the reduction of fluorescence intensity [142]

molecules participate in electron transfer reactions and increase the signal, even if not from the molecule of interest [153]. Electrochemical techniques are generally used in the development and design of innovative biosensors for their ease of miniaturization, high sensitivity, low cost and compatibility with advanced microfabrication technology [154]. The inclusion of nanomaterials in electrochemical biosensors amplifies signal response via the following mechanisms: lowering detection potentials, increasing current yield, improving stability and resistance to electrode fouling and enhancing biomolecule compatibility and functionalization [154].

Mazloum-Ardakani et al. [155] created a hybrid electrochemical sensor by using a modified GCE (glassy carbon electrode) to simultaneously detect glutathione (GSH), uric acid (UA) and tryptophan (Trp). The GCE was modified by immersion in a GQD solution at room temperature for 12 h. More recently, Hasanzadeh et al. synthesized magnetic graphene quantum dots (Fe_3O_4 MNPs-GQDs) and were used

for the detection of vitamin C at physiological pH. A +0.21 V decrease in the overvoltage of the vitamin C oxidation reaction was observed when electrodeposited magnetic GQDS on GCE were used as compared to using ordinary electrodes [156]. Another recent study involves decorating N-doped GQDs at N-doped carbon hollow nanospheres with Pd nanoparticles, by Xi et al. The composite was successfully used to detect cancer cells, made possible by the dual signal-amplifying effect caused by the material and with H_2O_2 as biomarker [157]. Detection of other analytes have also been studied, i.e., trinitrotoluene (0.2 ppb LOD) [158], Hg^{2+} (0.02 nM LOD) and Cu^{2+} (0.05 nM LOD) [159], H_2O_2 (0.12 uM LOD) [160], persulfate (0.2 uM LOD) [161].

4.5.9 Electrochemiluminescence (ECL) Sensor

ECL is a means of converting electrical energy into radiative energy by the production of reactive intermediates that emit light when excited as they undergo electron transfer reactions at electrode surface [162]. It is also referred as electrogenerated chemiluminescence, as it involves combining sensing strategies of chemiluminescence and electrochemistry [163]. The mechanism does not involve a light source as luminescence is produced at the electrode and controlled by changing the electrode potential [164]. This eliminates scattered light and luminescent impurities, common to fluorescent labels [165, 166]. Other advantages include controllable time and position of light-emitting reaction, high selectivity, elimination of self-quenching from side reactions, and ECL emitter regeneration [130]. Other articles cite ECL sensors being more facile and highly sensitive relative to PL sensors [167, 168].

Fundamental principles of ECL vary from ion annihilation mechanism, to using co-reactants and generating ECL from luminol. Most publications and commercially available ECL analytical instruments rely on co-reactant ECL technology [130]. With previously overwhelming use of $Rub(bpy)_3^{2+}$ as co-reactant, growing number of studies have shown alternatives for ECL emitters, one of which is through using QDs, as first reported by Ding et al. in 2002 which paved way for using semiconductor quantum dots for ECL studies [169]. However, it is the work of Li et al. in 2012 that pioneered the application of GQDs in ECL sensing [34]. With cysteine as masking agent and $S_2O_8^{2-}$ as co-reactant, Cd^{2+} was successfully detected through its quenching effect on GQD's ECL, Fig. 4.29. From then on, various GQD types and composites have been synthesized for ECL signal amplification [170], detection of ions [35, 171, 172] and bioanalytes [173–175], particularly for immunoassays and aptasensor development.

Though the number of studies on GQD-ECL application is limited, it is interesting to highlight various co-reactants used throughout the years, from the widely used peroxydisulfate ($S_2O_8^{2-}$) [34, 35, 172, 176, 177], to either hydrogen peroxide (H_2O_2) [170, 173], L-cysteine [171], dibutylethanolamine (DBAE) [178], nitrogen dioxide (NO_2) and/or dissolved oxygen (O_2) [179], each having distinction in its

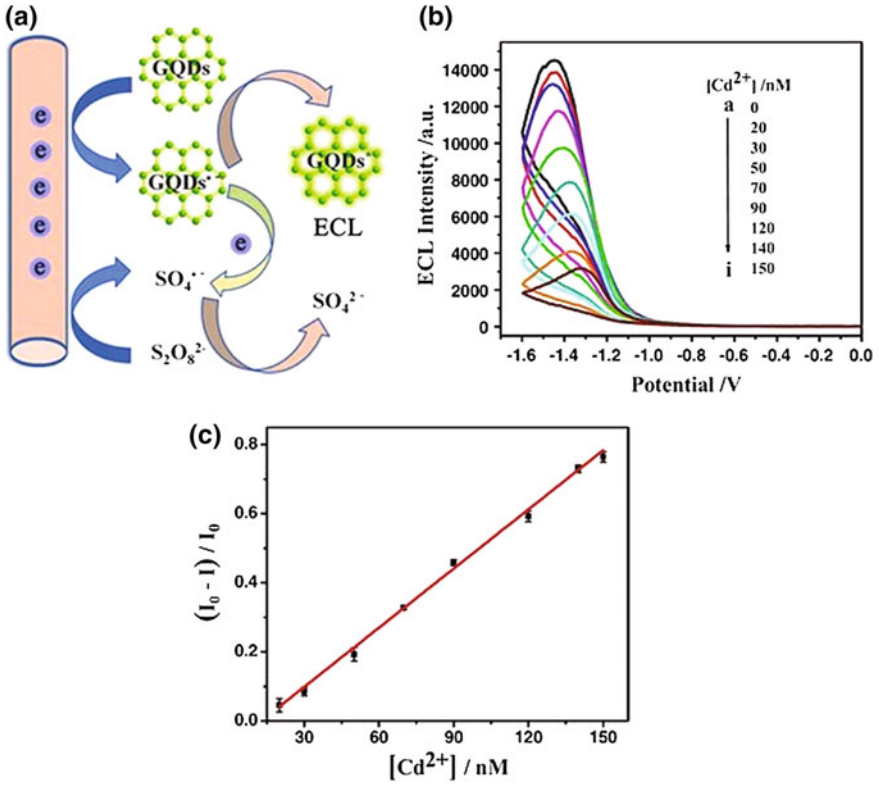

Fig. 4.29 **a** Schematic illustration of GQD-ECL mechanism. **b** ECL potential curves of GQDs in the presence of increasing concentrations of Cd^{2+}; quenching is evident. **c** Linear calibration plot for Cd^{2+} detection, with 13 nM of LOD and detection range of 20–150 nM [34]

possible ECL mechanism, as shown in Fig. 4.30. A co-reactant is any compound that can produce a reactive intermediate. It is highly useful when ECL solvent has a narrow potential window (i.e., water), as such species $R^{\bullet+}$ or $R^{\bullet-}$ cannot be formed. Criteria for co-reactant selection are found in the study of Choi [180]. General mechanisms of co-reactant ECL systems are discussed in detail from the following authors, Miao [130] and Richter [162].

Developments on GQD-ECL involve using non-radiative techniques, namely electrochemiluminescence resonance energy transfer (ERET). A first on the report of ERET between GQDs and AuNPs was conducted by Lu et al. for DNA damage detection [176]. A signal off–on mechanism was developed by linking AuNPs with single-stranded DNA (cp53 ssDNA) probe. The ECL signal of GQDs was quenched via non-covalent binding of AuNPs-ssDNA to GQDs. ECL was recovered as AuNPs-dsDNA that were formed between the hybridization of AuNPs-ssDNA and target p53 DNA have weak non-covalent interactions with GQDs. ECL response brought by fully hybridized AuNPs-dsDNA was then compared to using

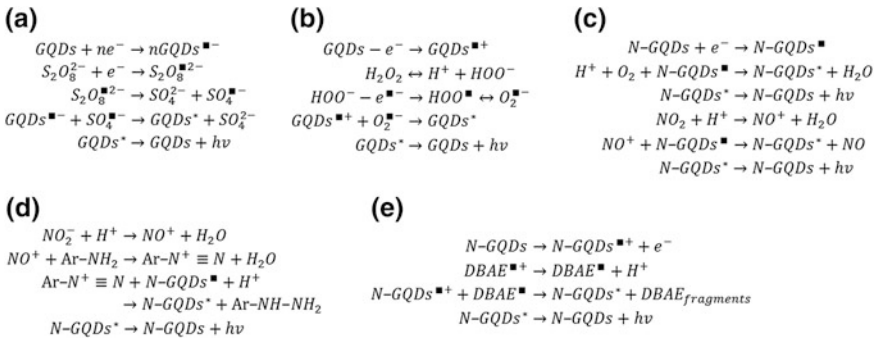

Fig. 4.30 Compiled possible ECL mechanisms of different co-reactants, namely **a** peroxydisulfate ($S_2O_8^{2-}$) [34], **b** hydrogen peroxide (H_2O_2) [170], **c** dissolved oxygen (O_2) [179], **d** nitrogen dioxide (NO_2) [179], **e** dibutylethanolamine (DBAE) [178]. Cation $R^{\bullet +}$ or anion $R^{\bullet -}$ radicals are formed upon electro-oxidation, resulting in excited-state GQDs (GQD*) as source of emitted light (*hv*)

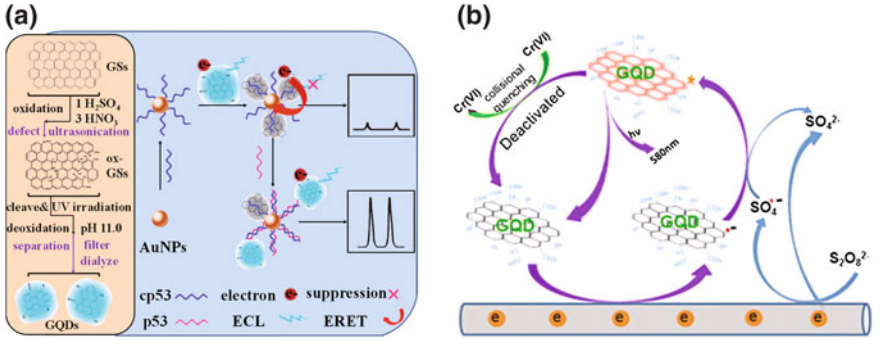

Fig. 4.31 Schematic representations of **a** AuNP-induced ECL dynamic quenching of GQDs [176] and **b** ECL reaction mechanism of GQDs/$S_2O_8^{2-}$ in the presence of Cr(VI) [35]

deliberately damaged p53 DNA, which recovered less of ECL signal, thus identifying DNA damage.

An illustrative comparison on applying ERET versus collisional quenching is shown in Fig. 4.31. The study by Chen et al. used ECL signals from GQDs, with $S_2O_8^{2-}$ as co-reactant, to detect hexavalent chromium in real water samples. A highly selective sensor with LOD of 20 nM runs on the principle of heavy atoms deactivating the excited state of luminophores through collisional quenching [35].

Studies involving the use of GQD composites as platforms for ECL sensing continue to grow. As shown in Table 4.3, the high performance of these composites in terms of sensitivity and selectivity make them effective as probes for monitoring environmental contaminants and detecting biomacromolecules.

4.5.10 Catalysis

4.5.10.1 Electrocatalysis—Oxygen Reduction Reaction (ORR) in Fuel Cells

Fuel cell (FC) technology is a promising solution for rising global energy demand [181–183]. It basically converts chemical energy to electrical energy by electrochemically reducing oxygen and oxidizing fuel into only water as the by-product [181]. Proton exchange membrane fuel cells (PEMFCs) and direct methanol fuel cells (DMFCs) are one of the attractive FC classifications for their low-temperature operations (<100 °C) and long life span [184] (i.e., 10,000 h [185], 20,000 h—7 kW [186]). Conventionally for both FC types, Pt or Pt-containing catalysts are anchored as cathode and anode. However, using such precious material accounts for 50% of the overall cost of the FC system [184], giving it a huge disadvantage for commercialization. Moreover, Pt-based electrodes are prone to time-dependent drift, CO deactivation and low tolerance for crossover effects [187, 188]. Metal-free catalysts, specifically carbon structures, are thus explored as feasible alternatives for having high fraction of sp^2 hybridization, high specific surface area, modifiable structures by doping and/or decorating with metals or non-metals, and inexpensive sources, varying from organic and inorganic precursors [189]. In particular, GQDs are advantageous for their abundant edge features as electrochemically catalyzed reactions mostly occur at the edge planes rather than the basal plane [190, 191]. When doped with heteroatoms, the electron neutrality is drastically changed, creating more active sites favorable for O_2 adsorption [189]. All these features could then dramatically reduce cost and increase FC efficiency.

Li et al. reported for the first time the solution chemistry approach to synthesize N-GQDs and dopant-free GQDs, with the purpose of investigating the effect of N-doping on the ORR catalytic activity. It was found that the catalytic performance increases with the size of N-GQDs, and the conjugation size in N-GQDs is a key parameter for further improving the catalytic activities [193]. As shown in Fig. 4.32 the N-containing 1, 2, and 11 GQDs show ORR onset potentials at −0.04, −0.10, and −0.14 V, respectively, relative to that for the commercial Pt/C catalyst. In addition, the cathodic current density increases with size of the QDs, indicating the improved catalytic activity of larger QDs, to highlight the electrocatalytic performance of the study.

Recent GQD-based ORR catalytic applications involve synthesizing GQDs into graphene composites as conducted by Jin et al. [194]. The new class of ORR catalyst hybrid has a Tafel slope of ca. 87.7 mV per decade, similar to that of Pt/C (40%) catalyst. Using the material follows the desired one-step $4e^-$ reduction path as the calculated transferred electron number (n) per oxygen molecule via the K-L equation was about 3.91. Another recent carbon-based composite comes from the study of Liu et al. [195]. They created a novel 3D graphene–aerogel-supported and GQD-modified γ-MnOOH nanotubes (γ-MnOOH NTs-GQD on GA) with comparable onset potential (0.11 vs. 0.13 V), half-wave potential (−0.23 vs. −0.17 V) and Tafel slope (82.7 vs. 78.5 mV/dec) to Pt/C (20%). It is also interesting to

Table 4.3 Compilation of GQD studies using ECL mechanism for sensing

Sensing strategy	Graphene quantum dot			Analyte	LOD (nM) (detection range)	Test of selectivity	Ref.
	Type/composite	Precursor	Preparation method				
ECL	GQD	Graphene oxide	Microwave-assisted cleaving and reduction	Cd^{2+}	13 (20–150)	Mg^{2+}, Ba^{2+}, Co^{2+}, Fe^{2+}, Fe^{3+}, Na^{+}, K^{+}, Zn^{2+}, Al^{3+}, Cu^{2+}, Pb^{2+}, Ni^{2+}	[34]
	SiO_2 NS/GQD/ssDNA2	Graphite oxide	Ultrasonication (cell crusher), hydrothermal	ATP	$1.5E^{-3}$ ($5E^{-3–5}$)	CTP, GTP, UTP	[170]
	GQD (luminophore)	Graphite oxide	Thermal reduction ultraviolet irradiation	p53 ssDNA	13 (25–400)		[176]
	GQD	Vulcan CX-72 carbon black	Chemical oxidation	Pb^{2+}	70 (1E2–1E3)	Hg^{2+}, Cu^{2+}, Co^{2+}, Fe^{3+}, Ni^{2+}, Ag^{+}, Ca^{2+}. Cd^{2+}, Mn^{2+}, Mg^{2+}, Ba^{2+}, Na^{+}, Li^{+}, $Cr_2O_7^{2-}$, Zn^{2+}	[171]
	MWCNTs/N-GQDs/Ab_2 (label)	Graphene oxide	Solvothermal	α-fetoprotein	$1.8E^{-5}$ ($7.3E^{-5}$–$1.5E^{-3}$)	CEA, CA-125, PSA	[178]
	GQD	Vulcan CX-72 carbon black	Chemical oxidation	Cr^{6+}	20 (50–$6E^{4}$)	MnO_4^{-}, ClO_4^{-}, ClO^{-}, Zn^{2+}, Ca^{2+}, Mg^{2+}, K^{+}, Na^{+}, Al^{3+}, Fe^{3+}, Fe^{2+}, Cu^{2+}, Co^{2+}, Hg^{2+}, Pb^{2+}, Ag^{+}, Cr^{3+}, Cd^{2+}	[35]
	GQD-Cu_2O NS on GCE	Carbon fibers	Acid treatment chemical exfoliation	PCP	0.03 (0.08–1232)	3-CP, 1,3,5-TCP, 2,4-DCP, Fe^{3+}, Fe^{2+}, Cu^{2+}, Cl^{-}	[192]
	Au/B-GQDs-DNA on Pt	B-Graphene rods	Electrolytic exfoliation	miRNAs-20a	($100–1E^{7}$)	Single-base mismatch miRNA, three-base mismatch miRNA, non-complementary miRNA	[177]

(continued)

Table 4.3 (continued)

Sensing strategy	Graphene quantum dot			Analyte	LOD (nM) (detection range)	Test of selectivity	Ref.
	Type/composite	Precursor	Preparation method				
	GQD-CS on Au	Carbon fibers	Acid treatment chemical exfoliation	$S_2O_8^{2-}$	3300 (1E4–1.5E8)	$S_2O_3^{2-}$, SO_4^{2-}, SO_3^{2-}, Na^+	[172]
	N-GQD/CS on GCE	Citric acid	Carbonization	Nitroaniline	5 (10–1000)	4-NCB, MB, benzene, hydroquinone, 2,4,6-TNP	[179]

CTP cytidine triphosphate, *GTP* guanosine triphosphate, *UTP* uridine triphosphate, *NS* nanospheres, *ATP* adenosine triphosphate, Ab_2 monoclonal antibody, *CEA* carcinoembryonic antigen, *CA-125* carcinoma antigen 125, *PSA* prostate-specific antigen, *CS* chitosan, *PCP* pentachlorophenol, *3-CP* 3-Chlorophenol, *1,3,5-TCP* 2,4,6-trichlorophenol, *2,4-DCP* 2,4-dichlorophenol, *miRNA* microRNA, *4-NCB* 4-nitrochlorobenzene, *MB* methylbenzene, *2,4,6-TNP* 2,4,6-trinitrophenol, *ATP* adenosine triphosphate, *GCE* glassy carbon electrode

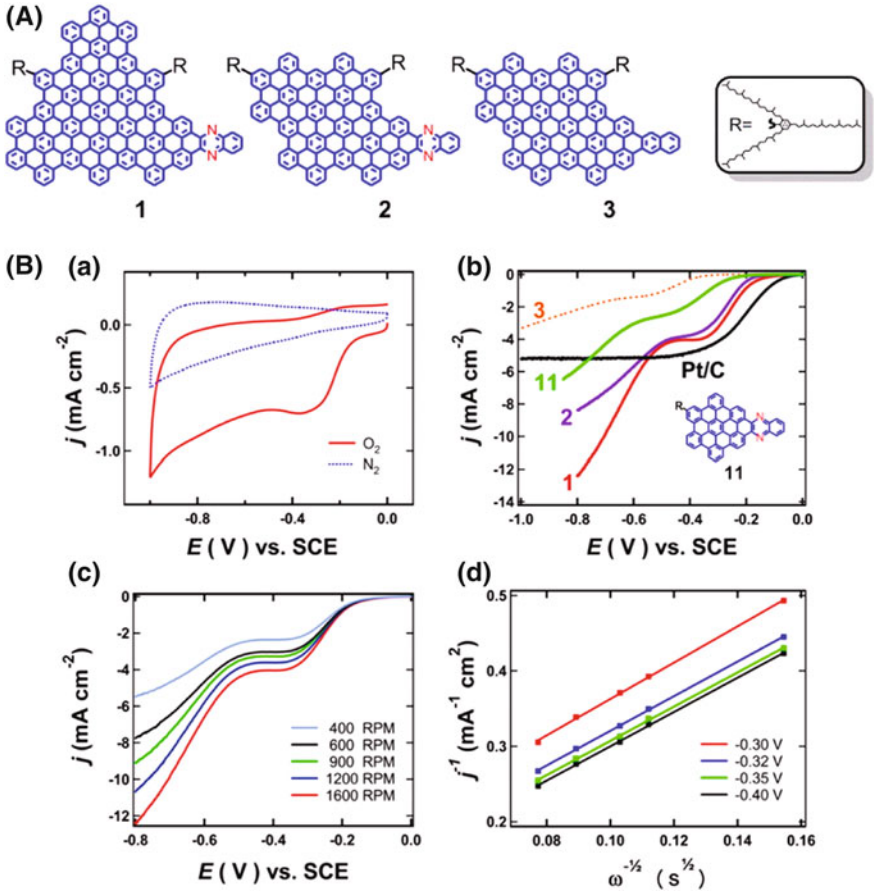

Fig. 4.32 Differing structures of N-doped GQDs labeled as 1,2, and undoped GQD 3 for size comparison studies. **a** Cyclic voltammograms of N-GQDs (*1*) on a glassy carbon in a nitrogen- and an oxygen (O_2)-saturated 0.1 M potassium hydroxide (KOH) solution; **b** LSV curves of molecules *1–3* and platinum/carbon (Pt/C) in an O_2-saturated 0.1 M KOH solution. The LSV curve for *11* is also given, which has a much smaller N-substituted heterocycle and the structure is shown in the inset; **c** LSVs of N-GQDs (*1*) in an O-saturated 0.1 M KOH solution at different rotating speeds; **d** Koutecky–Levich plots for N-GQDs (*1*), obtained from the data in (**c**) at various voltage values. A global fitting of the plots reveals that the number of electrons transferred per O molecule is 3.9 [193]

highlight how they obtained the charge transfer resistance (R_{ct}) of the hybrid, that is 3715 Ω, smaller than the hybrids without GQDs. This shows that the material as electrode exhibits much faster transport of electrons during ORR. Lastly, another important and recent study involves comparing the ORR activities of GQD-based composites in both alkaline and acidic electrolyte solution, as conducted by Zhang et al. [196]. Using nitrogen-doped GQDs anchored on thermally reduced graphene oxide as electrocatalyst, a different onset potential was obtained for the material

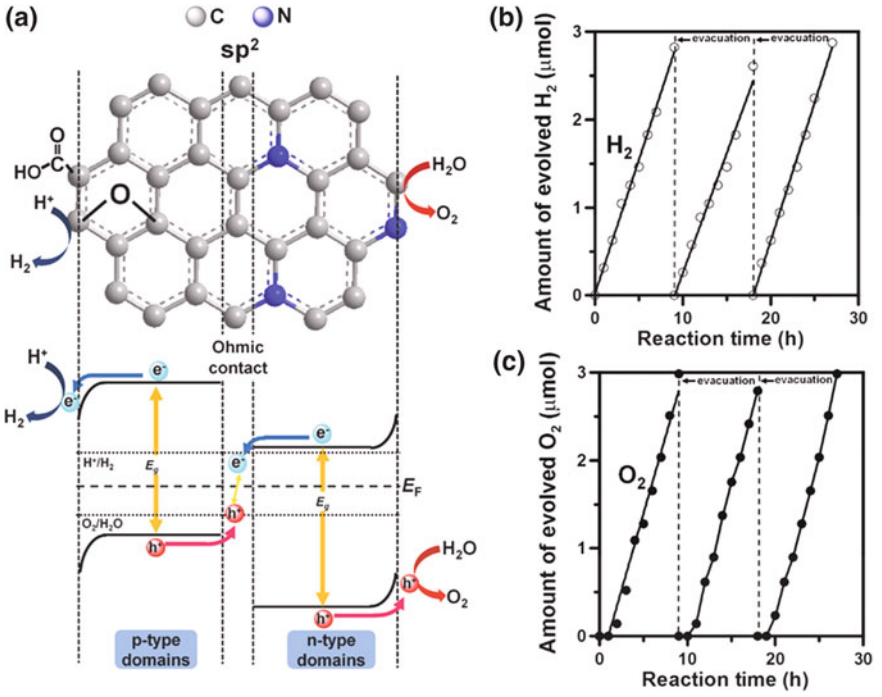

Fig. 4.33 **a** The configuration and energy diagram for the GQD photochemical diode consist of the p- and n-type domains connected through the sp^2 clusters as ohmic contact. Evolution of **b** H_2 and **c** O_2 over 1.2 g of GQDs [197]

immersed in 0.1 M KOH and 0.1 M $HClO_4$ solution, having values of 1.03 and 0.80 V, respectively. Both systems have desirable n values of 3.94 and for alkaline and 3.81 acidic electrolyte solution.

4.5.10.2 Photocatalysis

Yeh et al. synthesized nitrogen-doped graphene oxide quantum dots (GOQDs) to demonstrate the capability of graphene-based structures in catalyzing overall water splitting under visible light irradiation. With a bandgap of 2.2 eV, excitons were generated as the material was capable of absorbing visible light. Doping of GOQD and its inherent functional groups resulted in the formation of p- and n-type photochemical domains that were responsible for the production of hydrogen and oxygen gases, as shown in Fig. 4.33a and further illustrated in Fig. 4.33b and c. The metal-free catalyst shows the recent efforts of scientist on providing sustainable and environment-friendly strategy for photocatalytic water splitting [197].

Recent studies involve promoting the chemical stability of graphene-based photocatalysts by incorporating charge-mediating GO sheets in N-GOQDs

(photocatalyst). Chen et al. [198] discovered that by the vectorial electron transfer and relocation of active sites to the GO sheets, catalyzed hydrogen evolution was stable for 96 h under visible light. Furthermore, the GO sheets acted as electron sink to suppress charge recombination in the N-GOQDs and prevented reaction intermediates from the damaging its framework. Other recent GQD composites used in photocatalytic studies are: GQD-TiO_2, which reportedly shows a photocurrent enhancement of $\sim$70% for water oxidation compared to pristine TiO_2 [199]; 3-nm GQDs incorporated to mesoporous Bi_2MoO_6 frameworks which photocatalyzed 69% of pollutants RhB and BPA under stimulated sunlight within 30 min, that is 2.3 times higher than bare Bi_2MoO_6 [200]; and metal-free g-C_3N_4/GQD composites used as photocatalyst for H_2 evolution in water splitting, which had 2.16 times higher hydrogen evolution rate than the GQD-free material.

4.5.10.3 Energy-Related Application

Photovoltaics (PV)

Tang et al. [201] first studied the photoresponsive properties of N-GQDs and observed the material to emit broad spectral wavelengths covering deep ultraviolet, visible and NIR (300 to >1000 nm). It was attributed to its layered structure providing a large conjugated system with delocalized π electrons. With responsivity of 325 V/W at 405 nm and photoresponse ranging from 365 to 980 nm, a novel functional material was synthesized, capable of absorbing and emitting broad spectral ranges useful for photovoltaic applications.

From then on, heteroatom-doped GQDs continue to receive much attention for PV applications for its adjustable bandgap and multiple excitons generation capabilities. For example, doping GQDs with Cl have been found to increase carrier concentration and produce a high ratio of photocurrent to dark current at 10^5 under 405-nm laser irradiation [202]. S-GQDs were observed to have higher photocurrent than GQDs alone, as more electrons are generated from the naturally electron-donating S atom [141].

To date, studies involve the attractive benefits of GQDs in solar cells from either acting as a hole/electron transport agent [203], active layer additive in donor/acceptor blends [204] or sensitizers [205]. They can be also used as intermediate buffer layer between TiO_2 and poly(3-hexylthiophene) P3HT, forming a cascade of energy levels [206]. These desirable effects further opened the door for using GQDs as photovoltage and efficiency enhancers for dye-sensitized solar cells (DSSCs) [207] and quantum dot-sensitized solar cells (QDSCs) [208].

4.6 Prospect of GQDs

To sum up, due to GQDs unique optical, physical and chemical properties, it has wide application window, particularly biological applications. However, the research on GQDs is not yet proficient, and there is a huge development space for GQDs. Based on above PL discussion, there are some ambiguous PL phenomena such as excitation-dependent PL emission [13] and up-conversion PL [6, 11], needing to be interpreted. Recently, some researchers try to explain these phenomena by their experiment results, but still having some challenges. Additionally, quantum yield (QY) is also a significant factor for applications. The QY of GQDs, which varies with the fabrication method and the involved surface chemistry, needs to be further improved [2]. For example, the QY of red-luminescent GQDs usually get low. It will influence the application of biotechnology. Therefore, there are still many issues waiting to be settled for further solving.

Nevertheless, there is no doubt that it is a potential and novel material in the future. With their uniform size, excellent PL and high quantum yields, GQDs will be used in more creative applications [1].

References

1. L. Lin, M. Rong, F. Luo, D. Chen, Y. Wang, X. Chen, Luminescent graphene quantum dots as new fluorescent materials for environmental and biological applications. TrAC Trends Anal. Chem. **54**, 83–102 (2014)
2. Z. Wang, H. Zeng, L. Sun, Graphene quantum dots: versatile photoluminescence for energy, biomedical, and environmental applications. J. Mater. Chem. C **3**(6), 1157–1165 (2015)
3. L.A. Ponomarenko, F. Schedin, M.I. Katsnelson et al., Chaotic Dirac Billiard in graphene quantum dots. Science **320**(5874), 356–358 (2008)
4. S. Benítez-Martínez, M. Valcárcel, Graphene quantum dots in analytical science. TrAC Trends Anal. Chem. **72**, 93–113 (2015)
5. Y. Dong, J. Lin, Y. Chen, F. Fu, Y. Chi, G. Chen, Graphene quantum dots, graphene oxide, carbon quantum dots and graphite nanocrystals in coals. Nanoscale **6**(13), 7410–7415 (2014)
6. X.T. Zheng, A. Ananthanarayanan, K.Q. Luo, P. Chen, Glowing graphene quantum dots and carbon dots: properties, syntheses, and biological applications. Small **11**(14), 1620–1636 (2015)
7. X. Li, M. Rui, J. Song, Z. Shen, H. Zeng, Carbon and graphene quantum dots for optoelectronic and energy devices: a review. Adv. Func. Mater. **25**(31), 4929–4947 (2015)
8. S.H. Jin, D.H. Kim, G.H. Jun, S.H. Hong, S. Jeon, Tuning the photoluminescence of graphene quantum dots through the charge transfer effect of functional groups. ACS Nano. **7**(2), 1239–1245 (2013)
9. R. Ye, Z. Peng, A. Metzger et al., Bandgap engineering of coal-derived graphene quantum dots. ACS Appl. Mater. Interfaces. **7**(12), 7041–7048 (2015)
10. J. Shen, Y. Zhu, X. Yang, C. Li, Graphene quantum dots: emergent nanolights for bioimaging, sensors, catalysis and photovoltaic devices. Chem. Commun. (Camb.) **48**(31), 3686–3699 (2012)
11. L. Li, G. Wu, G. Yang, J. Peng, J. Zhao, J.J. Zhu, Focusing on luminescent graphene quantum dots: current status and future perspectives. Nanoscale. **5**(10), 4015–4039 (2013)

12. X. Li, S. Zhang, S.A. Kulinich, Y. Liu, H. Zeng, Engineering surface states of carbon dots to achieve controllable luminescence for solid-luminescent composites and sensitive Be^{2+} detection. Sci. Rep. **4** (2014)
13. Z. Gan, H. Xu, Y. Hao, Mechanism for excitation-dependent photoluminescence from graphene quantum dots and other graphene oxide derivatives: consensus, debates and challenges. Nanoscale **8**(15), 7794–7807 (2016)
14. R. Liu, D. Wu, X. Feng, K. Mullen, Bottom-up fabrication of photoluminescent graphene quantum dots with uniform morphology. J. Am. Chem. Soc. **133**(39), 15221–15223 (2011)
15. J. Tan, R. Zou, J. Zhang, W. Li, L. Zhang, D. Yue, Large-scale synthesis of N-doped carbon quantum dots and their phosphorescence properties in a polyurethane matrix. Nanoscale **8** (8), 4742–4747 (2016)
16. W.-J. Niu, Y. Li, R.-H. Zhu, D. Shan, Y.-R. Fan, X.-J. Zhang, Ethylenediamine-assisted hydrothermal synthesis of nitrogen-doped carbon quantum dots as fluorescent probes for sensitive biosensing and bioimaging. Sens. Actuators B Chem. **218**, 229–236 (2015)
17. S. Zhu, Q. Meng, L. Wang et al., Highly photoluminescent carbon dots for multicolor patterning, sensors, and bioimaging. Angew. Chem. Int. Ed. Engl. **52**(14), 3953–3957 (2013)
18. D. Pan, J. Zhang, Z. Li, M. Wu, Hydrothermal route for cutting graphene sheets into blue-luminescent graphene quantum dots. Adv. Mater. **22**(6), 734–738 (2010)
19. Z. Gan, S. Xiong, X. Wu et al., Mechanism of Photoluminescence from chemically derived graphene oxide: role of chemical reduction. Adv. Opt. Mat. **1**(12), 926–932 (2013)
20. Y. Deng, X. Chen, F. Wang, X. Zhang, D. Zhao, D. Shen, Environment-dependent photon emission from solid state carbon dots and its mechanism. Nanoscale **6**(17), 10388–10393 (2014)
21. S.K. Cushing, M. Li, F. Huang, N. Wu, Origin of strong excitation wavelength dependent fluorescence of graphene oxide. ACS Nano. **8**(1), 1002–1013 (2014)
22. Y. Dong, H. Pang, H.B. Yang et al., Carbon-based dots co-doped with nitrogen and sulfur for high quantum yield and excitation-independent emission. Angew. Chem. Int. Ed. **52**(30), 7800–7804 (2013)
23. T.F. Yeh, W.L. Huang, C.J. Chung et al., Elucidating quantum confinement in graphene oxide dots based on excitation-wavelength-independent photoluminescence. J. Phys. Chem. Lett. **7**(11), 2087–2092 (2016)
24. Z.-C. Yang, M. Wang, A.M. Yong et al., Intrinsically fluorescent carbon dots with tunable emission derived from hydrothermal treatment of glucose in the presence of monopotassium phosphate. Chem. Commun. **47**(42), 11615–11617 (2011)
25. S. Kim, S.W. Hwang, M.-K. Kim et al., Anomalous behaviors of visible luminescence from graphene quantum dots: interplay between size and shape. ACS Nano. **6**(9), 8203–8208 (2012)
26. H. Ding, S.-B. Yu, J.-S. Wei, H.-M. Xiong, Full-color light-emitting carbon dots with a surface-state-controlled luminescence mechanism. ACS Nano (2015)
27. H. Tetsuka, A. Nagoya, T. Fukusumi, T. Matsui, Molecularly designed, nitrogen-functionalized graphene quantum dots for optoelectronic devices. Adv. Mater. **28** (23), 4632–4638 (2016)
28. L. Cao, X. Wang, M.J. Meziani et al., Carbon dots for multiphoton bioimaging. J. Am. Chem. Soc. **129**(37), 11318–11319 (2007)
29. E. Lee, J. Ryu, J. Jang, Fabrication of graphene quantum dots via size-selective precipitation and their application in upconversion-based DSSCs. Chem. Commun. (Camb.) **49**(85), 9995–9997 (2013)
30. S. Zhu, J. Zhang, X. Liu et al., Graphene quantum dots with controllable surface oxidation, tunable fluorescence and up-conversion emission. RSC Adv. **2**(7), 2717 (2012)
31. J. Shen, Y. Zhu, C. Chen, X. Yang, C. Li, Facile preparation and upconversion luminescence of graphene quantum dots. Chem. Commun. (Camb.) **47**(9), 2580–2582 (2011)
32. X. Wen, P. Yu, Y.R. Toh, X. Ma, J. Tang, On the upconversion fluorescence in carbon nanodots and graphene quantum dots. Chem. Commun. (Camb.) **50**(36), 4703–4706 (2014)

33. C. Frigerio, D.S. Ribeiro, S.S. Rodrigues et al., Application of quantum dots as analytical tools in automated chemical analysis: a review. Anal. Chim. Acta **735**, 9–22 (2012)
34. L.-L. Li, J. Ji, R. Fei et al., A facile microwave avenue to electrochemiluminescent two-color graphene quantum dots. Adv. Func. Mater. **22**(14), 2971–2979 (2012)
35. Y. Chen, Y. Dong, H. Wu, C. Chen, Y. Chi, G. Chen, Electrochemiluminescence sensor for hexavalent chromium based on the graphene quantum dots/peroxodisulfate system. Electrochim. Acta **151**, 552–557 (2015)
36. X. Du, D. Jiang, Q. Liu, G. Zhu, H. Mao, K. Wang, Fabrication of graphene oxide decorated with nitrogen-doped graphene quantum dots and its enhanced electrochemiluminescence for ultrasensitive detection of pentachlorophenol. Analyst **140**(4), 1253–1259 (2015)
37. S. Zhu, J. Zhang, C. Qiao et al., Strongly green-photoluminescent graphene quantum dots for bioimaging applications. Chem. Commun. (Camb.) **47**(24), 6858–6860 (2011)
38. Y. Dong, C. Chen, X. Zheng et al., One-step and high yield simultaneous preparation of single- and multi-layer graphene quantum dots from CX-72 carbon black. J. Mater. Chem. **22**(18), 8764 (2012)
39. S. Zhu, J. Zhang, S. Tang et al., Surface chemistry routes to modulate the photoluminescence of graphene quantum dots: from fluorescence mechanism to up-conversion bioimaging applications. Adv. Func. Mater. **22**(22), 4732–4740 (2012)
40. J. Peng, W. Gao, B.K. Gupta et al., Graphene quantum dots derived from carbon fibers. Nano Lett. **12**(2), 844–849 (2012)
41. Y. Sun, S. Wang, C. Li et al., Large scale preparation of graphene quantum dots from graphite with tunable fluorescence properties. Phys. Chem. Chem. Phys. **15**(24), 9907–9913 (2013)
42. Y. Shin, J. Lee, J. Yang et al., Mass production of graphene quantum dots by one-pot synthesis directly from graphite in high yield. Small **10**(5), 866–870 (2014)
43. F. Yang, M. Zhao, B. Zheng, D. Xiao, L. Wu, Y. Guo, Influence of pH on the fluorescence properties of graphene quantum dots using ozonation pre-oxide hydrothermal synthesis. J. Mater. Chem. **22**(48), 25471 (2012)
44. H. Yoon, Y.H. Chang, S.H. Song et al., Intrinsic photoluminescence emission from subdomained graphene quantum dots. Adv. Mater. (2016)
45. M. Zhang, L. Bai, W. Shang et al., Facile synthesis of water-soluble, highly fluorescent graphene quantum dots as a robust biological label for stem cells. J. Mater. Chem. **22**(15), 7461 (2012)
46. Z. Zhang, J. Zhang, N. Chen, L. Qu, Graphene quantum dots: an emerging material for energy-related applications and beyond. Energy Environ. Sci. **5**(10), 8869 (2012)
47. G.S. Bumbrah, R.M. Sharma, Raman spectroscopy—basic principle, instrumentation and selected applications for the characterization of drugs of abuse. Egypt. J. Forensic Sci. **6**(3), 209–215 (2016)
48. D. Qu, M. Zheng, L. Zhang et al., Formation mechanism and optimization of highly luminescent N-doped graphene quantum dots. Sci. Rep. **4**, 5294 (2014)
49. Y. Shin, J. Park, D. Hyun et al., Acid-free and oxone oxidant-assisted solvothermal synthesis of graphene quantum dots using various natural carbon materials as resources. Nanoscale **7**(13), 5633–5637 (2015)
50. Z. Luo, G. Qi, K. Chen et al., Microwave-assisted preparation of white fluorescent graphene quantum dots as a novel phosphor for enhanced white-light-emitting diodes. Adv. Func. Mater. **26**(16), 2739–2744 (2016)
51. W. Zhang, Y. Liu, X. Meng et al., Graphenol defects induced blue emission enhancement in chemically reduced graphene quantum dots. Phys. Chem. Chem. Phys. **17**(34), 22361–22366 (2015)
52. P. Gong, K. Hou, X. Ye, L. Ma, J. Wang, S. Yang, Synthesis of highly luminescent fluorinated graphene quantum dots with tunable fluorine coverage and size. Mater. Lett. **143**, 112–115 (2015)
53. R. Ye, C. Xiang, J. Lin et al., Coal as an abundant source of graphene quantum dots. Nat. Commun. **4**, 2943 (2013)

54. M. Hassan, E. Haque, K.R. Reddy, A.I. Minett, J. Chen, V.G. Gomes, Edge-enriched graphene quantum dots for enhanced photo-luminescence and supercapacitance. Nanoscale **6**(20), 11988–11994 (2014)
55. L. Wang, W. Li, B. Wu et al., Facile synthesis of fluorescent graphene quantum dots from coffee grounds for bioimaging and sensing. Chem. Eng. J. **300**, 75–82 (2016)
56. L. Lin, S. Zhang, Creating high yield water soluble luminescent graphene quantum dots via exfoliating and disintegrating carbon nanotubes and graphite flakes. Chem. Commun. (Camb.) **48**(82), 10177–10179 (2012)
57. A. Gupta, G. Chen, P. Joshi, S. Tadigadapa, P.C. Eklund, Raman scattering from high-frequency phonons in supported n-graphene layer films. Nano Lett. **6**(12), 2667–2673 (2006)
58. Y. Dong, J. Shao, C. Chen et al., Blue luminescent graphene quantum dots and graphene oxide prepared by tuning the carbonization degree of citric acid. Carbon **50**(12), 4738–4743 (2012)
59. X. Zhou, Y. Zhang, C. Wang et al., Photo-fenton reaction of graphene oxide: a new strategy to prepare graphene quantum dots for DNA cleavage. ACS Nano **6**(8), 6592–6599 (2012)
60. J. Shen, Y. Zhu, X. Yang, J. Zong, J. Zhang, C. Li, One-pot hydrothermal synthesis of graphene quantum dots surface-passivated by polyethylene glycol and their photoelectric conversion under near-infrared light. New J. Chem. **36**(1), 97–101 (2012)
61. J. Lu, J. Yang, J. Wang, A. Lim, S. Wang, K.P. Loh, One-Pot synthesis of fluorescent carbon nanoribbons, nanoparticles, and graphene by the exfoliation of graphite in ionic liquids. ACS Nano **3**(8):2367–2375 (2009)
62. L. Zheng, Y. Chi, Y. Dong, J. Lin, B. Wang, Electrochemiluminescence of water-soluble carbon nanocrystals released electrochemically from graphite. J. Am. Chem. Soc. **131**(13), 4564–4565 (2009)
63. J. Zhou, C. Booker, R. Li et al., An electrochemical avenue to blue luminescent nanocrystals from multiwalled carbon nanotubes (MWCNTs). J. Am. Chem. Soc. **129**(4), 744–745 (2007)
64. Y. Li, Y. Hu, Y. Zhao et al., An electrochemical avenue to green-luminescent graphene quantum dots as potential electron-acceptors for photovoltaics. Adv. Mater. **23**(6), 776–780 (2011)
65. D.B. Shinde, V.K. Pillai, Electrochemical preparation of luminescent graphene quantum dots from multiwalled carbon nanotubes. Chemistry **18**(39), 12522–12528 (2012)
66. A. Ananthanarayanan, X. Wang, P. Routh et al., Facile synthesis of graphene quantum dots from 3D graphene and their application for Fe^{3+} sensing. Adv. Func. Mater. **24**(20), 3021–3026 (2014)
67. S. Zhuo, M. Shao, S.-T. Lee, Upconversion and downconversion fluorescent graphene quantum dots: ultrasonic preparation and photocatalysis. ACS Nano **6**(2), 1059–1064 (2012)
68. H. Li, X. He, Y. Liu et al., One-step ultrasonic synthesis of water-soluble carbon nanoparticles with excellent photoluminescent properties. Carbon **49**(2), 605–609 (2011)
69. L. Wang, X. Chen, Y. Lu, C. Liu, W. Yang, Carbon quantum dots displaying dual-wavelength photoluminescence and electrochemiluminescence prepared by high-energy ball milling. Carbon **94**, 472–478 (2015)
70. J. Lu, P.S.E. Yeo, C.K. Gan, P. Wu, K.P. Loh, Transforming C60 molecules into graphene quantum dots. Nat. Nano **6**(4), 247–252 (2011)
71. C.K. Chua, Z. Sofer, P. Šimek et al., Synthesis of strongly fluorescent graphene quantum dots by cage-opening buckminsterfullerene. ACS Nano **9**(3), 2548–2555 (2015)
72. H. Yang, W. Liu, C. Ma et al., Gold–silver nanocomposite-functionalized graphene based electrochemiluminescence immunosensor using graphene quantum dots coated porous PtPd nanochains as labels. Electrochim. Acta **123**, 470–476 (2014)
73. J. Gu, X. Zhang, A. Pang, J. Yang, Facile synthesis and photoluminescence characteristics of blue-emitting nitrogen-doped graphene quantum dots. Nanotechnology **27**(16), 165704 (2016)

74. J. Schneider, C.J. Reckmeier, Y. Xiong, et al. Molecular fluorescence in citric acid-based carbon dots. J. Phys. Chem. C. **121**(3), 2014–2022 (2017).
75. S. Qu, D. Zhou, D. Li et al., Toward efficient orange emissive carbon nanodots through conjugated sp-domain controlling and surface charges engineering. Adv. Mater. (2016)
76. F.A. Permatasari, A.H. Aimon, F. Iskandar, T. Ogi, K. Okuyama, Role of C-N configurations in the photoluminescence of graphene quantum dots synthesized by a hydrothermal route. Sci. Rep. **6**, 21042 (2016)
77. J.C. Hebden, S.R. Arridge, D.T. Delpy, Optical imaging in medicine: I. Experimental techniques. Phys. Med. Biol. **42**(5), 825 (1997)
78. T.F. Massoud, S.S. Gambhir, Molecular imaging in living subjects: seeing fundamental biological processes in a new light. Genes Dev. **17**(5), 545–580 (2003)
79. W. Cai, X. Chen, Nanoplatforms for targeted molecular imaging in living subjects. Small **3** (11), 1840–1854 (2007)
80. M. Xu, L.V. Wang, Photoacoustic imaging in biomedicine. Rev. Sci. Instrum. **77**(4), 041101 (2006)
81. Z. Liu, Z. Guo, H. Zhong, X. Qin, M. Wan, B. Yang, Graphene oxide based surface-enhanced Raman scattering probes for cancer cell imaging. Phys. Chem. Chem. Phys. **15**(8), 2961–2966 (2013)
82. M. Zhang, R.R. Naik, L. Dai, *Carbon Nanomaterials for Biomedical Applications*, vol. 5 (Springer, 2015)
83. X. Zhu, Y. Liu, P. Li, Z. Nie, J. Li, Applications of graphene and its derivatives in intracellular biosensing and bioimaging. Analyst **141**(15), 4541–4553 (2016)
84. A. Cayuela, M.L. Soriano, C. Carrillo-Carrion, M. Valcarcel, Semiconductor and carbon-based fluorescent nanodots: the need for consistency. Chem. Commun. (Camb.) **52** (7), 1311–1326 (2016)
85. D. Jiang, Y. Chen, N. Li et al., Synthesis of luminescent graphene quantum dots with high quantum yield and their toxicity study. PLoS ONE **10**(12), e0144906 (2015)
86. J.-E. Lee, I. In, H. Lee, K.D. Lee, J.H. Jeong, S.Y. Park, Target delivery and cell imaging using hyaluronic acid-functionalized graphene quantum dots. Mol. Pharm. **10**(10), 3736–3744 (2013)
87. K.L. Schroeder, R.V. Goreham, T. Nann, Graphene quantum dots for theranostics and bioimaging. Pharm. Res. (2016)
88. J. Lin, X. Chen, P. Huang, Graphene-based nanomaterials for bioimaging. Adv. Drug Deliv. Rev. (2016)
89. Y. Du, S. Guo, Chemically doped fluorescent carbon and graphene quantum dots for bioimaging, sensor, catalytic and photoelectronic applications. Nanoscale **8**(5), 2532–2543 (2016)
90. C. Moina, G. Ybarra, Fundamentals and applications of immunosensors. Adv. Immunoassay Technol. 65–80 (2012)
91. X. Wang, L. Chen, X. Su, S. Ai, Electrochemical immunosensor with graphene quantum dots and apoferritin-encapsulated Cu nanoparticles double-assisted signal amplification for detection of avian leukosis virus subgroup. J. Biosens. Bioelectron. **47**, 171–177 (2013)
92. H. Zhao, Y. Chang, M. Liu, S. Gao, H. Yu, X. Quan, A universal immunosensing strategy based on regulation of the interaction between graphene and graphene quantum dots. Chem. Commun. (Camb.) **49**(3), 234–236 (2013)
93. J. Tian, H. Zhao, X. Quan, Y. Zhang, H. Yu, S. Chen, Fabrication of graphene quantum dots/silicon nanowires nanohybrids for photoelectrochemical detection of microcystin-LR. Sens. Actuators B Chem. **196**, 532–538 (2014)
94. L. Li, W. Li, C. Ma, H. Yang, S. Ge, J. Yu, Paper-based electrochemiluminescence immunodevice for carcinoembryonic antigen using nanoporous gold-chitosan hybrids and graphene quantum dots functionalized Au@Pt. Sens. Actuators B Chem. **202**, 314–322 (2014)

95. H. Pei, S. Zhu, M. Yang, R. Kong, Y. Zheng, F. Qu, Graphene oxide quantum dots@silver core-shell nanocrystals as turn-on fluorescent nanoprobe for ultrasensitive detection of prostate specific antigen. Biosens. Bioelectron. **74**, 909–914 (2015)
96. Y. Dong, H. Wu, P. Shang, X. Zeng, Y. Chi, Immobilizing water-soluble graphene quantum dots with gold nanoparticles for a low potential electrochemiluminescence immunosensor. Nanoscale **7**(39), 16366–16371 (2015)
97. D. Bhatnagar, V. Kumar, A. Kumar, I. Kaur, Graphene quantum dots FRET based sensor for early detection of heart attack in human. Biosens. Bioelectron. **79**, 495–499 (2016)
98. D. Wu, Y. Liu, Y. Wang et al., Label-free electrochemiluminescent immunosensor for detection of prostate specific antigen based on aminated graphene quantum dots and carboxyl graphene quantum dots. Sci. Rep. **6**, 20511 (2016)
99. J. Jeevanandam, Y.S. Chan, M.K. Danquah, Nano-formulations of drugs: recent developments, impact and challenges. Biochimie (2016)
100. M.X. Zhao, B.J. Zhu, The research and applications of quantum dots as nano-carriers for targeted drug delivery and cancer therapy. Nanoscale Res. Lett. **11**(1), 207 (2016)
101. H. Chen, Z. Wang, S. Zong et al., A graphene quantum dot-based FRET system for nuclear-targeted and real-time monitoring of drug delivery. Nanoscale **7**(37), 15477–15486 (2015)
102. Z. Liu, J.T. Robinson, X. Sun, H. Dai, PEGylated nanographene oxide for delivery of water-insoluble cancer drugs. J. Am. Chem. Soc. **130**(33), 10876–10877 (2008)
103. N. Al Abdullah, J.E. Lee, I. In et al., Target delivery and cell imaging using hyaluronic acid-functionalized graphene quantum dots. Mol Pharm. **10**(10), 3736–3744 (2013)
104. C. Wang, C. Wu, X. Zhou et al., Enhancing cell nucleus accumulation and DNA cleavage activity of anti-cancer drug via graphene quantum dots. Sci. Rep. **3**, 2852 (2013)
105. X. Wang, X. Sun, J. Lao et al., Multifunctional graphene quantum dots for simultaneous targeted cellular imaging and drug delivery. Colloids Surf. B Biointerfaces **122**, 638–644 (2014)
106. P. Nigam, S. Waghmode, M. Louis, S. Wangnoo, P. Chavan, D. Sarkar, Graphene quantum dots conjugated albumin nanoparticles for targeted drug delivery and imaging of pancreatic cancer. J. Mat. Chem. B. **2**(21), 3190–3195 (2014)
107. O. Lv, Y. Tao, Y. Qin et al., Highly fluorescent and morphology-controllable graphene quantum dots-chitosan hybrid xerogels for in vivo imaging and pH-sensitive drug carrier. Mater. Sci. Eng. C Mater. Biol. Appl. **67**, 478–485 (2016)
108. X. Wang, G. Sun, N. Li, P. Chen, Quantum dots derived from two-dimensional materials and their applications for catalysis and energy. Chem. Soc. Rev. **45**(8), 2239–2262 (2016)
109. M. Bacon, S.J. Bradley, T. Nann, Graphene quantum dots. Part. Part. Syst. Charact. **31**(4), 415–428 (2014)
110. K. Hola, Y. Zhang, Y. Wang, E.P. Giannelis, R. Zboril, A.L. Rogach, Carbon dots—emerging light emitters for bioimaging, cancer therapy and optoelectronics. Nano Today **9** (5), 590–603 (2014)
111. Y. Zhang, C. Xie, H. Su et al., Employing heavy metal-free colloidal quantum dots in solution-processed white light-emitting diodes. Nano Lett. **11**(2), 329–332 (2010)
112. W. Chung, H. Jung, C.H. Lee, S.H. Kim, Fabrication of high color rendering index white LED using Cd-free wavelength tunable Zn doped CuInS2 nanocrystals. Opt. Express **20**(22), 25071–25076 (2012)
113. F. Wang, S. Pang, L. Wang, Q. Li, M. Kreiter, C. Liu, One-step synthesis of highly luminescent carbon dots in noncoordinating solvents. Chem. Mat. **22**(16), 4528–4530 (2010)
114. Z. Wu, D. Ma, Recent advances in white organic light-emitting diodes. Mat. Sci. Eng. R Rep. **107**, 1–42 (2016)
115. F. So, J. Kido, P. Burrows, Organic light-emitting devices for solid-state lighting. MRS Bull. **33**(07), 663–669 (2008)
116. Q. Wang, D. Ma, Management of charges and excitons for high-performance white organic light-emitting diodes. Chem. Soc. Rev. **39**(7), 2387–2398 (2010)

117. J. Chen, F. Zhao, D. Ma, Hybrid white OLEDs with fluorophors and phosphors. Mater. Today **17**(4), 175–183 (2014)
118. V. Gupta, N. Chaudhary, R. Srivastava, G.D. Sharma, R. Bhardwaj, S. Chand, Luminescent graphene quantum dots for organic photovoltaic devices. J. Am. Chem. Soc. **133**(26), 9960–9963 (2011)
119. L. Tang, R. Ji, X. Cao et al., Deep ultraviolet photoluminescence of water-soluble self-passivated graphene quantum dots. ACS Nano **6**(6), 5102–5110 (2012)
120. H. Tetsuka, A. Nagoya, R. Asahi, Highly luminescent flexible amino-functionalized graphene quantum dots@cellulose nanofiber–clay hybrids for white-light emitting diodes. J. Mater. Chem. C. **3**(15), 3536–3541 (2015)
121. R. Sekiya, Y. Uemura, H. Murakami, T. Haino, White-light-emitting edge-functionalized graphene quantum dots. Angew. Chem. Int. Ed. Engl. **53**(22), 5619–5623 (2014)
122. C.M. Luk, L.B. Tang, W.F. Zhang, S.F. Yu, K.S. Teng, S.P. Lau, An efficient and stable fluorescent graphene quantum dot–agar composite as a converting material in white light emitting diodes. J. Mater. Chem. **22**(42), 22378 (2012)
123. S. Mahesh, C.L. Lekshmi, K.D. Renuka, K. Joseph, Simple and cost-effective synthesis of fluorescent graphene quantum dots from honey: application as stable security ink and white-light emission. Part. Part. Syst. Charact. **33**(2), 70–74 (2016)
124. P. Roy, A.P. Periasamy, C. Chuang et al., Plant leaf-derived graphene quantum dots and applications for white LEDs. New J. Chem. **38**(10), 4946–4951 (2014)
125. T. Ghosh, E. Prasad, White-light emission from unmodified graphene oxide quantum dots. J. Phys. Chem. C. **119**(5), 2733–2742 (2015)
126. J. Kyu Kim, S. Bae, Y. Yi et al., Origin of white electroluminescence in graphene quantum dots embedded host/guest polymer light emitting diodes. Sci. Rep. 5, 11032 (2015)
127. W. Kwon, Y.H. Kim, C.L. Lee et al., Electroluminescence from graphene quantum dots prepared by amidative cutting of tattered graphite. Nano Lett. **14**(3), 1306–1311 (2014)
128. L. Su, X. Zhang, Y. Zhang, A.L. Rogach, Recent progress in quantum dot based white light-emitting devices. Top. Curr. Chem. **374**(4), 1–25 (2016)
129. S.H. Song, M.-H. Jang, J. Chung et al., Highly efficient light-emitting diode of graphene quantum dots fabricated from graphite intercalation compounds. Adv. Opt. Mat. **2**(11), 1016–1023 (2014)
130. W. Miao, Electrogenerated chemiluminescence and its biorelated applications. Chem. Rev. **108**(7), 2506–2553 (2008)
131. C.G. Zoski, *Handbook of Electrochemistry* (Elsevier, 2006)
132. M. Hakimi, A. Salehi, F.A. Boroumand, Fabrication and characterization of an ammonia gas sensor based on PEDOT-PSS with N-doped graphene quantum dots dopant. IEEE Sens. J. **16**(16), 6149–6154 (2016)
133. R. Sekiya, Y. Uemura, H. Murakami, T. Haino, White-light-emitting edge-functionalized graphene quantum dots. Angew. Chem. Int. Ed. **53**(22), 5619–5623 (2014)
134. D. Pan, L. Guo, J. Zhang et al., Cutting sp2 clusters in graphene sheets into colloidal graphene quantum dots with strong green fluorescence. J. Mater. Chem. **22**(8), 3314–3318 (2012)
135. F. Yuan, L. Ding, Y. Li et al., Multicolor fluorescent graphene quantum dots colorimetrically responsive to all-pH and a wide temperature range. Nanoscale **7**(27), 11727–11733 (2015)
136. Y. Dong, H. Pang, S. Ren, C. Chen, Y. Chi, T. Yu, Etching single-wall carbon nanotubes into green and yellow single-layer graphene quantum dots. Carbon **64**, 245–251 (2013)
137. X. Tan, Y. Li, X. Li, S. Zhou, L. Fan, S. Yang, Electrochemical synthesis of small-sized red fluorescent graphene quantum dots as a bioimaging platform. Chem. Commun. **51**(13), 2544–2546 (2015)
138. Z. Fan, Y. Li, X. Li et al., Surrounding media sensitive photoluminescence of boron-doped graphene quantum dots for highly fluorescent dyed crystals, chemical sensing and bioimaging. Carbon **70**, 149–156 (2014)

139. H. Sun, H. Ji, E. Ju, Y. Guan, J. Ren, X. Qu, Synthesis of fluorinated and nonfluorinated graphene quantum dots through a new top-down strategy for long-time cellular imaging. Chem. A Eur. J. **21**(9), 3791–3797 (2015)
140. D. Qu, M. Zheng, L. Zhang et al., Formation mechanism and optimization of highly luminescent N-doped graphene quantum dots. Sci. Rep. **4** (2014)
141. C.-B. Ma, Z.-T. Zhu, H.-X. Wang et al., A general solid-state synthesis of chemically-doped fluorescent graphene quantum dots for bioimaging and optoelectronic applications. Nanoscale **7**(22), 10162–10169 (2015)
142. J. Ju, W. Chen, Synthesis of highly fluorescent nitrogen-doped graphene quantum dots for sensitive, label-free detection of Fe(III) in aqueous media. Biosens. Bioelectron. **58**, 219–225 (2014)
143. S. Li, Y. Li, J. Cao, J. Zhu, L. Fan, X. Li, Sulfur-doped graphene quantum dots as a novel fluorescent probe for highly selective and sensitive detection of Fe(3+). Anal. Chem. **86**(20), 10201–10207 (2014)
144. A. Dutta Chowdhury, R. Doong, Highly sensitive and selective detection of nanomolar ferric ions using dopamine functionalized graphene quantum dots. ACS Appl. Mat. Interfaces (2016)
145. L. Li, L. Li, C. Wang et al., Synthesis of nitrogen-doped and amino acid-functionalized graphene quantum dots from glycine, and their application to the fluorometric determination of ferric ion. Microchim. Acta **182**(3–4), 763–770 (2014)
146. Z. Qian, J. Ma, X. Shan, H. Feng, L. Shao, J. Chen, Highly luminescent N-doped carbon quantum dots as an effective multifunctional fluorescence sensing platform. Chem. Eur. J. **20** (8), 2254–2263 (2014)
147. F. Wang, Z. Gu, W. Lei, W. Wang, X. Xia, Q. Hao, Graphene quantum dots as a fluorescent sensing platform for highly efficient detection of copper(II) ions. Sens. Actuators B: Chem. **190**, 516–522 (2014)
148. Y.X. Qi, M. Zhang, Q.Q. Fu, R. Liu, G.Y. Shi, Highly sensitive and selective fluorescent detection of cerebral lead(II) based on graphene quantum dot conjugates. Chem. Commun. (Camb.) **49**(90), 10599–10601 (2013)
149. B. Wang, S. Zhuo, L. Chen, Y. Zhang, Fluorescent graphene quantum dot nanoprobes for the sensitive and selective detection of mercury ions. Spectrochim Acta A Mol. Biomol. Spectrosc. **131**, 384–387 (2014)
150. F. Cai, X. Liu, S. Liu, H. Liu, Y. Huang, A simple one-pot synthesis of highly fluorescent nitrogen-doped graphene quantum dots for the detection of Cr(vi) in aqueous media. RSC Adv. **4**(94), 52016–52022 (2014)
151. T. Hallaj, M. Amjadi, J.L. Manzoori, R. Shokri, Chemiluminescence reaction of glucose-derived graphene quantum dots with hypochlorite, and its application to the determination of free chlorine. Microchim. Acta **182**(3–4), 789–796 (2014)
152. J.M. Bai, L. Zhang, R.P. Liang, J.D. Qiu, Graphene quantum dots combined with europium ions as photoluminescent probes for phosphate sensing. Chemistry **19**(12), 3822–3826 (2013)
153. S.E.K. Kirschbaum-Harriman, Investigating electrochemiluminescence (ECL) as highly sensitive and effective signaling means for microfluidic biosensors (2016)
154. S.A. Lim, M.U. Ahmed, Electrochemical immunosensors and their recent nanomaterial-based signal amplification strategies: a review. RSC Adv. **6**(30), 24995–25014 (2016)
155. M. Mazloum-Ardakani, R. Aghaei, M. Abdollahi-Alibeik, A. Moaddeli, Fabrication of modified glassy carbon electrode using graphene quantum dot, gold nanoparticles and 4-(4-mercaptophenyl)imino)methyl)benzene-1,2-diol by self-assembly method and investigation of their electrocatalytic activities. J. Electroanal. Chem. **738**, 113–122 (2015)
156. N. Shadjou, M. Hasanzadeh, F. Talebi, A.P. Marjani, Integration of beta-cyclodextrin into graphene quantum dot nano-structure and its application towards detection of Vitamin C at physiological pH: a new electrochemical approach. Mater. Sci. Eng. C Mater. Biol. Appl. **67**, 666–674 (2016)

157. J. Xi, C. Xie, Y. Zhang et al., Pd nanoparticles decorated n-doped graphene quantum dots@N-doped carbon hollow nanospheres with high electrochemical sensing performance in cancer detection. ACS Appl. Mater. Interfaces. **8**(34), 22563–22573 (2016)
158. Z. Cai, F. Li, P. Wu et al., Synthesis of nitrogen-doped graphene quantum dots at low temperature for electrochemical sensing trinitrotoluene. Anal. Chem. **87**(23), 11803–11811 (2015)
159. S.L. Ting, S.J. Ee, A. Ananthanarayanan, K.C. Leong, P. Chen, Graphene quantum dots functionalized gold nanoparticles for sensitive electrochemical detection of heavy metal ions. Electrochim. Acta **172**, 7–11 (2015)
160. J. Ju, W. Chen, In situ growth of surfactant-free gold nanoparticles on nitrogen-doped graphene quantum dots for electrochemical detection of hydrogen peroxide in biological environments. Anal. Chem. **87**(3), 1903–1910 (2015)
161. M. Roushani, Z. Abdi, Novel electrochemical sensor based on graphene quantum dots/riboflavin nanocomposite for the detection of persulfate. Sens. Actuators B: Chem. **201**, 503–510 (2014)
162. M.M. Richter, Electrochemiluminescence (ecl). Chem. Rev. **104**(6), 3003–3036 (2004)
163. H. Sun, L. Wu, W. Wei, X. Qu, Recent advances in graphene quantum dots for sensing. Mater. Today **16**(11), 433–442 (2013)
164. A. Zweig, A.K. Hoffmann, D.L. Maricle, A.H. Maurer, The mechanism of electrochemiluminescence. Chem. Commun. (Lon.) **3**, 106–108 (1967)
165. A.J. Bard, *Electrogenerated Chemiluminescence* (CRC Press, 2004)
166. A. Bard, J. Debad, J. Leland et al., *Encyclopedia of Analytical Chemistry: Applications, Theory and Instrumentation* (Meyers, RA, Ed, 2000)
167. R. Xie, Z. Wang, W. Zhou et al., Graphene quantum dots as smart probes for biosensing. Anal. Methods **8**(20), 4001–4016 (2016)
168. H. Zhou, J. Liu, S. Zhang, Quantum dot-based photoelectric conversion for biosensing applications. TrAC Trends Anal. Chem. **67**, 56–73 (2015)
169. Z. Ding, B.M. Quinn, S.K. Haram, L.E. Pell, B.A. Korgel, A.J. Bard, Electrochemistry and electrogenerated chemiluminescence from silicon nanocrystal quantum dots. Science **296** (5571), 1293–1297 (2002)
170. J. Lu, M. Yan, L. Ge et al., Electrochemiluminescence of blue-luminescent graphene quantum dots and its application in ultrasensitive aptasensor for adenosine triphosphate detection. Biosens. Bioelectron. **47**, 271–277 (2013)
171. Y. Dong, W. Tian, S. Ren, R. Dai, Y. Chi, G. Chen, Graphene quantum dots/L-cysteine coreactant electrochemiluminescence system and its application in sensing lead(II) ions. ACS Appl. Mater. Interfaces. **6**(3), 1646–1651 (2014)
172. Y. Yan, Q. Liu, H. Mao, K. Wang, The immobilization of graphene quantum dots by one-step electrodeposition and its application in peroxydisulfate electrochemiluminescence. J. Electroanal. Chem. **775**, 1–7 (2016)
173. J. Liu, X. He, K. Wang et al., A highly sensitive electrochemiluminescence assay for protein kinase based on double-quenching of graphene quantum dots by G-quadruplex-hemin and gold nanoparticles. Biosens. Bioelectron. **70**, 54–60 (2015)
174. R.P. Liang, W.B. Qiu, H.F. Zhao, C.Y. Xiang, J.D. Qiu, Electrochemiluminescence resonance energy transfer between graphene quantum dots and graphene oxide for sensitive protein kinase activity and inhibitor sensing. Anal. Chim. Acta **904**, 58–64 (2016)
175. H.F. Zhao, R.P. Liang, J.W. Wang, J.D. Qiu, A dual-potential electrochemiluminescence ratiometric approach based on graphene quantum dots and luminol for highly sensitive detection of protein kinase activity. Chem. Commun. (Camb.) **51**(63), 12669–12672 (2015)
176. Q. Lu, W. Wei, Z. Zhou, Z. Zhou, Y. Zhang, S. Liu, Electrochemiluminescence resonance energy transfer between graphene quantum dots and gold nanoparticles for DNA damage detection. Analyst **139**(10), 2404–2410 (2014)
177. T. Zhang, H. Zhao, G. Fan, Y. Li, L. Li, X. Quan, Electrolytic exfoliation synthesis of boron doped graphene quantum dots: a new luminescent material for electrochemiluminescence detection of oncogene microRNA-20a. Electrochim. Acta **190**, 1150–1158 (2016)

178. L. Zhang, L. Li, C. Ma, S. Ge, M. Yan, C. Bian, Detection of α-fetoprotein with an ultrasensitive electrochemiluminescence paper device based on green-luminescent nitrogen-doped graphene quantum dots. Sens. Actuators B: Chem. **221**, 799–806 (2015)
179. S. Chen, X. Chen, T. Xia, Q. Ma, A novel electrochemiluminescence sensor for the detection of nitroaniline based on the nitrogen-doped graphene quantum dots. Biosens. Bioelectron. **85**, 903–908 (2016)
180. K.J. Stevenson, D.A.V. Bout, Electrogenerated chemiluminescence with amine and benzoyl peroxide coreactants: reactivity and reaction mechanism studies (2003)
181. L. Dai, Y. Xue, L. Qu, H.-J. Choi, J.-B. Baek, Metal-free catalysts for oxygen reduction reaction. Chem. Rev. **115**(11), 4823–4892 (2015)
182. S. Basu, *Fuel Cell Science and Technology* (Springer, 2007)
183. R. Ramachandran, S.-M. Chen, G.P.G. Kumar, Recent developments in electrode materials for oxygen reduction reaction. Int. J. Electrochem. Sci. **10**(10), 8581–8606 (2015)
184. Y. Zheng, Y. Jiao, M. Jaroniec, Y. Jin, S.Z. Qiao, Nanostructured metal-free electrochemical catalysts for highly efficient oxygen reduction. Small **8**(23), 3550–3566 (2012)
185. A. Emadi, M. Ehsani, J.M. Miller, *Vehicular Electric Power Systems: Land, Sea, Air, and Space Vehicles* (CRC press, 2003)
186. N. Kimiaie, K. Wedlich, M. Hehemann et al., Results of a 20000h lifetime test of a 7 kW direct methanol fuel cell (DMFC) hybrid system-degradation of the DMFC stack and the energy storage. Energy Environ. Sci. **7**(9), 3013–3025 (2014)
187. X. Yu, S. Ye, Recent advances in activity and durability enhancement of Pt/C catalytic cathode in PEMFC: part II: degradation mechanism and durability enhancement of carbon supported platinum catalyst. J. Power Sour. **172**(1), 145–154 (2007)
188. M. Winter, R.J. Brodd, What are batteries, fuel cells, and supercapacitors? Chem. Rev. **104** (10), 4245–4270 (2004)
189. R. Zhou, M. Jaroniec, S.Z. Qiao, Nitrogen-doped carbon electrocatalysts decorated with transition metals for the oxygen reduction reaction. Chem. Cat. Chem. **7**(23), 3808–3817 (2015)
190. H. Kim, K. Lee, S.I. Woo, Y. Jung, On the mechanism of enhanced oxygen reduction reaction in nitrogen-doped graphene nanoribbons. Phys. Chem. Chem. Phys. **13**(39), 17505–17510 (2011)
191. D. Yu, E. Nagelli, F. Du, L. Dai, Metal-free carbon nanomaterials become more active than metal catalysts and last longer. J. Phys. Chem. Lett. **1**(14), 2165–2173 (2010)
192. Y. Yan, Q. Liu, X. Dong et al., Copper(I) oxide nanospheres decorated with graphene quantum dots display improved electrocatalytic activity for enhanced luminol electrochemiluminescence. Microchim. Acta **183**(5), 1591–1599 (2016)
193. Q. Li, S. Zhang, L. Dai, L. Li, Nitrogen-doped colloidal graphene quantum dots and their size-dependent electrocatalytic activity for the oxygen reduction reaction. J. Am. Chem. Soc. **134**(46), 18932–18935 (2012)
194. H. Jin, H. Huang, Y. He et al., Graphene quantum dots supported by graphene nanoribbons with ultrahigh electrocatalytic performance for oxygen reduction. J. Am. Chem. Soc. **137** (24), 7588–7591 (2015)
195. Y. Liu, W. Li, J. Li, H. Shen, Y. Li, Y. Guo, Graphene aerogel-supported and graphene quantum dots-modified γ-MnOOH nanotubes as a highly efficient electrocatalyst for oxygen reduction reaction. RSC Adv. **6**(49), 43116–43126 (2016)
196. B. Zhang, C. Xiao, Y. Xiang, B. Dong, S. Ding, Y. Tang, Nitrogen-doped graphene quantum dots anchored on thermally reduced graphene oxide as an electrocatalyst for the oxygen reduction reaction. Chem. Electro. Chem. **3**(6), 864–870 (2016)
197. T.F. Yeh, C.Y. Teng, S.J. Chen, H. Teng, Nitrogen-doped graphene oxide quantum dots as photocatalysts for overall water-splitting under visible light illumination. Adv. Mater. **26** (20), 3297–3303 (2014)
198. L.-C. Chen, T.-F. Yeh, Y.-L. Lee, H. Teng, Incorporating nitrogen-doped graphene oxide dots with graphene oxide sheets for stable and effective hydrogen production through photocatalytic water decomposition. Appl. Catal. A **521**, 118–124 (2016)

199. P. Sudhagar, I. Herraiz-Cardona, H. Park et al., Exploring graphene quantum dots/TiO_2 interface in photoelectrochemical reactions: solar to fuel conversion. Electrochim. Acta **187**, 249–255 (2016)
200. Y. Hao, X. Dong, X. Wang, S. Zhai, H. Ma, X. Zhang, Controllable electrostatic self-assembly of sub-3 nm graphene quantum dots incorporated into mesoporous Bi_2MoO_6 frameworks: efficient physical and chemical simultaneous co-catalysis for photocatalytic oxidation. J. Mater. Chem. A. **4**(21), 8298–8307 (2016)
201. L. Tang, R. Ji, X. Li et al., Deep ultraviolet to near-infrared emission and photoresponse in layered n-doped graphene quantum dots. ACS Nano **8**(6), 6312–6320 (2014)
202. J. Zhao, L. Tang, J. Xiang et al., Chlorine doped graphene quantum dots: preparation, properties, and photovoltaic detectors. Appl. Phys. Lett. **105**(11), 111116 (2014)
203. Z. Zhu, J. Ma, Z. Wang et al., Efficiency enhancement of perovskite solar cells through fast electron extraction: the role of graphene quantum dots. J. Am. Chem. Soc. **136**(10), 3760–3763 (2014)
204. J.K. Kim, M.J. Park, S.J. Kim et al., Balancing light absorptivity and carrier conductivity of graphene quantum dots for high-efficiency bulk heterojunction solar cells. ACS Nano **7**(8), 7207–7212 (2013)
205. A. Ali Tahir, H. Ullah, P. Sudhagar, M. Asri Mat Teridi, A. Devadoss, S. Sundaram, The application of graphene and its derivatives to energy conversion, storage, and environmental and biosensing devices. Chem. Rec. **16**(3), 1591–1634 (2016)
206. Y. Qin, Y. Cheng, L. Jiang et al., Top-down strategy toward versatile graphene quantum dots for organic/inorganic hybrid solar cells. ACS Sustain. Chem. Eng. **3**(4), 637–644 (2015)
207. X. Fang, M. Li, K. Guo et al., Graphene quantum dots optimization of dye-sensitized solar cells. Electrochim. Acta **137**, 634–638 (2014)
208. Y. Zhong, H. Zhang, D. Pan, L. Wang, X. Zhong, Graphene quantum dots assisted photovoltage and efficiency enhancement in CdSe quantum dot sensitized solar cells. J. Energy Chem. **24**(6), 722–728 (2015)

Chapter 5
Graphene/Metal Nanowire Hybrid Transparent Conductive Films

Iskandar Kholmanov, Giorgio Sberveglieri and Muhammad A. Alam

5.1 Introduction

Transparent conductive films (TCFs) are attracting significant interest due to their potential applications in a broad range of emerging device technologies. As a result, a new generation of TCF materials has been proposed [1, 2]. Figure 5.1 illustrates different types of thin films for TCF applications. Among the metal oxide films, indium tin oxide (ITO) is a mature technology and is widely used in various devices/systems. Other oxides, such as fluorine-doped tin oxide (FTO) and aluminum-doped zinc oxide (AZO) are used for specialized devices. ITO (or tin doped indium oxide) is a heavily doped n-type semiconductor with a bandgap of 4 eV. Doping increases electrical conductivity, while the wide bandgap provides the high transparency in the visible range of the spectrum needed for this class of devices [3]. However, the poor compatibility with organic materials, opaqueness to the infrared spectra, brittle ceramic structure and the uncertain availability of indium are some of the key challenges for the use of ITO films in TCFs applications, particularly in flexible and large area optoelectronic devices [2]. Moreover, it is known that indium can diffuse into the functional layers of organic photovoltaic (OPV) devices and organic light emitting diodes (OLEDs) [4, 5], introducing recombination centers that degrade device performance. These drawbacks of ITO

I. Kholmanov (✉)
Department of Mechanical Engineering, The University of Texas at Austin, Austin, TX 78712, USA
e-mail: iskandar.kholmanov@ino.it

I. Kholmanov · G. Sberveglieri
CNR-INO, Sensor Lab, The University of Brescia, via Branze 45, 25123 Brescia, Italy

M.A. Alam
School of Electrical and Computer Engineering and Birck Nanotechnology Center, Purdue University, West Lafayette, IN 47907, USA

Z.H. Khan (ed.), *Recent Trends in Nanomaterials*,
Advanced Structured Materials 83, DOI 10.1007/978-981-10-3842-6_5

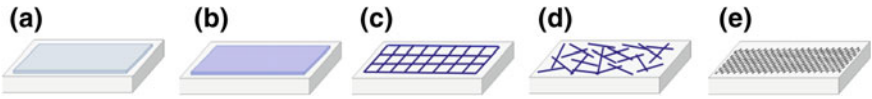

Fig. 5.1 An illustration of transparent conductive films composed of different materials: **a** ITO metal oxide, **b** conductive polymer, **c** periodic metal grid, **d** percolated random network of one-dimensional nanostructures, such as carbon nanotubes and metal nanowires, and **e** two-dimensional graphene

have stimulated intensive research in developing new materials that can meet the evolving requirements of the TCF market. For example, several other materials including conductive polymers, metal grids, metal nanowires (NWs), carbon nanotubes (CNTs) and graphene-based films have been investigated as alternatives to ITO (Fig. 5.1).

Conductive polymers, such as poly(3,4-ethylenedioxythiophene) polystyrene sulfonate (PEDOT:PSS) have a great potential to replace ITO for TCF applications. Conductive polymer films are inexpensive, mechanically flexible, and involves environmentally benign processing. However, their degradation under photochemical, thermal, oxidative, and mechanical processes limits their applications in a broad range of optoelectronic devices [6, 7].

Fully interconnected, periodic metal grid films offers high electrical conductivity [8], and the optical transparency of these films can be tuned by the geometry and density of the grid structure on the substrate surface. The lithographically-defined metal grid TCFs, however, are expensive, unsuited for applications in large area systems. In addition, the effect of chemical reactivity of metals on other functional parts of the devices is not yet fully investigated.

Nanostructured films based on percolated random network of one-dimensional (1D) metal nanowires (NWs) and CNTs, and continuous two-dimensional (2D) graphene conductive films are considered as promising alternatives to ITO because of their unique physical and chemical properties [1, 2]. Percolated and randomly oriented metal NW films, for example, have sheet resistance (R_s) and optical transmittance (T) comparable to/or better than ITO films. Compared to metal grid films, the NW films can be obtained using relatively low-cost fabrication methods. However, the high surface roughness, poor adhesion to some substrates, and high chemical reactivity of metal NW films limit their long-term applications or make them incompatible with functional parts of certain devices.

CNT films often present good thermal and chemical stabilities and good optical and electromechanical characteristics. These properties make them promising for TCFs applications [9, 10]. The electrical conductivity of CNT films is provided by charge transfer through percolated networks of nanotubes. The one of the main drawbacks of these films is their relatively high sheet resistance (R_s), mainly contributed from the nanotube-nanotube junction resistance [11, 12].

2D graphene, a recent nanomaterial with prominent Optoelectrical characteristics, is considered as another alternative to ITO for TCFs applications. Theoretical values of charge carrier mobility in graphene can be as high as 200,000 cm^2/V s,

demonstrating its remarkable transport properties [13]. Additionally, single layer graphene absorbs about 2.3% of visible light [14, 15]. Combined, these superior properties make graphene an excellent candidate for TCF applications. In spite of theoretically predicted superior electrical conductivity, graphene-based films have relatively high sheet resistances. TCFs fabricated using chemically modified graphene have a sheet resistance $R_s > 5$ kΩ/sq with an optical transmittance lower than 90% at 550 nm wavelength (T_{550}) [16, 17]. Single layer graphene films grown by chemical vapor deposition (CVD) has a typical sheet resistance of about $R_s > 1$ kΩ/sq with optical transmittance of about $T_{550} = 97.5\%$ [18].

Current ongoing research investigations are focused on development of advanced strategies to address the key issues and to improve the performance of single component nanostructured TCFs discussed above. One of the prominent concepts is development of *hybrid nanostructured films*, in which the shortcomings of single component TCFs is overcome by the presence of another component, and the overall performance of the hybrid films is improved due to synergy between individual components [19–21]. This concept opens up possibilities for developing next generation multi-component and multi-functional TCFs.

Given this summary of the various single and multi-component TCFs, we now consider these systems in detail. We begin with a review of single component 2D graphene (Sect. 5.2) and 1D metal nanowire (Sect. 5.3) films, to provide a baseline for our discussion of the multicomponent hybrid TCFs composed of these two components. In Sect. 5.4, we describe the fabrication and characterization of optical and electrical properties of RG-O/Cu NW hybrid films, as well as the multi-functionality of RG-O platelets in the films. Section 5.5 focuses on the fabrication and characterization of CVD-graphene/Ag NW hybrid films. This section also considers the heat dissipation properties of the CVD-graphene layer that improve the thermal stability of the hybrid films. In Sect. 5.6, applications of graphene/metal nanowire hybrid TCFs in electrochromic devices are presented, highlighting the advantages of the hybrid films over the corresponding single component TCFs. Section 5.7 summarizes and briefly presents the future challenges of nanostructured hybrid TCFs.

5.2 Graphene-Based Transparent Conductive Films

First graphene-based transparent conductive films were fabricated using graphene oxide (G-O) platelets obtained by solution-based oxidation and exfoliation of graphite (modified Hummers method) [17, 22–24]. G-O can be dispersed in water and form stable colloidal aqueous suspension. G-O platelets are decorated with oxygen-containing functional groups (such as carboxyl, hydroxyl, epoxy) located at both sides of the basal plane and at the edges. The presence of these functional groups results in a poor electrical conductivity of G-O. Different reduction methods, such as thermal, chemical and electrochemical approaches have developed to remove the functional groups and restore the graphitic structure of the platelets.

To achieve highly reduced G-O films by thermal treatment high-temperatures (>1000 °C) and ultrahigh vacuum (or a reducing environment) are required [17, 23–25]. Chemical reduction involves reducing agents such as hydrazine, [17, 26–28] N,N-dimethyl hydrazine, [23] and sodium borohydride [29] and because of their toxic properties, safety precautions must be taken when large quantities of these reagents are used. Electrochemical reduction involves changing the Fermi energy level of the electrode material surface and thus direct charge transfer is used to efficiently reduce G-O films on the electrode surface [30, 31]. Ongoing research in this field is actively progressing, and recently developed new methods using metal foils or particles allows facile reducing of G-O at near-room temperatures [32–35].

The reduced graphene oxide (RG-O) possesses substantially higher electrical conductivity compared to that of G-O. Conductive RG-O films are fabricated either by reduction of pre-deposited G-O films, or by deposition of RG-O dispersions on a substrate. The first approach is widely used because G-O dispersions can be easily deposited on a various kind of substrates forming continuous thin G-O films and can be subsequently reduced to obtain RG-O films (Fig. 5.2a, b). Although the electrical properties of the RG-O strongly depend on the degree of reduction, none of the existing reduction methods allows fabrication of RG-O films with sheet resistance $R_s < 1$ kΩ/sq with $T_{550} > 90\%$. Such high sheet resistance is partially contributed by large amount of structural defects formed during the fabrication (oxidation, exfoliation, sonication) processes. The defects can scatter the charge carriers, adversely affecting the transport properties of the RG-O platelets. In addition, because of a limited lateral size of RG-O platelets (from several nanometers up to some tens of micrometers (Fig. 5.2a) the continuous large-area films are formed by interconnected (mostly overlapped) platelets. Because of random orientation and absence of perfect hexagonal bonds between interconnected platelets, the platelet-platelet junctions may significantly contribute to the sheet resistance of the RG-O films. Residual impurities of chemicals used during

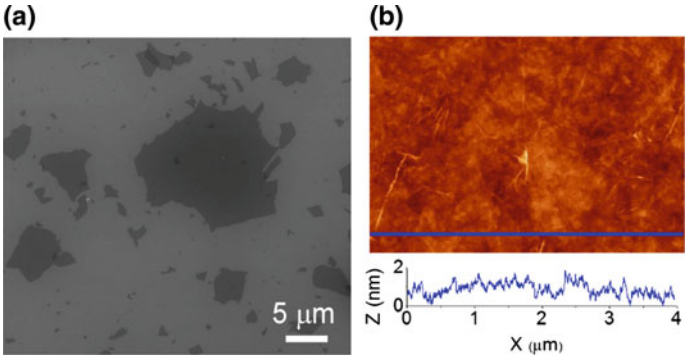

Fig. 5.2 **a** Scanning electron microscopy (SEM) image of RG-O platelets on a SiO_2/Si substrate. RG-O platelets with different sizes are shown. **b** Atomic force microscopy (AFM) image of thin RG-O films spin coated on a SiO_2/Si wafer. The line profile exhibits a relatively low surface of RG-O film. Reprinted with permission from [28]. Copyright 2013 American Chemical Society

solution-based oxidation exfoliation processes can also decrease the conductivity of RG-O films. These factors cannot be eliminated by the reduction processes and development of additional processing and treatments is required to restore the inherently high conductivity of graphene platelets.

In graphene grown by CVD of hydrocarbon gases on metal surfaces, the role of the factors adversely affecting the transport properties of the films, mentioned above for RGO films, is negligible. CVD growth method allows synthesizing of large-area single or few layer graphene films with structural qualities much higher than that of RG-O films [36, 37]. Due to these characteristics the potential of CVD-graphene for TCF applications is considerably higher compared to RG-O. However, typical monolayer CVD-graphene has a sheet resistance of about >1 kΩ/sq [18], markedly higher than that of ITO films. In addition, the charge carrier mobility in these CVD-graphene films is significantly lower [18] compared to that of mechanically exfoliated graphene [38] as well as theoretically calculated values [13]. The high sheet resistance of CVD-graphene films is contributed by different kind of defects formed during synthesis and transfer processes. Figure 5.3a shows a SEM image of a monolayer CVD-graphene grown on a polycrystalline Cu substrate. The graphene layer was grown continuously across the steps, facets and grain boundaries of the substrate. Different thermal contractions of the grown graphene layer and the metal substrate upon cooling yields line imperfections such as ripples and wrinkles, as observed in Fig. 5.3a [36]. Additional line disruptions are formed after the transfer of CVD-graphene onto SiO_2/Si substrates (Fig. 5.3b). These disruptions together with other structural defects, such as cracks, tears, point defects, etc., can scatter the charge carriers, adversely affecting charge carrier motilities and decreasing ballistic transport path lengths [13, 39, 40]. In addition, structurally CVD-graphene can be considered as a 1D polycrystalline layer with topological defects such as grain boundaries and crystal structure dislocations [41, 42]. Each graphene domain in CVD-graphene layer may have different crystallographic orientations, and the junctions between two neighboring domains form graphene grain boundaries.

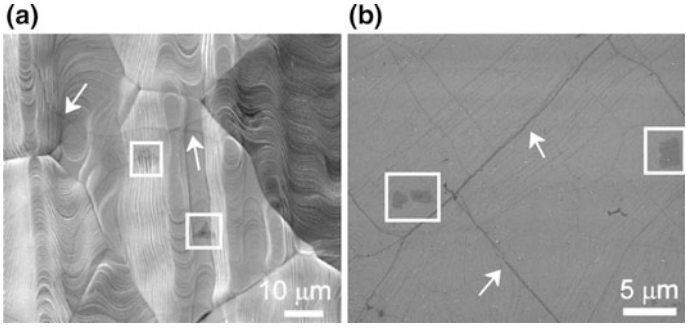

Fig. 5.3 SEM images of **a** CVD-graphene grown on a polycrystalline Cu substrate, and **b** CVD-graphene transferred onto a SiO_2/Si substrate. *Squared* areas contain dark islands that are bilayer CVD-graphene. *Arrows* indicate the line imperfections (folding, ripples and wrinkles) formed during the growth and/or transfer of CVD-graphene

These defects in graphene can essentially scatter the charge carriers and disturb the sp^2 delocalization of π electrons [41, 42]. Consequently the presence of such defects may lead to the low electrical conductivity decreasing the potential of CVD-graphene films for TCF applications.

Different approaches have been developed to minimize the role of defects and improve the electrical conductivity of CVD-graphene films. High temperature treatment to heal the structural defects, [43, 44] growing a larger grain size CVD-graphene to lower the density of grain boundaries [45], and various doping processes to increase the charge density [37] have been studied. However, to date these methods are yet to produce monolayer CVD-graphene films having a sheet resistance less than 100 Ω/sq that is required for many device applications.

In spite of above mentioned disadvantages, both RG-O and CVD-graphene are prominent candidate for next generation TCFs. One of the advantages of graphene-based films is their extremely low thicknesses (one-atom-thick for single layer graphene), compared to NW and CNT-based TCFs, and their 2D structure allows fabrication of continuous films. Another merit of graphene-based TCFs is their relatively high chemical stability that makes them consistent with functional components of diverse optoelectronic devices. Further research focused on development of new methods for production of less defective RG-O films, cost-effective fabrication, facile transfer and stable doping of CVD-graphene is needed in order to realize the full potential of graphene films for TCF applications, particularly, when they are used as a component in hybrid TCFs and provide additional functionalities, as described in the next sections.

5.3 Metal Nanowire-Based Transparent Conductive Films

Recently, thin films of percolated, randomly oriented metal NWs have received increased attention due to their excellent optical and electrical properties [2, 46, 47]. As other nanostructured films for TCF applications, metal NW films also exhibit good electromechanical performances retaining their stable electrical conductivity under mechanical strains. For practical applications mostly attractive metal nanowires are Cu (Fig. 5.4a) and Ag NWs (Fig. 5.4b) because of their relatively low-cost fabrication and good electrical conductivities [46, 47]. The NWs can be synthesized using simple wet-chemistry approaches, and large-area Ag and Cu NW transparent electrodes can be cheaply deposited using these NW solutions [46–48]. High optical transmittance in these mesh films is provided by open spaces between NWs, while good electrical conductivity is achieved due the percolated network of metal NWs. Therefore, optoelectrical properties of the films can be controlled by the density of the NWs in the film. Bottleneck in metal nanowires TCFs is NW–NW junction resistance. Mechanical pressing or heating of NW films can decrease the junction resistance, however, these processing might not be compatible with integrated devices. Recently developed plasmonic welding technique can substantially decrease the junction resistance between nanowires yielding metal NW

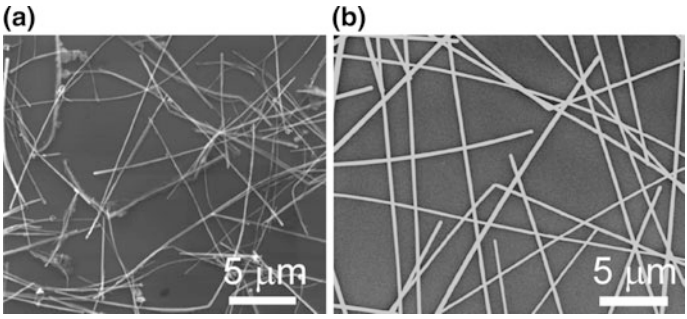

Fig. 5.4 SEM images of **a** Cu NWs with an average diameter less than 60 nm and average length longer than 20 μm (purchased from NanoForge), and **b** Ag NWs with an average diameter of 100–130 nm, and average length of 5–25 μm (purchased from SeaShell Technology) deposited onto SiO_2/Si substrate

films with a sheet resistance of 10 Ω/sq at 90% optical transmission [49]. Since this approach exclusively heats the NW–NW junctions, it can be used for NW films on plastic substrates without any damage. Another recent report has demonstrated the fabrication of metal nanotrough networks based on templating ultralong polymer nanofibers [50]. Because of the continuous network (absence of or very low electrical resistance at the nanotrough junctions), this approach allowed fabrication of metal nanotrough network films with a sheet resistance of 2 Ω/sq at 90% optical transmission.

Overall, in terms of optical transmittance and sheet resistance the metal NW films satisfy minimum application-specific requirements. However, large diameter (several tens of nanometers) as well as NW–NW junctions required for conductive network formation leads to undesirably increased surface roughness that can impede their applications in most of the sandwich-structured optoelectronic devices. In addition, metal NWs possess relatively high chemical reactivity. This may restrict the use of NW-based TCFs in certain optoelectronic devices in order to avoid the interaction (and subsequent degradation) of NWs with other active functional parts of devices. Moreover, at elevated temperatures the metal NWs transform into metal nanoparticle array that indicates the thermal instability of NWs [51]. Such instabilities may adversely affect the long term reliability of NW TCFs. Therefore, future research on the topic must address the chemical and thermal stabilities, optimization of structural and morphological characteristics, and compatibility of NWs with diverse device components.

The drawbacks of single component nanostructured transparent electrodes, such as graphene and NW films, can be minimized/eliminated in the hybrid films where shortcomings of one component are overcome by the second component, a concept originally proposed theoretically by Alam group at Purdue [19]. To date, various multi-component TCFs composed of two or more of the following structures: CNTs, metal NWs, metal grids, graphene, graphene oxide and conductive polymers, have been reported. Among these multi-component films, the hybrids of 2D graphenic

structures with 1D metal NWs are one of the most attractive ones, and therefore, here, we will discuss RG-O/Cu NW films (in Sect. 5.4), and CVD-graphene/Ag NW films (in Sect. 5.5).

5.4 RG-O/Cu NW Hybrid Transparent Conductive Films

Assembling of RG-O with Cu metal NWs is a promising strategy to overcome the drawbacks of the single component RG-O and Cu NW films. For preparation RG-O/Cu NW hybrid films, first the dispersion of Cu NWs were deposited onto a transparent substrate (mainly onto glass) using a spray-coating method [28]. Density of the Cu NWs on the substrate can be controlled by repeating the pulses of spray coating. After each sprayed pulse, the substrate was kept at 60 °C for about 2 min, and then nitrogen gas was finely blown to the substrate surface to dry completely the sprayed droplets. Figure 5.4a shows the SEM image of the typical spray-coated Cu NW film with random orientation of individual nanowires.

The RG-O can be obtained by depositing and subsequently reducing the G-O films produced. For this, first the graphite oxide composed of highly oxidized graphene platelets was produced using a modified Hummers method [23]. Stirring the graphite oxide particles in water for about 3 h, and subsequent sonication in an ultrasonic bath for about 45 min yield aqueous dispersions of G-O. Thin films of G-O can be produced by spin coating the dispersions onto target substrates. The reduction of the G-O films was performed by exposing the films to hydrazine ($N_2H_4 \cdot H_2O$) vapor at 90 °C for 24 h. The further reduction process was done by thermal annealing the films at 400 °C for 1 h at 1 atm pressure of an Ar (95%) + H (5%) gas mixture.

To fabricate RG-O/Cu NW hybrid films the RG-O films were transferred onto Cu NW films using an approach described elsewhere [28]. For this, a thin film of poly (methyl methacrylate) (PMMA) was deposited on top of the RG-O films on glass substrate by spin coating. The obtained PMMA/RG-O film was subsequently put into 1 M NaOH aqueous solution to delaminate the film from the substrate [52]. In order to remove the residual NaOH the delaminated PMMA/RG-O films were washed three times with de-ionized (DI) water, and then transferred on top of Cu NW films. Afterwards, the PMMA layer was removed with acetone, and the obtained RG-O/Cu NW films were put in a tube furnace to anneal at 180 °C for 30 min at 1 atm pressure of an Ar (95%) + H_2 (5%) gas mixture.

Figure 5.5a shows the optical transmittance and sheet resistance of the pure Cu NW and RG-O/Cu NW hybrid films. The Cu NW films with a low density of nanowires on the substrate surfaces have high optical transmittances (at 550 nm of $T_{550} > 95\%$). However the nanowires in such films do not form globally percolated network, and therefore the films are electrically non-conductive. Repeating the spray pulses can increase the density of NWs on the substrate surface and results in the formation of percolated networks yielding electrically conductive films. The average sheet resistance of such Cu NW films with optical transmittance of $T_{550} = 90\%$ is about $R_s = 295 \pm 19.5$ Ω/sq.

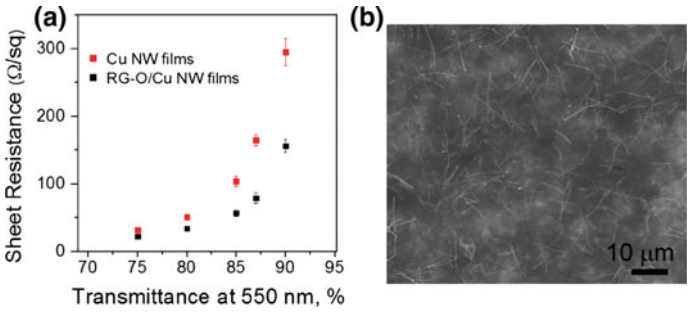

Fig. 5.5 **a** Sheet resistance versus optical transmittance for the pure Cu NW films and RG-O/Cu NW hybrid films. **b** SEM image of a typical RG-O/Cu NW film. Reprinted with permission from [28]. Copyright 2013 American Chemical Society

The RG-O films used in the hybrid films had an average sheet resistance of $R_s = 36.6 \pm 4.7$ kΩ/sq and optical transmittance of $T_{550} = 95.5\%$. The hybrid films had $R_s = 34 \pm 2.6$ Ω/sq at $T_{550} = 80\%$, which is lower than that of pure Cu NW films ($R_s = 51 \pm 4.0$ Ω/sq) and pure RG-O films ($R_s = 7.6 \pm 0.86$ kΩ/sq), each also at $T_{550} = 80\%$. The lower sheet resistance of the hybrid films can be ascribed to Cu NWs that can eliminate or decrease the platelet-platelet junction resistance in the RG-O films, and to the RG-O platelets that can bridge initially non-connected Cu NWs. The RG-O platelets have an average diameter of several micrometers, and can bridge two or more non-connected Cu NWs separated by any distance smaller than the platelet diameter. Figure 5.5b shows that the RG-O platelets cover the empty spaces between NWs providing a continuous 2D platform for charge carriers. Overall, the obtained results demonstrate that the multi-component hybrid films have better optoelectrical characteristics compared to the corresponding single-component films.

In addition to improving the overall conductivity, RG-O platelets can provide additional functionalities. For example, RG-O can act as an oxidation-resistant layer to protect the underneath Cu NWs. Pure Cu NW films are degraded under ambient conditions because of oxidation. Oxidation increases the sheet resistance of the nanowire films, and at higher temperatures this degradation process occurs even faster. The changes of the sheet resistances (R_s) of pure Cu NW and hybrid RG-O/Cu NW films over time in ambient atmosphere at room temperature and at 60 °C are shown in Fig. 5.6a. At room temperature the sheet resistance of the Cu NW films changes from 57 ± 2.5 to 69 ± 3.2 Ω/sq after 72 h. At 60 °C for the same time period the R_s of the nanowire films increases even more rapidly from 56 ± 2.5 to 94 ± 4.7 Ω/sq because of faster oxidation of metal nanowires at elevated temperatures [53]. In contrast, under the same conditions the hybrid films exhibit only minor (in average less than 3% both at room temperature and at 60 °C) changes in R_s. Overall, the minor increase in R_s of the hybrid films compared to that of the pure Cu NW films indicates the higher oxidation-resistance of the hybrid films that can be ascribed to the RG-O layers covering the nanowires.

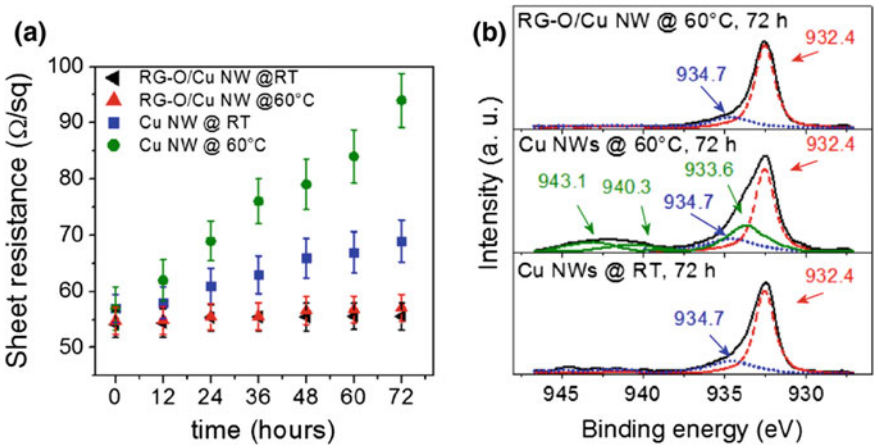

Fig. 5.6 **a** Sheet resistances changes over time for pure Cu NW films and RG-O/Cu NW hybrid films at room temperatures (RT) and at 60 °C. **b** Cu $2p_{3/2}$ XPS spectrum of Cu NW film kept at room temperature (*bottom*), and 60 °C (*middle*) for 72 h, and of RG-O/Cu NW films kept at 60 °C for 72 h (*top*). Reprinted with permission from [28]. Copyright 2013 American Chemical Society

X-ray photoelectron spectroscopy (XPS) studies are consistent with the above shown oxidation-resistance role of RG-O layers in the hybrid films. The high intensity peak (dashed red curve) at ~932.4 eV in the spectrum of the pure Cu NW films kept at room temperature (Fig. 5.6b, bottom spectrum) is ascribed to the overlap of Cu $2p_{3/2}$ and Cu_2O [54] spectral peaks. The low intensity peak (dotted blue curve) at ~934.7 eV is ascribed to $Cu(OH)_2$ [55]. In the spectrum for the Cu NW film kept at 60 °C for 72 h the deconvolution of the peak centered at ~932.4 eV shows the presence of CuO (933.6 eV), $Cu(OH)_2$ (934.7 eV) (dotted blue curve),and the shake-up satellites of CuO (940.3 and 943.1 eV) (solid dark green curves) (Fig. 5.6b, middle spectrum) [54]. The existence of the oxygen containing copper compounds indicate the higher level of oxidation of the Cu NW films compared to the RG-O/Cu NW films (Fig. 5.6b, top spectrum), where such compounds were not observed. These results demonstrate the higher oxidation-resistance of the RG-O/Cu NW hybrid films compared to the pure Cu NW films, and this can be assigned to the RG-O layers that protect the metal nanowires from oxidation.

In the RG-O/Cu NW hybrid films the Cu NWs are considered as the main electrically conductive component. RG-O in this films acts as a multifunctional component simultaneously addressing multiple issues: a continuous film that covers the empty spaces between Cu NWs; a 2D conductive platforma protective layer against oxidation of metal nanowires. Due to these synergistic effects the RG-O/Cu NW hybrid films exhibit higher performance compared to the corresponding single component films.

5.5 CVD-Graphene/Metal Nanowire Hybrid Transparent Conductive Films

CVD-graphene possesses better electrical conductivity compared to RG-O, and therefore it can be main electrically conductive component in the graphene-NW hybrid films. Here, we describe fabrication and optoelectrical properties of CVD-graphene/Ag NW hybrid films with sub-percolation density of Ag NWs. The pure sub-percolated Ag NW films do not form a global network, and therefore the entire film composed of sub-percolated Ag NWs has no electrical conductivity. In the CVD-graphene/Ag NW hybrid films with sub-percolated nanowire components each nanowire can locally contribute with high metallic conductivity to global electrical conductivity of the hybrid films. This allows estimating the contribution of individual metal nanowires (but not the network of NWs) in improving the electrical conductivity of the hybrid films.

CVD-graphene grown on Cu foil can be transferred onto arbitrary substrates using a wet transfer method [18]. Line disruptions in CVD-graphene, as were shown in the SEM images in Fig. 5.3, can be detected by Raman spectroscopy, as well (Fig. 5.7). Presence of defects that cause a double resonance involving transitions around two inequivalent K points of the first Brillouin zone of graphene results in the appearance of the Raman active D mode centered at $\sim$1365 cm^{-1} [56]. Bright lines on the Raman map shown in Fig. 5.7a correspond to the D mode of graphene and can be attributed to the line disruptions. Figure 5.7b shows the individual Raman spectra of graphene taken at areas marked with red, blue and dark cyan circles in the Raman map (Fig. 5.7a). The dark cyan and blue circled areas in the Raman map contain the bright lines (defects), and therefore, the corresponding

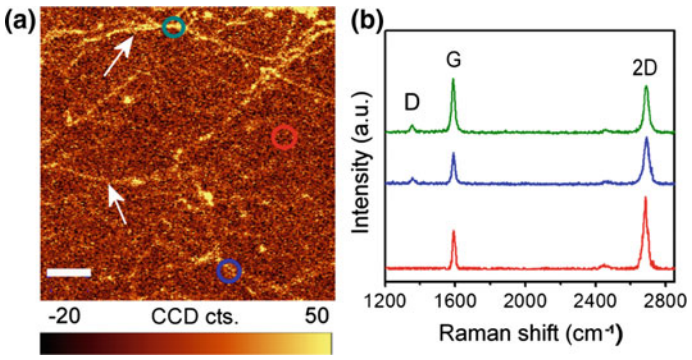

Fig. 5.7 **a** Raman map of CVD-graphene film on a SiO_2/Si substrate (1300–1400 cm^{-1}) around the D mode (1365 cm^{-1}). The line defects (ripples, folding and wrinkles) in the map are shown by the *white arrows*. The scale bar is 10 μm. **b** Raman spectra taken from the areas shown by *red*, *blue* and *dark cyan circles* in the Raman map in (**a**). Raman spectra were taken using WITEC Alpha 300, 100× objective, laser wavelength of 532 nm. Reprinted with permission from [20]. Copyright 2012 American Chemical Society

spectra in Fig. 5.7b show the clearly visible D peaks. Raman spectrum corresponding to the red circled area shows typical CVD-graphene with no observable D peaks. In addition to the D peaks, all three spectra in Fig. 5.7b have relatively high intensity G ($\sim$575 cm^{-1}) and 2D ($\sim$2680 cm^{-1}) peaks. The differences in intensity ratio of G and 2D peaks in blue and dark cyan spectra (I(2D)/I(G) $\approx$ 1.4 for blue, and $\approx$0.9 for dark cyan) indicate the variety of the line disruptions in CVD-graphene. Such transferred CVD-graphene films have a typical sheet resistance of about 1.35 $\pm$ 0.14 kΩ/sq. Thermal annealing at 170 °C for 1 h in a vacuum with a pressure of $p < 2 \times 10^{-2}$ Torr can lower the film sheet resistance to about 1.05 $\pm$ 0.11 kΩ/sq.

Ag NWs (Fig. 5.4b) dispersed in isopropyl alcohol (IPA) (20 mg/ml) was diluted with IPA in order to obtain 0.2, 0.6 and 1.0 mg/mL concentrated Ag NW dispersions. Ag NW films were made by spin coating (3000 rpm) these three dispersions on target substrates, yielding NW films with optical transmittance at 550 nm wavelength (T_{550}) of 98.6, 97.2 and 96.0%, respectively. These films were denoted as NW1, NW2, and NW3, respectively, and all these are non-conductive due to the sub-percolation network of the NWs. Higher (>1.0 mg/mL) concentrations of Ag NW dispersions yield electrically conductive (i.e., percolating) NW films (with $T_{550} < 96\%$), and here we do not consider such films in detail.

To fabricate CVD-graphene/Ag NW hybrid films, CVD-graphene was transferred from the original Cu substrate onto Ag NW films using a double PMMA layer coverage [20]. Figure 5.8a shows a SEM image of the obtained CVD-graphene/Ag NW hybrid films. The graphene layer conforms to the curved surface of the underlying NWs yielding larger contact area between nanowires and graphene layer. This structural feature may improve charge transfer between these two nanostructures resulting in improved conductivity of the hybrid film. The randomly oriented NWs in the hybrid film cross the line disruptions of the graphene (Fig. 5.8b) and can provide 1D pathway for charge transfer.

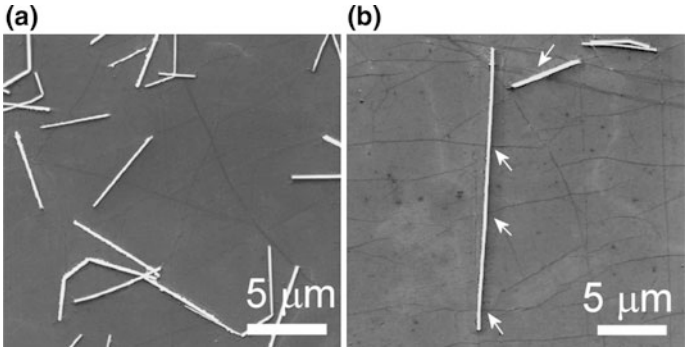

Fig. 5.8 SEM images of **a** a CVD-graphene/Ag NW films, and **b** graphene line disruptions crossing Ag NW shown by *arrows*. Reprinted with permission from [20]. Copyright 2012 American Chemical Society

Figure 5.9a shows the optical transmittance of CVD-graphene and CVD-graphene/Ag NW hybrid films with transparency of >90% in the presented spectral region (400–1000 nm). Optical transmittance vesus the R_s of the films measured after annealing at 170 °C for 1 h in a vacuum with a pressure of $p < 2 \times 10^{-2}$ Torr is depicted in Fig. 5.9b. The sheet resistance of the CVD-graphene/Ag NW films depends on the density of the Ag NWs. The CVD-graphene/NW3 films have the lowest sheet resistance $R_s = 64 \pm 6.1$ Ω/sq with $T_{550} = 93.6\%$ that is comparable to the values (30 Ω/sq for CVD-graphene/SiO_2 system) theoretically predicted for appropriately doped 'perfect' graphene when solely electron-phonon scattering is considered [40]. Such greatly improved conductivity of the hybrid films compared to pure typical CVD-graphene films ($R_s = 1.05 \pm 0.11$ kΩ/sq) can be ascribed to the Ag NWs that provide metallic 1D conductivity pathways. In these hybrid films, graphene is the main conductive component while Ag NWs contribute only locally because of their sub-percolation density.

Further decrease in the sheet resistance of the hybrid films can be achieved by increasing the density of Ag NWs or by adding another layer of graphene. For example, adding a second graphene layer onto the CVD-graphene/NW3 allows decreasing the films sheet resistance to about 24 (±3.6) Ω/sq with $T_{550} \approx 91\%$ (CVD-graphene × 2/NW3 in Fig. 5.9b).

In the presented CVD-graphene/sub-percolated Ag NW films the graphene layer is the main globally conductive component while Ag NWs are an additional component (globally non-conductive) that can locally contribute to the conductivity of the hybrid films. Using percolated NW films or metal grids yields hybrid films with further enhanced conductivities, as has been demonstrated recently [21, 57]. In such films metal structures are considered as main conductive components.

As in case of RG-O layer in RG-O/Cu NW hybrid films, demonstrated in the previous section, graphene in CVD-graphene/Ag NW hybrid films can also provide additional functionalities resulting in improved performance of the hybrid films.

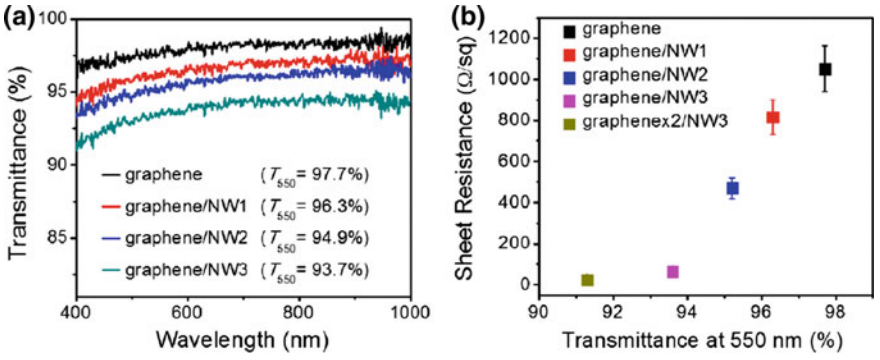

Fig. 5.9 **a** Optical transmittance of CVD-graphene and CVD-graphene/Ag NW films. **b** Sheet resistance versus optical transmittance for CVD-graphene and CVD-graphene/Ag NW films. Reprinted with permission from [20]. Copyright 2012 American Chemical Society

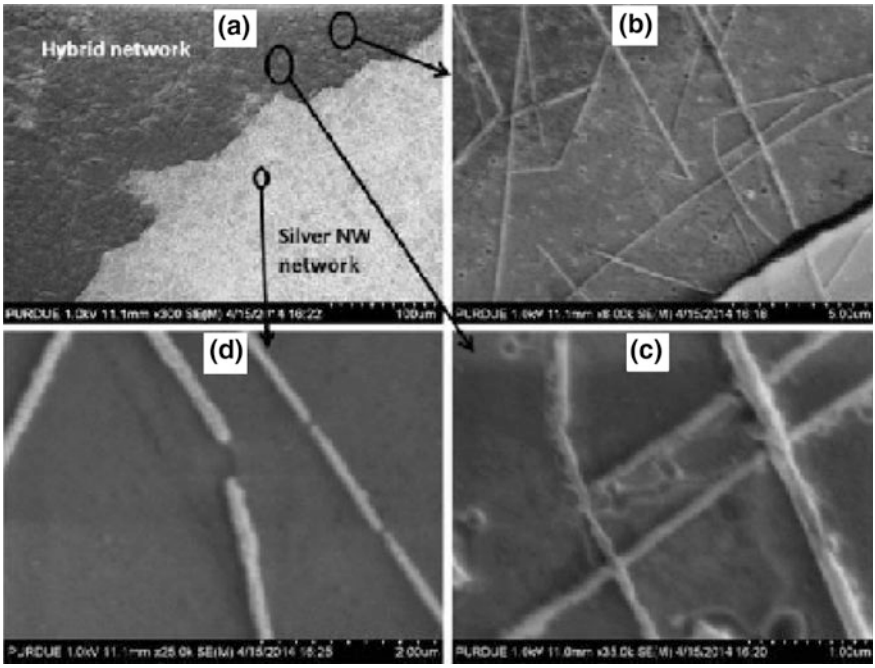

Fig. 5.10 SEM of silver nanowires after laser irradiation with intensity of 0.8 MW cm^{-2}: **a** A comparison between NW network region and hybrid NW network region (note the difference in the image contrast between the two regions). **b**, **c** High-magnification SEM images of two randomly located hybrid network regions. **d** High-magnification SEM view of a representative randomly located nanowire network region. Reprinted with permission from [51]. Copyright 2015 American Chemical Society

One of such functionalities of graphene, namely the protection of Ag NWs from harsh radiation environment has been recently studied [51]. For these studies thin films of CVD-graphene/Ag NWs (darker area in Fig. 5.10a) and pure Ag NWs (lighter area in Fig. 5.10a) were exposed to intense 248 nm KrF excimer laser beams with nanosecond pulses widths and with varied laser intensities corresponding to millions of W cm^{-2} power densities. It was demonstrated that after exposing to the laser beam the Ag NWs covered with graphene layer were not damaged (Fig. 5.10b, c), while the uncovered Ag NWs deformed, converted into nanosegments (Fig. 5.10d), and eventually into nanobeads along the length of the nanowires. In the CVD-graphene/Ag NW films, the graphene layer extracts and spreads the most of the thermal energy from the nanowires to the graphene lattice, thereby protecting the nanowires from thermal damaging. This functionality of the graphene layer enables using the hybrid films at elevated temperatures for longer terms compared to the pure Ag NW films.

It should be noted that the electromechanical performance of the hybrid films is another major advantage over ITO. Although all RG-O/Cu NW and CVD-graphene/Ag

NW hybrid films presented above were on rigid substrates, similar optoelectrical results for the films deposited on flexible substrates can be obtained because all thin film fabrication and processing are compatible with flexible substrates. In addition, excellent stability of numerous graphene/metal NW hybrid films under mechanical strains has been reported in recent literatures [34, 57, 58].

5.6 Applications of Graphene/Metal Nanowire Hybrid Films

As shown above, the hybrid films composed of RG-O or CVD-graphene and metal nanowires have a great potential for TCF applications due to their optoelectrical characteristics. The hybrid films have been recently tested in diverse optoelectronic devices, such as CdTe solar cells [59], light emitting diodes [60], single-pixel contact lenses [57] showing feasibility of the films as transparent electrodes in these devices. Some applications of the hybrid films have been summarized in recent literature [61]. Here, we show two examples of the applications of RG-O/Cu NW and CVD-graphene/Ag NW hybrid films as transparent electrodes in electrochromic (EC) devices. Using two different EC cells we highlight two different aspects of the hybrid films: (i) better performance of the hybrid TCF compared to single component NW TCFs, and (ii) hybrid TCFs can replace the conventional ITO in EC devices.

5.6.1 Application of RG-O/Cu NW Transparent Electrodes in EC Devices

Working principle of EC devices is based on the reversible change the optical properties of the EC material induced by an external electric field. These devices can be used for diverse applications, including displays, gas sensors, antiglare mirrors and smart windows. The latter application represents an important use to shadow buildings against direct solar radiation to reduce the heat load, and in majority cases requires large-area device fabrication. Below we provide more detailed description of EC device fabrication steps using the hybrid films as transparent electrodes. Most aspects of the fabrication of electrochromic devices can be applied for sandwich-structured optoelectronic devices, such as dye-sensitized solar cells and OLEDs.

The RG-O/Cu NW hybrid films were tested as transparent electrodes in Prussian blue (PB)-based electrochromic (EC) devices. This kind of EC device typically consists of a thin PB film deposited onto a transparent electrode, usually ITO. Here, RG-O/Cu NW hybrid films on glass substrates were used to replace ITO electrodes [28]. An aqueous solution of 0.05 M hydrochloric acid (HCl), 0.05 M iron(III)

chloride ($FeCl_3$), and 0.05 M potassium hexacyanoferrate (III) ($K_3[Fe(CN)_6]$) in a 1:2:2 ratio was used to electrochemically deposit PB films onto the RG-O/Cu NW transparent electrodes [62]. PB films with homogeneous thicknesses on top of the RG-O/Cu NW electrode can be obtained by applying a voltage to the RG-O/Cu NW electrode and Pt counter electrode, both immersed into the solution [63].

An external electric voltage applied to the RG-O/Cu NW transparent electrode of the EC device and the Pt counter electrode (Fig. 5.11a) induces an electrochemical reaction that results in reversible modulations of optical characteristics of PB layers. Electrochemical reduction of the PB layer converts a mixed-valence (Fe^{2+}, Fe^{3+}) compound into a single-valence (Fe^{2+}) compound (and vice versa upon oxidation) and changes the color of the PB layer from blue to colorless (from colorless to blue upon oxidation). This electrochemical reaction can be described as [63]:

$$(\text{blue})\ Fe_4^{3+}\left[Fe^{2+}(CN)_6\right]_3 + 4\,K^+ + 4e^- \Leftrightarrow (\text{colorless})\ K_4Fe_4^{2+}\left[Fe^{2+}(CN)_6\right]_3$$

The redox reactions leading to the coloration/bleaching of PB-based EC devices can be simply carried out using 1 M KCl aqueous solution as an electrolyte (Fig. 5.11a). Bleached colorless state of the EC device can be obtained by applying an external voltage (−0.6 V) to the RG-O/Cu NW TCF, and the blue colored state is achieved by applying a reverse external field. Figure 5.11b shows the optical transmittance spectra of the PB layer at the bleached (T_{550} = 79.2%) and colored (T_{550} = 36.4%) states. Typical times needed for the bleached-to-colored and colored-to-bleached processes in the tested EC devices are measured to be 75 and 95 s, respectively, which are similar to that of a PB EC device with an ITO electrode [62, 63].

In contrast the RG-O-Cu NW hybrid films, pure Cu NW transparent electrodes cannot work in the PB EC devices. This has been demonstrated using a two-area

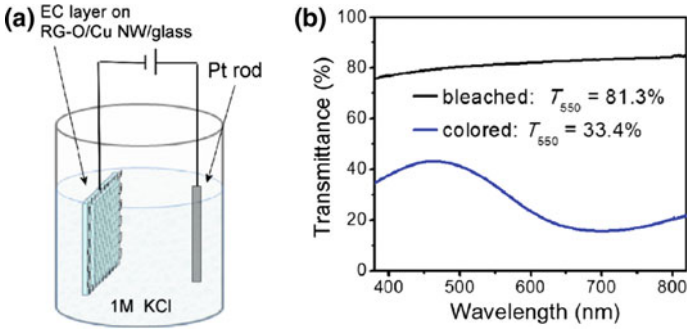

Fig. 5.11 **a** Schematic of an EC device with a PB layer deposited onto the RG-O/Cu NW electrode and Pt rod used as a counter electrode, both immersed into an electrolyte. **b** Optical transmittance of colored and bleached PB films deposited on a RG-O/Cu NW transparent electrode. Reprinted with permission from [28]. Copyright 2013 American Chemical Society

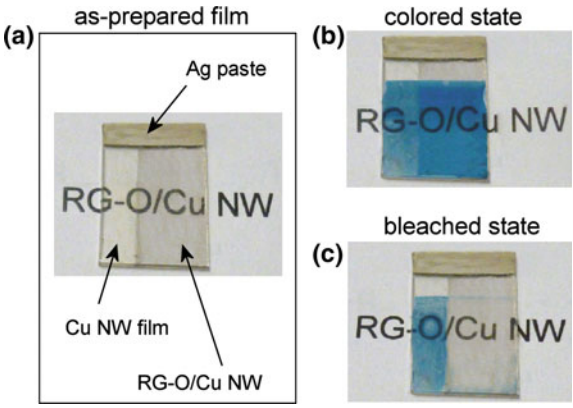

Fig. 5.12 Digital photograph of **a** as-prepared two-area transparent electrode with areas covered by a pure Cu NW film and a hybrid RG-O/Cu NW film, as shown by the *arrows* (*left*). PB EC layer on the two-area electrode **b** after coloration, and **c** bleaching processes. Reprinted with permission from [28]. Copyright 2013 American Chemical Society

transparent electrode (a glass substrate with one-half covered by RG-O/Cu NW hybrid film and the other by pure Cu NW film, as shown in Fig. 5.12a). After deposition of a PB layer onto this electrode, entire surface of the electrode has been homogeneously colored (Fig. 5.12b, colored state). In electrochemical bleaching, the PB layer deposited on the RG-O/Cu NW hybrid film has been bleached, while no bleaching of the PB on top of the pure Cu NW film occurred (Fig. 5.12c, bleached state). This can be explained by the fact that during the deposition of PB layers pure Cu NWs reacted with PB forming copper hexacyanoferrate compounds [64]. This reaction destroys the Cu NW network(s), the area of the electrode initially covered with pure Cu NWs has no electrical conductivity. In addition, immersing the electrode into the electrolyte solution leads to partial delamination of the Cu NWs from the electrode area covered with the pure Cu NW film, which also results in worsening the electrical conductivity of the pure Cu NW films. In contrast, the PB layer, deposited onto the electrode area covered with RG-O/Cu NW films, can be repeatedly electrochemically colored and bleached. This indicates that the RG-O platelets in RG-O/Cu NW films protect the Cu NWs from reacting with the PB layer. Also, no delamination of Cu NWs from the electrode area covered with RG-O/Cu NW film was observed.

The presented example demonstrates that RG-O/Cu NW hybrid films exhibit better performance compared to pure Cu NWs. However, it should be noted that lowering the RG-O thickness and/or increasing the cycling results in gradual degradation of RG-O/Cu NW hybrid films in the EC device. These observations indicate that currently, the nanostructured hybrid TCFs can be selectively used in certain type of devices, and further improvement is needed in order to expand their use in wider range of optoelectronic applications. In addition to the optical, electrical and mechanical properties of the hybrid films, their long-term use and material consistencies/inconsistencies of the hybrid films needs to be more rigorously studied.

5.6.2 *Application of CVD-Graphene/Ag NW Transparent Electrodes in EC Devices*

CVD-graphene/Ag NW films were used as a transparent electrode in another EC device with an electrochromic WO_3 layer [20]. This kind of EC devices consist of an EC thin film and an electrolyte layer sandwiched between two transparent electrodes (usually ITO electrodes). An external voltage applied to the electrodes can modulate the optical characteristics of the EC layer [65, 66]. Here, the CVD-graphene/Ag NW films on glass substrates were used to replace one of the two ITO TCFs as shown in Fig. 5.13a. Nanostructured sol-gel synthesized WO_3 films that exhibit improved performance of EC devices with fast coloration/bleaching kinetics were chosen as the EC layer [65–67]. However, direct spin-coating of sol-gel synthesized WO_3 onto CVD-graphene/Ag NW hybrid films with no buffer layer yields EC films with non-uniform thicknesses and inhomogeneous morphologies. Therefore, first, using thermal evaporation of WO_3 powder, a buffer layer—100 nm thick WO_3 film was deposited onto the CVD-graphene/Ag NW electrode. This buffer layer provides a good surface for spin coating of sol–gel prepared nanostructured WO_3 films onto it. The total thickness of the double layer WO_3 thin films with highly porous surface structure (Fig. 5.13b) was about 500 nm. A propylene/ethylene carbonate solution (1:1) containing 1 M $LiClO_4$ was chosen as a Li-conductive electrolyte. Figure 5.13a shows the schematic of complete EC device with WO_3 EC layers and electrolyte sandwiched between ITO and CVD-graphene/Ag NW transparent electrodes deposited on glass substrates.

An external voltage applied to the electrodes (3.0 V, negative to the CVD-graphene/Ag NW and positive to the ITO) induces the injection of electrons and intercalation of Li^+ cations into the WO_3 films and yields W^{+5} sites. Subsequently the charge transfer between the W^{+6} and W^{+5} states occurs in the WO_3 films. This process is accompanied with strong optical absorption leading to blue coloration of the WO_3 layers. The reaction is described as [66]:

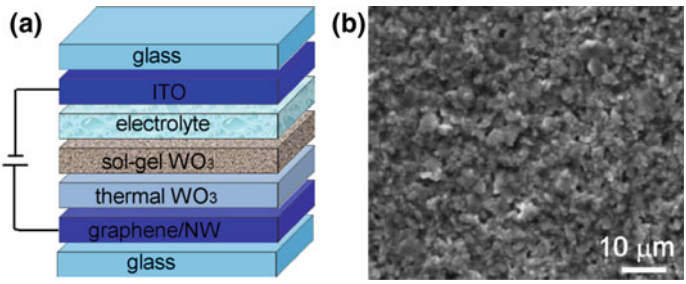

Fig. 5.13 **a** Schematic of an EC device. Reprinted with permission from [20]. Copyright 2012 American Chemical Society. **b** SEM image of double layer WO_3 film deposited onto CVD-graphene/Ag NW transparent conductive electrode

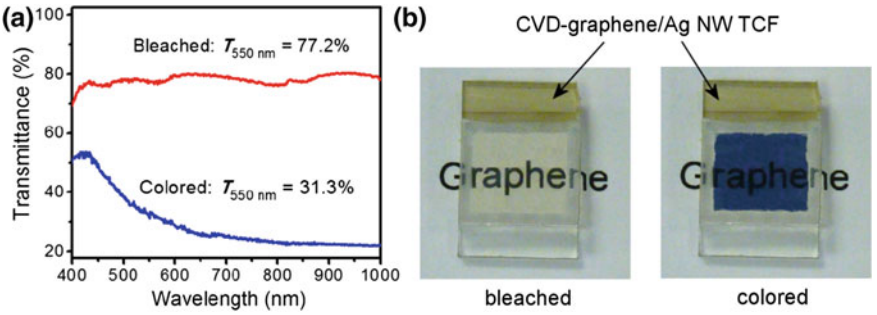

Fig. 5.14 **a** Optical transmittance spectra of the EC device in bleached and colored states. **b** Digital photographs of the bleached and colored EC devices with a background "Graphene". A conductive silver paste (*yellow area*) on top of the CVD-graphene/Ag NW electrode was used to improve the electrical contacts. Reprinted with permission from [20]. Copyright 2012 American Chemical Society

$$WO_3 + x[Li^+ + e^-] \rightarrow Li_xW^{+6}_{(1-x)}W^{+5}_x O^3,$$

where x is the fractional number of WO_3 lattice sites filled with Li cations. Extraction of Li^+ ions from the WO_3 layers and bleaching the EC film can be obtained by applying a reverse external voltage to the electrodes. Typical optical transmittance of the EC device in bleached (T_{550} = 77.2%) and colored (T_{550} = 31.3%) states is shown in Fig. 5.14a.

The photographs of the EC device in bleached and colored states are shown in Fig. 5.14b. The stable times of 115 and 205 s for 90% optical transmittance change from bleached-to-colored and from colored-to-bleached states, respectively are obtained after several initial coloration/bleaching cycles. These values are similar to that of a EC device with the same electrolyte and sol–gel EC film, but using two ITO electrodes [67].

The presented applications of the hybrid films in the EC devices demonstrate the feasibility of the graphene/metal NW hybrid films for TCF applications. Further research studies and optimization of properties of the hybrid films are needed to accelerate the practical application of graphene-metal nanowire hybrid films in various optoelectronic devices including displays, touch screens, solar cells, OLEDS, electromagnetic shielding and transparent heaters.

5.7 Conclusions and Future Challenges

Commercially available ITO transparent conductive films cannot meet the performance metrics of new TCF-based devices, especially in emerging technologies such as flexible displays, solar cells, transistors, sensors and energy storage systems. Hybrid films composed of two or more components not only exhibit better

performance compared to that of the corresponding single component films, but also they possess optical, electrical and mechanical properties similar or superior to that of conventionally used transparent oxide conductors.

The strategy to assemble 1D metal NWs and 2D graphene films allows one to obtain hybrid films with excellent control of nanoscale morphology, where the limitation of one component is compensated by the strengths of the other component. In terms of the two main TCF characteristics: optical transmittance and electrical conductivity, the hybrid films are comparable to or better than ITO films. Another advantage of the hybrid films over ITO films is their good electromechanical stabilities that make them suitable for flexible optoelectronic devices. Overall, the strategy to fabricate the hybrid films not only allows replacing ITO films, but also can provide a path to next generation TCFs with novel architectures and additional functionalities.

In spite of these advantages, today, the hybrid films have not yet fully expanded in the market to replace the ITO films in the existing and emerging optoelectronic device applications. The successful realization of a great potential of the hybrid films requires extensive investigation and comprehensive analysis of both fundamental and application-specific characteristics of the hybrid films. Furthermore, research and development addressing the following issues: (i) developing of advanced methods for fabrication of high-quality, low-cost and large-scale hybrid films; (ii) thermal, chemical, environmental stability of the films, (iii) optimization of compositional and structural performance, (iv) designing and assembling of components, and integration testing of hybrid films in a broad range of devices are vitally important to realize the potential of the hybrid transparent conductive films. In addition, to improve the feasibility of the hybrid films for practical applications, it is important to test the compatibility of the hybrid films with active parts of diverse optoelectronic devices, and studying, detecting and eliminating the film performance issues for long-term applications.

Acknowledgements Dr. Kholmanov thanks Prof. R. Ruoff for his collaboration, and would like to acknowledge the support from Tokyo Electron Ltd.—customized Semiconductor Research Corporation (Project#2009-OJ-1873). Prof. Alam will like to acknowledge his long term collaborations: Prof. D. Janes, Prof. J. Rogers, Prof. Shakouri, Dr. S. Das, Dr. R. Chen, Dr. C. Jeong. The work was supported by Semiconductor Research Corporation (Project # 2009-OJ-1873) and National Science Foundation Grant ECCS 1408346. Prof. Sberveglieri would like to acknowledge the support from European Union Research and Innovation Funding Program FP7 (Project# FP7-ICT-2013-10).

References

1. K. Ellmer, Nat. Photonics **6**, 9 (2012)
2. D.S. Hecht, L. Hu, G. Irvin, Adv. Mater. **23**, 1482 (2011)
3. T. Minami, Semicond. Sci. Technol. **20**, S35 (2005)
4. S.T. Lee, Z.Q. Gao, L.S. Hung, Appl. Phys. Lett. **75**, 1404 (1999)

5. M.P. de Jong, D.P.L. Simons, M.A. Reijme, L.J. van Ijzendoorn, A.W. Denier van der Gon, M.J.A. de Voigt, H.H. Brongersma, R.W. Gymer, Synth. Met. **110**, 1 (2000)
6. M. Jørgensen, K. Norrman, S.A. Gevorgyan, T. Tromholt, B. Andreasen, F.C. Krebs, Adv. Mater. **24**, 580 (2012)
7. S. Savagatrup et al., Energy Environ. Sci. **8**, 55 (2015)
8. M.G. Kang, L.J. Guo, Adv. Mater. **19**, 1391 (2007)
9. M. Zhang, S. Fang, A.A. Zakhidov, S.B. Lee, A.E. Aliev, C.D. Williams, K.R. Atkinson, R. H. Baughman, Science **309**, 1215 (2005)
10. F. Mirri, A.W.K. Ma, T.T. Hsu, N. Behabtu, S.L. Eichmann, C.C. Young, D.E. Tsentalovich, M. Pasquali, ACS Nano **6**, 9737 (2012)
11. Q. Cao, J.A. Rogers, Adv. Mater. **21**, 29 (2009)
12. N. Pimparkar, M.A. Alam, IEEE Electron Device Lett. **29**, 1037 (2008)
13. S.V. Morozov, K.S. Novoselov, M.I. Katsnelson, F. Schedin, D.C. Elias, J.A. Jaszczak, A.K. Geim, Phys. Rev. Lett. **100**, 016602 (2008)
14. A.B. Kuzmenko, E. van Heumen, F. Carbone, D. van der Marel, Phys. Rev. Lett. **100**, 117401 (2008)
15. R.R. Nair, P. Blake, A.N. Grigorenko, K.S. Novoselov, T.J. Booth, T. Stauber, N.M.R. Peres, A.K. Geim, Science **320**, 1308 (2008)
16. Q. Zheng, Z. Li, J. Yang, J.-K. Kim, Prog. Mater Sci. **64**, 200 (2014)
17. H.A. Becerril, J. Mao, Z. Liu, R.M. Stoltenberg, Z. Bao, Y. Chen, ACS Nano **2**, 463 (2008)
18. X. Li, Y. Zhu, W. Cai, M. Borysiak, B. Han, D. Chen, R.D. Piner, L. Colombo, R.S. Ruoff, Nano Lett. **9**, 4359 (2009)
19. C. Jeong, P. Nair, M. Khan, M. Lundstrom, M.A. Alam, Nano Lett. **11**, 5020 (2011)
20. I.N. Kholmanov et al., Nano Lett. **12**, 5679 (2012)
21. Y. Zhu, Z. Sun, Z. Yan, Z. Jin, J.M. Tour, ACS Nano **5**, 6472 (2011)
22. W.S. Hummers, R.E. Offeman, J. Am. Chem. Soc. **80**, 1339 (1958)
23. S. Stankovich, D.A. Dikin, G.H.B. Dommett, K.M. Kohlhaas, E.J. Zimney, E.A. Stach, R.D. Piner, S.T. Nguyen, R.S. Ruoff, Nature **442**, 282 (2006)
24. X. Wang, L. Zhi, K. Müllen, Nano Lett. **8**, 323 (2008)
25. V. Galstyan, E. Comini, I. Kholmanov, G. Faglia, G. Sberveglieri, Rsc Adv. **6**, 34225 (2016)
26. I.N. Kholmanov et al., ACS Nano **6**, 5157 (2012)
27. S. Gilje, S. Han, M. Wang, K.L. Wang, R.B. Kaner, Nano Lett. **7**, 3394 (2007)
28. I.N. Kholmanov et al., ACS Nano **7**, 1811 (2013)
29. H.-J. Shin et al., Adv. Func. Mater. **19**, 1987 (2009)
30. M. Zhou, Y. Wang, Y. Zhai, J. Zhai, W. Ren, F. Wang, S. Dong, Chemistry. Eur J **15**, 6116 (2009)
31. Y. Shao, J. Wang, M. Engelhard, C. Wang, Y. Lin, J. Mater. Chem. **20**, 743 (2010)
32. Z.-J. Fan, W. Kai, J. Yan, T. Wei, L.-J. Zhi, J. Feng, Y.-M. Ren, L.-P. Song, F. Wei, ACS Nano **5**, 191 (2011)
33. X. Mei, J. Ouyang, Carbon **49**, 5389 (2011)
34. S.H. Domingues et al., Carbon **63**, 454 (2013)
35. X. Wang, I. Kholmanov, H. Chou, R.S. Ruoff, ACS Nano **9**, 8737 (2015)
36. X. Li et al., Science **324**, 1312 (2009)
37. S. Bae et al., Nat Nano **5**, 574 (2010)
38. X. Du, I. Skachko, A. Barker, E.Y. Andrei, Nat Nano **3**, 491 (2008)
39. G.-X. Ni et al., ACS Nano **6**, 1158 (2012)
40. J.-H. Chen, C. Jang, S. Xiao, M. Ishigami, M.S. Fuhrer, Nat Nano **3**, 206 (2008)
41. P.Y. Huang et al., Nature **469**, 389 (2011)
42. O.V. Yazyev, S.G. Louie, Nat. Mater. **9**, 806 (2010)
43. I.N. Kholmanov, J. Edgeworth, E. Cavaliere, L. Gavioli, C. Magnuson, R.S. Ruoff, Adv. Mater. **23**, 1675 (2011)
44. S. Karoui, H. Amara, C. Bichara, F. Ducastelle, ACS Nano **4**, 6114 (2010)
45. Q. Yu et al., Nat. Mater. **10**, 443 (2011)
46. L. Hu, H.S. Kim, J.-Y. Lee, P. Peumans, Y. Cui, ACS Nano **4**, 2955 (2010)

47. A.R. Rathmell, B.J. Wiley, Adv. Mater. **23**, 4798 (2011)
48. D.-S. Leem, A. Edwards, M. Faist, J. Nelson, D.D.C. Bradley, J.C. de Mello, Adv. Mater. **23**, 4371 (2011)
49. E.C. Garnett, W. Cai, J.J. Cha, F. Mahmood, S.T. Connor, M. Greyson Christoforo, Y. Cui, M.D. McGehee, M.L. Brongersma, Nat. Mater. **11**, 241 (2012)
50. H. Wu et al., Nat Nano **8**, 421 (2013)
51. S.R. Das, Q. Nian, M. Saei, S. Jin, D. Back, P. Kumar, D.B. Janes, M.A. Alam, G.J. Cheng, ACS Nano **9**, 11121 (2015)
52. H. Yamaguchi, G. Eda, C. Mattevi, H. Kim, M. Chhowalla, ACS Nano **4**, 524 (2010)
53. A.R. Rathmell, M. Nguyen, M. Chi, B.J. Wiley, Nano Lett. **12**, 3193 (2012)
54. C.-K. Wu, M. Yin, S. O'Brien, J.T. Koberstein, Chem. Mater. **18**, 6054 (2006)
55. C.E. Dubé, B. Workie, S.P. Kounaves, A. Robbat, M.L. Aksub, G. Davies, J. Electrochem. Soc. **142**, 3357 (1995)
56. A.C. Ferrari, Solid State Commun. **143**, 47 (2007)
57. M.-S. Lee et al., Nano Lett. **13**, 2814 (2013)
58. B. Deng et al., Nano Lett. **15**, 4206 (2015)
59. J. Liang, H. Bi, D. Wan, F. Huang, Adv. Func. Mater. **22**, 1267 (2012)
60. J. Liang, L. Li, K. Tong, Z. Ren, W. Hu, X. Niu, Y. Chen, Q. Pei, ACS Nano **8**, 1590 (2014)
61. R. Das Suprem, S. Sadeque, C. Jeong, R. Chen, A. Alam Muhammad, B. Janes David, Nanophotonics, 180 (2016)
62. S. Lupu, C. Mihailciuc, L. Pigani, R. Seeber, N. Totir, C. Zanardi, Electrochem. Commun. **4**, 753 (2002)
63. A.A. Karyakin, Electroanalysis **13**, 813 (2001)
64. O. Makowski, J. Stroka, P.J. Kulesza, M.A. Malik, Z. Galus, J. Electroanal. Chem. **532**, 157 (2002)
65. M. Deepa, A.K. Srivastava, M. Kar, S.A. Agnihotry, J. Phys. D Appl. Phys. **39**, 1885 (2006)
66. P.R. Somani, S. Radhakrishnan, Mater. Chem. Phys. **77**, 117 (2003)
67. A.E. Aliev, H.W. Shin, Solid State Ionics **154–155**, 425 (2002)

Chapter 6
Antibacterial Applications of Nanomaterials

Ameer Azam, Mohd. Arshad, Sourabh Dwivedi and Md. Tanweer Ashraf

6.1 Introduction

Many serious threats due to infectious diseases are laid to serious threats to the public health worldwide. In order to resolve these problems, new pasteurization and antibacterial agents are demanded and studied. This is particularly with the outgrowth of bacterial strains due to antibiotic-resistant. In recent advances, nanotechnology has provided its huge potential effect on public health care and plays a significant role in controlling the infectious diseases. Nanoparticles (NPs) of metal oxides exhibit an advance class of materials which are in great demand for research work and health-related issues. Nowadays, nanoscale materials are being widely used for fundamental study and applied research. This is on account of its extraordinary properties due to size effect (nano scale), doping effect, synthesis conditions, and synthesis parameters [1]. Several materials are being used from centuries as bactericidal and bacteriostatic agents [2]. Silver, gold, and zinc, each with diverse properties and spectrums of activity, have been tested [2, 3]. At high temperature and pressure, inorganic antibacterial agents are found relatively more stable as compared with that of organic materials and metal oxide nano particles dust which are prescribed as firm antimicrobial agents [4, 5]. In view of these properties, a concourse of nanoscience and biology can deal with various biomedical problems. In this way, a revolution can take place in the field of public health, health-related issues, and medicines [6, 7]. In several fields of medical sciences such as imaging, sensing, targeted drug delivery, gene delivery systems, and artificial implant, nanotechnology is being utilized as a tool for searching new

A. Azam (✉) · Mohd. Arshad · S. Dwivedi
Department of Applied Physics, Aligarh Muslim University, Aligarh, India
e-mail: azam222@rediffmail.com

Md.T. Ashraf
Department of Applied Sciences and Humanities, Jamia Millia Islamia, New Delhi, India

Z.H. Khan (ed.), *Recent Trends in Nanomaterials*,
Advanced Structured Materials 83, DOI 10.1007/978-981-10-3842-6_6

avenues [8–12]. Because of the possibilities of being synthesized nanoscale organic and inorganic materials, one can have one's interest in applications in medical fields [13]. Due to stimulated effectiveness, the nanotechnology-based new drugs can fight with the conditions like cancer, pathogens like bacteria and fungi in human [14]. These drugs include polymers, metals, and ceramics [15–17].

Medically, pathogenic bacteria origins are a major health concern due to hospital-acquired infections that induce a large number of dyings and hospitalizations. If we want to be prepared against known and unknown pathogenic bacterial infections, a range of potential solutions have been researched in hope that new treatments and diagnostic techniques will be developed in future. A large number of research studies include execution of nanotechnology to develop new class of antibacterial nanomedicines with increased effectiveness and potentials [18, 19]. Nanomedicine is termed as the supervising, repairing, and check of biological systems at nanolevel in human beings and animals, by using engineered nanodevices and nanomaterials. In this chapter, we look at a range of potential antibacterial therapeutics materials which involve nanotechnology, most of which have been early phases of research and now they are having positive indication of applications in nanomedical therapy and drug development to control the pathogenic bacterial infection.

Nanocarriers such as polymers, dendrimers, liposomes, nanotubes, and nanorods have provided a novel platform for target-specific delivery as well as for diagnosis [20–23]. ZnO nanoparticles because of their stability and eco-friendly properties have some advantages over silver nanoparticles [13, 24–26]. ZnO powders have UV blocking property and absorb infrared radiation with intensity of 5–16.68 dB in the frequency range of 2.45–18 GHz [26, 27]. ZnO also comes out to increase wear-resistant phase and antisliding phase in composites due to its rich elastic moduli and strength [28]. Li et al. [29] has studied the enduringness of antibacterial activity of nano-ZnO-functionalized cotton fabric for sweating.

ZnO NPs have been utilized as antibacterial wallpapers for hospitals use to prevent nosocomial infection [30]. Antimicrobial activity of soaked ZnO onto cotton textiles has showed excellent results against two bacteria, *Staphylococcus aureus* and *Klebsiella pneumoniae* [26]. ZnO is presently used as the most promising antibacterial agent in both microscale and nanoscale formulations [31]. It is reported that ZnO NPs show better antibacterial activity than microrange particles. Temperature is also an important factor for medicine activity such as at high temperature; ZnO NPs have a significant effect on their antibacterial activity [32]. ZnO NPs are found as the best antibacterial agent against *Bacillus subtilis*, *Escherichia coli*, and *Pseudomonas fluorescence* as reported by Jiang et al. [33]. This is also reported that ZnO nanoparticles can be immensely used as an efficient antibacterial agent to defend agricultural materials from foodborne pathogens, especially *E. coli* O157:H7 [34]. *Staphylococcus* is also a major group of the foodborne pathogens that are generally related to community-gained nosocomial infections. Recently, many complexes and nanomaterials of cobalt showing antimicrobial activity have been synthesized [35–37]. But, there is no result over

antibacterial activity of Co- and Mg-doped ZnO while zinc, Co, and Mg are the essential elements for human and animal body in trace amount. We have, therefore, been motivated to take up this task, to determine the antimicrobial activities, both qualitatively and quantitatively, of Co- and Mg-doped ZnO NPs against gram-positive and gram-negative bacteria. Mg-doped ZnO has been proved to be an effective agent for the enhancement of antibacterial activities of nanocrystalline ZnO. In present investigations, we have studied the effect of pure Co- and Mg-doped ZnO NPs. Here, we have also optimized the doping concentrations of Co and Mg in ZnO for effective antimicrobial activity. Apart from ZnO, various other nanomaterials such as TiO_2, CuO, Fe_2O_3, graphene oxide, CNTs have also shown their antibacterial applications.

6.2 Mechanism of Antibacterial Action

Although, comprehensive activity mechanisms of antibacterial effect of ZnO nanoparticles have not been substantially studied, Sawai et al. [38–40] reported that the formation of H_2O_2 may be the prime factor of antibacterial activities. Stoimenov et al. [13] studied the antibacterial behavior of ZnO nanoparticles using chemiluminescence and oxygen electrode analysis, and they reported that the holding of particles on bacteria surface due to the electrostatic forces could be a possible responsible mechanism for its activities. And they have also studied that production of H_2O_2 takes place in the slurry of ZnO, and its concentration is directly proportional to the concentration of ZnO particle in the slurry. Some researchers suggested that the reason of production of H_2O_2 in ZnO slurry is the electrostatic interaction between the bacteria surface and NPs. Presence of ZnO NPs in growing medium causes damage to the cell membrane or cell wall of *E. coli*. Such damages may be partly due to direct interactions between ZnO NPs and bacteria membrane surface. Gedanken et al. [41] suggested that the effective mechanism of antibacterial activity is the production of reactive oxygen species (ROS). Effect of ZnO lattice constant on antibacterial activities has also been reported by Yamamoto et al. [42]. The antibacterial activities of ZnO have been found due to reaction of water with ZnO. From electron spin resonance (EPR) measurements, it has been observed that the aqueous suspensions of ZnO nanoparticles generate enhanced levels of reactive oxygen species (ROS), saying hydroxyl radicals. A remarkable increase of oxidative stress, beyond the level yielded by the ZnO itself, has been noticed by observing antibacterial treatment. Similarly, bacteria exposer to ZnO NPs results in an enhanced cellular incorporation of NPs and the bacterial cell damage due to free radical generation. Figure 6.1 shows the NPs and bacterial cell interaction and ROS generation by the surface of the bacterial cells. Here, zinc ions released from the ZnO NPs cause membrane dysfunction due to the interruption of electron transport system. Further, the NPs internalization is the main cause of cell bursting/swelling.

In case of graphene oxide (GO), it is generally considered that the antimicrobial effect present in grapheme oxide are due to its physical and chemical properties.

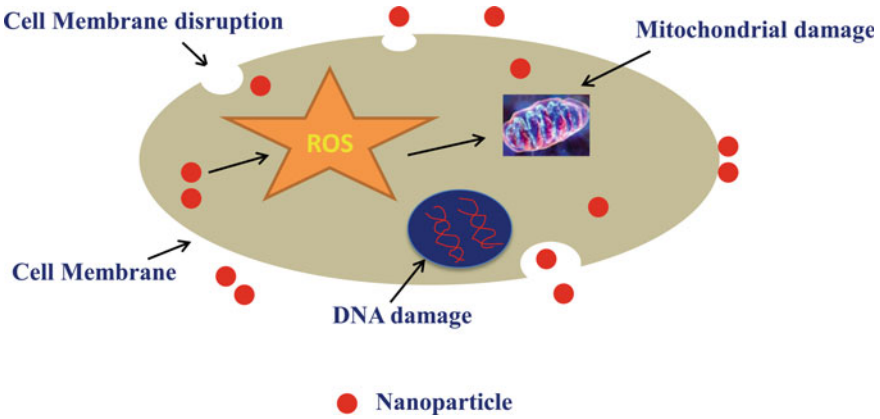

Fig. 6.1 Mechanisms of the disruption of bacterial cell by the interaction of NPs

The overproduction of reactive oxygen species (ROS) involves the chemical factor, and it was also detected to oxidize fatty acids which lead to the development of lipid peroxides that stimulate a chain reaction, finally leading to the decaying of the cell membrane followed by cell destruction [43].

6.3 Synthesis Procedure

A number of techniques are available for the preparation of pure and doped ZnO NPs [44]. Some methods are via chemical routes, and some are physical routes. The chemical methods consist of thermal hydrolysis methods [45], hydrothermal processing technique [46], and solgel route [47]. On the other hand, the physical methods are vapors condensation technique [48], spray pyrolysis technique [49], and thermochemical/flame decomposition of metal-organic precursors [50, 51]. Moreover, wet chemical method is one of the commercial methods for producing relatively huge amounts of NPs at lower cost. In a typical synthesis condition, citric acid is poured into 100 ml of distilled water and kept the solution on a magnetic stirrer until its pH becomes 1.5. Then after, measured amount of chlorides of zinc and the dopant are mixed together and dissolved. In the next step, we added 10 ml of ethylene glycol to the as-prepared above solution and again stirred it for 20 min. Later, sufficient amount of aqueous ammonia (15 mol/L) was poured dropwise into the as-prepared above solution and kept it for magnetic stirring of 30 min. The above-mentioned procedure resulted in the syntheses of a gel. The as-prepared gel was properly cleaned with water and alcohol and then it was dried at 115 °C for about 12 h in an incubator. Finally, this dried gel is further calcined at 400 °C for about 4 h. This resulted in the formation of pure and doped ZnO NPs.

6.4 Antibacterial Test Protocols

In order to have reliable quantitative data for materials screening in terms of antibacterial activities and inter-laboratory comparison, standard evaluation methods and criteria are necessary. Generally, evaluation methods for nanomaterials are adopted from long-standing in vitro microbiology protocols for antibiotics. Efficiency of the nanomaterial is evaluated on the basis of following parameters.

6.5 Antimicrobial Activity of Pure and Doped ZnO

Antimicrobial activities of the synthesized pure Co-doped ZnO NPs and Mg-doped ZnO NPs were performed against two gram-negative *E. coli* and *Pseudomonas aeroginosa* and two gram-positive *B. subtilis* and *S. aureus* bacteria using standard protocols as discussed above. The pure cultures of organisms were subculture on Müller-Hinton broth at 32 ± 2 °C on a rotary shaker at 120 rpm. Wells were cut, and bottom of the well was closed with a drop of molten agar (0.8% agar) to block leakage that may occur from base of the plate. About 100 µl (50 µg) of the as-prepared solution was supplied to each of the wells on all plates. After incubation at 30 ± 2 °C for 24 h, the different stages of zone of inhibition were determined. Solvent blank was used as negative control, and antibiotic ampicillin was used as a positive control. The above-mentioned bacteria were grown individually in nutrient broth to check the growth pattern in presence/absence of pure Co-doped ZnO and Mg-doped ZnO NPs. All bacteria strains growth pattern in the presence of Co-doped ZnO are shown in Fig. 6.2a–d, and bacterial growth patterns in the presence of Mg-doped ZnO are presented in Fig. 6.3a–d. In Fig. 6.2, we have observed growth pattern of *E. coli* in the absence and presence of pure ZnO and Co-doped ZnO NPs. In the absence of ZnO NPs, the optical density was recorded maximum, which indicates thrive growth of the strain in nutrient broth medium, while in the presence of ZnO and Co-doped ZnO NPs, it decreased with increasing concentration of Co in ZnO in nutrient broth medium, and similar result has been observed with strains *P. aeroginosa*, *S. aureus*, and *B. subtilis* in this study. It is clear from Fig. 6.3 that the growth pattern of *E. coli* is highly affected by the presence of ZnO and Mg-doped ZnO NPs. Similarly, in the absence of ZnO NPs, the optical density was recorded maximum, which indicates thrive growth of the strain in nutrient broth medium, while in the presence of ZnO and Mg-doped ZnO NPs, it decreases with increasing concentration of Mg in ZnO in nutrient broth medium. Similar result has been observed with bacterial strains *P. aeroginosa*, *S. aureus*, and *B. subtilis*.

Our results (Figs. 6.2 and 6.3) show that the enhancement of Co and Mg concentrations in ZnO NPs proportionally increases the bactericidal activity because particle size was found to decrease from 27.1 to 21.3 nm with the increase in Co

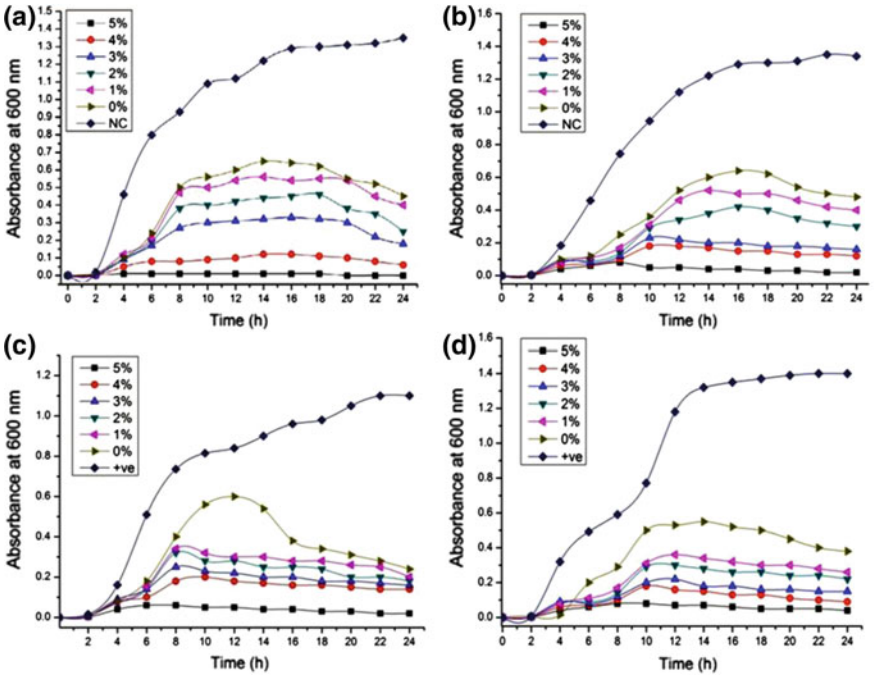

Fig. 6.2 Growth pattern of bacteria in the presence of 100 µg/ml of different percentages of Co-doped ZnO NPs and pure ZnO amended in nutrient broth medium, here **a** *E. coli* **b** *P. aeroginosa* **c** *B. subtilis* **d** S. *aureus*

concentration from 0 to 5%. Similarly, when Mg concentration increased from 0 to 12% in the form of doping in ZnO, the particle size was found to decrease from 36 to 13 nm. It is believed that the antibacterial activity of the material increased because the surface to volume ratio increased with the decrease in the particle size which leads to enhanced binding forces and generation of free radicals in bacterial cell or the reactive oxygen species.

6.5.1 Effect of Doping on Minimum Inhibitory Concentration (MIC)

Sterile Erlenmeyer flasks (250 ml), each containing 100-ml nutrient broth, were sonicated for 10 min after adding the NPs to prevent aggregation of the NPs. On the basis of results obtained, we have observed that some significant changes are found in the bactericidal properties of the NPs of pure and Co-doped ZnO for different concentrations of doping. Minimum inhibitory concentration was determined by

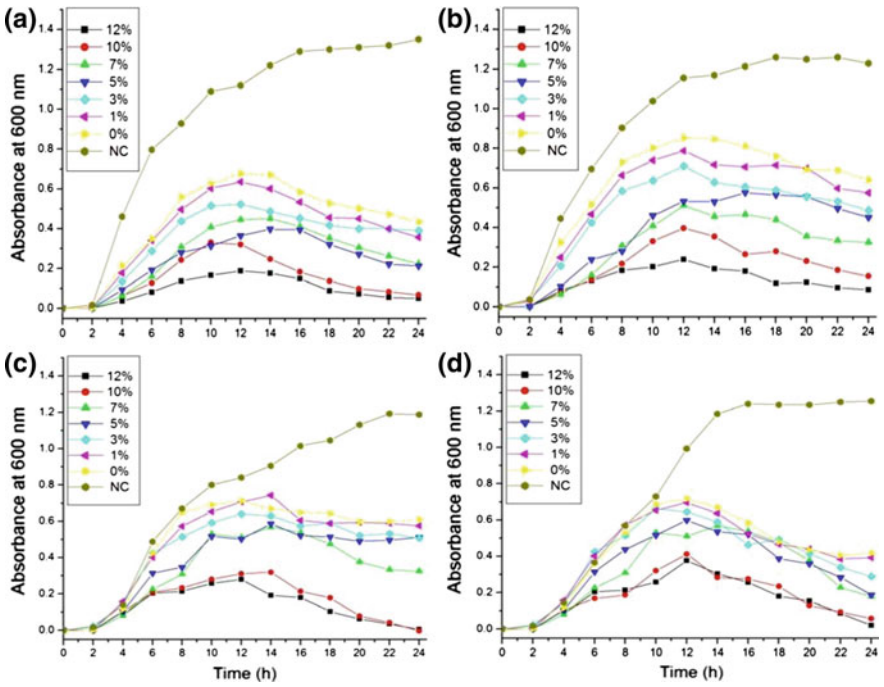

Fig. 6.3 Growth pattern of bacteria in the presence of 100 μg/ml of different percentages of Mg-doped ZnO NPs and pure ZnO amended in nutrient broth medium, here **a** *E. coli* **b** *P. aeroginosa* **c** *B. subtilis* **d** S. *aureus*

Table 6.1 MIC of ZnO NPs doping with increasing concentration of Co against gram-positive and gram-negative bacterial strains

Culture	MIC (μg/ml) of Zn particles doping with Co in %					
	0% Co	1% Co	2% Co	3% Co	4% Co	5% Co
E. coli	130	110	100	88	75	70
P. aeroginosa	125	115	105	100	85	80
B. subtilis	120	100	95	90	80	75
S. aureus	125	120	112	105	95	70

standard broth dilution method at NPs concentrations between 50 and 130 μg/ml of Co-doped and Co-undoped ZnO. MIC for pure ZnO NPs (27 nm) was estimated to be 120–130 μg/ml, while for 1–5% Co-doped ZnO (21 nm), the MIC was found to be between 70 and 120 μg/ml as shown in Table 6.1. In the case of Mg-doped ZnO NPs, minimum inhibitory concentration was determined at different nanoparticle concentrations ranging between 75 and 150 μg/ml. MIC for pure ZnO NPs (36.1 nm) was estimated to be 120–150 μg/ml, while for 1–12% Mg-doped ZnO (13.5 nm), the MIC lies between 75 and 150 μg/ml as shown in Table 6.2.

Table 6.2 MIC of ZnO NPs doping with increasing concentration of Mg against gram-positive and gram-negative bacterial strains

Culture	MIC (μg/ml) of Zn particles doping with Mg in %						
	0% Mg	1% Mg	3% Mg	5% Mg	7% Mg	10% Mg	12% Mg
E. coli	150	130	120	110	100	90	90
P. aeroginosa	140	125	110	100	90	80	80
B. subtilis	120	110	100	90	90	85	80
S. aureus	150	130	120	100	80	80	70

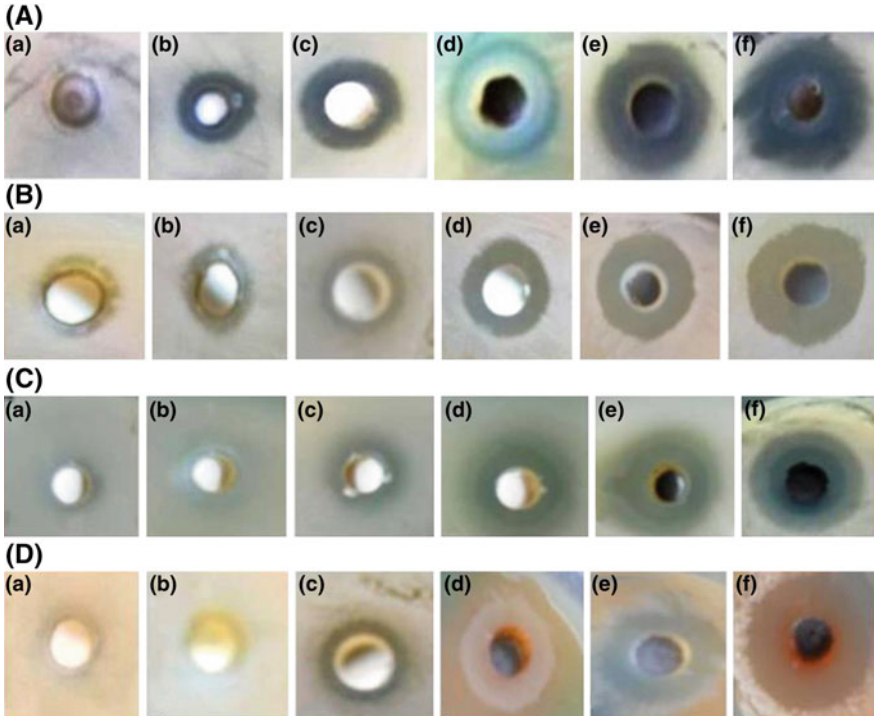

Fig. 6.4 Zone of inhibition pattern of pure and Co-doped ZnO NPs. Pure ZnO (*a*), 1% Co-doped ZnO (*b*), 2% Co-doped ZnO (*c*), 3% Co-doped ZnO (*d*), 4% Co-doped ZnO (*e*), 5% Co-doped ZnO (*f*) zone of inhibition growth of bacterial strain **A** *E.coli* **B** *P. aeroginosa* **C** *B. Subtilis* **D** *S. aureus*

6.5.2 *Effect of Doping on Zone of Inhibition (ZOI)*

Figures 6.4 and 6.5 show the well diffusion and paper disk diffusion methods that were performed on solid nutrient agar plates. The bacteria growth clearly has retarded in the form of zone of inhibition as shown in Fig. 6.4. *E. coli* growth pattern in the presence of ZnO NPs loaded in well has shown minimum growth at

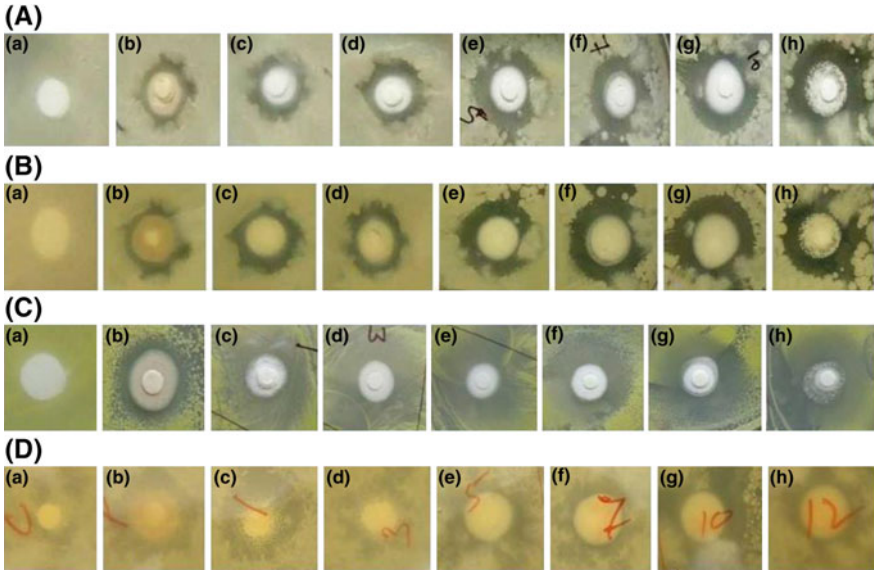

Fig. 6.5 Zone of inhibition pattern of pure and Mg-doped ZnO NPs. Control (*a*), pure ZnO (*b*), 1% Mg-doped ZnO (*c*), 3% Mg-doped ZnO (*d*), 5% Mg-doped ZnO (*e*), 7% Mg-doped ZnO (*f*), 10% Mg-doped ZnO (*g*), and 12% Mg-doped ZnO (*h*) zone of inhibition growth of bacterial strain **A** *E. coli* **B** *P. aeroginosa* **C** *S. aureus* **D** *B. subtilis*

1% Co-doped ZnO (Fig. 6.4A(b) and maximum growth at 5% Co-doped ZnO (Fig. 6.4A(f). Similar results are observed with *P. aeroginosa*, *S. aureus*, and *B. Subtilis* bacterial stains. It was observed that when Co concentration was increased in ZnO NPs, size of the particles was found to decrease and the killing efficacy in bacterial strains was found to increase. This is because of the increase in the chemical binding force and activation of reactive oxygen species. Clear zones of inhibition are scrutinized around the NPs loaded well with distinct variations in the susceptibility of bacteria toward pure ZnO and Co-doped ZnO. Increase of Co doping enhances antibacterial activity against both gram-positive (*B. Subtilis*, *S. aureus*) and gram-negative (*E. coli*, *P. aeroginosa*) bacterial strains. Here, maximum zone of inhibition of 5% Co-doped ZnO is found to be 23 ± 1.5 mm against *S. aureus* and lowest is 20 ± 2.0 against *P. aeroginosa* as shown in Table 6.3.

The bacterial growth clearly has retarded in the form of zone of inhibition as shown in Fig. 6.5. *E. coli* growth pattern in the presence of ZnO NPs loaded disk placed on nutrient agar petri plates has shown least inhibition zone in Fig. 6.5A(b) when 1% Mg-doped ZnO was used as an antimicrobial agent (Fig. 6.5A(c)) and maximum growth at 10% Mg-doped ZnO. Similar pattern occurs at 12% Mg-doped ZnO as shown in Table 6.4 and Fig. 6.5A(g, h).

Similar results of Mg-doped ZnO NPs were observed with *P. aeroginosa*, *S. aureus*, and *B. subtilis* bacterial stains. Increase of Mg doping enhances

Table 6.3 Zone of inhibition of bacterial growth in the presence of increasing percentage of Co-doped ZnO

Treatment	Diameter of zone of inhibition (mm)			
	E. coli	*P. aeroginosa*	*B. subtilis*	*S. aureus*
Pure ZnO	8 ± 0.5	10 ± 0.5	10 ± 0.5	09 ± 0.5
1% Co-doped ZnO	13 ± 1.0	12 ± 0.5	12 ± 1.0	10 ± 0.5
2% Co-doped ZnO	15 ± 1.0	14 ± 0.6	15 ± 0.5	13 ± 0.5
3% Co-doped ZnO	17 ± 0.8	16 ± 1.0	18 ± 1.0	20 ± 1.0
4% Co-doped ZnO	18 ± 1.0	19 ± 1.0	21 ± 1.0	22 ± 1.0
5% Co-doped ZnO	22 ± 1.0	20 ± 2.0	22 ± 1.0	23 ± 1.5

Table 6.4 Zone of inhibition of bacterial growth in the presence of increasing percentage of Mg-doped ZnO

Treatment	Diameter of zone of inhibition (mm)			
	E. coli	*P. aeroginosa*	*B. subtilis*	*S. aureus*
Pure ZnO	07 ± 0.5	09 ± 0.4	10 ± 0.6	08 ± 0.5
1% Mg-doped ZnO	08 ± 0.5	10 ± 0.6	12 ± .0.5	11 ± 0.4
3% Mg-doped ZnO	10 ± 0.6	10 ± 0.5	12 ± 0.5	14 ± 0.5
5% Mg-doped ZnO	15 ± 0.5	14 ± 0.7	14 ± 1.0	18 ± 1.2
7% Mg-doped ZnO	15 ± 1.0	16 ± 1.3	18 ± 0.8	20 ± 0.6
10% Mg-doped ZnO	17 ± 1.0	18 ± 1.0	20 ± 1.0	21 ± 1.0
12% Mg-doped ZnO	17 ± 0.8	18 ± 1.5	20 ± 1.2	21 ± 1.5

antibacterial activity against both gram-positive (*B. Subtilis*, *S. aureus*) and gram-negative (*E. coli*, *P. aeroginosa*) bacterial strains. Here, maximum zone of inhibition of 10% Mg-doped ZnO is found to be 21 ± 1.5 mm against *S. aureus* and lowest is 17 ± 1.0 against *E. coli* is shown in Table 6.4.

6.5.3 *Growth of Bacterial Cells in Presence of Co-doped ZnO*

Bacterial cultures of *B. subtilis* were grown in Co-doped ZnO nanomaterial treated and untreated medium in 250-ml flask on orbital shaker at 30 ± 2 °C overnight. Overnight grown culture was divided into two parts: one to check the growth of bacteria on sterile nutrient agar plate and other part of overnight growth culture of bacillus strain was centrifuged at 10,000 rpm at 4 °C for 10 min. The cells were washed three times with PBS and fixed overnight in 2% glutaraldehyde for the examination by scanning electron microscopy. This study confirmed that the effect of nanomaterial on the growth of bacterial cells at initial (0 min) time intervals has no effect on bacterial shape as shown in Fig. 6.6, while after 4-h incubation of

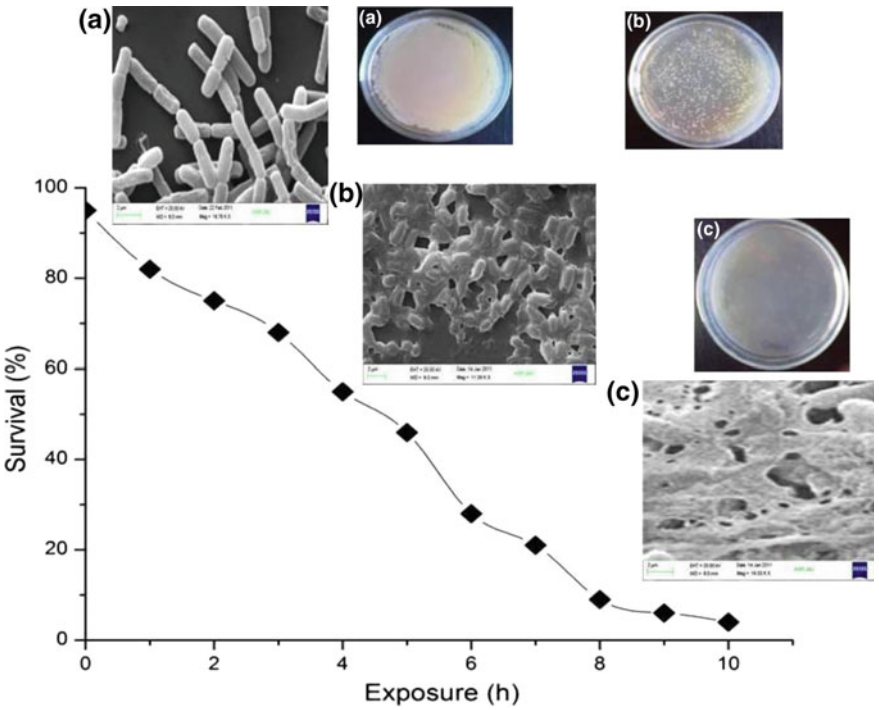

Fig. 6.6 Survival assay in the presence of ZnO NPs (100 μg/ml) in medium, SEM image, and growth on nutrient agar plate after different time intervals 2 h (**a**), after 6 h (**b**), and after 10 h (**c**)

bacterial culture with 100 μg/ml, the bacterial cells have partially distorted (Fig. 6.6), and after 10-h incubation of bacterial culture with 100 μg/ml, the bacterial cell was totally distorted which was confirmed by SEM analysis, and further bacterial growth check on sterile nutrient agar plate by spread plate method confirmed the efficacy of the pure and doped ZnO as antimicrobial agents.

6.6 Bacterial Biofilm

Biofilm is a complex microbial assembly irreversibly connected with different surface materials [52]. Biofilm is composed of extracellular polymeric substances (EPS), carbohydrate-binding proteins, and extracellular DNA (eDNA) [53]. The matrix is robust with high tensile strength and is responsible for keeping bacteria in close proximity and hydrated for interactions and exchange of DNA [54]. Biofilms form on food contact surfaces under appropriate environmental conditions. Biofilms are established by ubiquitous kind of microbial growth in nature. And they are essential for the growth of bacterial infections.

The mechanisms of biofilm resistance toward conventional drug include upregulated efflux pumps, mutations in drug target sites, β lactamase production, and adsorption of antibiotics onto the biofilm matrix which accounts for its slow penetration. The positively charged aminoglycoside antibiotics in the biofilm matrix are bind to the negatively charged polymers [55]. Several phenomena such as hypermutation of bacteria, transmission of drug resistance genes, and tolerance for antibiotics are caused by oxidative stress in biofilms [56]. Quorum sensing within the biofilms is also responsible for resistance to antimicrobials. *P. aeruginosa* is also reported the quorum-sensing-dependent tolerance toward different antimicrobial agents [57]. Quorum-sensing inhibitors such as furanone C-30 and C-56 on biofilm enhance the sensitiveness against tobramycin treatment [58].

6.6.1 Inhibition of Microbial Biofilm Using Nanoantibiotic

A variety of antimicrobial strategies are used to control the formation of bacteria biofilm. Studying the mechanism of bacterial cell–cell connection can offer a refreshing access to avoid biofilm growth. Applications of quorum-sensing inhibitors (QSIs) utilizing nanoparticles are most emerging methods for preventing quorum sensing and biofilm development. NPs are used as efficient bactericidal activities and antimicrobial activities of oxide of nanoparticles against pathogenic bacterial strains. These activities have already been reported by Ravikumar et al. [59–61]. Moreover, effects of ZnO on dental caries causing bacteria (*S. mutans*) have been broadly studied [62–64]. The nanoparticles with antimicrobial properties also exhibit antibiofouling activity. Biofilm growth can be forbidden by surface modification to restrict bacterial colonization [65]. The antimicrobial potential of silver nanoparticles (AgNPs) has the ability to preclude the biofilm development of multidrug resistance *E. coli* and *S. aureus* [66]. Decay of the bacterial cell membrane in biofilm has also been observed on the addition of AgNPs to *P. aeruginosa*. Zinc oxide nanoparticles are also able to produce reactive oxygen species (ROS) that interfere with *E. coli* and *S. aureus* biofilm formation [6, 68, 69]. Superparamagnetic iron oxide NPs (SPIONs) show highest antibacterial activity against biofilms using external magnetic fields [70]. The effects of ZnO nanoparticles, a potent quorum and virulence quencher for the *P. aeruginosa* strain, were tested against clinical isolates from cystic fibrosis patients. The nanomaterial inhibits the growth pattern of the number of microorganism and obstructs the formation of biofilms which make them a prospective candidate for fighting against the clinical infections.

6.7 Summary

Modifications in ZnO can be utilized to enhance the activity, making it appropriate for several biomedical-based applications. Doping of ZnO and coupling agents provide a number of applications for various health-related purposes. Further investigations referring to their activities on eukaryotic cells have to be performed before their technological applications in biomedical field. However, nanoparticles of Co- and Mg-doped ZnO could be suggested as an effective and potent antibacterial activity against the growth of both gram-positive and gram-negative bacteria. A treatment with Co-doped ZnO NPs results in bacterial cell growth inhibition, and its antibacterial action is excellent in both types of bacteria. ZnO NPs also exhibited significant inhibitory activity on bacteria and biofilm formation. The application of Co- and Mg-doped ZnO NP can be recommended as a protective agent against bacterial pathogens in therapy against infectious diseases. The future will probably witness important novel developments in applied nanoresearch regarding antimicrobial agents and composite systems by Co- and Mg-doped ZnO NP in efficient combinations with drugs.

References

1. M. Meyer, O. Kuusi, Nanotechnology: generalizations in an interdisciplinary field of science and technology. Int. J. Philos. Chem. **10**, 153–168 (2002)
2. F.J. Hernández-Sierra, F. Ruiz, D.C.C. Pena et al., The antimicrobial sensitivity of *Streptococcus mutans* to nanoparticles of silver, zinc oxide, and gold. Nanomed. Nanotech. Biol. Med. **4**, 237–240 (2008)
3. M. Oves, M.S. Khan, A. Zaidi et al., Antibacterial and cytotoxic efficacy of extracellular silver nanoparticles biofabricated from chromium reducing novel OS4 strain of *Stenotrophomonas maltophilia*. PLoS ONE **8**(3), e59140 (2013)
4. J. Sawai, Quantitative evaluation of antibacterial activities of metallic oxide powders (ZnO, MgO and CaO) by conductimetric assay. J. Microbiol. Methods **54**, 177–182 (2003)
5. A. Azam, A.S. Ahmed, M. Oves, Antimicrobial activity of metal oxide nanoparticles against gram-positive and gram-negative bacteria: a comparative study. Int. J. Nanomed. 6003–6009 (2012)
6. J. Musarrat, S. Dwivedi, B.R. Singh, A.A. Al-Khedhairy, A. Azam, A. Naqvi, Production of antimicrobial silver nanoparticles in water extracts of the fungus *Amylomyces rouxii* strain KSU-09. Biores. Technol. **101**(22), 8772–8776 (2010)
7. A. Vascashta, D. DimovaMalinovska, Nanostructured and nanoscale devices, sensors and detectors. Sci. Technol. Adv. Mater. **6**, 312 (2005)
8. R. Langer, Drug delivery. Drugs on target. Science **293**, 58–59 (2001)
9. K.H. Roy, Q. Mao, S.K. Huang et al., Oral gene delivery with chitosan–DNA nanoparticles generates immunologic protection in a murine model of peanut allergy. Nat. Med. **5**, 387 (1999)
10. E. Sachlors, D. Gotora, J.T. Czernuszka, Collagen scaffolds reinforced with biomimetic composite nano-sized carbonate-substituted hydroxyapatite crystals and shaped by rapid prototyping to contain internal microchannels. Tissue Eng. **12**, 2479 (2006)
11. Z.P. Xu, Q.H. Zeng, G.Q. Lu et al., Nanoscience and computational chemistry: research progress. Chem. Eng. Sci. **61**, 1027 (2006)

12. O.C. Farokhzad, J. Cheng, B.A. Teply, I. Sherifi, S. Jon, P.W. Kantoff, J.P. Richie, R. Langer, Targeted nanoparticle-aptamer bioconjugates for cancer chemotherapy in vivo. Natl. Acad. Sci. USA **103**, 6315 (2006)
13. P.K. Stoimenov, R.L. Klinger, G.L. Marchin et al., Synthesis of AgNPs by *Bacillus cereus* bacteria and their antimicrobial potential. Langmuir **18**, 6679 (2002)
14. I. Sondi, B. Salopek-Sondi, Silver nanoparticles as antimicrobial agent: a case study on *E. coli* as a model for gram-negative bacteria. J. Coll. Interface Sci **275**, 177 (2004)
15. A. Panacek, K. vitek, R.M. Prucek et.al., Silver colloid nanoparticles: synthesis, characterization, and their antibacterial activity. J. Phys. Chem B **110**, 16248 (2006)
16. A.H. Pfund, The light sensitiveness of copper oxide. Phys. Rev. **3**, 289 (1916)
17. A.E. Rakhshni, Preparation, characteristics and photovoltaic properties of cuprous oxide—a review. Solid State Electron. **29**(1), 7–17 (1986)
18. Y.W. Chun, T.J. Webster, The role of nanomedicine in growing tissues. Ann. Biomed. Eng. **37**(10), 2034–2047 (2009)
19. E. Weir, A. Lawlor, A. Whelan et al., The use of nanoparticles in anti-microbial materials and their characterization. E. Analyst. **133**(7), 835–845 (2008)
20. S. Pedroso, I.A. Guillen, Microarray and nanotechnology applications of functional nanoparticles Comb. Chem. High Throughput Screen. **9**(5), 389–397 (2006)
21. J.R. Kanwar, G. Mahidhara, R.K. Kanwar, Recent advances in nanoneurology for drug delivery to the brain. Curr. Nanosci. **5**(4), 441–448 (2009)
22. B. Sara, R.K. Kanwar, K. Khoshmanesh, Promises of nanotechnology for drug delivery to brain in neurodegenerative diseases. Curr. Nanosci. **5**(1), 26–32 (2009)
23. I. Yacoby, I. Benhar, Antibacterial nanomedicine. Nanomed **3**(3), 329–341 (2008)
24. G. Fu, P.S. Vary, C.T. Lin, Anatase TiO_2 nanocomposites for antimicrobial coatings. J. Phys. Chem. B **109**, 8889–8898 (2005)
25. M. Nirmala, A. Anukaliani, Synthesis and characterization of undoped and TM (Co, Mn) doped ZnO nanoparticles. Phys. B: Phys. Mat **406**, 911–915 (2011)
26. N. Vigneshwaran, S. Kumar, A.A. Kathe et al., Functional finishing of cotton fabrics using zinc oxide–soluble starch nanocomposites. Nanotechnology **17**, 5087–5095 (2006)
27. A. Becheri, M. Durr, P.L. Nostro et al., Synthesis and characterization of zinc oxide nanoparticles: application to textiles as UV-absorbers. J. Nanopart. Res. **10**, 679–689 (2007)
28. T. Xu, C.S. Xie, Tetrapod-Like nano-particle ZnO/Acrylic resin composite and its multi-function property. Prog. Org. Coat. **46**, 297–301 (2003)
29. Q. Li, S.L. Chen, W.C. Jiang, Durability of nano ZnO antibacterial cotton fabric to sweat. J. Appl. Polym. Sci. **103**, 412–416 (2007)
30. E. Richards, Antibacterial wallpaper. Chem. Tech. **11** (2006)
31. S. Nair, A. Sasidharan, V.V.D. Rani et al., Role of size scale of ZnO nanoparticles and microparticles on toxicity toward bacteria and osteoblast cancer cells. J. Mat. Sci. **20**, 235–241 (2009)
32. J. Sawai, H. Igarashi, A. Hashimoto et al., Evaluation of growth inhibitory effect of ceramics powder slurry on bacteria by conductance method. Chem. Eng. Jpn. **29**, 251–256 (1996)
33. W. Jiang, H. Mashayeikhi, B. Xing, Bacterial toxicity comparison between nano- and micro-scaled oxide particles. Environ. Pollut. **157**, 1619–1625 (2009)
34. Y. Liu, L. He, A. Mustapha, H. Li, Z.Q. Hu, Antibacterial activities of zinc oxide nanoparticles against *Escherichia coli* O157:H7. J. App. Microbiol. **107**, 1193–1201 (2009)
35. H. Lopez-Sandoval, M. Londono-Lemos, R. Garza-Velasco et al., Synthesis, structure and biological activities of cobalt(II) and zinc(II) coordination compounds with 2-benzimidazole derivatives. J. Inorg. Biochem. **102**, 1267–1276 (2008)
36. L. Saghatforoush, F. Chalabian, A. Aminkhani et al., Synthesis, spectroscopic characterization and antibacterial activity of new cobalt(II) complexes of unsymmetrical tetradentate (OSN2) schiff base ligands. Eur. J. Med. Chem. **44**, 4490–4495 (2009)
37. Rodrıguez-Arguelles MC, Cao R, A.M. Garcıa-Deibe et al., Antibacterial and antifungal activity of metal(II) complexes of acylhydrazones of 3-isatin and 3-(N-methyl) isatin. Polyhedron **28**, 2187–2195 (2009)

38. J. Sawai, E. Kawada, F. Kanou et al., Detection of active oxygen generated from ceramic powders having antibacterial activity. J. Chem. Eng. Jpn. **29**, 627–633 (1996)
39. J. Sawai, H. Kojima, H. Igarashi et al., *Escherichia coli* damage by ceramic powder slurries. J. Chem. Eng. Jpn. **30**, 1034–1039 (1997)
40. J. Sawai, S. Shoji, H. Igarashi et al., Hydrogen peroxide as an antibacterial factor in zinc oxide powder slurry. J. Bioeng. **86**, 521–522 (1998)
41. B.G. Applerot, A. Lipovsk, R. Dror, N. Perkas, Y. Nitzan, R. Lubart, A. Gedanken, Enhanced antibacterial activity of nanocrystalline ZnO due to increased ROS-mediated cell injury. Adv. Funct. Mater. **19**, 842 (2009)
42. O. Yamamoto, M. Komatsu, J. Sawai, et.al., Effect of lattice constant of zinc oxide on antibacterial characteristics. Mater. Sci. Mater. Med. **15**, 847 (2004)
43. R. Dastjerdi, M. Montazer, A review on the application of inorganic nano-structured materials in the modification of textiles: focus on anti-microbial properties. Coll. Surf. B: Biointerface **79**, 5–8 (2010)
44. I. Djerdj, J. Zvonko, A. Denis, N. Markus, Co-doped ZnO nanoparticles: minireview. Nanoscale **2**, 1096–1104 (2010)
45. H.K. Park, D.K. Kim, C.H. Kim, Effect of solvent on titania particle formation and morphology in thermal hydrolysis of $TiCl_4$. J. Am. Ceram. Soc. **80**, 743–749 (1997)
46. S.I. Hirano, Hydrothermal processing of ceramics. J. Am. Ceram. Soc. **66**, 1342–1344 (1987)
47. D. Vorkapic, T. Matsoukas, Effect of temperature and alcohols in the preparation of titania nanoparticles from alkoxides. J. Am. Ceram. Soc. **81**, 2815–2820 (1998)
48. C.G. Granqvist, R.A. Buhrman, Log-normal size distributions of ultrafine metal particles. J. App. Phys. **47**, 2200–2219 (1976)
49. T.T. Kodas, Generation of complex metal oxides by aerosol processes: superconducting ceramic particles and films. Adv. Mater. **6**, 180–192 (1989)
50. G.D. Ulrich, J.W. Riehl, Aggregation and growth of submicron oxide particles in flames. J. Coll. Interface Sci **87**, 257–265 (1982)
51. G. Skanadan, Y.J. Chen, N. Glumac, B.H. Kear, Synthesis of oxide nanoparticles in low pressure flames. Nanostruct. Mater. **11**, 149–158 (1999)
52. K. Pearson, K.E. Kartan, Biofilm development in bacteria. Adv. Appl. Microb. **57**, 79–111 (2005)
53. M. Kostakioti, M. Hadjifrangiskou, S.J. Hultgren, Bacterial biofilms: development, dispersal and therapeutic strategies in the dawn of the postantibiotic era. Cold Spring Harb. Perspect. Med. **3**, a010306 (2013)
54. H.C. Flemming, J. Wingender, The biofilm matrix. Nat. Rev. Microbiol. **8**, 623–633 (2010)
55. W.W. Nichols, S.M. Dorrington, M.P.E. Slack, H.L. Walmsley, Inhibition of tobramycin diffusion by binding to alginate. Antimicrob. Agents Chemother. **32**, 518–523 (1988)
56. N. Hoiby, T. Bjarnsholt, M. Givskov, S. Molin, O. Ciofu, Antibiotic resistance of bacterial biofilms. Int. J. Antimicrob. Agents **35**, 322–332 (2010)
57. T. Bjarnsholt, P.O. Jensen, M. Burmolle, M. Hentzer, J.A.J. Haagensen, H.P. Hougen, *Pseudomonas aeruginosa* tolerance to tobramycin, hydrogen peroxide and polymorphonuclear leukocytes is quorum-sensing dependent. Microbiology **151**, 373–383 (2005)
58. M. Hentzer, H. Wu, J.B. Andersen, Attenuation of *Pseudomonas aeruginosa* virulence by quorum sensing inhibitors. EMBO J. **22**, 3803–3815 (2003)
59. M. Fresta, G. Puglisi, G. Giammona, G. Cavallaro, N. Micali et al., Pefloxacine mesilate and ofloxacin loaded polyethylcyanoacrylate nanoparticles: characterization of the colloidal drug carrier formulation. J. Pharm. Sci. **84**, 895–902 (1995)
60. T. Hamouda, M. Hayes, Z. Cao, R. Tonda, K. Johnson et al., A novel surfactant nanoemulsion with broad-spectrum sporicidal activity against *Bacillus* species. J. Infect. Dis. **180**, 1939–1949 (1990)
61. S. Ravikumar, R. Gokulakrishnan, P. Boomi, In vitro antibacterial activity of the metal oxide nanoparticles against urinary tract infectious bacterial pathogens. Asian Pac. J. Trop. Dis. **2**, 85–89 (2012)

62. M. Eshad, J. Lellouche, S. Matalon, A. Gedanken, E. Banin, Sonochemical coating of ZnO and CuO nanoparticles inhibit *Streptococcus mutans* biofilm formation on teeth model. Langmuir **28**, 12288–12295 (2012)
63. R. Hernandez-Delgadillo, D. Velasco-Arias, D. Diaz, K. Arevalo-Niño, M. Garza-Enriquez et al., Zero valent bismuth nanoparticles inhibit *Streptococcus mutans* growth and formation of biofilm. Int. J. Nanomed. **7**, 2109–2113 (2012)
64. J.F. Hernández-Sierra, F. Ruiz, D.C. Pena, F. Martínez-Gutiérrez, A.E. Martínez et al., The antimicrobial sensitivity of *Streptococcus mutans* to nanoparticles of silver, zinc oxide, and gold. Nanomed **3**, 237–240 (2008)
65. J. Lellouche, A. Friedman, A. Gedanken, E. Banin, Antibacterial and antibiofilm properties of yttrium fluoride nanoparticles. Int. J Nanomed. **7**, 5611–5624 (2012)
66. K. Ali, S. Dwivedi, A. Azam, Q. Saquib, M.S. Al-Said, A.A. Alkhedhairy, J. Musarrat, Aloe vera extract functionalized zinc oxide nanoparticles as nanoantibiotics against multi-drug resistant clinical bacterial isolates. J. Coll. Interface Sci. **472**, 145–156 (2016)
67. K. Ali, B. Ahmed, S. Dwivedi, Q. Saquib, A.A. Al-Khedhairy, J. Musarrat, Microwave accelerated green synthesis of stable silver nanoparticles with *Eucalyptus globulus* leaf extract and their antibacterial and antibiofilm activity on clinical isolates. PLoS ONE **10**(7), e0131178 (2015)
68. S. Dwivedi, R. Wahab, F. Khan, Y.K. Mishra, J. Musarrat, A.A. Al-Khedhairy, Reactive oxygen species mediated bacterial biofilm inhibition via zinc oxide nanoparticles and their statistical determination. PLoS ONE **9**(11), e111289 (2014)
69. M.J. Hajipour, K.M. Fromm, A.A. Ashkarran, D.J. Aberasturi, I.R. Larramendi, T. Rojo, V. Serpooshan, Parak Wj, M. Mahmoudi, Antibacterial properties of nanoparticles. Trends Biotechnol. **30**, 499–511 (2012)
70. H. Park, H.-J. Park, J.A. Kim, S.H. Lee, Jh Kim, J. Yoon, T.H. Park, Inactivation of *Pseudomonas aeruginosa* PA01 biofilms by hyperthermia using super paramagnetic nanoparticles. J. Microbiol. Methods **84**, 41–45 (2011)

Chapter 7
Facile Synthesis of Large Surface Area Graphene and Its Applications

Mahe Talat, Prashant Tripathi and Onkar Nath Srivastava

7.1 Introduction

Carbon is an amazingly versatile element. Based on the atoms arrangement, it can create hard diamonds or soft graphite. One such creation of carbon is graphene obtained from graphite, which scientists have been considering for the better part of a hundred years, though not always by that name. Graphene could be groundbreaking for a wide variety of fields. It is a predetermined conclusion that graphene will revolutionize the world—the only question is whether it will do so directly, or indirectly. Earlier it was difficult to assume a stable 2D material until 2002, University of Manchester researcher Andre Geim became fascinated in graphene and challenged his PhD student to peel as few as 10–100 layers of graphene from a piece of graphite. His scholar succeeded in obtaining up to 1000 layers but could not achieve the desired number of layers. Geim tried a different approach of peeling using scotch tape and eventually, they were able to isolate graphene or more precisely a single layer of carbon atoms. Geim and his colleague Kostya Novoselov published their findings in "Science" in October 2004, further they received the Nobel Prize in physics in 2010 for their work.

In fact manufacturing it to market, affecting the world with graphene-based technologies, might undoubtedly be in the cards. But it is also simple to imagine that a range of specific, graphene-like materials tailored to each specific graphene-like application could beat graphene itself. Still, even if all the material achieved is exhilarating a new generation of 2D materials science, it will have been tremendously significant in determining the face of current technology. In simple terms,

M. Talat (✉) · P. Tripathi · O.N. Srivastava
Physics and Bioscience Division, Nanoscience and Nanotechnology Unit,
Banaras Hindu University, Varanasi, India
e-mail: mahetalat04@gmail.com

Z.H. Khan (ed.), *Recent Trends in Nanomaterials*,
Advanced Structured Materials 83, DOI 10.1007/978-981-10-3842-6_7

graphene is a single/thin layer of pure carbon; it is a single, tightly packed layer of carbon atoms that are bonded together in a hexagonal honeycomb lattice. In more specifically, it is an allotrope of carbon in the structure of a plane of sp^2 bonded atoms having a bond length of 0.142 nm. Stacked graphene layers form graphite having interplanar spacing of 0.335 nm. Bearing this in mind, one may be astonished to know that carbon is the second most abundant mass within the human body and the fourth most abundant element in the universe (by mass), after hydrogen, helium, and oxygen. This makes carbon the chemical basis for all existing life on this planet, so therefore graphene could well be an ecologically friendly, sustainable way out for a nearly unlimited number of applications. This also makes graphene as one of the most probable materials in the field of nanoscience and nanotechnology including electronics, EMI shielding, sensing, and biomedical devices as well as energy storage, biotechnological, medical, and many more. High quality as well as quantity of graphene is highly desired to fulfill the criteria of such applications.

The difficulty that prohibited graphene from initially being accessible for developmental research in commercial uses was that the creation of superior quality graphene was exceptionally costly, and complex procedure that involved the use of hazardous chemicals to grow graphene as a single layer by exposing platinum, nickel, or titanium carbide to ethylene or benzene at high temperatures. Graphene is still in an immature phase compared to developed materials like silicon and ITO. In order to make it widely adopted, it is needed that it should be producible in large quantities at a competitive price with that of existing materials.

Generally there are two approaches employed for graphene synthesis. In the first approach, a sheet of graphene is detached or peeled off from the graphite crystal, also known as exfoliation. While another method is depositing or growing graphene layer directly on a substrate surface, this growth can take place by two methods, i.e., either the carbon is already present in the substrate or it has to be added from outside. Based on this broad classification, several methods have been reported and used so far primarily divided into following categories: exfoliation, growth by self assembly using hydrocarbons (glucose, fructose, etc.), chemical vapor deposition, chemical methods, mechanical cleavage, etc.

Some of the methods reported for the growth by self assembly and exfoliation methods of graphene sheet from graphite are discussed below:

1. **Mechanical Cleavage**: The very famous "Scotch Tape Method" falls under the category of this micromechanical cleavage and was first exfoliated mechanically from graphite in 2004 [1]. The interlayer van der Waals force in graphite can be easily broken with interaction energy of $\sim$2 eV/nm, therefore, effortless exfoliation of layer of graphene using an adhesive tape can be done [2]. The multilayer of graphene gets adhered on the tape and after repeated peeling the few-layer graphene is obtained. Lastly, the tape's glue is removed from tape using, e.g., acetone and small flakes of irregular shapes and sizes are obtained ranging from nanometers to several tens of micrometers for single-layer graphene [3]. Main advantages of mechanical exfoliation are that it is safe and simple process. Obtaining few-layer graphene is easy without the use of

chemicals, thus the chances of impurity in the graphene so obtained are less, also does not require tedious sample preparation methods. However, there are certain limitations too, that yield obtained may not meet the requirements, also needs experienced manual labor. Regardless of the fact that tape residue does not seriously affect the quality of the graphene, it does make difficult to locate graphene sheet on the substrate.

2. **Sonication or Dispersion**: Graphene can be exfoliated by dispersing graphite in a liquid medium (organic solvent) in an ultrasonic bath for long hours and if required in some cases, voltage is applied followed by centrifugation [4]. Sonicating graphite at the crossing point (interface) of two immiscible liquids, generally organic solvents and water exfoliate macroscale graphene films. The graphene sheets are adsorbed to the high-energy boundary between the materials and are prevented from agglomeration. The sheets so obtained are up to about 95% transparent and conductive [5]. After the dispersion, the solution has to be centrifuged in order to remove the thicker flakes. The quality of the obtained graphene flakes is superior in accordance with the micromechanical exfoliation. Its size, however, is quite small; also, the controllability is not given. However, restacking is a major issue with this kind of graphene which can be overcome by adding surfactants like sodium dodecyl sulfate (SDS), tetramethylethylenediamine (TMEDA or TEMED), etc., before sonication.
3. **Chemical exfoliation methods**: Apart from mechanical exfoliation, sometimes chemicals are also used for obtaining graphene sheet. Chemical exfoliation methods based on the Hummers' method produce graphene oxide (GO) in bulk scale but need chemical or thermal reduction to partially recover the electronic properties of the graphene. This method has recently gained attention, owing to the advantages of potentially low-cost and solution-processed production [6–18]. However, the graphene produced by this method is severely damaged due to extensive oxidation. Beside this, the consequent reduction of GO sheets is associated with high temperature to reduce the graphitic structure [19–26]. The resistance acquired from the film obtained from reported reduced GO (rGO) was found from 1 k to 70 kΩ/sq (<80% transmittance) [21, 22, 27, 28] or from 31 kΩ/sq to 19 MΩ/sq (at 95% transmittance), [15, 22, 26, 29] which is much high than that of ITO. Some more exfoliation procedures have been attempted to get the highly conducting graphene sheets such as: (1) liquid-phase exfoliation of graphite by extensive sonication [30–34], and (2) intercalation and expansion of graphite with volatile agents [35–39]; but the size of graphene sheets is usually lesser than 1 μm^2. These small sheets were used to prepare transparent conducting (TC) film, and such small sheets exhibit transparency from 83 to 90% and resistance from 8000 to 5000 Ω/sq [30, 32, 35]. The large amounts of inter-sheet junctions and damage produced during exfoliation process are responsible for high resistance of TC films.
4. **Microwave-assisted synthesis**: Recent method introduced for the synthesis of graphene sheets is by combining chemical treatment with microwave radiation using eco-friendly chemicals. Microwave radiation can be used to produce strong expansion of the graphite worm in the thickness direction.

Microwave-based techniques such as solid-state microwave irradiation, and microwave-assisted solvothermal/hydrothermal process can provide effortless and rapid routes to synthesize nanomaterials without high temperature or high pressure. Furthermore, the microwave technique is largely helpful for a large-scale synthesis without difficult preparation conditions [40–43].
The classical preparation of graphene in conventional heating arrangement (furnace or oil bath), the environment-friendly microwave-assisted method has gained attention where the microwave-assisted solvothermal/hydrothermal methods can be adopted to treat GO or graphite [44, 45].

5. **Electrochemical Exfoliation**: The electrochemical exfoliation method is a green, facile, cost-effective, quick, and one-step process to produce high-quality graphene where a power supply, liquid solution (electrolyte), and electrodes are required. The working electrode is usually graphite rod/film/highly orientated pyrolytic graphite, graphite foil and can be used anode or cathode [46–49]. A potential is applied (current) which dissociates the graphite into small thin sheets either via cathodic reduction or anodic oxidation of the graphite source electrode. The electronic states of the graphene can be modifying by adjusting the external power supply. Electrochemical exfoliation and microwave-assisted graphene synthesis and some experimental results obtained by our group will be discussed in the last part of this chapter.
6. **Growth by Self Assembly**:

   (i) **Epitaxial growth**: Epitaxy is defined as a natural or artificial growth of crystals on a crystalline substrate that determines their orientation. It is a deposition of a crystalline overlayer on a crystalline substrate where there is registry between the two. However, in some cases, epitaxial graphene layers are held to surfaces weakly by van der Waal forces. The graphene produced through epitaxial growth methods provides high-quality materials but in limited quantities which drag its applications wherever large amount of graphene is required.

   (ii) **Chemical Vapor Deposition (CVD)**: High quality of graphene can be grown on catalytic metal substrate (Ni or Cu) by CVD method, which shows capability of growing large-area graphene, and can be used in various applications particularly in highly transparent and flexible conducting films [50–53]. Because carbon has extremely little solubility in Cu, thus it is an outstanding substrate for the growth of monolayer graphene sheet. During the process, Cu foil was annealed at high temperature d H_2/CH_4 together in a combination was flushed into the system to begin graphene growth on the Cu foil. Further, the system was cooled at room temperature once a continuous layer of graphene is formed. After the cooling of substrate, the solubility of carbon on the substrate reduces and the carbon precipitates to form single to few-layer graphene sheets. But more research should be done to reduce the production costs, particularly those related with the high-temperature system and costly substrates. Also, multistep transferring process involving the use of poly

(methylmethacrylate) and/or polydimethylsiloxane with toxic chemical process makes the process extensive [15, 16]. The necessity of expensive substrate materials for graphene growth is preventive in its applications for large-scale synthesis. Also difficulty exists in transferring the film to other surface (exfoliation), and achieving the uniform deposition of the carbon is a major issue which needs to be addressed.

7. **Electrochemical method and Microwave-assisted synthesis of graphene sheet**:

Electrochemical method is more advantageous over non-electrochemical solution phase processing methods in the sense that it is of single-step process, simple, and can be performed under ambient conditions. Moreover, this method takes smaller time (minutes to hours) to perform the complete exfoliation than chemical/sonication routes which generally run for several days [54, 55]. The graphene can be produced in milligram to gram by employing this approach [56, 57] with altering quality and purity which depend on the experimental procedures and electrolyte used. The lateral sizes of graphene sheets prepared by this method are very high that helps to reduce the number of inter-sheet junctions which enhances the electrical conductivity of the film thereby reduces the resistance. The sheet resistance of the electrochemically derived graphene was found to be ~0.015–0.21 K Ω/sq at 96% transparency which is far better than chemical exfoliation, liquid-phase exfoliation, etc., as discussed above. Beside this, the defect concentration is very low in contrast to chemical exfoliation and reduction. Hence, from the above discussion, it is obvious that the graphene derived through this route is of high quality, transparent, highly electric conductive, and can be useful in various applications including in areas of electronics, EMI shielding, composite materials, energy storage, sensors, conversion devices, and many more. In this part of the chapter, we have reviewed various work done on electrochemical exfoliation method for graphene preparation.

The essential elements used for electrochemical exfoliation experiment are graphite as working electrode, counter and reference electrode, electrolyte, and power source. Graphene source that is used as working electrode may be a graphite foil, graphite flakes, graphite rods, highly oriented pyrolytic graphite (HOPG), etc. [46–49]. The working electrode can be adhered by conducting carbon tape [47, 58] and silver glue [49, 59, 60]. A Pt wire, mess, plate, and graphite were placed parallel to working electrode as counter electrode. The working and counter electrodes are immersed into electrolyte keeping certain distance between them. A positive or negative potential is impressed to the working electrode based on requirements. Depending on the application of positive or negative potential on the working electrode, the phenomena are known as anodic or cathodic graphite exfoliation, respectively. In anodic exfoliation, a positive potential pulls out electron from the working electrode, namely graphite which leaves a positive charge. This positive charge attracts the negative ions from electrolyte and in the influence of potential these get intercalated between the graphite layers. The intercalating ions enhance the interlayer separation between graphite layers. Thus, decrease the van

der Waals force and help in exfoliation of graphite into thin sheets. The similar phenomenon occurs with cathodic exfoliation where a negative potential applied at working electrode (graphite) draws positively charged ions from the electrolyte. This positively charged ion goes between the interlayer spacing of graphite and causing expansion and exfoliation. Among anodic and cathodic exfoliation, anodic exfoliation is very common as it has higher exfoliation efficiency.

The elctecrochemical exfoliation of graphite anode for the preparation of graphene was first mentioned by Liu et al. [61]. In this experiment, they employed a mixture of ionic liquid (1-octyl-3-methylimidazolium hexafluorophosphate) with water as electrolyte. A 15 V potential was impressed between both graphite rods (electrodes) at room temperature, and after 6 h a black precipitate of graphitic nanosheets was attained at the bottom of the reactor. They have noticed the role of water in exfoliation of graphite. The oxidation of graphite edges by hydroxyl radicals opens the edges of graphite, due to this PF_6^- ions intercalate between the graphitic layers, and at an optimum potential the graphite electrode starts to dissociate into small black sheets which were found to be suspending in the electrolyte. However, the graphene obtained by Liu et al. were still contained with functionalities. After this report, several other approaches have been published [15, 16, 47–59, 61–63] using anodic exfoliation process.

Su et al. demonstrated a feasible electrochemical process to exfoliate graphite into graphene sheets [59]. In this report, they optimized multiple parameters such as electrolyte, pH, and applied voltage. They used various acidic solutions (HBr, HCl, HNO_3, and H_2SO_4) as electrolyte; however, H_2SO_4 was found the most efficient. They examined that low pH of the electrolyte results in huge amount of defects on the graphene due to strong oxidation with electrolyte. They added KOH with H_2SO_4 in order to increase the pH value of the electrolyte which lowers the exfoliation rate. The addition of the KOH results into larger number of bilayer graphene sheets. They also checked the effect of voltage applied on the electrochemical process. They found that if the working bias is less than 10 V, then the process was slow and inefficient while if the voltage applied is greater than 10 V, then the exfoliation rate was so quick that large and thick graphene sheets were generated. In this series, the electrochemical exfoliation was performed with sulfuric acid (H_2SO_4), highly oriented pyrolytic graphite (HOPG) and Pt wire employed as electrolyte, working electrode (anode) and counter electrode (cathode), respectively. Initially, a low bias of +1 V was impressed on the graphite electrode for the time period of 5–10 min which helped to wet the graphite electrode and probably caused intercalation of SO_4^{2-} ions into the grain boundary of the graphite electrode [57], after that the voltage was increased and set at +10 V for time span of 1 min. Before applying high bias, the graphite was a single piece, but on the application of high voltage (+10 V), the graphite electrode was quickly dissociated into thin small sheets and spreads on the surface of the electrolyte. The process was very efficient but the thin sheets synthesized in this experiment were associated with high levels of defects as the H_2SO_4 itself caused oxidation of graphite. To overcome this difficulty, KOH was added to the H_2SO_4 solution which lowers the acidity of the electrolyte. The experiment was optimized as a low bias of +2.5 V was first

impressed for the time period of 1 min which wets the surface of the graphite electrode and causes the gentle intercalation of the anions, after that high alternating voltages of +10 and −10 V were applied (switching +10 V, 2 s; −10 V, 5 s) which dissociates the graphite electrode into thin graphitic sheets. The +10 V was employed to oxidize the graphite sheets which dissociate it into thin sheets along with functional groups attached to it. The switching of negative bias (−10 V) helps to reduce the moieties generated during positive bias. The resulted thin graphitic sheets were found to be comprised of few to 30 μm lateral size with mostly (>60%) bilayered (A–B stacked) character. The level of defects produced in this experiment was lower than that produced by conventional chemical methods. The film prepared by using these thin graphene sheets displayed excellent conductivity and very high transparency. This film can be utilized in the area of flexible electronics. The yield of the graphene obtained with this method was 5–8 wt% which was very low. To enhance the yield of graphene, our group (Prashant et al.) heated the electrolyte at different temperatures and investigated the results. We found that the yield of the graphene synthesized using H_2SO_4-KOH-DW electrolyte enhances 4.5 times at 80 °C in comparison with room temperature [49]. The detailed mechanism will be discussed in the next section. Prashant et al. in another work used pure alkaline electrolyte and examined its effect on the resulted graphene sheets. It was found that the use of alkaline electrolyte resulted into high-quality graphene with almost no disorder [60].

Parvez et al. also demonstrated the electrochemical exfoliation of graphite using H_2SO_4 aqueous electrolyte [58] and investigated the role of concentration of H_2SO_4 on the exfoliation efficiency. They used different concentrations of 0.1, 1, and 5 M H_2SO_4 electrolytes and checked the exfoliation efficiency. A positive potential (+10 V) was applied for the time span of 2 min to dissociate the graphite sheets into thin graphitic sheets. The process was optimized with 0.1 M H_2SO_4 solution. This is most probably because higher concentration of solutions produced larger and thicker graphitic. They have tried lower concentration of H_2SO_4 (0.01 and 0.05 M) also as electrolyte, the electrochemical exfoliation efficiency was reduced and more potential was required. This is most likely due to inefficient quantity of anions present in electrolyte. In the same report, they used pure H_2SO_4 and a 1:1 H_2SO_4/acetic acid mixture as electrolyte but almost no exfoliation was observed. This confirms the role of water in exfoliation of graphite that generates oxygen and hydroxyl radicals that help in intercalation of anions and exfoliation of graphite. High-quality graphene containing large lateral size ($\sim$10 μm), low oxygen content ($\sim$7.5 wt%), and low sheet resistance (4.8 kΩ/sq) for a single EG sheets were observed using 0.1 M H_2SO_4 as electrolyte.

Some works also have been mentioned by other workers, e.g., Liu et al. [48], Rao et al. [62], Parvez et al. [47], Motta and coworkers [63], etc. Liu et al. has used two graphite electrodes as working and counter electrode in aqueous electrolytes (H_2SO_4 or H_3PO_4) and applied alternate +7 and −7 V potentials that produce thick multilayered graphene flakes (thickness $\sim$3–9 nm) with lateral size in the range of 1–5 μm, and the amount of oxidation was comparatively small [48]. Rao et al. used $NaOH/H_2O_2/H_2O$ as electrolyte and checked the electrochemical exfoliation

efficiency. They optimized the exfoliation process by using 3.0 M NaOH and 130 mM H_2O_2 solutions as electrolyte and the working bias potential of +1 V for 10 min followed by +3 V for more 10 min keeping temperature of ~25 °C. High quality of graphene sheets was found consisted with 3–6 layers at a yield of 95% [62]. Parvez et al. [47] have tested in 2014 a series of salts, e.g., $(NH_4)_2SO_4$, Na_2SO_4, K_2SO_4, NH_4Cl, $NaNO_3$, $NaClO_4$, etc., with water as electrolyte and studied their exfoliation outcomes. Sulfate ions were observed to have better exfoliation efficiency as compared to other anions. The better results were found with 0.1 M $(NH_4)_2SO_4$ aqueous solution at a +10 V voltage. They claimed that the use of the optimized electrolyte enables to produce flakes of larger than 5 μm in lateral size with most of the flakes (85%) of 1–3 layers. Motta and coworkers [63] have employed sonication throughout the electrochemical process using 0.15 M Na_2SO_4 and 0.01 M sodium dodecyl sulfate (SDS) as an electrolyte. The electrochemical cell was located in a sonication bath, and a potential difference of 6 V was impressed. It took nearly an hour to consume the graphite entirely. They claimed that most of the flakes are bilayer; however, the process without sonication consisted with mostly four layers of graphene.

Prashant et al. have reported large-scale synthesis of electrochemically exfoliated graphene and investigated the heating effect of the electrolyte on the yield and quality of the graphene [49]. They used different electrolytes (2.0 M H_2SO_4, 0.2 M H_2SO_4, H_2SO_4 + KOH + DW, H_3PO_4 + KOH + DW, $HClO_4$ + NaOH + DW) and performed heating-assisted electrochemical exfoliation experiment with these. An improved result was observed with H_2SO_4 + KOH + DW electrolyte. To notice the effect of temperature, electrolyte solution was heated on a hot plate. When the desired steady temperature was attained, the potential difference was applied between the two electrodes. After application of higher voltages (±10 V), the graphite foil started to exfoliate into the thin small sheets and dispersed into the electrolyte. The resulted sheets were then cleaned over and over with double-distilled water using vacuum filtration technique. After washing, the sheets were put in vacuum oven for drying and then suspended in water using sonication for 20 min. In order to get rid from thick sheets, the suspended sheets were then centrifuged at 4000 rpm for 30 min. The yield of the graphene sheets was estimated by guessing the portions of graphene and graphite sheets present in the solution after centrifugation. This was done by measuring the mass of the floated sheets in supernatant (graphene) and precipitated sheets at bottom (graphite). The enhancement in the yield is given in Table 7.1. It was noticed a significant enhancement in the yield of H_2SO_4 + KOH + DW as electrolyte. They found a 4.5 times increase in the yield of graphene at 80 °C (yield; 77%) in comparison with room temperature (yield; 17%) for H_2SO_4 + KOH + DW as electrolyte. They have discussed a plausible mechanism in details for higher yield which was based on the thermal expansion. Two effects are responsible for enhancement in the yield: (i) Heating of electrolyte resulted in an increase in graphitic interlayer spacing [64]. The expression for the expansion of interlayer spacing is given as $d = 3.3525 + 90.54 \times 10^{-6}\ T + (6.33 \times 10^{-9})\ T^2 = 3.3525 + 90.54 \times 10^{-6}$ TÅ [65]. By using this expression, the interlayer distance between the graphite sheets

Table 7.1 Outcome of graphene yield on heating the electrolyte at various temperatures [49]

	Percentage yield of graphene (wt%) at different temperatures			
Electrolyte	RT (300 K)	40 °C (313 K)	60 °C (333 K)	80 °C (353 K)
2.0 M H_2SO_4	~6	~6.30	~7	~8
0.2 M H_2SO_4	~7	~8	~12	~13
H_2SO_4 + KOH + DW	**~17**	**~28**	**~44**	**~77**
H_3PO_4 + KOH + DW	~12	~13	~19	~35
$HClO_4$ + NaOH + DW	~13	~17	~24	~43

will increase from 3.3525 (~3.35 Å) at room temperature to 3.3595 (~3.36 Å) at 80 °C. However, this increment in the interlayer distance is very small but van der Waals potential varies approx as $1/d^6$. A small increase in the interlayer spacing will result in d^6 times reducing in the van der Waals potential between the two layers. Thus, the sulfate ions will be easier to intercalate between the layers and thereby will lead to efficient exfoliation. (ii) The second effect is due to the thermal vibration of the ions generated by heating the electrolyte [66]. The thermal vibration effective at higher temperature will be isotropic, and the vibration vertical to the basal graphitic planes will create a perpendicular jerk on the consecutive graphitic layers in the influence of the applied electric field. This will eventually help in increasing the exfoliation efficiency of the graphene. They predicted that both effect collectively help in increasing the graphene yield. To confirm the quality of the exfoliated sheets Raman, XPS, FTIR, AFM, SEM, TEM/HRTEM and TGA technique were used. This high-yield graphene can be used in applications like EMI shielding where relatively large quantity of graphene is desired.

Extensive development of the electronic and home appliances, telecommunication devices, many commercial and industrial equipments, etc., are main cause of EMI [66]. These appliances/equipments/devices emit electromagnetic waves which interfere with the normal action of other close by appliances/equipments/devices which affect the performance and lifetime of these sources. These radiations also have bad impact on human health such as symptoms of insomnia; nervousness, and headache [66]. To avoid malfunctioning, health hazards, etc., electronic equipments/appliances must be protected in a way that the incoming and outgoing interference are filtered [66]. To shield from such pollutants and to make safer surroundings, search for some new materials is highly desired which can have better absorption of electromagnetic waves in microwave frequency region. For practical applications lightweight, portable, flexible, corrosion resistant, and cost-effective EMI shielding material are highly desirable which could protect the surroundings from such emissions [49]. In this prospects, graphene is very efficient material due to its high aspect ratio, high electrical and thermal conductivity, light-weight, non-corrodible nature, and processing benefits, but for EMI shielding application graphene is desired in large amount. The large quantity heating-assisted graphene synthesised from electrochemical method is one-step-ahead process for preparation

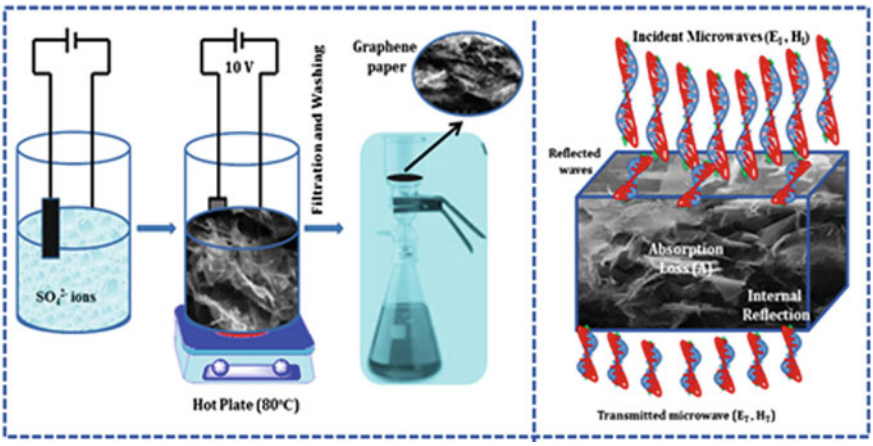

Fig. 7.1 Schematic diagram of the electrochemical exfoliation process for the preparation of graphene and its use in EMI shielding [49]

of graphene which was used for EMI shielding application. The schematic illustration of the experiment performed for graphene synthesis and its use in EMI shielding is shown in Fig. 7.1. Various characterization techniques were employed to investigate the graphene sheets, e.g., Raman, XPS, FTIR, AFM, SEM, TEM/HRTEM, and TGA. Typical SEM and TEM micrographs are given in Fig. 7.2 [49]. TEM and SEM techniques are used to explore the morphology as well as microstructure of the as-prepared graphene sheets as shown in Fig. 7.2 [49]. The thin graphene sheets were found (two to four layers) with interlayer spacing of 0.36 nm which was further stacked and formed graphene block and used for EMI shielding measurements.

The as-synthesized graphene was sonicated in water for 1 h followed by filtration and drying on filter paper at 100 °C. After that, graphene blocks were cut into rectangular shape. These blocks have thickness of 0.25 mm and consisting of stacked graphene sheets. This block was inserted into Cu sample holder and shielding measurement was performed. They have also looked into the thickness effect (0.5, 0.75 and 1 mm) of the graphene blocks on the electromagnetic effectiveness performances. The EMI shielding performances were measured with Agilent E8362B Vector Network Analyzer (12.4–18.0 GHz).

The variation of shielding effectiveness due to absorption (SE_A), reflection (SE_R), and transmission (SE_T) of graphene block at fixed frequency (12.4 GHz) is shown in Fig. 7.3a which revealed that by increasing the thickness of the graphene block, SE_A varies from 9.14 to 37.71 dB, while SE_R was found to be almost constant (7.5 dB). As a result, the total shielding effectiveness (SE_{Tot}) for graphene blocks of different thicknesses 0.25, 0.50, 0.75, and 1 mm was measured as 17.23, 26.23, 32.39, and 46.35 dB, respectively. Figure 7.3b exhibits the SE versus frequency (12.4–18.00 GHz) graph. It is clear from the above discussion that for the stacked sheets the SE mainly deals with the absorption; however, reflection was

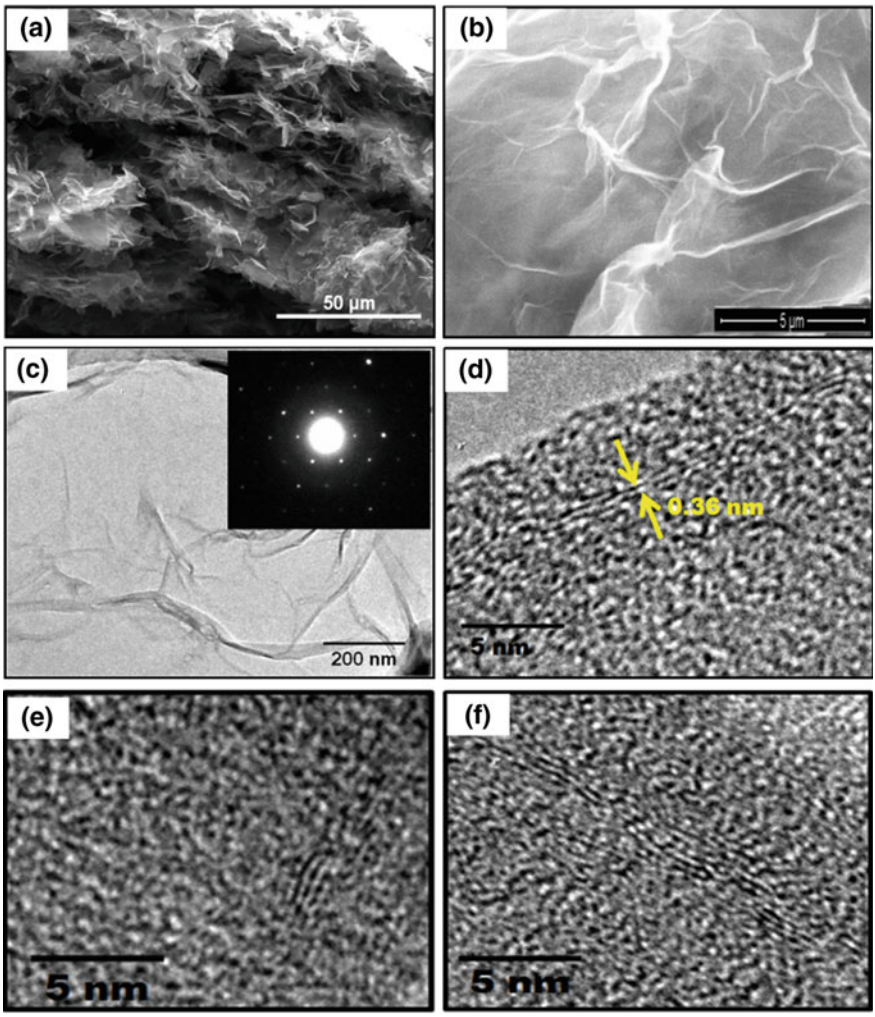

Fig. 7.2 **a** SEM micrograph of the cross section of graphene block. **b** SEM micrograph of graphene sheet. **c** Typical TEM micrograph and corresponding SAD pattern (*inset*) of as-prepared graphene. **d**, **e**, and **f** Demonstrate the HRTEM micrographs of as-prepared thin sheets of graphene [49]

almost constant. In this paper, Prashant et al. discussed the three reasons for SE phenomena to occur. First, the enormously thin and high polar character of the stacked sheets provides more prospects to induce polarization with EM wave that will help in improving the dielectric losses. Second, stacked graphene sheets improve the conductive paths which will help in increasing the shielding by changing microwave energy in the form of heat. Third, due to the stacked nature of the sheets, multiple internal reflections of electromagnetic waves occur which help

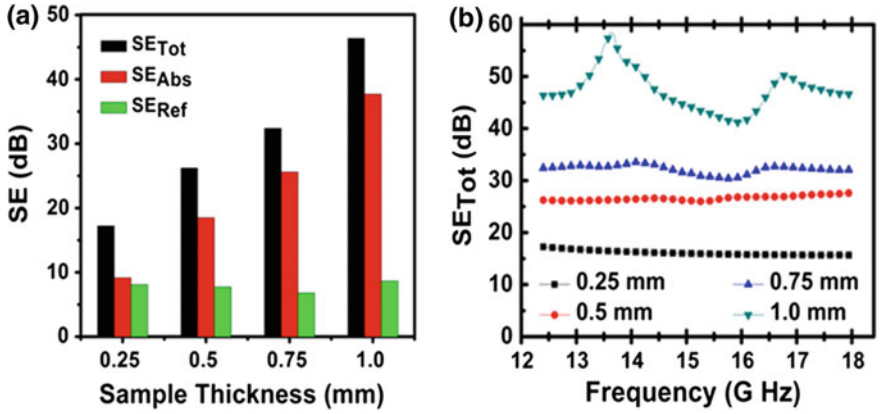

Fig. 7.3 **a** Shielding effectiveness SE_A, SE_R, and SE_T of graphene blocks at fixed frequency (12.4 GHz) for various thicknesses. **b** SE_A, SE_R, and SE_T versus frequency graph (in the range of 12.4–18.0 GHz) for various blocks of graphene [49]

in improving the attenuation of EM waves. They proposed that current work may be indicative for future work where the graphene yield and quality can be increased using this concept and can be used in EMI shielding and other possible applications.

The high quality and quantity of graphene is necessary for their realistic use in various applications such as electronics, optoelectronics, composite materials, and energy-storage devices [47, 58]. Therefore, the electrochemical method will be the milestone in the above applications.

8. **Microwave-Assisted Method of Graphene Synthesis**:

The microwave-assisted synthesis of graphene has abundant benefits. Foremost, the microwave-assisted method requires less time exclusive of complex synthesis procedure. Microwave-based system can offer a rapid and successful approach to heat the material uniformly from the core. While in conventional heating methods, heat is transferred from the exterior toward the interior of the material using heating mantle, water/oil bath, or any other heat source, which is comparatively slow and incompetent. Microwave-assisted method is economical, also as the amount of the used chemicals is greatly reduced compared to usual method of synthesis reported so far. Next, the average size of the graphene synthesized from microwave-based method can be generously proportioned than that prepared by other conventional heating methods. Finally, the graphene produced from microwave-based technology is of high quality with controlled structure and residual functional groups [67]. Since microwave-irradiated method of graphene synthesis is not only easy but also nonhazardous. Therefore, we have synthesized graphene sheet in our lab through this route also.

Slightly modified Hummer's method was used to prepare graphite oxide from graphite powder. In a characteristic experiment, graphite powder was treated with

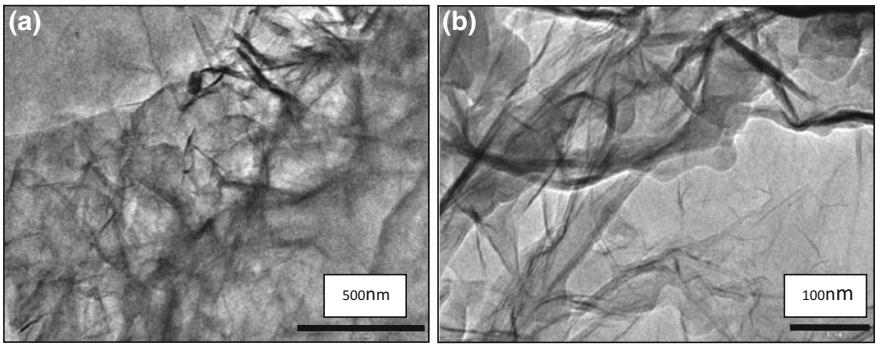

Fig. 7.4 TEM micrograph of microwave-assisted synthesis of graphene sheet (a and b)

H_2SO_4 and H_3PO_4 in the 9:1 ratio and $KMnO_4$ was added. As obtained graphite oxide was heated at 80 °C in vacuum to remove moisture and grinded into fine powder. As obtained fine powder of graphite oxide was irradiated for about 1 min at 900 W in microwave oven (LG Model No: MJ3286BFUM), and then the sample was cooled to ambient temperature.

Above is the TEM micrograph given (Fig. 7.4), it can be observed in these images that sheets of graphene are exfoliated, and a thin wrinkle-like structure is obtained. In Fig. 7.4b at 100 nm, it is clearly observed that the few-layer graphene sheets are obtained. Sheets are so thin that at the edges it frill and rolled due to thermal vibrations, edge instabilities, and thermodynamically unstable (inter-atomic) interactions.

7.2 Conclusions

Graphene has attracted an enormous attention recently for its very well-known electrical, physical, and chemical properties. However, this carbon material continues to surprise scientists who are engaged in this study. High expectations are being placed for this magical 2D material, as it promises much in a variety of applications that include electronic devices, supercapacitors, batteries, drug delivery, biomedical applications, composites, flexible transparent displays, sensing devices, and energy storage. Low-cost element of the sixth most abundant element on earth makes it a smart pick to replace classical materials used for super capacitors, energy storage, batteries, etc. But there will always be a hunt to look for a novel synthesis method which should be non-hazardous, low cost with high-quality graphene sheets having large surface area. This chapter has discussed some of the prominent methods of graphene synthesis developed so far. We have discussed the facile method of graphene synthesis being employed in our laboratory for various applications, particularly in EMI shielding. Still lot more is left to

explore this magnificent material which scientists hope to witness in future research.

Acknowledgements Authors gratefully acknowledge UGC, MNRE, DST, and BHU. One of the authors (M.T) acknowledges the financial support from DST (WOS-A scheme File no. SR/WOS-A/PM-25/2016). Authors are also thankful to group members of the Nanoscience unit and Hydrogen Energy Centre, Dept. of Physics, BHU for the fruitful discussions.

References

1. K.S. Novoselov et al., Science **306**, 666 (2004)
2. A.K. Geim, P. Kim, Carbon wonderland. Sci. Am. (2008)
3. A.K. Geim, A.H. MacDonald, Graphene: exploring carbon flatland. Phys. Today **60**(8), 35–41 (2007)
4. Y. Hernandez, V. Nicolosi, M. Lotya, F.M. Blighe, Z. Sun, S. De, I.T. McGovern, B. Holland, M. Byrne, Y.K. Gun'Ko, J.J. Boland, P. Niraj, G. Duesberg, S. Krishnamurthy, R. Goodhue, J. Hutchison, V. Scardaci, A.C. Ferrari, J.N. Coleman, High-yield production of graphene by liquid-phase exfoliation of graphite. Nat. Nanotechnol. **3**(9), 563–568 (2008)
5. S.J. Woltornist, A.J. Oyer, J.-M.Y. Carrillo, A.V. Dobrynin, D.H. Adamson, Conductive thin films of pristine graphene by solvent interface trapping. ACS Nano **7**(8), 7062–7066 (2013). doi:10.1021/nn402371c
6. J.K. Wassei, R.B. Kaner, Graphene, a promising transparent conductor. Mater. Today **13**, 52–59 (2010)
7. G. Eda, G. Fanchini, M. Chhowalla, Large-area ultrathin films of reduced graphene oxide as a transparent and flexible electronic material. Nat. Nanotechnol. **3**, 270–274 (2008)
8. S. Stankovich, D.A. Dikin, R.D. Piner, K.A. Kohlhaas, A. Kleinhammes, Y. Jia, Y. Wu, S. T. Nguyen, R.S. Ruoff, Synthesis of graphene-based nanosheets via chemical reduction of exfoliated graphite oxide. Carbon **45**, 1558–1565 (2007)
9. S. Park, R.S. Ruoff, Chemical methods for the production of graphenes. Nat. Nanotechnol. **4**, 217–224 (2009)
10. S. Park, J. An, I. Jung, R.D. Piner, S.J. An, X. Li, A. Velamakanni, R.S. Ruoff, Colloidal suspensions of highly reduced graphene oxide in a wide variety of organic solvents. Nano Lett. **9**, 1593–1597 (2009)
11. Z. Luo, Y. Lu, L.A. Somers, A.T.C. Johnson, High yield preparation of macroscopic graphene oxide membranes. J. Am. Chem. Soc. **131**, 898–899 (2009)
12. C. Gomez-Navarro, R.T. Weitz, A.M. Bittner, M. Scolari, A. Mews, M. Burghard, K. Kern, Electronic transport properties of individual chemically reduced graphene oxide sheets. Nano Lett. **9**, 2206 (2009)
13. G. Williams, B. Seger, P.V. Kamat, TiO_2-graphene nanocomposites UV-assisted photocatalytic reduction of graphene oxide. ACS Nano **2**, 1487–1491 (2008)
14. A.A. Green, M.C. Hersam, Solution phase production of graphene with controlled thickness via density differentiation. Nano Lett. **9**, 4031–4036 (2009)
15. L.J. Cote, F. Kim, J. Huang, Langmuir-blodgett assembly of graphite oxide single layers. J. Am. Chem. Soc. **131**, 1043–1049 (2009)
16. D. Li, M.B. Muller, S. Gilje, R.B. Kaner, G.G. Wallace, Processable aqueous dispersions of graphene nanosheets. Nat. Nanotechnol. **3**, 101–105 (2008)
17. W. Gao, L.B. Alemany, L. Ci, P.M. Ajayan, New insights into the structure and reduction of graphite oxide. Nat. Chem. **1**, 403–408 (2009)

18. C.M. Chen, Q.H. Yang, Y.G. Yang, W. Lv, Y.F. Wen, P.X. Hou, M.Z. Wang, H.M. Cheng, Self-assembled free-standing graphite oxide membrane. Adv. Mater. **21**, 3007–3011 (2009)
19. X. Li, H. Wang, J.T. Robinson, H. Sanchez, G. Diankov, H. Dai, Simultaneous nitrogen doping and reduction of graphene oxide. J. Am. Chem. Soc. **131**, 15939–15944 (2009)
20. V. López, R.S. Sundaram, C. Gómez-Navarro, D. Olea, M. Burghard, J. Gómez-Herrero, F. Zamora, K. Kern, Chemical vapor deposition repair of graphene oxide: a route to highly-conductive graphene monolayers. Adv. Mater. **21**, 4683–4686 (2009)
21. H.A. Becerril, J. Mao, Z. Liu, R.M. Stoltenberg, Z. Bao, Y. Chen, Evaluation of solution-processed reduced graphene oxide films as transparent conductors. ACS Nano **2**, 463–470 (2008)
22. J. Wu, H.A. Becerril, Z. Bao, Z. Liu, Y. Chen, P. Peumans, Organic solar cells with solution-processed graphene transparent electrodes. Appl. Phys. Lett. **92**, 263302-1 (2008)
23. X. Wu, M. Sprinkle, X. Li, F. Ming, C. Berger, W.A. de Heer, Epitaxial-graphene/graphene-oxide junction: an essential step towards epitaxial graphene electronics. Phys. Rev. Lett. **101**, 026801-1 (2008)
24. S. Stankovich, R.D. Piner, X. Chen, N. Wu, S.T. Nguyen, R.S. Ruoff, Stable aqueous dispersions of graphitic nanoplatelets via the reduction of exfoliated graphite oxide in the presence of poly(sodium 4-styrenesulfonate). J. Mater. Chem. **16**, 155–158 (2006)
25. C.-Y. Su, Y. Xu, W. Zhang, J. Zhao, X. Tang, C.-H. Tsai, L.-J. Li, Electrical and spectroscopic characterizations of ultra-large reduced graphene oxide monolayers. Chem. Mater. **21**, 5674–5680 (2009)
26. C.Y. Su, Y. Xu, W. Zhang, J. Zhao, A. Liu, X. Tang, C.-H. Tsai, Y. Huang, L.J. Li, Highly efficient restoration of graphitic structure in graphene oxide using alcohol vapors. ACS Nano **4**, 5285–5292 (2010)
27. X. Wang, L. Zhi, K. Müllen, Transparent, conductive raphene electrodes for dye-sensitized solar cells. Nano Lett. **8**, 323–327 (2008)
28. G. Eda, Y.Y. Lin, S. Miller, C.-W. Chen, W.-F. Su, M. Chhowalla, Transparent and conducting electrodes for organic electronics from reduced graphene oxide. Appl. Phys. Lett. **92**, 233305 (2008)
29. Y.W. Zhu, W.W. Cai, R.D. Piner, A. Velamakanni, R.S. Ruoff, Transparent self-assembled films of reduced graphene oxide platelets. Appl. Phys. Lett. **95**, 103104 (2009)
30. Y. Hernandez, V. Nicolosi, M. Lotya, F.M. Blighe, Z. Sun, S. De, I.T. McGovern, B. Holland, M. Byrne, Y.K. Gun'Ko et al., High-yield production of graphene by liquid-phase exfoliation of graphite. Nat. Nanotechnol. **3**, 563–568 (2008)
31. P. Blake, P.D. Brimicombe, R.R. Nair, T.J. Booth, D. Jiang, F. Schedin, L.A. Ponomarenko, S.V. Morozov, H.F. Gleeson, E.W. Hill et al., Graphene-based liquid crystal device. Nano Lett. **8**, 1704–1708 (2008)
32. S. De, P.J. King, M. Lotya, A. O'Neill, E.M. Doherty, Y. Hernandez, G.S. Duesberg, J.N. Coleman, Flexible, transparent, conducting films of randomly stacked graphene from surfactant-stabilized, oxide-free graphene dispersions. Small **6**, 458–464 (2010)
33. S. Biswas, L.T. Drzal, A novel approach to create a highly ordered monolayer film of graphene nanosheets at the liquid-liquid interface. Nano Lett. **9**, 167–172 (2009)
34. W.T. Gu, W. Zhang, X.M. Li, H.W. Zhu, J.Q. Wei, Z. Li, Q.K. Shu, C. Wang, K.L. Wang, W.C. Shen et al., Graphene sheets from worm-like exfoliated graphite. J. Mater. Chem. **19**, 3367–3369 (2009)
35. X. Li, G. Zhang, X. Bai, X. Sun, X. Wang, E. Wang, H. Dai, Highly conducting graphene sheets and langmuir-blodgett films. Nat. Nanotechnol. **3**, 538–542 (2008)
36. C. Valles, C. Drummond, H. Saadaoui, C.A. Furtado, M. He, O. Roubeau, L. Ortolani, M. Monthioux, A. Penicaud, Solutions of negatively charged graphene sheets and ribbons. J. Am. Chem. Soc. **130**, 15802–15804 (2008)
37. J.H. Lee, D.W. Shin, V.G. Makotchenko, A.S. Nazarov, V.E. Fedorov, Y.H. Kim, J.Y. Choi, J.M. Kim, J.B. Yoo, One-step exfoliation synthesis of easily soluble graphite and transparent conducting graphene sheets. Adv. Mater. **21**, 4383–4387 (2009)

38. J. Lu, J.X. Yang, J. Wang, A. Lim, S. Wang, K.P. Loh, One-pot synthesis of fluorescent carbon nanoribbons, nanoparticles, and graphene by the exfoliation of graphite in ionic liquids. ACS Nano **3**, 2367–2375 (2009)
39. N. Liu, F. Luo, H. Wu, Y. Liu, C. Zhang, J. Chen, One-step ionic-liquid-assisted electrochemical synthesis of ionic-liquid-functionalized graphene sheets directly from graphite. Adv. Funct. Mater. **18**, 1518–1525 (2008)
40. D.L. Boxall, C.M. Lukehart, Rapid synthesis of Pt or Pd/carbon nanocomposites using microwave irradiation. Chem. Mater. **13**, 806–810 (2001)
41. K.W. Gallis, C.C. Landry, Rapid calcination of nanostructured silicate composites by microwave irradiation. Adv. Mater. **13**, 23–26 (2001)
42. J. Liang, Z.X. Deng, X. Jiang, F.L. Li, Y.D. Li, Photoluminescence of tetragonal ZrO_2 nanoparticles synthesized by microwave irradiation. Inorg. Chem. **41**, 3602–3604 (2002)
43. C.R. Patra, G. Alexandra, S. Patra et al., Microwave approach for the synthesis of rhabdophane-type lanthanide orthophosphate (Ln = La, Ce, Nd, Sm, Eu, Gd and Tb) nanorods under solvothermal conditions. New J. Chem. **29**, 733–739 (2005)
44. W.F. Chen, L.F. Yan, P.R. Bangal, Preparation of graphene by the rapid and mild thermal reduction of graphene oxide induced by microwaves. Carbon **48**, 1146–1152 (2010)
45. M.A.H. Hassan, V. Abdelsayed, A.E.R.S. Khder et al., Microwave synthesis of graphene sheets supporting metal nanocrystals in aqueous and organic media. J. Mater. Chem. **19**, 3832–3837 (2009)
46. J. Wang, K.K. Manga, Q. Bao, K.P. Loh, High-yield synthesis of few-layer graphene flakes through electrochemical expansion of graphite in propylene carbonate electrolyte. J. Am. Chem. Soc. **133**, 8888–8891 (2011)
47. K. Parvez, Z.S. Wu, R. Li, X. Liu, R. Graf, X. Feng et al., Exfoliation of graphite into graphene in aqueous solutions of inorganic salts. J. Am. Chem. Soc. **136**, 6083–6091 (2014)
48. J. Liu, H. Yang, S.G. Zhen, C.K. Poh, A. Chaurasia, J. Luo et al., A green approach to the synthesis of high-quality graphene oxide flakes via electrochemical exfoliation of pencil core. RSC Adv **3**, 11745–11750 (2013)
49. P. Tripathi, C.R. Prakash Patel, A. Dixit, A.P. Singh, P. Kumar, M.A. Shaz, R. Srivastava, G. Gupta, S.K. Dhawan, B.K. Gupta, O.N. Srivastava, High yield synthesis of electrolyte heating assisted electrochemically exfoliated graphene for electromagnetic interference shielding applications. RSC Adv. **5**, 19074–19081 (2015)
50. A. Reina, X. Jia, J. Ho, D. Nezich, H. Son, V. Bulovic, M.S. Dresselhaus, J. Kong, Large area, few-layer graphene films on arbitrary substrates by chemical vapor deposition. Nano Lett. **9**, 30–35 (2009)
51. X. Li, W. Cai, J. An, S. Kim, J. Nah, D. Yang, R. Piner, A. Velamakanni, I. Jung, E. Tutuc et al., Large-area synthesis of high-quality and uniform graphene films on copper foils. Science **324**, 1312–1314 (2009)
52. S. Bae, H.K. Kim, Y.B. Lee, X.F. Xu, J.S. Park, Y. Zheng, J. Balakrishnan, T. Lei, H.R. Kim, Y. Song et al., Roll-to-roll production of 30-inch graphene films for transparent electrodes. Nat. Nanotechnol. **5**, 574–578 (2010)
53. X.S. Li, Y.W. Zhu, W.W. Cai, M. Borysiak, B.Y. Han, D. Chen, R.D. Piner, L. Colombo, R.S. Ruoff, Transfer of large-area graphene films for high-performance transparent conductive electrodes. Nano Lett. **9**, 4359–4363 (2009)
54. U. Khan, J.N. Coleman, Small **6**, 864–871 (2010)
55. M. Lotya, P.J. King, U. Khan, S. De, J.N. Coleman, ACS Nano **4**, 3155–3162 (2010)
56. G. Wang, B. Wang, J. Park, Y. Wang, B. Sun, J. Yao, Carbon **47**, 3242–3246 (2009)
57. M. Alanyalıoğlu, J.J. Segura, J. Oró-Solè, N. Casañ-Pastor, Carbon **50**, 142–152 (2012)
58. K. Parvez, R. Li, S.R. Puniredd, Y. Hernandez, F. Hinkel, S. Wang et al., Electrochemically exfoliated graphene as solution-processable, highly conductive electrodes for organic electronics. ACS Nano **7**, 3598–3606 (2013)
59. C.Y. Su, A.Y. Lu, Y. Xu, F.R. Chen, A.N. Khlobystov, L.J. Li, High-quality thin graphene films from fast electrochemical exfoliation. ACS Nano **5**, 2332–2339 (2011)

60. P. Tripathi, C. Ravi Prakash Patel, M.A. Shaz, O.N. Srivastava, Synthesis of high-quality graphene through electrochemical exfoliation of graphite in alkaline electrolyte. http://arxiv.org/ftp/arxiv/papers/1310/1310.7371.pdf (2012)
61. N. Liu, F. Luo, H. Wu, Y. Liu, C. Zhang, J. Chen, Adv. Funct. Mater. **18**, 1518 (2008)
62. K.S. Rao, J. Senthilnathan, Y.F. Liu, M. Yoshimura, Role of peroxide ions in formation of graphene nanosheets by electrochemical exfoliation of graphite. Sci. Rep. **4** (2014)
63. J. Liu, M. Notarianni, G. Will, V.T. Tiong, H. Wang, N. Motta, Electrochemically exfoliated graphene for electrode films: effect of graphene flake thickness on the sheet resistance and capacitive properties. Langmuir **29**, 13307–13314 (2013)
64. J.B. Nelson, D.P. Riley, Proc. Phys. Soc. Lon. **57**, 477–486 (1945)
65. Z. Liu, J.Z. Liu, Y. Cheng, Z. Li, L. Wang, Q. Zheng, Phys. Rev. B: Condens. Matter Mater. Phys. **85**, 205418 (2012)
66. Sima Kashi, R.K. Gupta, T. Baum, N. Kao, S.N. Bhattacharya, Morphology, electromagnetic properties and electromagnetic interference shielding performance of poly lactide/graphene nanoplatelet nanocomposites. Mater. Des. **95**, 119–126 (2016)
67. W. Sun, H. Li, Y. Wang, Microwave-assisted synthesis of graphene nanocomposites: recent developments on lithium-ion batteries. Reports in Electrochemistry, p. 5 (2015)

Chapter 8
Carbon Nanomaterials Derived from Graphene and Graphene Oxide Nanosheets

Ling Bing Kong, Wenxiu Que, Kun Zhou, Sean Li and Tianshu Zhang

8.1 Brief Introduction

Graphene is one of the hottest two-dimensional (2D) materials, which has attracted much attention all around the world and was first used to stand for isolated single atom thick carbon sheet [1], while it now represents all 2D carbon materials with sheet-like or flake-like structures [2, 3]. Besides monolayer (single atomic layer) graphene, ultrathin multilayered carbon materials derived from graphite through exfoliation are also called graphene or graphene-based materials. Furthermore, graphene oxide and various chemically modified graphenes have emerged abruptly [3]. Graphene and graphene oxide have been developed into various one-dimensional (1D),

L.B. Kong (✉)
School of Materials Science and Engineering, Nanyang Technological University, 50 Nanyang Avenue, 639798 Singapore, Singapore
e-mail: elbkong@ntu.edu.sg

W. Que (✉)
Electronic Materials Research Laboratory, School of Electronic and Information Engineering, Xi'an Jiaotong University, 710049 Xi'an, Shaanxi, People's Republic of China
e-mail: wxque@xjtu.edu.cn

K. Zhou
School of Mechanical & Aerospace Engineering, Nanyang Technological University, 639798 Singapore, Singapore
e-mail: kzhou@ntu.edu.sg

S. Li
School of Materials Science and Engineering, The University of New South Wales, Sydney, Australia
e-mail: sean.li@unsw.edu.au

T. Zhang
Anhui Target Advanced Ceramics Technology Co. Ltd., Hefei, Anhui, People's Republic of China
e-mail: 13335516617@163.com

Z.H. Khan (ed.), *Recent Trends in Nanomaterials*,
Advanced Structured Materials 83, DOI 10.1007/978-981-10-3842-6_8

two-dimensional (2D), and three-dimensional (3D) architectures [4, 5]. Among them, 1D structures are also known as fibers or yarns, while 2D ones are called papers or sheets.

Graphene fibers (GFs) have been fabricated by using various methods. They have numerous unique properties, such as high mechanical flexibility, low density, and potential functionalization capability [6]. These special properties make them potential candidates for various applications in different areas, such as photovoltaic cells, supercapacitors, flexible fiber-type actuators, and so on. Graphene-based 2D materials have been reported in the open literature [7–9].

Besides, some applications, e.g., energy storage, environmental protection, and biological issues, required 3D structures [10–13]. The 3D structured graphene materials could have high specific surface areas, strong mechanical properties and rapid mass, and charge transport kinetics, due to the synergistic effect of the 3D porous structures and the intrinsic high conductivity of graphene. 3D graphene structures have also various other names, such as networks, foams, sponges, hydrogels, and aerogels, which will not be specifically emphasized in this chapter and just follow the original references.

8.2 Graphene Fibers (1D)

8.2.1 Solution Processing from Graphene Oxide (GO)

It was found that liquid crystals (LCs) could be formed in suspensions of soluble chemically oxidized graphene or GO nanosheets, which follow a twist-grain-boundary (TGB) phase-like model, with simultaneous lamellar ordering and long-range helical frustrations, so that they can be continuously spun into macroscopic GO fibers [14–17]. The presence of the lamellar structures makes the GO LCs to achieve concentrations that are sufficiently high for efficient alignment and effective coagulation. For instance, a simple syringe injection method has been developed to fabricate GO fibers, which were through 5 wt% NaOH–methanol solution as the coagulation bath [14]. GFs could be obtained by simply reducing the GO fibers in hydroiodic acid. The GFs exhibited a mechanical strength of 140 MPa at an ultimate elongation of 5.8% and a high conductivity of 2.5×10^4 S m^{-1}. In addition, the GFs displayed high mechanical flexibility, so that they could be used to fabricate special patterns and complex textiles.

Experimental results indicated that concentration of the GO LCs played a crucial role in determining whether fibers could be spun out or not [14]. For example, the GO LCs with a concentration of 0.76 led to brittle fibers, while the 2.0% samples were collapsed belts. To obtain continuous fibers, the LC dispersions should have a sufficiently high concentration, e.g., $\varphi = 5.7\%$. In addition, diameters of the fibers could be controlled in the range 50–100 μm, while the spinning rate was hundreds of centimeters per minute, by adjusting the size of nozzle and the drawing speed,

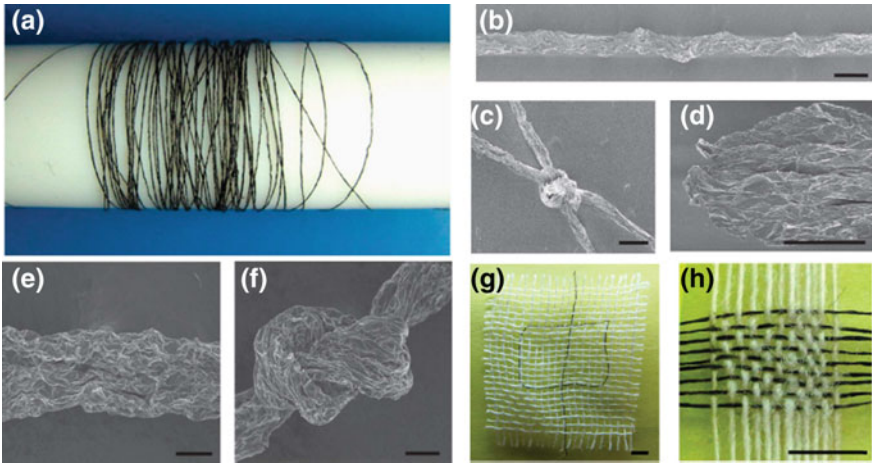

Fig. 8.1 Macroscopic GO fibers and chemically reduced graphene fibers. **a** Photograph of four-meter-long GO fiber wound on a Teflon drum (diameter = 2 cm). **b** SEM image of the fiber and **c** typical tighten knots. **d** Fracture morphology of the GO fiber after tensile tests. The surface-winkled morphology (**e**) and the tighten knot (**f**) of the graphene fiber. **j** A Chinese character ('中', Zhong) pattern knitted in the cotton network (*white*) using two graphene fibers (*black*). **k** A mat of graphene fibers (*horizontal*) woven together with cotton threads (*vertical*). Scale bars = 50 μm (**b**–**f**) and 2 mm (**g**, **h**). Reproduced with permission from [14], Copyright © 2011, Macmillan Publishers Limited

with examples shown in Fig. 8.1a, b. Figure 8.1c demonstrated that the fibers were not broken as the knots were tightened. As compared to the traditional carbon fibers, the GO fibers had much higher flexibility and torsion resisting capability.

The GO fibers exhibited a typical plastic deformation at room temperature, which was attributed to the possible stretching of the crumbled GO nanosheets, as well as the displacements of the GO nanosheets, as shown in Fig. 8.1d. The fibers possessed a Young's modulus of 5.4 GPa at small deformation in the elastic region and demonstrated fracture elongations of 6.8–10.1%, which were greater than those of filtrated GO papers (~0.4%) by more than one order of magnitude [18]. Also, the GO fibers showed a fracture strength of 102 MPa, which was within the range of filtrated GO papers, i.e., 70–130 MPa [4].

After the GO fibers were reduced through chemical reduction in 40% hydroiodic acid, the fiber shrunk in diameter, accompanied by the presence of a gray metallic luster. Meanwhile, the interlayer spacing was decreased from 8.9 Å ($2\theta = 9.86°$) to 3.7 Å ($2\theta = 24.25°$), according to XRD analysis results, with the latter to be close to the interlayer spacing of graphite (3.35 Å). The reduction led to an increase in both the Young's modulus (7.7 GPa) and fracture strength (140 MPa), while a fracture elongation of about 5.8% was also retained. The enhancement in mechanical strength was attributed to the stronger interactions between the graphene nanosheets, due to the much denser layer stacking. Similarly, crumbled graphene nanosheets were stretched when subject to tensile stress, which resulted in

the high fracture elongation of the graphene fiber, as shown in Fig. 8.1e. High flexibility of the graphene fibers was clearly shown in Fig. 8.1f–h.

This approach has also been applied to GO aerogel fibers, which had a "porous core–dense shell" structure, by combining spinning and ice-templating, from GO LCs [19]. Due to the interior uniform alignment of the GO nanosheets, the fibers possessed high tensile strength and high compression strength. The porous GO fibers could be reduced through chemical reduction and annealing process to obtain graphene fibers, without losing the porous structure, while gaining high electrical conductivity. This unique type of fibers had both high porosity and high mechanical strength and electrical conductivity, which could not be possible in most general materials.

Unique biomimetic composite fibers have been fabricated by using wet-spinning method combined with the liquid crystal self-templating (LCST) approach [20]. In the composite fibers, guest compounds, such as polymers and inorganic nanoparticles, could be homogeneously dispersed in the interchannels of LC GO nanosheets. The nacre-mimetic fibers exhibited a highly ordered hierarchical structure. The concurrent effect of ultrahigh aspect ratio, well-preserved alignment of the GO nanosheets, uniform single-molecule interlayer of polymers, and the presence of hydrogen bonding arrays ensured the formation of the macroscopic-assembled artificial nacre, with a high σ of 555 MPa and toughness of 18 MJ m^{-3}, which were 2–17 times higher than those of natural nacre (80–135 MPa and 0.1–1.8 MJ m^{-3}) [21, 22]. With an ultralow density of 1.0 g m^{-3}, the fibers possessed an optimal specific strength of as high as 652 N m g^{-1}, which was nearly two times that of most metals and alloys. The reduced composite fibers possessed a high electrical conductivity of 5261 S m^{-1}.

A one-step method is used to fabricate graphene fibers at large scale, through in situ reduction in basic coagulation baths [23]. Liquid crystallinity of the suspension was dependent on concentration and size of the GO nanosheets, which had a directional effect on processability of the LCs. Two types of fiber wet-spinning systems were employed to develop the graphene fibers. Spinability of the GO dispersions was evaluated by using the "petri dish method," in which the GO dispersion was injected at the flow rate of 5–10 ml h^{-1} into a rotating petri dish with coagulation bath that was rotated at 30–60 rpm. A custom-built wet-spinning apparatus was also used to study the continuous wet-spinning process. All the as-spun gel fibers were washed with 25 vol% ethanol–water and then air-dried at room temperature under tension, so as to obtain dried GO fibers. Two methods, i.e., (i) overnight annealing at 220 °C in vacuum and (ii) hydrazine vapor treatment at 80 °C for 3 h, were conducted to reduce the GO fibers to rGO fibers.

Figure 8.2a shows a POM image of the GO gel fibers, with birefringence being clearly observed, confirming the highly ordered GO domains that were retained during from the LC suspensions. It is well known that the formation of mono-domains of GO nanosheets requires a long timescale, if no external driving force is applied. One way to promote the alignment of LC GO is the application of external magnetic field. In this case, it took 5 h to form uniform LCs [23]. In contrast, macroscopic alignment during wet-spinning occurred almost immediately

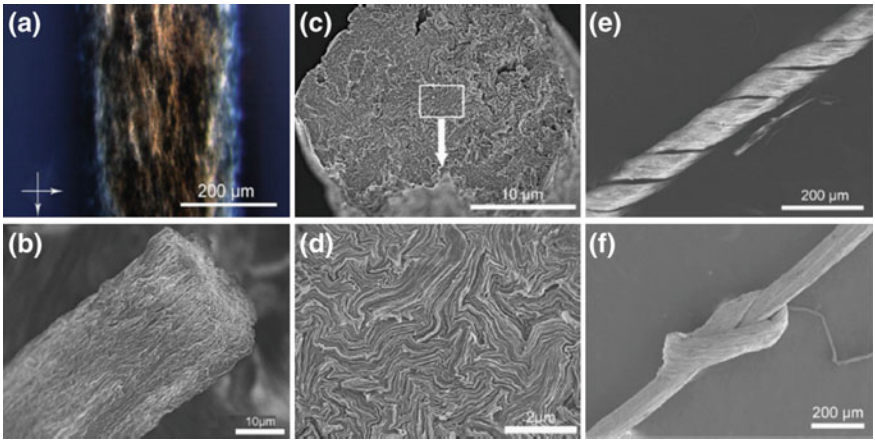

Fig. 8.2 **a** Polarized optical microscopy (POM) image of the as-spun GO gel fiber showing birefringence that confirmed the presence of ordered LC domains, with the *arrows* indicating the direction of polarizers. SEM images of as-spun GO fibers: **b** corrugated surface and **c** near-circular cross section. **d** Close view SEM image of cross section of the GO fiber shown in (**b**) revealing GO nanosheet planes that were oriented along the fiber axis. **e**, **f** SEM images of the crumpled and knotted rGO yarns (reduced by annealing) showing their high flexibility. Reproduced with permission from [23], Copyright © 2013, WILEY-VCH Verlag GmbH & Co. KGaA, Weinheim

(within several seconds), which was ascribed to the action of the shear stress generated through the spinneret, because of the 2D feature of the GO nanosheets. Microstructure analysis indicated that, in the dry fibers, the GO nanosheets were stacked in a layer-by-layer way, with only a slight degree of folding. Meanwhile, they were orientated in the direction of the fiber axis, as shown in Fig. 8.2b–d.

A similar wet-spinning assembly approach was reported to fabricate graphene fibers with GO solutions combined with chemical reduction [24]. GO fibers were developed by spinning GO dispersions in a coagulation bath of hexadecyltrimethyl ammonium bromide (CTAB) solution. This is the first report in which the assembly of GO nanosheets into macroscopic fibers was realized at low GO concentrations. The assembly mechanism of the GO fibers was clarified. The graphene fibers exhibited promising mechanical strength, high electrical conductivity, and high flexibility. Multifunctionality could be achieved through in situ or post-synthesis integration of various functional nanomaterials into the GO fibers.

In a separate study, graphene fibers were fabricated by using the wet-spinning and coagulation process, with focus on the understanding of the processing structure–property relationship [25]. Processing parameters include graphene dimension, spinning conditions, fiber density, and orientation in achieving optimum properties. It was found that both mechanical strength and electrical conductivity of the graphene fibers were closely related to the degree of orientation of graphene nanosheets in the fibers. The interaction between graphene nanosheets could be enhanced by using the solution of high GO concentration graphene nanosheets of

large size, which led to fibers with high electrical and mechanical properties. Also, mechanical properties of the fibers were more strongly influenced by the fiber packing density-related defects.

Because of the intrinsic alignment of the GO nanosheets along the long axis direction of the fibers, these wet-spun GO fibers generally have a low-tensile modulus. To address this problem, it is necessary to use large GO nanosheets as the building blocks to assemble fibers [26]. By doing this, modulus could be increased by one order of magnitude. For example, two types of GO nanosheets are used: (i) large flake GO (LFGO) nanosheets, with an average diameter of 22 μm; and (ii) small flake GO (SFGO) nanosheets, with an average diameter of 9 μm. Expectedly, the LFGO fibers demonstrated much higher mechanical performances than the SFGO fibers, in specific stress, specific modulus, and elongation by 178, 188, and 278%, respectively.

A coaxial two-capillary spinning strategy was developed to continuously to fabricate graphene-based hollow fibers (HFs) with well-controlled morphology [27]. Continuous GO-HFs and necklace-like HFs (nGO-HFs) could be spun out directly from concentrated GO suspensions. Graphene HFs (G-HFs) could be obtained through chemical reduction. The GO-HFs had a tensile strength of 140 MPa. They exhibited a typical elongation at break of about 2.8%, which was attributed to the possible displacement of the GO nanosheets within the walls. Furthermore, simultaneous functionalization of the GO-HFs could be achieved by introducing functional components directly into the core flow or mixing them with the initial GO suspension. By using thermal annealing, the GO-HFs could be converted to G-HFs, whereas their flexibility was not influenced while mechanical strength was improved.

A modified wet-spinning method was reported to produce graphene fibers by applying a shear stress [28]. The fibers fabricated in this way exhibited a macroscopic ribbon-like structure with high flexibility. Such ribbon-like graphene fibers could find a wide range of applications, such as elastic strain sensors, flexible counter electrodes for fiber solar cells, and fabric electrodes for supercapacitors. Figure 8.3a shows a schematic diagram of the spinning setup. The GO nanosheets with few layers were several micrometers in size. Aqueous GO suspension had a concentration of 6 mg ml^{-1}, which was injected by using a syringe pump into a chitosan solution placed on a stage that was rotated constantly at a speed of 10 rpm. The GO ribbons were collected by using a glass rod placed vertically in the chitosan solution.

During the spinning, the fluid flow direction was controlled to be perpendicular to the direction in which the GO suspension was injected (downward). Continuous ribbons were produced due to the presence of the shear stress. The ribbons exhibited a flat morphology, with a width-to-thickness ratio of up to 100, as shown in Fig. 8.3b. Photographs of the experimental setup, together with the glass rod, are shown in Fig. 8.3c–e. There were two reasons responsible for the formation of the ribbon structure, i.e., (i) electrostatic interaction between the GO nanosheets and chitosan in the coagulation bath, and (ii) the larger shear fluid velocity compared with the injection rate of the GO suspension. The width of the ribbons in the range

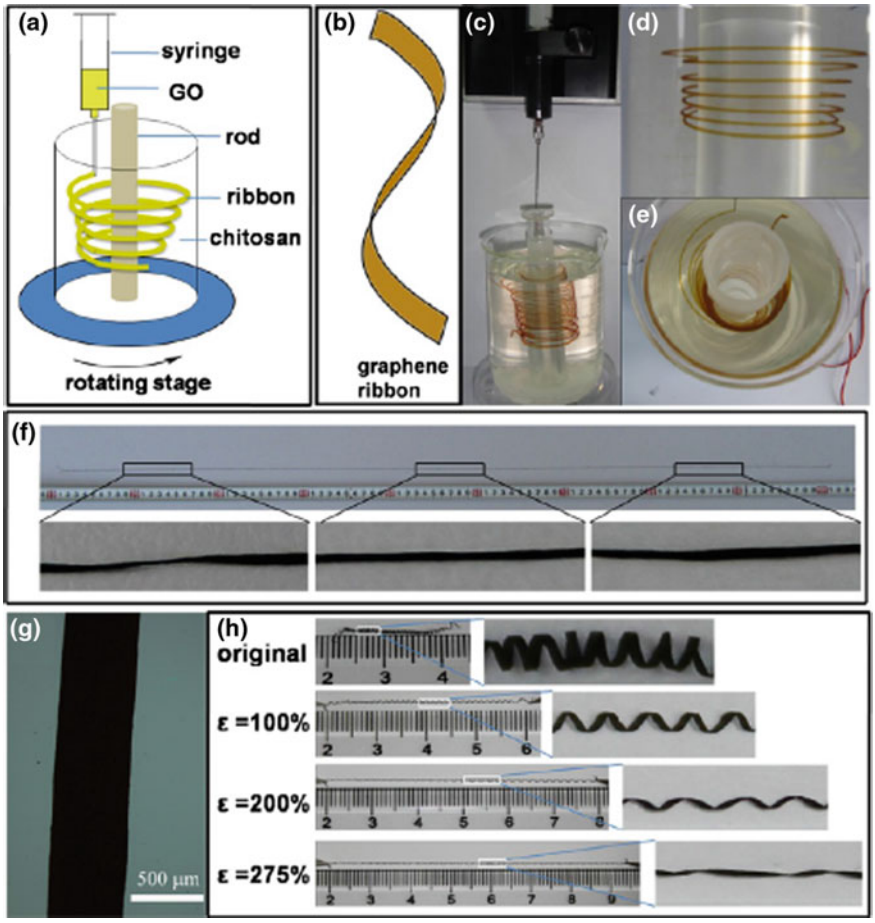

Fig. 8.3 Fabrication process and microstructures of the continuous graphene ribbons. **a** Schematic diagram of the wet-spinning setup. **b** Illustration of the flexible ribbon structure. **c** Photograph of the setup with a uniform GO ribbon spun in the chitosan solution. **d** Photograph of a single ribbon rotated around the collecting rod. **e** Top view of the setup. **f** Photograph of a 1-m-long and 300-μm-wide graphene ribbon after chemical reduction. **g** Optical image of a 500-μm-wide ribbon. **h** A ribbon made into spiral shape and then stretched to large strains. Reproduced with permission from [28], Copyright © 2013, American Chemical Society

of 200–500 μm was determined by the diameter of the tilted opening of a needle. Other factors included concentration of the GO suspension and chitosan, injection rate of the GO suspension and rotation speed of chitosan, which could be optimized to tailor morphology and property of the final ribbons.

Chemical reduction in hydroiodic acid was used to convert GO ribbons to rGO ribbon, accompanied by a color change from brown to black, as shown in Fig. 8.3f, g. The rGO ribbons possessed conductivities of 100–150 S cm^{-1}.

Figure 8.3h indicated that rGO ribbons showed very high flexibility. Wet ribbons could be wound onto a thin glass capillary to form a stable helical item after drying. When the spring-like structure was stretched, the twisted ribbon was not fractured and the shape could be recovered to a large extent.

Mechanical properties of the graphene ribbons had a close relation with orientation of the wrinkles. According to uniaxial tension testing results, oriented samples exhibited a relatively small failure strain of $\varepsilon < 4\%$, while those with random wrinkles demonstrated larger failure strain of $\varepsilon > 9\%$. In the oriented samples, the presence of tensile stress during the drying process triggered the alignment of the graphene nanosheets, thus leading to a denser stacking between the graphene layers and hence higher strengths (>100 MPa). In contrast, the highly wrinkled structure of the samples with random wrinkles possessed a lower strength due to larger intersheet distance, corresponding to a moderate tensile strain (up to about 14%) before fracture. It was also found that thickness of the ribbons was decreased with increasing fluid velocity, and the tensile strength of the graphene ribbons was increased with decreasing thickness over the range 7–1.5 μm. This was simply because thicker ribbons had more voids or defects.

8.2.2 Hydrothermal Approach

Hydrothermal treatment can facilitate spontaneous assembly and reduction in GO nanosheets, leading to graphene network via the strong interlayer π–π stacking between the graphene nanosheets [13]. A simple one-step dimensionally confined hydrothermal method was used to produce graphene fibers from aqueous GO suspensions [29]. A glass pipeline with an interdiameter of 0.4 mm was used as the reactor. GO suspension with a concentration of 8 mg ml^{-1} was injected into the glass pipeline, with the two ends being sealed, which was then treated at 230 °C for 2 h. Graphene fibers fit with the geometry of the pipeline were finally formed, with a diameter of 150 μm in wet state. The graphene fibers were collected from the pipeline by using N_2 flow and then air-dried. After drying, length of the fibers was not changed, while they were shrunk in diameter to $\sim$35 μm, due to the loss of water. The graphene fibers exhibited a very high flexibility, so that they could be woven into meshwork-like and cloth-like structures manually. The graphene fibers network could also be embedded into polydimethylsiloxane (PDMS) matrix by casting a mixed and degassed PDMS prepolymer on graphene fiber meshes, followed by thermal curing.

Figure 8.4a shows a graphene fiber with a length of 63 cm and a diameter of 33 μm. The process was very productive, where 1 ml GO suspension of 8 mg ml^{-1} yield graphene fiber of >6 m. Also, diameter and length of the fibers could be readily controlled either by using pipelines with different lengths and inner diameters or adopting GO suspensions with different concentrations. The large shrinkage

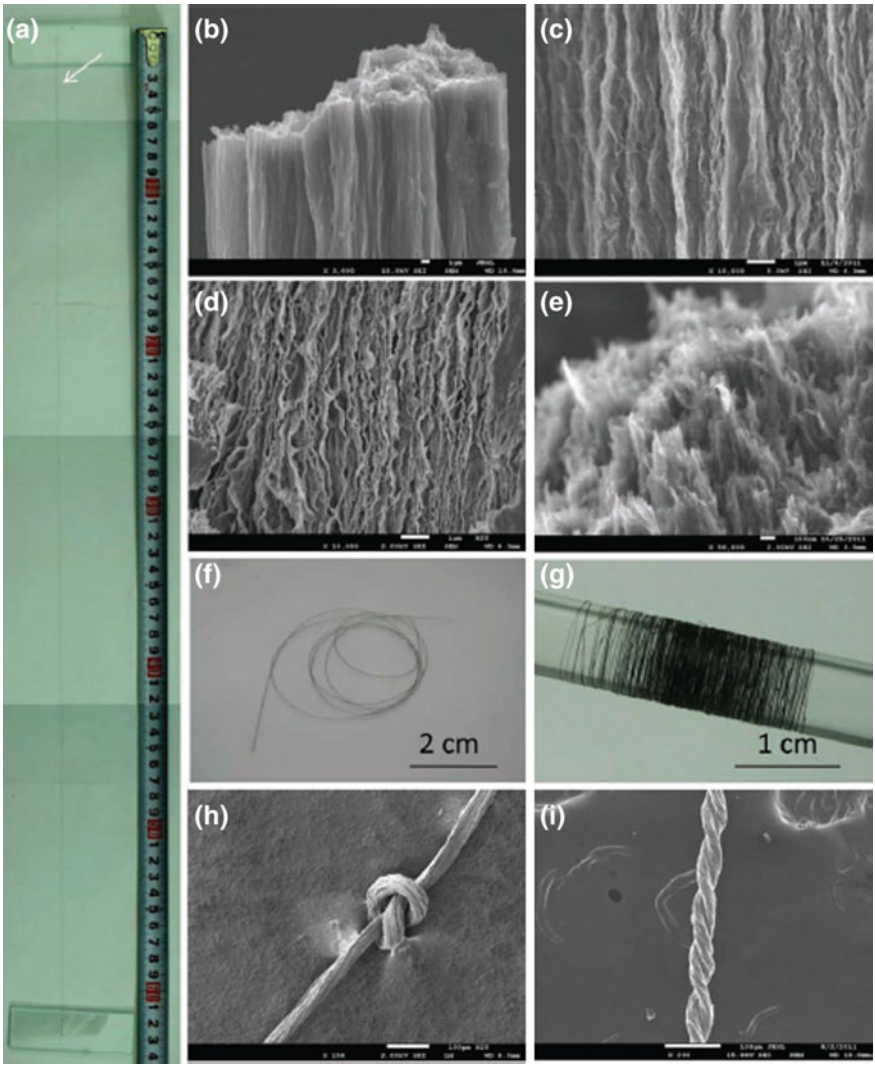

Fig. 8.4 Morphology and flexibility of the graphene fibers. **a** Photograph of a dry graphene fiber with a diameter of ~33 μm and a length of 63 cm. **b** SEM image of the broken part of a graphene fiber (scale bar = 1 μm). **c**, **d** Axial external surface and inner cross section SEM images of the graphene fiber, respectively (scale bars = 1 μm). **e** High-resolution SEM image of the broken section in (**b**) (scale bar = 100 nm). **f** Photograph of a wet graphene fiber coiled individually in water. **g** Photograph of dry graphene fibers coiled into bundle around a glass rod. **h**, **i** SEM images of the knotted and two-ply graphene fibers (scale bars = 100 μm). Reproduced with permission from [29], Copyright © 2012, WILEY-VCH Verlag GmbH & Co. KGaA, Weinheim

in diameter of the fibers during the drying process would produce surface tension forces that could promote spontaneous orientation of graphene nanosheets. The capillary force caused by the evaporation of water molecules led to a close packing of the porous graphene nanosheets. As a result, the fibers were densely packed and certainly aligned in the direction of axis, of the fibers, as shown in Fig. 8.4b–e. Figure 8.4e shows SEM image of a broken fiber, with the individual graphene nanosheets and their packing entanglement being clearly observed.

The dried graphene fibers had a Raman ratio of about 6:1, while the ratio of the wet fibers was close to 1:1, which further implied that the graphene nanosheets in the dried fibers were highly aligned parallel to the axis. Because no aggregation and preformed orientation were observed in initial GO suspensions before and after they were injected into the pipeline, the alignment of the graphene nanosheets in the direction of fiber axis was mainly ascribed to the effect of capillary-induced shear force and surface tension induced during dry process. The graphene fibers could be curved into coils and enlaced in bundles in wet and dry states, as shown in Fig. 8.4f, g. The fiber was not broken as the knot was tightened (Fig. 8.4h), while two-ply yarn could be made by twisting two fibers (Fig. 8.4i).

The hydrothermally as-derived graphene fibers possessed tensile strength of up to 180 MPa, which was increased to 420 MPa after they were thermally treated at 800 °C for 2 h in vacuum. Due to their relatively density of 0.23 g cm^{-3}, the fibers reached a density-normalized failure stress of 782 MPa (g $cm^{-3})^{-1}$. Typical elongations at the beak of the graphene fibers were in the range 3–6%. The graphene fibers exhibited an electrical conductivity of $\sim$10 S cm^{-1}. The electrical conductivity was nearly not affected when the fibers were bent over 1000 cycles. Due to their high flexibility and mechanical strength, the graphene fibers could be shaped to various geometries. In addition, functional components could be incorporated into the graphene fibers to further amplify their functionality. Because the as-obtained wet graphene fibers were highly porous, they can be used as host to incorporate other components during the drying process.

Another hydrothermal method led to a dually geometric confinement approach, which enabled meter-long hollow GFs (hGFs) with tunable diameters [30]. The hGFs were microtubings (μGTs), which could find potential applications for fluidics, catalysis, purification, separation, sensing, and environmental protection. The meter-long μGTs had diameters tunable in the range 40–150 μm. The μGTs could be shaped to have hierarchical multichannels. In addition, selectively site-specific functionalization could be realized on outer wall, inner wall, outer/inner wall, and within wall, in a well-controlled way, which made it possible to create μGTs with desired properties for targeted applications, such as stimulus-responsive devices and self-powered micromotors. The μGTs had stable flexibility and strong mechanical strength. The wet μGTs could have various predesigned configurations realized through the Cu wires. The predesigned structures were well retained after drying.

8.2.3 *Chemical Vapor Deposition (CVD)*

Chemical vapor deposition (CVD) graphene films have been used to fabricate graphene fivers through self-assembly [31]. The graphene fibers were porous and continuous with tunable diameter and pore distribution. They were also mechanically flexible with high electrical conductivity. Graphene films were grown on Cu foils by a CVD method, with methane as the precursor. Four steps were involved in the 2D film to 1D fiber transformation process, as shown in Fig. 8.5a–d. Firstly, free-standing CVD graphene films were made to float in water after the substrates

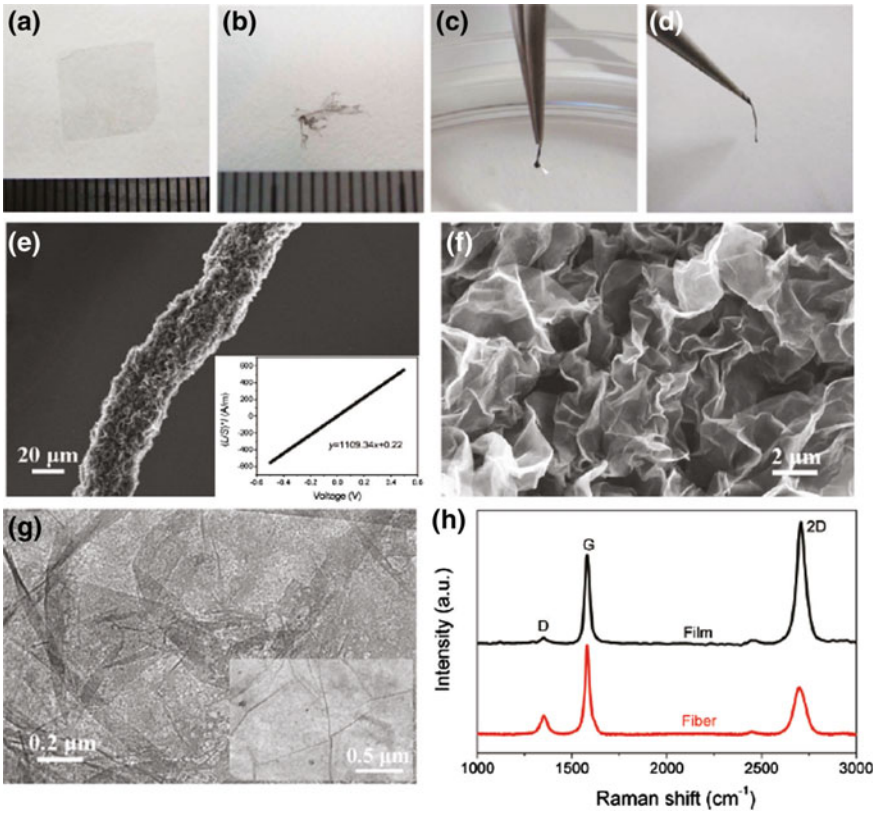

Fig. 8.5 Graphene fibers through the film to fiber self-assembly. **a** Free-standing graphene film on deionized water surface. **b** Scrolled and wrapped graphene film when transferred onto ethanol. **c** Graphene fiber drawn out of ethanol. **d** Porous and wrinkled structure of the dried fibers. **e** Low-magnification SEM image of a graphene fiber, with the inset showing the current density–voltage curve, yielding a conductivity of 1000 S m^{-1}. **f** SEM and **g** TEM images of the graphene fiber, showing wrinkled and porous structure, with the *inset* showing TEM image of pristine graphene film. **h** Raman spectra of the graphene film and the fiber. Reproduced with permission from [31], Copyright © 2011, American Chemical Society

were etched (Fig. 8.5a). Secondly, the graphene films were collected and transferred onto the surface of ethanol. Once the graphene films were put on ethanol, their edges immediately scrolled up, thus leading to agglomerates, which sank into the liquid (Fig. 8.5b). Thirdly, the graphene films were picked out (Fig. 8.5c), which shrank into fibers after the evaporation of ethanol (Fig. 8.5d). Eventually, graphene fibers were obtained after drying.

Figure 8.5e indicated that the fibers obtained from 1 cm^2 films had a diameter of 20–50 μm. Geometric size of the fibers was mainly determined by the size of the original graphene films and could be controlled to change other parameters, e.g., the drawing rate. The graphene fibers were mechanically flexible, so that they could be conveniently manipulated. They exhibited an electrical conductivity of 1000 S m^{-1}, as shown in the inset of Fig. 8.5e, due to the high quality of the CVD-derived graphene nanosheets. Figure 8.5f shows SEM image of the fibers, which were wrinkled and highly porous. The porous structure forms upon ethanol evaporation during the drying process. The pores were formed by the scrolled graphene nanosheets, as shown in Fig. 8.5g. Figure 8.5h shows typical Raman spectra of the graphene film and the fiber.

The self-assembly process experienced two stages, i.e., (i) scrolling of the film to form the fiber and (ii) shrinking of the fiber. The scrolling process was facilitated by the surface tension. Generally, because graphene films are relatively hydrophobic, they can be wetted by most organic solvents. Once being contacted with ethanol, the graphene film became very flexible. At the same time, solvent evaporation played an important role in the formation of graphene porous structure. After the fiber was formed, its surface was still covered by a liquid layer of ethanol. Pore size of the porous graphene fibers could be controlled by controlling the rate of solvent evaporation. Due to their porous structure, the graphene fibers could be used as electrodes of electrochemical devices. They could also be further functionalized by incorporating other components.

A similar CVD method has been employed to directly grow graphene layers on Cu meshes [32]. After deposition, the Cu wires were etched out with $FeCl_3$/HCl aqueous solution, so that hGFs with a network configuration were developed, which was named as graphene-based woven fabrics (GWFs). The GWFs could be transferred onto polydimethylsiloxane (PDMS) substrates, thus forming graphene-based woven fabric/PDMS hybrid films, which could find various applications. The GWFs possessed various special structural and characteristic features. Firstly, they exhibited high structural integrity, with much higher mechanical strength than polycrystalline graphene films. Secondly, there were micron-sized holes present in the GWFs, so that they were highly permeable, as compared with graphene monolayers. Also, they had unique exponential resistive response to external loadings, which could be used to develop strain sensors. Two applications have been demonstrated by using the GWFs, i.e., (i) GWFs/polymer composites and (ii) GWFs/semiconductor solar cells.

3D graphene networks have been obtained through substrate-assisted reduction and assembly of GO (SARA-GO) [33]. GO nanosheets were reduced and assembled into 3D networks on various substrates, including active metals of Zn, Fe, and

Cu, inert metals of Ag, Pt, and Au, semiconducting Si wafer, nonmetallic carbon-based films and even indium-tin oxide (ITO)-coated glass. Various graphene assemblies have been developed, including microtubes, four-way pipes, spiral tubes, multichannel networks, and micropatterns, which could be used to fabricate binder-free rechargeable lithium-ion batteries (LiBs).

8.2.4 Graphene Ribbon Fibers from Unzipped CNTs

Graphene nanoribbons with high aspect ratios can be obtained by unzipping CNTs [34–37]. These graphene ribbons have been used to prepare graphene fibers. A scalable method has been developed to fabricate long and narrow graphene nanoribbons, with which large graphene nanoribbon sheets were assembled and aligned first, while macroscopic neat graphene nanoribbon fibers were then obtained by twisting the sheets [38]. The graphene ribbon fibers showed high conductivity and good mechanical performance. The graphene ribbons were prepared by unzipping aligned nanotubes through oxidation, which were then reduced through thermal reduction. The graphene nanoribbons were highly aligned before and after the reduction process, which was confirmed by polarized infrared spectra. The graphene nanoribbon yarns exhibited a much higher electrochemical performance than the conventional twist-spun MWCNT yarns, which was attributed to incomplete reduction in the graphene nanoribbons. Most importantly, the conversion process could be scaled up for industrial production for applications as woven electrodes of fuel cells, supercapacitors and batteries.

Similarly, GONRs and chemically reduced graphene nanoribbons can also be dispersed with high concentrations in chlorosulfonic acid to form anisotropic LC phases for wet spinning of GFs [39]. The graphene oxide nanoribbons (GONRs) were prepared by unzipping MWCNTs through oxidation. The GONRs fibers could be thermally reduced (tr) into trGNR fibers. Alternatively, GONRs could be chemically reduced (cr) with hydrazine to crGNRs, with which were crGNR fibers were fabricated through spinning. As the crGNR fibers were further annealed (a), a-crGNR fibers were obtained.

Both the crGNRs and GONRs could be dispersed in chlorosulfonic acid to form anisotropic liquid crystal phases at room temperature. Diethyl ether (boiling point b_p = 35 °C, viscosity = 0.224 cP at 25 °C) was used as the coagulation bath solvent. The spinning apparatus included a spinning chamber with a piston. The piston was connected to a pressure controller at one end of the chamber, while a spinneret (capillary tube) was affixed to the other end of the chamber. The lyotropic materials were extruded, through the small spinneret, into the coagulation bath with an air gap to produce aligned ribbons within the as-spun fibers. The ribbons had an average length of 4 μm and widths of >100 nm. AFM analysis indicated that the height of the ribbon was about 1.2 nm, implying that the ribbons were single-layer graphene. 2 wt% GONRs and crGNRs were studied by using polarized optical microscope (POM).

It has been demonstrated that cross-sectional shape of wet-spun fibers is closely related to the coagulation conditions. A coagulation bath should meet certain requirements. For example, the GONRs should not be soluble in the coagulation bath. The cross-sectional shape of the wet-spun fibers is determined by the deformability of the coagulated layers and the mass transfer rate difference. It means that the coagulation rate should be sufficiently high, so that the coagulated layers will have low gradient at the interface near the surface layer. In this case, the coagulated outer layers will not collapse toward the core, thus leading to fibers with a circular shape. The mass transfer rate difference should be sufficiently low, in order to maintain a state where the solvent diffusion rate out of the fiber should be similar to the absorption rate of the nonsolvent. If the two rates are largely different, an irregular cross-sectional shape will likely be produced. Also, the viscosity of the bath should be as sufficiently low, to avoid surface etching of the fibers when going through the bath, thus leading to desirable surface morphology.

Water was first tested to prepare GONR solutions, due to the fact that it is easier to handle as compared to chlorosulfonic acid. Liquid crystal phase was observed in 5 wt% GONR aqueous solution. Ethyl acetate, methyl acetate, and diethyl ether were used as the coagulation bath, which all could not result in fibers with promising morphologies. Therefore, water was not suitable to develop GONR fibers. Instead, chlorosulfonic acid had to be employed as the solvent.

Figure 8.6 shows SEM images of the GONR fibers spun from 8 wt% chlorosulfonic acid solution, with diethyl ether solvent as the coagulant bath, clearly indicating that the fiber possessed a nearly perfect circular cross-sectional shape. The GONR fibers spun with different air gaps had an average diameter of 54 μm, tensile strength of 33.2 MPa, modulus of 3.2 GPa, and elongation of 1.64%. They were highly flexible. As shown in Fig. 8.2c, the fiber could be easily knotted into a loop with a minimum diameter of about 1 mm. The as-spun GONR fiber had porosity, measured by using the BET method, corresponding to a surface area of 58 $m^2\ g^{-1}$.

Surface morphologies of the 1050 °C trGNR with 1.3 g force (gf) pretension are shown in Fig. 8.7a, b. The diameter of the fiber was decreased because the oxygen

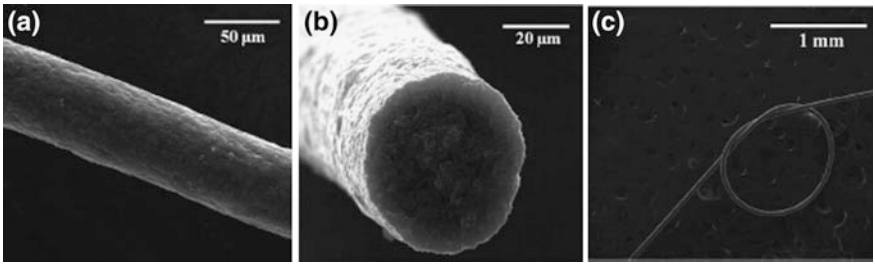

Fig. 8.6 Morphologies of the GONR fibers spun from the 8 wt% suspension. **a** Surface morphology of the as-spun fiber. **b** Transverse cross-sectional morphology. **c** Fiber knotted into a loop. Reproduced with permission from [39], Copyright © 2013, American Chemical Society

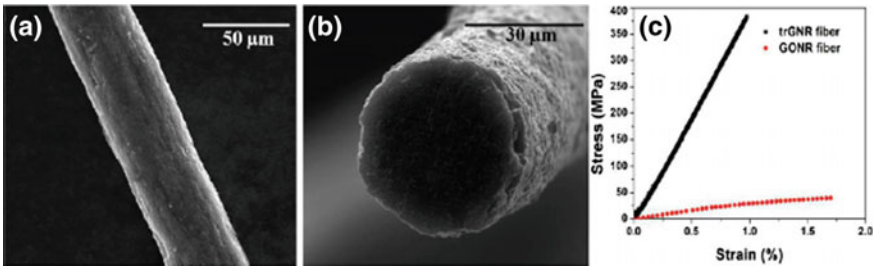

Fig. 8.7 **a** Surface morphology of the 1050 °C annealed trGNR fiber. **b** Cross-sectional morphology of the 1050 °C annealed trGNR fiber. **c** Typical stress–strain curve of the as-spun GONR fiber (12-cm air gap) and 1050 °C annealed trGNR fiber (12-cm air gap) with 1.3-gf pretension. Reproduced with permission from [39], Copyright © 2013, American Chemical Society

functional groups and some voids were removed due to the thermal reduction. Optimized mechanical performances of the fiber included a tensile strength of 383 MPa, a modulus of 39.9 GPa and an elongation to break of 0.97%. A representative stress–strain curve is shown in Fig. 8.7c. The tensile strength and modulus were increased by nearly one order of magnitude, when compared with the as-spun GONR fibers. Higher molecular alignment leads to higher tensile modulus. The trGNR fibers showed higher tensile modulus than the graphene fibers fabricated by using other methods ($\sim$10 GPa), as discussed before [14, 24, 29]. Due to the presence of residual microvoids, density of annealed trGNR fiber was 0.88 g cm^{-3}, which was less than half of that of conventional carbon fibers of 1.75–2.2 g cm^{-3} [40]. As a result, specific strength of the trGNR fiber was 430 kN * m kg^{-1}. Microstructure of the fibers could be improved by using high-temperature thermal annealing. Electrical conductivity of the fibers could be significantly increased by removing the oxygen groups and aligning graphene ribbons.

8.2.5 Other Methods

An electrophoretic self-assembly method was used to fabricate polymer-free and surfactant-free fibers from rGO nanoribbons [41]. Because no additive was contained in the fibers, it was possible to monitor the state of oxidation as the graphene oxide nanoribbons (GONRs) were reduced. This state could be correlated to the property of the fibers for different applications. Electrical and field emission properties of the fibers as a function of oxidation state of the GO nanosheets were evaluated. Especially for field emission, the rGONR fibers exhibited a low threshold electric field of 0.7 V μm^{-1} and a giant current density of 400 A cm^{-2}. Additionally, the fibers were stable at a high current density of 300 A cm^{-2}.

The GONRs were prepared by unzipping CVD-produced carbon MWCNTs with solution of $KMnO_4$ in sulfuric acid. The optimal concentration of $KMnO_4$, in order

to unzip the MWCNTs with a diameter of about 10 nm in the axis direction, was in the range 800–900 wt%, with respect to the amount of the MWCNTs. For example, 30 mg of MWCNTs powder was dispersed in 30 ml H_2SO_4, in which 250 mg $KMnO_4$ was added. The mixture was then heated at 55 °C for 30 min first. After that, the temperature was increased to 65 °C so that oxidation reaction was completed, which was then increased to 70 °C, followed by cooling to room temperature. The GONRs were collected after thorough washing and drying. The dried GONRs were dispersed in a mixture solvent of DMF/H_2O with a volumetric ratio of 9:1. Chemical reduction in GONRs was achieved with hydrazine monohydrate (1 μl for 3 mg GO) at 80 °C for 12 h. Well-dispersed colloidal solutions were obtained after ultrasonication for 10 min.

A graphitic tip was used as a positive electrode which was immersed into the chemically reduced GONR colloidal suspension in a Teflon vessel in which a counter electrode was embedded. The immersed tip was separated by about 5 mm away from the counter electrode. A constant voltage in the range 1–2 V was applied between the electrodes during the withdrawal process of the graphitic tip, which was at 0.1 mm min^{-1}, at 20–25 °C and 18–23% relative humidity. For thermal reduction, the chemically reduced GONR fibers treated in Ar at atmospheric pressure, at temperatures of 200, 500, and 800 °C for 1 h. The rGONRs had widths of 15–35 nm and thicknesses of 2.5–6.0 nm, corresponding to few-layer stacks. Also, rGONR fibers could be derived directly from reduced GONR solution.

A scalable self-assembly method at the liquid/air interface was reported to prepare GO fibers from aqueous GO suspensions, without using any polymer or surfactant [42]. The GO fibers were mechanically flexible, while their electrical conductivity could be significantly increased by using a low-temperature hydrothermal treatment at 180 °C for 5 h. When stable GO suspensions were kept a beaker of 2000 ml at room temperature, GO fibers were assembled and grew at the liquid/air interface in two-week time. The GO fibers were stable, free-standing, and floating on surface of the GO solution, which could be transferred onto arbitrary substrates. After washing and drying, dried GO fibers were obtained, which were intertwined into GO fiber films before they were transferred onto SiO_2/Si substrates. The GO fiber films were hydrothermally treated together with the SiO_2/Si substrates. Diameter and length of the fibers were controlled by either changing the size of the containers or controlling the times of ultrasonic treatment and self-assembly process.

8.3 Graphene-Based Free-Standing Papers (2D)

Free-standing papers or membranes based on graphene nanosheets have attracted much attention, due to their potential applications, especially in flexible electronic and energy storage devices [18, 43, 44]. Among various methods, vacuum filtration of G/GO suspensions through a porous membrane filter has been the most widely used technique to fabricate G/GO papers [45–95]. Other methods included solution

casting [96–102], tape casting [103], electrospray deposition (ESD) [104], electrophoretic deposition (EPD) [105], interface self-assembly [106, 107], cryogel [108], pyrolyzed asphalt [109], hydrothermal synthesis [70], and chemical vapor deposition (CVD) [110, 111],

8.3.1 Membrane Vacuum Filtration

Membrane vacuum filtration is the simplest and most straightforward method to prepare G/GO papers. Solvents are passed through the porous membranes, while G/GO nanosheets are blocked by the membranes as films. The films are then peeled off as free-standing papers after a certain degree of drying. For instance, GO papers with thicknesses in the range 1–30 μm have been fabricated by using this technique [18]. Structural characterization of GO paper indicated that the compliant GO nanosheets were interlocked/tiled together parallel in the horizontal direction, i.e., the formation of the ordered structures was attributed to the flow-directed assembly process. The GO paper exhibited high flexibility and strong mechanical properties. Compared with the conventional carbon- and clay-based papers, the extraordinary mechanical properties of the GO paper were originated from the strong van der Waals interactions and hydrogen bonding within GO nanosheets.

GO nanosheets were dispersed in water to form GO suspension at a concentration of 3 mg ml^{-1}. Thickness of the GO papers was controlled by adjusting the volume of the colloidal suspension. The GO paper prepared in this way could be cut by using a razor blade. The papers were uniform, while they were dark brown under transmitted white light and almost black in reflection as the thickness was > 5 μm, as shown in Fig. 8.8a–c. SEM images revealed that the highly oriented nanolayers were closely packed through almost the entire cross section of the papers, with less densely packed "wavy" skin layers with thicknesses in the range 100–200 nm, as shown in Fig. 8.8e–g. The layered structure was also confirmed by XRD patterns. Layer-to-layer distance or *d*-spacing of the GO papers was about 0.83 nm, corresponding to the presence of one-molecule-thick layer of water interacting with the GO nanosheets through hydrogen bonding [112]. Average dimension of the ordered stack of GO nanosheets in the papers oriented perpendicularly to the diffracting plane was about 5.2 ± 0.2 nm, corresponding to 6–7 stacked GO nanosheets.

With three regimes of deformation in the stress–strain curves, i.e., straightening, almost linear (or "elastic"), and plastic, mechanical behavior of the GO papers was similar to that of most paper-like or foil-like materials, but had very high stiffness. Despite the presence of different levels of wrinkling and "waviness" in the GO papers at different length scales, the initial straightening during the tensile loading was not very pronounced. During the rupture of the GO papers that were loaded beyond the "elastic" regime, no pull-out of their lamellae was observed. Instead, nearly straight and flat fracture surfaces were formed, as shown in Fig. 8.8e–g. This was attributed to

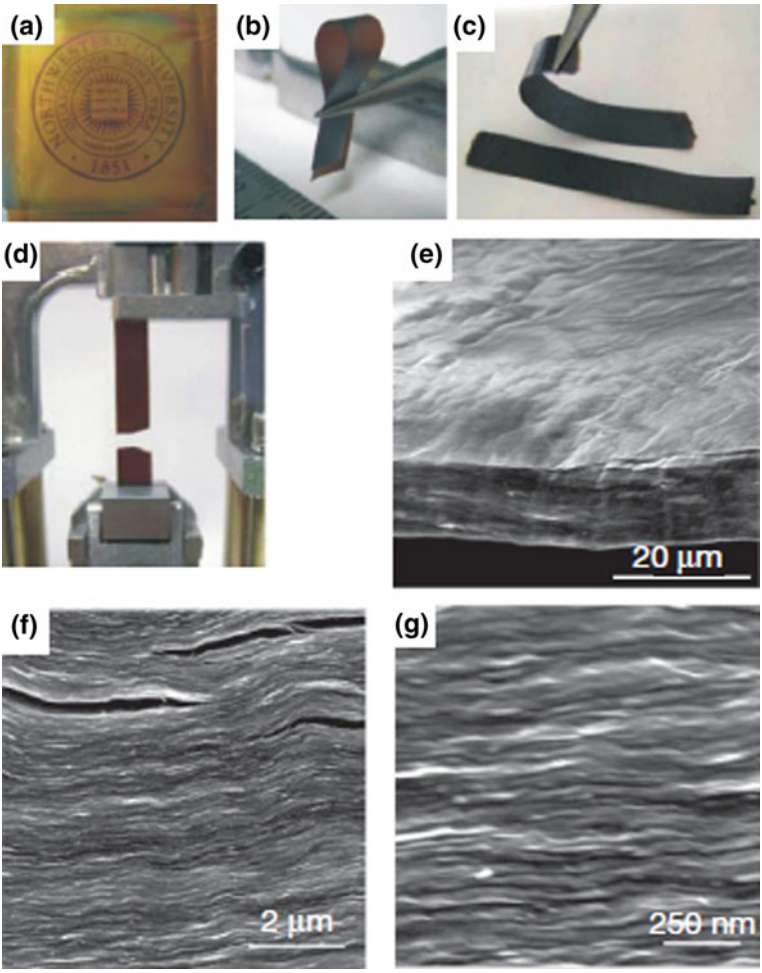

Fig. 8.8 Morphology and structure of the GO papers. **a**–**d** Photographs of the GO papers: **a** about 1-μm-thick film, **b** folded about 5-μm-thick semi-transparent film, **c** folded about 25-μm-thick strip and **d** strip after fracture after tensile loading. **e**–**g** Low-, middle-, and high-resolution SEM side-view images of the ~10-μm-thick papers. Reproduced with permission from [18], Copyright © 2007, Macmillan Publishers Limited

their high homogeneity and strong interlayer interaction. The GO papers exhibited an average modulus of 32 GPa, with the highest value to 42 ± 2 GPa.

Because GO papers are nonconductive, which cannot be directly used for some applications, e.g., electrodes of LiBs and supercapacitors, where high electrical conductivity is critical to maintain a high performance. As a result, it is desired to reduce GO papers into rGO papers. Various reduction methods have been employed to reduce GO papers, including hydrazine hydrate reduction [83],

photothermal reduction [113], supercritical ethanol reduction [106], and thermal reduction [114, 115].

Due to the highly conjugated structure, graphene and graphene-based materials have extraordinary electrical properties, which thus could be controlled by manipulating the degree of the in-sheet conjugation. This approach has been applied to graphene papers, whose conductivities could vary over a wide range of 0.001–100 S cm^{-1} [84]. The objective was achieved at the molecular level, through either covalent bonding or π–π stacking interactions by using either monofunctional or bifunctional molecules. Functional molecules, including monoaryl diazonium salts (MDS), bifunctional aryl diazonium salts (BDS), and bipyrene terminal molecular wire (BPMW), have been used for such a purpose. It was found that both MDS ad BDS led to a decrease in conductivity of the graphene papers, with BDS having a finer modification effect. In contrast, the graphene papers modified with BPMW had higher electrical conductivity that of the other two groups of samples.

Graphene papers consist of tightly stacked graphene nanosheets, thus leading to poor permeability, which could limit their applications where high permeability and tunable layer spacing are required. A simple method was developed to modulate the layer spacing of GO papers, by using the temperature-dependent decomposition reaction of ammonium nitrate (AN, NH_4NO_3) [85]. Different form the commonly used intercalation method, this approach could tailor the layer spacing of GO papers over a very large range of 123–20,000%, but without the presence of any guest molecules. With such a wide range of expansion amplitude, the GO papers could find various applications, such as highly efficient exclusion of small organic molecules, separation of ultrathin nanoparticles, and loading of polar and nonpolar guest molecules. Moreover, once the GO papers were reduced to rGO papers, with high electrical conductivity, the papers could be used for flexible paper-based electrochemical devices.

Besides wet-chemical exfoliated GO and graphene nanosheets, chemical vapor deposition (CVD)-derived graphenes have also been used to fabricate graphene papers by using vacuum membrane filtration [74]. The graphene papers from the CVD-derived graphene exhibited superior electrochemical performances, with a capacity of 1200 mAh g^{-1} at 50 mA g^{-1} as electrodes of supercapacitors and excellent cycling characteristics as anodes of lithium-ion rechargeable batteries. The CVD graphene nanosheets had a lateral size at the order of hundreds of micrometers, with a production at gram scale, by using a layered Fe containing natural mineral, expanded vermiculite, as template. Due to the large sheet size of the CVD graphene nanosheets, the obtained graphene papers were highly flexible with a loose stacking state. Moreover, graphene-carbon nanotube (G-CNT) hybrids could also be synthesized in just one step.

Graphene quantum dots (GQDs) have been proposed to be a stabilizer to achieve aqueous dispersions of graphene nanosheets [70]. GQDs have both special atomic structure and surface chemistry, with one- to few-layered graphene nanosheets that have a lateral dimension smaller than 100 nm [116–118]. Due to the 2D sp^2 carbon structure, GQDs are expected to be able to strongly attach to the basal plane of graphene nanosheets through van der Waals attractions, i.e., π–π stacking. Also,

GQDs contain same hydrophilic surface groups, such as carboxyl, hydroxyl, and epoxy groups, as GO, due to the similarity in their synthetic processing [119, 120]. Owing to the presence of these hydrophilic groups, GQDs have high solubility in water, so that they could promote the dispersion of the intrinsically hydrophobic graphene nanosheets. With the incorporation of GQDs, commercially available graphene powder could be well dispersed in water, which led to highly flexible and highly conductive graphene papers by using the vacuum filtration technique.

The graphene dispersions were prepared involving three steps: (i) dispersing graphene powder in GQDs solution, (ii) removing excess GQDs, and (iii) re-dispersing the graphene slurry. In this case, the presence of the GQDs played was a crucial requirement to stabilize the graphene nanosheets in water. There could be two mechanisms governing the enhanced dispersion of graphene. Firstly, the surface of the graphene was modified due to the absorption of the GQDs, so that the graphene nanosheets became to be negatively charged and thus electrostatically stabilized in water. Secondly, the GQDs were uniformly distributed to surround the graphene nanosheets, so that they were blocked from one another. As a consequence, agglomeration of the graphene nanosheets was effectively prevented.

Figure 8.9a shows a photograph of the free-standing graphene papers with a diameter of about 3.8 cm, which were highly flexible and bendable. A free-standing and bendable paper with a diameter of about 3.8 cm (Fig. 8.9a) was obtained after peeling off the membrane. Cross-sectional SEM images of the graphene papers are shown in Fig. 8.9b, c, at low- and high-magnifications. The graphene nanosheets were highly oriented in the plane of the papers, which suggested that the graphene nanosheets were deposited on the filter membrane in parallel direction. The completely dried graphene papers had apparent densities in the range 1.22–1.51 g cm^{-3}.

The presence of partially π–π stacking between the adjacent graphene nanosheets is confirmed by the XRD results, as shown in Fig. 8.9d. The graphene papers had a relatively strong peak at 23.7°, corresponding to plane spacing of d_{002} = 0.37 nm. Electric conductivity of the graphene paper was up to 7240 S m^{-1} at room temperature. It was found that the average conductivity was decreased from 7240 to 2506 S m^{-1}, as the content of the GQDs was increased from 7.0 to 28.8%. Therefore, the content of the GQDs in the graphene papers should be controlled at a sufficiently low level. For a graphene paper with a thickness of 18.0 μm, tensile strength, ultimate tensile strain, and Young's modulus were 91.2 MPa, 1.7% and 5.3 GPa, respectively. Therefore, this approach could be a new route to develop flexible graphene papers with controllable properties.

Graphene or GO papers have a nanoscale "brick-and-mortar" structure, in which the interaction between adjacent nanosheets could be mediated by intercalated solvents [121–123]. There have been reports on mechanical properties of the papers, together with strategies to improve their mechanical strength [121, 124]. However, in order to realize "materials design" for such special paper materials, it is necessary to clearly understand the formation mechanisms. As seen in the above discussion, vacuum membrane filtration has been the major technique to develop various G/GO papers, which involves the flow-directed assembly of graphene or GO nanosheets, as their suspensions are filtered over a supporting membrane.

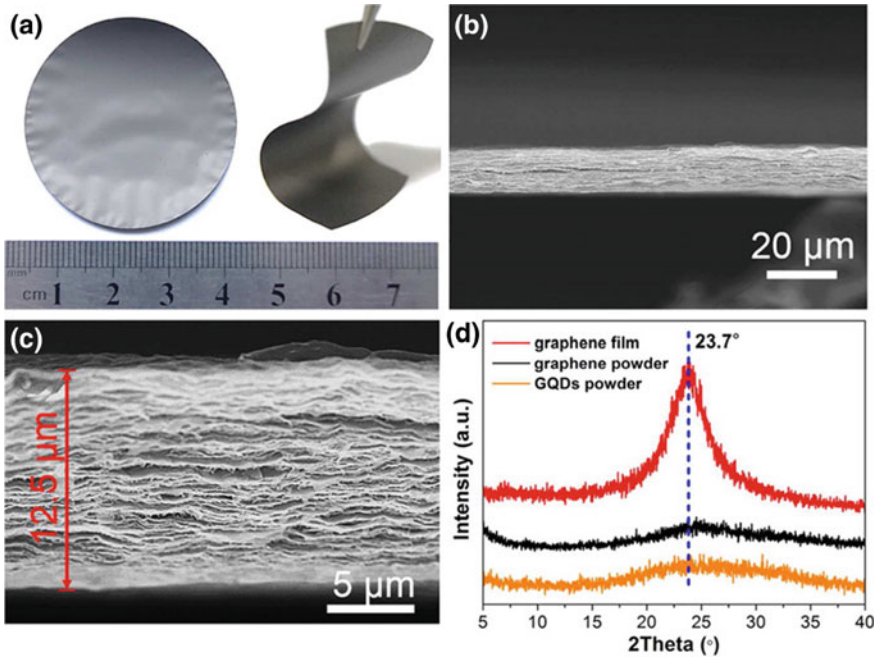

Fig. 8.9 **a** Photographs of the flexible graphene papers with metallic luster. **b**, **c** Low- and high-magnification cross-sectional SEM images of the graphene papers, illustrating the uniform thickness (12.5 μm) and layered structure. **d** XRD patterns of the graphene paper, graphene powder, and GQDs, with a peak observed for the graphene paper confirming the π–π stacking of the graphene nanosheets formed during the paper filtration process. Reproduced with permission from [74], Copyright © 2015, American Chemical Society

Obviously, the papers with well-aligned G/GO nanosheets are derived from suspensions in which all the nanosheets are entirely randomly distributed. Also, it has been observed that the layered structures could be swelled by several solvent molecules without destroying the layered structures [112, 125], while the swelling is reversible, i.e., after drying in air the original structures are completely recovered [69, 94].

It has been suggested that a gelation process of the graphene nanosheets took place at the solution–filter membrane interface during filtration, which was related to the formation of mechanically strong, highly conductive, and anisotropic graphene papers [50]. More importantly, various organic or inorganic components could be incorporated into the graphene papers to form composites or hybrids [126, 127].

In a separate study, three formation mechanisms have been considered to explain the wide range of possible ordering sequences during the fabrication of GO papers through vacuum membrane filtration [53]. In brief, they were two extreme cases, i.e., highly ordered layering and complete disordering, together with the cases in

between the two extreme two. At the highly ordered layering end, order structure was developed as the nanosheets were deposited. At the other end, the GO nanosheets were randomly distributed during the filtration process, until they were aligned due to the geometric confinement caused by the removal of the solvents. The third mechanism was known as semi-ordered accumulation, which resulted in the formation of loosely stacked nanosheets at surface of the filter membranes. During the removal of the solvents, the semi-ordered layers were transferred to layered structures, owing to the filtration-induced compression. Experimental results suggested that the semi-ordered accumulation mechanism has governed the formation of GO papers through vacuum membrane filtration.

8.3.2 Other Methods

8.3.2.1 Solvent Direct Evaporation

A direct solvent evaporation method was used to fabricate GO papers from GO suspension with mild heating [100]. The GO thin papers had an average thickness of about 8.4 μm, which exhibited excellent EMI shielding effectiveness of 20 dB and high in-plane thermal conductivity of 1100 W m^{-1} K^{-1}, as well as high mechanical flexibility and structure integrity withstanding repeated bending. Figure 8.10a shows a schematic diagram describing fabrication process of the GO thin papers through direct evaporation. GO suspensions were poured into Teflon dishes, which were heated gently at 50–60 °C to evaporate the water, so that flexible dark brown GO papers were formed. Obviously, thickness of the papers could be well controlled from microns to ten microns by controlling the volume and concentration of the GO suspensions. Also, this method has no limit in size of the GO papers. In this respect, it was advantageous over the vacuum membrane filtration method discussed above.

Figure 8.10b shows photograph of the GO paper with a dimension of about 400 cm^2 made simply by using a mold of that size. The GO papers were sufficiently flexible, so that they could be rolled and folded, as shown in Fig. 8.10c. SEM observations indicated that the GO papers had smooth with a few thin ripples, as shown in Fig. 8.10d. The multilayered structure was maintained through almost the entire cross sections, as shown in Fig. 8.10e, f, without difference from that of their vacuum filtration counterparts. During the evaporation of water, concentration of the GO suspensions was gradually increased, so that the sheet-to-sheet interactions were facilitated, thus leading to self-alignment of the GO nanosheets due to their relatively large lateral dimension.

The GO papers were thermally annealed at 2000 °C for further reduction and graphitization, which resulted in graphene papers (denoted as GF-2000) [128, 129]. The GF-2000 sample exhibited almost no variation in physical dimension as compared the as-obtained GO papers, whereas it became darker and black with a shiny metallic luster, as observed in Fig. 8.10c. Figure 8.10d shows SEM image of

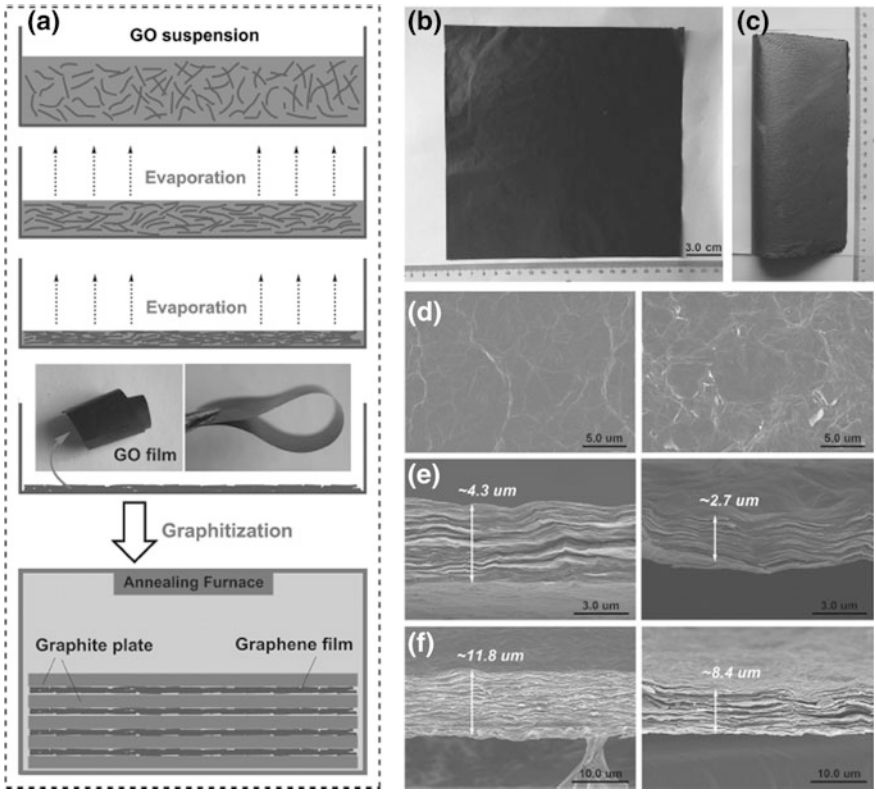

Fig. 8.10 **a** Schematic diagram of the self-assembly process to obtain the GO papers through evaporation and thermal graphitization treatment. The *inset* shows photographs of the flexible GO papers. **b** Photograph of the free-standing and dark brown GO paper with a dimension of 20 cm × 20 cm. **c** Photograph of the free-standing and shiny metallic GF-2000 (20 cm × 20 cm) folded on a paper. **d** Surface SEM images of the GO paper (*left*) and GF-2000 sample (*right*). **e**, **f** Cross-sectional SEM images of the GO paper and GF-2000 sample (with different thicknesses). Reproduced with permission from [100], Copyright © 2014, WILEY-VCH Verlag GmbH & Co. KGaA, Weinheim

the GF-2000 sample, indicating its smooth surface and the presence of ripples. Cross-sectional SEM images of the GF-2000 sample are shown in Fig. 8.10e, f, illustrating the highly oriented multilayer stacking of the graphene nanosheets. The thicknesses were decreased from 4.3 and 11.8 μm to 2.7 and 8.4 μm, respectively, due to the removal of the oxygen groups and water molecules.

8.3.2.2 Tape Casting

Most of the methods that have been available in the open literature to fabricate G/GO papers are limited only at the laboratory scale. Tape casting is a promising

candidate that can be used to address this problem, as demonstrated in a recent study [103]. Polymer graphene composite tapes were prepared first, while the polymer was subsequently removed through thermolysis, which led to large-scale graphene papers with a network structure. The graphene tapes exhibited high surface area, excellent electrical conductivity, and promising mechanical strength.

Figure 8.11 shows the process of tape casting, in which the colloidal suspension was cast through a slit by moving the substrate relative to a doctor blade. The graphene used in the tape casting should have sufficiently large quantities, which was produced through the simultaneous thermal exfoliation and reduction in GO powder. Besides the oxygen-containing functionalities as stated earlier, the graphene network contained lattice defects and vacancies, as shown in the inset of Fig. 8.11. The functionalized graphene nanosheets (FGSs) could be distinguished according to their oxygen contents, which was expressed as carbon-to-oxygen ratio (C/O in mol/mol). Wrinkles were formed on the graphene nanosheets, due to the presence of the defects and oxygen-containing groups, which decreased the contact area in between the adjacent graphene nanosheets and also prevented the re-stacking. This happening could be an advantage for applications that require high surface area. Moreover, chemical activity of the FGSs was increased because of the defect sites and the functional groups, which could find applications in electrochemical sensors, catalysts, and fuel cells.

To fabricate graphene tapes with high surface areas by using the tape casting method, the pre-requirement was to prepare highly dispersed suspensions of FGSs. A triblock copolymer surfactant (ethylene oxide)$_{100}$-(propylene oxide)$_{65}$-(ethylene oxide)$_{100}$, or $EO_{100}PO_{65}EO_{100}$ in short, was used to disperse the FGSs in water. The amount of the surfactant needed to disperse the nanosheets was determined according to the concentrations of the FGSs in the supernatant of suspensions containing different amounts of surfactants, which were compared with the initial overall suspension concentrations. The amount of FGSs in the supernatant was increased with increasing concentration of the surfactant, corresponding to a

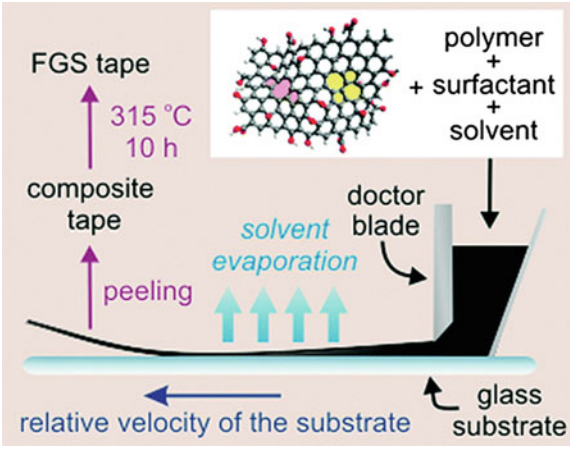

Fig. 8.11 Schematic diagram describing the fabrication of the FGS tapes with tape casting. The FGS schematic shows defective and wrinkled structure of the graphene nanosheets. Oxygen functional groups are shown in *red*, with a 5-8-5 defect in *pink* and a 5-7-7-5 defect in *yellow*. Reproduced with permission from [103], Copyright © 2011, American Chemical Society

continuous enhancement in stability of the suspensions. As the surfactant-to-FGSs ratio reached 1 (g/g), the concentration of the FGSs was saturated, implying that they were sterically stabilized suspensions, i.e., the suspension stability was increased as the surface coverage of the particles increased [130].

Hydrophobic PO chains of the $EO_{100}PO_{65}EO_{100}$ molecules were adsorbed on surfaces of the graphene nanosheets, while their hydrophilic EO chains were extended into water [131]. Due to the high solubility of EO in water, the EO chains with strong repulsive interaction among themselves acted as a barrier which prevented the FGSs from aggregation. As the surfactant molecules could not fully cover the FGSs, the strong van der Waals forces would bring them together to form aggregation. Once the FGSs were entirely covered by the surfactant molecules, their dispersion concentration would be saturated. The decrease in supernatant concentration over time implied the sedimentation of the FGSs in the suspensions. This result suggests aggregation of FGSs. This observation was mainly attributed to the van der Waals interactions if the weakly adsorbed surfactant molecules were desorbed. Because the time used for both the tape casting and drying processes was sufficiently short, and the negative effect of desorption of the triblock copolymer from the FGSs was not observed.

Besides the requirement of high-quality dispersions during the casting process, the suspensions should also have a good flowing behavior to pass through the gap between the blade and substrate under shear, as shown in Fig. 8.11. At the same time, the shape and thickness of the cast tape should be maintained as the shearing force disappeared after passing through the blade. Although these behaviors are closely related to the properties of the suspensions, effects of the substrate wettability and the contact line pinning are also significant to a certain degree. It was found that, under the shear rates used in the casting, i.e., about 100 s^{-1}, the suspensions indeed exhibited shear thinning behavior. This was simply because both the PEO solutions and the FGS suspensions had shear thinning behavior, owing to the disentanglement of the PEO molecules, the break-up of the FGS network, and the shear-induced orientation of both the FGSs and the PEO molecules [132, 133].

Viscosities of the FGS tape casting suspensions were variable over one order of magnitude at a given strain rate. The higher the concentration of FGSs, the lower the viscosity that suspensions would have. The viscosity was also increased with increasing content of PEO, so that the PEO solution with higher viscosity could be used as a thickening agent to adjust viscosity of the suspensions. As the shear rate was decreased from 100 to 1 s^{-1}, the viscosity of the suspension required 1–2 s to return. As a result, the viscosity of the suspensions was increased suddenly in several seconds when they were cast. If nonwetting substrates were used, the contact line could not be effectively pinned [134]. Consequently, the suspension would be pulled away from the substrate, thus being condensed into a formless puddle. Therefore, it is necessary to use wetting substrates to maintain the shape of tapes during evaporation of the solvents.

8.3.2.3 Electro-spray Deposition

Another approach to large area free-standing graphene papers is called direct electro-spray deposition (ESD), by combining a continuous roll-to-roll process and simple water exfoliation from highly hydrophilic aluminum substrates [104]. ESD has been widely used to deposit various thin films, because of its advantages, such as mass scale capacity, less material loss, and high precision of property controlling [135–137]. Charged mono-dispersed fine droplets are generated due to the repulsion forces among them. Size of the droplets can be well controlled by adjusting the flow rate and electric field applied to the injection nozzles and substrates, with smallest diameter to be hundreds of nanometers. The graphene papers fabricated in this way can have a wide range of thickness from hundreds of nanometers to hundreds of micrometers. They can be deposited on various substrates [138, 139].

The assembly and alignment of the graphene nanosheets in the final papers could be well controlled by controlling the ESD processing parameters and further improved through mechanical compaction upon water exfoliation. In addition, thermal annealing was employed to heal the structural defects and remove the functional groups in the graphene nanosheets, so that their thermal and electrical properties were further improved [140, 141]. It was found that the optimal thermal annealing temperature was 2200 °C, which led to defect-free, highly aligned, and light-weight (density ≈ 2.1 g cm^{-3}) graphene papers. The annealed graphene papers exhibited thermal and electrical conductivities of 1238.3 W m^{-1} K^{-1} and 1.57×10^5 S m^{-1}, respectively.

Well-dispersed graphene suspensions were used to deposit the graphene papers by using the ESD process. During the deposition, an electric voltage of 11.5 kV was applied between the injection nozzle and substrate which were separated by 2–3.5 cm to maintain a stable cone-jet mode. The graphene suspension was pushed through the nozzle at flow rates of 50–100 μl min^{-1}, by using a syringe pump, so as to generate well-dispersed fine droplets that were then deposited on the heated substrate to form a uniform film. By controlling the solution concentration and the time of deposition, films with desired thicknesses would be readily obtained. After deposition, the Al foils coated with the graphene films were immersed into water, so that free-standing graphene papers were peeled off from the substrate, as shown in Fig. 8.12a–g. The graphene papers had well-retained geometry without visible fracture.

Due to the difference in surface properties and wettability, the graphene papers could be easily peeled off from the Al foils. The Al foil was more hydrophilic than the graphene papers, as shown in Fig. 8.12j, k. When the graphene-coated Al foils were immersed in water, water molecules could penetrate the graphene films to reach the Al-graphene interface. Therefore, wet films were at the interface between the graphene layers and the hydrophilic Al substrate, so that the graphene papers were obtained when they were separated from the Al substrate.

The ESD system could be integrated with a continuous roll-to-roll process [104]. Graphene strips and graphene rolls could be produced by using the integrated system. Although the large area free-standing graphene papers were derived

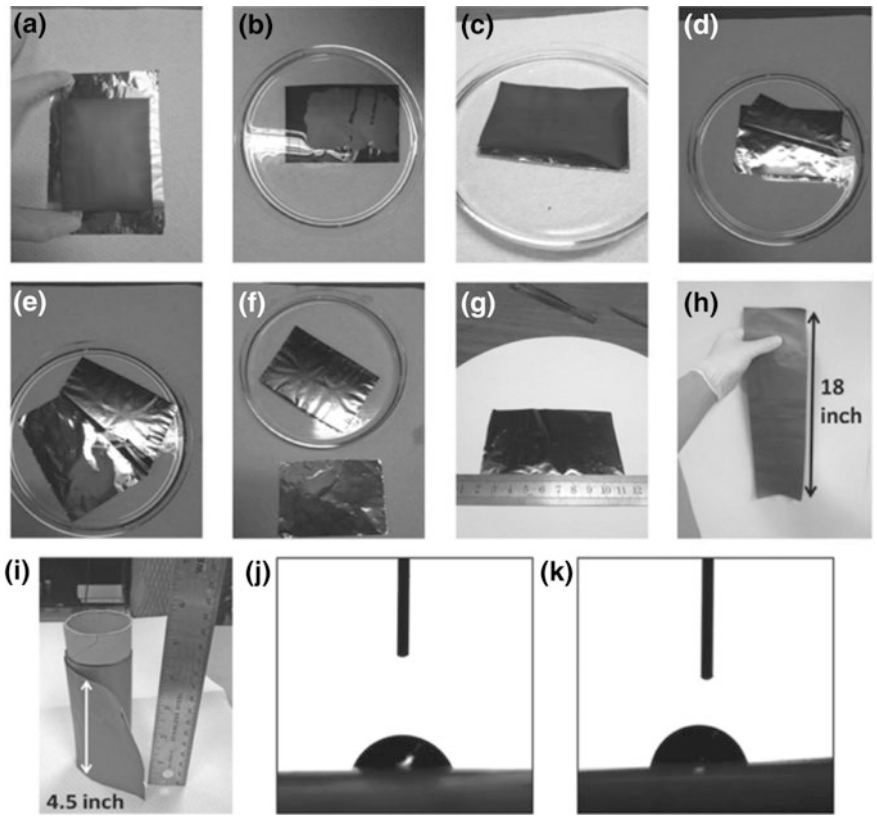

Fig. 8.12 **a** Electrospray deposited (ESD) graphene films on Al foils. **b–f** Photographs of the samples immersed in water for different time durations: **b** 30 s, **c** 2 min, **d** 4 min, **e** 7 min, and **f** 9 min. **g** Photograph of a graphene paper (9 × 6 cm^2) peeled off from the Al foil and dried at room temperature. **h**, **i** Photographs of a 18 in. graphene paper strip (**h**) and a paper roll with 4.5 in. width (**i**) made by using the ESD integrated with roll-to-roll process. **j**, **k** Contact angle measurements of the Al substrate (64°, **j**) and the graphene paper (78°, **k**). Reproduced with permission from [104], Copyright © 2014, WILEY-VCH Verlag GmbH & Co. KGaA, Weinheim

without using polymer binders, they had pretty high flexibility, so that they could be rolled without the presence of visible damage, as shown in Fig. 8.12h, i. Due to their high flexibility, the graphene papers could be processed into different shapes, with desired dimensions and geometries.

8.3.2.4 Interface Self-Assembly

Interface-induced self-assembly is also a promising method to construct graphene papers [142–145]. In this respect, the amphiphilic characteristic of GO nanosheets is beneficial to form an oriented packing at the liquid–air interface. As the thickness

is sufficiently large, free-standing GO papers could be obtained. This method has several advantages. Firstly, it is time saving and low energy consuming. For example, the GO membranes could be formed within 1 h. In contrast, the vacuum filtration method needs to take hours or even days to achieve similar thickness. Secondly, the GO suspensions could be repeatedly used, as long as the concentrations meet the requirement of membrane formation. Therefore, this process is sustainable and thus cost-effective. Thirdly, the thickness can be readily controlled by controlling the assembly time duration, while the size of the membrane simply determined by the area of the liquid–air interface, i.e., the dimension of the reactors.

A facile self-assembly approach has been reported to obtain macroscopic GO membranes at a liquid–air interface by evaporating GO hydrosols [142]. In the experiment, 200 ml GO suspension in water with a concentration of 2 mg ml^{-1} was treated ultrasonically for 30 min, followed by high-speed centrifugation at 5000 rpm for 20 min to remove impurities, as shown in Fig. 8.13a. By heating a stable hydrosol of GO to 353 K, a smooth and condensed GO thin film was formed at the liquid–air interface, as shown in Fig. 8.13b. Further drying and reduction

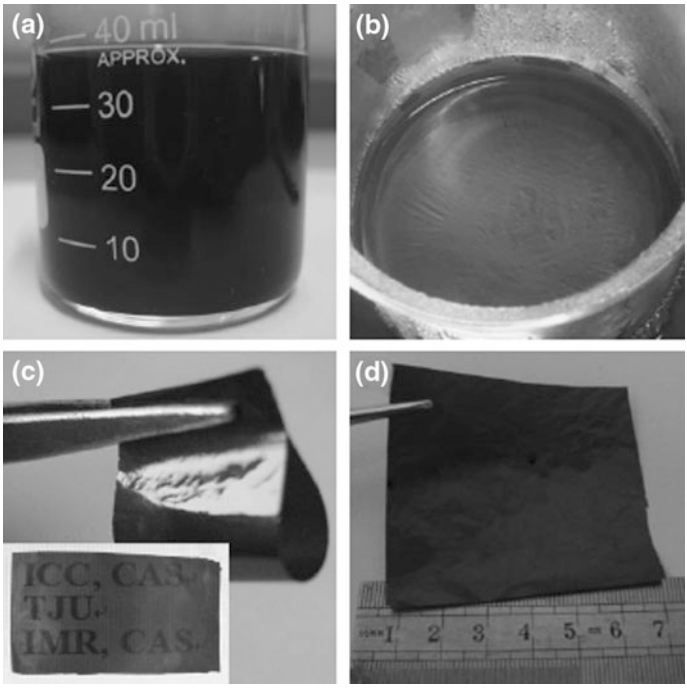

Fig. 8.13 **a** Photograph of the GO colloid suspension with a concentration of 2 mg ml^{-1} kept stable for two weeks. **b** A film self-assembled at the liquid–air interface after heating at 80 °C for 15 min. **c** Photograph of a flexible and semi-transparent GO paper (15 mm × 30 mm). **d** Photograph of a large-area (about 60 mm × 60 mm) GO paper. Reproduced with permission from [142], Copyright © 2009, WILEY-VCH Verlag GmbH & Co. KGaA, Weinheim

treatment yielded a flexible, semi-transparent, and free-standing graphene papers with thicknesses in the range 0.5–20 μm, which could be tailored by controlling the evaporation time of the hydrosol, as shown in Fig. 8.13c. For example, GO papers with thicknesses of 5 and 10 μm were obtained after heating for 20 and 40 min, respectively. The size of the flexible GO paper was only limited by the area of the liquid/air interface, so that large papers could be easily obtained by using large reaction vehicles (Fig. 8.13d).

As the hydrosol was heated, Brownian motion of the GO nanosheets was sped up in the suspension. Due to the evaporation of water, the liquid level of the hydrosol gradually decreased, so that collision and interaction among the GO nanosheets became more frequently and stronger. As a result, they migrated up to the liquid–air interface as the water molecules escaped from the hydrosol. The liquid–air interface offered a smooth space to host the 2D GO nanosheets. As the GO nanosheets reached the interface, they tended to aggregate to form a multi-layered structure. This layer would become thicker and thicker, as new GO nanosheets were transferred near to the interface and accumulated, due to the strong interlayer van der Waals interactions. XRD results indicated that the average thickness of the ordered stack was 8.2 ± 0.1 nm, implying that the stacking structure consisted of 10–11 layers of graphene oxide nanosheets. Finally, macroscopic membranes with a thickness of several micrometers were developed over the whole liquid–air interface.

8.3.2.5 Chemical Vapor Deposition (CVD)

A chemical vapor deposition (CVD) process was used to fabricate graphene papers [110]. Firstly, graphene pellets were synthesized by the CVD method, with inexpensive nickel powder as the catalyst. The graphene pellets were then processed into graphene papers by using mechanical pressing. The graphene papers exhibited high electrical conductivity of up to 1136 ± 32 S cm^{-1} and a breaking stress at 22 ± 1.4 MPa. Moreover, the graphene paper with a thickness of 50 μm demonstrated 60 dB electromagnetic interference (EMI) shielding effectiveness.

Nickel powder with average particle size of 2–3 μm and specific surface area of 0.68 m^2 g^{-1} in was pressed into pellets of 6.4 cm in diameter. The nickel pellet was placed on a quartz platform inside a quartz tube to grow graphene nanosheets by using CVD. The nickel pellet was heated up to 1000 °C in a tube furnace in Ar (1000 sccm). H_2 (325 sccm) was then purged into the tube for 15 min, to eliminate any metal catalyst oxide. After that, CH_4 was introduced for 5 min. Various hydrocarbon flow rates were tested, including 12, 15, 18, 25, and 28 sccm, corresponding to concentrations of 0.9, 1.1, 1.3, 1.9, and 2.1 vol%, respectively. The furnace was then cooled to room temperature at a rate of 100 °C min1 in Ar (1000 sccm) and H_2 (325 sccm). The nickel pellet was shrunk by about 30% after the CVD synthesis. The final 3D graphene structure in the form of the pellet was obtained by etching out the nickel from the graphene–nickel pellet with HCl (3 M) at 80 °C for 10 h. The graphene pellet was washed with water to remove residual

acid and dried at room temperature. Graphene paper was obtained by compressing the graphene pellet with a presser between two flat steel plates. Thickness of the graphene papers was controlled by controlling the compression load.

Another example of CVD processing is the development of freestanding, flexible, and transparent graphene paper (FFT-GP) from prism-like graphene (PLG) building blocks [111]. This freestanding paper possessed a large-area PLG structure, which could be transferred onto any other substrates. The PLG building blocks were connected in a face-to-face way and homogeneously aligned on silicon substrates. A single piece of FFT-GP were both highly transparent and flexible. It also maintained the electrical and physical properties of 2D graphene nanosheet, i.e., high electrical conductivity and large surface area. Such FFT-GP could find potential applications in transparent and stretchable supercapacitors.

8.4 Graphene 3D Monoliths

8.4.1 Solution Processes

For practical applications, small graphene nanosheets usually need to be constructed or assembled into macroscopic materials [146–151]. However, due to the extremely large aspect ratio, graphene nanosheets tend to aggregate or restack into the graphitic structure as they are brought together, which has been a critical issue encountered in this process. If these problems cannot be addressed, the advantageous structures and properties of graphene nanosheets cannot be well utilized as macroscopic materials. Therefore, it has been widely accepted that integration of 2D graphene nanosheets into 3D macroscopic structures, such as porous films, scaffolds, and networks, is the first step toward high-performance graphene-based materials in terms of their practical applications [10–13, 152]. In this section, the main strategies that have been used to 3D graphene architectures will be summarized.

8.4.1.1 Gelation of GO

According to polymer science and physical chemistry, CMGs are 2D amphiphilic-conjugated polyelectrolytes that consist of hydrophobic basal planes attached with hydrophilic oxygenated functional groups [153]. There is a hydrophilic–hydrophobic balance between the interplanar van der Waals force and the electrostatic repulsion, which determines the properties and thus their self-assembly behaviors of the CMGs solutions or suspensions. As discussed previously, in general, GO is soluble in water, while graphene (or rGO) nanosheets are insoluble. However, it has been found that rGO aqueous dispersion was stable at certain concentrations [154]. For example, there was a critical concentration of 0.5 mg ml^{-1}, below which stable

rGO solutions were obtained, while gelation occurred once the concentration was above this critical value. Currently, solution-based self-assembly, following the principles of colloid chemistry, has been one of the most versatile techniques reported in the open literature to develop 3D graphene architectures with hierarchical structures and special properties [152].

Gelation of GO dispersions has been acknowledged to be a simple yet feasible approach to fabricate porous 3D GO networks [155–162]. As stated earlier, GO nanosheets soluble in water due to the edge-bound carboxyl moieties, together with the large amount of hydrophilic epoxy and hydroxyl groups on their basal planes [163]. GO stable aqueous dispersion can reach concentrations of up to 10 mg ml^{-1} [164].

To promote the gelation of GO nanosheets in water suspension, various additives have been explored. One example is poly(vinyl alcohol) (PVA), which is water soluble and a widely available polymer [155]. It acted as a cross-linking agent to boost the interactions of the 2D GO nanosheets, so as to enhance the GO gelation. GO/PVA hybrid hydrogels could be derived from the mixtures of GO and PVA aqueous solutions, which were heavily shaked for 10 s and then sonicated for 20 min. The strong hydrogen bonding interaction between the hydroxyl-rich PVA chains and oxygen-containing groups on the GO nanosheets facilitated the formation of the cross-linking between the two species. Because the number of cross-linking sites was sufficiently large, stable GO composite hydrogels were produced by forming GO networks.

The gelation process was strongly influenced by the concentration of the cross-linking agent used in the experiments. GO/PVA mixtures containing 5 mg ml^{-1} GO and PVA with various weight ratios, $r_{P/G}$, were studied. For PVA, there were low critical gelation concentrations and high critical gelation concentrations. A small amount of PVA, i.e., $r_{P/G}$ = 1:20, would be able to significantly increase the viscosity of the GO solution. For the GO/PVA mixtures with 5 mg ml^{-1} GO, the gelation was only observed as the $r_{P/G}$ was in the range between 1:10 and 1:2. Further increasing the PVA content would facilitate a gel–sol transition. As $r_{P/G}$ = 1:1, viscosity of the GO/PVA mixture was close to that of pure GO solution. This observation implied that the interactions between the GO nanosheets and the PVA molecules were different in the mixtures with low and high PVA concentrations.

Pure GO, GO/PVA mixed solutions, and typical gels were lyophilized for morphological study. The freeze-dried sample derived from the 5 mg ml^{-1} GO retained its original shape and volume, while the sample from the 1 mg ml^{-1} GO demonstrated an obvious shrinkage caused by the lyophilization. Therefore, the 5 mg ml^{-1} GO suspension was like a semi-diluted solution, so that the GO volume fraction was sufficiently large to form a GO network, after all water was removed.

Figure 8.14a shows SEM image of the GO network of sheets. Similarly, all the samples with PVA could retain their volumes after the lyophilization process. If only a small amount of PVA was added into the GO solution, e.g., $r_{P/G}$ = 1:20, the morphology of lyophilized sample was not changed, i.e., the GO nanosheets were in extended states, as shown in Fig. 8.14b. The lyophilized gel derived from the

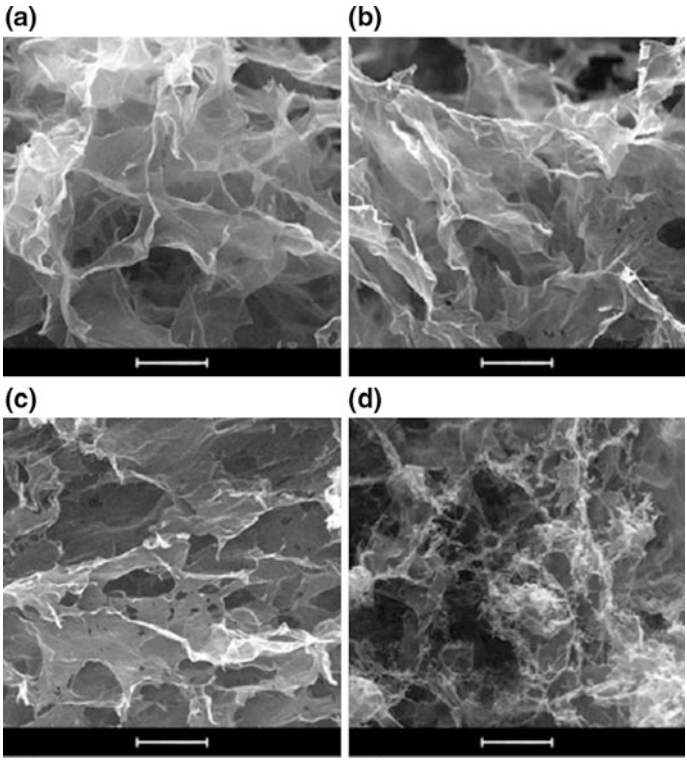

Fig. 8.14 SEM images of lyophilized 5 mg ml^{-1} GO (**a**) and GO/PVA blends (**b**–**d**) with different ratios $r_{P/G}$: **b** 1:20, **c** 1:5 and **d** 1:1. Scale bar = 5 μm. Reproduced with permission from [155], Copyright © 2010, The Royal Society of Chemistry

mixture with $r_{P/G}$ = 1:5 had a similar morphology, as shown in Fig. 8.14c. As the $r_{P/G}$ was increased to 1:1, the sample would have a different morphology after lyophilization, as shown in Fig. 8.14d. There were wire-like structures in the sample, implying that the GO nanosheets were rolled up either in the solution or during the lyophilization process.

There have been other cross-linkers for GO gelation, such as DNA [156], protein [158], synthetic polymers with cationic charges and hydrogen bonding acceptors [157, 160], small quaternary ammonium salts, and metal ions [157], through regulating the balance between the electrostatic repulsion, hydrophobic interactions, and hydrogen bonding of GO-based colloidal suspensions. In this regard, DNA is an important category of biological building blocks, which could be used to noncovalently functionalize or promote the assembly of GO nanosheets. In GO/DNA composite assemblies, single-stranded DNA (ssDNA) chains flatly would lay on surface of the GO nanosheets through π–π stacking interactions [165–167]. A simple and efficient approach was developed to trigger 3D self-assembly of GO nanosheets into multifunctional hydrogels by using in situ-formed ssDNA chains

[156]. The GO/DNA composite self-assembled hydrogels (GO/DNA SH) had a high water content of 99%. They were mechanically strong, had self-healing ability, and showed high environmental stability and dye-loading capacity.

A strategy has been developed to obtain ultralight chemically converted graphene aerogels with high compressibility [168]. In order to prevent the restacking of graphene nanosheets during the assembly progress, a functionalization-lyophilization-microwave treatment approach was strategically adopted. GO nanosheets were functionalized in a controllable way, which were then assembled into monolithic functionalized graphene hydrogel (FGH) in ethylenediamine (EDA) aqueous solution. Finally, microwave irradiation (MWI) was employed to remove the functional groups, in order to produce ultralight graphene aerogel (ULGA) that exhibited outstanding elasticity. Such aerogel could find potential applications in the areas of energy dissipation and vibration damping.

Figure 8.15a shows the synthesis steps of the graphene aerogel with extremely low density. Firstly, a basic and weak reducing agent, i.e., EDA, was mixed into the GO colloidal solution to realize the functionalization of the GO nanosheets, so that would self-assembly into 3D network. The GO suspension initially became black, then turned into sticky, and finally converted into hydrogel, as shown in Fig. 8.15b. It was observed that the final hydrogel experienced almost zero volume shrinkage after gelation. After the lyophilization process, functionalized graphene aerogel (FGA) was derived from the FGH by removing all the solvent. The FGA was further treated with MWI, thus leading to ULGA. After being treated with MWI, the aerogel had change in color from black to metallic gray, while the 3D network was

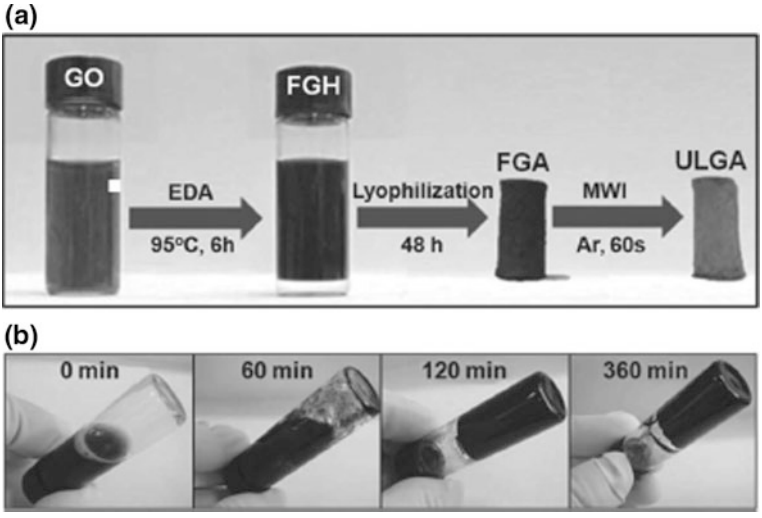

Fig. 8.15 **a** Illustration of the fabrication process of the ultralight graphene aerogel (ULGA). **b** Photographs of time-dependent formation process of the functionalized graphene hydrogel (FGH). Reproduced with permission from [168], Copyright © 2013, WILEY-VCH Verlag GmbH & Co. KGaA, Weinheim

well retained, which implied that the ULGA was sufficiently strong to survive the MWI treatment. It was readily attributed to the strong interconnection of graphene nanosheet building blocks.

A special synthetic route was devised to fabricate 3D GO hydrogels and aerogels, through self-assembly of 2D GO nanosheets that were cross-linked by using layered double hydroxides (LDHs) [169]. Recently, LDHs have formed a new class of multifunctional materials, with inorganic nanolamellar and positively charged frameworks, which have found various potential applications [170–175]. The LDH + GO hydrogels were fabricated through a one-step method, without using any hydrothermal processing or other additives. With an optimal ratio of organic and inorganic components, the Mg–Al LDHs served as a cross-linking agent, which effectively suppressed the restacking of the GO nanosheets. Instead, uniformly cross-linked GO nanosheets were assembled into 3D network structures, through various interactions, including strong hydrogen bonds and relatively weak electrostatic and cation–π interactions. The GO-based hybrid aerogels possessed strong hydrophilic behaviors and demonstrated extraordinary structural stability in aqueous solutions, thus making them for potential applications as absorbents. As a consequence, the LDH + GO hybrid aerogels exhibited strong capability to remove dyes and heavy metal pollutants from water. Due to their well-retained 3D monolithic structures, they could be easily separated, recovered, and reused.

Two sets of experiments were conducted to synthesize the LDH + GO hydrogels. In the first experiment, the amount of LDH powder was controlled at 5 mg ml^{-1}, while concentration of the homogeneous GO suspension was decreased from 5 to 1 mg ml^{-1}, so that five samples were obtained with LDH:GO ratios of 1:1, 2:1, 3:1, 4:1, and 5:1. In the second experiment, the GO concentration was fixed at 5 mg ml^{-1}, whereas the concentration of the LDH was increased from 1 to 5 mg ml^{-1}, which also led to five samples, with LDH:GO ratios of 1:5, 1:4, 1:3, 1:2, and 1:1. Once the LDHs wereadded to the GO suspensions, the mixtures were heavily shaken for homogenization and then sonicated for 1 h. The mixtures were kept at room temperature for 1 h to obtain LDH + GO hydrogels, as 3D dark-brown monoliths, which were further freeze-dried to form LDH + GO aerogels.

Figure 8.16 shows representative SEM images of the hydrogels, indicating that they consisted of porous randomly oriented 3D GO frameworks. Micro-scale morphology of the LDH + GO aerogels had a close relation to the concentration of the LDHs. It was found that the higher the concentration of the LDHs, the larger the assembled GO layers would be. For example, the pure GO aerogels contained numerous smaller GO pieces with small-sized fractals, whereas the presence of the LDHs obviously led to larger pieces, and the size was increased with increasing amount of LDHs. For instance, in the 1:1 LDH + GO aerogel, large pieces of flat sheets were observed. Therefore, it could be concluded that the LDHs had played an important role in assembling of the GO nanosheets into hydrogels with strong 3D network structures.

Additive-free GO hydrogels have been prepared by tuning pH value [157] and using ultrasonication of the GO aqueous suspensions [159]. As mentioned earlier,

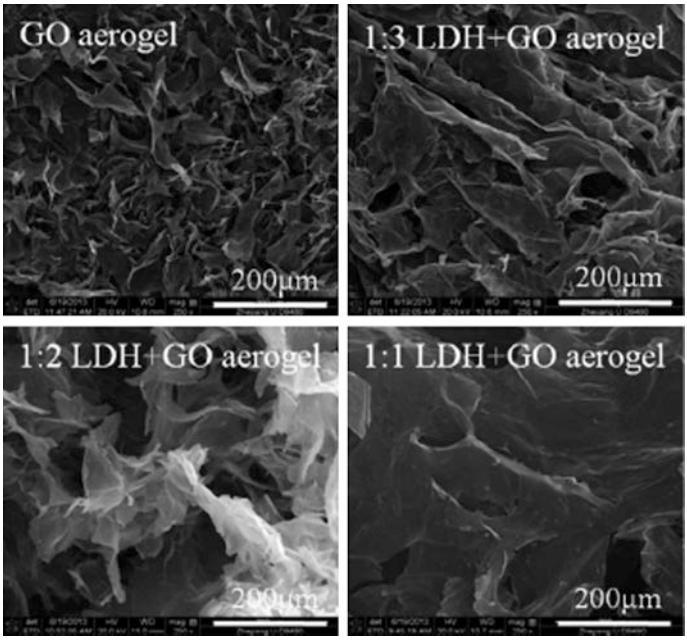

Fig. 8.16 SEM images of the pure GO aerogel and LDH + GO aerogels with various ratios of LDH and GO. Reproduced with permission from [169], Copyright © 2014, The Royal Society of Chemistry

the ionized carboxyl groups on the edges allowed the GO nanosheets to be dispersed in water through the electrostatic repulsion among them. In this case, acidification of the GO suspension would weaken the repulsion force, owing to the protonation of the carboxyl groups. It has been confirmed that GO nanosheets became unstable in a strong acidic aqueous environment, due to the insufficient mutual repulsion forces [157, 176]. As the GO concentration was sufficiently high, hydrogel could be formed, instead of the presence of an amorphous precipitation [157]. More recently, it was found that ultrasonication could be used to convert aqueous GO suspensions into hydrogels, which had much smaller channels as compared with the aerogels derived from the parent GO suspension [159]. The sonication fractured the GO aggregates into smaller fragments, so that new sheet edges were present, but without the stabilizing carboxyl groups. This surface chemistry change triggered the gelation of the GO suspensions. More importantly, such GO hydrogels exhibited very low critical gelation concentrations (CGC), in the range 0.050–0.125 mg ml^{-1}, which was dependent on the power of the ultrasonic treatment.

Purified GO aqueous suspensions (50 ml) were diluted to concentration of 2 mg ml^{-1} and sonicated with a probe sonicator set at 30% amplitude with alternating pulse and rest periods of 10 s each for different time durations (30–120 min). GO nanosheets are electrostatically stable in water due the edge-bound carboxylic

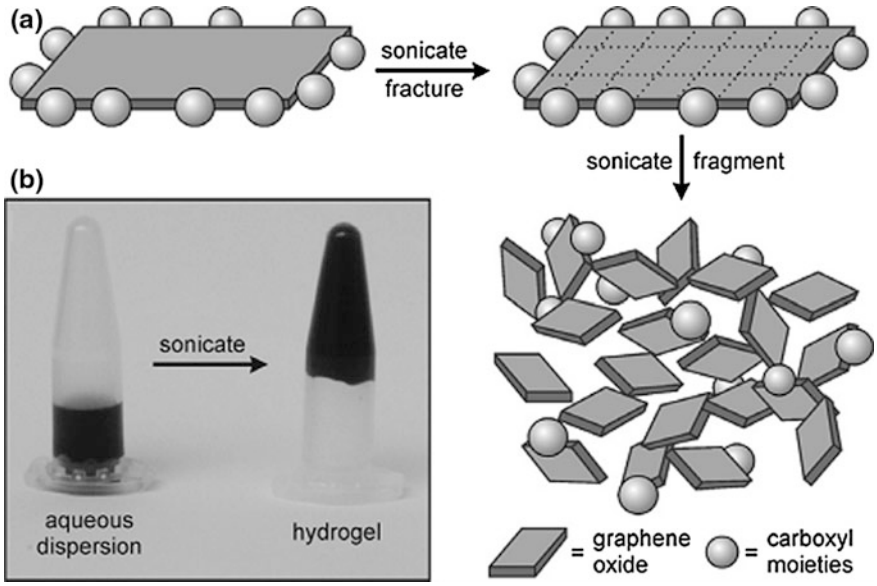

Fig. 8.17 **a** Schematic diagram illustrating the fracture and fragmentation of the GO nanosheet due to the ultrasonication, thus decreasing the coverage of carboxyl moieties (*spheres*) at the edges of the GO nanosheet fragments responsible for the gelation. **b** Photograph demonstrating the conversion of the GO aqueous suspension (*left*) into hydrogel (*right*) after the sonication treatment. Reproduced with permission from [159], Copyright © 2012, Elsevier

acid moieties. The aqueous dispersibility of GO nanosheets can be further enhanced by oxidizing the hydroxyl moieties into carboxyl groups on the basal planes. It was hypothesized that fracturing of the GO nanosheets to smaller fragments without the carboxylic acid groups along their freshly exposed edges would lead to decrease in dispersion capability, while irreversible aggregation was not induced, as shown in Fig. 8.17a.

After ultrasonication for 30 min, the dilute GO aqueous dispersion of 2 mg ml^{-1} was gelated, as shown in Fig. 8.17b. Dynamic light scattering (DLS) results indicated that average hydrodynamic diameter of the GO nanosheets was decreased from 590 to 250 nm after the ultrasonic treatment. As the sonication duration was increased to 120 min, stronger gel was formed. At the same time, hydrodynamic diameters of the GO nanosheets were further decreased to 80 nm. Although the lateral dimension of the GO nanosheets was decreased due to the ultrasonic treatment, zeta potentials of the GO suspension and the resultant hydrogels were kept almost constant at 56 ± 4 mV, which was still above the value of 30 mV required to prevent particle aggregation [154]. This suggested that the ultrasonic treatment caused negligible loss of the negatively charged functional groups. Therefore, it was more likely that the gelation was attributed to the fragmentation of the GO nanosheets that created new unfunctionalized edges which destabilized the suspensions.

In addition to the reduction in lateral size, surface chemistry of the GO nanosheets was also altered by the sonication treatment, which could be another factor to trigger the gelation of the suspensions. However, spectral characterization results, including XPS, FT-IR, and NMR, indicated that no obvious change was observed in chemical composition of GO after sonication for 120 min. This further confirmed that the destabilization of the GO nanosheets was caused by reduced carboxyl coverage at the edges of the newly formed fragments. Driving forces for the gelation included van der Waals attraction, hydrogen bonding between the functional groups, and π–π stacking of the residual sp^2-hybridized regions on the GO nanosheet basal plane. The hydrogels were fragile in nature, suggesting the weak balance between the hydrophobic interactions and hydrogen bonding.

8.4.1.2 Centrifugal Evaporation-Induced Assembly of GO

Vacuum centrifugal evaporation has been demonstrated as a strategy to fabricate additive-free GO hierarchical structures [177]. It can be used produce large-scale GO sponges with a 3D interconnected network structure. The combination of vacuum evaporation and centrifugal force sped up the solvent evaporation while retaining the sample shape and morphology due to the effect of foaming or bumping. Once 1 ml GO colloidal suspension was formed in 2 ml Eppendorf tube (Fig. 8.18a), evaporation process was initiated in a speed vacuum concentrator, so that possible sedimentation of the GO nanosheets was effectively prevented.

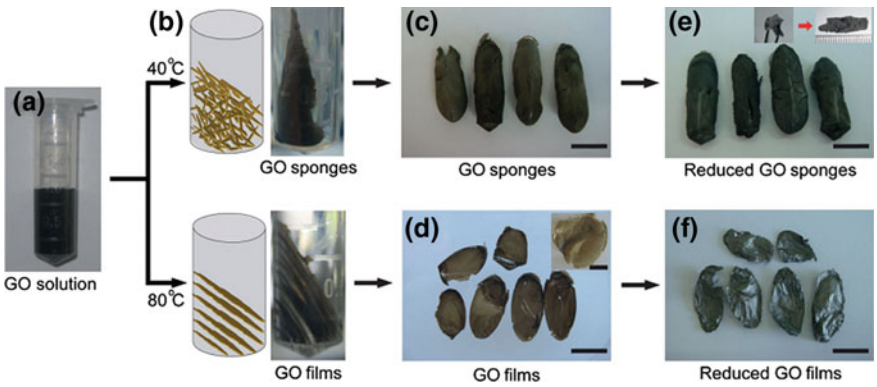

Fig. 8.18 Synthetic process of the fabrication of GO sponges and thin sheets by using the rapid vacuum centrifugation. **a** 1 ml GO solution (3 mg ml^{-1}) in a 2-ml microtube. **b** Schematic diagram showing production of the GO sponges and films at different temperatures, each with a photograph of the sample. **c** Photographs of GO sponges. **d** Free-standing GO thin sheets, with the *inset* showing photograph of the GO thin sheet with diameter of 3 cm. **e** Photographs of the rGO sponges derived from the GO sponges after thermal annealing in H_2/Ar at 800 °C for 12. **f** Free-standing graphene thin sheets. Scale bars = 1 cm (**c**–**f**). Reproduced with permission from [177], Copyright © 2010, WILEY-VCH Verlag GmbH & Co. KGaA, Weinheim

Concentration of the GO colloidal suspension was varied in the range from 2 to 5 mg ml^{-1}, at temperatures of 40, 60, and 80 °C. At the low temperature of 40 °C, the GO nanosheets were assembled into sponges with 3D porous networks. The driving force for the assembly was van der Waals forces, because during the water evaporation the outward centrifugal force was dominant over the upward evaporation force. After thermal annealing in H_2/Ar (50 cc min^{-1}) at 800 °C for 12 h, the GO sponges were reduced to graphene sponges, with large surface area and porous structure.

Figure 8.18 shows the formation process of the GO sponges and thin sheets. The experiments were started from homogeneous suspensions of single-layered GO nanosheets. The suspensions were placed on the rotor plate fixed in the vacuum chamber, with the vacuum centrifugal evaporator be operated at a rotating speed of 1800 rpm at a vacuum level of 10^{-4} torr. The as-formed GO sponges could be directly collected from the microtube by using a tweezer, which were brown in color and of a cotton-like soft morphology, as shown in Fig. 8.18c. Higher temperatures at 60 and 80 °C led to a sponge-sheet mixtures and sheets, respectively. The sponge and film morphologies were well retained after thermal reduction, with graphitic color and metallic luster, as shown in Fig. 8.18e, f. The rGO sponge exhibited high mechanical strength, as shown in the inset of Fig. 8.18e, which was obviously ascribed to the strong network structure formed by the GO nanosheets.

The individual GO nanosheets, with sizes in the range from 200 nm to 5 μm, were cross-linked to form GO-assembled network with a size of about 30 μm. The network was constructed through mainly edge-to-edge and partially edge-to-surface interactions. In the near inner wall regions of the GO sponges, there were GO nanosheets that were stacked in parallel fashion, with a relatively uniform thickness and narrow size distribution, caused by the centrifugal force. After thermal reduction, porosity of the GO sponges was reduced, while the porous structure was somehow collapsed, due to removal of the functional groups. The randomly connected morphology of the GO sponges was still retained, while the large surface area was not destroyed.

8.4.1.3 In Situ Gelation of RGO

3D rGO architecture would have more functions as compared with their GO counterparts, due to the recovered aromatic structure and thus enhanced conductivity. One of the simplest methods to develop 3D rGO architectures is self-assembly of rGO in situ. The reduction in GO increases the van der Waals forces between adjacent graphene basal planes, resulting in rGO gelation or precipitation. As stated earlier, the force balance between electrostatic repulsion and interplanar van der Waals interaction dominates the formation of rGO gels. Various reduction methods have been employed to reduce GO and trigger in situ gelation of rGO hydrogels.

Hydrothermal Reduction in GO

Hydrothermal or solvothermal reduction has been the most widely used method for such a purpose [13, 178–181]. For example, 3D rGO interconnected networks were fabricated by using a hydrothermal process with the aid of noble-metal nanocrystals (Au, Ag, Pd, Ir, Rh, Pt, etc.) [179]. The hydrothermal treatment was conducted with GO suspensions (1.0 mg ml^{-1}), together with noble-metal salt and glucose in a Teflon-lined stainless steel autoclave. The as-synthesized 3D microstructures were then freeze-dried to have good mechanical strength. Microstructures of the 3D structures, including porosity and pore size, are controlled by adjusting the GO concentration.

A simple yet effective approach has been reported to produce nanoscaled pores on graphene nanosheets by activating the graphene aerogels (GA) with H_3PO_4 [182]. Due to its mild characteristics, H_3PO_4 could be used to generate nanopores, while preventing the severe corrosion to the experimental facilities and thus mitigating the environmental problems. As schematically shown in Fig. 8.19a, the hydrothermally derived GAs in the presence of urea were impregnated with H_3PO_4 solution of different concentrations (Fig. 8.19b, c). The GAs were then subject to the activation treatment at 800 °C in the flowing N_2 gas for 90 min. The activated GA (aGA) (Fig. 8.19d) retained the macroscopic morphology of the original aerogel (Fig. 8.19c), while exhibiting an enormously enlarged specific surface area (SSA). The aGA possessed extraordinary electrochemical performance when used as electrodes of supercapacitors. They were much superior to respect to the pristine GA, in terms of specific capacitance, rate capability, and other parameters.

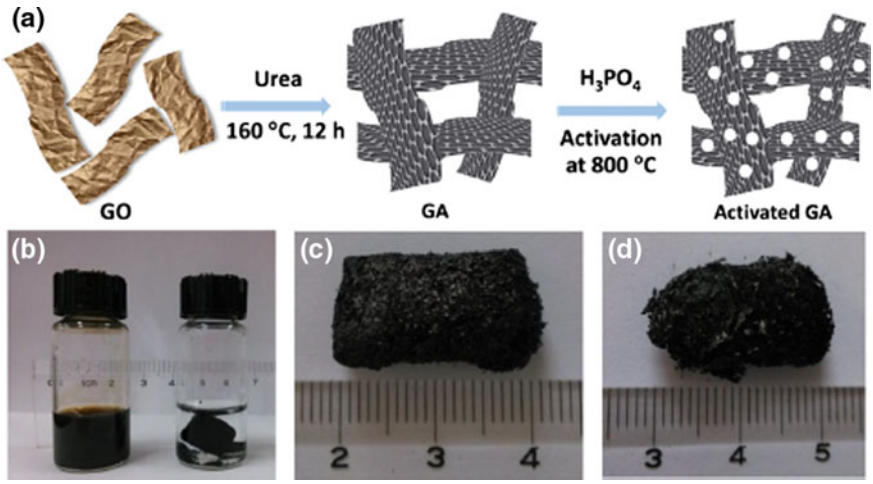

Fig. 8.19 **a** Schematic diagram showing formation process of the aGA monoliths with H_3PO_4. **b** Photographs of the GO dispersion (1 mg ml^{-1}) before and after hydrothermal reduction with urea. Photograph of the as-obtained GA (**c**) and aGA-0.5 (**d**). Reproduced with permission from [182], Copyright © 2015, Elsevier

GO suspension with a concentration of 4 mg ml^{-1} was used for the experiments. Monolith GA was first obtained by hydrothermal gelation of GO with the aid of urea. For example, 0.85 g urea and 10 ml GO suspension (4 mg ml^{-1}) were added into 30 ml water to form a diluted GO dispersion of 1 mg ml^{-1}. After stirring for 1 h, the suspension was hydrothermally treated at 160 °C for 12 h. The products were thoroughly washed with water until the pH value of the filtrate was close to 7. They were then freeze-dried for 24 h to obtain free-standing GA monoliths. The GA monoliths were impregnated with H_3PO_4 solution at concentrations of 0.2, 0.5, 1.0, and 1.2 M. After that, the samples were dried and then activated at 800 °C for 90 min in flowing N_2. The activated GA samples were labeled as aGA-x, where x is the concentration of the H_3PO_4 solution used in the impregnation experiments. In comparison, the GA sample without the H_3PO_4 impregnation was thermally annealed at 800 °C, which denoted aGA-800.

A simple hydrothermal method was developed to prepare rGO aerogels with variable and controllable surface wettability by using different amino acids as both cross-linkers and reducing agents [183]. For example, the cys-rGO aerogels obtained in the presence of L-cysteine (L-cys) were hydrophobic with extraordinary adsorption capacity to treat oil and organic solvent contaminated water, while the lys-rGO aerogels derived from L-lysine (L-lys) were hydrophilic, so as to be potential adsorbents to remove heavy metal ions from water.

It has been reported that rGO hydrogels could be directly obtained by hydrothermally treating GO aqueous suspension at appropriate concentrations without using any other reagents [13]. To prepare the self-assembled graphene hydrogels (SGH), a 2.0 mg ml^{-1} aqueous dispersion was sealed in a Teflon-lined autoclave and hydrothermally heated at 180°C for 12 h. Figure 8.20a shows the photographs of the sample before and after the hydrothermal experiment. The resulting rGO hydrogel contained 97.4 wt% water and 2.6 wt% rGO, with an interconnected 3D porous structure. The rGO hydrogels had an electrical conductive of 5×10^{-3} S cm^{-1}, high thermal stability over 25–100 °C, and high mechanical strength with storage modulus of 470 ± 20 kPa. Furthermore, its structure and properties can be easily tuned by changing the concentration of GO dispersion and hydrothermal reaction time.

Figure 8.20b shows the photographs of three SGH columns with a diameter of about 0.8 cm each, which were mechanically strong to support 100 g weight with almost no deformation. SEM images of the SGHs after freeze-drying are shown in Fig. 8.20c–e, demonstrating that they had well-developed interconnected 3D porous network structure. The pores exhibited sizes in the range from submicrometer to several micrometers, while the wall of the pore walls consisted of thin layers of tightly stacked graphene nanosheets. The formation of the physical cross-linking sites of the framework in the SGH was attributed to the partial overlapping or coalescing of the highly flexible graphene nanosheets, as shown in Fig. 8.20e. Therefore, it was the inherent flexibility of the graphene nanosheets that led to the porous 3D macrostructures.

I–V curve of the SGH is shown in Fig. 8.20f, with an Ohmic linear relationship and high electrical conductivity, due to the recovery of the π-conjugated system,

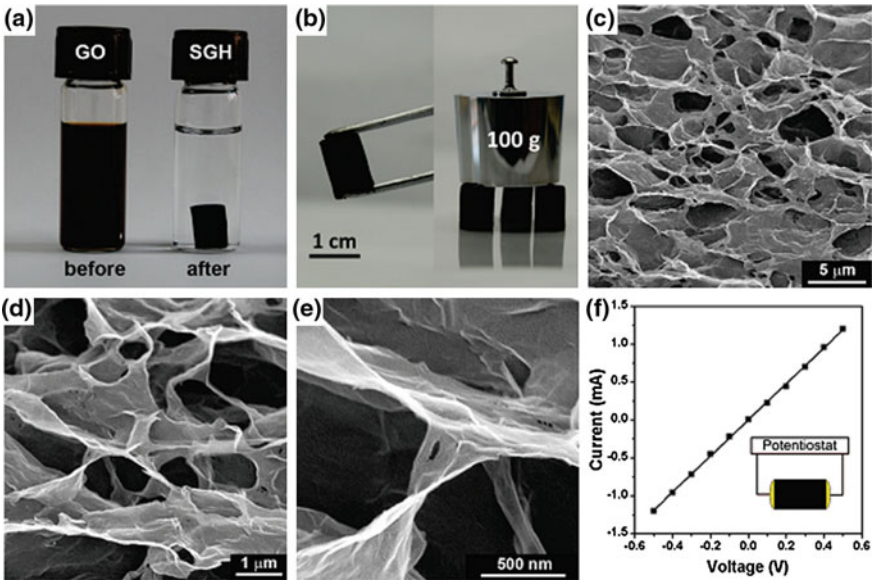

Fig. 8.20 **a** Photographs of the 2 mg ml^{-1} homogeneous GO aqueous suspension before and after hydrothermal reduction at 180 °C for 12 h. **b** Photographs of the strong SGH that could support a heavy weight. **c–e** SEM images at different magnifications of the SGHs showing their interior porous microstructures. **f** Room temperature *I–V* curve of the SGH exhibiting Ohmic characteristic, with inset showing the two-probe method for the conductivity measurement. Reproduced with permission from [13], Copyright © 2010, American Chemical Society

because the GO nanosheets were hydrothermally reduced to rGO, as confirmed by XRD patterns. The freeze-dried SGH possessed an interlayer spacing of about 3.76 Å, which was much smaller than that of the GO precursor (6.94 Å) but slightly larger than that of natural graphite (3.36 Å). This observation implied that the graphene nanosheets in the SGH took π–π stacking, while there were still residual oxygenated functional groups. With these residual hydrophilic oxygenated groups, the rGO nanosheets would encapsulate water molecules during the self-assembly process. The freeze-dried SGH exhibited a broad XRD peak, suggesting the decreased ordering of the graphene nanosheets and the presence of few-layer stacked graphene nanosheets.

Chemical Reduction in GO

Self-assembly of in situ-formed rGO through chemical reduction in GO has been extensively studied. Various reducing agents, such as sodium ascorbate [184], L-ascorbic acid [185], hypophosphorous acid–iodine [186], $NaHSO_3$ [187, 188], Na_2S, HI, and hydroquinone [187], have been used to fabricate 3D graphene architectures through the in situ self-assembly of rGO nanosheets. Similar to the

hydrothermal approaches, chemical reduction in GO promoted hydrophobic and π–π interactions between the graphene nanosheets, so as to trigger the self-assembly to 3D framework structures, with pore sizes ranging from sub-micrometer to several micrometers. Examples are discussed as follows.

High-performance 3D self-assembled graphene hydrogels (SGHs) have been fabricated through chemical reduction in aqueous GO dispersions by using sodium ascorbate as the reducing agent [184]. Pure SGHs exhibited a high specific capacitance of 240 F g^{-1}, when they were used as electrodes of supercapacitors. To prepare the SGHs, 6 ml GO aqueous suspension with a concentration of 2 mg ml^{-1} was loaded in a 15-ml glass vial, into which 24 mg sodium ascorbate was added. The sodium ascorbate was dissolved completely after sonication for 5 min, leading to a homogeneous yellow-brown solution, which was then heated at 90 °C for 1.5 h to obtain the SGH. The excess sodium ascorbate was removed through dialysis.

Figure 8.21a shows the photographs of the GO aqueous suspension (2 mg ml^{-1}), with the addition of sodium ascorbate (left), along with a piece of SGH (right). The SGHs exhibited were mechanically strong, so that they appeared as free-standing cylinders. Interior microstructures of the as-prepared SGHs were characterized by

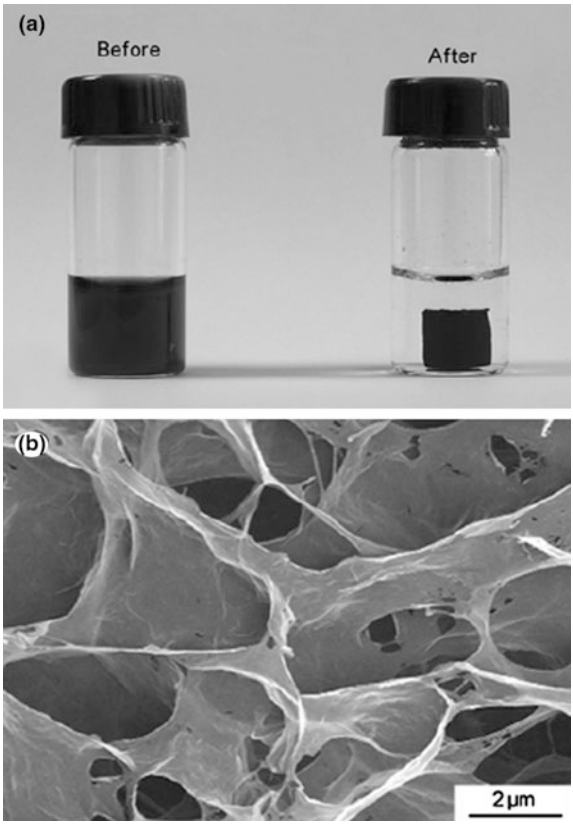

Fig. 8.21 **a** Photograph of an aqueous mixture of GO (2 mg ml^{-1}) and sodium ascorbate before (*left*) and after (*right*) chemical reduction at 90 °C for 1.5 h. **b** SEM image of SGHs. Reproduced with permission from [184], Copyright © 2011, Elsevier

using SEM. Figure 8.21b shows a representative SEM of the graphene hydrogels, in which a well-developed cross-linked 3D porous structure was clearly observed, with pores having sizes ranging from submicrometer to several micrometers.

Both microstructure and properties of the SGH were strongly dependent on several factors, including concentration (c_{GO}) of the starting GO suspensions, heating temperature, and reaction time. Among them, c_{GO} played the most important role. As the concentration of the GO suspension was too low, e.g., c_{GO} = 0.5 mg ml^{-1}, only black-colored rGO powder was formed. At intermediate concentration, e.g., c_{GO} = 0.5 mg ml^{-1}, although SGHs could be obtained, they were mechanically weak. As the concentration of the GO suspensions was increased to 2 mg ml^{-1} and above, the SGHs would have sufficiently high mechanical strength. Rheological testing results indicated that the samples derived from the suspensions with c_{GO} = 2 and 3 mg ml^{-1} had almost the same mechanical strength. Therefore, the optimal c_{GO} was 2 mg ml^{-1}. The heating temperature and reaction time could be combined to prepare mechanically strong SGHs. The heating temperature could be from room temperature to 90 °C. The higher the reaction temperature, the shorter the reaction time required.

A facile method was employed to produce chemically converted graphene xerogel (CCGX) through chemical reduction in GO suspension with the presence of hypophosphorous acid and iodine (HPA-I) at 90 °C for 12 h [186]. The reduction in GO in an aqueous solution of HPA-I resulted in stable graphene hydrogel (GH), which was then freeze-dried to form the CCGX with very low density. The CCGX possessed a C/O atomic ratio of 14.7. Due to high degree of reduction, the CCGX exhibited extraordinary electrical properties, with an electrical conductivity (EC) of about 500 S m^{-1}. More importantly, by using HPA-I as the reducing agent, the hydrogelation could be observed at a very low GO concentration of 0.5 mg ml^{-1}, so that ultralow density xerogel could be obtained by using this method.

A method to prepare 3D architectures of graphene was developed, through in situ self-assembly of graphene nanosheets that were reduced from GO by using mild chemical reduction at 95 °C and ambient pressure without stirring [187]. The reducing agents used to reduce the GO included $NaHSO_3$, Na_2S, Vitamin C, HI, and hydroquinone. Both graphene hydrogels and aerogels with 3D architectures could be fabricated by the method, while their shapes could be controlled by simply using reactors with desirable shapes. The graphene 3D architectures exhibited low density, high mechanical strength, thermal stability, electrical conductivity, and specific capacitance, thus making them promising candidates for applications in supercapacitors, hydrogen storage, and supports of catalysts.

Aqueous GO suspensions at concentrations of 0.1–2.0 mg ml^{-1} were added with various reducing agents, including $NaHSO_3$, Na_2S, Vitamin C, HI, and hydroquinone, at contents of 27–54 mmol ml^{-1}. The resultant suspensions were heated at 95 °C for 30 min or 3 h without stirring to form graphene hydrogels. The as-obtained graphene hydrogels were dialyzed against deionized water for 3 days to remove the residual inorganic compounds. To obtain aerogels, the dried graphene hydrogels were freeze-dried to remove the absorbed water molecules.

$NaHSO_3$ can be used to reduce GO in aqueous suspension, which is considered as a mild reducing agent [189]. If the reduction is conducted under stirring, the final products are aggregates or precipitates, due to the crude self-assembly of the quickly formed hydrophobic rGO nanosheets. Given the steric hindrance effect of rGO nanosheets with micrometer sizes, if the reaction is not disturbed, it is expected to produce 3D rGO architecture. With increasing degree of reduction, the partially reduced GO nanosheets would start to aggregate, owing to the increase in hydrophobicity. Some rGO nanosheets were assembled with high degree of orientation, while others could be aggregated randomly. Finally, as more and more water molecules were driven out from the aggregates, compact 3D architectures were obtained consequently.

More recently, a one-step strategy was developed to prepare macroscopic graphene–iron oxide hydrogels with 3D interconnected network structures, by using the synergistic effects of self-assembly of GO nanosheets and in situ deposition of the metal oxide nanoparticles, including α-FeOOH nanorods and magnetic Fe_3O_4 nanoparticles [190]. The GO nanosheets were reduced by the ferrous ions that acted as a reducing agent under mild conditions. The compositions of the graphene hydrogels could be readily controlled by adjusting the pH value of the starting GO suspensions. As the oil-saturated graphene–α-FeOOH superhydrophobic aerogel was burnt directly, 3D hematite α-Fe_2O_3 monoliths with porous microstructures were formed. More importantly, the separable and cost-effective graphene/metal oxide hydrogels and aerogels exhibited extraordinary capability to remove heavy metal ions and oils from water, thus making them potential candidates as efficient adsorbents in water purification and other waster-related applications.

In the experiments, a certain amount of $FeSO_4$ (0.0625–1 mmol) was quickly added into 10 ml GO aqueous suspension of 2 mg ml^{-1} in a 25-ml cylindrical sampler vial. The suspensions were then adjusted to pH = 3–11 with ammonia. All the reactions were carried out at 90 °C in an oil bath for 6 h without stirring, leading the appearance of 3D black monoliths. The samples were thoroughly washed with distilled water and freeze-dried into aerogels.

Figure 8.22a shows the photographs of the mixture of 10 ml GO suspension (2 mg ml^{-1}) and $FeSO_4$ (0.5 mmol) that was sealed in an oil bath at 90 °C for different time durations. After reaction for 0.5 h, the GO suspension became black, due to the reduction in the GO nanosheets, which were still dispersible in water. Therefore, no aggregate was observed, but the sample was slightly floating from bottom of the vessel. As the reaction time was prolonged, graphene monolith was formed and floated on top of the water. Finally, the black aggregate was further shrunk, leading to the formation of a columnar hydrogel. After reaction for 6 h, a well-developed black columnar hydrogel a diameter of 10 mm and height of 7 mm was obtained, as shown in Fig. 8.22b. No isolated graphene nanosheets were present elsewhere, so the transparent liquid was left in the vessel.

The as-synthesized graphene hydrogel contained about 95.8 wt% water, with a microstructure of well-defined and interconnected 3D network, as shown in Fig. 8.22c. The 3D network was uniformly dispersed with pores of several micrometers in size. A large number of nanoparticles were homogenously

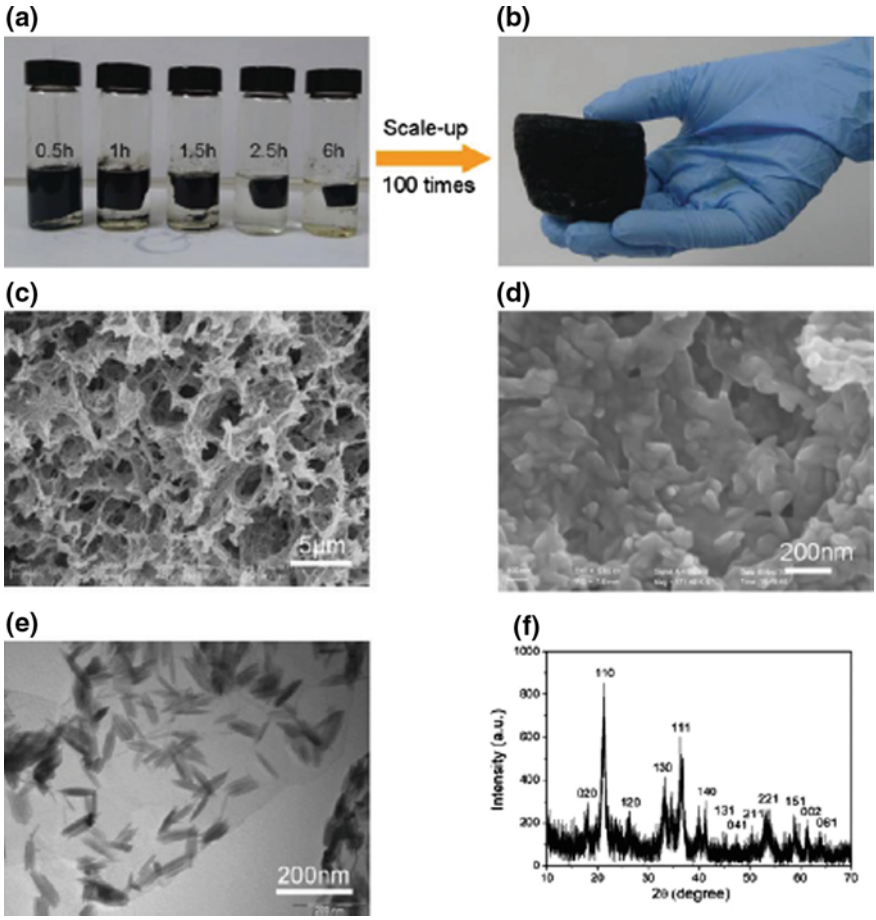

Fig. 8.22 **a** Photographs of samples after reaction for different times, showing the time-dependent formation process of the hydrogels derived from 10 ml of GO (2 mg ml^{-1}) suspensions at pH = 3 in the presence of 0.5 mmol $FeSO_4$. **b** Photograph of the hydrogels prepared by using 1000 ml GO suspension and 50 mmol $FeSO_4$. **c**, **d** Low- and high-magnification SEM images of the hydrogel. **e** TEM image of the freeze-dried graphene–α-FeOOH hydrogel. **f** XRD pattern of the graphene/α-FeOOH aerogel. Reproduced with permission from [190], Copyright © 2012, American Chemical Society

distributed on the graphene nanosheets, as shown in Fig. 8.22d. Figure 8.22e shows TEM image of the nanoparticles, which had a rod-like morphology with a size of about 60 nm. XRD pattern in Fig. 8.22f indicated that the nanoparticles were orthorhombic α-FeOOH.

Properties of the graphene–α-FeOOH hydrogels were closely dependent on the amount of the reducing agent Fe(II). The higher the content of $FeSO_4$ used in the GO suspension, the more the α-FeOOH nanorods produced in the 3D network graphene hydrogels. It was found that the graphene/α-FeOOH hydrogels were

superhydrophobic and highly porous. When they adsorbed oils and nonpolar organic solvents, water was left, so that they could be used as a suction skimmer in marine oil-spill recovery.

8.4.2 *Interface Self-Assembly*

Interface self-assembly has been shown to be an effective way to fabricate G/GO thin sheets, as discussed in last chapter. In this section, porous graphene-layered free-standing films, which have been classified as a new type of 3D architectures, are presented. These porous films have shown various advantages as compared with 3D porous scaffolds. For example, porous films can be directly used as active electrode materials for electrochemical applications without the requirement of tailoring their dimensions [191]. Various methods have been developed to fabricate graphene-based porous free-standing films, which are discussed as follows.

8.4.2.1 Breath-Figure-Templated Assembly

Breath-figure, a widely used procedure for fabricating large-area porous polymer films, has been applied to the self-assembly of polystyrene-grafted GO (PS–GO) into macroporous films [192]. GO nanosheets were self-assembled into mechanically flexible, macroporous 3D free-standing large-scale films with tunable porous microstructures. Figure 8.23a shows schematic diagram of the breath-figure method. The polymer-grafted GO nanosheets were synthesized and dispersed in an organic solvent. The dispersion was then cast onto proper substrates, which were exposed to a stream of humid air flow. Due to the evaporation of the volatile organic solvent, spontaneous condensation and close packing of aqueous droplets occurred at surface of the organic solution. Polymer-grafted GO-based macroporous films were developed on the substrates after completely drying, from which flexible robust macroporous films consisting of rGO nanosheets were derived after pyrolysis. In addition, electrical properties and chemical reactivity of the 3D rGO assemblies could be further increased by using nitrogen doping (N-doping).

The polymer-grafted GO nanosheets were prepared by using the surface-initiated atom transfer radical polymerization (ATRP) [193–195]. The polystyrene-grafted graphene oxide (PS-GO) nanosheets could be well dispersed in benzene. Drop casting the PS-GO/benzene dispersion with a concentration of 5 mg ml^{-1} onto a SiO_2 substrate resulted in highly flexible macroporous film after the evaporation of the solvent, which could be transferred to the flexible poly(ethylene terephalate) (PET) substrate, as shown in Fig. 8.23b. The film had a thickness of 3.8 μm. After pyrolysis, the GO was thermally reduced to rGO, which thus became superhydrophobic, as shown in Fig. 8.23c.

SEM images of the rGO macroporous films are shown in Fig. 8.23d, e. The sample was characterized by closely packed macropores with a nanoscale rim

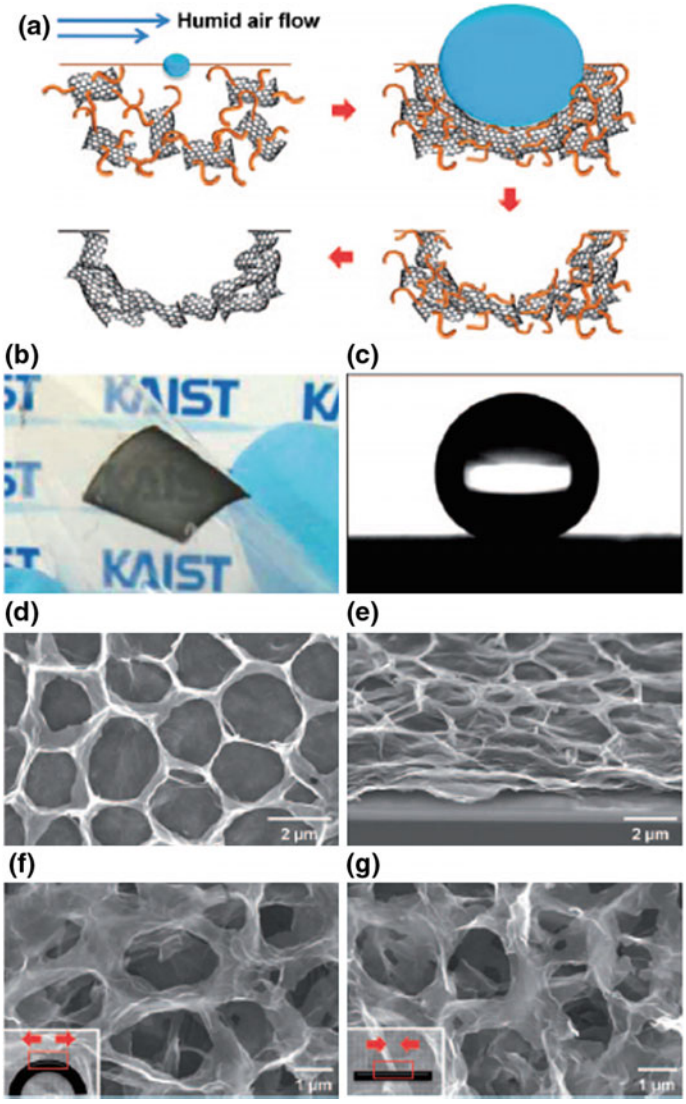

Fig. 8.23 **a** Self-assembly procedure of the rGO into macroporous free-standing films. **b** Photograph of the flexible semi-transparent macroporous rGO film on PET. **c** A water contact angle of 152° was observed for the superhydrophobic macroporous rGO film. **d** Plane view and **e** 60-tilted SEM images of the rGO film. **f**, **g** Plane view SEM images of the porous rGO film upon (**f**) and after (**g**) deformation. Reproduced with permission from [192], Copyright © 2010, Wiley-VCH Verlag GmbH & Co. KGaA, Weinheim

thickness. The rGO-assembled films were highly flexible and robust. Figure 8.23f shows a plane view SEM image of a concave film with a radius of curvature of about 2 mm, in which the pores were slightly elongated, but without damaging the macropore morphology. The porous structure was quickly recovered as the film was return to flat state, as shown in Fig. 8.23g.

8.4.2.2 Flow-Directed Self-Assembly

Leavening Strategy

More recently, another approach based on flow-directed self-assembly of GO followed by a leavening strategy was developed to prepare rGO film with 3D interconnected macroporous structures [12]. Leavening is usually a process applied for increasing the volume of breads or cakes before or during baking or steaming by forming porous structures. Leavening has been demonstrated to be an effective approach to transfer compact graphene structures into porous one, by finding a proper leavening procedure. Because unstable GO can be chemically reduced with mild heating to yield rGO, accompanied by the production of gaseous species such as H_2O and CO_2 [163, 196–198]; if the gas released during the chemical reduction in the GO could be controlled properly, rGO foams could be obtained, similar to the formation of leavened bread. It was found that the rGO foams prepared in this way possessed structures with open pores and continuous cross-links of the rGO nanosheets. They could find potential applications as electrodes of supercapacitors and absorbents for selective absorption of oil and organic solvents for clean environment.

Figure 8.24 shows a schematic diagram of the experimental procedure. In the experiment, GO aqueous dispersions with a concentration of about 2.5 mg ml^{-1} were prepared. With the suspensions, nacre-like layer-structured films were fabricated by using flow-directed assembly of the GO nanosheets. A porous anodized aluminum oxide (AAO) membrane with a pore diameter of 20 nm was used to filter the GO aqueous suspension to obtain desired samples. Therefore, thickness of GO films could be controlled by controlling concentration and volume of the GO suspensions. The films were the peeled off from the AAO membranes. The free-standing GO films were put into a Teflon (polytetrafluoroethylene) vessel of 50 ml together with 80 μl hydrazine monohydrate. To avoid direct contact, the GO films were suspended well above the hydrazine monohydrate level. Hydrothermal treatment was carried out at 90 °C for 10 h. The foam structured film experienced a 50-fold volume expansion and 30% mass loss. During the reduction in GO to rGO by the hydrazine vapor, rapid evolution of gaseous species occurred, leading the formation of the porous films. Porosity of the rGO foams could be controlled by controlling the amount of hydrazine used in the reduction reaction.

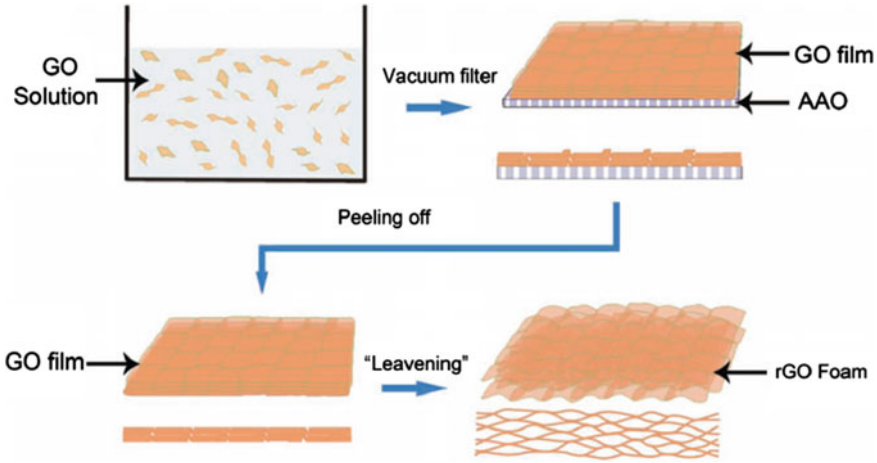

Fig. 8.24 Schematic diagram showing the leavening process to prepare the rGO foams. Reproduced with permission from [12], Copyright © 2012, Wiley-VCH Verlag GmbH & Co. KGaA, Weinheim

KOH Activation of RGO Porous Structures

Chemical activation has been shown to be a useful procedure to produce porous carbon-based materials, which has also been employed to create highly conductive and porous rGO films [199, 200]. To realize the activation, GO suspensions were added with KOH at certain concentrations. The suspensions were then heated at 100 °C to evaporate the water, thus leading to the formation a thickened "ink paste." After that, GO/KOH composite films were deposited by using vacuum filtration. After drying, the precursor films were activated in argon at 800 °C for 1 h. The activated rGO films were free standing with a smooth surface and uniform thicknesses. The flexible activated rGO porous films had a high in-plane electrical conductivity and high specific surface area. One example is discussed in more detailed way as follows.

The activated reduced graphene oxide films were named aGO [200]. The aGO films were mechanically flexible, physically free-standing, and highly porous, with an extremely high specific surface areas of 2400 $m^2\ g^{-1}$ and a very high in-plane electrical conductivity of 5880 S m^{-1}. They had a very low H content of <0.5 wt% and a high C/O atomic ratio of 14. The C/O atomic ratio was higher than that of typical chemically converted graphene nanosheets. Figure 8.25 shows schematic diagram to describe the processing steps of the film-like aGO porous thin sheets. Firstly, GO aqueous colloidal suspensions with a typical concentration of 1 mg ml^{-1} were added with 1 M KOH dropwise, which were then heated in an oil bath at 100 °C under constant stirring to evaporate the water, until an ink pastes were obtained. The pastes contained GO nanosheets evenly dispersed with KOH

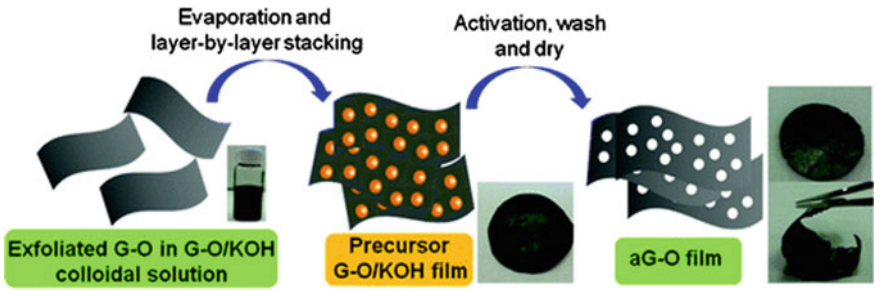

Fig. 8.25 Schematic diagram depicting the experimental steps to produce the aGO film. Reproduced with permission from [200], Copyright © 2012, American Chemical Society

together with small amount of water, which were then used to deposit films by using brief vacuum filtration with PTFE membrane.

8.4.3 Templating Approaches

Template-guided methods are also effective to develop 3D graphene architectures. This type of approaches can be used to fabricate 3D porous graphene networks, with well-defined and shaped structures in the forms of either 3D scaffolds or layered films [201–206]. The methods will be demonstrated and discussed by using four groups of samples, including template-directed CVD, ice-templating, PS colloidal temperate, and lithography method, in a detailed way.

8.4.3.1 Templated Chemical Vapor Deposition (CVD)

Various rGO samples have been fabricated by different methods, some of which could be used to produce large-scale products. However, most the rGO materials still have a relatively low electrical conductivity, which has limited their applications in some areas, especially those that require high electrical conductivity. The main reason for that is the poor quality of the graphene nanosheets made by using those methods. Chemical vapor deposition (CVD) has been acknowledged to be an effective approach to produce high-quality graphene nanosheets [207–213].

A 3D graphene macroscopic structure with a foam-like network, i.e., graphene foam (GF), has been fabricated by using a template-directed CVD method [202]. Unlike the structures formed with the chemically derived graphene nanosheets of relatively small lateral sizes, the GF fabricated by using the templated CVD method was a monolithic graphene 3D network, which facilitated charge carriers to migrate with remarkably low resistance, due to the high-quality continuous CVD-derived graphene nanosheets. Therefore, this type of GFs would have excellent electrical and mechanical properties.

8.4.3.2 Ice-Templated Unidirectional Freezing

Unidirectional freezing, also described as ice-segregation-induced self-assembly (ISISA), is a well-known wet shaping technique to form porous materials, with unique porous microstructures [214–219]. This technique has also been applied to fabricate 3D graphene macroporous scaffolds, as well as their hybrids [201, 220, 221]. Several examples are presented in the following section to demonstrate the versatility of the technique.

A template-directed method has been used to prepare graphene–polymer nanocomposites with highly ordered 3D architectures, including sponge-like macroporous scaffolds and hollow micrometer-sized spheres [201]. The sponge-like macroporous scaffolds were obtained by using the ice-segregation-induced self-assembly (ISISA) of frozen aqueous dispersions, where were homogeneous mixtures of polystyrene sulfonate grafted graphene nanosheets (PSS-G) and poly (vinylalcohol) (PVA), as shown in Fig. 8.26i. By directionally freeze casting the PSS-G or GO aqueous dispersions, free-standing monoliths with a high surface area were obtained, which were constructed by internally aligned macro- and mesoscale pores. Also, PSS-G-coated polymer microparticles or hollow micrometer-sized

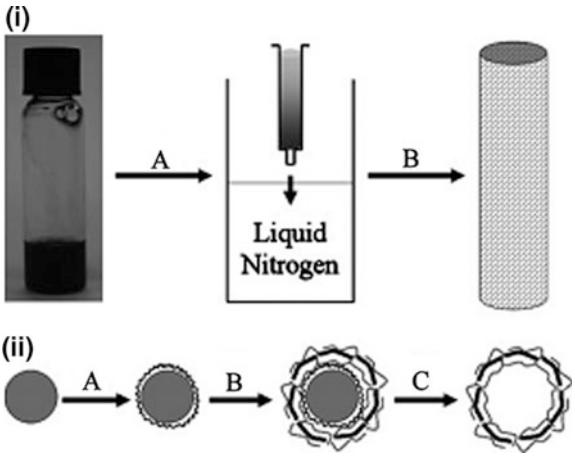

Fig. 8.26 Fabrication of the graphene–polymer nanocomposites with highly ordered 3D architectures. **i** Schematic diagram showing the formation process of the macroporous PSS-G/PVA monoliths by using the ice-segregation-induced self-assembly (ISISA): (*A*) homogeneous aqueous mixture of PVA and PSS-G (optical image) was transferred into an insulin syringe and unidirectionally frozen by immersing into liquid nitrogen at dipping rates of 2 and 5.9 mm min^{-1}, whereas (*B*) the frozen scaffold was then freeze-dried to sublime the ice crystals to produce macroporous monolith. **ii** Schematic diagram showing colloidal templating process to form the hollow PSS-G microspheres: (*A*) functionalization of the polystyrene beads with poly(allylamine hydrochloride) (PAH), (*B*) electrostatically induced templating of the negatively charged PSS-G nanosheets on the positively charged bead surface, and (*C*) removal of the core template by treatment with toluene to create hollow PSS-G microspheres. Reproduced with permission from [201], Copyright © 2009, WILEY-VCH Verlag GmbH & Co. KGaA, Weinheim

PSS-G spheres were fabricated by depositing the negatively charged PSS-G dispersions on surface of the positively charged polymer beads, as shown in Fig. 8.26ii. The PSS-G nanosheets had lateral sizes in the range from 500 nm to >1 μm and thickness of 1.5–2 nm.

In a separate study, the ISISA approach was extended to fabricate macroporous rGO–Pt/Nafion hybrid films and 3D scaffolds, in which two steps were engaged [203]. Firstly, a porous network was derived from the aqueous suspensions of Nafion, GO, and chloroplatinic acid, by using ice-templating. Secondly, the porous network was reduced to result in graphene-supported Pt nanoparticles on Nafion scaffolds. Figure 8.26i shows a schematic diagram illustrating the formation process of the ice-templating technique. The porous hybrids exhibited both ionic and electronic conductivities along with catalytic activity, making them potential candidates for fuel cell and biosensor applications.

More recently, ice-templating strategy has been employed to realize uniform distribution of nitrogen-doped graphene nanosheets, in order to achieve unique three-dimensional morphology of graphene-based materials, with enhanced electrochemical stability and ion transport network specifically for superior capacitor applications [220]. To synthesize nitrogen-doped rGO (N-rGO), 20 ml GO solution with a concentration of 5 mg ml^{-1} was diluted by adding 10 ml deionized water and sonicated for 1 h to develop a homogeneous suspension. Melamine was used as the source of nitrogen, which was dissolved in deionized water by heating at 80 °C for 30 min to form melamine solution. The GO and melamine solutions were mixed thoroughly with a mass ratio of 1:5 and then frozen in liquid nitrogen. After that, the samples were thawed following the phase diagram of water. To obtain N-rGO powder, the GO/melamine sponge type monoliths were annealed at 900 °C for 30 min in Ar. Undoped samples of rGO were prepared similarly for comparison. During annealing process, oxygen molecules were detached, which created active sites for nitrogen atoms to be incorporated into the honeycomb lattice of graphene.

8.4.4 3D Printing

The conventional manufacturing is known as subtractive process, in which unwanted portion was removed from a work piece in order to fabricate an item with desired shapes. In contrast, additive manufacturing (AM), also called 3D printing, is to create objects from 3D model data by joining materials, generally in a layer-by-layer way [222]. Therefore, 3D printing is superior over the traditional subtractive manufacturing [223–228]. For example, it can be used produce complex items and parts that are made of expensive materials. Complex items are those that have special characteristics, such as complicated geometries, internal features, engineered porosity, and material gradients. Also, it is suitable high-level customization with small scale production. More recently, 3D printing has been employed to produce graphene-based complicated items with special functionalities [229–234]. Representative examples are discussed in the following section.

Recently, electrically conductive, mechanically resilient and biocompatible scaffolds with a high graphene content of 60 vol% in solid have been developed by using 3D printing, with printable graphene inks [232]. The 3D graphene (3DG) inks were synthesized with graphene nanosheets and the biocompatible, biodegradable, and hyperelastic polyester polylactide-co-glycolide (PLG). The 3D printing was conducted at room temperature by using an extrusion method to obtain self-supporting user-defined structures with high fidelity and precision. The graphene-based structures were mechanically strong while maintaining high flexibility. Moreover, the structures had pretty high electrical conductivity, which could be used as electrically conducting scaffolds for potential applications in tissue regenerative engineering.

A 3D printing strategy has been demonstrated to fabricate 3D graphene aerogels with designed macroscopic architectures [233]. The approach was based on the precise deposition of GO ink filaments on a pre-defined tool path. Two key challenges were encountered in this process, i.e., (i) development of printable graphene-based inks and (ii) retaining the intrinsic properties of single graphene nanosheets in the final 3D printed structures, such as large specific surface area, strong mechanical properties, and high electrical conductivity.

The printed 3D graphene aerogel microlattices exhibited extraordinary structural stability and micro-architecture accuracy, as shown in Fig. 8.27a, b, which suggested that the inks possessed high quality for the 3D printing process. After the removal of the silica fillers, randomly distributed large-sized pores were left in the graphene aerogels, as shown in Fig. 8.27c, d. It also indicated that the microstructure of the 3D printed graphene aerogels could be tailored by modifying the compositions of the GO inks. It has been accepted that gelation chemistry has a significant effect on microstructural of the final hydrogels [235]. To confirm this in the 3D printed structures, two gelation reactions were examined, i.e., (i) basic solution of $(NH4)_2CO_3$ to directly cross-link the graphene nanosheets through the functional groups and (ii) resorcinol (R) and formaldehyde (F) with sodium carbonate to catalyze and link the graphene nanosheets. With the organic solgel chemistry (R–F solution), the GO networks had more open pores (Fig. 8.27d), as compared to those through the gelation based on native functionality of the GO nanosheets (Fig. 8.27c). A series of graphene aerogel microlattices with varying thickness and large area graphene aerogel honeycomb have been printed to demonstrate the versatility of the technique, as shown in Fig. 8.27e, f.

8.4.5 Miscellaneous

Spark plasma sintering (SPS) has recently been widely used to consolidate nanostructured ceramics, metals, and CNT-reinforced composites [236–240]. SPS is a sintering method that applies high pressure, high temperature, along with a pulsing current through the material during sintering [241]. The current leads to the formation of plasma in the form of micro-discharge, due to impurities on the

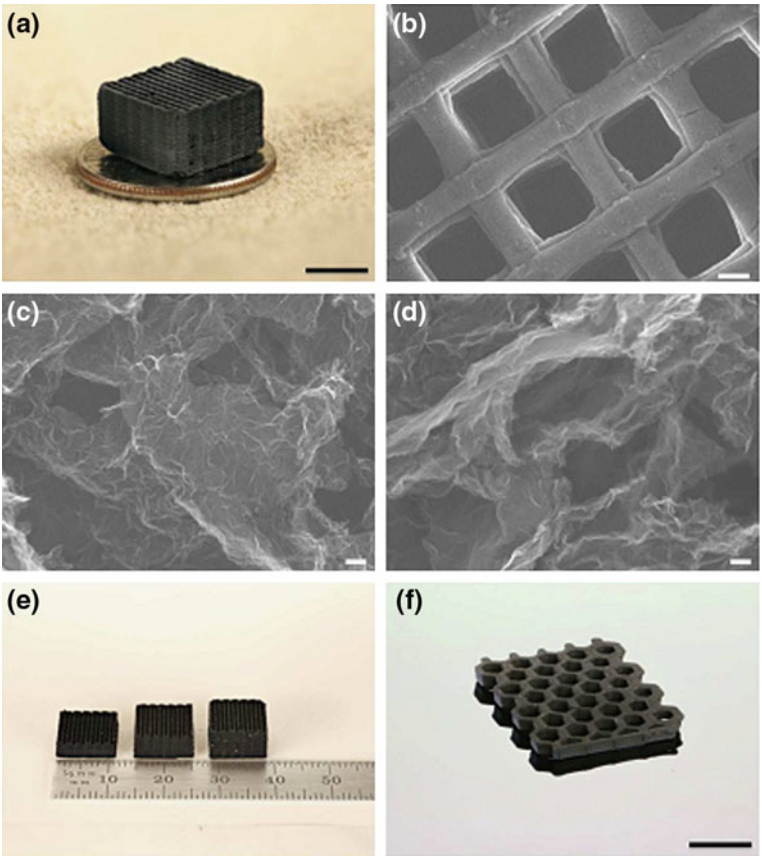

Fig. 8.27 Morphology and structure of the graphene aerogels. **a** Photograph of the 3D printed graphene aerogel microlattice. SEM images of the samples: **b** 3D printed graphene aerogel microlattice, **c** graphene aerogel without R–F after etching and **d** graphene aerogel with 4 wt% R–F after etching. **f** Photograph of the 3D printed graphene aerogel microlattices with varying thickness and **f** the 3D printed graphene aerogel honeycomb. Scale bars = 5 mm (**a**), 200 μm (**b**), 100 nm (**c**, **d**), and 1 cm (**f**). Reproduced with permission from [233], Copyright © 2015, Macmillan Publishers Limited

particle surfaces. The plasma provides with an enhanced heat transfer effect, so as to produce better bonding of the sintered materials. This technique has various advantages over the conventional sintering technologies, including high densification rate, short sintering times, controlled grain growth, and enhanced bonding between composite components. More recently, SPS has been used to consolidate graphene-reinforced composites based on aluminum oxide [242–244] and silicon nitride [245], at pressures of 35–60 MPa and temperatures of 1000–1650 °C. It was found that the SPS processing had no any negative effect on the graphene nanosheets, which were almost defect free in the composites.

Inspired by those observations, a bulk sample of graphene nanosheets has been prepared by using SPS technique at an extremely high temperature of 1850 °C and a pressure of 80 MPa [246]. Structure of the graphene nanosheets remained unchanged after the SPS processing at such an extremely high temperature. Graphene nanosheets were less vulnerable, as compared with CNTs, due probably to the special structure [247–250]. Graphene nanosheets are 2D-like, while CNTs are tubular-like. Comparatively, tubular-like structured CNTs are vulnerable to buckling and collapse at high pressures.

8.5 Concluding Remarks

Various strategies have been developed to fabricate graphene fibers, graphene papers, and bulk-like structures. Although significant progress has been made, we are facing various challenges. For instance, mechanical strength and electric conductivity of the GFs are still below the expected levels for high-performance applications. There is also a lack of standard to guide or regulate the processing of the GFs.

Obviously, the majority of free-standing 2D graphene materials have been developed by using vacuum membrane filtration, which, however, has several serious shortcomings, such as low deposition rate and limited sizes. This could restrict their practical applications, especially when large area samples are required. Therefore, solution casting or evaporation methods are expected to be more applicable in terms of large-scale production, which should be deserved for more exploration.

Various strategies and approaches have been developed to fabricate 3D graphene-based architectures, such as self-assembly, templated growth, solgel synthesis, and lithography patterning technology. There are also challenges that need to be addressed in the near future in terms of practical applications of the 3D graphene-based structures. For example, the capability of synthesizing high-quality nanosheets with desired physical and chemical properties should be established. Also, problems of restacking of the single-layer graphene building blocks, porosity and mechanical strength, purity and electrical conductivity, formation mechanisms of the 3D structures, especially for those derived from solutions or suspensions, should be paid more attention. Nevertheless, it is quite optimistic that this new group of materials will continuously be among the hot topics in terms of research.

References

1. K.S. Novoselov, A.K. Geim, S.V. Morozov, D. Jiang, Y. Zhang, S.V. Dubonos et al., Electric field effect in atomically thin carbon films. Science **306**, 666–669 (2004)

2. A. Bianco, H.M. Cheng, T. Enoki, Y. Gogotsi, R.H. Hurt, N. Koratkar et al., All in the graphene family—a recommended nomenclature for two-dimensional carbon materials. Carbon **65**, 1–6 (2013)
3. A.K. Geim, K.S. Novoselov, The rise of graphene. Nat. Mater. **6**, 183–191 (2007)
4. O.C. Compton, S.T. Nguyen, Graphene oxide, highly reduced graphene oxide, and graphene: versatile building blocks for carbon-based materials. Small **6**, 711–723 (2010)
5. J.Y. Luo, H.D. Jang, T. Sun, L. Xiao, Z. He, A.P. Katsoulidis et al., Compression and aggregation-resistant particles of crumpled soft sheets. ACS Nano **5**, 8943–8949 (2011)
6. H.H. Cheng, C.G. Hu, Y. Zhao, L.T. Qu, Graphene fiber: a new material platform for unique applications. NPG Asia Mater. **6**, e113 (2014)
7. D.Q. Wu, F.B. Zhang, H.W. Liang, X.L. Feng, Nanocomposites and macroscopic materials: assembly of chemically modified graphene sheets. Chem. Soc. Rev. **41**, 6160–6177 (2012)
8. G. Eda, M. Chhowalla, Chemically derived graphene oxide: towards large-area thin-film electronics and optoelectronics. Adv. Mater. **22**, 2392–2415 (2010)
9. J.H. Du, S.F. Pei, L.P. Ma, H.M. Cheng, 25th anniversary article: carbon nanotube- and graphene-based transparent conductive films for optoelectronic devices. Adv. Mater. **26**, 1958–1991 (2014)
10. Q.W. Chen, L.Y. Zhang, G.H. Chen, Facile preparation of graphene-copper nanoparticle composite by in situ chemical reduction for electrochemical sensing of carbohydrates. Anal. Chem. **84**, 171–178 (2012)
11. F. Yavari, Z.P. Chen, A.V. Thomas, W.C. Ren, H.M. Cheng, N. Koratkar, High sensitivity gas detection using a macroscopic three-dimensional graphene foam network. Sci. Rep. **1**, 166 (2011)
12. Z.Q. Niu, J. Chen, H.H. Hng, J. Ma, X.D. Chen, A leavening strategy to prepare reduced graphene oxide foams. Adv. Mater. **24**, 4144–4150 (2012)
13. Y.X. Xu, K.X. Sheng, C. Li, G.Q. Shi, Self-assembled graphene hydrogel via a one-step hydrothermal process. ACS Nano **4**, 4324–4330 (2010)
14. Z. Xu, C. Gao, Graphene chiral liquid crystals and macroscopic assembled fibres. Nat. Commun. **2**, 571 (2011)
15. B. Dan, N. Behabtu, A. Martinez, J.S. Evans, D.V. Kosynkin, J.M. Tour et al., Liquid crystals of aqueous, giant graphene oxide flakes. Soft Matter **7**, 11154–11159 (2011)
16. B. Konkena, S. Vasudevan, Glass, gel, and liquid crystals: arrested states of graphene oxide aqueous dispersions. J. Phys. Chem. C **118**, 21706–21713 (2014)
17. Z. Xu, C. Gao, Aqueous liquid crystals of graphene oxide. ACS Nano **5**, 2908–2915 (2011)
18. D.A. Dikin, S. Stankovich, E.J. Zimney, R.D. Piner, G.H.B. Dommett, G. Evmenenko et al., Preparation and characterization of graphene oxide paper. Nature **448**, 457–460 (2007)
19. Z. Xu, Y. Zhang, P.G. Li, C. Gao, Strong, conductive, lightweight, neat graphene aerogel fibers with aligned pores. ACS Nano **6**, 7103–7113 (2012)
20. X.Z. Hu, Z.P. Xu, Z. Liu, C. Gao, Liquid crystal self-templating approach to ultrastrong and tough biomimic composites. Sci. Rep. **3**, 2374 (2013)
21. H.B. Yao, H.Y. Fang, X.H. Wang, S.H. Yu, Hierarchical assembly of micro-/nano-building blocks: bio-inspired rigid structural functional materials. Chem. Soc. Rev. **40**, 3764–3785 (2011)
22. J.F. Wang, Q.F. Cheng, Z.Y. Tang, Layered nanocomposites inspired by the structure and mechanical properties of nacre. Chem. Soc. Rev. **41**, 1111–1129 (2012)
23. R. Jalili, S.H. Aboutalebi, D. Esrafilzadeh, R.L. Shepherd, J. Chen, S. Aminorroaya-Yamini et al., Scalable one-step wet-spinning of graphene fibers and yarns from liquid crystalline dispersions of graphene oxide: towards multifunctional textiles. Adv. Func. Mater. **23**, 5345–5354 (2013)
24. H.P. Cong, X.C. Ren, P. Wang, S.H. Yu, Wet-spinning assembly of continuous, neat, and macroscopic graphene fibers. Sci. Rep. **2**, 613 (2012)
25. L. Chen, Y.L. He, S.G. Chai, H. Qiang, F. Chen, Q. Fu, Toward high performance graphene fibers. Nanoscale **5**, 5809–5815 (2013)

26. C.S. Xiang, C.C. Young, X. Wang, Z. Yan, C.C. Hwang, G. Cerioti et al., Large flake graphene oxide fibers with unconventional 100% knot efficiency and highly aligned small flake graphene oxide fibers. Adv. Mater. **25**, 4592–4597 (2013)
27. Y. Zhao, C.C. Jiang, C.G. Hu, Z.L. Dong, J.L. Xue, Y.N. Meng et al., Large-scale spinning assembly of neat, morphology-defined, graphene-based hollow fibers. ACS Nano **7**, 2406–2412 (2013)
28. J.K. Sun, Y.H. Li, Q.Y. Peng, S.C. Hou, D.C. Zou, Y.Y. Shang et al., Macroscopic, flexible, high-performance graphene ribbons. ACS Nano **7**, 10225–10232 (2013)
29. Z.L. Dong, C.C. Jiang, H.H. Cheng, Y. Zhao, G.Q. Shi, L. Jiang et al., Facile fabrication of light, flexible and multifunctional graphene fibers. Adv. Mater. **24**, 1856–1861 (2012)
30. C.G. Hu, Y. Zhao, H.H. Cheng, Y.H. Wang, Z.L. Dong, C.C. Jiang et al., Graphene microtubings: controlled fabrication and site-specific functionalization. Nano Lett. **12**, 5879–5884 (2012)
31. X.M. Li, T.S. Zhao, K.L. Wang, Y. Yang, J.Q. Wei, F.Y. Kang et al., Directly drawing self-assembled, porous, and monolithic graphene fiber from chemical vapor deposition grown graphene film and its electrochemical properties. Langmuir **27**, 12164–12171 (2011)
32. X. Li, P.Z. Sun, L.L. Fan, M. Zhu, K.L. Wang, M.L. Zhong et al., Multifunctional graphene woven fabrics. Sci. Rep. **2**, 395 (2012)
33. C.G. Hu, X.Q. Zhai, L.L. Liu, Y. Zhao, L. Jiang, L.T. Qu, Spontaneous reduction and assembly of graphene oxide into three-dimensional graphene network on arbitrary conductive substrates. Sci. Rep. **3**, 2065 (2013)
34. D.V. Kosynkin, A.L. Higginbotham, A. Sinitskii, J.R. Lomeda, A. Dimiev, B.K. Price et al., Longitudinal unzipping of carbon nanotubes to form graphene nanoribbons. Nature **458**, 872–876 (2009)
35. L.Y. Jiao, X.R. Wang, G. Diankov, H.L. Wang, H.J. Dai, Facile synthesis of high-quality graphene nanoribbons. Nat. Nanotechnol. **5**, 321–325 (2010)
36. L.Y. Jiao, L. Zhang, X.R. Wang, G. Diankov, H.J. Dai, Narrow graphene nanoribbons from carbon nanotubes. Nature **458**, 877–880 (2009)
37. A.G. Cano-Marquez, F.J. Rodriguez-Macias, J. Campos-Delgado, C.G. Espinosa-Gonzalez, F. Tristan-Lopez, D. Ramirez-Gonzalez et al., Ex-MWNTs: graphene sheets and ribbons produced by lithium intercalation and exfoliation of carbon nanotubes. Nano Lett. **9**, 1527–1533 (2009)
38. J. Carretero-Gonzalez, E. Castillo-Martinez, M. Dias-Lima, M. Acik, D.M. Rogers, J. Sovich et al., Oriented graphene nanoribbon yarn and sheet from aligned multi-walled carbon nanotube sheets. Adv. Mater. **24**, 5695–5701 (2012)
39. C.S. Xiang, N. Behabtu, Y.D. Liu, H.G. Chae, C.C. Young, B. Genorio et al., Graphene nanoribbons as an advanced precursor for making carbon fiber. ACS Nano **7**, 1628–1637 (2013)
40. M.L. Minus, S. Kumar, The processing, properties, and structure of carbon fibers. JOM **57**, 52–58 (2005)
41. E.Y. Jang, J. Carretero-Gonzalez, A. Choi, W.J. Kim, M.E. Kozlov, T. Kim et al., Fibers of reduced graphene oxide nanoribbons. Nanotechnology **23**, 235601 (2012)
42. Z.S. Tian, C.X. Xu, J.T. Li, G.Y. Zhu, Z.L. Shi, Y. Lin, Self-assembled free-standing graphene oxide fibers. ACS Appl. Mater. Interfaces **5**, 1489–1493 (2013)
43. R.H. Baughman, C.X. Cui, A.A. Zakhidov, Z. Iqbal, J.N. Barisci, G.M. Spinks et al., Carbon nanotube actuators. Science **284**, 1340–1344 (1999)
44. F. Hennrich, S. Lebedkin, S. Malik, J. Tracy, M. Barczewski, H. Rosner et al., Preparation, characterization and applications of free-standing single walled carbon nanotube thin films. Phys. Chem. Chem. Phys. **4**, 2273–2277 (2002)
45. H. Chen, M.B. Muller, K.J. Gilmore, G.G. Wallace, D. Li, Mechanically strong, electrically conductive, and biocompatible graphene paper. Adv. Mater. **20**, 3557–3561 (2008)
46. W.B. Hu, C. Peng, W.J. Luo, M. Lv, X.M. Li, D. Li et al., Graphene-based antibacterial paper. ACS Nano **4**, 4317–4323 (2010)

47. G.Y. He, H.Q. Chen, J.W. Zhu, F.L. Bei, X.Q. Sun, X. Wang, Synthesis and characterization of graphene paper with controllable properties via chemical reduction. J. Mater. Chem. **21**, 14631–14638 (2011)
48. M. Lian, J.C. Fan, Z.X. Shi, S. Zhang, H. Li, J. Yin, Gelatin-assisted fabrication of graphene-based nacre with high strength, toughness, and electrical conductivity. Carbon **89**, 279–289 (2015)
49. H. Gwon, H.S. Kim, K.U. Lee, D.H. Seo, Y.C. Park, Y.S. Lee et al., Flexible energy storage devices based on graphene paper. Energy Environ. Sci. **4**, 1277–1283 (2011)
50. X.W. Yang, L. Qiu, C. Cheng, Y.Z. Wu, Z.F. Ma, D. Li, Ordered gelation of chemically converted graphene for next-generation electroconductive hydrogel films. Angew. Chem. Int. Ed. **50**, 7325–7328 (2011)
51. Q.F. Cheng, M.X. Wu, M.Z. Li, L. Jiang, Z.Y. Tang, Ultratough artificial nacre based on conjugated cross-linked graphene oxide. Angew. Chem. Int. Ed. **52**, 3750–3755 (2013)
52. S.J. Park, K.S. Lee, G. Bozoklu, W.W. Cai, S.T. Nguyen, R.S. Ruoff, Graphene oxide papers modified by divalent ions—enhancing mechanical properties via chemical cross-linking. ACS Nano **2**, 572–578 (2008)
53. K.W. Putz, O.C. Compton, C. Segar, Z. An, S.T. Nguyen, L.C. Brinson, Evolution of order during vacuum-assisted self-assembly of graphene oxide paper and associated polymer nanocomposites. ACS Nano **5**, 6601–6609 (2011)
54. A. Sumboja, C.Y. Foo, X. Wang, P.S. Lee, Large areal mass, flexible and free-standing reduced graphene oxide/manganese dioxide paper for asymmetric supercapacitor device. Adv. Mater. **25**, 2809–2815 (2013)
55. Y. Tian, Y.W. Cao, Y. Wang, W.L. Yang, J.C. Feng, Realizing ultrahigh modulus and high strength of macroscopic graphene oxide papers through crosslinking of mussel-inspired polymers. Adv. Mater. **25**, 2980–2983 (2013)
56. W. Guo, C. Cheng, Y.Z. Wu, Y.N. Jiang, J. Gao, D. Li et al., Bio-inspired two-dimensional nanofluidic generators based on a layered graphene hydrogel membrane. Adv. Mater. **25**, 6064–6068 (2013)
57. H.Y. Liu, H.T. Wang, X.W. Zhang, Facile fabrication of freestanding ultrathin reduced graphene oxide membranes for water purification. Adv. Mater. **27**, 249–254 (2015)
58. D.D. Han, Y.L. Zhang, H.B. Jiang, H. Xia, J. Feng, Q.D. Chen et al., Moisture-responsive graphene paper prepared by self-controlled photoreduction. Adv. Mater. **27**, 332–338 (2015)
59. S.H. Ha, Y.S. Jeong, Y.J. Lee, Free standing reduced graphene oxide film cathodes for lithium ion batteries. ACS Appl. Mater. Interfaces **5**, 12295–12303 (2013)
60. Z.L. Hou, W.L. Song, P. Wang, M.J. Meziani, C.Y. Kong, A. Anderson et al., Flexible graphene-graphene composites of superior thermal and electrical transport properties. ACS Appl. Mater. Interfaces **6**, 15026–15032 (2014)
61. Y.F. Li, Y.Z. Liu, W.Z. Shen, Y.G. Yang, M.Z. Wang, Y.F. Wen, Free-standing optoelectronic graphene-CdS-graphene oxide composite paper produced by vacuum-assisted self-assembly. Appl. Phys. A-Mater. Sci. Process. **106**, 779–784 (2012)
62. J.L. Xiang, L.T. Drzal, Thermal conductivity of exfoliated graphite nanoplatelet paper. Carbon **49**, 773–778 (2011)
63. C. Valles, J.D. Nunez, A.M. Benito, W.K. Maser, Flexible conductive graphene paper obtained by direct and gentle annealing of graphene oxide paper. Carbon **50**, 835–844 (2012)
64. S. Park, J.W. Suk, J.H. An, J. Oh, S. Lee, W. Lee et al., The effect of concentration of graphene nanoplatelets on mechanical and electrical properties of reduced graphene oxide papers. Carbon **50**, 4573–4578 (2012)
65. W. Lee, J.U. Lee, B.M. Jung, J.H. Byun, J.W. Yi, S.B. Lee et al., Simultaneous enhancement of mechanical, electrical and thermal properties of graphene oxide paper by embedding dopamine. Carbon **65**, 296–304 (2013)
66. D.Y. Kim, M.K. Kim, D.W. Kim, J.D. Suk, O.O. Park, Y.K. Kang, Flexible binder-free graphene paper cathodes for high-performance Li-O_2 batteries. Carbon **93**, 625–635 (2015)

67. L. Paliotta, G. De Bellis, A. Tamburrano, F. Marra, A. Rinaldi, S.K. Balijepalli et al., Highly conductive multilayer-graphene paper as a flexible lightweight electromagnetic shield. Carbon **89**, 260–271 (2015)
68. P. Kumar, F. Shahzad, S.G. Yu, S.M. Hong, Y.H. Kim, C.M. Koo, Large-area reduced graphene oxide thin film with excellent thermal conductivity and electromagnetic interference shielding effectiveness. Carbon **94**, 494–500 (2015)
69. S. Stankovich, D.A. Dikin, O.C. Compton, G.H.B. Dommett, R.S. Ruoff, S.T. Nguyen, Systematic post-assembly modification of graphene oxide paper with primary alkylamines. Chem. Mater. **22**, 4153–4157 (2010)
70. P. He, J. Sun, S.Y. Tian, S.W. Yang, S.J. Ding, G.Q. Ding et al., Processable aqueous dispersions of graphene stabilized by graphene quantum dots. Chem. Mater. **27**, 218–226 (2015)
71. X.Q. Zhang, S.H. Wan, J.B. Pu, L.P. Wang, X.Q. Liu, Highly hydrophobic and adhesive performance of graphene films. J. Mater. Chem. **21**, 12251–12258 (2011)
72. C. Zhang, W.W. Tjiu, W. Fan, Z. Yang, S. Huang, T.X. Liu, Aqueous stabilization of graphene sheets using exfoliated montmorillonite nanoplatelets for multifunctional free-standing hybrid films via vacuum-assisted self-assembly. J. Mater. Chem. **21**, 18011–18017 (2011)
73. S.D. Zhang, Q.H. Tao, Z.Y. Wang, Z.P. Zhang, Controlled heat release of new thermal storage materials: the case of polyethylene glycol intercalated into graphene oxide paper. J. Mater. Chem. **22**, 20166–20169 (2012)
74. G.Q. Ning, C.G. Xu, Y.M. Cao, X. Zhu, Z.M. Jiang, Z.J. Fan et al., Chemical vapor deposition derived flexible graphene paper and its application as high performance anodes for lithium rechargeable batteries. J. Mater. Chem. A **1**, 408–414 (2013)
75. K.W. Shu, C.Y. Wang, S. Li, C. Zhao, Y. Yang, H.K. Liu et al., Flexible free-standing graphene paper with interconnected porous structure for energy storage. J. Mater. Chem. A **3**, 4428–4434 (2015)
76. C. Cheng, J.W. Zhu, X.W. Yang, L. Qiu, Y.F. Wang, D. Li, Dynamic electrosorption analysis: a viable liquid-phase characterization method for porous carbon? J. Mater. Chem. A **1**, 9332–9340 (2013)
77. J.U. Lee, W. Lee, J.W. Yi, S.S. Yoon, S.B. Lee, B.M. Jung et al., Preparation of highly stacked graphene papers via site-selective functionalization of graphene oxide. J. Mat. Chem. A **1**, 12893–12899 (2013)
78. Z.Q. Jiang, Y.L. Shi, Z.J. Jiang, X.N. Tian, L.J. Luo, W.H. Chen, High performance of a free-standing sulfonic acid functionalized holey graphene oxide paper as a proton conducting polymer electrolyte for airbreathing direct methanol fuel cells. J. Mater. Chem. A **2**, 6494–6503 (2014)
79. W.L. Song, X.T. Guan, L.Z. Fan, W.Q. Cao, C.Y. Wang, Q.L. Zhao et al., Magnetic and conductive graphene papers toward thin layers of effective electromagnetic shielding. J. Mater. Chem. A **3**, 2097–2107 (2015)
80. Q. Liu, L.Q. Liu, K. Xie, Y.N. Meng, H.P. Wu, G.R. Wang et al., Synergistic effect of a rGO/PANI nanocomposite electrode based air working ionic actuator with a large actuation stroke and long-term durability. J. Mater. Chem. A. **3**, 8380–8388 (2015)
81. J.F. Ping, Y.X. Wang, K. Fan, W.Z. Tang, J. Wu, Y.B. Ying, High-performance flexible potentiometric sensing devices using free-standing graphene paper. J. Mater. Chem. B **1**, 4781–4791 (2013)
82. I.W.P. Chen, S.H. Saint Jhou, W. Chen, Preparation of high-quality graphene sheets and their applications in highly conductive papers and a high-performance electromechanical actuator. J. Mater. Chem. C **1**, 5970–5975 (2013)
83. A. Abouimrane, O.C. Compton, K. Amine, S.T. Nguyen, Non-annealed graphene paper as a binder-free anode for lithium-ion batteries. J. Phys. Chem. C **114**, 12800–12804 (2010)
84. J.Q. Liu, R. Wang, L. Cui, J.G. Tang, Z. Liu, Q.S. Kong et al., Using molecular level modification to tune the conductivity of graphene papers. J. Phys. Chem. C **116**, 17939–17946 (2012)

85. J.M. Zhu, L.W. Zhu, Z.F. Lu, L. Gu, S.L. Cao, X.B. Cao, Selectively expanding graphene oxide paper for creating multifunctional carbon materials. J. Phys. Chem. C **116**, 23075–23082 (2012)
86. T. Cetinkaya, S. Ozcan, M. Uysal, M.O. Guler, H. Akbulut, Free-standing flexible graphene oxide paper electrode for rechargeable Li-O_2 batteries. J. Power Sources **267**, 140–147 (2014)
87. M.H. Yang, S.H. Ko, J.S. Im, B.G. Choi, Free-standing molybdenum disulfide/graphene composite paper as a binder- and carbon-free anode for lithium-ion batteries. J. Power Sources **288**, 76–81 (2015)
88. H.B. Huang, Z.G. Song, N. Wei, L. Shi, Y.Y. Mao, Y.L. Ying et al., Ultrafast viscous water flow through nanostrand-channelled graphene oxide membranes. Nat. Communi. **4**, 2979 (2013)
89. Y.X. Xu, C.Y. Chen, Z.P. Zhao, Z.Y. Lin, C. Lee, X. Xu et al., Solution processable holey graphene oxide and Its derived macrostructures for high-performance supercapacitors. Nano Lett. **15**, 4605–4610 (2015)
90. D. Zhong, Q.L. Yang, L. Guo, S.X. Dou, K.S. Liu, L. Jiang, Fusion of nacre, mussel, and lotus leaf: bio-inspired graphene composite paper with multifunctional integration. Nanoscale **5**, 5758–5764 (2013)
91. A.B. Dichiara, T.J. Sherwood, J. Benton-Smith, J.C. Wilson, S.J. Weinstein, R.E. Rogers, Free-standing carbon nanotube/graphene hybrid papers as next generation adsorbents. Nanoscale **6**, 6322–6327 (2014)
92. X.Y. Huang, C.Y. Zhi, P.K. Jiang, D. Golberg, Y. Bando, T. Tanaka, Temperature-dependent electrical property transition of graphene oxide paper. Nanotechnology **23**, 455705 (2012)
93. H. Bi, J. Chen, W. Zhao, S.R. Sun, Y.F. Tang, T.Q. Lin et al., Highly conductive, free-standing and flexible graphene papers for energy conversion and storage devices. RSC Adv. **3**, 8454–8460 (2013)
94. S.J. Park, J.H. An, J.W. Suk, R.S. Ruoff, Graphene-Based Actuators. Small **6**, 210–212 (2010)
95. J.W. Zhang, G. Shi, C. Jiang, S. Ju, D.Z. Jiang, 3D bridged carbon nanoring/graphene hybrid paper as a high-performance lateral heat spreader. Small **11**, 6197–6204 (2015)
96. F. Xiao, Y.Q. Li, H.C. Gao, S.B. Ge, H.W. Duan, Growth of coral-like PtAu-MnO_2 binary nanocomposites on free-standing graphene paper for flexible nonenzymatic glucose sensors. Biosens. Bioelectron. **41**, 417–423 (2013)
97. F. Xiao, J.B. Song, H.C. Gao, X.L. Zan, R. Xu, H.W. Duan, Coating graphene paper with 2D-assembly of electrocatalytic nanoparticles: a modular approach toward high-performance flexible electrodes. ACS Nano **6**, 100–110 (2012)
98. W. Cui, M.Z. Li, J.Y. Liu, B. Wang, C. Zhang, L. Jiang et al., A strong integrated strength and toughness artificial nacre based on dopamine cross-linked graphene oxide. ACS Nano **8**, 9511–9517 (2014)
99. F. Xiao, Y.Q. Li, X.L. Zan, K. Liao, R. Xu, H.W. Duan, Growth of metal-metal oxide nanostructures on freestanding graphene paper for flexible biosensors. Adv. Func. Mater. **22**, 2487–2494 (2012)
100. B. Shen, W.T. Zhai, W.G. Zheng, Ultrathin flexible graphene film: An excellent thermal conducting material with efficient EMI shielding. Adv. Func. Mater. **24**, 4542–4548 (2014)
101. M. Zhang, L. Huang, J. Chen, C. Li, G.Q. Shi, Ultratough, ultrastrong, and highly conductive graphene films with arbitrary sizes. Adv. Mater. **26**, 7588–7592 (2014)
102. S.J. Yang, J.H. Kang, H.S. Jung, T.H. Kim, C.R. Park, Preparation of a freestanding, macroporous reduced graphene oxide film as an efficient and recyclable sorbent for oils and organic solvents. J. Mater. Chem. A **1**, 9427–9432 (2013)
103. S. Korkut, J.D. Roy-Mayhew, D.M. Dabbs, D.L. Milius, I.A. Aksay, High surface area tapes produced with functionalized graphene. ACS Nano **5**, 5214–5222 (2011)
104. G.Q. Xin, H.T. Sun, T. Hu, H.R. Fard, X. Sun, N. Koratkar et al., Large-area freestanding graphene paper for superior thermal management. Adv. Mater. **26**, 4521–4526 (2014)

105. M. Wang, D. Le Dai, J.S. Oh, M. Nguyen Thi, S.H. Kim, S.C. Hong et al., Large-area, conductive and flexible reduced graphene oxide (rGO) membrane fabricated by electrophoretic deposition (EPD). ACS Appl. Mater. Interfaces **6**, 1747–1753 (2014)
106. S.Y. Liu, K. Chen, Y. Fu, S.Y. Yu, Z.H. Bao, Reduced graphene oxide paper by supercritical ethanol treatment and its electrochemical properties. Appl. Surf. Sci. **258**, 5299–5303 (2012)
107. C.M. Chen, J.Q. Huang, Q. Zhang, W.Z. Gong, Q.H. Yang, M.Z. Wang et al., Annealing a graphene oxide film to produce a free standing high conductive graphene film. Carbon **50**, 659–667 (2012)
108. K.W. Shu, C.Y. Wang, M. Wang, C. Zhao, G.G. Wallace, Graphene cryogel papers with enhanced mechanical strength for high performance lithium battery anodes. J. Mater. Chem. A **2**, 1325–1331 (2014)
109. I.F. Cheng, Y.Q. Xie, R.A. Gonzales, P.R. Brejna, J.P. Sundararajan, B.A.F. Kengne et al., Synthesis of graphene paper from pyrolyzed asphalt. Carbon **49**, 2852–2861 (2011)
110. L. Zhang, N.T. Alvarez, M.X. Zhang, M. Haase, R. Malik, D. Mast et al., Preparation and characterization of graphene paper for electromagnetic interference shielding. Carbon **82**, 353–359 (2015)
111. N. Li, G.Z. Yang, Y. Sun, H.W. Song, H. Cui, G.W. Yang et al., Free-standing and transparent graphene membrane of polyhedron box-shaped basic building units directly grown using a NaCl template for flexible transparent and stretchable solid-state supercapacitors. Nano Lett. **15**, 3195–3203 (2015)
112. A. Lerf, A. Buchsteiner, J. Pieper, S. Schottl, I. Dekany, T. Szabo et al., Hydration behavior and dynamics of water molecules in graphite oxide. J. Phys. Chem. Solids **67**, 1106–1110 (2006)
113. R. Mukherjee, A.V. Thomas, A. Krishnamurthy, N. Koratkar, Photothermally reduced graphene as high-power anodes for lithium-ion batteries. ACS Nano **6**, 7867–7878 (2012)
114. Y.H. Hu, X.F. Li, D.S. Geng, M. Cai, R.Y. Li, X.L. Sun, Influence of paper thickness on the electrochemical performances of graphene papers as an anode for lithium ion batteries. Electrochim. Acta **91**, 227–233 (2013)
115. X. Zhao, C.M. Hayner, M.C. Kung, H.H. Kung, Flexible holey graphene paper electrodes with enhanced rate capability for energy storage applications. ACS Nano **5**, 8739–8749 (2011)
116. Z.H. Jin, P. Owour, S.D. Lei, L.H. Ge, Graphene, graphene quantum dots and their applications in optoelectronics. Curr. Opin. Colloid Interface Sci. **20**, 439–453 (2015)
117. X.J. Zhou, S.W. Guo, J.Y. Zhang, Solution-processable graphene quantum dots. ChemPhysChem **14**, 2627–2640 (2013)
118. I. Ozfidan, M. Korkusinski, P. Hawrylak, Electronic properties and electron-electron interactions in graphene quantum dots. Phys. Status Solidi-Rapid Res. Lett. **10**, 13–23 (2016)
119. J. Peng, W. Gao, B.K. Gupta, Z. Liu, R. Romero-Aburto, L.H. Ge et al., Graphene puantum dots derived from carbon fibers. Nano Lett. **12**, 844–849 (2012)
120. S.W. Yang, J. Sun, X.B. Li, W. Zhou, Z.Y. Wang, P. He et al., Large-scale fabrication of heavy doped carbon quantum dots with tunable-photoluminescence and sensitive fluorescence detection. J. Mater. Chem. A **2**, 8660–8667 (2014)
121. N.V. Medhekar, A. Ramasubramaniam, R.S. Ruoff, V.B. Shenoy, Hydrogen bond networks in graphene oxide composite paper: structure and mechanical properties. ACS Nano **4**, 2300–2306 (2010)
122. K.W. Putz, O.C. Compton, M.J. Palmeri, S.T. Nguyen, L.C. Brinson, High-nanofiller-content graphene oxide-polymer nanocomposites via vacuum-assisted self-assembly. Adv. Func. Mater. **20**, 3322–3329 (2010)
123. X.W. Yang, C. Cheng, Y.F. Wang, L. Qiu, D. Li, Liquid-mediated dense integration of graphene materials for compact capacitive energy storage. Science **341**, 534–537 (2013)

124. O.C. Compton, D.A. Dikin, K.W. Putz, L.C. Brinson, S.T. Nguyen, Electrically conductive "alkylated" graphene paper via chemical reduction of amine-functionalized graphene oxide paper. Adv. Mater. **22**, 892–896 (2010)
125. I. Dekany, R. Kruger-Grasser, A. Weiss, Selective liquid sorption properties of hydrophobized graphite oxide nanostructures. Colloid Polym. Sci. **276**, 570–576 (1998)
126. S. Park, N. Mohanty, J.W. Suk, A. Nagaraja, J.H. An, R.D. Piner et al., Biocompatible, robust free-standing paper composed of a TWEEN/graphene composite. Adv. Mater. **22**, 17361740 (2010)
127. J.J. Liang, Y.F. Xu, D. Sui, L. Zhang, Y. Huang, Y.F. Ma et al., Flexible, magnetic, and electrically conductive graphene/Fe_3O_4 paper and its application for magnetic-controlled switches. J. Phys. Chem. C **114**, 17465–17471 (2010)
128. R. Rozada, J.I. Paredes, S. Villar-Rodil, A. Martinez-Alonso, J.M.D. Tascon, Towards full repair of defects in reduced graphene oxide films by two-step graphitization. Nano Res. **6**, 216–233 (2013)
129. T. Ghosh, C. Biswas, J.S. Oh, G. Arabale, T.S. Hwang, L. Nguyen Dang et al., Solution-processed graphite membrane from reassembled graphene oxide. Chem. Mater. **24**, 594–599 (2012)
130. Y. Almog, J. Klein, Interactions between mica surfaces in a polystyrene-cyclopentane solution near the theta-temperature. J. Colloid Interface Sci. **106**, 33–44 (1985)
131. P. Alexandridis, T.A. Hatton, Poly(ethylene oxide)-poly(propylene oxide)-poly(ethylene oxide) block-copolymer surfactants in aqueous-solutions and at interfaces—thermodynamics, structure, dynamics, and modeling. Colloids Surfaces A Physicochem. Eng. Aspects **96**, 1–46 (1995)
132. K.W. Ebagninin, A. Benchabane, K. Bekkour, Rheological characterization of poly(ethylene oxide) solutions of different molecular weights. J. Colloid Interface Sci. **336**, 360–367 (2009)
133. I. Bihannic, C. Baravian, J.F.L. Duval, E. Paineau, F. Meneau, P. Levitz et al., Orientational order of colloidal disk-shaped particles under shear-flow conditions: a rheological-small-angle X-ray scattering study. J. Phys. Chem. B **114**, 16347–16355 (2010)
134. E.L. Decker, S. Garoff, Contact line structure and dynamics on surfaces with contact angle hysteresis. Langmuir **13**, 6321–6332 (1997)
135. A. Jaworek, A.T. Sobczyk, Electrospraying route to nanotechnology: An overview. J. Electrostat. **66**, 197–219 (2008)
136. M. Pal, U. Pal, Y. Gracia, J.M. Jimenez, F. Perez-Rodriguez, Effects of crystallization and dopant concentration on the emission behavior of TiO_2: Eu nanophosphors. Nanoscale Res. Lett. **7**, 1 (2012)
137. Y.N. Meng, G.Q. Xin, J.W. Nam, S.M. Cho, H.Y. Chae, Electrospray deposition of carbon nanotube thin films for flexible transparent electrodes. J. Nanosci. Nanotechnol. **13**, 6125–6129 (2013)
138. M. Mustafa, M.N. Awais, G. Pooniah, K.H. Choi, J.B. Ko, Y.H. Doh, Electrospray deposition of a graphene-oxide thin film, its characterization and investigation of its resistive switching performance. J. Korean Phys. Soc. **61**, 470–475 (2012)
139. C.K. Lee, K.W. Park, S.W. Hwang, S.B. Lee, J.K. Shim, Direct electrospray deposition of graphene onto paper and effect of binder on its surface resistance. J. Nanosci. Nanotechnol. **13**, 7108–7111 (2013)
140. M.H. Jin, T.H. Kim, S.C. Lim, D.L. Duong, H.J. Shin, Y.W. Jo et al., Facile physical route to highly crystalline graphene. Adv. Func. Mater. **21**, 3496–3501 (2011)
141. L. Song, F. Khoerunnisa, W. Gao, W.H. Dou, T. Hayashi, K. Kaneko et al., Effect of high-temperature thermal treatment on the structure and adsorption properties of reduced graphene oxide. Carbon **52**, 608–612 (2013)
142. C.M. Chen, Q.H. Yang, Y.G. Yang, W. Lv, Y.F. Wen, P.X. Hou et al., Self-assembled free-standing graphite oxide membrane. Adv. Mater. **21**, 3007–3011 (2009)
143. J.Y. Kim, L.J. Cote, F. Kim, W. Yuan, K.R. Shull, J.X. Huang, Graphene oxide sheets at interfaces. J. Am. Chem. Soc. **132**, 8180–8186 (2010)

144. L. Chen, L.L. Huang, J.H. Zhu, Stitching graphene oxide sheets into a membrane at a liquid/liquid interface. Chem. Commun. **50**, 15944–15947 (2014)
145. F. Kim, L.J. Cote, J.X. Huang, Graphene oxide: Surface activity and two-dimensional assembly. Adv. Mater. **22**, 1954–1958 (2010)
146. H. Bai, C. Li, G.Q. Shi, Functional composite materials based on chemically converted graphene. Adv. Mater. **23**, 1089–1115 (2011)
147. X.J. Wan, Y. Huang, Y.S. Chen, Focusing on energy and optoelectronic applications: a journey for graphene and graphene oxide at large scale. Acc. Chem. Res. **45**, 598–607 (2012)
148. X. Huang, X.Y. Qi, F. Boey, H. Zhang, Graphene-based composites. Chem. Soc. Rev. **41**, 666–686 (2012)
149. B. Luo, S.M. Liu, L.J. Zhi, Chemical approaches toward graphene-based nanomaterials and their applications in energy-related areas. Small **8**, 630–646 (2012)
150. Y.Q. Sun, Q. Wu, G.Q. Shi, Graphene based new energy materials. Energy Environ. Sci. **4**, 1113–1132 (2011)
151. W.R. Yang, K.R. Ratinac, S.P. Ringer, P. Thordarson, J.J. Gooding, F. Braet, Carbon nanomaterials in biosensors: Should you use nanotubes or graphene? Angew. Chem. Int. Ed. **49**, 2114–2138 (2010)
152. Y.X. Xu, G.Q. Shi, Assembly of chemically modified graphene: methods and applications. J. Mater. Chem. **21**, 3311–3323 (2011)
153. D. Li, R.B. Kaner, Materials science—graphene-based materials. Science **320**, 1170–1171 (2008)
154. D. Li, M.B. Mueller, S. Gilje, R.B. Kaner, G.G. Wallace, Processable aqueous dispersions of graphene nanosheets. Nat. Nanotechnol. **3**, 101–105 (2008)
155. H. Bai, C. Li, X.L. Wang, G.Q. Shi, A pH-sensitive graphene oxide composite hydrogel. Chem. Commun. **46**, 2376–2378 (2010)
156. Y.X. Xu, Q. Wu, Y.Q. Sun, H. Bai, G.Q. Shi, Three-dimensional self-assembly of graphene oxide and DNA into multifunctional hydrogels. ACS Nano **4**, 7358–7362 (2010)
157. H. Bai, C. Li, X.L. Wang, G.Q. Shi, On the gelation of graphene oxide. J. Phys. Chem. C **115**, 5545–5551 (2011)
158. C.C. Huang, H. Bai, C. Li, G.Q. Shi, A graphene oxide/hemoglobin composite hydrogel for enzymatic catalysis in organic solvents. Chem. Commun. **47**, 4962–4964 (2011)
159. O.C. Compton, Z. An, K.W. Putz, B.J. Hong, B.G. Hauser, L.C. Brinson et al., Additive-free hydrogelation of graphene oxide by ultrasonication. Carbon **50**, 3399–3406 (2012)
160. A. Sahu, W.I. Choi, G.Y. Tae, A stimuli-sensitive injectable graphene oxide composite hydrogel. Chem. Commun. **48**, 5820–5822 (2012)
161. J. Zhang, Y.W. Cao, J.C. Feng, P.Y. Wu, Graphene-oxide-sheet-induced gelation of cellulose and promoted mechanical properties of composite aerogels. J. Phys. Chem. C **116**, 8063–8068 (2012)
162. X. Wang, L.L. Lu, Z.L. Yu, X.W. Xu, Y.R. Zheng, S.H. Yu, Scalable template synthesis of resorcinol-formaldehyde/graphene oxide composite aerogels with tunable densities and mechanical properties. Angew. Chem. Int. Ed. **54**, 2397–2401 (2015)
163. D.R. Dreyer, S. Park, C.W. Bielawski, R.S. Ruoff, The chemistry of graphene oxide. Chem. Soc. Rev. **39**, 228–240 (2010)
164. Y.R. Lin, G.J. Ehlert, C. Bukowsky, H.A. Sodano, Superhydrophobic functionalized graphene aerogels. ACS Appl. Mater. Interfaces **3**, 2200–2203 (2011)
165. N. Mohanty, V. Berry, Graphene-based single-bacterium resolution biodevice and DNA transistor: interfacing graphene derivatives with nanoscale and microscale biocomponents. Nano Lett. **8**, 4469–4476 (2008)
166. A.J. Patil, J.L. Vickery, T.B. Scott, S. Mann, Aqueous stabilization and self-assembly of graphene sheets into layered bio-nanocomposites using DNA. Adv. Mater. **21**, 3159–3164 (2009)

167. S.J. He, B. Song, D. Li, C.F. Zhu, W.P. Qi, Y.Q. Wen et al., A graphene nanoprobe for rapid, sensitive, and multicolor fluorescent DNA analysis. Adv. Func. Mater. **20**, 453–459 (2010)
168. H. Hu, Z.B. Zhao, W.B. Wan, Y. Gogotsi, J.S. Qiu, Ultralight and highly compressible graphene aerogels. Adv. Mater. **25**, 2219–2223 (2013)
169. Q.L. Fang, B.L. Chen, Self-assembly of graphene oxide aerogels by layered double hydroxides cross-linking and their application in water purification. J. Mater. Chem. A **2**, 8941–8951 (2014)
170. G.L. Fan, F. Li, D.G. Evans, X.F. Duan, Catalytic applications of layered double hydroxides: recent advances and perspectives. Chem. Soc. Rev. **43**, 7040–7066 (2014)
171. C.M. Li, M. Wei, D.G. Evans, X.F. Duan, Layered double hydroxide-based nanomaterials as highly efficient catalysts and adsorbents. Small **10**, 4469–4486 (2014)
172. Li W, Yan D, Gao R, Lu J, Wei M, Duan X. Recent advances in stimuli-responsive photofunctional materials based on accommodation of chromophore into layered double hydroxide nanogallery. J. Nanomaterials. 2013:586462
173. J. Qu, Q.W. Zhang, X.W. Li, X.M. He, S.X. Song, Mechanochemical approaches to synthesize layered double hydroxides: a review. Appl. Clay Sci. **119**, 185–192 (2016)
174. Q. Wang, D. O'Hare, Recent advances in the synthesis and application of layered double hydroxide (LDH) nanosheets. Chem. Rev. **112**, 4124–4155 (2012)
175. K. Zhang, Z.P. Xu, J. Lu, Z.Y. Tang, H.J. Zhao, D.A. Good et al., Potential for layered double hydroxides-based, innovative drug delivery systems. Int. J. Mol. Sci. **15**, 7409–7428 (2014)
176. X.L. Wang, H. Bai, G.Q. Shi, Size fractionation of graphene oxide sheets by pH-assisted selective sedimentation. J. Am. Chem. Soc. **133**, 6338–6342 (2011)
177. F. Liu, T.S. Seo, A controllable self-assembly method for large-scale synthesis of graphene sponges and free-standing graphene films. Adv. Func. Mater. **20**, 1930–1936 (2010)
178. J.Y. Cao, Y.M. Wang, P. Xiao, Y.C. Chen, Y. Zhou, J.H. Ouyang et al., Hollow graphene spheres self-assembled from graphene oxide sheets by a one-step hydrothermal process. Carbon **56**, 389–391 (2013)
179. Z.H. Tang, S.L. Shen, J. Zhuang, X. Wang, Noble-metal-promoted three-dimensional macroassembly of single-layered graphene oxide. Angew. Chem. Int. Ed. **49**, 4603–4607 (2010)
180. Y.Q. Sun, Q. Wu, G.Q. Shi, Supercapacitors based on self-assembled graphene organogel. Phys. Chem. Chem. Phys. **13**, 17249–17254 (2011)
181. J.P. Zhao, W.C. Ren, H.M. Cheng, Graphene sponge for efficient and repeatable adsorption and desorption of water contaminations. J. Mater. Chem. **22**, 20197–20202 (2012)
182. X.X. Sun, P. Cheng, H.J. Wang, H. Xu, L.Q. Dang, Z.H. Liu et al., Activation of graphene aerogel with phosphoric acid for enhanced electrocapacitive performance. Carbon **92**, 1–10 (2015)
183. W.J. Liu, Y.K. Wang, Z.H. Li, Tuning of surface wettability of RGO-based aerogels for various adsorbates in water using different amino acids. Chem. Commun. **50**, 10311–10314 (2014)
184. K.X. Sheng, Y.X. Xu, C. Li, G.Q. Shi, High-performance self-assembled graphene hydrogels prepared by chemical reduction of graphene oxide. New Carbon Mater. **26**, 9–15 (2011)
185. X. Zhang, Z.Y. Sui, B. Xu, S.F. Yue, Y.J. Luo, W.C. Zhan et al., Mechanically strong and highly conductive graphene aerogel and its use as electrodes for electrochemical power sources. J. Mater. Chem. **21**, 6494–6497 (2011)
186. P. Hai Dinh, P. Viet Hung, C. Tran Viet, N.P. Thuy-Duong, J.S. Chung, E.W. Shin et al., Synthesis of the chemically converted graphene xerogel with superior electrical conductivity. Chem. Commun. **47**, 9672–9674 (2011)
187. W.F. Chen, L.F. Yan, In situ self-assembly of mild chemical reduction graphene for three-dimensional architectures. Nanoscale **3**, 3132–3137 (2011)

188. W.F. Chen, S.R. Li, C.H. Chen, L.F. Yan, Self-assembly and embedding of nanoparticles by in situ reduced graphene for preparation of a 3D graphene/nanoparticle aerogel. Adv. Mater. **23**, 5679–5683 (2011)
189. W.F. Chen, L.F. Yan, P.R. Bangal, Chemical reduction of graphene oxide to graphene by sulfur-containing compounds. J. Phys. Chem. C **114**, 19885–19890 (2010)
190. H.P. Cong, X.C. Ren, P. Wang, S.H. Yu, Macroscopic multifunctional graphene-based hydrogels and aerogels by a metal ion induced self-assembly process. ACS Nano **6**, 2693–2703 (2012)
191. X.W. Yang, J.W. Zhu, L. Qiu, D. Li, Bioinspired effective prevention of restacking in multilayered graphene films: towards the next generation of high-performance supercapacitors. Adv. Mater. **23**, 2833–2838 (2011)
192. S.H. Lee, H.W. Kim, J.O. Hwang, W.J. Lee, J. Kwon, C.W. Bielawski et al., Three-dimensional self-assembly of graphene oxide platelets into mechanically flexible macroporous carbon films. Angew. Chem. International Ed. **49**, 10084–10088 (2010)
193. N. Ayres, Atom transfer radical polymerization: a robust and versatile route for polymer synthesis. Polym. Rev. **51**, 138–162 (2011)
194. K. Matyjaszewski, Atom transfer radical polymerization: From mechanisms to applications. Isr. J. Chem. **52**, 206–220 (2012)
195. K. Matyjaszewski, J.H. Xia, Atom transfer radical polymerization. Chem. Rev. **101**, 2921–2990 (2001)
196. S. Stankovich, D.A. Dikin, R.D. Piner, K.A. Kohlhaas, A. Kleinhammes, Y.Y. Jia et al., Synthesis of graphene-based nanosheets via chemical reduction of exfoliated graphite oxide. Carbon **45**, 1558–1565 (2007)
197. S.J. An, Y.W. Zhu, S.H. Lee, M.D. Stoller, T. Emilsson, S.J. Park et al., Thin film fabrication and simultaneous anodic reduction of deposited graphene oxide platelets by electrophoretic deposition. J. Phys. Chem. Lett. **1**, 1259–1263 (2010)
198. X.F. Gao, J. Jang, S. Nagase, Hydrazine and thermal reduction of graphene oxide: reaction mechanisms, product dtructures, and reaction design. J. Phys. Chem. C **114**, 832–842 (2010)
199. Y.W. Zhu, S. Murali, M.D. Stoller, K.J. Ganesh, W.W. Cai, P.J. Ferreira et al., Carbon-based supercapacitors produced by activation of graphene. Science **332**, 1537–1541 (2011)
200. L.L. Zhang, X. Zhao, M.D. Stoller, Y.W. Zhu, H.X. Ji, S. Murali et al., Highly conductive and porous activated reduced graphene oxide films for high-power supercapacitors. Nano Lett. **12**, 1806–1812 (2012)
201. J.L. Vickery, A.J. Patil, S. Mann, Fabrication of graphene-polymer nanocomposites with higher-order three-dimensional architectures. Adv. Mater. **21**, 2180–2184 (2009)
202. Z.P. Chen, W.C. Ren, L.B. Gao, B.L. Liu, S.F. Pei, H.M. Cheng, Three-dimensional flexible and conductive interconnected graphene networks grown by chemical vapour deposition. Nat. Mater. **10**, 424–428 (2011)
203. L. Estevez, A. Kelarakis, Q.M. Gong, E.H. Da'as, E.P. Giannelis, Multifunctional graphene/platinum/nafion hybrids via ice templating. J. Am. Chem. Soc. **133**, 6122–6125 (2011)
204. B.G. Choi, M. Yang, W.H. Hong, J.W. Choi, Y.S. Huh, 3D macroporous graphene frameworks for supercapacitors with high energy and power densities. ACS Nano **6**, 4020–4028 (2012)
205. H.M. Sun, L.Y. Cao, L.H. Lu, Bacteria promoted hierarchical carbon materials for high-performance supercapacitor. Energy Environ. Sci. **5**, 6206–6213 (2012)
206. X.Y. Xiao, T.E. Beechem, M.T. Brumbach, T.N. Lambert, D.J. Davis, J.R. Michael et al., Lithographically defined three-dimensional graphene structures. ACS Nano **6**, 3573–3579 (2012)
207. M. Batzill, The surface science of graphene: metal interfaces, CVD synthesis, nanoribbons, chemical modifications, and defects. Surf. Sci. Rep. **67**, 83–115 (2012)

208. P.L. Huang, S.C. Lin, C.Y. Yeh, H.H. Kuo, S.H. Huang, G.R. Lin et al., Stable mode-locked fiber laser based on CVD fabricated graphene saturable absorber. Opt. Express **20**, 2460–2465 (2012)
209. E. Kibena, M. Mooste, J. Kozlova, M. Marandi, V. Sammelselg, K. Tammeveski, Surface and electrochemical characterisation of CVD grown graphene sheets. Electrochem. Commun. **35**, 26–29 (2013)
210. J.R. Kyle, A. Guvenc, W. Wang, M. Ghazinejad, J. Lin, S.R. Guo et al., Centimeter-scale high-resolution metrology of entire CVD-grown graphene sheets. Small **7**, 2599–2606 (2011)
211. R. Munoz, C. Gomez-Aleixandre, Review of CVD synthesis of graphene. Chem. Vap. Deposition **19**, 297–322 (2013)
212. A.W. Tsen, L. Brown, R.W. Havener, J. Park, Polycrystallinity and stacking in CVD graphene. Acc. Chem. Res. **46**, 2286–2296 (2013)
213. T. Yamada, J. Kim, M. Ishihara, M. Hasegawa, Low-temperature graphene synthesis using microwave plasma CVD. J. Phys. D-Appl. Phys. **46**, 063001 (2013)
214. W.L. Li, K. Lu, J.Y. Walz, Freeze casting of porous materials: review of critical factors in microstructure evolution. Int. Mater. Rev. **57**, 37–60 (2012)
215. S. Deville, Ice-templating, freeze casting: Beyond materials processing. J. Mater. Res. **28**, 2202–2219 (2013)
216. V. Medri, D. Sciti, D.D. Fabbriche, A. Piancastelli, E. Landi, Ice templating of ZrB_2–SiC systems. Ceram. Int. **41**, 10324–10330 (2015)
217. E. Papa, V. Medri, P. Benito, A. Vaccari, S. Bugani, J. Jaroszewicz et al., Synthesis of porous hierarchical geopolymer monoliths by ice-templating. Microporous Mesoporous Mater. **215**, 206–214 (2015)
218. S. Deville, E. Saiz, A.P. Tomsia, Ice-templated porous alumina structures. Acta Mater. **55**, 1965–1974 (2007)
219. M.C. Gutierrez, M.L. Ferrer, F. del Monte, Ice-templated materials: sophisticated structures exhibiting enhanced functionalities obtained after unidirectional freezing and ice-segregation-induced self-assembly. Chem. Mater. **20**, 634–648 (2008)
220. M. Kota, X. Yu, S.H. Yeon, H.W. Cheong, H.S. Park, Ice-templated three dimensional nitrogen doped graphene for enhanced supercapacitor performance. J. Power Sources **303**, 372–378 (2016)
221. K.H. Lee, Y.W. Lee, S.W. Lee, J.S. Ha, S.S. Lee, J.G. Son, Ice-templated self-assembly of $VOPO_4$-graphene nanocomposites for vertically porous 3D supercapacitor electrodes. Sci. Rep. **5**, 13696 (2015)
222. J.A. Slotwinski, E.J. Garboczi, Metrology needs for metal additive manufacturing powders. JOM **67**, 538–543 (2015)
223. J. Deckers, J. Vleugels, J.P. Kruthl, Additive manufacturing of ceramics: a review. J. Ceram. Sci. Technol. **5**, 245–260 (2014)
224. S.M. Giannitelli, P. Mozetic, M. Trombetta, A. Rainer, Combined additive manufacturing approaches in tissue engineering. Acta Biomater. **24**, 1–11 (2015)
225. R. Gmeiner, U. Deisinger, J. Schoenherr, B. Lechner, R. Detsch, A.R. Boccaccini et al., Additive manufacturing of bioactive glasses and silicate bioceramics. J. Ceram. Sci. Technol. **6**, 75–86 (2015)
226. A.R. Studart, Additive manufacturing of biologically-inspired materials. Chem. Soc. Rev. **45**, 359–376 (2016)
227. N. Travitzky, A. Bonet, B. Dermeik, T. Fey, I. Filbert-Demut, L. Schlier et al., Additive manufacturing of ceramic-based materials. Adv. Eng. Mater. **16**, 729–754 (2014)
228. S. Yang, Y.Y.F. Zhao, Additive manufacturing-enabled design theory and methodology: a critical review. Int. J. Adv. Manuf. Technol. **80**, 327–342 (2015)
229. J.H. Kim, W.S. Chang, D.H. Kim, J.R. Yang, J.T. Han, G.W. Lee et al., 3D printing of reduced graphene oxide nanowires. Adv. Mater. **27**, 157–161 (2015)
230. D. Lin, S.Y. Jin, F. Zhang, C. Wang, Y.Q. Wang, C. Zhou, et al. 3D stereolithography printing of graphene oxide reinforced complex architectures. Nanotechnology. 2015; 26

231. Z.X. Yang, C.Z. Yan, J.H. Liu, S. Chabi, Y.D. Xia, Y.Q. Zhu, Designing 3D graphene networks via a 3D-printed Ni template. RSC Adv. **5**, 29397–29400 (2015)
232. A.E. Jakus, E.B. Secor, A.L. Rutz, S.W. Jordan, M.C. Hersam, R.N. Shah, Three-dimensional printing of high-content graphene scaffolds for electronic and biomedical applications. ACS Nano **9**, 4636–4648 (2015)
233. C.F. Zhu, T.Y.J. Han, E.B. Duoss, A.M. Golobic, J.D. Kuntz, C.M. Spadaccini et al., Highly compressible 3D periodic graphene aerogel microlattices. Nat. Commun. **6**, 6962 (2015)
234. S.S. Duan, K. Yang, Z.H. Wang, M.T. Chen, L. Zhang, H.B. Zhang et al., Fabrication of highly stretchable conductors based on 3D printed porous poly(dimethylsiloxane) and conductive carbon nanotubes/graphene network. ACS Appl. Mater. Interfaces **8**, 2187–2192 (2016)
235. M.A. Worsley, T.Y. Olson, J.R.I. Lee, Willey TrM, M.H. Nielsen, S.K. Roberts et al., High surface area, sp^2-cross-linked three-dimensional graphene monoliths. J. Phys. Chem. Lett. **2**, 921–925 (2011)
236. Z.A. Munir, U. Anselmi-Tamburini, M. Ohyanagi, The effect of electric field and pressure on the synthesis and consolidation of materials: A review of the spark plasma sintering method. J. Mater. Sci. **41**, 763–777 (2006)
237. E.A. Olevsky, S. Kandukuri, L. Froyen, Consolidation enhancement in spark-plasma sintering: impact of high heating rates. J. Appl. Phys. **102**, 114913 (2007)
238. N. Saheb, Z. Iqbal, A. Khalil, A.S. Hakeem, N. Al Aqeeli, T. Laoui et al. Spark plasma sintering of metals and metal matrix nanocomposites: a review. J. Nanomater. 2012:983470
239. L.J. Wang, J.F. Zhang, W. Jiang, Recent development in reactive synthesis of nanostructured bulk materials by spark plasma sintering. Int. J. Refract Metal Hard Mater. **39**, 103–112 (2013)
240. M.S. Yurlova, V.D. Demenyuk, L.Y. Lebedeva, D.V. Dudina, E.G. Grigoryev, E.A. Olevsky, Electric pulse consolidation: an alternative to spark plasma sintering. J. Mater. Sci. **49**, 952–985 (2014)
241. K. Lu, Sintering of nanoceramics. Int. Mater. Rev. **53**, 21–38 (2008)
242. T. He, J.L. Li, L.J. Wang, J.J. Zhu, W. Jiang, Preparation and consolidation of alumina/graphene composite powders. Mater. Trans. **50**, 749–751 (2009)
243. K. Wang, Y.F. Wang, Z.J. Fan, J. Yan, T. Wei, Preparation of graphene nanosheet/alumina composites by spark plasma sintering. Mater. Res. Bull. **46**, 315–318 (2011)
244. Y.C. Fan, L.J. Wang, J.L. Li, J.Q. Li, S.K. Sun, F. Chen et al., Preparation and electrical properties of graphene nanosheet/Al_2O_3 composites. Carbon **48**, 1743–1749 (2010)
245. L.S. Walker, V.R. Marotto, M.A. Rafiee, N. Koratkar, E.L. Corral, Toughening in graphene ceramic composites. ACS Nano **5**, 3182–3190 (2011)
246. A. Nieto, D. Lahiri, A. Agarwal, Synthesis and properties of bulk graphene nanoplatelets consolidated by spark plasma sintering. Carbon **50**, 4068–4077 (2012)
247. B. Apak, F.C. Sahin, C-CNT produced by spark plasma sintering. Acta Phys. Pol. A **127**, 1029–1031 (2015)
248. J.L. Li, G.Z. Bai, J.W. Feng, W. Jiang, Microstructure and mechanical properties of hot-pressed carbon nanotubes compacted by spark plasma sintering. Carbon **43**, 2649–2653 (2005)
249. Y. Sato, H. Nishizaka, S. Sawano, A. Yoshinaka, K. Hirano, S. Hashiguchi et al., Influence of the structure of the nanotube on the mechanical properties of binder-free multi-walled carbon nanotube solids. Carbon **50**, 34–39 (2012)
250. G. Yamamoto, Y. Sato, T. Takahashi, M. Omori, T. Hashida, A. Okubo et al., Single-walled carbon nanotube-derived novel structural material. J. Mater. Res. **21**, 1537–1542 (2006)

Chapter 9
GaN Nanowall Network: Laser Assisted Molecular Beam Epitaxy Growth and Properties

M. Senthil Kumar and Sunil S. Kushvaha

9.1 Introduction

Group III-nitride materials, such as InN, GaN, AlN and their alloys, are the well-established semiconductors for the fabrication of high efficiency blue/green light emitting diodes (LEDs) and laser diodes (LDs) [1–3]. III-nitride LEDs are also the backbone for the current solid state lighting technology [4, 5]. Because of small size, light weight, high efficiency and long life time, nitride LEDs find a wide range of applications in the field of room lighting, displays, traffic lights, automobiles, etc. The excellent physical properties of group III-nitrides such as direct bandgap with a large tunability, high carrier mobility, high electron saturation velocity, high breakdown field, good mechanical and thermal conductivity, radiation hardness etc. are behind this success and make III-nitrides second most important semiconductors after silicon. Some of the important properties of wurtzite III-nitride semiconductors are listed in Table 9.1 [6–8]. Currently, III-nitrides are being explored for their potential applications in the field of short wavelength optoelectronics, high power electronics, photovoltaics and spintronics as well. Efficient AlGaN based ultraviolet (UV) LEDs are soon expected to replace UV lamps as they are free from ozone generation and mercury. On the other hand, the in-built spontaneous and piezo-electric polarization fields of GaN have led the way to realize AlGaN/GaN heterostructure based high electron mobility transistors (HEMTs) for micro- and millimeter-wave power electronics [9, 10]. Due to their robust nature, GaN based HEMTs can be used in extreme environmental applications such as space, satellite, and military systems.

M. Senthil Kumar (✉) · S.S. Kushvaha (✉)
CSIR-National Physical Laboratory, Dr. K.S. Krishnan Road,
New Delhi 110012, India
e-mail: senthilmk@nplindia.org

S.S. Kushvaha
e-mail: kushvahas@nplindia.org

Z.H. Khan (ed.), *Recent Trends in Nanomaterials*,
Advanced Structured Materials 83, DOI 10.1007/978-981-10-3842-6_9

Table 9.1 Important physical properties of wurtzite III-nitride semiconductors [6–8]

Property		InN	GaN	AlN
Lattice constants	a (Å)	3.533	3.189	3.112
	c (Å)	5.693	5.185	4.982
Band gap energy E_g (eV) at 300 K		0.64	3.43	6.14
Exciton binding energy (meV)		9	34	60
Thermal expansion	$\Delta a/a$ (K^{-1})	3.8×10^{-6}	5.6×10^{-6}	4.2×10^{-6}
	$\Delta c/c$ (K^{-1})	2.9×10^{-6}	3.2×10^{-6}	5.3×10^{-6}
Thermal conductivity (W cm^{-1} K^{-1})		~0.8	1.3	2.85
Dielectric constant (ε_r)		10.5	8.9	8.5
Density ρ (g cm^{-3})		6.81	6.15	3.23
Melting point (K)		2146	2791	3487
Decomposition temperature (K)		630	850	1040
Binding energy (eV)		1.98	2.20	2.88

III-nitride device structures are generally grown on foreign substrates due to the lack of large-sized bulk GaN substrates, using metal organic chemical vapor deposition (MOCVD) and molecular beam epitaxy (MBE) techniques. The MOCVD and MBE techniques employ a high temperature process for III-nitride growth that limits the choice of substrate materials mostly to sapphire and Si due to their high thermal stability and commercial viability. The large lattice and thermal mismatch of GaN with sapphire and Si lead to generation of a high density of threading dislocations in the order of 10^8–10^{10} cm^{-2} in the grown GaN epitaxial layer [11–13]. The threading dislocations propagate from the GaN/substrate interface even to the surface deteriorating the optical and electrical properties of GaN based devices. Whereas, there are several other closely lattice- and thermal-matched substrates like $LiGaO_2$, ZnO, etc. available for GaN growth but they are vulnerable to higher growth temperatures above 600 °C. Therefore, development of a low temperature growth process is essential for group III-nitrides to further enhance their device performance. Laser molecular beam epitaxy (LMBE) is a relatively new technique for developing group III-nitride semiconductors but it can offer a low temperature growth process as the adequate kinetic energy for the precursors is supplied by the laser power itself. Low temperature growth of III-nitride epitaxial layers has already been demonstrated on various kinds of substrates including metals by using LMBE technique [14–18]. We have recently reported a low temperature growth of GaN layers on sapphire substrate by LMBE using laser ablation of liquid Ga and solid GaN targets under r.f. plasma ambient [19–24].

In recent years, GaN based nanostructures such as nanowires, nanorods, nanotubes and nanowalls are gaining a great research interest as they are dislocation-free and strain-free, and also have a large surface area-to-volume ratio. One dimensional (1D) nanostructures such as nanorods and nanotubes have enormous potential as fundamental building blocks for nanoscale electronic and optoelectronic devices. Few devices based on GaN 1D nanostructures such as field

effect transistors, p-n junctions, LEDs, Lasers and photo-detectors have been successfully demonstrated [25–29]. However, the fabrication of devices on individual 1D nanostructure is difficult due to the complications involved in their handling process. Here, two-dimensional (2D) nanowall network structures are convenient for the fabrication of nano-devices with their material continuity in the lateral direction and also show very interesting structural, optical and electrical properties. Especially, the electron mobility in c-axis oriented wedge-shaped GaN nanowall network grown on sapphire is estimated to be several orders of magnitude larger than that in GaN bulk and the electron mobility increases with the reduction of the average width of the wall [30, 31]. ZnO nanowall network based gas sensors, field emitters, and UV detectors have been reported in literature though GaN nanowall based devices are yet to be realized [32, 33].

Spontaneous formation of GaN nanowalls has been achieved by few researchers by using either plasma-assisted or ion-beam-assisted MBE techniques [30, 34, 35]. However, the growth of III-nitride nanostructures by LMBE technique is extremely limited [36]. In this chapter, we present the homo- and hetero-epitaxial growth of GaN nanowall network on GaN template and sapphire (0001) substrate using LMBE and discuss their structural, optical and electronic properties as characterized by various techniques.

9.2 Growth of GaN Nanowall Network by LMBE Technique

The growth of GaN nanowall network was carried out on 3.5 μm thick MOCVD grown GaN template on sapphire (0001) and bare sapphire (0001) substrates using an ultra-high vacuum (UHV) LMBE growth technique. The growth system was equipped with reflection high energy electron diffraction (RHEED) for in situ monitoring, residual gas analyzer and r.f. N_2 plasma source to supply additional nitrogen radicals. The base pressure of the LMBE growth chamber is $\sim 2 \times 10^{-10}$ Torr which is maintained by combination of various UHV pumps such as turbo molecular pump, titanium sublimation pump and ion pump. The schematic diagram of LMBE growth technique is represented in Fig. 9.1. A high quality HVPE grown solid, polycrystalline GaN target with a purity of 99.9999% was used as target material and semiconductor grade N_2 gas was used as the gas source in r.f. nitrogen plasma cell. A resistive heater was employed to raise the substrate temperature via infra red (IR) radiation. The back side of the GaN template and sapphire substrate was coated with a ~1 μm thick layer of molybdenum to increase the absorption of IR heat radiation and uniform heat distribution. The substrates were cleaned using standard organic solvents followed by de-ionized water. The substrates were initially heated in the entry load lock chamber for several hours at 200 °C to remove surface adsorbates and were then transferred into the growth chamber. The substrate temperature and the growth duration were kept

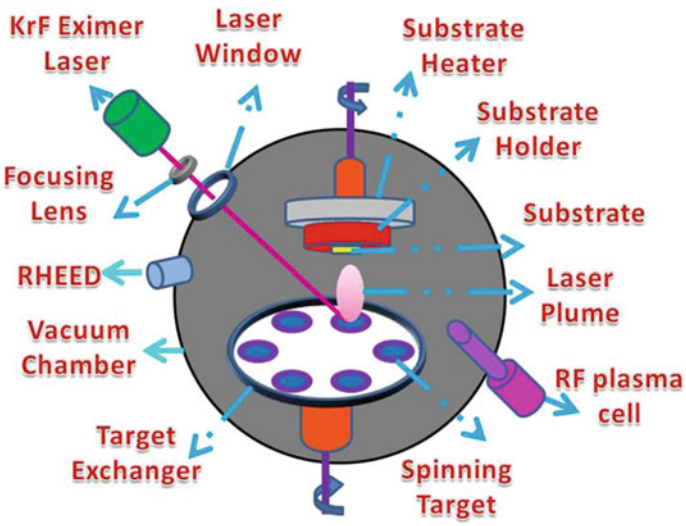

Fig. 9.1 Schematic diagram of laser molecular beam epitaxy (LMBE) growth technique

constant as 700 °C and 2 h, respectively. In case of sapphire substrate, it was thermally cleaned at 850 °C for 10 min in UHV condition followed by surface nitridation and GaN buffer growth at low temperature prior to the main GaN growth. A KrF excimer laser of 248 nm wavelength and 25 ns pulse width was used to ablate the GaN target with an energy density of ~ 3 J/cm^2 and a laser repetition rate varying between 10 and 40 Hz. The r.f. nitrogen radicals were also supplied during the ablation of GaN target to provide N-rich growth condition for nanowall growth. The nitrogen gas flow and r.f. plasma power were fixed at 0.4 sccm and 250 W, respectively. The substrate cleaning and GaN growth were monitored in situ using RHEED operated at 25 kV. The effect of wet-etching on the GaN nanowalls grown on GaN template was also studied with KOH solution of 2M concentration for 30 min at room temperature.

9.3 Characterization of GaN Nanowall Network Grown by LMBE Technique

The structural properties of grown GaN samples were characterized using high resolution X-ray diffraction (HR-XRD) and Raman spectroscopy. The X-ray rocking curve (XRC) measurements along GaN (0002) and (10-12) planes were used to characterize the crystalline quality. The broadening of rocking curve is generally used to estimate the defects such as dislocation density and mosaic spread in the epitaxial layer. Here, the rocking curves of the GaN layers for (0002) and (10-12) diffraction planes were recorded in incident beam configuration using a

multilayer graded mirror with channel-cut 2-bounce Ge (220) monochromator using Cu Kα1 radiation. A scintillation detector was used to record the diffracted beam from the homo-epitaxial GaN for measurements of rocking curve. The micro-Raman spectra were collected in backscattering geometry using an excitation source of 514.5 nm wavelength. The plan- and 45° tilt-view surface morphologies of GaN nanowalls were analyzed by using a field-emission scanning electron microscopy (FE-SEM) with a 5 kV electron source.

The quantitative analysis of crystalline quality was also carried out using Rutherford backscattering geometry (RBS) technique. A well-collimated (divergence $\sim 0.05°$) He^{++} ion beam of energy 3 meV from 1.7 MV Pelletron accelerator was used for the RBS/channeling measurements. The backscattered particles were detected using a surface barrier Si detector at an angle of 165° with respect to the incident beam. The optical emission properties were characterized using photoluminescence (PL) spectroscopy at room temperature with a 266 nm laser line as an excitation source. To investigate the electronic structures, X-ray photoelectron spectroscopy (XPS) measurements were carried out using monochromatic Al K_α and non-monochromatic dual anode (Al K_α and Mg K_α) X-ray sources housed in an UHV Multi Probe Surface Analysis System from Omicron at room temperature. An electrical contact was established between the sample surface and grounded sample plate with a highly conducting UHV compatible Ag paint in order to minimize charging during the XPS measurements of GaN nanowalls and GaN template samples. All binding energies have been referenced to the Fermi edge of an Ar+ sputtered clean polycrystalline Ag foil whereas charging correction was done using C 1s (284.8 eV) core-level binding energy [22]. Overall experimental energy resolution with 20 eV analyzer pass energy for monochromatic Al Kα (1486.7 eV) and non-monochromatic Mg Kα (1253.5 eV) is 0.45 and 0.9 eV, respectively [22].

9.4 Properties of Homoepitaxial GaN Nanowall Network Grown on GaN Template

9.4.1 Structural Properties

The cleaning of GaN template and LMBE growth of GaN were monitored by in situ RHEED technique. The RHEED observation of GaN template showed a streaky pattern along [11-20] and [10-10] directions as presented in Fig. 9.2a, which is the sign of an atomically flat surface suitable for epitaxial growth. During the LMBE GaN growth, the streaky pattern changed to aligned spotty features indicating an epitaxial three-dimensional (3D) growth of GaN under the adopted experimental conditions and the respective RHEED patterns are given in Fig. 9.2b. The twist and tilt in the GaN template and LMBE GaN were examined using symmetric and asymmetric XRC measurements, respectively. The symmetric (0002) plane and asymmetric (10-12) plane XRCs of GaN template are presented in Fig. 9.3. The full

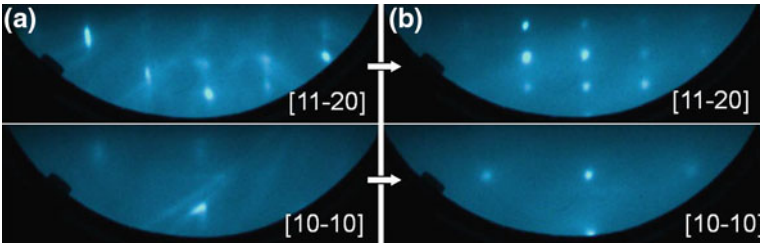

Fig. 9.2 RHEED patterns of **a** GaN template and **b** homoepitaxial GaN growth during LMBE technique, taken along [11-20] and [10-10] directions

width at half maximum (FWHM) of XRC is an indication of crystalline quality of the grown layers. The XRC FWHM values of (0002) and (10-12) planes of GaN template was obtained as 292 and 375 arc-sec, respectively, whereas, the values increased to 310 and 436 arc-sec for the LMBE grown GaN at 10 Hz. The values further increased as a function of laser repetition rate as shown in Fig. 9.4. A maximum of 320 and 468 arc-sec were obtained along (0002) and (10-10) planes for the GaN grown at 30 Hz (the respective XRCs are shown in Fig. 9.3). These observations exhibit that the crystalline quality of GaN is slightly distorted during LMBE growth especially at higher laser repetition rates up to 30 Hz. However, the asymmetric XRC FWHM value decreased significantly for the LMBE GaN grown at 40 Hz.

Surface morphology of the LMBE grown GaN samples on GaN template were characterized by FESEM and the plan- and and 45° tilted-view FESEM images are shown in Fig. 9.5. For the GaN grown at the low repetition rate of 10 Hz, highly dense, un-coalesced GaN islands are observed. The respective 45° tilt-view FESEM image shows an elongated GaN growth in the lateral direction as in Fig. 9.5a. Further increase in the laser frequency to 20 Hz leads to the formation of GaN nanowall network structure with a large number of hexagonal-shaped pores of size ranging from 90 to 120 nm. The nanowall width is tapered from the base towards the top with a tip width of about 20–30 nm as seen in Fig. 9.5b. The well-defined GaN nanowall network with a pore size of 120–180 nm has been observed for 30 Hz growth (Fig. 9.5c). The individual GaN nanowalls have a tip width of about 10–15 nm that overlap and interlace with one another to form a continuous network structure. In comparison, the pore size of the GaN nanowall network increased with increasing laser repetition rate from 20 to 30 Hz while the tip width decreased dramatically. For 40 Hz growth, the GaN layer of coalesced islands has been obtained with presence of a high density of surface pits. The surface pits are inverted hexagonal pyramids formed due to the remnants of island coalescence process and are characteristics of GaN growth.

Growth mode of GaN based materials shows a sharp sensitivity to the Ga/N flux ratio prevailing on the growth front. Under Ga-rich flux condition, i.e. N/Ga ratio <1, GaN grows in 2D mode yielding an atomically flat surface while N-rich condition with N/Ga ratio >1 mostly promotes a 3D growth of rough surface [37, 38].

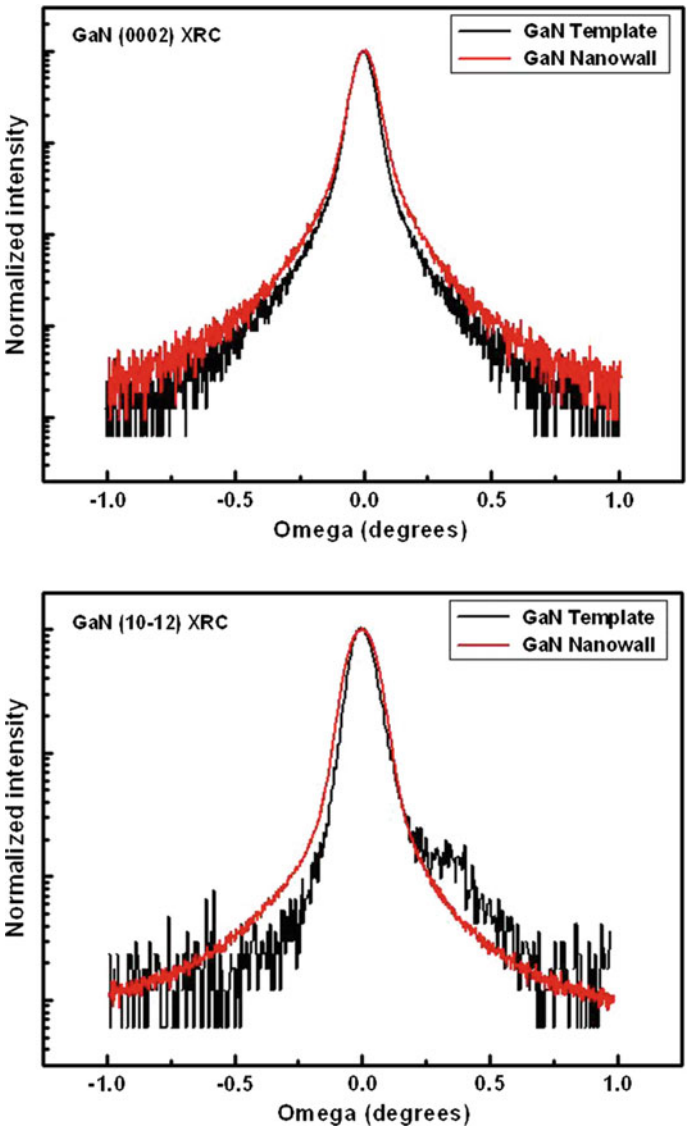

Fig. 9.3 High resolution X-ray rocking curves of GaN template and GaN nanowalls grown at 30 Hz: **a** (0002) and **b** (10-12) planes

The nanowall network is basically a vertically grown structure and the researchers have obtained growth of GaN nanowall network on different substrates under a highly nitrogen-rich flux condition using conventional MBE technique [34, 39–42]. Zhong and Hane have studied the effect of Ga/N flux ratio on the growth of GaN on Si (111) substrate by varying the N to Ga ratio from 180 to 980. The nanowall

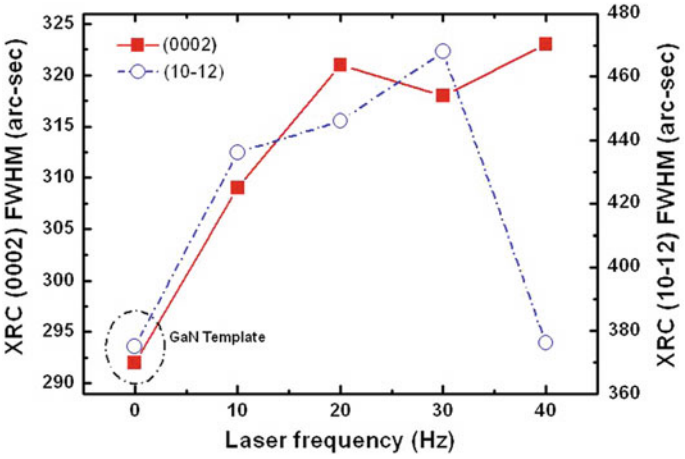

Fig. 9.4 X-ray rocking curve full width at half maximum (FWHM) of GaN template and LMBE grown GaN as a function of laser frequency

width could be controlled from 30 to 200 nm by adjusting the N/Ga flux ratio in the above range [34]. Poppitz et al. achieved growth of porous GaN nanowall network on SiC using ion-beam-assisted MBE in the temperature range 750–850 °C by keeping the N ion to Ga atom ratio between 2.7 and 6.3 [35]. Spontaneous growth of GaN nanowalls on sapphire (0001) has been reported under the N/Ga ratio of 100 by Kesaria et al. [39]. In the LMBE growth of GaN nanowall, the in situ RHEED showed the 3D growth with a spotty pattern indicating the N-rich flux condition.

Based on the experimental conditions and the observed results, a possible growth mechanism can be proposed for GaN nanowall network structure. As discussed earlier, the available reports unanimously suggest that nitrogen-rich growth condition is the most fundamental requirement for the formation of GaN nanowall structure. In addition, the large lattice and thermal mismatch between GaN and foreign substrates like sapphire and Si are also considered to understand the growth mechanism of nanowall structure as the relative biaxial stress can relax via formation of 3D structures [34, 39–42]. However, in case of GaN nanowall growth on thick GaN template, the contribution of in-plane stress will be a minimum. Hence, the growth mechanism of LMBE grown homoepitaxial GaN nanowall network can be understood on the basis of N-rich growth condition and high flux rates. In LMBE GaN growth, the laser ablation process of solid polycrystalline GaN target was carried out under the r.f. activated nitrogen plasma ambient, which is a N-rich flux situation prone for 3D growth. In addition, the surface kinetics of adatoms should also be considered as the increase in flux rate greatly influences the growth process of epitaxial layers. When the laser frequency is increased from 10 to 40 Hz, there is a multifold increase of flux rate for the GaN growth. While the low flux rate at 10 Hz results in un-coalesced GaN islands the high flux at 40 Hz leads to formation of a coalesced layer with a high density of large pits. The GaN nanowall network

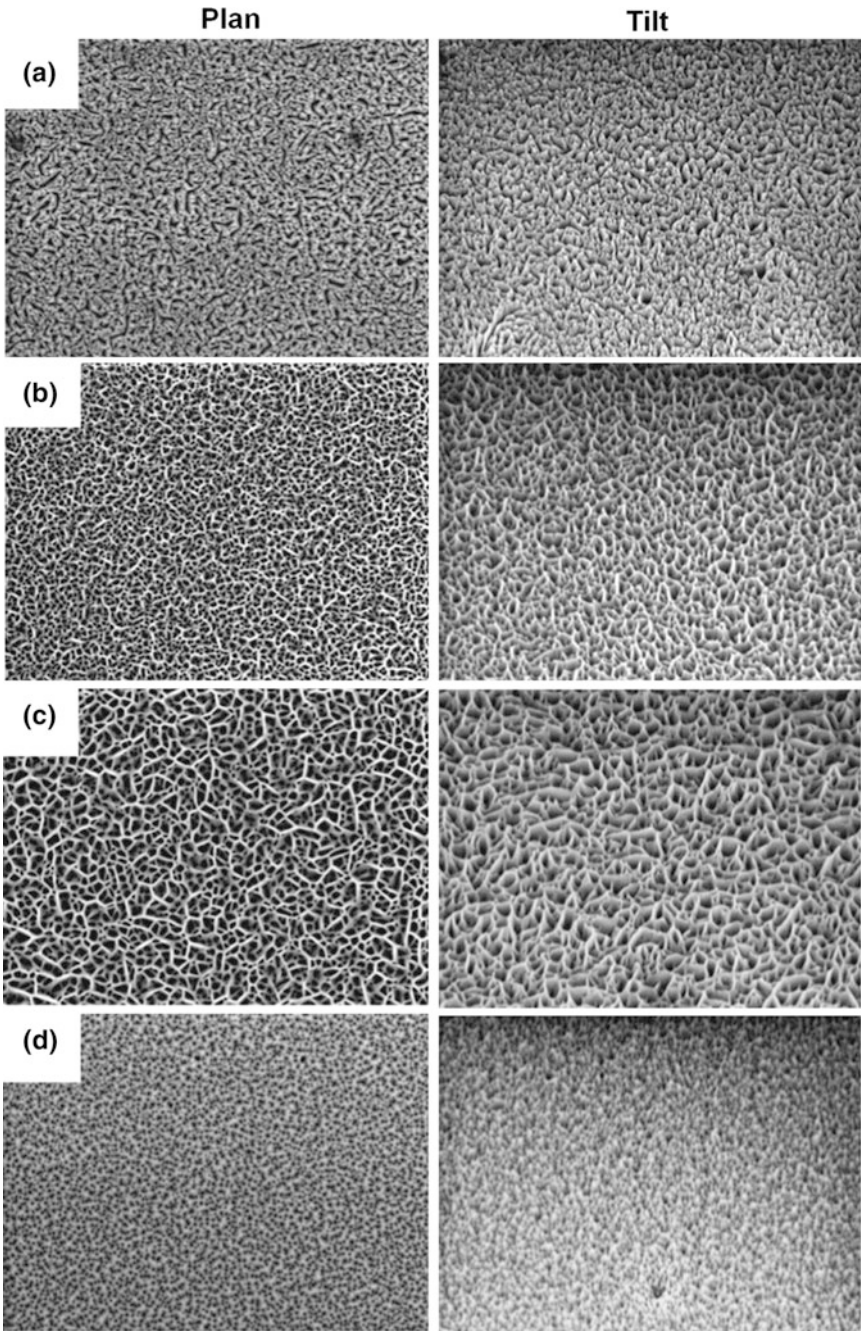

Fig. 9.5 Plan- and 45° tilt-view FESEM images of GaN structures grown on GaN template at various laser frequencies: **a** 10 Hz, **b** 20 Hz, **c** 30 Hz and **d** 40 Hz

structures are obtained only for the intermediate flux rates at 20–30 Hz. With increase in flux rate, the diffusion length of surface adatoms decreases due to limited surface mobility by impinging flux, which sets on a vertical growth. At 10 Hz, the flux is not sufficient to form a continuous layer in the designated growth duration of 2 h. At intermediate flux conditions i.e., 20 and 30 Hz, the GaN nanowall network is formed due to diffusion limited vertical growth in the lateral direction, which leads to nanowall formation. High density GaN nucleation islands due to higher flux rate at 40 Hz tend to form a layer structure by early coalescence among them. From the statistical analyses of nanowall network dimensions obtained for 20 and 30 Hz, it is understood that the increase of pore size at higher frequency occurs due to low surface diffusion of GaN adatoms by the increased flux rate. Moreover, the sticking coefficient of Ga atoms is relatively higher at GaN (0001) plane compared to other planes, which can further contribute towards the 3D growth [42, 43]. The above results are evident that GaN nanowalls could be grown homoepitaxially on GaN template at higher flux rates under N-rich flux condition using LMBE technique.

Raman spectroscopy has been applied to evaluate the crystalline quality and the presence of in-plane strain in the LMBE grown GaN structures. The Raman spectra of GaN grown at various laser frequencies were recorded at room temperature in backscattering geometry and are presented in Fig. 9.6. GaN normally crystallizes in hexagonal wrutzite structure and the Raman active modes of wurtzite GaN are A_1 (LO), A_1 (TO), E_1 (LO), E_1 (TO), E_2 (low) and E_2 (high). According to Raman selection rules, only E_2 (high) and A_1 (LO) phonon modes are expected in the backscattering geometry with laser beam incident on GaN (0001) surface.

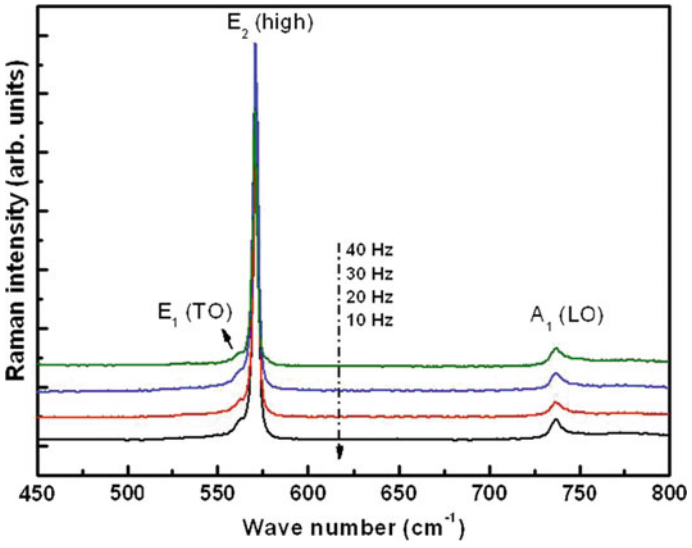

Fig. 9.6 Room temperature Raman spectra of LMBE grown GaN at various laser frequencies

By analyzing the line shape, FWHM value and shift of E_2 (high) peak, the crystalline quality and the in-plane stress/strain in the GaN layer can be accessed while the A_1 (LO) mode gives information on the carrier concentration and electron mobility [44, 45]. For the LMBE GaN, a strong E_2 (high) mode and A_1 (LO) mode are seen at 571.3 and 736.8 cm^{-1}, respectively. Compared to the E_2 (high) position of stress-free GaN at 567.6 cm^{-1}, a peak shift of about 3.7 cm^{-1} has been obtained for GaN template as well as LMBE grown GaN structures indicating a presence of in-plane compressive strain [46]. It is noted that there is no change in the intrinsic strain of the template over LMBE growth of GaN. The position and width of GaN Raman modes of all samples have been analyzed with Lorentzian peak fit. It is found that the peak position and FWHM of both E_2 (high) and A_1 (LO) modes remain almost same with increase of laser frequency from 10 to 40 Hz. There is a shoulder peak near E_2 (high) mode at 561.8 cm^{-1}, which is assigned to E_1 (TO) mode. The peak width of E_1 (TO) mode monotonically varies from 6.0 to 11.2 cm^{-1} with increase of frequency from 10 to 40 Hz. The increase of FWHM value of E_1 (TO) mode with respect to laser frequency indicates the increased structural defects as in good agreement with HRXRD analysis.

Rutherford backscattering experiments were performed to characterize the crystalline nature of the GaN nanowall network structure. The RBS/ion channeling spectra of GaN template and LMBE grown GaN nanowall network structures are given in Fig. 9.7. The ion channeling yield (the ratio of the backscattering yield of aligned direction to that from the random direction in the near surface region) is very low about 3.2% for the GaN template. The low RBS yield in the aligned direction is an indication of the high crystalline order of the grown GaN layer that is revealing the very high order of lattice arrangements. The ion channeling yield for the GaN nanowall network structures increased to 9.8% indicating a slight disorder of crystallinity during LMBE growth. The RBS observation is consistent with the HRXRD and Raman data.

9.4.2 Optical Properties

Optical emission properties of the LMBE grown GaN structures in the frequency range 10–40 Hz have been characterized by room temperature PL measurements and the respective PL spectra are presented in Fig. 9.8. The PL data were acquired under the same measurement parameters such as incident beam aperture size and laser power for all samples. In common, a strong UV emission at ~362 nm (3.43 eV) and a broad, weak deep-band emission centered at the wavelength of 540 nm (2.30 eV) are obtained for the GaN template and LMBE grown GaN samples. Bulk wurtzite GaN exhibit a near band edge (NBE) emission at ~3.4 eV and defects related peaks in the range of 1.4–2.8 eV at room temperature [47]. The shift in NBE position compared to bulk GaN is related to the stress present in the GaN template itself. It has been observed that the E_2 (high) Raman shift of 4.2 cm^{-1} due to biaxial stress in GaN layer makes a 27 meV of blue shift in NBE peak

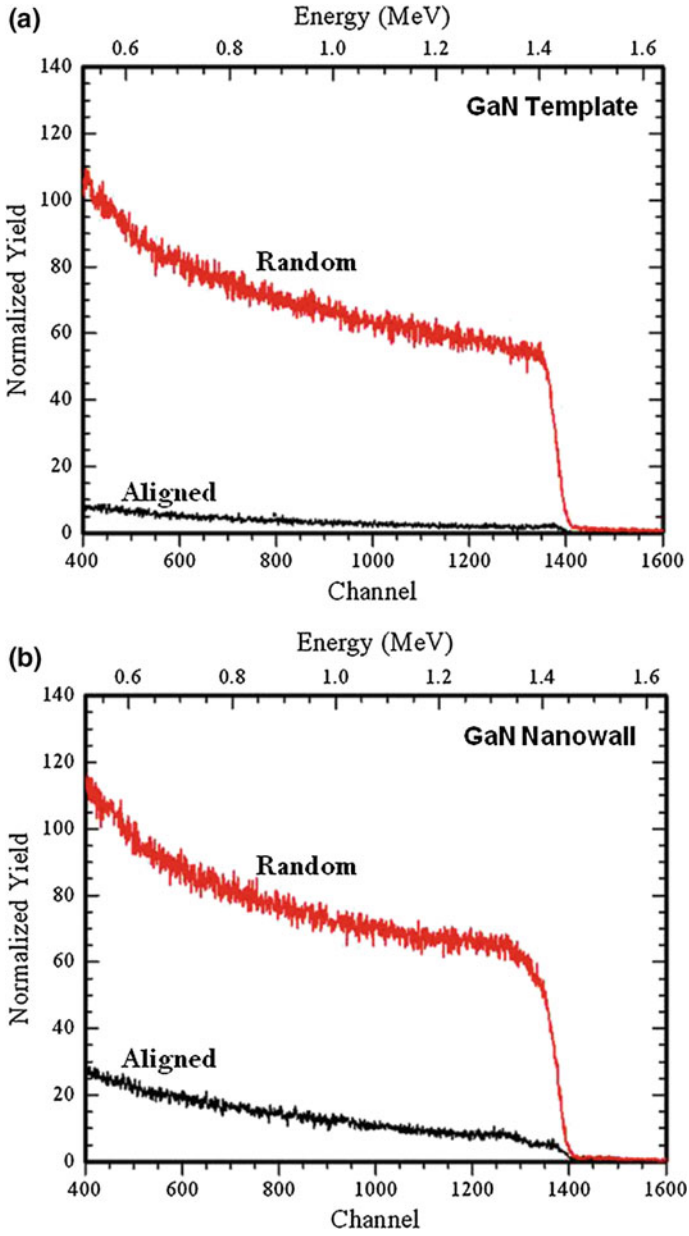

Fig. 9.7 Rutherford backscattering spectroscopy of **a** GaN template and **b** LMBE grown GaN nanowall network structure

position [24, 46]. The deep band emission is the characteristic yellow luminescence (YL) of GaN associated with intrinsic crystalline defects. The contribution of GaN template in the PL data of LMBE GaN samples is possible and the obtained PL data for all the samples cab be the combined effect of the template and the LMBE grown GaN. At the same time, the notable change in the spectral features and NBE/YL intensity ratio can provide information on the optical properties of the LMBE grown GaN. The NBE/YL intensity ratio of the template and LMBE grown GaN at 10, 20, 30 and 40 Hz are obtained to be 43, 37, 18, 17 and 11, respectively. Compared to GaN template, the ratio decreased as a function of laser frequency. It indicates the generation of structural defects during LMBE growth, which are responsible for YL emission [48]. In the literature, there are contradictory results about the presence of YL peak intensity in GaN nanowall network. While few reports claim a negligible YL emission for GaN nanowall network [41, 49], some researchers observed prominent defect related peaks [42, 48].

For the GaN nanowall network structure grown at 30 Hz, an additional peak at the higher energy region above NBE is observed as noted in the respective PL spectrum. To analyze the higher energy emission, the PL data was fitted using Lorentzian function and the position of new emission peak is identified to be 352 nm (3.52 eV). It should be mentioned that the higher energy peak with a blue shift of 90 meV from NBE emission is observed only for the GaN nanowalls network having a tip width of 10–15 nm. The GaN nanowall network with tip width of 20–30 nm grown at 20 Hz did not exhibit any higher energy emission. Recently, Bhasker et al. have reported that the NBE of GaN nanowalls of tip width $\sim$10 nm is shifted by 60 meV towards higher energy side compared to that of the

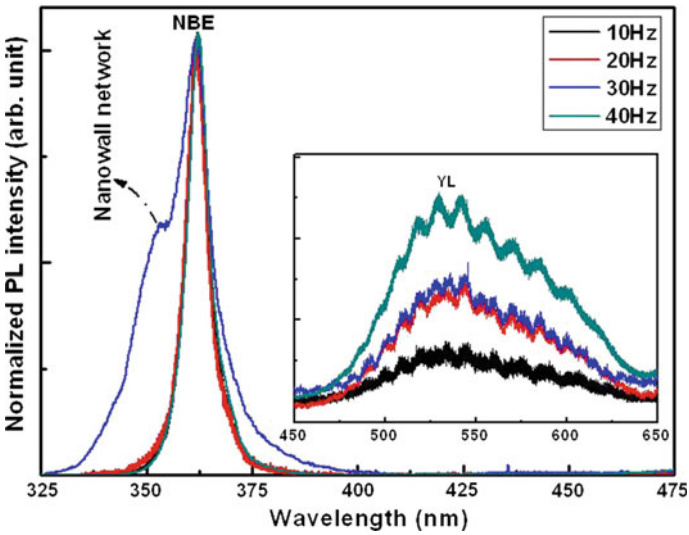

Fig. 9.8 Room temperature photoluminescence spectra of LMBE grown GaN at various laser frequencies (*Inset* yellow luminescence)

GaN epitaxial layer and the enhancement of the band gap was explained on the basis of carrier confinement effect in the nanowall structures [49]. Similarly, in case of ZnO nanowalls grown on GaN template, the room temperature PL spectrum showed a blue shift of NBE attributed to the quantum confinement effect [50]. GaN nanowires of diameter comparable to Bohr exciton radius of GaN, i.e., $\sim$11 nm, also exhibited a PL blue shift induced by quantum confinement effect induced [51]. Similarly, in the LMBE grown GaN nanowalls, the higher energy PL peak is observed for wall width of 10–15 nm that is comparable to the Bohr exciton radius of GaN. Therefore, the PL emission at 3.52 eV of GaN nanowall network is assigned to quantum confinement of the charge carriers [36].

9.4.3 Electronic Structure

The electronic structure of GaN template and GaN nanowall network were characterized using XPS studies [36]. Also, the XPS core level spectroscopy is one the most powerful technique to determine the surface chemical composition. A monochromatic Al K_α source was employed to study the Ga 3d core level as it is free from additional X-ray satellites and offers a high energy resolution better than non-monochromatic X-ray source. But, at the same time, it makes the N 1s core level analysis more complicated as the N 1s spectrum overlaps with the broad Ga Auger features and is not suitable to determine the chemical composition of GaN. Hence, N 1s core level data was acquired using a non-monochromatic Mg K_α source as the Ga Auger features do not overlap with the N 1s core level any more [22]. The Ga 3d and N 1s core level spectra of GaN template and GaN nanowall network measured using Al Kα and Mg Kα sources, respectively, are shown in Fig. 9.9a, b. To determine accurate peak positions and relative contribution of different components, the χ^2 iterative fit of Ga 3d and N 1s core level spectra were carried out. Ga 3d core level spectra of GaN template can be fitted using 3 components such as Ga–N, Ga–O, and N 2s while the fitting of Ga 3d core level spectrum of GaN nanowall network was done with 4 components, i.e. with an additional Ga–Ga component. As seen, in both cases, the Ga 3d core level spectrum is mainly dominated by Ga–N peak which appears at 19.95 $\pm$ 0.05 eV for GaN template and at 20.1 $\pm$ 0.05 eV for GaN nanowall network. The peak position and FWHM values for GaN template are close to the earlier reports [52, 53]. The FWHM is relatively large for the GaN nanowall network. Ga–O component, assigned to the formation of Ga_2O_3, is observed at 1.2 eV higher binding energy (BE) side compared to main peak. It might be due to surface oxidation of GaN upon exposure to atmospheric ambient [54, 55]. Ga–Ga component is located at 1.0 eV lower BE side compared to main peak and it can be related to uncoordinated/metallic Ga atoms [53, 54]. Relative percentage of Ga–O varies very little (7.2–7.9) between the GaN template and the nanowall network indicating a similar amount of surface oxidation.

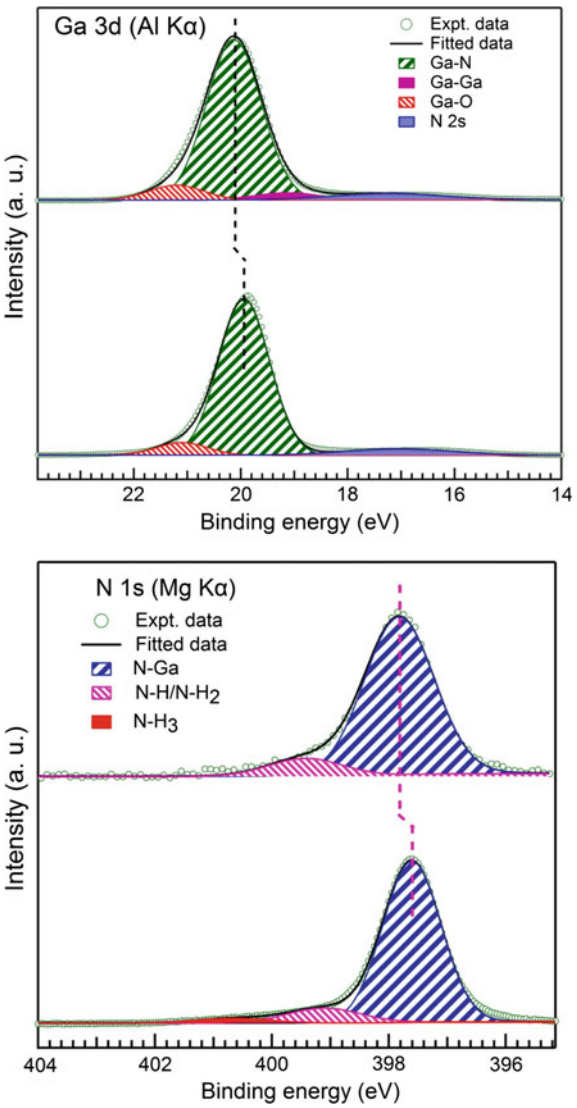

Fig. 9.9 X-ray photoemission spectra of GaN template and GaN nanowall network: Ga 3d and N 1s core levels

In case of N 1s core level, the spectra can be fitted by 2 components such as major N–Ga and surface contamination related N–H/N–H_2 peaks. The N–Ga peak dominates the spectra and N–H/N–H_2 component appears at 1.5 eV higher BE side [53, 56]. For the GaN template, a small feature at 3.0 eV higher BE side is obtained and can be attributed to NH_3 contamination occurred during MOCVD growth [56]. N–Ga peak for GaN template and nanowall network appear at 397.6 ± 0.05 and 397.8 ± 0.05 eV, respectively. To calculate the surface chemical composition of the GaN, area under the curve of Ga 3d and N 1s core levels have been normalized

using respective photo-ionization cross sections, inelastic mean free path and analyzer transmission function [22, 57, 58]. The Ga/N ratio for GaN template and GaN nanowall network are calculated to be 1.04 ± 0.05 and 2.03 ± 0.1, respectively. It clearly indicates that the LMBE grown GaN nanowall network is rich in Ga content. It has been reported that Ga-rich surface may result due to formation of Ga adlayer and/or Ga droplets and it can result in surface reconstructions [59–61]. Surface sensitivity of XPS can be tuned by varying the photoemission angle. From angle dependent photoemission measurements, the Ga/N ratio was found to be nearly same within the experimental error and therefore, the possibility of excess Ga at nanowall surface can be excluded [36]. The large Ga/N ratio of the LMBE grown GaN nanowall network suggests that it will have a large number of N vacancy related defects; it can be correlated with the more defective nature of the LMBE grown GaN as observed by the large X-ray rocking width and the enhanced peak intensity of YL band in PL spectrum [62]. Ga 3d and N 1s core levels of the GaN nanowall network shifts towards higher BE side by 0.15–0.2 eV, respectively, compared to the GaN template and such shifts have been attributed to the presence of N vacancies in GaN [63–66]. In recent past, N vacancies have emerged as major point defect in bulk and nanostructured GaN [67–69]. Fitting of Ga 3d core level spectrum of the LMBE grown nanowall network also confirmed the formation of uncoordinated Ga atoms, possibly located at interstitial sites, pointing towards the presence of N vacancies.

The VB spectra of GaN template and LMBE grown GaN nanowall network measured using Al K_α source are given in Fig. 9.9. The VB spectra can be satisfactorily fitted using 3 components corresponding to features A, B and C. The peaks A and C are associated to Ga 4p-N 2p and Ga 4s-N 2p hybridized states, respectively, with N 2p dominant character and the peak B has been attributed to mixed orbitals and/or surface adsorbates [70]. For the GaN template, the features A, B and C appeared at 4.5 ± 0.5, 6.92 ± 0.5, and 9.1 ± 0.5, respectively. Line shape and energy position of dominant features of the VB spectra are in good agreement with the earlier reports [70–72]. Similar to Ga 3d and N 1s core levels, the FWHM of VB peaks for GaN nanowall network are found to be higher compared to GaN template which could be correlated to the increased structural defects. Also, there is a very small shift of A and C peaks towards higher BE for the GaN nanowalls with respect to GaN template. These observations indicate that a redistribution of spectral weight takes place in GaN nanowall and it can be attributed to the change in Ga/N ratio and the consequent change in Ga–N hybridization.

The near E_F VB spectra of GaN template and nanowalls are presented in Fig. 9.10. The position of valence band maxima (VBM) has been found to lie at 2.67 ± 0.05, and 2.78 ± 0.05 eV below the surface Fermi level for GaN template and GaN nanowall network, respectively. Since GaN has a bandgap of about 3.4 eV at room temperature the VBM positions indicate that GaN template and nanowalls have n-type electrical conductivity. Also, in comparison with GaN template, the VBM of GaN nanowall network is shifted by ∼0.1 eV towards higher BE, which may be correlated to the increase in band gap as revealed by room temperature PL. In contrast, the N vacancy induced change in surface band bending

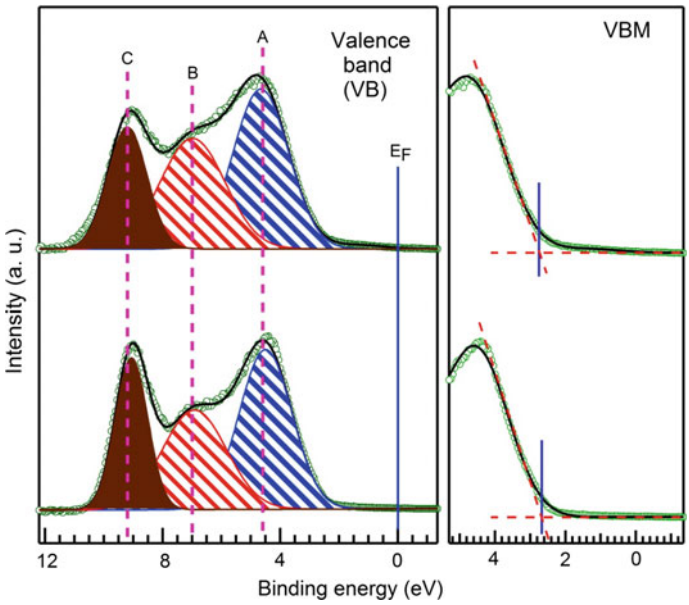

Fig. 9.10 X-ray photoemission valence band spectra of GaN template and GaN nanowall network

may also shift VBM and Ga 3d and N 1s core levels. N vacancy related donor states may increase near surface electron concentration resulting in positive surface charge that will result in a reduction of positive space charge in the depletion region and lower the band bending. In addition the surface oxidation level of GaN can also affect the VBM and core level BE [73]. As the surface oxidation level is similar in GaN template and nanowalls the related effect on peak shift would be insignificant. It is noted that any evidence of presence of metallic states related to uncoordinated Ga atoms is not found as there is no spectral weight around E_F.

9.4.4 Effect of Wet-Etching

The surface morphology of wet-etched GaN nanowall network grown at 30 Hz is shown in Fig. 9.11. The room temperature KOH wet-etching largely modifies the GaN nanowall structure. The sharp edge and pore areas of the nanowall network are etched-out thereby increasing the nanowall edge width and pore size. In addition, numerous, small-sized pores are newly revealed in the surface.

The room temperature PL spectra of GaN nanowall network before and after wet-etching are given in Fig. 9.12. After the wet-etching, the higher energy PL emission peak at $\sim$3.52 eV assigned to the GaN nanowall network totally disappeared from the spectrum. The GaN NBE peak becomes sharper and the YL

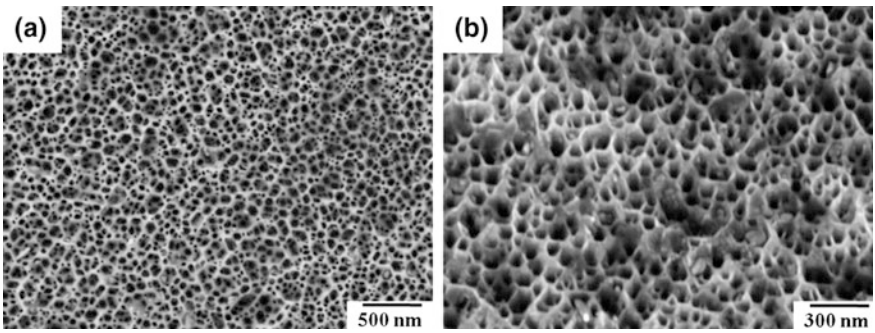

Fig. 9.11 **a** Plan- and **b** 45° tilt-view FESEM images of wet-etched GaN nanowall network structure

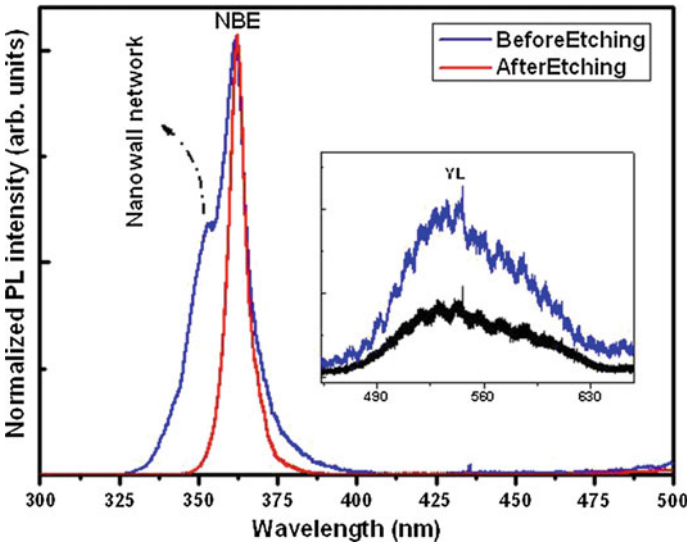

Fig. 9.12 Room temperature photoluminescence spectra of as-grown and wet-etched GaN nanowall network structure (*Inset* yellow luminescence)

emission intensity is also reduced. The NBE/YL intensity ratio increased from 20 to 41 after etching. The absence of higher energy peak above NBE confirms that the emission at $\sim$3.52 eV belongs to the GaN nanowalls due to quantum confinement effect. The reduction of NBE peak width and YL intensity of wet-etched GaN nanowalls are attributed to the removal of relatively defective LMBE grown GaN material.

9.5 Properties of Heteroepitaxial GaN Nanowall Network Grown on Sapphire (0001)

Growth of heteroepitaxial GaN nanowall network structure has been achieved on pre-nitridated sapphire substrate under similar experimental conditions employed for the growth on GaN template by LMBE. Only, the laser frequency and growth time were maintained as 10 Hz and 3 h, respectively. The in situ RHEED patterns recorded after sapphire cleaning and during GaN growth are given in Fig. 9.13. The RHEED indicated a clean and atomically flat sapphire surface with short streaky features. The RHEED obtained during GaN growth revealed a 3D growth of GaN with 30° in-plane rotation with respect to sapphire substrate [74]. Figure 9.14 shows the surface morphology of heteroepitaxial GaN nanowall network in plan- and 45° tilt-views. The nanowall network formation is analogous to that grown on GaN template. The nanowalls have a tip width of 9–20 nm and a pore size of 50–120 nm.

The room temperature photoluminescence spectrum of GaN nanowalls grown on sapphire substrate is presented in Fig. 9.15. A strong UV emission around 3.5 eV (∼355 nm) related to GaN nanowalls appeared with a blue shift of about 100 meV

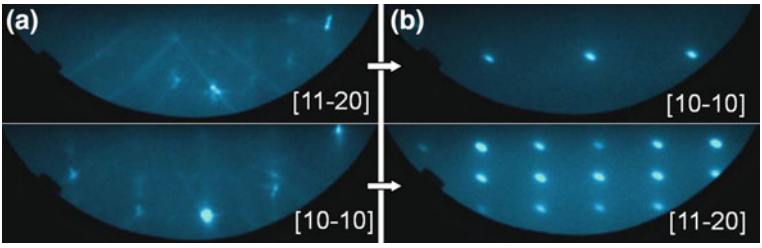

Fig. 9.13 **a** RHEED patterns of (**a**) thermally cleaned sapphire (0001) substrate and **b** heteroepitaxial GaN nanowall growth during LMBE, taken along [11-20] and [10-10] directions

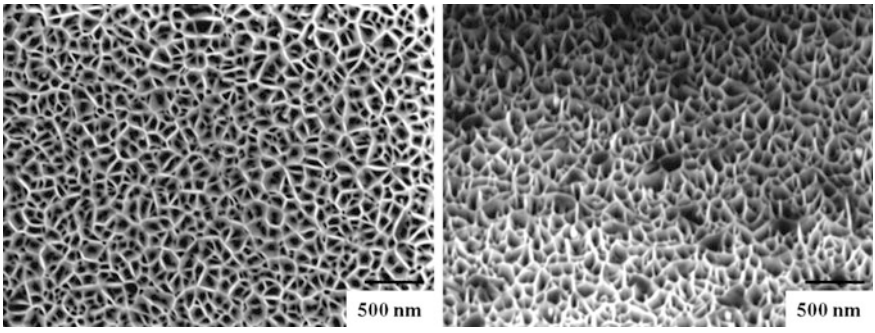

Fig. 9.14 Plan and 45° tilt view FESEM images of heteroepitaxial GaN nanowall network grown on sapphire (0001) substrate

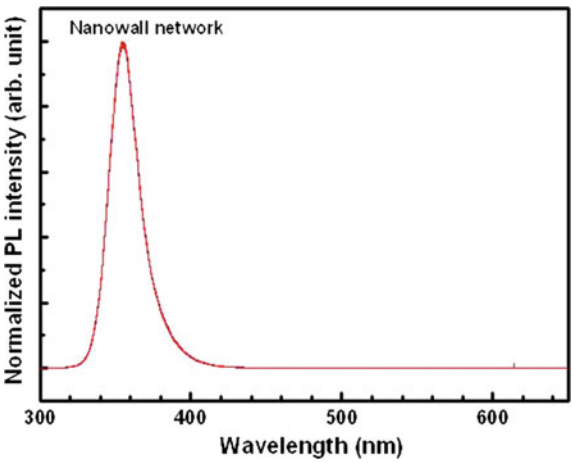

Fig. 9.15 Room temperature photoluminescence spectrum of heteroepitaxial GaN nanowall network grown on sapphire (0001) substrate

from the band energy of bulk GaN. The higher energy emission is due to the carrier confinement in nanowall edges of thin width comparable to Bohr radius of GaN as discussed in the previous section. The YL band intensity is found to be negligible, which denotes the good structural properties of the grown GaN nanowalls. Thus, the LMBE growth technique demonstrates a great promise for producing homo- and hetero-epitaxial GaN nanowall network under suitable experimental conditions that can be employed in realizing nitride nano-devices for various unique applications [32, 33, 75].

9.6 Concluding Remarks and Future Perspective

Homoepitaxial GaN nanowall network were grown on GaN template by laser ablation of solid GaN target in presence of r.f. nitrogen plasma by using LMBE technique. The role of laser frequency is found to be critical in the formation of GaN nanowall structure in LMBE growth. The GaN nanowall width decreases as a function of laser frequency and nanowall network with edge width of 10–15 nm and pore size of 120–180 nm are obtained at 30 Hz. The structural, electronic and optical properties of the GaN nanowall structures have been characterized. HRXRD, Raman and RBS studies indicate that the crystalline quality of LMBE grown GaN nanowalls are slightly changed as compared to that of MOCVD grown GaN template. The room temperature PL measurement shows a high energy emission from GaN nanowall network at 3.52 eV due to the quantum confinement of carriers at the nanowall edges. An increased width of GaN nanowall has been obtained after a wet-chemical etching in KOH and consequently, the nanowall related PL emission disappeared confirming the presence of quantum confinement effect only in thinner nanowall structures. Heteroepitaxial GaN nanowall network of

edge with <15 nm were also grown on sapphire (0001) substrate by LMBE. A higher energy PL emission from the heteroepitaxially grown nanowall is obtained around 3.5 eV at room temperature due to carrier confinement. Similar to conventional MBE, N-rich flux condition is found to be favorable to achieve GaN nanowall network structure by LMBE growth.

The LMBE grown GaN nanowall network with a large surface area and confined charge carriers will have potential technological applications in the area of field emission and high temperature sensing. The porous network structure can also be used for surface texturing of light emitters and solar cells to improve their output efficiency.

Acknowledgements The authors would like to thank Dr. K.K. Maurya, Dr. Ajay K. Shukla, Dr. Dilip K. Singh, Ms. Mandeep Kaur, Dr. B.S. Yadav (SSPL, Delhi) and Mr. Sunil Ojha (IUAC, New Delhi) for the assistance in sample characterizations. The financial support by Council of Scientific and Industrial Research (CSIR) through network project PSC-0109 is also gratefully acknowledged.

References

1. S. Nakamura, T. Mukai, M. Senoh, Candela-class high-brightness InGaN/AlGaN double heterostructure blue light emitting diodes. Appl. Phys. Lett. **64**, 1687 (1994)
2. S. Nakamura, M. Senoh, S. Nagahama, N. Iwasa, T. Yamada, T. Matsushita, H. Kiyoku, Y. Sugimoto, T. Kozaki, H. Umemoto, M. Sano, K. Chocho, Continuous-wave operation of InGaN/GaN/AlGaN based laser diodes grown on GaN substrates. Appl. Phys. Lett. **72**, 2014 (1998)
3. F.A. Ponce, D.P. Bour, Nitride-based semiconductors for blue and green light-emitting devices. Nature **386**, 351 (1997)
4. S. Nakamura, G. Fasol, *The Blue Laser Diode—GaN Based Light Emitters and Lasers* (Springer, Berlin, 1997)
5. S.C. Allen, A.J. Steck, A nearly ideal phosphor-converted white light emitting diode. Appl. Phys. Lett. **92**, 143309 (2008)
6. J. Wu, When group-III nitrides go infrared: new properties and perspectives. J. Appl. Phys. **106**, 011101 (2009)
7. H. Morkoc, *Nitride Semiconductors and Devices* (Springer, New York, 1999)
8. O. Ambacher, Growth and applications of group III-nitrides. J. Phys. D Appl. Phys. **31**, 2653 (1998)
9. M. Shur, B. Gelmont, M.A. Khan, Electron mobility in two-dimensional electron gas in AIGaN/GaN heterostructures and in bulk GaN. J. Electron. Mater. **25**, 777 (1996)
10. T. Brazzini, M.A. Casbon, H. Sun, M.J. Uren, J. Lees, P.J. Tasker, H. Jung, H. Blanck, M. Kuball, Electroluminescence of hot electrons in AlGaN/GaN high-electron-mobility transistors under radio frequency operation. Appl. Phys. Lett. **106**, 213502 (2015)
11. H.-Y. Shin, S.K. Kwon, Y.I. Chang, M.J. Cho, K.H. Park, Reducing dislocation density in GaN films using a cone-shaped patterned sapphire substrate. J. Cryst. Growth **311**, 4167 (2009)
12. V.E. Bougrov, M.A. Odnoblyudov, A.E. Romanov, T. Lang, O.V. Konstantinov, Threading dislocation density reduction in two-stage growth of GaN layers. Phys. Stat. Sol. (a) **203**, R25 (2006)

13. X. Weng, J.D. Acord, A. Jain, E.C. Dickey, J.M. Redwing, Evolution of threading dislocation density and stress in GaN films grown on (111) Si substrates by metalorganic chemical vapor deposition. J. Electron. Mater. **36**, 346 (2007)
14. K. Okamoto, S. Inoue, N. Matsuki, T.-W. Kim, J. Ohto, M. Oshima, H. Fujioka, A. Ishii, Epitaxial growth of GaN films grown on single crystal Fe substrates. Appl. Phys. Lett. **93**, 251906 (2008)
15. A. Kobayashi, S. Kawano, K. Ueno, J. Ohta, H. Fujioka, H. Amani, S. Nagao, H. Horie, Growth of a-plane GaN on lattice-matched ZnO substrates using a room-temperature buffer layer. Appl. Phys. Lett. **91**, 191905 (2007)
16. K. Sakurada, A. Kobayashi, Y. Kawaguchi, J. Ohta, H. Fujioka, Low temperature epitaxial growth of GaN films on $LiGaO_2$ substrates. Appl. Phys. Lett. **90**, 211913 (2007)
17. Y. Kawaguchi, J. Ohta, A. Kobayashi, H. Fujioka, Room-temperature epitaxial growth of GaN on lattice-matched ZrB_2 substrates by pulsed-laser deposition. Appl. Phys. Lett. **87**, 221907 (2005)
18. R.D. Vispute, V. Talyansky, R.P. Sharma, S. Choopun, M. Downes, T. Venkatesan, K.A. Jones, A.A. Iliadis, M. Asif Khan, J.W. Yang, Growth of epitaxial GaN films by pulsed laser deposition. Appl. Phys. Lett. **71**, 102 (1997)
19. M. Senthil Kumar, S.S. Kushvaha, K.K. Maurya, Low temperature growth of GaN epitaxial layers on sapphire (0001) by pulsed laser deposition using liquid Gallium target. Sci. Adv. Mater. **6**, 1215 (2014)
20. S.S. Kushvaha, M. Senthil Kumar, K.K. Maurya, M.K. Dalai, N.D. Sharma, Highly c-axis oriented growth of GaN film on sapphire (0001) by laser molecular beam epitaxy using HVPE grown GaN bulk target. AIP Adv. **3**, 092109 (2013)
21. M. Senthil Kumar, S.S. Kushvaha, K.K. Maurya, K. Saravanan, S. Ojha, High resolution X-ray diffraction and Rutherford backscattering spectroscopy studies on laser molecular beam epitaxy grown GaN layers on sapphire (0001). Adv. Sci. Lett. **20**, 1406 (2014)
22. S.S. Kushvaha, M. Senthil Kumar, M. Maheshwari, A.K. Shukla, P. Pal, K.K. Maurya, Structural and electronic properties of epitaxial GaN layer grown on sapphire (0001) using laser molecular beam epitaxy. Mater. Res. Express **1**, 035903 (2014)
23. M. Senthil Kumar, K.M.K. Srivatsa, S.S. Kushvaha, Detection of dislocation-related midgap levels in pulsed laser deposited GaN by photo-induced current transient spectroscopy. Phys. Stat. Sol. (b) **252**, 800 (2015)
24. S.S. Kushvaha, M. Senthil Kumar, B.S. Yadav, P.K. Tyagi, S. Ojha, K.K. Maurya, B.P. Singh, Influence of laser repetition rate on the structural and optical properties of GaN layers grown on sapphire (0001) by laser molecular beam epitaxy. Cryst. Eng. Comm. **18**, 744 (2016)
25. Z. Zhong, F. Qian, D. Wang, C.M. Lieber, Synthesis of p-type gallium nitride nanowires for electronic and photonic nanodevices. Nano Lett. **3**, 343 (2003)
26. Y. Huang, X. Duan, Y. Cui, C.M. Lieber, Gallium nitride nanowire nanodevices. Nano Lett. **2**, 101 (2002)
27. A.T.M.G. Sarwar, S.D. Carnevale, F. Yang, T.F. Kent, J.J. Jamison, D.W. McComb, R.C. Myers, Semiconductor nanowire light-emitting diodes grown on metal: a direction toward large-scale fabrication of nanowire devices. Small **11**, 5402 (2015)
28. Z. Mi, S. Zhao, S.Y. Woo, M. Bugnet, M. Djavid, X. Liu, J. Kang, X. Kong, W. Ji, H. Guo, Z. Liu, G.A. Botton, Molecular beam epitaxial growth and characterization of Al(Ga)N nanowire deep ultraviolet light emitting diodes and lasers. J. Phys. D Appl. Phys. **49**, 364006 (2016)
29. R. Calarco, M. Marso, T. Richter, A.I. Aykanat, R. Meijers, A.V.T. Hart, T. Stoica, H. Lüth, Size-dependent photoconductivity in MBE-grown GaN-nanowires. Nano Lett. **5**, 981 (2008)
30. H.P. Bhasker, V. Thakur, S.M. Shivaprasad, S. Dhar, Quantum coherence of electrons in random networks of c-axis oriented wedge-shaped GaN nanowalls grown by molecular beam epitaxy. J. Phys. D Appl. Phys. **48**, 255302 (2015)
31. H.P. Bhasker, V. Thakur, M. Kesaria, S.M. Shivaprasad, S. Dhar, Transport and optical properties of c-axis oriented wedge shaped GaN nanowall network grown by molecular beam epitaxy. AIP Conf. Proc. **1583**, 252 (2014)

32. C.-H. Lee, Y.-J. Kim, J. Lee, Y.J. Hong, J.-M. Jeon, M. Kim, S. Hong, G.-C. Yi, Scalable network electrical devices using ZnO nanowalls. Nanotechnology **22**, 055205 (2011)
33. B.Q. Cao, T. Matsumoto, M. Matsumoto, M. Higashihata, D. Nakamura, T. Okada, ZnO nanowalls grown with high-pressure PLD and their applications as field emitters and UV detectors. J. Phys. Chem. C **113**, 10975 (2009)
34. A. Zhong, K. Hane, Growth of GaN nanowall network on Si (111) substrate by molecular beam epitaxy. Nanoscale Res. Lett. **7**, 686 (2012)
35. D. Poppitz, A. Lotnyk, J.W. Gerlach, B. Rauschenbach, Microstructure of porous gallium nitride nanowall networks. Acta Mater. **65**, 98 (2014)
36. S.S. Kushvaha, M. Senthil Kumar, A.K. Shukla, B.S. Yadav, D.K. Singh, M. Jewariya, S.R. Ragam, K.K. Maurya, Structural, optical and electronic properties of homoepitaxial GaN nanowalls grown on GaN template by laser molecular beam epitaxy. RSC Adv. **5**, 87818 (2015)
37. E.J. Tarsa, B. Heying, X.H. Wu, P. Fini, S.P. DenBaars, J.S. Speck, Homoepitaxial growth of GaN under Ga-stable and N-stable conditions by plasma-assisted molecular beam epitaxy. J. Appl. Phys. **82**, 5472 (1997)
38. B. Heying, R. Averbeck, L.F. Chen, E. Haus, H. Riechert, J.S. Speck, Control of GaN surface morphologies using plasma-assisted molecular beam epitaxy. J. Appl. Phys. **88**, 1855 (2000)
39. M. Kesaria, S. Shetty, S.M. Shivaprasad, Evidence for dislocation induced spontaneous formation of GaN nanowalls and nanocolumns on bare C-plane sapphire. Cryst. Growth Des. **11**, 4900 (2011)
40. A. Zhong, K. Hane, Characterization of GaN nanowall network and optical property of InGaN/GaN quantum wells by molecular beam epitaxy. Jpn. J. Appl. Phys. **52**, 08JE13 (2013)
41. V. Thakur, M. Kesaria, S.M. Shivaprasad, Enhanced band edge luminescence from stress and defect free GaN nanowall network morphology. Solid State Comm. **171**, 8 (2013)
42. M. Kesaria, S.M. Shivaprasad, Nitrogen flux induced GaN nanostructure nucleation at misfit dislocations on Al_2O_3 (0001). Appl. Phys. Lett. **99**, 143105 (2011)
43. K.A. Bertness, A. Roshko, L.M. Mansfield, T.E. Harvey, N.A. Sanford, Mechanism for spontaneous growth of GaN nanowires with molecular beam epitaxy. J. Cryst. Growth **310**, 3154 (2008)
44. Z.C. Feng, W. Wang, S.J. Chua, P.X. Zhang, K.P.J. Williams, G.D. Pitt, Raman scattering properties of GaN thin films grown on sapphire under visible and ultraviolet excitation. J. Raman Spectrosc. **32**, 840 (2001)
45. A. Kasic, D. Gogova, H. Larsson, C. Hemmingsson, I. Ivanov, B. Monemar, C. Bundesmann, M. Schubert, Micro-Raman scattering profiling studies on HVPE-grown free-standing GaN. Phys. Stat. Sol. (a) **201**, 2773 (2004)
46. V.Y. Davydov, Y.E. Kitaev, I.N. Goncharuk, A.N. Smirnov, J. Graul, O. Semchinova, D. Uffman, M.B. Smirnov, A.P. Mirgorodsky, R.A. Evarestov, Phonon dispersion and Raman scattering in hexagonal GaN and AlN. Phys. Rev. B **58**, 12899 (1998)
47. M.A. Reshchikov, H. Morkoc, Luminescence properties of defects in GaN. J. Appl. Phys. **97**, 061301 (2005)
48. M. Kesaria, S. Shetty, S.M. Shivaprasad, Spontaneous formation of GaN nanostructures by molecular beam epitaxy. J. Cryst. Growth **326**, 191 (2011)
49. H.P. Bhasker, S. Dhar, A. Sain, M. Kesaria, S.M. Shivaprasad, High electron mobility through the edge states in random networks of c-axis oriented wedge-shaped GaN nanowalls grown by molecular beam epitaxy. Appl. Phys. Lett. **101**, 132109 (2012)
50. C.C. Wu, D.S. Wuu, T.N. Chen, T.E. Yu, P.R. Lin, R.H. Horng, H.Y. Lai, Growth and characterization of epitaxial ZnO Nanowall networks using metal organic chemical vapor deposition. Jpn. J. Appl. Phys. **47**, 746 (2008)
51. B. Ha, S.H. Seo, J.H. Cho, C.S. Yoon, J. Yoo, G.C. Yi, C.Y. Park, C.J. Lee, Optical and field emission properties of thin single-crystalline GaN nanowires. J. Phys. Chem. B **109**, 11095 (2005)
52. M.R. Coan, J.H. Woo, D. Johnson, I.R. Gatabi, H.R. Harris, Band offset measurements of the GaN/dielectric interfaces. J. Appl. Phys. **112**, 024508 (2012)

53. D. Li, M. Sumiya, S. Fuke, D. Yang, D. Que, Y. Suzuki, Y. Fukuda, Selective etching of GaN polar surface in potassium hydroxide solution studied by X-ray photoelectron spectroscopy. J. Appl. Phys. **90**, 4219 (2001)
54. S.D. Wolter, B.P. Luther, D.L. Waltemyer, C. Önneby, S.E. Mohney, R.J. Molnar, X-ray photoelectron spectroscopy and X-ray diffraction study of the thermal oxide on gallium nitride. Appl. Phys. Lett. **70**, 2156 (1997)
55. M. Petravic, V.A. Coleman, K.J. Kim, B. Kim, G. Li, Defect acceptor and donor in ion-bombarded GaN. J. Vac. Sci. Technol. A **23**, 1340 (2005)
56. Y.-J. Lin, C.-D. Tsai, Y.-T. Lyu, C.-T. Lee, X-ray photoelectron spectroscopy study of (NH4) 2Sx-treated Mg-doped GaN layers. Appl. Phys. Lett. **77**, 687 (2000)
57. J.J. Yeh, I. Lindau, Atomic subshell photoionization cross sections and asymmetry parameters: $1 \leq Z \leq 103$. At. Data Nucl. Data Tables **32**, 1 (1985)
58. S. Tanuma, C.J. Powell, D.R. Penn, Calculations of electron inelastic mean free paths. V. data for 14 organic compounds over the 50–2000 eV range. Surf. Interface Anal. **21**, 165 (1993)
59. G. Koblmüller, J. Brown, R. Averbeck, H. Riechert, P. Pongratz, J.S. Speck, Continuous evolution of Ga adlayer coverages during plasma-assisted molecular-beam epitaxy of (0001) GaN. Appl. Phys. Lett. **86**, 041908 (2005)
60. S.H. Xu, H. Wu, X.Q. Dai, W.P. Lau, L.X. Zheng, M.H. Xie, S.Y. Tong, Direct observation of a Ga adlayer on a GaN (0001) surface by LEED Patterson inversion. Phys. Rev. B **67**, 125409 (2003)
61. A.R. Smith, R.M. Feenstra, D.W. Greve, J. Neugebauer, J.E. Northrup, Reconstructions of the GaN(000-1) Surface. Phys. Rev. Lett. **79**, 3934 (1997)
62. W. Lei, D. Liu, J. Zhang, B. Liu, P. Zhu, T. Cui, Q. Cui, G. Zou, AlN nanostructures: tunable architectures and optical properties. Chem. Comm. 1365 (2009)
63. K.A. Rickert, A.B. Ellis, F.J. Himpsel, J. Sun, T.F. Kuech, N–GaN surface treatments for metal contacts studied via X-ray photoemission spectroscopy. Appl. Phys. Lett. **80**, 204 (2002)
64. H.W. Jang, J.L. Lee, Origin of the abnormal behavior of contact resistance in ohmic contacts to laser-irradiated n-type GaN. Appl. Phys. Lett. **94**, 182108 (2009)
65. T. Hashizume, R. Nakasaki, Discrete surface state related to nitrogen-vacancy defect on plasma-treated GaN surfaces. Appl. Phys. Lett. **80**, 4564 (2002)
66. Y.J. Lin, Y.L. Chu, Effect of reactive ion etching-induced defects on the surface band bending of heavily Mg-doped p-type GaN. J. Appl. Phys. **97**, 104904 (2005)
67. M.G. Ganchenkova, R.M. Nieminen, Nitrogen vacancies as major point defects in gallium nitride. Phys. Rev. Lett. **96**, 196402 (2006)
68. D.J. Carter, M. Fuchs, C. Stampfl, Vacancies in GaN bulk and nanowires: effect of self-interaction corrections. J. Phys. Condens. Matter **24**, 255801 (2012)
69. F. Gao, E.J. Bylaska, A. El-Azab, W.J. Webber, Wannier orbitals and bonding properties of interstitial and antisite defects in GaN. Appl. Phys. Lett. **85**, 5565 (2004)
70. W.R.L. Lambrecht, B. Segall, S. Strite, G. Martin, A. Agarwal, H. Morkoc, A. Rockett, X-ray photoelectron spectroscopy and theory of the valence band and semicore Ga 3d states in GaN. Phys. Rev. B **50**, 14155 (1994)
71. P. Lorenz, T. Haensel, R. Gutt, R.J. Koch, J.A. Schaefer, S. Krischok, Analysis of polar GaN surfaces with photoelectron and high resolution electron energy loss spectroscopy. Phys. Stat. Sol. (b) **247**, 1658 (2010)
72. D. Skuridina, D.V. Dinh, B. Lacroix, P. Ruterana, M. Hoffmann, Z. Sitar, M. Pristovsek, M. Kneissl, P. Vogt, Polarity determination of polar and semipolar (11-22) InN and GaN layers by valence band photoemission spectroscopy. J. Appl. Phys. **114**, 173503 (2013)
73. M.A. Garcia, S.D. Wolter, T.-H. Kim, S. Choi, J. Baier, A. Brown, M. Losurdo, G. Bruno, Surface oxide relationships to band bending in GaN. Appl. Phys. Lett. **88**, 013506 (2006)
74. S.S. Kushvaha, M. Senthil Kumar, *Advances in Nanomaterials* (Springer, India, 2016)
75. S. Siddhanta, V. Thakur, C. Narayana, S.M. Shivaprasad, Universal metal-semiconductor hybrid nanostructured SERS substrate for biosensing. ACS Appl. Mater. Interfaces. **4**, 5807 (2012)

Chapter 10
Density Functional Theory (DFT) Study of Novel 2D and 3D Materials

Fayyaz Hussain, Muhammad Imran and Hafeez Ullah

10.1 Introduction

In modern era, conventional semiconductors exhibiting ferromagnetism called diluted magnetic semiconductors (DMSs) are acquired after doping various kinds of transition metals (TMs). In the last 20 years, at the room temperature, DMSs have exhibited auspicious ferromagnetism. As a result, an incredible interest has been bred for the forthcoming spintronics applications [1–3]. It opens new inroads of DMSs for the future spintronics materials having distinguished features and potential applications comprising of fast memory speed, ultra-grade lowers the power consumption, logic photonic devices, and bio-detectors [4–7]. The ferromagnetism at room temperature could be obtained by the magnetic doping of materials (semiconductors) having wide band gap [1]; usually, ferromagnetism at room temperature has been found in TiO_2, GaN, ZnO doped with Cr, Co, Fe, and Mn [8–10]. For doping elements, local magnetic moments are not the finest way, so in DMSs, local magnetic cluster has been exposed for being ferromagnetic (FM) that is not worthy for the FM [11–14]. The Cu being a hot dopant has

F. Hussain (✉)
Material Simulation Research Laboratory (MSRL), Department of Physics, Bahauddin Zakariya University, Multan 60800, Pakistan
e-mail: fayyazhussain248@yahoo.com

H. Ullah (✉)
Department of Physics, The Islamia University of Bahawalpur, Bahawalpur 63100, Pakistan
e-mail: hafeezullah79@gmail.com

M. Imran
Department of Physics, Govt. College University Faisalabad, Faisalabad 38000, Pakistan
e-mail: imraniub86@gmail.com

Z.H. Khan (ed.), *Recent Trends in Nanomaterials*,
Advanced Structured Materials 83, DOI 10.1007/978-981-10-3842-6_10

acquired theoretical as well as experimental attention. Currently several experimental attempts have been reported to predict the ferromagnetism in Cu doped ZnO at room temperature [15–19].

Metal and the metal oxide (M/O) system is extensively used in all kinds of catalysis and microelectronics functions such as Schottky barrier diode, laser diode, and ultraviolet (UV) diode [20, 21]. Most recent attempts to decrease the dimension of electronic devices (as small as one atom thick) have been done using boron nitride and graphene like nanomaterials [22–25]. For this reason, lots of studies have been done on monolayer based BN nanostructure and graphene, for example, nanoflakes, nanoribbons, and their hybrid structures [26–30]. Most recent attempt has been prolonged toward other materials of two dimensions (2D). ZnO is known to be very favorable for the fabrication of UV light emitter and microelectronics, for catalysis, and for gas sensing [31, 32]. The crystal that has polar surfaces, such as low-index surface of ZnO [33], it displays stronger surface reconstruction and is generally enough stable [34]. Currently, Tseng et al. adop sol-gel technique to synthesis ZnO nanostructure in 1D, 2D, and 3D spherical crystals [35]. Therefore, nanosheet of ZnO is a powerful applicant for catalysis and microelectronic functions.

Diamond (film) acts as a fantastic practical material because of its precious characteristics such as extraordinary carrier mobility (for holes: 1600 $cm^2\ V^{-1}\ s^{-1}$ and for electrons: 2200 $cm^2\ V^{-1}\ s^{-1}$), sharp energy gap ($\sim$5.5 eV), good thermal conductivity (2600 $W\ m^{-1}\ K^{-1}$) hence has prospective commercial applications, such as photodiode, radiation detectors, and heterojunction [36]. In addition, in diamond, the doping of outsized atomic elements is not appropriate since they produce greater lattice distortion while doping of smaller sized elements plays very important role in order to boost its value for electrochemical and electronics devices [37–39]. It is too easy to achieve thin films of p-type diamond by doping boron in diamond [40–42]. However, it is much harder to fabricate thin films of n-type diamond by doping As, P, N, S, Na, Li, etc. [43–48] because in diamond structure between C–C, there is smaller lattice space. It is assumed that the incorporation of bcc tantalum film into diamond will be helpful to decrease resistivity without declining mechanical properties, since Ta is chemically active, ductile, and soft and its resistivity is smaller (15–70 μΩ cm) [49].

Latest advanced studies suggest that the magnetization in carbon (diamond) is because of the defects in it [50–54] which tend to make this material a powerful candidate for future spintronics applications [55, 56]. In addition, the thin films of p-type can be simply obtained after boron doping [42, 57]. While it is more challenging to acquire n-type diamond [43, 44], further its progress is very important for electronic progress applications and many more materials [58]. The indium dopant is considered to be the finest donor in order to develop an n-type diamond. However, it has been a challenging feature for computational field to develop a theoretical model of oxygen-doped diamond due to its chemical nature.

10.2 The Method of Calculations

All calculations are carried out within plane-wave density functional theory (DFT) by employing the Vienna ab initio simulation package (VASP) [59, 60]. The generalized gradient approximation (GGA) with the Perdew, Burke, and Ernzerhof (PBE) of function and projector augmented wave (PAW) potential are selected in all these DFT calculations [61–63]. The vacuum surface is set to be 14 Å for the 2D system along c-direction, and it is not required for 3D materials calculations. The convergence tests for both systems of total energy with respect to the electron wave function are expanded using plane waves with a cutoff energy of 400 eV. The ionic position, cell volume, and lattice parameters of the system are fully relaxed with conjugate gradient method until the Hellmann Feynman forces are smaller than 0.02 eV/Å and the energy convergence criteria are met 1×10^{-5} eV. Hybrid Functional corrections (HSE 06) [64] have been applied to get more accurate band gap. The popular scheme for this calculation is Monkhorst-pack (MP) [65, 66] which is applied for K-point sampling.

10.3 Results and Discussion

10.3.1 Diluted Magnetic Semiconductors (DMSs)

The (0001) surface of GaN is renowned not only from the theoretical perspective but from the experimental too [67–74]. Currently to find out a fairly stable structure, numerous positions of adatom have been examined. On (0001) surface of GaN, T1, T4, and H3 positions are highly symmetric points, as reported T4 be the more auspicious site for adsorption [75]. We remove one Ga atom and substitute a Cu atom. After the substitution, the lattice parameter (−0.006 Å) changes slightly. Basically, this happens because of the different atomic radius of Ga from Cu and all the bond lengths of Cu-N3 system are of 2.0 Å. In GaN (2D layer), the magnetization per Cu atom is 2.0 μB and is in harmony to Wu et al. [76], but its value is larger than the value of ZnO doped with Cu [77]. Figure 10.1 shows the spin charge density of N-2p and Cu-3d.

The FM coupling is noticed to be the stronger coupling in N-2p atoms because these are close to Cu-3d showing that the Cu-3d atom being responsible for FM coupling in the system. Figure 10.2 shows the resolved spin band structure of GaN 2D layer.

The majority spin channel (blue) is for semiconductor while the minority spin channel (red) exhibits metallic characteristic with sufficient unfilled states on the right side of Fermi level as reported in also Ref. [76].

The unfilled states are extremely valuable for conduction charge carriers (compulsory for adequate spin polarized current) [79, 80]; hence, its 2D Cu-doped GaN layer is suggested to be used as injection of spin charge carriers. In the previous study of magnetic coupling, similar method was adopted [76].

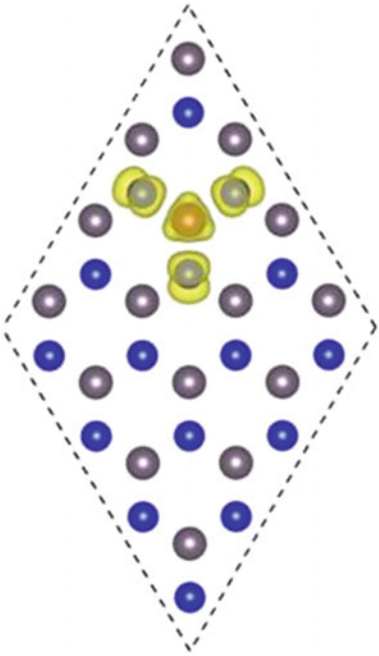

Fig. 10.1 Isosurface of spin charge density of 2D GaN layer doped with 6.25% of Cu [78]

We substitute, for antiferromagnetic (AFM) and FM coupling, two Cu atoms along c-direction separated 5.82 Å distant apart. For both systems, the total energy is calculated and the results indicate FM state to be the ground state having energy of 173 meV, that is, lower energy than AFM state. In DOS, p and d orbitals are represented by the red and blue curves, respectively, shown in Fig. 10.3 exhibiting semiconducting character. In 2D GaN DMSs doped with Cu to understand the responsible mechanism for the stabilization of FM state in Fig. 10.4, the projected density of states (PDOSs) plot for Cu and its nearest neighboring N atoms are shown.

The majority spin channel shows the coupling between N-2p and Cu-3d is strong; in case of Cu-3d, an interaction peak is noticed at −0.43 eV which overlaps with N-2p in Cu-N3, while for Cu-3d, the second interaction peak is noticed at −0.37 eV which overlaps with N-2p through smaller magnetization. In case of minority spin channel, the significant contribution toward the unoccupied states is because of 2p state of three connecting N atoms. These features specify that the coupling of Cu atom with its three neighbor atoms of N is a strong coupling. Due to the strong hybridization, a finite magnetization has been persuaded on Cu and its neighboring N atoms. The magnetization of 0.25 μB is carried by each N atom, and in case of Cu atom, the magnetization is of the magnitude of 0.56 μB. This value of magnetization is similar for N as deliberated in Ref. [76] while the value of magnetization of 0.14 μB in case of Cu is smaller in GaN 2D layer than GaN bulk, however, greater as compared to Mn in the Mn-doped GaN [81]. The magnetization

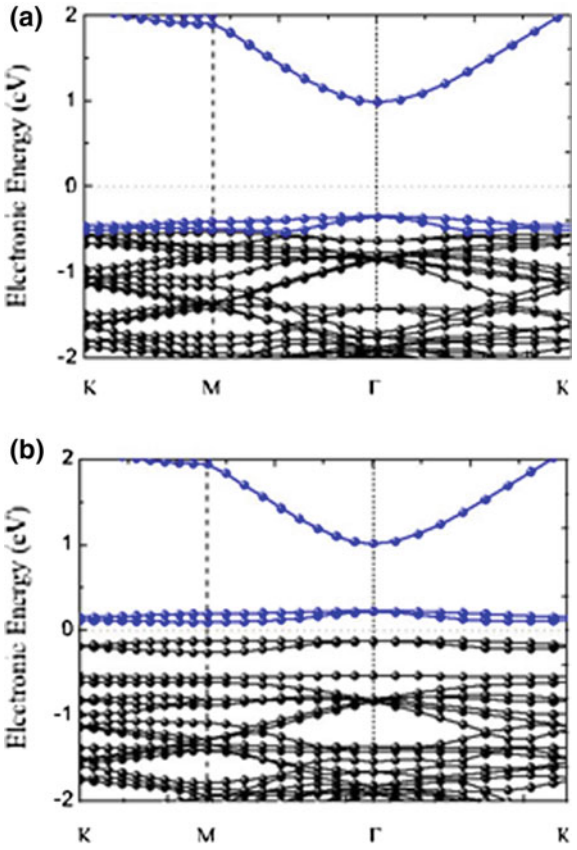

Fig. 10.2 Band structure of **a** majority spin **b** minority spin of 2D GaN layer doped with 6.25% of Cu [78]

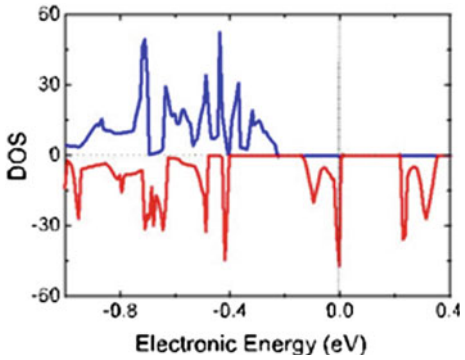

Fig. 10.3 Spin polarized DOSs of Cu-3d and N-2p [78]

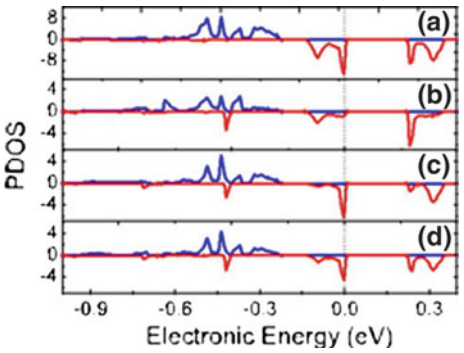

Fig. 10.4 Spin PDOSs of Cu-3d (**a**) and N-2p of the N atoms in CuN_3 structure (**b–d**) [78]

of every single N atom linked to Mn is smaller than 0.02 μB instead of greater magnetization of 4 μB of Mn; hence, in case of Cu-doped 2D GaN for ferromagnetism, the hybridization of p-d orbitals is responsible.

10.3.2 Semiconductor and Metal Interface

For a metal/semiconductor contact, the charge carriers on the two sides of the interface redistribute and reach an equilibrium state upon adjusting the Fermi levels of the two phases. The schematic diagram of the energy band structures of ZnO and Cu metal before and after contact is shown in Fig. 10.5.

However, in present study, we just consider ZnO layer to be atomically thin, and the band arrangement for multilayer sheets of ZnO with Cu assumed to be like single sheet because of layers' weak interaction [82]. So as to study the relative energy level shifting of Cu and ZnO, a reference vacuum level of (2D) Cu, ZnO, and Cu-ZnO hybrid system is aligned. Physically, for the alignment of Fermi level across interface, the electrons are transferred from the substrate (Cu) toward the semiconducting layer (ZnO); as a result, the electrons accumulate at interface in the form of extremely thin region. Hence, after the achievement of the state of equilibrium of electronic charge, further flow from metal layer toward the semiconductor layer slows down. Figure 10.6a shows the addition in carrier charge density at interface than ZnO layer, due to the deposition of ZnO monolayer under equilibrium, upon metal substrate. In order to calculate the work function, Fermi level is subtracted from electrostatic potential [83]. In Fig. 10.6, we have lined up a (uniform) reference vacuum level to study the relative energy level shift of 2D ZnO layer.

The value of work function for polar (0001) ZnO is estimated to be 4.68 eV. In case of ZnO films, the value of work function calculated using Schottky barrier model lies in the range from 4.45 to 4.50 eV [84]. The value of effective work

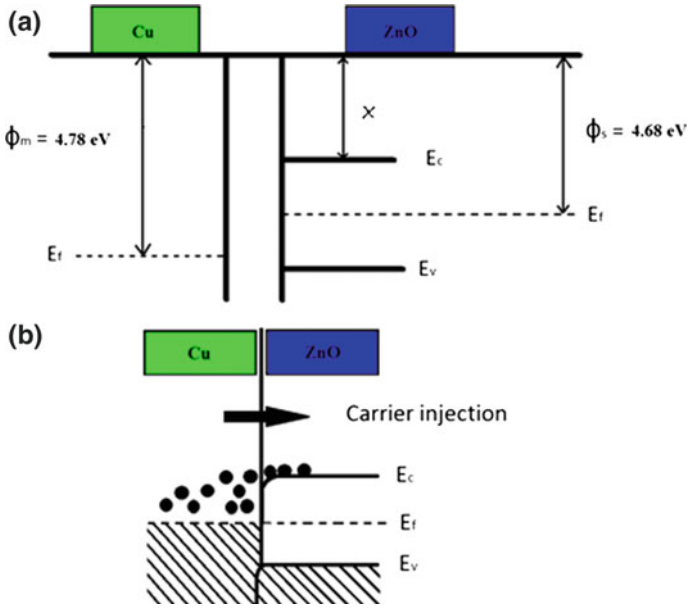

Fig. 10.5 Schematic diagrams of the energy band structures of ZnO and Cu metal. **a** Before contact and **b** after contact

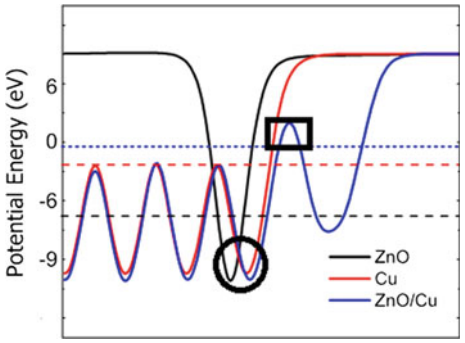

Fig. 10.6 Work function plot, potential lineups of ZnO, Cu, and ZnO–Cu hybrid. The *black rectangular box* indicates the tunneling barrier and *circle* shows shifting of energy states

function for n-type ZnO has been reported to be 4.45 eV, and the value of 4.29 eV has been reported for electron affinity of ZnO [85]. Furthermore, it is found that in ZnO the presence of oxygen defect causes its work function to be reduced. The value of work function in case of Cu substrate calculated is 4.78 eV. This value of work function is in close agreement with that of experimentally estimated value of 4.54 eV for Cu [86]. In the consequence, the development of Schottky contact at the interface of Cu and ZnO 2D monolayer is expected, along with the accumulation of electrons (majority carriers) in between the interfacial layer and within the layer of ZnO. A large number of carriers inject into semiconductor (ZnO) layer,

when the difference of work function is greater. It is the leading reason of which conductivity of multilayer structure has been increased. The injection of majority carrier electrons occurs from Cu substrate toward ZnO layer. These electrons attract the positively charged ions after their accumulation in conduction band. Figure 10.6 exhibits the transfer of charge from Cu substrate to ZnO monolayer. Recently, the established electric field has its direction from positively charged atoms (Cu) toward the conduction band electrons. An observed tunneling barrier at interface is shown by a black rectangular box in Fig. 10.6. Tunneling probability has been estimated at ZnO–Cu interface system, supposing a square potential barrier of width 1.12 Å and height 0.97 eV. This behavior has a good accordance with recent study of Ag-G system presented by Gong et al. [87] also with experimental results of Vogel et al. [88]. The contact can be a Schottky or an ohmic. The type of interface between semiconductor and the metal and the alignment of Fermi surface determines the sort of contact. This also relies on the kind of majority carriers (holes or electrons) and also on the work function (φ) of semiconducting materials and the metal. In the case of n-type semiconductor, a Schottky barrier is formed when the work function of metal (φ_M) used for contact is greater than the work function of semiconductor (φ_S). In our current work, the work function of Cu (φ_M) is greater than that of ZnO (φ_S), so the contact is Schottky contact. According to the Davidos, Mott, and Schottky theories [89], the height of barrier (φ_B) can be found using following equation:

$$\varphi_B = \varphi_M - \chi_S$$

The symbol χ_S represents the electron affinity of semiconducting material.

The existence of oxide layer because of pinning must cause a large value of φ_B (shift of the height of barrier) through some charge transfer. For essential shift of levels to be occurred, the massive charge transfer and the definite value of shifted charge could be relatively small. Because of this transfer of charge, an attractive force due to ionization develops at interface and causes change in the Fermi level making it act as a slightly forward bias efficiently; therefore, the height of Schottky barrier and band bending will be lessened. In 1947, Bardeen explained this Schottky barrier height in his theory [90].

For both systems, Fig. 10.7 displays the PDOS in which the ZnO valence band is mostly comprised of p-orbital of oxygen and d-orbital of Zn. In case of Cu, the conduction as well as valence bands are mainly comprised of d-orbital.

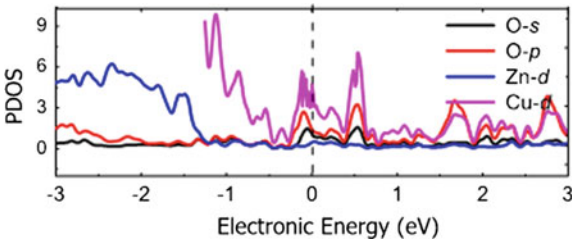

Fig. 10.7 PDOS after contact of hybrid system ZnO/Cu

In the case of hybrid system, the contribution of s and p atomic orbitals of O atom in the conduction band is small while the 3d Cu atom orbital is larger. For both ZnO and Cu phases, there exist sharp peaks in the region of low energy of conduction as well as valance band. For Cu, these peaks are more obvious. The hybridization of d-d orbitals is responsible for sharpness of peaks, and these peaks can be separated into two groups below and above the Fermi level, respectively. In comparison with pure Cu, the 3d-Cu states in the case of hybrid system of valance band states shift forward to higher energy near Fermi level. Figure 10.7 clarifies that in case of pristine ZnO layer, only contribution for valance band is from hybridization of s-p orbital of O atom. Anyhow, in case of hybrid system, the p states of O atom have major component in the conduction band also around Fermi level that is chiefly due to the hybridization of O-p and 3d-4s states of Cu. Additionally, the shifting of Zn-3d states toward valance band makes a sharp peak of value −2.35 eV.

10.3.3 Effects of Tantalum Incorporation into Diamond Films

In order to understand the electronic properties of the Ta-incorporated diamond films, their band structures (BSs) have been elaborated by using first principle calculations which are reported in [91]. The diamond films BSs substitutionally doped with Ta impurity, and pure diamond film's BSs energy gap is ∼4.4 eV [92]. Band structures of 1.56% Ta-doped diamond films, for minority (↓) and majority (↑) electronic spins reported in [91]. The formation of impurity states occur within the region of band gaps near conduction band minimum (CBM). From band structure plot of Ta-incorporated diamond, the distribution of a large number of (n-type) impurity states between Fermi level and conduction band can be observed. Spin-up and spin-down electrons may contribute to the formation of such impurity levels and thus resulting in complexity of band structure. This causes CBM to extend toward Fermi level; resulting band gap energy is decreased. In this way, existence of these impurity states may help electrons to transit from valence band to conduction band. In the similar way, Ta insertion enhances the electrical conductivity of diamond and makes it an effective semiconductor. Similar trend is also reported by Zhang et al. [39]. Furthermore, incorporated-Ta in diamond acts like a donor, i.e., it donates electrons to diamond. Moreover, it can also be noticed that insertion of Ta in diamond causes its band structure to shift downwards as compared to that of pure diamond. Ta-incorporated diamond has a slightly deeper donor level, thus it creates ∼2.0 eV of energy gap for majority spin (↑) and for minority spin (↓) ∼1.9 eV of charge carriers as in [91]. Thus, decrease in band gap energy enhances the electrical conductivity of Ta-doped diamond films, and they act as a good semiconductor. The total densities of states for different percentages of Ta atoms doped in diamond lattice (1.56, 3.12 and 6.25% Ta) are presented in [91].

Due to the increasing percentage of Ta in diamond lattice, more levels are created in the conduction band, consequently, it meets the Fermi level and hence reduces the band gap. With the increasing content of Ta, some of such local impurity levels are also created in valence band. With the increase of Ta in the diamond lattice, band gap decreases; but, after an abrupt fall, the decrease is not very prominent as Ta starts reacting with carbon atoms forming TaC. Consequently, relative to that of pure diamond films, the energy gap of a substituted diamond abruptly falls to a very low value and thus of Ta-inserted diamond films.

10.3.4 Effects of Oxygen Incorporation into Diamond Films

The Band structures of diamond, which are incorporated with substitutional impurity of 1.56% oxygen, for majority and minority electron spins are presented in [91]. The formation of impurity states occur within the region of band gaps near conduction band minimum (CBM). In addition, Fermi level exists below CBM, therefore, inserted-oxygen in diamond behaves as a donor i.e., oxygen donates electrons to diamond. Furthermore, it can also be noticed that incorporation of oxygen in diamond causes its band structure to shift downwards as compared to that of pure diamond. Oxygen-substituted diamond has a slightly deeper donor level, thus it creates $\sim$1.34 eV of energy gap for majority spin and $\sim$1.10 eV for minority spin. BSs of oxygen-incorporated diamond with 3.12% of oxygen for spin-up and spin-down electrons are demonstrated and reported in [91], so that the impact of increasing oxygen concentration in diamond lattice can be seen. This causes the extension of CBM toward Fermi level; hence, band gap energy decreases further to $\sim$0.46 eV in case of spin-up electrons and $\sim$0.44 eV in case of spin-down electrons. Because of decrease in band gap energy, the electrical conductivity of oxygen-inserted diamond films enhances, thus making it a good semiconductor. Similar trend is reported by Zhang et al. [93]; anyhow, the various values of band gap energy can be associated with varied contents of oxygen insertion. Furthermore, the current DFT studies confirm that the insertion of oxygen into diamond structure enhances its electrical conductivity, thus oxygen-incorporated diamond films act as a semiconductor [94].

It is evident that the impurity states that occur in the region of band gap tend to extend CBM to Fermi level. It causes the band gap to decrease, and oxygen-incorporated diamond acts like a semiconductor. The partial density of states of diamond films doped with oxygen is presented in [91] and confirms the filling of both valence and conduction bands by 2p-O states. The appearance of the band at -55 eV confirms the shifting of CBM toward the Fermi level. By this behavior, the donor nature of oxygen has been approved. The present findings contradict the results of Long et al. [95] according to whom the oxygen plays the role of acceptor in diamond lattice through the creation of impurity states close to VBM. But our findings seem to be in good accord with the findings of Zhou et al. [93].

The isosurface charge density of the oxygen-doped diamond films is presented in [91]. For different regions, the charge density distribution is illustrated by different colors. The excess (positive) density of charge (blue) is observed across atoms that is seemed to be decreasing with the increasing distance from center as shown by the variation of colors from purple color to orange color (which describes negative charge density). The creation of single bond after the electrons sharing by two atoms is represented by blue color. It is clear that there is relatively greater charge between O and C atoms as compared to that of C and C atoms. This shows the stronger bonding of C–O as compared to C–C bonds. Between O and C atoms, the greater charge value exhibits that the oxygen defect combination can show as vacancy character (of defect states) related to bonds of C-atom. Same findings have been reported by Long et al. [95], however, in contradiction to that of Gali et al. [96], by whom the nature of chemical bonds between C–O is weaker due to the longer bond lengths of C–O relative to C–C bonds that cause in oxygen-incorporated diamond the lattice distortion.

10.4 Summary

In summary, it can be deduced that the electronic properties of Cu-doped 2D GaN calculated using DFT. The Cu dopants when Cu doped into 2D GaN monolayer, it become spin polarized; furthermore, this spin polarization calculation magnetizes p electrons of the three neighboring N atoms with help of p-d hybridization. The ferromagnetic coupling states are preferable among all Cu dopants rather than that of AFM coupling in Cu-doped 2D GaN. Hence, Cu is promising nonmagnetic dopant for 2D GaN monolayer to fabricate 2D-based DMSs, which are promising materials with reducing size and should be free from magnetic precipitates. The adsorption properties and the electronic interaction between Cu and deposited 2D ZnO atomically sheet have been performed using DFT. We predict that the Schottky contact is formed at the ZnO/Cu interface, and the charge accumulation has been observed at the interfacial layer of this hybrid system. There is a large amount of charge transfer between the 2D ZnO and Cu substrate. It is predicted that the electronic charges are accumulated at the interface as well as on the Zn and O atoms.

Band structure calculations lead to the semiconducting behavior of Ta-incorporated diamond films due to the creation of defects states inside the band gap region extending toward conduction band minimum. Resent DFT results support the behavior observed for the experimental electrical resistivity findings. Thus, tantalum incorporation in diamond films can be useful to fabricate n-type semiconducting diamond films for industrial applications. Electronic properties of oxygen-doped diamond have been studied using DFT calculations. It is observed that the highest occupied molecular orbital is localized at oxygen atom. In addition, C_4–O bond lengths are equivalent to those of C–C bonds of diamond indicating no lattice distortions in the oxygen-doped diamond. The substitution of oxygen into

diamond is thermodynamically favorable because of negative formation energy. Band structure calculations of oxygen-doped diamond demonstrate the creation of impurity states inside the band gap region which extend CBM toward Fermi level resulting in decrease of band gap energy, and hence, oxygen-doped diamond behaves as a semiconductor. The spin projected density of states calculations reveal significant contributions of O-2p states at the Fermi level with no appreciable magnetic moments appearing on oxygen or carbon atoms for all C_1–C_4 configurations leading to nonmagnetic semiconducting behavior of oxygen-doped diamond. Present DFT results verify that by adding oxygen into diamond lattice increases its conductivity and oxygen-doped diamond films behave like a semiconductor.

References

1. T. Dietl, H. Ohno, F. Matsukura, J. Cibert, D. Ferrand, Zener model description of ferromagnetism in zinc-blende magnetic semiconductors. Science **287**, 1019 (2000)
2. T. Dietl, A ten-year perspective on dilute magnetic semiconductors and oxides. Nat. Mater. **9**, 965 (2010)
3. I. Zutic, J. Fabian, S.D. Sarma, Spintronics: fundamentals and applications. Rev. Mod. Phys. **76**, 323 (2004)
4. S.D. Sarma, Ferromagnetic semiconductors: a giant appears in spintronics. Nat. Mater. **2**, 292 (2003)
5. I. Malajovich, J.J. Berry, N. Samarth, D.D. Awschalom, Persistent sourcing of coherent spins for multifunctional semiconductor spintronics. Nature **411**, 770 (2001)
6. H. Ohno, Making nonmagnetic semiconductors ferromagnetic. Science **281**, 951 (1998)
7. S.A. Wolf, D.D. Awschalom, R.A. Buhrman, J.M. Daughton, S.V. Molnar, M.L. Roukes, A. Y. Chtchelkanova, D.M. Treger, Spintronics: a spin-based electronics vision for the future. Science **294**, 1488 (2001)
8. J.S. Lee, J.D. Lim, Z.G. Khim, Y.D. Park, S.J. Pearton, S.N.G. Chu, Magnetic and structural properties of Co, Cr, V ion-implanted GaN. J. Appl. Phys. **93**, 4512 (2003)
9. J.R. Neal, A.J. Behan, R.M. Ibrahim, H.J. Blythe, M. Ziese, A.M. Fox, G.A. Gehring, Room-temperature magneto-optics of ferromagnetic transition-metal-doped ZnO thin films. Phys. Rev. Lett. **96**, 197208 (2006)
10. Y. Matsumoto, M. Murakami, T. Shono, T. Hasegawa, T. Fukumura, P. Ahmet, T. Chikyow, M. Kawasaki, S. Koshihara, H. Koinuma, Room-temperature ferromagnetism in transparent transition metal-doped titanium dioxide. Science **291**, 854 (2001)
11. M. Zaja, J. Gosk, E. Granka, M. Kaminska, A. Twardowski, B. Strojek, T. Szyszko, S. Podsiadlo, Possible origin of ferromagnetism in (Ga,Mn)N. J. Appl. Phys. **93**, 4715 (2003)
12. J.Y. Kim, J.H. Park, B.G. Park, H.J. Noh, S.J. Oh, J.S. Yang, D.H. Kim, S.D. Bu, W. Noh, H. J. Lin, H.H. Hsieh, C.T. Chen, Ferromagnetism induced by clustered co in co-doped anatase TiO_2 thin films. Phys. Rev. Lett. **90**, 017401 (2003)
13. K. Ando, H. Saito, Z. Jin, T. Fukumura, M. Kawasaki, Y. Matsumoto, H. Koinuma, Magneto-optical properties of ZnO-based diluted magnetic semiconductors. J. Appl. Phys. **89**, 7284 (2001)
14. S. Sonoda, S. Shimizu, T. Sasaki, Y. Yamamoto, H. Hori, Magnetic and transport characteristics on high Curie temperature ferromagnet of Mn-doped GaN. J. Appl. Phys. **91**, 7911 (2002)

15. D.B. Buchholz, R.P.H. Chang, J.H. Song, J.B. Ketterson, Room-temperature ferromagnetism in Cu-doped ZnO thin films. J. Appl. Phys. Lett. **87**, 082504 (2005)
16. M.S. Park, B.I. Min, Ferromagnetism in ZnO codoped with transition metals: Zn 1− x(FeCo)x O and Zn 1− x(FeCu)x O. Phys. Rev. B **68**, 224436 (2003)
17. C.H. Chien, S.H. Chiou, G.Y. Guo, Y.D. Yao, Electronic structure and magnetic moments of 3d transition metal-doped ZnO. J. Magn. Magn. Mater. **282**, 275 (2004)
18. X. Feng, Electronic structures and ferromagnetism of Cu-and Mn-doped ZnO. J. Phys.: Condens. Matter **16**, 4251 (2004)
19. L.H. Ye, A.J. Freeman, B. Delley, Half-metallic ferromagnetism in Cu-doped ZnO: density functional calculations. Phys. Rev. B **73**, 033203 (2006)
20. U. Grossner, S. Gabrielsen, T.M. Borseth, J. Grillenberger, A.Y. Kuznetsov, G. Svensson, Palladium Schottky barrier contacts to hydrothermally grown n-ZnO and shallow electron states. Appl. Phys. Lett. **85**, 2259 (2004)
21. H. Endo, M. Sugibuchi, K. Takahashi, S. Goto, S. Sugimura, K. Hane, Y. Kashi-waba, Schottky ultraviolet photodiode using a ZnO hydrothermally grown single crystal substrate. Appl. Phys. Lett. **90**, 121906 (2007)
22. C.L. Phillips, P.D. Bristowe, First principles study of the adhesion asymmetry of a metal/oxide interface. J. Mater. Sci. **43**, 3960 (2008)
23. K.S. Novoselov, A.K. Geim, S.V. Morozov, D. Jiang, Y. Zhang, S.V. Dubonos, V. Grigorieva, A.A. Firsov, Electric field effect in atomically thin carbon films. Science **306**, 666 (2004)
24. Y.B. Zhang, Y.W. Tan, H.L. Stormer, P. Kim, Experimental observation of the quantum Hall effect and Berry's phase in graphene. Nature **438**, 201 (2005)
25. K.S. Novoselov, A.K. Geim, S.V. Morozov, Two-dimensional atomic crystals. Proc. Natl. Acad. Sci. USA **102**, 10451 (2005)
26. Y.W. Son, M.L. Cohen, S.G. Louie, Half-metallic graphene nanoribbons. Nature **444**, 347 (2006)
27. E.J. Kan, Z.Y. Li, J.L. Yang, J.G.J. Hou, Half-metallicity in edge-modified zigzag graphene nanoribbons. Am. Chem. Soc. **130**, 4224 (2008)
28. O. Hod, V. Barone, J.E. Peralta, G.E. Scuseria, Enhanced half-metallicity in edge-oxidized zigzag graphene nanoribbons. Nano Lett. **7**, 2295 (2007)
29. W. Chen, Y.F. Li, G.T. Yu, C.Z. Li, S.B. Zhang, Z. Zhou, Z.F.J. Chen, Hydrogenation: a simple approach to realize semiconductor—half-metal—metal transition in boron nitride nanoribbons. Am. Chem. Soc. **132**, 1699 (2010)
30. M.S. Si et al., Intrinsic ferromagnetism in hexagonal boron nitride nanosheets. J. Chem. Phys. **140**, 204701 (2014)
31. Z.K. Tang, G.K.L. Wong, P. Yu, M. Kawasaki, A. Ohtomo, H. Koinuma, Y. Segawa, Room-temperature ultraviolet laser emission from self-assembled ZnO microcrystallite thin films. Appl. Phys. Lett. **72**, 3270 (1998)
32. O. Dulub, U. Diebold, G. Kresse, Novel stabilization mechanism on polar surfaces: ZnO (0001)-Zn. Phys. Rev. Lett. **90**, 016102 (2003)
33. C. Noguera, Polar oxide surfaces. J. Phys.: Condens. Matter **12**, 367 (2000)
34. A. Wander, F. Schedin, P. Steadman, A. Norris, R. McGrath, T.S. Turner, G. Thorn-ton, N.M. Harrison, Stability of polar oxide surfaces. Phys. Rev. Lett. **86**, 3811 (2001)
35. Y.K. Tseng, M.H. Chuang, Y.C. Chen, C.H. Wu, Synthesis of 1d, 2d, and 3d ZnO polycrystalline nanostructures using the sol-gel method. J. Nanotechnol. **8**, 712850 (2012)
36. M. Ullah, E. Ahmed, F. Hussain, A.M. Rana, R. Raza, Electronic structure calculations of oxygen-doped diamond using DFT technique. Microelectr. Eng. **146**, 26 (2015)
37. D. Lu, H.D. Li, S.H. Cheng, J.J. Yuan, X.Y. Lv, Fabrication and characteristics of nitrogen doped nanocrystalline diamond/p-type silicon heterojunction. Nano-Micro Lett. **2**, 56 (2010)
38. Y. Koide, M.Y. Liao, J. Alvarez, M. Imura, K. Sueishi, F. Yoshifusa, Schottky photodiode using submicron thick diamond epilayer for flame sensing. Nano-Micro Lett. **1**, 30 (2009)

39. Y. Zhang, L. Zhang, J. Zhao, L. Wang, G. Zhao, Y. Zhang, Doping of vanadium to nanocrystalline diamond films by hot filament chemical vapor deposition. Nanoscale Res. Lett. **7**, 441 (2012)
40. Z.J. Li, L. Wang, Y.J. Su, P. Liu, Y.F. Zhang, Semiconducting single-walled carbon nanotubes synthesized by S-doping. Nano-Micro Lett. **1**, 9 (2009)
41. S. Yamanaka, H. Watanabe, S. Masai, D. Takenuchi, H. Okushi, K. Kajimura, High-quality B-doped homoepitaxial diamond films using trimethylboron. Jpn. J. Appl. Phys. **37**, 1129 (1998)
42. A.T. Collins, The electronic and optical properties of diamond; do they favour device applications? Mater. Res. Soc. Symp. Proc. **162**, 3 (1990)
43. N. Fujimoro, T. Imai, H. Nakahata, H. Shiomi, Y. Nishibayashi, Epitaxial growth of diamond and diamond devices. Mater. Res. Soc. Symp. Proc. **162**, 23 (1990)
44. Y. Saito, Diamond synthesis from methane-hydrogen-water mixed gas using a microwave plasma. J. Mater. Sci. **23**, 842 (1988)
45. R. Kalish, Doping of diamond. Carbon **37**, 781 (1999)
46. S.A. Kajihara, A. Antonelli, J. Bernholc, R. Car, Nitrogen and potential n-type dopants in diamond. Phys. Rev. Lett. **66**, 2010 (1991)
47. S. Prawer, D.N. Jamieson, R.J. Walker, K.K. Lee, F. Watt, R. Kalish, Lattice substitution of phosphorous in diamond by MeV ion implantation and pulsed laser annealing. Diamond Films Technol. **6**, 351 (1997)
48. M.E. Zvanut, W.E. Carlos, J.A. Freitas Jr., K.D. Jamison, R.P. Hellmer, Identification of phosphorus in diamond thin films using electron paramagnetic resonance spectroscopy. Appl. Phys. Lett. **65**, 2287 (1994)
49. N. Arshi, J. Lu, C.G. Lee, B.H. Koo, F. Ahmed, Power-dependent structural, morphological and electrical properties of electron beam evaporated tantalum films. Electron. Mater. Lett. **9**, 841 (2013)
50. S. Talapatra, P.G. Ganesan, T. Kim, R. Vajtai, M. Huang, M. Shima, G. Ramanath, D. Srivastava, S.C. Deevi, P.M. Ajayan, Irradiation-induced magnetism in carbon nanostructures. Phys. Rev. Lett. **95**, 097201 (2005)
51. H. Ohldag, T. Tyliszczak, R. Hohne, D. Spemann, P. Esquinazi, M. Ungureanu, T. Butz, π-electron ferromagnetism in metal-free carbon probed by soft X-ray dichroism. Phys. Rev. Lett. **97**, 187204 (2007)
52. Y. Zhang, S. Talapatra, S. Kar, R. Vajtai, S.K. Nayak, P.M. Ajayan, First-principles study of defect-induced magnetism in carbon. Phys. Rev. Lett. **99**, 107201 (2007)
53. W.L. Wang, S. Meng, E. Kaxiras, Graphene nanoflakes with large spin. Nano Lett. **8**, 241 (2008)
54. Y.-W. Son, M.L. Cohen, S.G. Louie, Half-metallic graphene nanoribbons. Nature **444**, 347 (2006)
55. H. Ohno, Making nonmagnetic semiconductors ferromagnetic. Science **281**, 951 (1998)
56. S.A. Wolf, D.D. Awschalom, R.A. Buhrman, J.M. Daughton, S. von Molnár, M.L. Roukes, A.Y. Chtchelkanova, D.M. Treger, Spintronics: a spin-based electronics vision for the future. Science **294**, 1488 (2001)
57. S. Yamanaka, H. Watanabe, S. Masai, D. Takenuchi, H. Okushi, K. Kajimura, High-quality B-doped homoepitaxial diamond films using trimethylboron. Jpn. J. Appl. Phys. **37**, 1129 (1998)
58. S.B. Zhang, J.E. Northrup, Chemical potential dependence of defect formation energies in GaAs: application to Ga self-diffusion. Phys. Rev. Lett. **67**, 2339 (1991)
59. D.W. Boukhvalov, First principles modeling of the interactions of iron impurities with graphene and graphite. Phys. Status Solidi B **248**, 1347 (2011)
60. P.A. Brown, C. Xu, K.L. Shuford, Periodic trends of pnictogen substitution into a graphene monovacancy: a first-principles investigation. Chem. Mater. **26**, 5735 (2014)
61. D.W. Boukhvalov, M.I. Katsnelson, Destruction of graphene by metal adatoms. Appl. Phys. Lett. **95**, 023109 (2009)

62. G. Li, F. Li, X. Wang, M. Zhao, X. Liu, Gold atom and dimer adsorbed on perfect and defective graphene and boron nitride monolayer: A first-principles study. Physica E **59**, 235 (2014)
63. D. Xu, J. Zhao, X. Wang, A density functional theory study of the adsorption of bimetallic FenPtm clusters on defective graphene: structural, electronic and magnetic properties. J. Nanopart. Res. **15**, 1 (2013)
64. L.Y. Isseroff, E.A. Carter, Electronic structure of pure and doped cuprous oxide with copper vacancies: suppression of trap states. Chem. Mater. **25**, 253 (2013)
65. P. Blake, P.D. Brimicombe, R.R. Nair, T.J. Booth, D. Jiang, F. Schedin, L.A. Ponomarenko et al., Graphene-based liquid crystal device. Nano lett. **8**, 1704 (2008)
66. L. Feng, Simulation of crystal, electronic and magnetic structures, and gas adsorption of two dimensional materials, **20**, 5 (2014)
67. C.G. Van de Walle, J. Neugebauer, First-principles surface phase diagram for hydrogen on GaN surfaces. Phys. Rev. Lett. **88**, 066103 (2002)
68. Q.Z. Xue, Q.K. Xue, R.Z. Bakhtizin, Y. Hasegawa, I.S.T. Tsong, T. Sakurai, T. Ohno, Atomistic investigation of various GaN (0001) phases on the 6 H-SiC (0001) surface. Phys. Rev. B **59**, 12604 (1999)
69. A.R. Smith, R.M. Feenstra, D.W. Greve, M.S. Shin, M. Skowronski, J. Neugebauer, J.E. Northrup, GaN (0001) surface structures studied using scanning tunneling microscopy and first-principles total energy calculations. Surf. Sci. **423**, 70 (1999)
70. Q.K. Xue, Q.Z. Xue, R.Z. Bakhtizin, Y. Hasegawa, I.S.T. Tsong, T. Sakurai, T. Ohno, Structures of GaN (0001)-(2 $\times$ 2), -(4 $\times$ 4), and -(5 $\times$ 5) surface reconstructions. Phys. Rev. Lett. **82**, 3074 (1999)
71. A.R. Smith, R.M. Feenstra, D.W. Greve, J. Neugebauer, J.E. Northrup, Reconstructions of the GaN (000 1) surface. Phys. Rev. Lett. **79**, 3934 (1997)
72. T. Strasser, C. Solterbeck, F. Starrost, W. Schattke, Valence-band photoemission from the GaN (0001) surface. Phys. Rev. B **60**, 11577 (1999)
73. A.L. Rosa, J. Neugebauer, First-principles calculations of the structural and electronic properties of clean GaN (0001) surfaces. Phys. Rev. B **73**, 205346 (2006)
74. F.H. Wang, P. Krüger, J. Pollmann, Electronic structure of 1 $\times$ 1 GaN (0001) and GaN (0001) surfaces. Phys. Rev. B **64**, 035305 (2001)
75. R.G. Hernandez, W.L. Perez, M.G.M. Armenta, M.J.A. Rodríguez, Vanadium adsorption and incorporation at the GaN (0001) surface: a first-principles study. Phys. Rev. B **81**, 195407 (2010)
76. R.Q. Wu, G.W. Peng, L. Liu, Y.P. Feng, Ferromagnetism in Mg-doped AlN from ab initio study. Appl. Phys. Lett. **89**, 142501 (2006)
77. D.B. Buchholz, R.P.H. Chang, J.Y. Song, J.B. Ketterson, Room-temperature ferromagnetism in Cu-doped ZnO thin films. Appl. Phys. Lett. **87**, 082504 (2005)
78. F. Hussain, Y.Q. Cai, M.J.I. Khan, M. Imran, M. Rashid, H. Ullah, E. Ahmad, F. Kousar, S. A. Ahmad, Enhanced ferromagnetic properties of Cu doped two-dimensional GaN monolayer. Int. J. of Mod. Phys. **26**, 1 (2015)
79. Y. Ohno, D.K. Young, B. Beschoten, F. Matsukura, H. Ohno, D.D. Awschalom, Electrical spin injection in a ferromagnetic semiconductor heterostructure. Nature **402**, 790 (1999)
80. R. Fiederling, M. Keim, W. Reuscher, G. Ossau, A. Schmidt, A. Waag, L.W. Molenkamp, Injection and detection of a spin-polarized current in a light-emitting diode. Nature **402**, 787 (1999)
81. B. Sanyal, O. Bengone, S. Mirbit, Electronic structure and magnetism of Mn-doped GaN. Phys. Rev. B **68**, 205210 (2003)
82. S. Larentis, J.R. Tolsma, B. Fallahazad, D.C. Dillen, K. Kim, A.H. MacDonald, E. Tutuc, Band offset and negative compressibility in graphene-MoS_2 heterostructures. Nano Lett. **14**, 2039 (2014)
83. K.B. Sundaram, A. Khan, Work function determination of zinc oxide films. J. Vac. Sci. Technol. A **15**, 2 (1997)

84. Y.Q. Cai, A. Zhang, Y.P. Feng, C. Zhang, H.F. Teoh, G.W. Ho, Strain effects on work functions of pristine and potassium-decorated carbon nanotubes. J. Chem. Phys. **131**, 224701 (2009)
85. S. Ju, S. Kim, S. Mohammadi, D.B. Janes, Y.G. Ha, A. Facchetti, T.J. Marks, Interface studies of ZnO nanowire transistors using low-frequency noise and temperature-dependent I-V measurements. Appl. Phys. Lett. **92**, 022104 (2008)
86. V. Dose, W. Altmann, A. Goldmann, U. Kolac, J. Rogozik, Image-potential states observed by inverse photoemission. Phys. Rev. Lett. **52**, 1919 (1984)
87. A. Venugopal, L. Colombo, E.M. Vogel, Contact resistance in few and multilayer graphene devices. Appl. Phys. Lett. **96**, 013512 (2010)
88. C. Gong, G. Lee, B. Shan, E.M. Vogel, R.M. Wallace, K. Cho, First-principles study of metal graphene interfaces. J. Appl. Phys. **108**, 123711 (2010)
89. R. Tung, Formation of an electric dipole at metal-semiconductor interfaces. Phys. Rev. B. **64**, 20 (2001)
90. J. Bardeen, Surface states and rectification at a metal semi-conductor contact. Phys. Rev. **71**, 717 (1947)
91. M. Ullah, E. Ahmed, F. Hussain, A.M. Rana, R. Raza, H. Ullah, Electronic structure calculations of oxygen-doped diamond using DFT technique. Microelectron. Eng. **146**, 26 (2015)
92. C.X. Yan, Y. Dai, B.B. Huang, DFT study of halogen impurity in diamond. J. Phys. D Appl. Phys. **42**, 145407 (2009)
93. H. Zhou, Y. Yokoi, H. Tamura, S. Takami, M. Kubo, A. Miyamoto, Quantum chemical calculations of sulfur doping reactions in diamond CVD. Jpn. J. Appl. Phys. **40**, 2830 (2001)
94. M. Ullah, E. Ahmed, I.U. Hassan, M.J. Jackson, W. Ahmed, Controlling properties of micro crystalline diamond films using oxygen in a hot filament chemical vapor deposition system. J. Manuf. Technol. Res. **3**, 153 (2011)
95. R. Long, Y. Dai, L. Yu, Structural and electronic properties of oxygen-adsorbed diamond (100) surface. J. Phys. Chem. C **111**, 855 (2007)
96. A. Gali, J.E. Lowther, P. Deak, Defect states of substitutional oxygen in diamond. J. Phys.: Condens. Matter **13**, 11607 (2001)

Chapter 11
Prospects of Nanostructured ZrO_2 as a Point-of-Care Diagnostics

Pramod K. Gupta, Zishan Husain Khan and Pratima R. Solanki

11.1 Introduction

In the last few decades, various types of metal oxide nanoparticles (MONPs), have extensively been utilized as an immobilizing matrix for the development of efficient biosensors [1–3]. Due to unique properties such as high surface-to-volume ratio, surface activity, catalytic efficiency, and strong adsorption. Among MONPs, zirconium dioxide (ZrO_2) was identified as a bioceramic material by the German chemist Martin Heinrich Klaproth in 1789 [3]. ZrO_2 was obtained from naturally occurring zirconium silicate (zircon, $ZrSiO_4$) or baddeleyite (monoclinic m-ZrO_2). ZrO_2 nanostructures honored with remarkable properties including stable surface area at high temperatures, oxidation and reduction properties, porosity, good mechanical strength, hardness, shock resistance, wear strength, low frictional resistance, low thermal conductivity, corrosion resistance, ionic conductivity, chemical inertness, wide optical bandgap, excellent thermal stability, pH stability, lack of toxicity, higher isoelectric point (about 9.5), and good biocompatibility [4–8]. Table 11.1 represents the various physical properties of nanostructured ZrO_2. These unique properties of ZrO_2 elicited interest toward its utilization in diverse applications such as oxygen sensors, nanoelectronic devices, ceramic biomaterial, fuel cell electrolytes, solar energy converters, piezoelectric devices, ceramic condensers, and optical amplifiers

P.K. Gupta · P.R. Solanki (✉)
Special Centre for Nanoscience, Jawaharlal Nehru University,
New Delhi 110067, India
e-mail: partima@mail.jnu.ac.in; pratimarsolanki@gmail.com

P.K. Gupta · Z.H. Khan
Department of Applied Sciences and Humanities, Jamia Millia Islamia,
New Delhi 110025, India

Z.H. Khan (ed.), *Recent Trends in Nanomaterials*,
Advanced Structured Materials 83, DOI 10.1007/978-981-10-3842-6_11

Table 11.1 Summarizes the physical properties of the ZrO_2

Property	Value	Property	Value
Color	White	Melting point	2715 °C
Formula weight	123.22 g/mol	Coefficient of thermal expansion at −80 °C	8×10^{-6} cm/cm/°C
Solubility	**Soluble** in HF, Conc. H_2SO_4, molten glass **Insoluble** in water, alkalies, organic solvent	Density	Monoclinic—5.68 g/mL Tetragonal—5.86 g/mL Cubic—6.29 g/mL
Boiling point	4300 °C	Heat of fusion	20.8 kg Cal/mol
Heat of formation at 298 K	261.5 kg Cal/mol	Thermal conductivity at 100 °C	0.004 Cal s/cm/cm^2/°C
Entropy of formation at 298 K	46.5 Cal	Refractive index (η_D)	2.13

[9–11]. Besides this, excellent biocompatibility, with no reported cases of toxicity, non-allergic or sensitivity, and good electrochemical activity, make it more reliable biomaterial for fabrication of electrochemical biosensors [12, 13]. Moreover, the presence of oxygen moieties on ZrO_2 NPs provides a suitable microenvironment for binding of biomolecules (proteins, nucleic acids) and encourages electron transfer between the electrode surface and active site of the biomolecules [14–16].

The pure ZrO_2 is found in three polymorphic phases depending on temperature [17]. ZrO_2 can exhibit phase transformation from one structure to another as a function of temperature as follows:

$$\text{Monoclinic} \overset{1170\,^\circ\text{C}}{\rightleftharpoons} \text{Tetragonal} \overset{2370\,^\circ\text{C}}{\rightleftharpoons} \text{Cubic} \overset{2680\,^\circ\text{C}}{\rightleftharpoons} \text{Liquid} \tag{11.1}$$

ZrO_2 is found as a monoclinic crystal structure in the temperature ranging from room temperature to 1170 °C. The monoclinic crystal structure of ZrO_2 gets transformed into tetragonal crystal structure at the temperature >1170 and <2370 °C. Further, at a higher temperature (>2370 °C), the tetragonal crystal structure gets transformed into the cubic crystal structure. The phase transformations occur due to shrinkage/expansion during heating/cooling of the material [18]. However, to develop a highly sensitive and stable electrochemical sensor, it is essential that transducer material has high electrochemical activity as well as the stable (pure) crystal structure. Moreover, electrochemical activity of the material depends upon its electronic conductivity that can be enhanced by doping of higher conducting material in the host material [19–21]. The type of dopant also has the capability to influence the phase, crystallite size and crystallinity of synthesized NPs [19, 22]. The crystalline phase of ZrO_2 can be altered by doping with divalent or trivalent metal oxides impurities such as alkaline and rare earth metal oxides (Al_2O_3, MgO, CaO, Y_2O_3, and La_2O_3) or transition metal oxides (CuO, Cr_2O_3, Fe_2O_3, CeO_2, MnO, and NiO) [9, 23, 24]. Addition of a small percentage of dopant mentioned above can alter the phase of

ZrO_2 to tetragonal or cubic crystal structure as well as properties of the material. ZrO_2 has energy equivalent to the 4d and 5s levels, and this allows most of the zirconium chemistry to involve the four electrons in these two levels. The Zr^{4+} is a highly charged ion with a relatively large radius (0.86 Å) [25]. The metal ions, used as dopants for ZrO_2, are smaller in ionic radius size and valency compare to Zr ions may result in the generation of lattice defects and a decrease in the number of unit cells in crystalline. The crystal lattice defects generated due to oxygen vacancies in the crystalline which may play a significant role in stabilization of pure phase ZrO_2. The major problem in utilizing ZrO_2 NPs in applications is its aggregation and cracking. As a solution, ZrO_2-based nanocomposites can avoid the aggregation of ZrO_2 and enhance the toughness of ceramics system by controlling the phase transformation. The mechanical degradation characteristic due to the slow spontaneous transformation of crystalline phase from tetragonal to monoclinic ("known as aging") [26] was observed. There are six types of stabilized ZrO_2 available such as tetragonal ZrO_2 polycrystals (TZP), partially stabilized ZrO_2 (PSZ), fully stabilized ZrO_2 (FSZ), transformation toughened ceramics (TTC), ZrO_2 toughened alumina (ZTA), and transformation toughened ZrO_2 (TTZ) [27]. Among these TZP, PSZ and ZTA are utilizing in the field of dentistry [28].

The sensors are devices that record a physical, chemical, or biological change and transform that into a measurable signal. The sensor encloses with three major components: recognition element, transducer, and signal processor. The recognition element allows the selective detection of a specific analyte or a group of analytes, thus diminishing interferences from other sample components. Besides this, transducer registers the signals and converts it into another measurable form. The work of a signal processor is to collect, simplify, and display the signal. Electrochemical biosensors are a subclass of chemical sensors that combine the sensitivity of electroanalytical methods with the inherent bioselectivity of the biological component. Electrochemical biosensors contain a biological recognition element (proteins, antibodies, nucleic acids, cells, and enzymes tissues) that selectively reacts with the target analytes and produces an electrical signal that is related to the concentration of the analyte being studied. Figure 11.1 shows the scheme of biosensing platform based on different biorecognition elements. The biosensor's performance is usually experimentally evaluated based on its sensitivity, limit of detection (LOD), linear and dynamic ranges, the reproducibility or precision of the response, selectivity, and its response to interferences. Some of these sensor devices have reached the commercial stage and are routinely used in clinical, environmental, industrial, and agricultural applications.

The aim of this chapter is to focus on the interaction studies of nanostructured ZrO_2 with different biomolecules include enzymes, antibodies, and DNA for the development of electrochemical biosensors for point-of-care diagnostics.

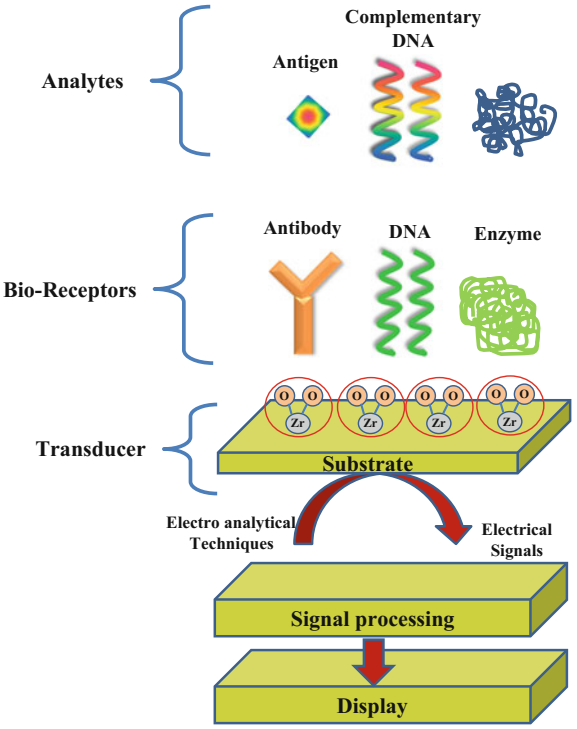

Fig. 11.1 Schematic representation of ZrO_2-based biosensing platform

11.2 Synthesis and Characterizations of ZrO_2 Nanostructures

The development of easy and reproducible synthesis technique for the production of nanostructured ZrO_2 is of great importance. Crystalline structure properties of ZrO_2 are reliant on synthesis method and thermal treatment involved in the growth of nanomaterial. Moreover, structural properties such as particle shape, size, and phase of nanomaterials have a great impression on the physiochemical characteristics. Figure 11.2 represents the different shapes of nanostructured ZrO_2 reported in the literature. The exploration of an appropriate synthesis method for the production of nanostructured ZrO_2 with controlled morphology and particle size is critical. Till now, various synthesis methods have been employed to prepare ZrO_2 nanostructures [29]. All these nanostructured ZrO_2 synthesis methods are divided into mainly two groups: liquid-phase methods and gas-phase methods. Table 11.2 shows the different synthesis methods with their size and morphological behavior. The liquid phase methods are also known as wet-chemical synthesis, which involves sol-gel, precipitation, hydrothermal, emulsion precipitation, solvothermal, sonochemical, and microwave irradiation synthesis methods. As the name "liquid phase method" suggests, the chemical reactions in the medium of solution resulting in precipitates

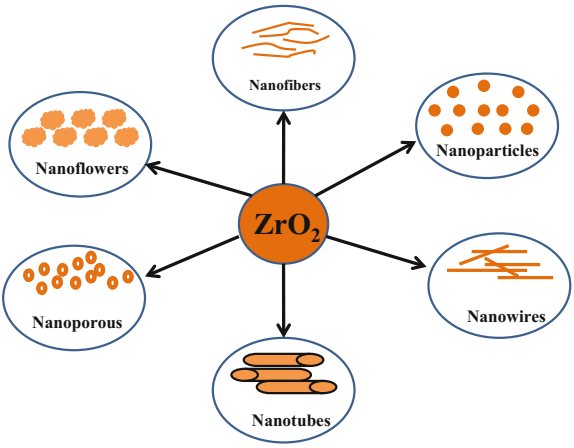

Fig. 11.2 Different shapes of nanostructured ZrO_2

Table 11.2 Different synthesis methods for nanostructured ZrO_2

	Method	Morphology	Size (nm)	Ref.
Liquid phase	Co-precipitation	Spherical-shaped ZrO_2 NPs coated SiO_2 NPs	20–50	[30]
	Hydrothermal	Hexagonal and sheet-type	50	[15]
	Solvothermal	Nanorods	100	[31]
	Emulsion precipitation	NPs	5–20	[32]
	Hydrolysis	Spherical-shaped ZrO_2 NPs	9	[33]
	Sol-gel	Spherical-shaped NPs	7 ± 1	[4]
	Microwave assist sol-gel	NPs	5–10	[34]
	Electrochemical deposition	Core-shell/Fe_3O_4–ZrO_2	~50	[35]
Vapor phase	Physical vapor deposition	Spherical-shaped NPs	60	[36]
	Spray pyrolysis	NPs	14–17	[37]
	Ion beams irradiation	Spherical-shaped NPs	8 ± 3	[38]
	Templated assist	Nanotube	60–80	[39]

or crystals and concluding products can be achieved through thermal decomposition or dehydration resulting product. On the other hand, gas-phase methods include laser ablation, inert gas condensation, physical evaporation, selective laser heating, chemical vapor synthesis, and microwave plasma synthesis. In these approaches, the nanostructured ZrO_2 is gained via the collections of precursor vapor. Among the methods mentioned above, the wet-chemical method is extensively employed to synthesize nanostructured ZrO_2 due to its ease and cost-effectiveness. During the synthesis of ZrO_2 through liquid ways (precipitation and microemulsion synthesis)

it is essential that the reaction conditions must be controlled, which make the experiment more complex. Thus, sol-gel and hydrothermal synthesis methods are favored to produce nanostructured ZrO_2. Hydrothermal synthesis is reported to be a soft chemical route with a significant advantage like the formation of crystalline products at low temperature. In the hydrothermal method, reacting solution is sealed in a high-pressure reaction kettle and the grain size of samples could be controlled in several nanometers owing to the relatively low reaction temperature. During the hydrothermal synthesis of nanomaterial, the surrounding conditions such as temperature and pressure were kept at >100 °C and above 1 atm, respectively. Finally, under the applied surrounding conditions ZrO_2 sols formed through chemical reactions in an aqueous or organo-aqueous medium and rapid growth of crystals provide nanostructures of ZrO_2. Moreover, the pH value of the medium solution has a great impact on the crystal structure and particle size of the synthesized ZrO_2. The nanostructured ZrO_2 particles under 10 nm have been produced via hydrothermal synthesis at pH 10–11. The hydrothermal process was found preferable because using this method crystal size can be controlled and miniaturized by altering the process conditions. The reaction such as hydrolysis, co-precipitation, oxidation, decomposition, and complex ion also can be performed using the hydrothermal method. In this way, it is feasible to clarify the influence of nanometer-size effect on phase stability systematically. However, agglomeration phenomena of ZrO_2 NPs were observed in hydrothermal synthesis method, which can change the structural/mechanical properties and stability. ZrO_2-based nanocomposites were also synthesized *via* a hydrothermal method to avoid the aggregation of NPs in big clusters. Moreover, a surfactant such as a cetrimonium bromide (CTAB) [15], polyethylene glycol (PEG), and graphene oxide (GO) were also used to prevent the aggregation of nanostructured ZrO_2.

Till now, different ZrO_2 nanostructures such as NPs, nanowires, nanofibers, nanoflowers, nanorods, and nanoporous have been reported using different characterization techniques such as X-ray diffraction (XRD), transmission electron microscopy (TEM), atomic force microscopy (AFM), and scanning electron microscopy (SEM) of ZrO_2 NPs synthesized through hydrothermal and co-precipitation methods.

Figure 11.3 shows the XRD patterns of (a) hydrothermally synthesized ZrO_2 NPs and (b) aluminum (Al)-doped ZrO_2 NPs synthesized by co-precipitation method. The XRD patterns for hydrothermally synthesized ZrO_2 NPs contain diffraction peaks correspond to both monoclinic (m) and tetragonal (t) crystalline phases marked by “m” and “t” symbols, respectively, whereas for Al-doped ZrO_2 NPs, diffraction peaks only correspond to tetragonal phase are observed and no any peak related to monoclinic phase. It is suggested that the doping in ZrO_2 produced stabilize pure tetragonal ZrO_2 NPs.

Bare ZrO_2 NPs and ZrO_2-RGO nanocomposite were also synthesized through hydrothermal method to investigate the degree of aggregation of NPs. Figure 11.4 shows the surface morphology of synthesized ZrO_2 NPs using co-precipitation

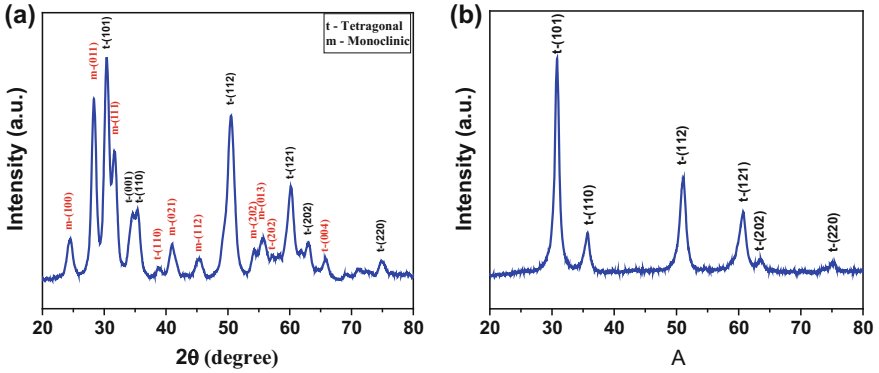

Fig. 11.3 **a** XRD patterns of ZrO_2NPs and **b** Al-doped ZrO_2 NPs

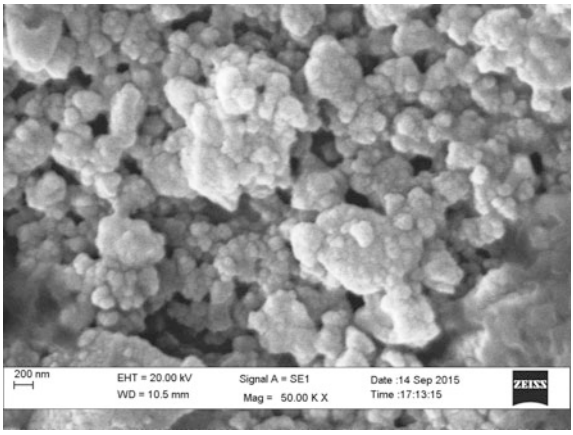

Fig. 11.4 SEM image of hydrothermal synthesized ZrO_2 NP

method. A high degree of aggregation of NPs can be easily observed. It was very difficult to observe the shape and size of synthesized NPs due to such high aggregation of NPs. To minimize the aggregation, ZrO_2-based nanocomposite with other materials such as GO or reduced GO was also explored using the hydrothermal method.

For more precise investigation, TEM images of bare ZrO_2 NPs and ZrO_2 NPs decorated onto RGO sheets were analyzed (Fig. 11.5a, b). TEM images clearly indicated that a dense magnitude of ZrO_2 NPs (sizes of 6–7 nm) is uniformly decorated on the RGO sheet (image b). This dense dispersion of NPs on RGO sheet is just a visual matter caused by TEM imaging. In fact, unlike the SEM images, TEM images show ZrO_2 NPs on both sides of RGO sheets, and thus, the contribution of the significant amount of NPs was observed as a dense dispersion of NPs on RGO sheets surface. RGO sheets exhibited typical wrinkle morphology and paper-like structure with fragile layers. The presence of small size NPs reveals that

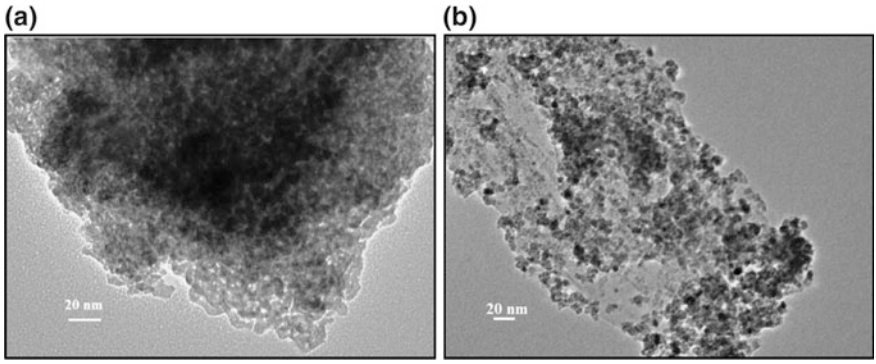

Fig. 11.5 TEM image of hydrothermally synthesized **a** bare ZrO_2 NPs and **b** ZrO_2 NPs decorated on RGO sheets

hydrothermal synthesized NPs facilitate an excellent microenvironment for rapid crystal growth of ZrO_2. The good dispersion of ZrO_2 NPs on RGO surface prevents aggregation of ZrO_2NPs as well as restacking of RGO sheets, which increases the stability of the exfoliated RGO sheets.

These characterization techniques revealed that the synthesis techniques have a great impact on the crystallinity, morphology, and physicochemical properties of synthesized ZrO_2 nanostructures. Besides this, template-assisted ZrO_2 synthesis characterizes a suitable and versatile method for producing 1-D nanostructures. It was also obtained that synthesis of ZrO_2 nanostructures in the presence of nitrogen-containing reducing agents may lead to the doping of nitrogen by replacing oxygen atoms.

11.3 Biological Properties of ZrO_2

The unique properties of ZrO_2 such as higher isoelectric point (9.5), chemical inertness, lack of toxicity, pH stability and availability of oxygen groups make it an ideal material for immobilization of biomolecules. [40] High biocompatibility of ZrO_2 is confirmed by both studies in vitro and in vivo. A higher biocompatibility of bioceramic ZrO_2 is also observed in the case where ZrO_2 was completely purified from its radioactive contents. Bioceramic ZrO_2 is inserted in the body and has no adverse local or general tissue reactions. The highly polished surface of ZrO_2 prostheses provides the ability to contact easily with gum tissue to assist in the structural maintenance of gingival. Moreover, chemical inertness of bioceramic ZrO_2 provides good cell adhesion, and therefore, no hostile systemic reactions are associated with it. However, degradation of ZrO_2 particles from synthesis process or at low temperature promotes the immune localized inflammatory responses [41]. Toxicity of ZrO_2 is comparably lower than titanium oxide and similar to alumina. It was confirmed using

in vitro tests. ZrO_2 was first used for medical purposes in 1969 for orthopedic application. It was proposed as a new material for hip head replacement instead of titanium or alumina prostheses. Often ZrO_2 convoyed radioactive elements such as thorium (Th) and uranium (U), having along half-life. Due to the presence of radioactive materials with ZrO_2, two types of radiations alpha and gamma were observed. For ZrO_2-based bioceramics, used in surgical implants, a significant quantity of alpha emissions was observed due to higher ionization of ZrO_2. The radiated alpha particles may damage the cell of hard and soft tissues. The purification of ZrO_2 from radioactive materials is a challenging and expensive. From the previous literature, it is concluded that the level of gamma radiation associated with ZrO_2 is not worrisome. Recently, ZrO_2 nanogel was utilized for the entrapment of biomolecules (hemoglobin, myoglobin and the protein). The analytical characteristics of the developed biosensor proved that the nanogel preserved catalytic activity and an excellent hydration microenvironment for the enzyme. Due to its lack of toxicity, excellent conductivity, and affinity to bind with groups containing oxygen, the ZrO_2 nanogels became attractive for the construction of biosensors. Also, some works in the literature have reported that ZrO_2 has a strong affinity with the phosphoric group. Therefore, ZrO_2 is used as a capturing agent for selectively enriching free organophosphate pesticides (OPPs) and phosphorylated proteins. Meanwhile, there are few reports of a nanocomposite of three-dimensional ordered macroporous polyaniline (OMP) combined with ZrO_2 NPs being used to detect methyl parathion (MP) [42].

11.4 ZrO_2-Based Biosensors

The nanostructured ZrO_2 is issued extensively for the development of immunosensor, enzymatic, and DNA biosensor for point care diagnosis.

11.4.1 ZrO_2-Based Immunosensors

By a literature survey of last two decades, it is found that the electrochemical immunoassays and immunosensors are an appropriate solution to fabricate portable devices for the purpose of point-of-care testing or on-site monitoring of chemicals agents. Different strategies were employed for fabrication of an electrochemical immunosensors for clinical diagnosis and environmental toxicant monitoring. Table 11.3 demonstrates the list of immunosensors fabricated for clinical diagnosis and environmental toxicant monitoring. Liu et al. [43] reported ZrO_2 NPs as selective sorbents to capture the phosphorylated acetylcholinesterase (AChE) adduct. ZrO_2 NPs, which were pre-coated on a screen-printed electrode (SPE) through electrodeposition and quantum dots (QD) tagged monoclonal anti-AChE fabricated a model sensor for paraoxon detection. Using voltammetric

Table 11.3 Represents the ZrO_2-based immunosensors reported in literature

Surface/matrix	Transducers	Target molecules	Detection range	Detection limit	Sensitivity	Ref.
APTES/ZrO_2/ITO	DPV	CYFRA-21-1	2–16 ng mL^{-1}	0.08 ng mL^{-1}	2.2 mA mL ng^{-1}	[15]
ZrO_2–RGO	DPV	CYFRA-21-1	2–22 ng mL^{-1}	0.122 ng mL^{-1}	0.756 μA mL ng^{-1}	[16]
GA-ZrO_2/ITO electrode	**EIS**	*Vibrio cholerae*	50–400 ng mL^{-1}	0.74 ng mL^{-1}	0.03 ng^{-1} mL^{-1} cm^{-2}	[4]
ZrO_2-coated SPE surface	SWV	Paraoxon	10 pM–4 nM	8.0 pM	–	[43]
Fe_3O_4/ZrO_2 NPs	CV	CEA	0.008–200 ng mL^{-1}	5 pg mL^{-1}		[35]
ssDNA/ZrO_2/ITO	DPV	*Vibrio cholerae*	1×10^{-8}–10 nM	1×10^{-8} nM	0.48 mA/nM cm^{-2}	[45]
Serine/nZrO_2	DPV	CYFRA-21-1	0.01–29 ng mL^{-1}	0.01 ng mL^{-1}	0.295 mA mL ng^{-1}	[44]
SPCE | MWCNTs/(PDDA/Hemin/AuNPs)	Amperometric	Clenbuterol	0.003–100 μg L^{-1}	1.0 ng L^{-1}		[46]

Anti-cytokeratin fragment (anti-CYFRA-21-1); square-wave voltammetry (SWV); carcinoembryonic antigen (CEA)

technique biosensing results were obtained as linear detection of phosphorylated AChE in range from 10 pM to 4 nM, and the limit of detection of 8.0 pM. The biocompatible materials were used to make the material more suitable for the immobilization of biomolecules including antibodies which result in improved biosensing properties like sensitivity, self-life etc. In this context, different biocompatible materials were explored for the functionalization of ZrO_2 NPs. The amino acids and proteins are well-known biocompatible organic molecule containing amine ($–NH_2$) and carboxylic acid (–COOH) functional groups, which make it a promising linker to offer a sufficient immobilization of desired biomolecules (antibodies, nucleic acid, etc.). Bagbi et al. [4] fabricated a nanocomposite of gelatin A (GA), which behaves as a stabilizing agent to avoid aggregation of ZrO_2 NPs to form a network assemble due to the interaction between the sufficient oxygen and nitrogen atoms. They have created a thin film of GA-ZrO_2 nanocomposite onto an indium tin oxide (ITO)-coated glass substrate by a simple drop casting method. This nanocomposite was used for immobilization of monoclonal antibodies (Ab) specific to *Vibrio cholerae* (*Vc*) followed by bovine serum albumin (BSA) for antigen *Vc* detection using electrochemical techniques. The results were obtained with excellent linearity in the range of 50–400 ng mL^{-1} with a low limit of detection of 0.74 ng mL^{-1}, sensitivity as 0.03 Ω ng mL^{-1} cm^{-2}, and reproducibility more than 10 times. It is reported that the sandwich-type immune complex assay is needed to confirm the accuracy of antibodies–antigen interaction further. Gan et al. [35] proposed an amperometric sandwich immunosensor comprising of magnetic DNA-tagged nanoprobes. They formed a core/shell (Fe_3O_4/ZrO_2 NPs) structure and functionalized it with horseradish peroxidase (HRP)-labeled anti-carcinoembryonic (anti-CEA) antibodies (HRP-CEAAb2) to form an immunosensing probe. Further, to project immunoassay, o-phenylenediamine (OPD) and CEA antibody were immobilized onto Au NPs/CHIT/GCE to construct CEA recognition. In this way, a sandwich-type immune complex was formed between secondary antibodies modified HRP-CEAAb2/Fe_3O_4/ZrO_2 NPs and Au NPs/CHIT/GCE [35]. Dissimilar to the conventional nanostructured-based electrochemical immunoassays, sandwich-type immunoassays were involved both electron mediators and enzyme labels that apparently make simpler the electrochemical measurement process. This sensing method showed detection of CEA in the range of 0.008–200 ng/mL, with a detection limit of 5 pg/mL. ZrO_2 NPs-based immunosensing platform for oral cancer detection was also fabricated by Kumar et al. [15]. They have synthesized ZrO_2 NPs through hydrothermal method, silanized using 3-aminopropyltriethoxysilane (APTES), and then electrophoretically deposited onto ITO. APTES/ZrO_2/ITO electrode was further functionalized with anti-cytokeratin fragment (anti-CYFRA-21-1) and BSA. BSA/anti-CYFRA-21-1/APTES/ZrO_2/ITO was used to electrochemically detect the salivary CYFRA-21-1 antigen that was used as a biomarker for the detection of oral cancer and resulted in a high sensitivity of 2.2 mA mL ng^{-1} with a detection range of 2–16 ng mL^{-1}, the detection limit of 0.08 ng mL^{-1}. Further, Kumar et al. [44] have fabricated serine functionalized nanostructured ZrO_2 (serine/nZrO_2)-based immunosensor for oral cancer detection. They found biosensing parameters as a wide linear range (0.01–29 ng mL^{-1}), the detection limit

(0.01 ng mL^{-1}), and a quick response time (6 min) for detection of the CYFRA-21-1 antigen. Further, they have synthesized the uniformly decorated reduced graphene oxide (RGO) with ZrO_2 NPs and reported that the RGO avoid the coagulation of the ZrO_2 NPs with enhancement in electrochemical performance of ZrO_2–RGO nanocomposite [16]. The ZrO_2–RGO nanocomposite-based immunosensor was used for detection of CYFRA-21-1 biomarker in the saliva of oral cancer patients using differential pulse voltammetry (DPV). These studies show the interaction between the ZrO_2 and antibodies occurred due to the high isoelectric point ($\sim$9.5) of ZrO_2 helps in increasing interaction with a different biomolecule that consists of low isoelectric point (IEP, $\sim$4–5) via electrostatic interactions.

11.4.2 Enzymatic Biosensor

In recent years, nanostructured ZrO_2 was used to develop enzymatic electrochemical biosensors. Enzyme electrodes combine the specificity of enzymes with the analytical power of electrochemical devices and are extremely useful for clinical diagnostics or environmental monitoring. The different enzymatic biosensors are mentioned in the Table 11.4. The ZrO_2 NPs-decorated graphene nanosheets (ZrO_2 NPs-GNs) were electrochemically deposited on GCE to construct an enzymeless biosensor for the detection of organophosphate pesticides (OPs) [14]. Electrochemical synthesis of hybrid ZrO_2 NPs-GNs without the use of hazard chemical to RGO was observed as environment-friendly and far from any contamination. Hybrid composite provided enhanced electrochemical activity as well as oxygen moieties to capture OPs. The enzymeless sensor showed the sensitivity of 107.3 ng mL^{-1} for detection of methyl parathion (MP) in the range of 0.002–0.9 g mL^{-1} with a detection limit of 0.6 ng mL^{-1}. The ZrO_2-based electrochemical biosensor was fabricated for urea detection by applying bi-enzyme [urease (Urs) and glutamate dehydrogenase (GLDH)] onto electrochemically deposited ZrO_2 film [6]. The fabricated Urs-GLDH/ZrO_2/Au bioelectrode resulted in a linear detection in the range of 5–100 mg dL^{-1} with the sensitivity of 0.071 μA/(mM cm^{-2}) and an extended storage stability up to 4 months at 4 °C. Shukla et al. [47] have developed an electrochemical urea biosensor through electro-co-deposition of ZrO_2-polypropylene imine dendrimer (ZrO_2-PPI) nanocomposite onto screen-printed carbon electrode (SPCE). The electrolyte for electro-co-deposition was formed by dispersing sol-gel-synthesized ZrO_2 NPs in PPI solution. High active surface area of both PPI and ZrO_2 NPs resulted in improved electrocatalytic properties and immobilization of Urs enzyme on ZrO_2-PPI/SPCE bioelectrode. The amperometric biosensor achieved a sensitivity of 3.89 A mM^{-1} cm^{-2} and detection range of 0.01–2.99 mM with a fast response time of $\sim$4 s for urea detection. Uslu et al. introduced one another urea biosensor based on titania–ZrO_2 (TiO_2–ZrO_2) nanocomposite [5]. They have co-immobilized Urs and GLDH onto TiO_2–ZrO_2/ITO electrode nanocomposite and combined it

Table 11.4 Exhibits the biosensing characteristics of the different enzymatic biosensor

S. No.	Surface/matrix	Transducers	Target molecule	Detection range	Detection limit	Sensitivity	Ref.
1.	ZrO_2NPs-GNs/GCE	SWV	Methyl parathion	0.002–0.9 ng mL^{-1}	0.6 ng mL^{-1}	107.3 ng mL^{-1}	[14]
2.	Urs-GLDH/ZrO_2/Au	DPV	Urea	5–100 mg dL^{-1}	5 mg dL^{-1}	0.071 μA/(mM cm^{-2})	[6]
3.	Urs/ZrO_2-PPI/SPCE	Amperometry	Urea	0.01–2.99 mM		3.89 μA mM^{-1} cm^{-2}	[47]
4.	Urs-GLDH/TiO_2–ZrO_2/ITO	Microfluidic-based CV	Urea	0.8–16.6 mM	0.44 mM	2.74 mA mM^{-1} cm^{-2}	[54]
5.	AChE–ChO/c-MWCNT/ZrO_2NPs/GCE	Amperometric	Choline	0.01–200 μm	0.01 μm		[48]
6.	*GOx/GLU/CHITOSAN/Pt*	Chronoamperometry	Glucose	1.25×10^{-5}–9.5×10^{-3} M	1.0×10^{-5} M	0.028 μA mM^{-1}	[49]
7.	GOx/chitosan/α-ZrP	Amperometric	Glucose	0.25–8.0 mM		0.076 mM	[50]
8.	Hb/ZrO_2/[BMIM]BF_4/CHI/GCE	CV	Hemoglobin	0.5–500 μmol L^{-1}	0.2 μmol L^{-1}	0.0631 μmol L^{-1}	[39]
9.	Hb/HZMS-SA/Au	Amperometric	H_2O_2	1.75 μM–4.9 mM	0.6 μM	1.832 μM	[51]
10.	HRP/ZrO_2–CS–AuNPs	Amperometric	H_2O_2	7.8×10^{-7}–3.7×10^{-3} mol L^{-1}	3.2×10^{-7}	11.10 mM	[52]
11.	Hb–DNA/ZrO_2/Au	Amperometric	H_2O_2	1.1 μM–2.3 mM	0.5 μM		[53]
12.	ChOx/ZrONPs/ITO	CV	Cholesterol	0.26–10.34 mM	0.01 mM	0.70 μA mM^{-1} cm^{-2}	[40]
13.	(SiO_2@ZrONPs)/chitosan	Amperometric	Bilirubin	0.02–250 mM	0.1 nM		[30]

with the microfluidics mediator-free sensor. The fabricated mediator-free microfluidics biosensor showed a linear detection of urea in the range of 5–100 mg/dL with sensitivity of 2.74 mA [Log mM]$^{-1}$ cm^{-2} and detection limit of 0.07 mg/dL. Other than this, a bi-enzymatic biosensor for choline detection was constructed by Pundir et al. [48] by co-immobilization of AChE and choline oxidase (ChO) onto electrodeposited (carboxylated MWCNTs-ZrO_2 NPs) nanocomposite. For a healthy person, level of choline in serum sample was measured in the range of 9.0–12.8 μmol/L, whereas it was in the range of 5.0–8.4 μmol/L for a person who has Alzheimer's disease. Sodium dodecyl benzenesulfonate as anionic surfactant facilitates a good dispersion of nanostructured ZrO_2 in the medium of polymer solution such as CHIT solution. Using this concept, Yang et al. [49] fabricated a nanoporous CHIT/Pt electrode and used as an immobilization matrix for the glucose oxidase (GOx) enzyme directly (without any linker). They found that direct immobilization of GOx onto CHIT/Pt provides more bioactivity compared to GOx immobilized cross-linked by glutaraldehyde (GLU). The fabricated biosensor was capable of linear detection of glucose in the range of 1.25×10^{-5}–9.5×10^{-3} M with a detection limit of 1.0×10^{-5} M and sensitivity of 0.028 μA mM^{-1}. Whereas, a layer of negatively charged sulfonate groups of Nafion films on top of the ZrO_2/CHIT/GO*x* electrode was used to minimize the influence of chemical interferents in the amperometric determination of glucose. Liu et al. [50] constructed another glucose biosensor based on GOx chitosan/α-zirconium phosphate (GOx/CHIT/α-ZrP). This biocomposite (GOx-CHIT) was intercalated between the interlayers of α-ZrP and deposited onto a glassy carbon electrode (GCE). For hybrid GOx/CHIT/α-ZrP/GCE bioelectrode, a high electron transfer rate constant (7.48 ± 3.52 s^{-1}) with a linear glucose detection range of 0.25–8.0 was observed. Ma et al. [39] have synthesized alumina template assist highly ordered ZrO_2 nanotubes by liquid phase deposition technique. They deposited a uniformly dispersed CHIT solution containing 1-butyl-3-methylimidazolium tetrafluoroborate ionic liquid ([BMIM]BF_4), ZrO_2 nanotubes and hemoglobin (Hb) onto GCE surface to develop a biocompatible immobilizing matrix for Hb. An enhancement in direct electrochemistry Hb was achieved due to the synergic effects of ZrO_2 nanotubes and [BMIM]BF_4. In the series of ZrO_2-based enzymatic biosensors, a biosensor for the detection of hydrogen peroxide (H_2O_2) was fabricated by deposition of hollow ZrO_2 microstructures—sodium alginate (HZMS-SA) nanocomposite onto the gold electrode [51]. The porous structure of HZMS provided a high surface area for the immobilization of Hb and enhanced the electron transfer rate. Hb/HZMS-SA/Au biosensor detected H_2O_2 in the linear range of 1.75 μM–4.9 mM with a high sensitivity of 1.832 μM and low detection limit of 0.6 μM. Wang et al. [52] reported another electrochemical sensor for H_2O_2 detection. They electrodeposited flower-like polymer–copper nanostructure composite (pPA–FCu) onto the gold electrode and then modified the electrode as HRP/ZrO_2–CS–AuNPs/pPA–FCu/gold electrode. Using same procedure, HRP/ZrO_2–CS–AuNPs/gold electrode was also fabricated to observe the significant use of pPA–FCu. They found that presence of pPA–FCu enhanced the redox electrochemical activity and excellent catalytic efficiency for H_2O_2. It was also observed that ZrO_2–CS–AuNPs had an excellent

film-forming ability, high stability and provided an excellent microenvironment for immobilization of enzyme. The fabricated HRP/ZrO_2–CS–AuNPs/gold bioelectrode showed a linear detection of H_2O_2 in range from 7.80×10^{-7} to 3.7×10^{-3} mol L^{-1} with a detection limit of 3.2×10^{-7} mol L^{-1}. Yang et al. [53] presented a novel electrochemical biosensor based on Hb-doped DNA/ZrO_2 polyion complex membrane (PIC) for the detection of H_2O_2. They observed a high rate of electron exchange between Hb and Au electrode in the presence of DNA and ZrO_2 NPs. Moreover, Hb–DNA/ZrO_2 polyion complex membranes were capable of resisting interferences from anionic species in the sample. The developed Hb–DNA/ZrO_2/Au biosensor detected H_2O_2 (in milk) ranging from 1.1 μM to 2.3 mM with a detection limit of 0.5 μM. Kaushik et al. [40] introduced a biosensor based on sol-gel-synthesized ZrO_2 NPs for the detection of cholesterol. Cholesterol oxidase (ChOx) was immobilized on the surface of ZrO_2NPs/ITO via physisorption. The fabricated ChOx/ZrO_2NPs/ITO biosensor showed an enhanced electron transport and sensitivity of 0.70 μA mM^{-1} cm^{-2} with a low detection limit of 0.01 mM in cholesterol range of 0.26–10.34 mM. Batra et al. [30] fabricated ZrO_2-coated silica NPs (SiO_2@ZrONPs) based highly sensitive electrochemical biosensor for the detection of bilirubin. The SiO_2@ZrONPs composite with CHIT was electrodeposited onto Au electrode to develop a matrix for the covalent immobilization of bilirubin oxidase (BOx). The larger effective surface area of SiO_2@ZrONPs/CHIT/Au compared to CHIT/Au provided higher electrochemical current. Because SiO_2@ZrONPs acted as electron transfer mediator that helped in enhancing the biosensor response and thus increased sensitivity.

11.4.3 DNA Biosensor

DNA biosensors, based on nucleic acid recognition processes, are rapidly being developed toward the goal of rapid, simple, and inexpensive testing of genetic and infectious diseases. Electrochemical hybridization biosensors rely on the immobilization of a single-stranded (ss) DNA probe. It is found that ZrO_2 exhibited high affinity toward the phosphate group. Thus, it is a very suitable material for adsorption of DNA for development of electrochemical biosensor. Most of the electrochemical biosensors are based on hybridization technique, and their response studies are being monitored in the presence of electroactive catalysts such as methylene blue and ruthenium complexes. ZrO_2 has high affinity to bind with the freely available bases of DNA. After the hybridization of probe DNA with the complementary sequence or mismatch, DNA sequences and response monitored in the presence of the electroactive catalysts. During the measurement of reaction studies of DNA probe, intercalated electroactive catalysts oxidized or reduced. Table 11.5 exhibits the different DNA biosensor reported in the literature for clinical diagnosis. Solanki et al. [55] fabricated an electrochemical sensor based on hybridization technique using methylene blue as a catalyst. The ssDNA probe of 16s rRNA coding region of *Escherichia coli* immobilized on a thin film of ZrO_2 NPs biosensor and hybridized

Table 11.5 Exhibits the DNA biosensor reported in the literature

Surface/matrix	Transducers	Detection limit	Linearity	Ref.
ZrO_2/ITO electrode	Electrochemical	10^{-6} pM	10^{-6}–10^{6} pM	[55]
ZrO_2/ITO electrode	Electrochemical	1×10^{-8} nM	1×10^{-8}–1×10^{-9} nM	[45]
ZrO_2/diamond	Electrochemical	1.3×10^{-10} M for CV 4.5×10^{-12} M for DPV	10^{-10}–10^{-7} M	[56]
ZrO_2 NPs/Au	DPV	2.25×10^{-10}–2.25×10^{-8} mol l^{-1}	1.0×10^{-10} mol l^{-1}	[8]
ZrO_2 NPs	DPV	0.065 ng μL^{-1}	640–0.065 ng L^{-1}	[57]
ZrO_2-chitosan		0.00078 μM	0.00078–0.05 μM	
ZrO_2/nanoSPAN membrane	EIS	3.4×10^{-13} M	1.0×10^{-12} M–1.0×10^{-6} M	[58]
ZrO_2-CPE	DPV			[59]
ZrO_2NPs/NG/GCE	EIS	3.1×10^{-11} mol/L	1.0×10^{-10}–1.0×10^{-6} mol/L	[60]
CHIT–CeO_2–ZrO2/Au	DPV	1.0×10^{-13} M	1.63×10^{-13} M–1.63×10^{-8} M	[61]
ZrO_2/ERGO/Au	DPV	1.21×10^{-14} mol L^{-1}	1.0×10^{-13}–1.0×10^{-7} mol L^{-1}	[62]

with complementary, non-complementary, and genomic DNA. The ssDNA/ZrO_2/ITO bioelectrode exhibits high sensitivity toward hybridization detection (10^{-6}–10^{6} pM complementary DNA) using DPV technique. Further, they have used this platform for *V. cholera* [O1 gene] detection. This genosensor exhibits sensitivity of 0.48 mA/nM cm^{-2} for complementary DNA and 2.34 mA/nM cm^{-2} for genomic DNA [45]. Liu et al. [56] deposited a ZrO_2 thin film on the diamond electrode to fabricate a simple and effective DNA biosensor. DNA functionalized DNA/ZrO_2/diamond bioelectrode showed an enhanced redox activity for redox mediator methylene blue and highly sensitive detection of complementary DNA concentration in the range of 10^{-10}–10^{-7} M in the solution. Zhu et al. also reported a DNA biosensor based on ZrO_2 thin film [8]. They electrodeposited ZrO_2 NPs onto Au electrode and immobilized ssDNA probe with phosphate groups after fabrication. The bioelectrode (ssDNA/ZrO_2/Au) was exposed to complementary ssDNA in solution. The DNA hybridization related to the target DNA concentration was observed in the range of 2.25×10^{-10}–2.25×10^{-8} mol L^{-1} with a detection limit of 1.0×10^{-10} mol l^{-1}. The thin film of ZrO_2 NPs of size 35 nm was electrochemically deposited onto gold (Au) surface and utilized to immobilize 21-mer ssDNA-specific to *Mycobacterium tuberculosis*. It was observed that the thin film of ZrO_2 NPs had limitation due to aggregation and cracking that can be overcome by modifying these NPs with the polymers or other materials to prepare a nanocomposite. Das et al. [57] fabricated a nanocomposite of ZrO_2 NPs with CHIT. It is a well-studied material consisting of the amino group which provides a hydrophilic

environment for further modification with desired biomolecules. This nanocomposite was used for immobilization of biotinylated probe DNA specific to *M. tuberculosis*, and results found target detection limit up to 0.00078 μM with a sensitivity of 6.38×10^{-6} A μM^{-1}. A membrane-based biosensor for detection of DNA hybridization was formed using ZrO_2 microparticles and self-doped polyaniline nanofibers (nanoSPAN, a copolymer of aniline, and m-aminobenzenesulfonic acid) [58]. In the immobilization matrix, high electron transfer property of nano SPAN, the affinity of ZrO_2 microparticles toward oxygen-containing groups, and high surface areas, both materials significantly improved the loading of ssDNA. Electrochemical biosensor successfully detected DNA in the linear range of 1.0×10^{-12} M–1.0×10^{-6} M with a detection limit of 3.4×10^{-13} M. Zuo et al. [59] constructed a polishable DNA biosensor based on ZrO_2 modified carbon paste electrode. They observed a high selectivity and sensitivity of biosensor hybridization detection ($\leq 2 \times 10^{-10}$ M complementary DNA detectable). The biosensor fabricated using simple techniques was highly reproducible with a quick polishing step. Zhang et al. [60] electrodeposited gold (NG) and ZrO_2 NPs on GCE, using cyclic voltammetry, to develop a novel architecture of electrochemical biosensor for the detection of DNA hybridization. Using affinity of binding of ZrO_2 NPs with phosphate groups, DNA probes (ssDNA) were attached to the ZrO_2/NG/GCE electrode. The hybridization of ssDNA with the complementary DNA (cDNA) was observed regarding cathodic peak current in the range of 1.0×10^{-10}–1.0×10^{-6} mol/L with a detection limit of 3.1×10^{-11}. One-step electrodeposition of nanocomposite CeO_2–ZrO_2 hollow spheres and CHIT were performed on Au electrode to construct electrochemical DNA biosensor [61]. The high electroactive area of cerium oxide (CeO_2)–ZrO_2 nanocomposite helped in enhancement of electron transfer rate, and using MB as an electrochemical indicator, CHIT–CeO_2–ZrO_2/Au biosensor achieved the detection of DNA hybridization over a wide range of 1.63×10^{-13} M–1.63×10^{-8} M with a detection limit of 1.0×10^{-13} M. Yang et al. [62] compared the biosensing behavior of two kinds of electrochemically reduced graphene oxide (ERGO) and ZrO_2 nanocomposites for DNA sensing, one-step electrodeposited ZrO_2–ERGO and the second step wise electrodeposited ZrO_2/ERGNO. They found that little globules nanostructured ZrO_2–ERGO/Au has large surface area and high sensitivity toward the detection of DNA hybridization in the range of 1.0×10^{-13}–1.0×10^{-7} mol L^{-1} limit of detection 1.21×10^{-14} mol L^{-1}.

11.5 Conclusions

The high affinity of nanostructured ZrO_2 toward phosphatic groups, high isoelectric point, chemical inertness, lack of toxicity, availability of oxygen groups, and its excellent biocompatibility makes it more suitable environment of the immobilization of antibody, DNA, and enzymes. Besides this high conductivity, stability, pH stability, and redox properties of ZrO_2 promoted its applications in the development

of electrochemical biosensing devices. Different morphologies of nanostructured ZrO_2 such as spherical-shaped NPs, nanorods, nanoflowers, and nanofibers have been synthesized and utilized in the fabrication of immunosensors, enzymatic and DNA biosensors. Out of the above morphologies, ZrO_2 NPs have been extensively used in biosensing applications. Synthesis of ZrO_2-based nanocomposite not only minimized the aggregation of NPs and cracking of thin films but also enhanced the electrochemical properties of material. The hybrid interface of ZrO_2 with CHIT, GO, RGO, CNTs, polymers, and other metal oxides provides a higher rate of charge transfer than the individual materials during electrochemical reactions. Further, functionalization of nanostructured ZrO_2 with amino acids enhanced its stability, immobilization of biomolecules, and electrochemical electron transfer rate constant. The new approaches and concepts of biosensing have opened the door to great applications of electrochemical devices in the area of biomedical sciences. Electrochemical biosensing devices are inexpensive, fast, simple, and easy to use and thus enormously convenient for providing the diagnostic information. Such properties of nanostructured ZrO_2 make it uniquely qualified for meeting the demands for the development of electrochemical biosensors for point-of-care diagnostics.

References

1. P.R. Solanki et al., Nanostructured metal oxide-based biosensors. NPG Asia Mater. **3**(1), 17–24 (2011)
2. P.K. Gupta, Z.H. Khan, P.R. Solanki, One-step electrodeposited porous ZnO thin film based immunosensor for detection of *Vibrio cholerae* toxin. J. Electrochem. Soc. **163**(7), B309–B318 (2016)
3. S. Pilathadka, D. Vahalová, T. Vosáhlo, The Zirconia: a new dental ceramic material. An overview. Prague Med. Rep. **108**(1), 5–12 (2007)
4. Y. Bagbi et al., Immunosensor based on nanocomposite of nanostructured zirconium oxide and gelatin-A. Int. J. Biol. Macromol. **82**, 480–487 (2016)
5. İ. Uslu et al., Synthesis and characterization of boron doped alumina stabilized zirconia fibers. Fibers Polym. **12**(3), 303–309 (2011)
6. G. Sumana et al., A novel urea biosensor based on zirconia. Thin Solid Films **519**(3), 1187–1191 (2010)
7. L. Liang et al., Annealing effect on the optical properties and laser-induced damage resistance of solgel-derived ZrO_2 films. JOSA B **24**(5), 1066–1074 (2007)
8. N. Zhu et al., Electrochemical detection of DNA hybridization using methylene blue and electro-deposited zirconia thin films on gold electrodes. Anal. Chim. Acta **510**(2), 163–168 (2004)
9. M. Bhagwat et al., Rietveld refinement study of nanocrystalline copper doped zirconia. Mater. Res. Bull. **38**(13), 1713–1724 (2003)
10. M. Aslam et al., Preparation, characterization and mechanistic features of zirconia films on bare and functionalized gold surfaces. J. Mater. Chem. **10**(7), 1737–1743 (2000)
11. I. Birkby, R. Stevens, Applications of Zirconia Ceramics. in *Key Engineering Materials* (Trans Tech Publication, 1996)
12. C. Piconi, G. Maccauro, Zirconia as a ceramic biomaterial. Biomaterials **20**(1), 1–25 (1999)

13. P.F. Manicone, P.R. Iommetti, L. Raffaelli, An overview of zirconia ceramics: basic properties and clinical applications. J. Dent. **35**(11), 819–826 (2007)
14. J. Gong et al., Facile synthesis of zirconia nanoparticles-decorated graphene hybrid nanosheets for an enzymeless methyl parathion sensor. Sens. Actuators B: Chem. **162**(1), 341–347 (2012)
15. S. Kumar, et al., Biofunctionalized nanostructured zirconia for biomedical application: a smart approach for oral cancer detection. Adv. Sci. **2**(8) (2015)
16. S. Kumar et al., Nanostructured zirconia decorated reduced graphene oxide based efficient biosensing platform for non-invasive oral cancer detection. Biosens. Bioelectron. **78**, 497–504 (2016)
17. L. Bai et al., Hydroxypropyl-β-cyclodextrin as a versatile additive for the formation of metastable tetragonal zirconia exhibiting high thermal stability. CrystEngComm **15**(11), 2076–2083 (2013)
18. F. Drymiotis et al., Monocrystal elastic constants of the negative-thermal-expansion compound zirconium tungstate (ZrW_2O_8). Phys. Rev. Lett. **93**(2), 025502 (2004)
19. S. Azad et al., Nanoscale effects on ion conductance of layer-by-layer structures of gadolinia-doped ceria and zirconia. Appl. Phys. Lett. **86**(13), 131906 (2005)
20. X. Guo, R. Waser, Electrical properties of the grain boundaries of oxygen ion conductors: acceptor-doped zirconia and ceria. Prog. Mater. Sci. **51**(2), 151–210 (2006)
21. P.G. Bruce, *Solid state electrochemistry*, vol. 5. (Cambridge University Press, 1997)
22. P. Li, I.W. Chen, J.E. Penner-Hahn, Effect of dopants on zirconia stabilization—an X-ray absorption study: I, trivalent dopants. J. Am. Ceram. Soc. **77**(1), 118–128 (1994)
23. M. Bocanegra-Bernal, S.D. De La Torre, Phase transitions in zirconium dioxide and related materials for high performance engineering ceramics. J. Mater. Sci. **37**(23), 4947–4971 (2002)
24. J.H. Lee et al., Electrical conductivity and defect structure of CeO_2-ZrO_2 mixed oxide. J. Mater. Sci. **37**(6), 1165–1171 (2002)
25. Q.F. Deng et al., High-surface-area $Ce_{0.8}Zr_{0.2}O_2$ solid solutions supported Ni catalysts for ammonia decomposition to hydrogen. Int. J. Hydrogen Energy **37**(21), 15901–15907 (2012)
26. D. Ragurajan, M. Satgunam, M. Golieskardi, The role of magnesium oxide on the mechanical properties of y-tzp ceramic (2014)
27. J. Park, *Bioceramics: Properties, Characterizations, and Applications*, vol. 741 (Springer Science & Business Media, 2009)
28. M. Sekar et al., Zirconia as a bioceramic material. Indian J. Restor. Dentist. **3**(1), 1–7 (2014)
29. H. Chen, C. Ding, Nanostructured zirconia coating prepared by atmospheric plasma spraying. Surf. Coat. Technol. **150**(1), 31–36 (2002)
30. B. Batra et al., Construction of an amperometric bilirubin biosensor based on covalent immobilization of bilirubin oxidase onto zirconia coated silica nanoparticles/chitosan hybrid film. Biosens. Bioelectron. **44**, 64–69 (2013)
31. X.L. Liu et al., Solvothermal synthesis and characterization of ZrO_2 nanostructures using zirconium precursor. Mater. Lett. **64**(14), 1591–1594 (2010)
32. F. Woudenberg et al., Nanostructured dense ZrO_2 thin films from nanoparticles obtained by emulsion precipitation. J. Am. Ceram. Soc. **87**(8), 1430–1435 (2004)
33. O. Vasylkiv, Y. Sakka, Synthesis and colloidal processing of zirconia nanopowder. J. Am. Ceram. Soc. **84**(11), 2489–2494 (2001)
34. R. Dwivedi et al., Microwave assisted sol–gel synthesis of tetragonal zirconia nanoparticles. J. Alloy. Compd. **509**(24), 6848–6851 (2011)
35. N. Gan, L. Jia, L. Zheng, A sandwich electrochemical immunosensor using magnetic DNA nanoprobes for carcinoembryonic antigen. Int. J. Mol. Sci. **12**(11), 7410–7423 (2011)
36. H. Huang et al., Ultrafast thermal plasma physical vapor deposition of yttria-stabilized zirconia for novel thermal barrier coatings. J. Therm. Spray Technol. **15**(1), 83–91 (2006)
37. P. Peshev et al., Spray pyrolysis deposition of nanostructured zirconia thin films. Mater. Sci. Eng.: B **97**(1), 106–110 (2003)

38. J. Lian et al., Ion beam-induced amorphous-to-tetragonal phase transformation and grain growth of nanocrystalline zirconia. Nanotechnology **20**(24), 245303 (2009)
39. Y. Ma et al., Direct electron transfer of hemoglobin in a biocompatible electrochemical system based on zirconium dioxide nanotubes and ionic liquid. Bioelectrochemistry **84**, 6–10 (2012)
40. P. Kaushik et al., Sol-gel derived nanostructured zirconia for cholesterol detection. J. Nanosci. Lett. **3**, 23 (2013)
41. C.Â.M. Volpato, et al., *Application of Zirconia in Dentistry: Biological, Mechanical and Optical Considerations* (INTECH Open Access Publisher, 2011)
42. Y. Wang et al., A novel electrochemical sensor based on zirconia/ordered macroporous polyaniline for ultrasensitive detection of pesticides. Analyst **140**(2), 560–566 (2015)
43. G. Liu et al., Nanoparticle-based electrochemical immunosensor for the detection of phosphorylated acetylcholinesterase: an exposure biomarker of organophosphate pesticides and nerve agents. Chem. A Eur. J. **14**(32), 9951–9959 (2008)
44. S. Kumar et al., A biocompatible serine functionalized nanostructured zirconia based biosensing platform for non-invasive oral cancer detection. RSC Adv. **6**(80), 77037–77046 (2016)
45. P.R. Solanki et al., Sol–gel derived nanostructured metal oxide platform for bacterial detection. Electroanalysis **23**(11), 2699–2708 (2011)
46. Z. Pan et al., Amperometric immunosensor for determination of clenbuterol based on enzyme-antibody coimmobilized ZrO_2 nano probes as signal tag. Chin. J. Anal. Chem. **41**(6), 828–834 (2013)
47. S.K. Shukla et al., Zirconia-poly (propylene imine) dendrimer nanocomposite based electrochemical urea biosensor. Enzym. Microb. Technol. **66**, 48–55 (2014)
48. S. Pundir et al., Amperometric choline biosensor based on multiwalled carbon nanotubes/zirconium oxide nanoparticles electrodeposited on glassy carbon electrode. Anal. Biochem. **427**(1), 26–32 (2012)
49. Y. Yang et al., Amperometric glucose biosensor based on a surface treated nanoporous ZrO_2/Chitosan composite film as immobilization matrix. Anal. Chim. Acta **525**(2), 213–220 (2004)
50. L.M. Liu et al., A mediator-free glucose biosensor based on glucose oxidase/chitosan/α-zirconium phosphate ternary biocomposite. Anal. Biochem. **445**, 24–29 (2014)
51. J. Xu, C. Liu, Y. Teng, Direct electrochemistry and electrocatalysis of hydrogen peroxide using hemoglobin immobilized in hollow zirconium dioxide spheres and sodium alginate films. Microchim. Acta **169**(1–2), 181–186 (2010)
52. J. Wang et al., Using flowerlike polymer–copper nanostructure composite and novel organic–inorganic hybrid material to construct an amperometric biosensor for hydrogen peroxide. Colloids Surf.: B **75**(2), 425–431 (2010)
53. J. Yang, X. Wang, H. Shi, An electrochemical DNA biosensor for highly sensitive detection of phosphinothricin acetyltransferase gene sequence based on polyaniline-(mesoporous nanozirconia)/poly-tyrosine film. Sens. Actuators B: Chem. **162**(1), 178–183 (2012)
54. S. Srivastava et al., Mediator-free microfluidics biosensor based on titania–zirconia nanocomposite for urea detection. RSC Adv. **3**(1), 228–235 (2013)
55. P.R. Solanki et al., Nanostructured zirconium oxide based genosensor for *Escherichia coli* detection. Electrochem. Commun. **11**(12), 2272–2277 (2009)
56. B. Liu, J. Hu, J.S. Foord, Electrochemical detection of DNA hybridization by a zirconia modified diamond electrode. Electrochem. Commun. **19**, 46–49 (2012)
57. M. Das, G. Sumana, B. Malhotra, Zirconia based nucleic acid sensor for *Mycobacterium tuberculosis* detection. Appl. Phys. Lett. **96**(13), 133703 (2010)
58. T. Yang et al., Synergistic membrane of ZrO_2/self-doped polyaniline nanofibres fabricated by controllable electrodeposition for DNA hybridization detection. J. Electroanal. Chem. **656**(1), 140–146 (2011)
59. S.H. Zuo et al., Electrochemical detection of DNA hybridization by using a zirconia modified renewable carbon paste electrode. Bioelectrochemistry **74**(2), 223–226 (2009)

60. W. Zhang et al., DNA hybridization and phosphinothricin acetyltransferase gene sequence detection based on zirconia/nanogold film modified electrode. Appl. Surf. Sci. **254**(15), 4750–4756 (2008)
61. Q. Wang et al., Electrochemical characterization and DNA sensing application of a sphere-like CeO_2–ZrO_2 and chitosan nanocomposite formed on a gold electrode by one-step electrodeposition. Electrochim. Acta **62**, 250–255 (2012)
62. T. Yang et al., Comparative studies on zirconia and graphene composites obtained by one-step and stepwise electrodeposition for deoxyribonucleic acid sensing. Anal. Chim. Acta **786**, 29–33 (2013)